Science

SPECIAL ISSUE

Cancer Immunology and Immunotherapy

CONTENTS

41 & 128

How cells dampen gene noise

11, 22, & 49

36

CONTENTS

40 & 102
A look at what keeps engines running smoothly

3 APRIL 2015 • VOLUME 348 • ISSUE 6230

ON THE COVER

Cancer immunotherapy harnesses the power of the immune system to kill tumors. These therapies aim to activate and expand T cells, such as those shown in blue, to specifically kill tumors (black). Current approaches include antibodies targeting inhibitory proteins on T cells, adoptive T cell therapy, and tumor vaccines, among others. See page 54.
Illustration: Valerie Altounian/Science

Published by AAAS

Science

1200 New York Avenue, NW, Washington, DC 20005
Bateman House, 82-88 Hills Road, Cambridge, UK CB2 1LQ

AAAS

Science serves as a forum for discussion of important issues related to the advancement of science by publishing material on which a consensus has been reached as well as including the presentation of minority of conflicting points of view. Accordingly, all articles published in *Science*—including editorials, news and comment, and books reviews—are signed and reflect the individual views of the authors and not official points of view adopted by AAAS or the institutions with which the authors are affiliated.

INFORMATION FOR AUTHORS See pages 678 and 679 of the 6 February 2015 issue or access www.sciencemag.org/about/authors

Published by AAAS

A community for disaster science

During disasters such as the 2010 Deepwater Horizon oil spill, engaging the expertise of the academic community helped responders make critical decisions. A major barrier to such engagement, however, is the cultural gap between academia's reward system and that which prevails in the disaster response community. Given the importance of developing smart approaches to disasters, whether natural or human-caused, we need to bridge this gap.

Responders are often focused on ending an emergency quickly, with minimal damage. Academics are driven to understand the basic science of these events first, as a basis for proposed actions. Each community is used to speaking to different audiences and delivering answers on their own time scales. But these differences should not discourage attempts to connect these communities.

One approach is to foster a cohesive community of interdisciplinary disaster scientists: researchers who focus on crises that severely disrupt the environment or threaten human health, and can apply scientific methods in a timely manner to understand how to prevent, mitigate, respond to, or recover from such events. Disaster scientists could come from a range of disciplines: environmental science, human health, toxic chemistry, geophysics, ecology, atmospheric science, oceanography, and the social sciences. A disaster science community could develop its own unique culture. It is well known in the disaster response community that the preparation that takes place in the years, months, and days before an event ever occurs is what truly makes the difference in reducing response time, improving coordination, and ultimately reducing impacts. In the same vein, disaster scientists would benefit from consistently interacting with the response community. The worst time to be exchanging business cards is during a crisis. Trust takes time to establish. Researchers could learn to liaise with federally authorized responders (such as the U.S. Coast Guard), police, firefighters, and others responding to oil spills, forest fires, earthquakes, hurricanes, and other emergencies. Researchers would develop ties with relevant industries (oil companies, utilities, insurance companies, etc.) and help all sides identify vulnerabilities, increase resilience, and better coordinate the scientific response. Together, responders and affected industries could create funds to support prioritized research.

The advantage of building a community for all disasters, rather than for just one type, is that researchers maintain momentum between emergencies, which may be decades or more apart for any one class. Every disaster poses similar challenges: knowing when to speak to the press and what to say; how to develop "no regrets" actions; how to communicate with decision-makers and the public; how to keep proprietary industry information confidential; how to get rapid, actionable peer review of relevant analyses and proposed actions.

So how can such a community be fostered? Scientific societies could create focus groups and thematic sessions. The American Geophysical Union's existing Focus Group on Natural Hazards could be broadened to include disaster science. Universities could create interdisciplinary centers to pull together the relevant disciplines. The Science Partnerships Enabling Rapid Response project at the Center for Ocean Solutions is currently proposing structures and mechanisms that will enable ongoing community building and rapid information exchange between federal responders and disaster scientists.*

As U.S. Geological Survey director during the Deepwater Horizon spill, I worked with many researchers who cared not whether they got a peer-reviewed publication out of their efforts; they felt it their duty to respond to the limits of their ability. I worked with first responders who craved good scientific information for making decisions. But that might not always be the case. By creating a community for disaster science, we can encourage and better reward such selfless service.

– **Marcia McNutt**
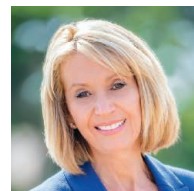
Marcia McNutt
Editor-in-Chief
Science *Journals*

> *"The worst time to be exchanging business cards is during a crisis."*

PHOTO: (TOP RIGHT) STACEY PENTLAND PHOTOGRAPHY; (INSET) JOEL SARTORE/GETTY IMAGES

NEWS

IN BRIEF

'Little Foot's' big footprint

From his beautifully preserved head (shown) to his fairly small feet, "Little Foot"—an australopithecine and cousin to the famous "Lucy"—is the most complete hominin skeleton ever found. Now, a new study in *Nature* this week supports the idea that Little Foot may also be old enough to be an ancestor of the more than 3-million-year-old human line. Since the fossil was discovered in South Africa's Sterkfontein Caves in the early 1990s, most of its anatomy remains unpublished, and researchers have argued bitterly about its age (*Science*, 21 March 2014, p. 1294). The skeleton can't be dated directly—it's too old for radiocarbon—and it is confusingly sandwiched between a younger limestone and older rock that is closer to the time when the cave formed. Depending on what is dated, age estimates range from 2.2 million years to more than 3 million years old. The team behind the new study thinks the older rock corresponds most closely to the fossil's age; they used aluminum-beryllium to date that rock and concluded that Little Foot died 3.67 million years ago. But some skeptics argue that the research team still might be dating the wrong rocks. http://scim.ag/littlefootage

AROUND THE WORLD

Error led to vessel's sinking

TAIPEI | The 10 October sinking of Taiwan's *Ocean Researcher V* resulted from human error, Wen-chung Chi, director-general of the country's Maritime and Port Bureau, told local press last week. A day into a cruise to study atmospheric pollution, *Ocean Researcher V*, in service under the Taiwan Ocean Research Institute (TORI) in Kaohsiung, headed back to port because of bad weather. The ship drifted off course, struck two submerged reefs, and sank near the Penghu Islands 260 kilometers southwest of Taipei. The accident claimed the lives of two researchers and rendered the research ship a total loss. Chi said that a review of the ship's voyage data recorder and other evidence indicated that the crew should have been alerted that the ship had drifted off course. TORI will have a similar ship built as replacement, says the institute's director, Hui-Ling Lin. http://scim.ag/Taiwansinking

U.S. tackles antibiotic resistance

WASHINGTON, D.C. | The White House last week announced a 5-year action plan to respond to the continued rise in drug-resistant bacteria. The plan describes steps that will be taken across several government agencies to prevent the misuse of existing antibiotics, track the appearance and spread of dangerous pathogens, and encourage the development of new drugs. It would establish stewardship programs at acute care hospitals and a network of regional labs to detect resistant strains. Although some urged the White House to take more aggressive action to ban the use of antibiotics in livestock, many praised the new plan as an ambitious first step. "This is the most serious proposal on this issue from any U.S. president, ever," says Boston University health law professor Kevin Outterson.

Scientists' media contact curbed

LONDON | Government scientists in the United Kingdom must now get permission from agency ministers before speaking to the media, according to a recent change in the Civil Service Code for public workers. Advocates for science communication last week expressed "deep concern" about the change. "We believe this will have a negative impact on the public understanding of science and the quality of the public discourse on some of the most important and contentious issues of our times," wrote

the Science Media Centre in London, the Association of British Science Writers, and Stempra, a network of science public relations workers. Similar restrictions on media contact in Canada have led to long delays in granting interviews with scientists and the omission of Canadian research from media stories. http://scim.ag/UKmediarest

Mexico submits climate plan

MEXICO CITY | Mexico will cut its greenhouse gas emissions 22% by the year 2030, the country pledged to the United Nations on 27 March. It is the first developing country to submit its climate action plan in advance of the Paris summit in December, where world leaders hope to hammer out a global climate change accord. Mexico now contributes 1.4% of global greenhouse gas emissions. "As a developing country, we want to participate," said Roberto Dondisch Glowinski, who represents Mexico in the U.N. climate talks, in an interview with the website ClimateWire. "Believe me, these numbers are not going to be easy for us, but we are committed."

New plan for asteroid mission

WASHINGTON, D.C. | Rather than bag up an entire asteroid, NASA has decided to pluck a boulder off an asteroid's surface and bring it back to the vicinity of Earth, officials in charge of the Asteroid Redirect Mission (ARM) announced last week. The $1.25 billion mission, to launch in December 2020, would send a robotic spacecraft to rendezvous with an asteroid in 2022. The spacecraft will first collect a boulder several meters across from the asteroid; it will then orbit the asteroid for up to 400 days to test out an idea for defending Earth from an asteroid impact: using the spacecraft's own gravitational field to subtly alter the asteroid's orbit. The spacecraft would then bring the snatched rock back in 2025. But some scientists are skeptical about the mission, due to concerns that its costs could eat into science mission funding. ARM has also drawn skepticism from Congress, which will decide whether to fund it. http://scim.ag/bouldersnatch

NEWSMAKERS

NIAID head treats Ebola patients

Anthony Fauci is head of the National Institute of Allergy and Infectious Diseases, part of the National Institutes of Health (NIH) in Bethesda, Maryland.
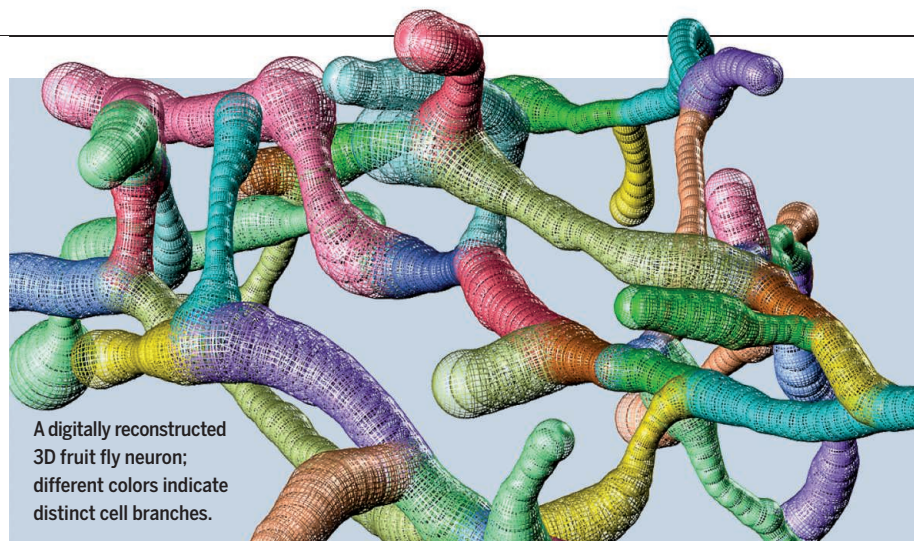
A digitally reconstructed 3D fruit fly neuron; different colors indicate distinct cell branches.

A gallery of brain cells

Got 3D microscopic images of neurons from a bee brain? How about brain cells from fruit fly larvae, mice—or people? BigNeuron wants your data. Whether a neuron branches like a chandelier or spreads like a pyramid, a brain cell's shape is one of the most important clues about its function, says project leader Hanchuan Peng, a neuroscientist at the Allen Institute for Brain Science in Seattle, Washington. However, different labs use incompatible methods to digitally reconstruct neurons, making their data hard to share, Peng says. BigNeuron, announced 31 March, will collect images of neurons from labs worldwide, then host hackathons to put the data in an online, public platform. Free, easy access to a vast library of brain cell types will help researchers better understand how information flows between neurons, Peng says: After all, the brain's complex connectivity, which produces all thoughts and behavior, "doesn't just come out of the air."

He wields a $4.4 billion research budget and has a punishing schedule. But in recent weeks, Fauci, 74, has reserved 2 hours on most days to put on a protective plastic suit and help treat a U.S. health care worker (who has not been identified) who became infected with Ebola in Sierra Leone. "I do believe that one gets unique insights into disease when you actually physically interact with patients," says Fauci, who also helped treat Dallas nurse Nina Pham last October during her stay at NIH's Clinical Center. He adds he also wanted to show his staff that he wouldn't ask them to do anything he wouldn't do himself. http://scim.ag/FauciEbola

FINDINGS

Tiny warbler crosses big ocean

A boreal songbird that fits in the palm of your hand still piles on enough fat to fly from Canada to the Caribbean islands. Some ornithologists suspected that the blackpoll warbler common in North America's subarctic evergreen forests takes a direct route over the Atlantic Ocean to South America for the winter. But because a blackpoll weighs just 12 grams, slightly more than a U.S. half dollar, others doubted the bird could make it that far. To find out, two teams of scientists put dime-sized devices that record daylight and time on 20 blackpolls preparing to travel south. Postjourney, the team retrieved five of the tags—which showed that blackpolls do fly about 2500 kilometers over water, stopping off in the Caribbean en route to Venezuela, the teams report in a joint paper this week in *Biology Letters*.

Tagged blackpoll warbler

Some doctors argue that mitochondria may help infertile couples produce embryos by in vitro fertilization.

REPRODUCTIVE MEDICINE

Eggs' power plants energize new IVF debate

Firm adding energy-generating mitochondria to egg cells has already produced human pregnancies

By **Jennifer Couzin-Frankel**

Derived from bacteria, mitochondria are our cells' energy-producing powerhouses. Now, a Massachusetts company is convinced that these microscopic cylinders are also key to conceiving a baby, and it has persuaded several groups of physicians outside the United States to test that controversial premise in women with fertility problems. More than 10 women are pregnant via the firm's proprietary in vitro fertilization (IVF) method, which adds a bolus of a woman's own mitochondria to her mature egg.

Meanwhile, the U.S. Food and Drug Administration (FDA) has erected roadblocks in front of a fertility specialist and a stem cell biologist who want to clinically test the mitochondrial hypothesis in the United States. The duo would like to harness a different IVF strategy: swapping out a woman's mitochondria by transferring chromosomes from her egg into an egg from another woman. The technique, called mitochondrial replacement therapy (MRT), was just legalized in the United Kingdom to prevent rare genetic diseases (*Science*, 6 February, p. 590). But even before that, the two researchers applied for permission to use it in women who are struggling to conceive. FDA said it needs far more data before allowing the work to proceed.

A central question for both IVF strategies is whether faulty or aging mitochondria actually drive infertility, and whether correcting that problem restores eggs to health. OvaScience, the Cambridge-based biotech firm, says the results it presented at a meeting in San Francisco last week answer that. In one small cohort of women with fertility issues, the company achieved a pregnancy rate of 35%. "We are so excited," says Michelle Dipp, OvaScience's CEO.

That enthusiasm is far from universal. John Eppig, a reproductive biologist at Jackson Laboratory in Bar Harbor, Maine, says he is "highly troubled" that the company has already made the leap to human pregnancies. No published animal studies with a control group have been done to test whether this approach can improve fertility—let alone whether it is safe for offspring, Eppig says. "What are the consequences" of adding mitochondria to an egg cell? he asks. "We really don't know."

MRT, the technique legalized in the United Kingdom, is in some respects even more of a lightning rod, because the resulting baby, with mitochondrial DNA from a donor and the rest of its DNA from mom and dad, would have three genetic parents (see diagram, p. 15). The United Kingdom approved MRT in February, but not for infertility: It's permitted only to prevent babies from inheriting potentially fatal mutations harbored in their mother's mitochondria. (Most DNA is in the nucleus, but each mitochondrion also has some.) In the United States, there are no laws prohibiting MRT, but FDA hasn't given anyone a green light to try it. Last year, the agency asked the Institute of Medicine to weigh the pros and cons of MRT. The institute's second meeting was this week, and it's expected to issue a report in 2016.

FDA has flexed its muscles in this arena before. In 2001, it stopped physicians from squirting cytoplasm, which contains mitochondria, from a healthy woman's egg into the egg of a woman who had been unable to conceive. But before FDA stepped in, 17 babies were born, most healthy, but not all. Now teenagers, they are often cited as proof of mitochondria's value in fertility. "All we're doing is copying that exact same concept," Dipp says, albeit with a woman's own mitochondria. "Adding mitochondria improves IVF success rates."

Yet one of the physicians who led the cytoplasmic transfer effort nearly 20 years ago contends it's impossible to draw such a clean conclusion. This was "a pilot experiment, not a randomized study," says Jacques Cohen, a clinical embryologist at Reprogenetics, a company in Livingston, New Jersey. Cohen and his colleagues were certainly encouraged that several women who had failed many IVF cycles were able to have a baby. But, he points out, the numbers were small, there was no control group, and cytoplasm contains a lot of factors beyond mitochondria that could explain any success the method had.

Evidence that faulty mitochondria impede fertility remains preliminary, agrees Jennifer Kawwass, a reproductive endocrinologist at Emory University in Atlanta, who has studied the safety of IVF. More important, she says: "We also don't know the degree to which fixing it improves anything."

Stem cell biologist Ali Brivanlou of Rockefeller University in New York City, one of

the investigators who asked FDA to permit MRT in infertile woman, says human tests are the best way to resolve the issue. At this point, he adds, "one can make the argument that it is almost unethical not to provide care" to women who would welcome it. The pushback against MRT is emotional, not science-based, adds fertility specialist Norbert Gleicher of the Center for Human Reproduction six blocks away, who is working with Brivanlou and would treat any women involved. The technique has produced seemingly healthy offspring in monkeys. Furthermore, Gleicher notes, "we manipulate eggs and embryos in many other procedures."

FDA is wary, however. The agency wrote that MRT "has not been sufficiently established … to support a first-in-human study," according to communications provided by a lawyer assisting Gleicher and Brivanlou. FDA didn't completely shut the door, requesting additional lab studies of human eggs and animal studies to demonstrate safety and effectiveness. It also said that any clinical test of MRT would need stringent cell-processing guidelines, strict enrollment criteria, and, ideally, a control group. The agency recommended following babies into adulthood and tracking their own offspring, if possible. Brivanlou and Gleicher say that many of the demands are too costly for them or any fertility center. (FDA declined to speak with *Science* about the case.)

Dipp says OvaScience believes it doesn't need FDA's blessing to try its treatment, called Augment, in the United States, although the firm is in a "low-level ongoing dialogue" with the agency. It's already offering Augment in Canada, Turkey, and Dubai. Physicians isolate "immature" eggs from a small piece of tissue removed from the lin-

ing of a woman's ovaries. They extract mitochondria from the cells and deliver them to the IVF clinic, where they're injected, along with sperm, into a woman's mature eggs. The resulting embryo is transferred as usual.

"The Augment procedure shows real promise," said Robert Casper of the Toronto Centre for Advanced Reproductive Technology in Canada, during a conference call last week at which OvaScience discussed its results. Out of 26 women treated at Casper's clinic, 17 had embryo transfers. In nine, a pregnancy took hold. All of these women were 40 and under, all had failed between one and three IVF cycles, and they often had poor-quality eggs or embryos. "This population would probably have a pregnancy rate less than 10%" if they had simply had another cycle of conventional IVF, Casper said. At the San Francisco meeting, doctors from Turkey also reported one ongoing pregnancy with Augment.

But Glenn Schattman, a fertility specialist at Weill Cornell Medical College in New York City, says OvaScience's results are "not that impressive." Many of his patients have failed two IVF cycles at another clinic before they reach him, yet many get pregnant. Schattman considers a control group essential. Cohen agrees that OvaScience's technology warrants a randomized trial, though he acknowledges it's difficult to control all the variables in IVF, such as age.

But the company has no such plans. "The fertility [industry] just doesn't do trials," Dipp says. As for MRT, Gleicher is considering offering that option outside the United States. Kawwass notes that infertile couples themselves may demand it. "Once an intervention has any hope," she says, "they want the intervention." ∎

Can mitochondria overcome infertility?

OvaScience's IVF method (left) transfers mitochondria from immature to mature eggs. Another method (right) would transfer an infertile woman's DNA-containing nucleus into a donor egg, which has its own mitochondria.

Egg recharging

Immature egg
Mitochondrial transfer
Mature egg
Sperm
Embryo
Implantation

Swapping nucleus

Mother's egg
Donor egg
Nucleus transfer
Implantation
Embryo
Mother
Donor
Sperm

DIAGRAM: G. GRULLÓN/SCIENCE

A child-killing toxin emerges from shadows

Scientists link mystery deaths in India to consumption of lychees

By **Priyanka Pulla**, *in Bangalore, India*

Residents of Muzaffarpur have good reason to dread the arrival of summer. As the heat builds before the monsoon rains, hundreds of young children in this district in the north Indian state of Bihar come down with an illness that kills many victims and leaves others brain-damaged. Now, scientists believe they may have unmasked the mystery culprit: a toxin in the sweet red lychee fruit for which Bihar is known.

Investigators long suspected that something to do with lychee orchards was making the children sick. In Muzaffarpur, outbreaks peak in May and June, when the white-fleshed berry is harvested. But for years, they chased phantom causes.

Now, a trio of teams has zeroed in on the lychee itself. After a 2-year investigation, the U.S. Centers for Disease Control and Prevention (CDC) and the Indian National Centre for Disease Control (NCDC) suggest in the 30 January issue of *Morbidity and Mortality Weekly Report* that the illness results from crashing blood sugar levels, likely due to a lychee toxin known to cause hypoglycemia in rats. Two other groups finger the toxin in *Current Science* and in the May issue of *Emerging Infectious Diseases*.

The mechanism appears to explain similar illnesses in lychee-growing regions of Bangladesh and Vietnam. And it underscores the threat of similar toxins present in related fruits in West Africa and the Caribbean, as well as in a mushroom revealed a few years ago as the cause of unexplained sudden deaths in southwestern China's Yunnan province (*Science*, 16 March 2012, p. 1293). "We need to approach these disorders with a global understanding," says Peter Spencer, a neurotoxicologist at Oregon Health & Science University in Portland.

In Bihar, where the illness kills about 200 children a year, the hallmark symptoms are consistent: Children under the age of 15 are jolted awake in the middle of the night
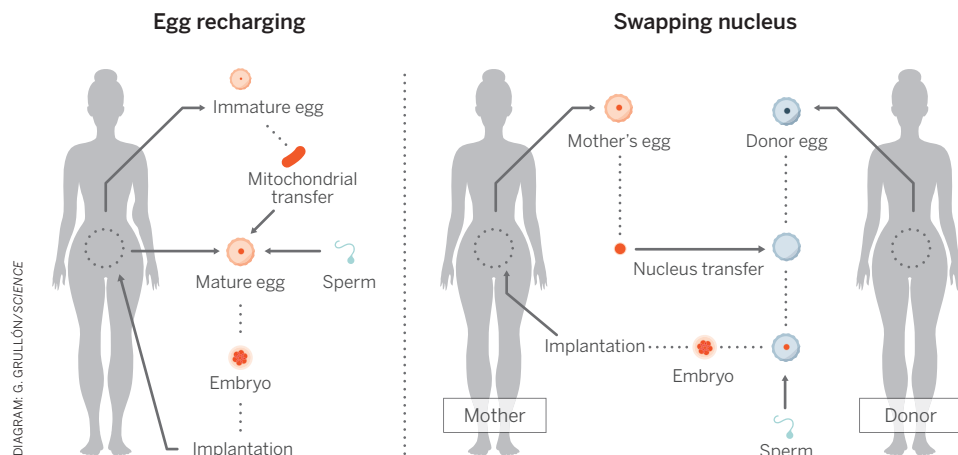
with seizures, mental confusion, and memory loss. A third or so become comatose and die. In Vietnam, where the disease is called Ac Mong, or "nightmare" encephalitis, victims tend to run high temperatures; many in India do not. Still, says Arnaud Fontanet, an epidemiologist at the Institut Pasteur in Paris who has studied the illness in Vietnam, "I am convinced that we are dealing with the same phenomenon."

Until now, Indian authorities were inclined to believe that the lychee illness was a form of viral encephalitis, a disease that causes brain inflammation. In 2013 and 2014, some 1.8 million children in Bihar were vaccinated against the Japanese encephalitis virus, transmitted by mosquitoes and endemic in the region. Fontanet's group, too, pointed to a viral cause in a 2012 paper in *Emerging Infectious Diseases*, in which they found high levels of cytokines and other signs of inflammation in the cerebrospinal fluid of patients in Vietnam. In 2012, a team at the International Centre for Diarrhoeal Disease Research, Bangladesh suggested another possible cause: a mix of pesticides sprayed on lychee trees.

Hoping to get to the bottom of the mystery, teams led by epidemiologists Aakash Shrivastava of NCDC and Padmini Srikantiah of CDC joined forces in 2013 to study 133 children admitted to Muzaffarpur's two main referral hospitals. They found no

Bihar state is known for prodigious production of lychees—and a malady linked to the fruit.

evidence of viruses or brain inflammation in those children or in another set of patients studied last summer. They did find that the children consistently had low blood glucose, with the lowest levels in the fatal cases.

Acting on the data, NCDC advised Muzaffarpur health officials in June 2013 to give patients intravenous dextrose to raise their blood sugar. As a result, Srikantiah says, the mortality rate in Bihar in 2014 was about 29% lower than in the previous year.

At about the time that NCDC and CDC flagged low blood sugar as a contributing factor, T. Jacob John, a retired virologist in Vellore, was drawing a bead on the likely culprit. John and Arun Shah, a pediatrician practicing in Muzaffarpur, had studied 26 children admitted to a Muzaffarpur hospital last June. They, too, found no signs of brain inflammation, but markedly low blood

glucose, which they treated with dextrose. Then John found a report on Jamaican vomiting sickness, an illness triggered by eating unripe ackee fruit, a Caribbean relative of the lychee. That malady is brought on by hypoglycin, an ackee toxin that is structurally similar to a compound in lychee seeds with a jaw-breaking name: methylenecyclopropylglycine (MCPG). John also uncovered a 1991 paper in which researchers had described a hypoglycemic illness in rats fed MCPG. "Nobody had looked at this data for 25 years," John says.

Last year, after the NCDC-CDC team's search for brain inflammation and viruses found nothing, the investigation's focus turned to MCPG. The toxin works by inhibiting fatty acid metabolism, which in turn blocks glucose production in cells. This could explain why children fall ill in the middle of the night, when blood glucose ebbs to its lowest levels. The team is now analyzing blood and urine samples from victims for MCPG metabolites; results are due this summer.

Although Fontanet is not ready to let some as-yet-unknown virus off the hook, he now plans to look for evidence that a lychee toxin may play a role in the illness in Vietnam. But Srikantiah says that puzzles remain. For instance, she asks, "Why do some children fall ill, while others don't?" One clue is that many victims who succumbed were malnourished: "the poorest of the poor, living in subhuman conditions," as Shah describes his patients. For an undernourished child with low glycogen and glucose stores, heavy consumption of any fruit in the soapberry family—ackees, lychees, rambutans, and longans—"probably has the potential to result in toxic hypoglycemic syndrome," Spencer and two colleagues write in *Emerging Infectious Diseases*.

Another question is just how the children ingest MCPG. The toxin is known to occur in the hard, inedible lychee seed. Srikantiah's team is now trying to ascertain whether it's also in the flesh of certain lychee varieties. That could help explain why the illness strikes some lychee-growing regions and not others. Spencer suggests that toxin levels may vary in lychees, as they do in ackee fruit, depending on factors such as cultivar, soil conditions, and ripeness.

NCDC is now looking for risk factors that would help it craft a government advisory on how to avoid contracting the illness. ∎

Bihar's grim harvest

In a familiar pattern, the number of patients admitted to two hospitals in Muzaffarpur, India, with unexplained acute neurologic illness crested in mid-June—at the height of the lychee harvest.

MARINE SCIENCE
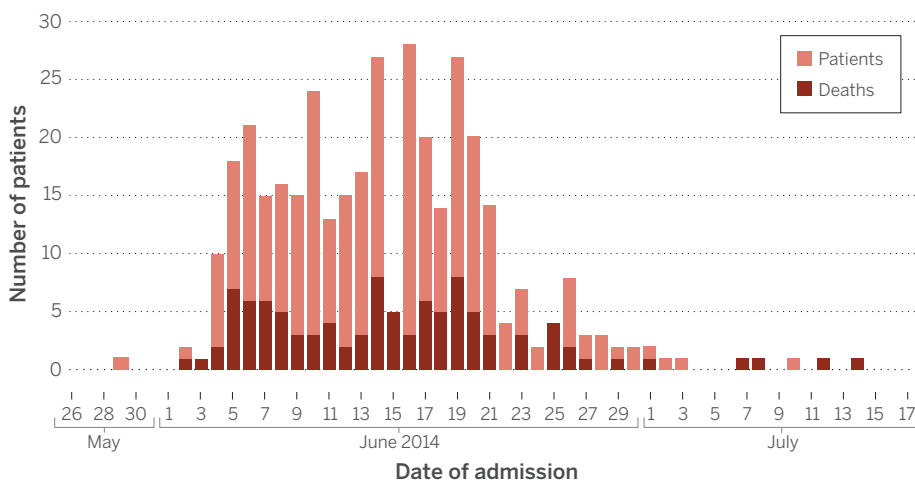
'The Blob' invades Pacific, flummoxing climate experts

Persistent mass of warm water is reshuffling ocean currents, marine ecosystems, and inland weather

By **Eli Kintisch**

Marine biologist Robert Pitman thought he'd seen it all after decades of conducting marine mammal surveys off the coast of southern California. But little prepared him for what he noticed off the bow of his team's research vessel this past October: a pod of pygmy killer whales, a tropical species typically found 2500 km to the south. "There was a moment of disbelief," recalls Pitman, who works at the National Oceanic and Atmospheric Administration's (NOAA's) Southwest Fisheries Science Center in San Diego, California.

It's aqua incognita these days for Pitman and other researchers studying the northeastern Pacific. Over the past 18 months, a gargantuan mass of unusually warm ocean water—dubbed The Blob—has hovered off North America's west coast, setting sea temperature records, scrambling weather and ecosystems, and threatening to disrupt fisheries worth billions of dollars. The Blob's freakish longevity has prompted researchers to redesign long-planned research cruises. And although scientists say global warming probably isn't a major cause of The Blob, others say it offers a preview of the disruptions that will accompany climate change.

The Blob, composed of water between 1°C and 4°C warmer than usual, has had three phases (see graphic, p. 18). Blob 1.0 appeared off Alaska's southern coast in fall 2013 and persisted for about 8 months. The mass of water—nearly 2000 km wide and 100 m deep—appears to have been main-

Tropical species, such as this pygmy killer whale, are appearing off California.

tained by a cyclical weather pattern that created a massive "ridge" of high atmospheric pressure that dominated the weather over western North America. The ridge deflected winds that usually stir up cold deep water and push cool water and air from high latitudes south along the Pacific coast.

Blob 2.0 appeared in the spring of 2014, after the high pressure dissipated, with patches of warm water spreading along the coast from Alaska to central Mexico. Tropical winds seemed to be a key driver, but physical oceanographers also noted unusually cool waters on the opposite side of the ocean, in the northwest Pacific. That pattern suggested the involvement of a major climate pattern known as the Pacific Decadal Oscillation, which can drive up temperatures in the eastern Pacific for periods of 4 to 20 years. Blob 3.0 appeared last month, as the warm pool split into two distinct patches, one off Washington state, the other off Baja California in Mexico. The reasons for the split aren't clear.

The Blob isn't just affecting the ocean. Inland, it has contributed to a number of unusual weather events in the Pacific Northwest, says Nick Bond, Washington state's climatologist, who is based in Seattle. In the summer of 2014, it likely contributed to unseasonably muggy conditions that produced high thunderstorm and lightning activity, including one July 2014 storm that sparked the biggest wildfire in the state's history. During that storm, Bond says, firefighters "couldn't keep up with the lightning strikes."

Researchers worry that The Blob is having an even bigger impact on marine eco-

PHOTO: JIM WATT/GETTY IMAGES

systems, reshuffling key food webs. For instance, it weakened currents that deliver nutrients from the subarctic to the mid-Pacific. There, the nutrients normally help fuel phytoplankton blooms in a feature known as the transition zone chlorophyll front, creating a lush feeding ground for marine life. But the front has moved 240 km farther north than usual, leaving relatively barren waters where species usually gather to feed.

Closer to shore, The Blob's warmer and therefore less dense surface water has formed a cap that, together with the changing winds, keeps cooler, more nutrient-rich waters from reaching the surface, says physical oceanographer Kris Holderied of NOAA's Kasitsna Bay Laboratory in Homer, Alaska. That means that surface-dwelling phytoplankton, a key food source for marine animals, may not be getting the nutrients they need to thrive. Already, scientists have documented an overall drop in populations of copepods, tiny crustaceans that graze on phytoplankton, off the Oregon coast. At the same time, they've seen an unprecedented jump in tiny sea creatures that normally live in the tropics—even in the Gulf of Alaska.

"It's fun to see some new animals I don't know," says Bill Peterson of NOAA's Northwest Fisheries Science Center in Seattle, who has rerouted some of his research cruises to study The Blob. But he and other researchers fear that the loss of phytoplankton, and the fact that some of the newly arrived plankton have relatively low nutritional value, could be contributing to a wave of die-offs further up the food chain. Some blame The Blob for deaths of thousands of seabirds called Cassin's auklets along the Pacific coast this past winter, as well as the starvation of thousands of sea lions along the California coast. "Evidence of hardship is mounting," says retired oceanographer Frank Whitney, who lives outside Victoria, Canada.

A growing concern is the fate of the multibillion-dollar Pacific salmon fishery. Juvenile salmon heading out to sea from their birth rivers "may have nothing to eat" if The Blob doesn't dissipate, Peterson says.

Several modeling teams are planning to convene early next year to share results of their Blob studies. A key question is whether the warming planet is responsible. Several recent papers have concluded it is not: The high-pressure ridge that birthed The Blob is a result of natural variability, researchers believe, not human-caused climate change. And the relatively modest climate-driven warming of the oceans seen so far probably isn't a major factor, adds James Overland, a NOAA climate scien-

tist at the Pacific Marine Environmental Laboratory in Seattle. "But you can't rule out a small global warming component to The Blob, or that in the future we won't see more phenomena like this," he says. Long-lasting atmospheric features, such as the persistent high-pressure ridge that spawned The Blob, may be more likely in the future, he says.

One thing is clear to oceanographer Russell Hopcroft of the University of Alaska, Fairbanks: The Blob provides a window into the kind of changes that could occur in the Pacific's warmer future. "What we're seeing now," he says, "is what we expected [to see] in a few decades." ∎

In hot water

Since appearing off the coast of Alaska (top), a pool of unusually warm surface waters has stretched south (middle) and then broken in two (bottom).

4 December 2013

29 October 2014

18 March 2015

Change in °C from base period, 1971–2000

−2 −1.5 −1 −0.5 0.5 1 1.5 2 2.5 3 3.5
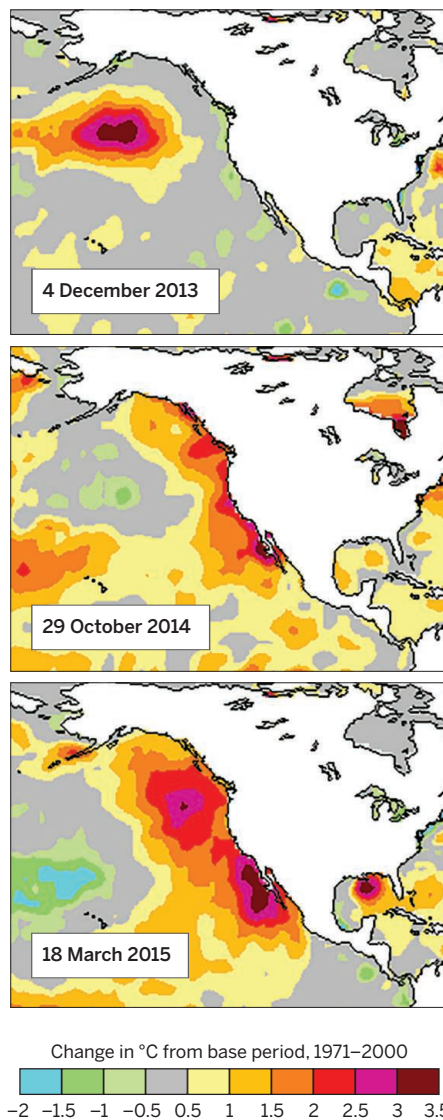
Hoax-detecting software spots fake papers

Springer jumps into sham submissions arms race

By **John Bohannon**

It all started as a prank in 2005. Three computer science Ph.D. students at the Massachusetts Institute of Technology—Jeremy Stribling, Max Krohn, and Dan Aguayo—created a program to generate nonsensical computer science research papers. The goal, says Stribling, now a software engineer in Palo Alto, California, was "to expose the lack of peer review at low-quality conferences that essentially scam researchers with publication and conference fees."

The program—dubbed SCIgen—soon found users across the globe, and before long its automatically generated creations were being accepted by scientific conferences and published in purportedly peer-reviewed journals. But SCIgen may have finally met its match. Last week, academic publisher Springer released SciDetect, a freely available program to automatically detect automatically generated papers.

SCIgen uses a "context-free grammar" to create word salad that looks like reasonable text from a distance but is easily spotted as nonsense by a human reader. For example:

> After years of compelling research into access points, we confirm the visualization of kernels. Amphibious approaches are particularly theoretical when it comes to the refinement of massive multiplayer online role-playing games.

SCIgen also generates impressive-looking but meaningless data plots, flow charts, and citations. SCIgen's first victim was the World Multi-Conference on Systemics, Cybernetics, and Informatics (WMSCI), a meeting that the trio suspected of not properly vetting submissions. Indeed, WMSCI accepted two of their nonsense papers.

The trio then put SCIgen online as a free service, encouraging researchers to "auto-generate submissions to conferences that you suspect might have very low submission standards." And submit they did. Over the past decade, researchers have pulled

MAPS: NOAA (3)

numerous pranks on journals and conferences that claim to use human peer reviewers. Variations on SCIgen have appeared for other fields, from mathematics to postmodern theory. (This author continued the tradition by using a different fake paper-generating method [*Science*, 4 October 2013, p. 60].)

The bad publicity for publishers mounted in 2013, when 85 SCIgen papers were found in the published proceedings of 24 different computer science conferences between 2008 and 2011. More were soon discovered, and 122 nonsense conference papers were ultimately retracted by Springer, the academic publishing giant based in Heidelberg, Germany, and by the Institute of Electrical and Electronic Engineers, based in New York City.

Rather than being created as pranks, many of the fake papers seemed to be coming from China, where they were "bought by academics and students" to pad their publication records, says the lead researcher behind the investigation, Cyril Labbé, a computer scientist at Joseph Fourier University in Grenoble, France. Later that year, an investigation by *Science* uncovered an underground market for fake academic credentials, in which some peddlers may have used SCIgen to save themselves the effort of writing "authentic" fake papers by hand (*Science*, 29 November 2013, p. 1035).

In the wake of that public relations nightmare, Springer approached Labbé for help. He agreed, for a price—enough to fund a 3-year Ph.D. student, Springer says. Labbé's method for finding the nonsense papers was sophisticated, requiring a statistical technique similar to spam e-mail detection, but based on grammatical patterns rather than on keywords like "Viagra."

The result is SciDetect, a program to automatically detect papers created with SCIgen and similar programs. Its purpose, according to Springer, is to "ensure that unfair methods and quick cheats do not go unnoticed."

But some think publishers may be more interested in avoiding embarrassment than in raising standards. "Anyone with a modicum of English language proficiency should be able to detect a paper written by SCIgen or similar software," says Philip Davis, an independent researcher who consults for the publishing industry. "To me, this appears to be a move by a publisher to protect itself against the unwillingness of journal editors to weed out these fraudulent papers themselves." Or as Paul Ginsparg, who founded arXiv, the physics preprint archive, puts it, "It's wonderful that Springer has moved to eliminate articles generated by software that intentionally produces nonsense, but what about unintentionally nonsensical articles produced by human authors?"

In an e-mail exchange with *Science*, the Springer representative wrote, "We agree with what Cyril Labbé says in his quote [in a 23 March press release]: 'Software cannot replace peer reviews and academic evaluation, but SciDetect lends publishers an additional hand in the fight against fraud and fake papers.' " She added that no SCIgen gibberish articles have been submitted to Springer conferences or journals since the 2013 retractions.

As for the pranksters, they will just have to work harder, says Stribling, the SCIgen creator. "I'm willing to bet if someone wanted to declare an arms race, they could come up with another way to generate papers that would fool [SciDetect] again for a while." ∎
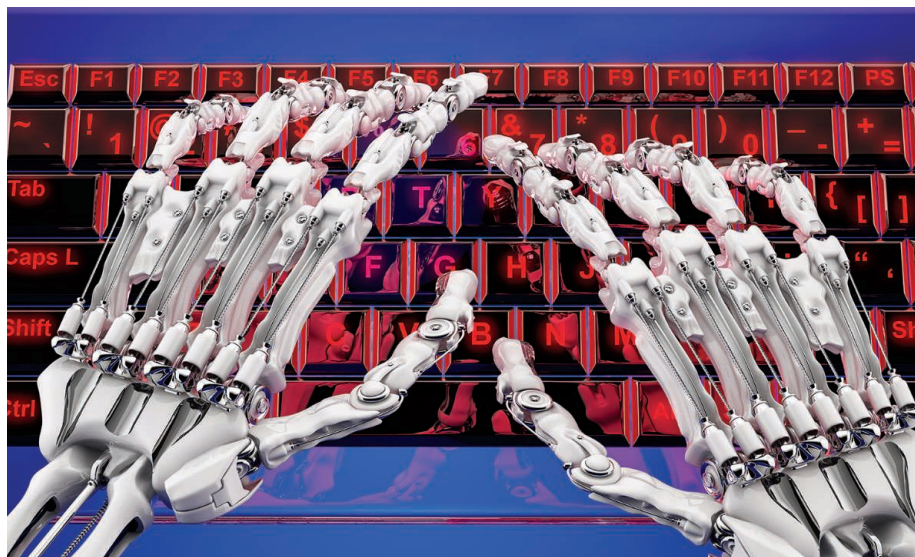
An automated paper-writing program has met its match in an automated detection system.

INFECTIOUS DISEASES

As Ebola wanes, trials jockey for patients

Researchers debate ending some trials to allow others to go forward

By **Kai Kupferschmidt**

For all the suffering it has caused, West Africa's Ebola epidemic could help save lives in the future by allowing scientists to test candidate drugs and vaccines. But recent successes in reining in the epidemic have created a problem for the international teams running clinical trials: Patients are becoming scarce. That creates moral and scientific quandaries—and even arguments between research teams competing for access to patients.

In its 25 March weekly report, the World Health Organization (WHO) reported only 79 new cases, down from more than 10 times that number during the height of the epidemic. Most are in shrinking areas around the capitals of Sierra Leone and Guinea; Liberia has had just one case in the past month. The slowdown is leading some to ask: Should trials of less promising treatments be terminated prematurely to make room for studies of the most promising drugs, which arrived on the scene later? "The window to conduct these trials is closing and we need to prioritize the drugs we think have the best chance of success," says Lisa Hensley, a microbiologist at the U.S. National Institutes of Health (NIH) in Frederick, Maryland.

Monkey studies have persuaded researchers that the most promising candidate treatments are an antibody cocktail called ZMapp, and TKM-Ebola, a drug based on a small RNA that blocks the expression of three of the virus's proteins. Neither was available in sufficient quantities last fall when researchers began designing the studies, so they launched trials of other, less auspicious therapies, including a Japanese influenza drug named favipiravir; serum and blood from recovered patients, which contain Ebola antibodies; and interferon, a drug that activates the immune system.

Now, the two favorites are readily available and trials are starting. On 11 March, University of Oxford researchers launched a study of TKM-Ebola in Sierra Leone; a study of ZMapp co-organized by NIH began in Liberia 2 weeks earlier. But the two are jostling for space with treatments already in testing—and with each other. (Vaccine trials are seeing similar rivalries [http://scim.ag/Ebolavactests].)

The teams testing less-promising treatments in Guinea aren't ready to pack their bags, however. And leaders of the TKM-Ebola trial are wary as well, as NIH contemplates expanding its ZMapp trial beyond Liberia, where the virus is almost gone. Testing ZMapp at sites where other studies are

A woman takes part in an Ebola vaccine trial in the Liberian capital Monrovia.

running would "jeopardize ongoing trials and lead to conflict," says Peter Horby, the lead investigator of the TKM-Ebola study.

Clifford Lane, who coordinates NIH's trial, says Sierra Leone's government will decide which treatment units should participate. But the ministries of health in Sierra Leone and Guinea did not respond to calls and e-mails to discuss the issue. All three countries are short on scientific, regulatory, and ethical expertise needed to make the important decisions, and the debates are held mostly between Western experts, many of them with a stake in the outcome. Nigerian virologist Oyewale Tomori says the rush to move in with studies last fall reminded him of the 1884 partition of Africa.

An expert panel at WHO regularly updates a list of the studies it regards as the most urgent, but it has no real powers. At its latest meeting, the group gave ZMapp and TKM-Ebola top priority but didn't recommend stopping other trials. "If you stop the trial then basically all the infrastructure comes down," says WHO's Martin Friede, who coordinates the panel's work. The committee did convince an Italian charity to end a trial with the heart drug amiodarone at its Ebola treatment unit in Sierra Leone, however, and instead work with the ZMapp trial. Doctors Without Borders' Armand Sprecher says the studies with convalescent blood and favipiravir have become questionable as well: "You can make a good argument to say: 'Stop these trials.' " Thomas Geisbert of the University of Texas Medical Branch in Galveston has the same view of the interferon trial. "That trial should never have happened," says Geisbert, who has tested many candidate drugs. "We showed years ago in primates that there is little or no effect in animals."

Aborting any trial to start another is problematic if it means that both end up without answers, says Trudie Lang of the University of Oxford in the United Kingdom. "If this happens, the patients who have received an experimental drug cannot contribute anything and their data and samples are wasted. This is highly unethical." And definitive negative results can be helpful, too, Friede says. If the interferon study—which the WHO panel accorded a low priority—is terminated without a clear outcome, for example, people may be tempted to try it again in the next outbreak.

Eleanor Fish, an immunologist at the University of Toronto in Canada, who helped set up the interferon study and began enrolling Guinean patients last week, agrees. She says the receptor for interferon β differs in humans and primates, and only a trial will show whether the drug is effective. In any case, she adds, there was little else available when the trial was designed. "The truth is it has just taken a heck of a long time to get this up and running," Fish says. "And now we are being hammered about how we can do this when there are other drugs available." ∎

PHOTO: AP PHOTO/ABBAS DULLEH

FEATURES

DEEPWATER HORIZON

AFTER THE OIL

Five years on, the world's largest accidental marine spill has left subtle scars on the Gulf of Mexico

By **Warren Cornwall**, in Barataria Bay, Louisiana

The scene of one of the nation's most dramatic environmental disasters is serene now. Waist-tall marsh grasses shiver in the wind, the tan and green carpet stretching to a hazy blue horizon. The quiet is broken only by small waves clapping a rhythm on the metal hull of a skiff, beached at the edge of the latte-colored Gulf of Mexico. At first glance, it's hard to see anything amiss.

But Linda Hooper-Bui kneels in a patch of grass, pulls up a clod of jet-black earth, and holds it to her nose. "Ooh, smell *that*, baby," exclaims the entomologist. A sniff delivers a swift kick reminiscent of motor oil.

Nearly 5 years after BP's *Deepwater Horizon* oil rig exploded on 20 April 2010, killing 11 workers and unleashing an 87-day undersea geyser of oil that spewed at least 518 million liters, the disaster's legacy is still evident here—if you dig. Barataria Bay, a pocket of islands, inlets, and bayous, endured some of the heaviest oiling, creating scenes of devastation replayed endlessly on screens around the globe. And the bay quickly became a magnet for researchers

PODCAST

To hear a podcast with author Warren Cornwall, see http://scim.ag/pod_6230.

like Hooper-Bui, who are seeking to understand the spill's impacts.

Today, the scientists are finding both damage and remarkable resilience. The oil has clearly left its mark on the ecosystem, affecting organisms small and large, from soil microbes to bottlenose dolphins. But nature has bounced back in surprising ways. Shrimp scavenge the sea floor. Brown pelicans wheel overhead. Barataria Bay hasn't gone to hell after *Deepwater*. But it's not the Garden of Eden, either.

The story, however, isn't over. After 5 years, researchers remain uncertain about whether this biological tapestry, frayed by oil, might still unravel in unexpected ways. And the concerns aren't just ecological: What the scientists learn could affect billions of dollars in environmental fines and the livelihoods of thousands of Gulf Coast families.

IN LATE MAY 2010, the oil barged into Barataria Bay like a drunken brawler, pouring through narrow gaps in nearby barrier islands, then lurching back and forth with the tides, currents, and winds. It left some areas untouched. Others, like the shoreline

Cleanup crews burn off oil from the *Deepwater* spill in June 2010.

of Bay Jimmy, were coated in muck ranging in consistency from peanut butter to mousse. Many of the disaster's most heart-rending images came from that area—pelicans staring out through a coating of brown goo, a dolphin surfacing in an oil slick, the carcass of an oil-bathed turtle. In the end, 675 kilometers of Louisiana marsh were oiled.

Scientists were soon on the scene, making the most of what amounted to the largest uncontrolled experiment of their lives. Hooper-Bui, for example, left her lab at Louisiana State University (LSU), Baton Rouge, to set up study plots in oiled and unoiled marsh, hoping to chart the fate of ants (her specialty) and other insects. The underlying question: What happens when you take a coastal marsh ecosystem and dunk it in oil?

Now she is back at the marsh to offer some answers—and to discuss some mys-

A chunk of the solidified oil from the *Deepwater* spill now provides shelter to small crabs.

teries that are still stumping scientists. Take the case of the shrunken ant heads. Hooper-Bui chooses a patch of dry grass and starts examining the stalks. Decked out in waders, a camouflage jacket, and a bright pink hood, she's a diminutive dynamo, peppering her scientific patter with exclamations and jokes. (At one point, she holds up an abandoned foam float used to mark crab traps: "What's this?" she asks. "A Bui with a buoy!")

Eventually, a colleague hands her what she is seeking: a stem with a single, tiny black and red ant scurrying along the outside. Hooper-Bui gently peels open the hollow stalk to reveal a swarm of acrobat ants, named for the way they point their abdomens in the air when pestered. The ants, which typically prey on other insects, live in the dry stems, in colonies 1 to 2 meters across.

In the years after the spill, the ants essentially disappeared from Hooper-Bui's oiled study sites. New colonies got started each spring but vanished by the end of summer. Measurements of the ants' bodies yielded a clue: Those in the oiled areas had smaller heads, a sure sign of malnourishment.

Hooper-Bui has documented a decline of other insects on oiled sites, and ex-

periments with caged katydids left in the marsh suggest the insects are killed by substances released by buried oil. In summer during low tides, the heat can crack the old oil caked on the marsh surface and let relatively fresh oil ooze up. The fumes might be killing insects that the ants like to eat, or keeping the ants from leaving their grass stems to look for food, something Hooper-Bui has observed in lab tests. "They'd rather starve to death when there's oil present," she says.

So, as the ants swarm onto her hand in early 2015, Hooper-Bui is thrilled. "This is the first time we've seen the ants start to come back and stay [in an oiled area]. … It's very exciting." The finding fits with signs of an uptick Hooper-Bui started seeing last year. In places hit by the spill, ant colonies had climbed back to 10% of normal, and other insect numbers were higher, too. "We're cautiously saying that there might be recovery," she says.

THE INSECTS ARE AMONG the clearest examples that the spill is still an ecological force. But there are others. At the marsh's edge, clumps of marsh grass hang in midair over the water, their pale roots suspended where the soil below has washed away.

Marsh erosion was one of the biggest threats to the bay even before the spill. Channels dug by the oil industry have chopped up the marsh, exposing more of it to erosion and killing vegetation by altering water flow patterns. Flood control projects along the Mississippi River starve the bay of fresh sediment from upstream. But soon after the spill, scientists watched erosion go into overdrive. It doubled in some areas, one study found, because oil killed the vegetation that held marsh muck in place. Over the next year and a half, as vegetation grew back on the remaining dirt, erosion rates subsided.

However, the oil may continue to boost erosion by weakening plant roots or by altering bacteria populations deep in the soil, according to a separate study. Oil acts like a fertilizer, fueling a boom in carbon-eating microbes that feast on the petroleum. Those same bacteria can eat away at the layer of rich organic matter that helps bind the marsh together, says Eugene Turner, a colleague of Hooper-Bui's at LSU and a leading expert on the decline of Louisiana's

A web of impacts

Louisiana's Barataria Bay was one of the places hardest hit by the *Deepwater Horizon* spill. Five years later, researchers are still studying its impact. Among their findings so far:

1. Oil-eating bacteria increased; may have helped accelerate marsh erosion

2. Acrobat ants (*Crematogaster pilosa*) disappeared from oiled sites; may be recovering along with other insects

3. There are fewer snails (*Littoraria irrorata*) in oiled sites; some signs of recovery

4. Where oil killed plant roots, erosion increased; mixed evidence of recovery

5. Seaside sparrows (*Ammodramus maritimus*) build fewer nests and hatch fewer chicks in oiled areas; no clear population impact

6. Blue crabs (*Callinectes sapidus*) have shown no signs of population decline; studies continue

7. Microflora and fauna, including algae and invertebrates, have mostly recovered; some populations remain low

8. Shrimp populations initially increased in oiled estuaries; not clear why

9. Larval oysters (*Crassostrea virginica*) may be more likely to survive and grow faster in unoiled areas

10. Oil may have killed thousands of brown pelicans (*Pelecanus occidenatlis*) Gulf-wide; no clear lasting impact

11. Bottlenose dolphins (*Tursiops truncatus*) are less healthy than Florida dolphins not affected by the spill

12. Gulf killifish (*Fundulus grandis*) show genetic evidence of exposure to toxic chemicals; no obvious population change

Thousands of brown pelicans may have died after the oil hit (*above*), but populations along the Gulf Coast appear to be healthy today (*top*).

wetlands. Turner found that erosion in some oiled areas started accelerating several years after the spill and that it appears tied to the weakening of this deep layer. He estimates the spill has led to the loss of up to 5 square kilometers of coastal wetlands in Louisiana.

Witnessed firsthand, the pace of erosion in Barataria Bay—whatever the cause—is startling. Five years ago, researchers placed plastic poles along the marsh's shoreline, to mark places hit by oil. Today, the poles stand 20 meters offshore, surrounded by water.

PAST THE POLES, out in the open water, live some of the oil's more photogenic victims: Barataria Bay's bottlenose dolphins. Roughly 1800 of the mammals live in the bay, feasting on fish and shrimp. In 2011, a checkup of 29 dolphins found serious problems associated with oil toxicity: nearly a third had moderate to severe lung disease, many suffered from suppressed hormone levels, and a quarter were severely underweight. Overall, it was a much worse report card than for similar dolphins in Florida, untouched by the spill.

New research suggests a link between the oil and a rash of dolphin deaths. An unusual cluster of at least 128 strandings occurred in the bay between August 2010

and the end of 2011. It's part of a Gulf-wide pattern that started shortly before the spill and continues today, adding up to more than 1250 deaths. Some of the strandings happened prior to the spill, researchers say. But a February study in *PLOS ONE* by government and private scientists identified a surge of strandings exactly where the spill hit hardest, in Barataria and coastal areas of Mississippi and Alabama.

"The cumulative evidence to date supports that the *Deepwater Horizon* oil spill is a causal factor for poor dolphin health and increased mortality," says Lori Schwacke of the National Oceanic and Atmospheric Administration in Charleston, South Carolina, who is helping lead

that agency's investigation of how the spill affected dolphins.

The blowout also left a big, but largely unseen, stain on the bottom of the Gulf. Oil sank to the sea floor over more than 3200 square kilometers—an area roughly the size of Rhode Island—according to one study. Near the wellhead, scientists found patches of coral apparently killed or damaged by the oil. As much as 17 kilometers from the center of the spill, the pollution seems to have upended the structure of seafloor communities of small creatures such as worms, tiny crustaceans, snails, and clams, reducing their diversity.

OTHER PARTS of Barataria Bay's ecosystem have proved startlingly resilient. Brown pelicans were a poster child of the oil spill's horrors, for instance, but there's no sign the population as a whole has fallen. Shrimp numbers in the bay actually rose the year after the spill. Researchers don't know if that was because state officials barred fishing for a time, or because the oil somehow caused shrimp to grow more slowly and linger in shallow water, boosting the counts. The bay's seaside sparrows, which nest in grasses, had fewer and less productive nests in oiled areas, accord-

Critics question plans to spray dispersant in future deep spills

By **Warren Cornwall**

In the early weeks of the 2010 *Deepwater Horizon* oil spill, as the ruptured wellhead spewed plumes of oil, desperate engineers took a gamble on a tactic they had never tried before. They rigged a hose to inject a toxic dispersant, normally used to break up surface oil slicks, into the hot, gas-rich petroleum jetting from the sea floor 1500 meters below the Gulf of Mexico's surface. They hoped the dispersant, which chemically acts like a soap, would break up much of the oil into a fine undersea mist, preventing it from bubbling up to the surface and smothering shorelines.

Today, many observers consider the move a remarkable success and say that it helped blunt the spill's impacts on coastal ecosystems (see main story, p. 22). As a result, U.S. and international agencies are starting to write the use of deep-sea dispersant into plans for handling future spills. The oil industry is designing special dispersant hardware for wellheads.

But a few scientists question whether pumping 2.9 million liters of the chemicals into the deep sea really did much good (and whether it may actually have harmed sea life). If a similar spill occurred today, "I would definitely say not to use the [deep-sea] dispersant," says Claire Paris, an oceanographer at the University of Miami in Florida and one of the researchers raising concerns. In February, she co-authored a paper online in *Chemical Engineering Science* that concluded the dispersant reduced the amount of floating oil by just 1% to 3%.

The debate centers on a seemingly simple question: How big were the droplets of oil that billowed, like ash clouds from a volcano, from the busted wellhead? If they were relatively large—more than 100 to 300 microns, depending on who you ask—they would have been buoyant, and the dispersant could have helped stop their swift rise by breaking them up. Smaller droplets, however, can become suspended in the water like fog and may never surface, meaning dispersant may not make much difference.

Paris and her research partner, chemical engineer Zachary Aman, used one of the world's toughest blenders to try to solve the puzzle. The mixer, housed at Aman's lab at the University of Western Australia, Crawley, is the size of a champagne glass, made of industrial sapphire strong enough to contain pressures 120 times greater than that found at Earth's surface—roughly the same as 1200 meters beneath the ocean surface. After oil impregnated with natural gas is mixed with salt water, stainless steel blades spin at up to 2000 revolutions per minute, generating turbulence that shreds the oil into drops. A high-speed camera captures the action.

In blender experiments, the researchers found that the pressure and turbulence at the *Deepwater* wellhead would have created droplets so small—80 microns in diameter on average—that many wouldn't reach the surface. That suggests "you may not get a huge benefit from the dispersant," Aman says.

Skeptics argue that Aman is committing a crucial error by likening the forces created by a spinning blender to the turbulence created at a gushing pipe, which acts more like the nozzle of a fire hose. Aman's findings also run counter to other studies that find bigger droplets, critics note. "We think they definitely made a mistake, and this is a hot-button policy question," says Scott Socolofsky, an engineer at Texas A&M University, College Station.

Labs around the world are now trying to find a more definitive answer. In the United States, Canada, and Germany, groups are preparing to run tests that better approximate deep-sea drilling conditions. Aman himself is fine-tuning computer models that he believes will create a more realistic picture of the forces at play near the wellhead.

But given the difficulty of mimicking the conditions at an undersea blowout, it's not clear that "if we have this conversation in 2 years that we're going to be any better off," says Steve Lehmann, a senior science adviser at the National Oceanic and Atmospheric Administration in Lowell, Massachusetts, who deals with spill response. And that, he says, "is a concern" for officials who will have to decide whether deep-sea dispersant should be de rigueur. ∎

Researchers use this high-pressure chamber to study how oil behaves under conditions like those at the *Deepwater* wellhead.

A gusher of money for research and restoration

The 2010 *Deepwater Horizon* disaster produced more than a plume of oil. It has also created a gusher of money from the responsible parties, BP and Transocean. The cash includes donations, economic damage payments to Gulf residents and businesses, and civil and criminal penalties. Ultimately, a substantial fraction will go to environmental restoration and research in the five Gulf Coast states affected by the spill. The full sum isn't clear, because BP is still liable for up to $13.7 billion in pollution fines in a case before a federal judge and potentially billions more to repair environmental damage that is being assessed.

$5.4
billion so far
with billions
more to come

ENVIRONMENTAL RESTORATION
$4.4+ billion

$2.554 billion
in criminal fines to the National Fish and Wildlife Foundation for environmental restoration in Gulf watershed

$750 million
in Clean Water Act civil fines for restoration in five Gulf states; **additional $8 billion possible**

$1 billion
to address natural resource damage; more possible

$100 million
in migratory bird fines to the North American Wetlands Conservation Fund for protection of habitat

RESEARCH
$1+ billion

$500 million
BP donation to create 10-year Gulf of Mexico Research Initiative, to study spill impacts and mitigation techniques

$500 million
in criminal fines to National Academies to create 30-year Gulf Research Program on understanding and reducing health and environmental risks from Gulf energy development

$40 million
in Clean Water Act civil fines to establish federal and state Gulf research centers; **up to $550 million** more possible

Other funds for natural resource damage assessment studies

ing to one study. Yet that doesn't appear to have translated into a drop in overall numbers in the region. In short, there's no sign the spill pushed the bay off some kind of ecological cliff.

Perhaps most puzzling is the state of the fish, which show clear signs of toxic exposure yet appear to be flourishing. In hard-hit waters, common minnows called Gulf killifish carried genetic markers associated with growth abnormalities, stress, gill damage, and heightened immune response for up to a year after the spill. Scientists have found no evidence, however, that these apparent physiological changes have caused fish numbers to drop in Louisiana's estuaries. They're left with unanswered questions. Has there really been no change? Is any change so subtle it hasn't been detected yet? Or is it too soon to know?

To Ed Overton, an LSU chemist who has spent years tracking the chemical changes in the *Deepwater* oil that washed ashore, the overall message is upbeat—even though he's found toxic chemicals in the oil that could persist in the bay for years. "I think the big story is, it's remarkable how Mother Nature can cure herself," he says. "It's really hard to find permanent impacts. Now folks down in the deep water might say 'Oh we had some impacts down there.' But those impacts were confined to a pretty small area."

Others aren't so sanguine.

Some point to the cautionary tale of the herring in Alaska's Prince William Sound. In 1993, 4 years after the *Exxon Valdez* ran aground in the sound and dumped 42 million liters of oil into the frigid waters, the herring population there crashed. It took another decade before several scientists concluded the fish's decline had actually started in 1989 and was likely tied to the spill.

The take-home message may be that "different components of the ecosystem have very different responses to oiling," says ecologist Brian Silliman of Duke University's Marine Lab in Beaufort, North Carolina, who specializes in saltwater marshes and studied erosion in Barataria Bay. "Some people say it's resilient and back to normal. But that's just one component of the ecosystem. When is it all back to normal?"

THAT ISN'T JUST a scientific question. At stake are billions of dollars, with repercussions in courtrooms, corporate boardrooms, and local businesses that rely on the Gulf.

Eventually—perhaps by 2016—BP and the other companies blamed for the spill are likely to be handed a very big bill for the environmental damage. They've already paid huge economic damage settlements and criminal and civil fines, with more to

come (see sidebar, p. 27). But another potentially huge bill is still being tallied by federal and state agencies. It involves completing what is known as the Natural Resource Damage Assessment (NRDA), and NRDA's final price tag will hinge on what scientists say the spill did to the environment and how long the damage lasted. (BP has already made a voluntary down payment of $1 billion for its NRDA bill.)

It's possible government scientists have already arrived at some answers that they aren't making public. Some research is being kept secret for now, because the NRDA findings could wind up in court. For example, the Louisiana Department of Wildlife and Fisheries declined to discuss whether it has seen changes in lucrative species such as

things cleaned up, and you're very much going to say things have come back, things look good," says Kyle Graham, executive director of Louisiana's Coastal Protection and Restoration Authority in Baton Rouge. "We're going to take probably a slower, more methodical approach to truly assessing what that injury looks like."

Amid the sniping, locals are sometimes left to draw their own conclusions about what exactly the oil spill did to the bay and whether it will recover.

Pete Vujnovich recently sat in the cramped cabin of his oyster boat, the *Miss Eva*, in a marina near the little town of Port Sulphur, chain-smoking Marlboro 100's and pondering the state of the Barataria Bay oyster fishery. As a third-generation oyster-

of oysters in the bay, some in places with oil, others in places that had dodged the spill, to see how mature oysters fared. They didn't find a difference. There were more intriguing findings when they put out blank ceramic and concrete tiles and watched how many baby oysters settled on them. In 2013, fewer settled on the oil-zone tiles. Those that did colonize the tiles grew more slowly in spots where, in addition to oil, they faced a second stressor: low water salinity. That suggests the spill might have compounded the effects of stressful conditions.

It's possible the spill will never yield some secrets. At Bay Jimmy, Hooper-Bui picks up a black, Frisbee-sized chunk of what looks like asphalt mixed with rubber.

Linda Hooper-Bui looks for signs of life on Cat Island in Barataria Bay.

oysters, shrimp, or blue crabs.

In the meantime, BP is mounting a publicity campaign declaring the Gulf is largely back to normal. Citing studies that found much of the oil has decomposed and few signs of a drop in wildlife numbers, in mid-March the company issued a lengthy report laying out its case. "[T]he most dire predictions made after the spill did not come to pass," said Laura Folse, BP's executive vice president for response and environmental restoration, in a statement. "The Gulf is showing strong signs of environmental recovery."

Those claims have drawn swift responses from Gulf state and federal officials working on the damage assessment. "If you're BP, you're absolutely making the case that you've taken care of things, you've gotten

man, he's come to understand the fickleness of his crop. Salinity, water temperature, and parasites all influence how many oysters he hauls off the mounds of rock and oyster shells dumped on the bottom of the bay to form artificial reefs. "We've had peaks and valleys of production," he says. But recent years have seen "one of the lowest lows."

After the spill, he bought rock and shell for replenishing some of his reefs with money from a compensation fund set up by BP. Those areas seem to be doing well. But older reefs are much less fertile than they were before, he says. Overall, he estimates his haul is still 20% below what it was before the spill. "That's the million-dollar question. Was it the oil?" he asks.

Scientists don't have an answer for him. In 2012 and 2013, researchers put cages

This slab of fossilized spill, several centimeters thick, is one of the most visible mementos of that long-stanched gusher of crude at the bottom of the Gulf. The ground along the marsh's edge here is paved with the stuff.

Yet marsh grass is growing through it. And as Hooper-Bui flips over the chunk of dried tar, she reveals two small brown crabs clinging to the underside. It's impossible to see what's going on in the crabs' tiny bodies—whether their cells bear damage caused by the oil that they call home, or whether they have found some way to survive, even thrive, in such intimacy with the *Deepwater Horizon*'s legacy. ∎

Warren Cornwall is a freelance writer in Bellingham, Washington.

DEEPWATER HORIZON

AFTER THE OIL

Five years on, the world's largest accidental marine spill has left subtle scars on the Gulf of Mexico

By **Warren Cornwall**, in Barataria Bay, Louisiana

The scene of one of the nation's most dramatic environmental disasters is serene now. Waist-tall marsh grasses shiver in the wind, the tan and green carpet stretching to a hazy blue horizon. The quiet is broken only by small waves clapping a rhythm on the metal hull of a skiff, beached at the edge of the latte-colored Gulf of Mexico. At first glance, it's hard to see anything amiss.

But Linda Hooper-Bui kneels in a patch of grass, pulls up a clod of jet-black earth, and holds it to her nose. "Ooh, smell *that*, baby," exclaims the entomologist. A sniff delivers a swift kick reminiscent of motor oil.

Nearly 5 years after BP's *Deepwater Horizon* oil rig exploded on 20 April 2010, killing 11 workers and unleashing an 87-day undersea geyser of oil that spewed at least 518 million liters, the disaster's legacy is still evident here—if you dig. Barataria Bay, a pocket of islands, inlets, and bayous, endured some of the heaviest oiling, creating scenes of devastation replayed endlessly on screens around the globe. And the bay quickly became a magnet for researchers

PODCAST

To hear a podcast with author Warren Cornwall, see http://scim.ag/pod_6230.

like Hooper-Bui, who are seeking to understand the spill's impacts.

Today, the scientists are finding both damage and remarkable resilience. The oil has clearly left its mark on the ecosystem, affecting organisms small and large, from soil microbes to bottlenose dolphins. But nature has bounced back in surprising ways. Shrimp scavenge the sea floor. Brown pelicans wheel overhead. Barataria Bay hasn't gone to hell after *Deepwater*. But it's not the Garden of Eden, either.

The story, however, isn't over. After 5 years, researchers remain uncertain about whether this biological tapestry, frayed by oil, might still unravel in unexpected ways. And the concerns aren't just ecological: What the scientists learn could affect billions of dollars in environmental fines and the livelihoods of thousands of Gulf Coast families.

IN LATE MAY 2010, the oil barged into Barataria Bay like a drunken brawler, pouring through narrow gaps in nearby barrier islands, then lurching back and forth with the tides, currents, and winds. It left some areas untouched. Others, like the shoreline

PHOTO: © JOEL SARTORE/NATIONAL GEOGRAPHIC CREATIVE/CORBIS

Cleanup crews burn off oil from the *Deepwater* spill in June 2010.

of Bay Jimmy, were coated in muck ranging in consistency from peanut butter to mousse. Many of the disaster's most heart-rending images came from that area—pelicans staring out through a coating of brown goo, a dolphin surfacing in an oil slick, the carcass of an oil-bathed turtle. In the end, 675 kilometers of Louisiana marsh were oiled.

Scientists were soon on the scene, making the most of what amounted to the largest uncontrolled experiment of their lives. Hooper-Bui, for example, left her lab at Louisiana State University (LSU), Baton Rouge, to set up study plots in oiled and unoiled marsh, hoping to chart the fate of ants (her specialty) and other insects. The underlying question: What happens when you take a coastal marsh ecosystem and dunk it in oil?

Now she is back at the marsh to offer some answers—and to discuss some mys-

A chunk of the solidified oil from the *Deepwater* spill now provides shelter to small crabs.

teries that are still stumping scientists. Take the case of the shrunken ant heads. Hooper-Bui chooses a patch of dry grass and starts examining the stalks. Decked out in waders, a camouflage jacket, and a bright pink hood, she's a diminutive dynamo, peppering her scientific patter with exclamations and jokes. (At one point, she holds up an abandoned foam float used

to mark crab traps: "What's this?" she asks. "A Bui with a buoy!")

Eventually, a colleague hands her what she is seeking: a stem with a single, tiny black and red ant scurrying along the outside. Hooper-Bui gently peels open the hollow stalk to reveal a swarm of acrobat ants, named for the way they point their abdomens in the air when pestered. The ants, which typically prey on other insects, live in the dry stems, in colonies 1 to 2 meters across.

In the years after the spill, the ants essentially disappeared from Hooper-Bui's oiled study sites. New colonies got started each spring but vanished by the end of summer. Measurements of the ants' bodies yielded a clue: Those in the oiled areas had smaller heads, a sure sign of malnourishment.

Hooper-Bui has documented a decline of other insects on oiled sites, and ex-

periments with caged katydids left in the marsh suggest the insects are killed by substances released by buried oil. In summer during low tides, the heat can crack the old oil caked on the marsh surface and let relatively fresh oil ooze up. The fumes might be killing insects that the ants like to eat, or keeping the ants from leaving their grass stems to look for food, something Hooper-Bui has observed in lab tests. "They'd rather starve to death when there's oil present," she says.

So, as the ants swarm onto her hand in early 2015, Hooper-Bui is thrilled. "This is the first time we've seen the ants start to come back and stay [in an oiled area]. … It's very exciting." The finding fits with signs of an uptick Hooper-Bui started seeing last year. In places hit by the spill, ant colonies had climbed back to 10% of normal, and other insect numbers were higher, too. "We're cautiously saying that there might be recovery," she says.

THE INSECTS ARE AMONG the clearest examples that the spill is still an ecological force. But there are others. At the marsh's edge, clumps of marsh grass hang in midair over the water, their pale roots suspended where the soil below has washed away.

Marsh erosion was one of the biggest threats to the bay even before the spill. Channels dug by the oil industry have chopped up the marsh, exposing more of it to erosion and killing vegetation by altering water flow patterns. Flood control projects along the Mississippi River starve the bay of fresh sediment from upstream. But soon after the spill, scientists watched erosion go into overdrive. It doubled in some areas, one study found, because oil killed the vegetation that held marsh muck in place. Over the next year and a half, as vegetation grew back on the remaining dirt, erosion rates subsided.

However, the oil may continue to boost erosion by weakening plant roots or by altering bacteria populations deep in the soil, according to a separate study. Oil acts like a fertilizer, fueling a boom in carbon-eating microbes that feast on the petroleum. Those same bacteria can eat away at the layer of rich organic matter that helps bind the marsh together, says Eugene Turner, a colleague of Hooper-Bui's at LSU and a leading expert on the decline of Louisiana's

A web of impacts

Louisiana's Barataria Bay was one of the places hardest hit by the *Deepwater Horizon* spill. Five years later, researchers are still studying its impact. Among their findings so far:

1. Oil-eating bacteria increased; may have helped accelerate marsh erosion

2. Acrobat ants (*Crematogaster pilosa*) disappeared from oiled sites; may be recovering along with other insects

3. There are fewer snails (*Littoraria irrorata*) in oiled sites; some signs of recovery

4. Where oil killed plant roots, erosion increased; mixed evidence of recovery

5. Seaside sparrows (*Ammodramus maritimus*) build fewer nests and hatch fewer chicks in oiled areas; no clear population impact

6. Blue crabs (*Callinectes sapidus*) have shown no signs of population decline; studies continue

7. Microflora and fauna, including algae and invertebrates, have mostly recovered; some populations remain low

8. Shrimp populations initially increased in oiled estuaries; not clear why

9. Larval oysters (*Crassostrea virginica*) may be more likely to survive and grow faster in unoiled areas

10. Oil may have killed thousands of brown pelicans (*Pelecanus occidenatlis*) Gulf-wide; no clear lasting impact

11. Bottlenose dolphins (*Tursiops truncatus*) are less healthy than Florida dolphins not affected by the spill

12. Gulf killifish (*Fundulus grandis*) show genetic evidence of exposure to toxic chemicals; no obvious population change

Thousands of brown pelicans may have died after the oil hit (*above*), but populations along the Gulf Coast appear to be healthy today (*top*).

wetlands. Turner found that erosion in some oiled areas started accelerating several years after the spill and that it appears tied to the weakening of this deep layer. He estimates the spill has led to the loss of up to 5 square kilometers of coastal wetlands in Louisiana.

Witnessed firsthand, the pace of erosion in Barataria Bay—whatever the cause—is startling. Five years ago, researchers placed plastic poles along the marsh's shoreline, to mark places hit by oil. Today, the poles stand 20 meters offshore, surrounded by water.

PAST THE POLES, out in the open water, live some of the oil's more photogenic victims: Barataria Bay's bottlenose dolphins. Roughly 1800 of the mammals live in the bay, feasting on fish and shrimp. In 2011, a checkup of 29 dolphins found serious problems associated with oil toxicity: nearly a third had moderate to severe lung disease, many suffered from suppressed hormone levels, and a quarter were severely underweight. Overall, it was a much worse report card than for similar dolphins in Florida, untouched by the spill.

New research suggests a link between the oil and a rash of dolphin deaths. An unusual cluster of at least 128 strandings occurred in the bay between August 2010 and the end of 2011. It's part of a Gulf-wide pattern that started shortly before the spill and continues today, adding up to more than 1250 deaths. Some of the strandings happened prior to the spill, researchers say. But a February study in *PLOS ONE* by government and private scientists identified a surge of strandings exactly where the spill hit hardest, in Barataria and coastal areas of Mississippi and Alabama.

"The cumulative evidence to date supports that the *Deepwater Horizon* oil spill is a causal factor for poor dolphin health and increased mortality," says Lori Schwacke of the National Oceanic and Atmospheric Administration in Charleston, South Carolina, who is helping lead

that agency's investigation of how the spill affected dolphins.

The blowout also left a big, but largely unseen, stain on the bottom of the Gulf. Oil sank to the sea floor over more than 3200 square kilometers—an area roughly the size of Rhode Island—according to one study. Near the wellhead, scientists found patches of coral apparently killed or damaged by the oil. As much as 17 kilometers from the center of the spill, the pollution seems to have upended the structure of seafloor communities of small creatures such as worms, tiny crustaceans, snails, and clams, reducing their diversity.

OTHER PARTS of Barataria Bay's ecosystem have proved startlingly resilient. Brown pelicans were a poster child of the oil spill's horrors, for instance, but there's no sign the population as a whole has fallen. Shrimp numbers in the bay actually rose the year after the spill. Researchers don't know if that was because state officials barred fishing for a time, or because the oil somehow caused shrimp to grow more slowly and linger in shallow water, boosting the counts. The bay's seaside sparrows, which nest in grasses, had fewer and less productive nests in oiled areas, accord-

Critics question plans to spray dispersant in future deep spills

By **Warren Cornwall**

In the early weeks of the 2010 *Deepwater Horizon* oil spill, as the ruptured wellhead spewed plumes of oil, desperate engineers took a gamble on a tactic they had never tried before. They rigged a hose to inject a toxic dispersant, normally used to break up surface oil slicks, into the hot, gas-rich petroleum jetting from the sea floor 1500 meters below the Gulf of Mexico's surface. They hoped the dispersant, which chemically acts like a soap, would break up much of the oil into a fine undersea mist, preventing it from bubbling up to the surface and smothering shorelines.

Today, many observers consider the move a remarkable success and say that it helped blunt the spill's impacts on coastal ecosystems (see main story, p. 22). As a result, U.S. and international agencies are starting to write the use of deep-sea dispersant into plans for handling future spills. The oil industry is designing special dispersant hardware for wellheads.

But a few scientists question whether pumping 2.9 million liters of the chemicals into the deep sea really did much good (and whether it may actually have harmed sea life). If a similar spill occurred today, "I would definitely say not to use the [deep-sea] dispersant," says Claire Paris, an oceanographer at the University of Miami in Florida and one of the researchers raising concerns. In February, she co-authored a paper online in *Chemical Engineering Science* that concluded the dispersant reduced the amount of floating oil by just 1% to 3%.

The debate centers on a seemingly simple question: How big were the droplets of oil that billowed, like ash clouds from a volcano, from the busted wellhead? If they were relatively large—more than 100 to 300 microns, depending on who you ask—they would have been buoyant, and the dispersant could have helped stop their swift rise by breaking them up. Smaller droplets, however, can become suspended in the water like fog and may never surface, meaning dispersant may not make much difference.

Paris and her research partner, chemical engineer Zachary Aman, used one of the world's toughest blenders to try to solve the puzzle. The mixer, housed at Aman's lab at the University of Western Australia, Crawley, is the size of a champagne glass, made of industrial sapphire strong enough to contain pressures 120 times greater than that found at Earth's surface—roughly the same as 1200 meters beneath the ocean surface. After oil impregnated with natural gas is mixed with salt water, stainless steel blades spin at up to 2000 revolutions per minute, generating turbulence that shreds the oil into drops. A high-speed camera captures the action.

In blender experiments, the researchers found that the pressure and turbulence at the *Deepwater* wellhead would have created droplets so small—80 microns in diameter on average—that many wouldn't reach the surface. That suggests "you may not get a huge benefit from the dispersant," Aman says.

Skeptics argue that Aman is committing a crucial error by likening the forces created by a spinning blender to the turbulence created at a gushing pipe, which acts more like the nozzle of a fire hose. Aman's findings also run counter to other studies that find bigger droplets, critics note. "We think they definitely made a mistake, and this is a hot-button policy question," says Scott Socolofsky, an engineer at Texas A&M University, College Station.

Labs around the world are now trying to find a more definitive answer. In the United States, Canada, and Germany, groups are preparing to run tests that better approximate deep-sea drilling conditions. Aman himself is fine-tuning computer models that he believes will create a more realistic picture of the forces at play near the wellhead.

But given the difficulty of mimicking the conditions at an undersea blowout, it's not clear that "if we have this conversation in 2 years that we're going to be any better off," says Steve Lehmann, a senior science adviser at the National Oceanic and Atmospheric Administration in Lowell, Massachusetts, who deals with spill response. And that, he says, "is a concern" for officials who will have to decide whether deep-sea dispersant should be de rigueur. ∎

Researchers use this high-pressure chamber to study how oil behaves under conditions like those at the *Deepwater* wellhead.

A gusher of money for research and restoration

The 2010 *Deepwater Horizon* disaster produced more than a plume of oil. It has also created a gusher of money from the responsible parties, BP and Transocean. The cash includes donations, economic damage payments to Gulf residents and businesses, and civil and criminal penalties. Ultimately, a substantial fraction will go to environmental restoration and research in the five Gulf Coast states affected by the spill. The full sum isn't clear, because BP is still liable for up to $13.7 billion in pollution fines in a case before a federal judge and potentially billions more to repair environmental damage that is being assessed.

$5.4
billion so far
with billions
more to come

ENVIRONMENTAL RESTORATION
$4.4+ billion

$2.554 billion
in criminal fines to the National Fish and Wildlife Foundation for environmental restoration in Gulf watershed

$750 million
in Clean Water Act civil fines for restoration in five Gulf states; **additional $8 billion possible**

$1 billion
to address natural resource damage; more possible

$100 million
in migratory bird fines to the North American Wetlands Conservation Fund for protection of habitat

RESEARCH
$1+ billion

$500 million
BP donation to create 10-year Gulf of Mexico Research Initiative, to study spill impacts and mitigation techniques

$500 million
in criminal fines to National Academies to create 30-year Gulf Research Program on understanding and reducing health and environmental risks from Gulf energy development

$40 million
in Clean Water Act civil fines to establish federal and state Gulf research centers; **up to $550 million** more possible

Other funds for natural resource damage assessment studies

ing to one study. Yet that doesn't appear to have translated into a drop in overall numbers in the region. In short, there's no sign the spill pushed the bay off some kind of ecological cliff.

Perhaps most puzzling is the state of the fish, which show clear signs of toxic exposure yet appear to be flourishing. In hard-hit waters, common minnows called Gulf killifish carried genetic markers associated with growth abnormalities, stress, gill damage, and heightened immune response for up to a year after the spill. Scientists have found no evidence, however, that these apparent physiological changes have caused fish numbers to drop in Louisiana's estuaries. They're left with unanswered questions. Has there really been no change? Is any change so subtle it hasn't been detected yet? Or is it too soon to know?

To Ed Overton, an LSU chemist who has spent years tracking the chemical changes in the *Deepwater* oil that washed ashore, the overall message is upbeat—even though he's found toxic chemicals in the oil that could persist in the bay for years. "I think the big story is, it's remarkable how Mother Nature can cure herself," he says. "It's really hard to find permanent impacts. Now folks down in the deep water might say 'Oh we had some impacts down there.' But those impacts were confined to a pretty small area."

Others aren't so sanguine.

Some point to the cautionary tale of the herring in Alaska's Prince William Sound. In 1993, 4 years after the *Exxon Valdez* ran aground in the sound and dumped 42 million liters of oil into the frigid waters, the herring population there crashed. It took another decade before several scientists concluded the fish's decline had actually started in 1989 and was likely tied to the spill.

The take-home message may be that "different components of the ecosystem have very different responses to oiling," says ecologist Brian Silliman of Duke University's Marine Lab in Beaufort, North Carolina, who specializes in saltwater marshes and studied erosion in Barataria Bay. "Some people say it's resilient and back to normal. But that's just one component of the ecosystem. When is it all back to normal?"

THAT ISN'T JUST a scientific question. At stake are billions of dollars, with repercussions in courtrooms, corporate boardrooms, and local businesses that rely on the Gulf.

Eventually—perhaps by 2016—BP and the other companies blamed for the spill are likely to be handed a very big bill for the environmental damage. They've already paid huge economic damage settlements and criminal and civil fines, with more to

come (see sidebar, p. 27). But another potentially huge bill is still being tallied by federal and state agencies. It involves completing what is known as the Natural Resource Damage Assessment (NRDA), and NRDA's final price tag will hinge on what scientists say the spill did to the environment and how long the damage lasted. (BP has already made a voluntary down payment of $1 billion for its NRDA bill.)

It's possible government scientists have already arrived at some answers that they aren't making public. Some research is being kept secret for now, because the NRDA findings could wind up in court. For example, the Louisiana Department of Wildlife and Fisheries declined to discuss whether it has seen changes in lucrative species such as

things cleaned up, and you're very much going to say things have come back, things look good," says Kyle Graham, executive director of Louisiana's Coastal Protection and Restoration Authority in Baton Rouge. "We're going to take probably a slower, more methodical approach to truly assessing what that injury looks like."

Amid the sniping, locals are sometimes left to draw their own conclusions about what exactly the oil spill did to the bay and whether it will recover.

Pete Vujnovich recently sat in the cramped cabin of his oyster boat, the *Miss Eva*, in a marina near the little town of Port Sulphur, chain-smoking Marlboro 100's and pondering the state of the Barataria Bay oyster fishery. As a third-generation oyster-

of oysters in the bay, some in places with oil, others in places that had dodged the spill, to see how mature oysters fared. They didn't find a difference. There were more intriguing findings when they put out blank ceramic and concrete tiles and watched how many baby oysters settled on them. In 2013, fewer settled on the oil-zone tiles. Those that did colonize the tiles grew more slowly in spots where, in addition to oil, they faced a second stressor: low water salinity. That suggests the spill might have compounded the effects of stressful conditions.

It's possible the spill will never yield some secrets. At Bay Jimmy, Hooper-Bui picks up a black, Frisbee-sized chunk of what looks like asphalt mixed with rubber.

Linda Hooper-Bui looks for signs of life on Cat Island in Barataria Bay.

PHOTO: © BRYAN TARNOWSKI

oysters, shrimp, or blue crabs.

In the meantime, BP is mounting a publicity campaign declaring the Gulf is largely back to normal. Citing studies that found much of the oil has decomposed and few signs of a drop in wildlife numbers, in mid-March the company issued a lengthy report laying out its case. "[T]he most dire predictions made after the spill did not come to pass," said Laura Folse, BP's executive vice president for response and environmental restoration, in a statement. "The Gulf is showing strong signs of environmental recovery."

Those claims have drawn swift responses from Gulf state and federal officials working on the damage assessment. "If you're BP, you're absolutely making the case that you've taken care of things, you've gotten

man, he's come to understand the fickleness of his crop. Salinity, water temperature, and parasites all influence how many oysters he hauls off the mounds of rock and oyster shells dumped on the bottom of the bay to form artificial reefs. "We've had peaks and valleys of production," he says. But recent years have seen "one of the lowest lows."

After the spill, he bought rock and shell for replenishing some of his reefs with money from a compensation fund set up by BP. Those areas seem to be doing well. But older reefs are much less fertile than they were before, he says. Overall, he estimates his haul is still 20% below what it was before the spill. "That's the million-dollar question. Was it the oil?" he asks.

Scientists don't have an answer for him. In 2012 and 2013, researchers put cages

This slab of fossilized spill, several centimeters thick, is one of the most visible mementos of that long-stanched gusher of crude at the bottom of the Gulf. The ground along the marsh's edge here is paved with the stuff.

Yet marsh grass is growing through it. And as Hooper-Bui flips over the chunk of dried tar, she reveals two small brown crabs clinging to the underside. It's impossible to see what's going on in the crabs' tiny bodies—whether their cells bear damage caused by the oil that they call home, or whether they have found some way to survive, even thrive, in such intimacy with the *Deepwater Horizon*'s legacy. ∎

Warren Cornwall is a freelance writer in Bellingham, Washington.

The human epoch *p. 38*

Fighting friction losses *p. 40*

NextGen's tools for the future

In January, we asked young scientists to name and describe a currently nonexistent invention that would make them more effective scientists. We heard from hundreds of scientists from dozens of countries. They described inventions that streamlined bench work, organization, communication, literature review, article writing, and idea generation. A sample of their

NEXTGEN VOICES responses can be found below.

To allow for as many voices as possible, in some cases we have printed excerpts of longer submissions (indicated by ellipses) and lightly copyedited original text for clarity. To read the complete versions, as well as many more, go to http://scim.ag/NG14R. Follow *Science*'s NextGen VOICES survey on Twitter with the hashtag #NextGenSci.

TEMPORARY HUMAN COPIER
Be in multiple places!

HAVE AN experiment and meeting scheduled at the same time? Tired of not being able to be in multiple places at once? Fear no more! With the Temporary Human Copier (THC), you will be able to be in multiple places at once. The patented THC will allow you to copy yourself, memories and all! No need to worry about THC taking over your life; it will self-destruct into a puff of smoke after a predetermined amount of time. Act now and we will include a wireless memory device that records everything your copy sees and hears!...

Matthew Kruger

School of Biological Sciences, Washington State University Vancouver, Vancouver, WA 98686, USA. E-mail: Matthew.kruger@email.wsu.edu

ILLUSTRATION: GWEN KERAVAL / WWW.GWENKERAVAL.COM; PHOTO COURTESY OF THE AUTHOR

COGNILYST
Increase your lab efficiency!

COGNILYST LOOKS like a slick pair of lab goggles but goes far beyond protecting your eyes. Cognilyst tracks your every lab movement and annotates your environment through a holographic display. Cognilyst learns your protocols, detects manual errors, and correlates protocol variations with your results. Cognilyst generates simplified labeling schemes and remembers where you store your samples. Multiple Cognilysts can work together, allowing exceptional tracking of reagent and supply use within labs and unprecedented ease of collaboration between labs. Cognilyst also tracks your focus through EEG, recommends rest, and provides electrical stimulation to enhance attention for those extended experiments.

Brendan J. Hussey

Department of Cell and Systems Biology, University of Toronto Mississauga, Mississauga, ON, L5L 1C6, Canada. E-mail: bjohnhussey@gmail.com

THE CALIBOT
Calibrate your instruments in seconds!

HAVING TROUBLE repeating an experiment from a paper or patent? Not sure you are using exactly the same instrument condition? Let CALIBOT help you. Simply select the publication you are following on CALIBOT. Then connect CALIBOT to the controller of your instrument. With a database containing instrument conditions from research labs all over the world, CALIBOT will calibrate your instrument to exactly the same conditions as the one used in the publication. Temperature distribution, mass flow, circuit signal delay, and many other parameters: CALIBOT covers them all....

Wei Wang

Fujian Institute of Research on the Structure of Matter, Chinese Academy of Sciences, Fuzhou, Fujian, 350108, China. E-mail: wangwei@fjirsm.ac.cn

DISSECT-O-MATIC
Dissect biological samples automatically!

INTRODUCING THE Dissect-O-Matic! Tired of endless hours with eyes scrunched and back hunched over a dissection microscope? Then this is the device for you! The newly designed Dissect-O-Matic is a fully automated system to dissect, block, stain, and mount biological samples for microscopy imaging. Simply select from menu options to specify species, tissue type, and staining method, and the Dissect-O-Matic will take it from there! This ergonomic instrument may even be interfaced to your microscope to fully automate the next stage of specimen imaging for a truly streamlined, carefree research experience!

Masha G. Savelieff

Life Sciences Institute, University of Michigan, Ann Arbor, MI 48109, USA. E-mail: savelief@umich.edu

CELL SUBMARINE
Look inside a living cell!

...BRING YOUR favorite cell a little closer with the first Cell Submarine. Aliquot one Cell Submarine into your cell culture dish. The Cell Submarine, equipped with a florescent-detecting camera, will begin beaming back images from inside the cell. This nanoscale sub can navigate through channels to seek out your favorite cell components. Cell Submarine can be directed using your phone as a remote.

Blair Roszell

Institute for Environmental Medicine, University of Pennsylvania, Philadelphia, PA 19104, USA. E-mail: blair.roszell@gmail.com

GROW ALREADY
Grow trees 100 times faster!

DOES PROGRESSING through your Ph.D. in ecology literally feel like watching trees grow? Are you envious of cellular biologists who grow their organisms in petri dishes in mere weeks? Measuring the response of long-lived organisms to treatment manipulations can take decades. Eliminate the long wait time by using our specially formulated Grow Already tea, guaranteed to grow trees up to 100 times faster! Use Grow Already to obtain experimental results quicker and graduate in an acceptable amount of time!

Mailea R. Miller-Pierce

School of Biological Sciences, Washington State University, Vancouver, Vancouver, WA 98686, USA. E-mail: m.miller-pierce@email.wsu.edu

MISAT
Preserve archaeological sites and samples!

ANCIENT GENETIC material is incredibly fragile. In an archaeological context, biological tissues are bombarded by exogenous DNA, and ultimately, human contamination. The Minimally-invasive Sample Acquisition Tool (MiSAT) combines core-drilling technology with a higher-resolution successor to modern ground-penetrating radar. Once you've identified a burial, MiSAT deploys a probe to extract a sample with almost surgical precision—all while preserving the stratigraphy of the site and limiting human contact before entering the lab.

Vincent M. Battista

Department of Molecular, Cellular, and Developmental Biology, Yale University, New Haven, CT 06520, USA. E-mail:vincent.battista@yale.edu

AUTOSYRINX DARTS
Collect blood from free-ranging animals!

FIELD WORKERS: Do you find yourself daydreaming about serum samples from your free-ranging study subjects? With the AutoSyrinx, your daydream just became a reality! Our patented rounds flip the function of dart guns on its head: Instead of putting a dart's contents into the animal's bloodstream, this device fills its lightweight barrel with a sample of the animal's blood! After extraction, which takes place nearly instantaneously, the dart ejects itself; the lightweight body of the round barely perturbs the animal being sampled.

Morgan E. Chaney

Department of Anthropology, Kent State University, Kent, OH 44242, USA. E-mail:mchaney1@kent.edu

FALSE POSITIVE DETECTOR
Detect spurious results!

SCIENTISTS traditionally accept a 5% chance that a statistically significant result is actually a false positive. That means 1 out of 20 findings is deceptively spurious, luring scientists down twisted paths lined with failures to replicate, wasted money, and lost time. Why take that 5% chance when the False

Positive Detector can make it 0%? Simply scan your data with the False Positive Detector, which reports back, "True result: Submit for publication" or "False positive: Back to the drawing board." For an extra $100 per month, access the False Positive File Drawer of unpublished null results, which will save you even more time!

Rosa Li

Department of Psychology and Neuroscience, Center for Cognitive Neuroscience, Duke University, Durham, NC 27708, USA. E-mail: rosa.li@duke.edu

CHEMBIO-IMPACTOMICS
Predict the biological impact of molecules!

MOST DRUG candidates fail in the approval process due to safety and/or efficacy issues. Chembioimpactomics offers you an experimentally and computationally verified database/platform for an economically productive, effective, and safe drug discovery program. Upload any designed structure/s into our platform and get a list of proteins and/or other macromolecules the designed molecule/s and resulting metabolites could inhibit or activate in the human system and/or in pathogenic organisms. The platform is derived from intensive experimental data involving macromolecules, drugs, synthetic libraries, natural products, and metabolites. It correlates molecular structures to their complete biological impact.

Idrees Mohammed

Department of Chemistry, New York University Abu Dhabi, Saadiyat Island, Abu Dhabi, United Arab Emirates. E-mail: dr.idreesmohammed@yahoo.com

PERFECTALIZER
Make physics equations valid!

ARE YOU TIRED of the equations of kinematics, thermodynamics, and statics being invalid? …The Perfectalizer…creates a perfect enviroment! All your ropes are massless, all your absorbers are perfect, all your emitters are perfect, all your pivots are frictionless, and you do not have to worry about air resistance! …"Perfect" is a subjective claim….The Perfectalizer has a very distinct look. Imagine God's face with

Darwin's beard, wrapped in a controversy and smothered with hard plastic.

Noel I. Robles

Yuma, AZ 85364, USA. E-mail: noelrobles177@gmail.com

TIME MACHINE
Improve your career prospects!

THIS PERSONAL, one-of-a-kind instrument allows you to instantly optimize experimental conditions and to perform experiments that always work the first time. As a result, your peers will be impressed by your ability to consistently generate and prove paradigm-shifting research hypotheses. This product also allows you to predict grant review panel and journal editor criticisms, preventing you from worrying about funding or struggling to publish. Limit of one Nobel Prize per user.

Michael G. Kemp

Department of Biochemistry and Biophysics, University of North Carolina, Chapel Hill, NC 27599, USA. E-mail: michael_kemp@med.unc.edu

EPIPHANY GENERATOR
Connect apparently unrelated concepts!

WHO'D HAVE thought that a light beam plus a falling elevator would lead to General Relativity? Or that magnetism plus a size-changing flask would lead to the Bose-Einstein condensate? Or that radar plus a metal container would lead to the microwave oven? The Epiphany Generator application throws concept words or pictures together, two at a time, on your screen! You make the connection. Doesn't make sense? Move on. Something new? Bingo! To survive academically, you must be creative and nonlinear. The Epiphany Generator can help.

Hemachander Subramanian

Integrated Mathematical Oncology Department, Moffitt Cancer Center, Tampa, FL 33612, USA. E-mail: hemachander@gmail.com

THE RISK METER
Measure a project's ethical repercussions!

WHEN CONDUCTING research, it is imperative that you remain cognizant of the potential ethical dilemmas that may arise as a consequence

of your discoveries. With this simple device, you can instantaneously gauge the risk level of unethical developments stemming from your work. Simply input your concept, and the Risk Meter assigns a numerical "risk number" to your current project! Armed with this knowledge, you can proceed forward with a more complete understanding of the potential of your research. The machine also serves as a gentle reminder for the ethics and obligations associated with scientific investigation.

Henry Zhou

Vagelos Scholars Program in the Molecular Life Sciences, University of Pennsylvania, Philadelphia, PA 19104, USA. E-mail: henryz@sas.upenn.edu

THE TOWER OF BABEL
Remove knowledge barriers!

INTERDISCIPLINARY research has led to some of the most exciting innovations in the human history, such as quantum computing and 3D bioprinting, but is often hindered by jargon, background knowledge requirements, and experts' inability to appreciate advances in other fields. The Tower of Babel software leverages artificial intelligence and big data analytics to mine research articles, patents, and textbooks in all fields; answer your queries pertaining to other domains in plain language; actively point out newly developed technologies potentially relevant to your studies; and update its databases automatically. This software will facilitate interdisciplinary research by removing the knowledge barriers across disciplines.

Kun-Hsing Yu

Biomedical Informatics Training Program, Stanford University, Stanford, CA 94305, USA. E-mail: khyu@stanford.edu

TRANSLATE IT! SCIENCE EDITION
Translate research for any audience!

HAVE YOU EVER faced blank stares at the dinner table when grandma asks you about your work? Have you spent countless hours on a presentation or grant application to target a multidisciplinary audience but still felt like they did not get it? Have you wished you had prepared your elevator speech when you ran into an unexpected investor? Then the Translate It! SCIENCE Edition software is

right for you! This software translates Word and PowerPoint files to accessible language with the click of a button, and its mobile application helps you share your research with all when you are on the go.

Karina R. Vega-Villa

Wenatchee Valley College, Wenatchee, WA 98801, USA. E-mail: vegavilla1@gmail.com
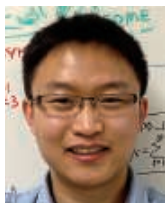
SLEEP PAPER READER
Read journal articles while sleeping!

OVERWHELMED BY papers? Having trouble keeping up with latest research? Are experiments taking too much time away from reading? No worries, Sleep Paper Reader (SPR) comes to the rescue! Simply wear the device while you sleep, and wake up with the latest publications all stuffed in your brain. You can even comment and share with friends in your dreams!...

Isaac T. S. Li

Center for the Physics of Living Cells, Department of Physics, University of Illinois at Urbana-Champaign, Urbana, IL 61801, USA. E-mail: isaac.li@gmail.com

QKNOWLEDGE
Keep up with current literature!

WE FIRMLY believe that scientists should spend less time diving into junk and more doing experiments...QKnowledge is an AI system that can parse publications, solve inconsistencies between them, and present them in a single easy-to-read document. Just power it on, connect it to the Internet and a printer, use your natural voice to tell it what you are looking for, and print the generated document.

Miguel Piñeiro Feick

Department of Neuroscience and Centro Interdisciplinario de Neurociencia de Valparaíso, Universidad de Valparaíso, Valparaíso, Chile. E-mail: miguel.pineiro@cinv.cl

WRI-ROBOT
Write your paper in hours!

...WRI-ROBOT will process your raw data results into figures and tables according to your vision through a simple interactive process. Wri-Robot will then use your key ideas, conclusions, and suggested references to generate a manuscript free of plagiarism and of original writing quality. Imagine your paper being ready for submission within hours of collecting the last experimental results. With the Wri-Robot, you will be a much more productive scientist, always ready to start the next project.

Islam M. Mosa

Department of Chemistry, University of Connecticut, Storrs, CT 06269, USA and Department of Chemistry, Faculty of Science, Tanta University, Tanta, Egypt. E-mail: islam.mosa@uconn.edu

SUBMIT NOW:
POSTDOCS REIMAGINED

Add your voice to *Science!* Our new NextGen VOICES survey is now open:

Is the idea of the postdoc position obsolete in today's scientific landscape? If so, what should replace it? If not, what one change would you make to improve it?

To submit, go to http://scim.ag/NG_15

Deadline for submissions is 15 May. A selection of the best responses will be published in the 3 July issue of *Science*. Submissions should be 200 words or less. Anonymous submissions will not be considered.

TURINGMAIL
Intelligently respond to every e-mail!

FED UP with beginning every e-mail reply with an apology for your slow response? Let TuringMail free you from this burden of guilt. TuringMail is the first automated, intelligent e-mail response service, fooling colleagues or students into believing you're an attentive collaborator or tutor. Every commitment TuringMail makes on your behalf will be carefully calibrated to ensure the most favorable cost/benefit ratio according to your diary and specified career priorities. To ensure TuringMail's deceptive ability, in addition to a monthly fee, users must answer one e-mail per week as a contribution to TuringMail's central knowledge base.

Rory Bingham

School of Geographical Sciences, University of Bristol, Bristol, BS8 1SS, UK. E-mail: rory.bingham@bristol.ac.uk

PEER-REVIEWER FILTER CRÈME
Filter out bad peer reviewers!

WORKED HARD FOR over a year on a paper? Feel like your reviewers are missing the point? Then purchase the new peer-reviewer filter crème today! Simply apply to your manuscript, rub in, and watch as your publication number goes up!...

Dan Hewitt

Lancaster Environment Centre, Lancaster University, Bangor, LL57 1AH, UK. E-mail: vulpesvulpes@live.co.uk

HOPE GENERATOR
Find hope when you have none!

DID YOU LOSE your way in your research? Haven't got any publishable results? This product is for you. The pocket size device generates hope to continue your meaningless research by creating artificial hope for you. By affecting your emotional state on a daily basis, it encourages you to carry on. Don't wait for the inspiration to come. It never will. Just keep calm and use the Hope Generator....

Emre Ozan Polat

Department of Electronics and Nanoscale Engineering, University of Glasgow, Glasgow, G128QQ, UK. E-mail: emreozan.polat@glasgow.ac.uk

BIOTECHNOLOGY

A prudent path forward for genomic engineering and germline gene modification

A framework for open discourse on the use of CRISPR-Cas9 technology to manipulate the human genome is urgently needed

By David Baltimore,[1] Paul Berg,[2]
Michael Botchan,[3,4] Dana Carroll,[5]
R. Alta Charo,[6] George Church,[7]
Jacob E. Corn,[4] George Q. Daley,[8,9]
Jennifer A. Doudna,[4,10*] Marsha Fenner,[4]
Henry T. Greely,[11] Martin Jinek,[12]
G. Steven Martin,[13] Edward Penhoet,[14]
Jennifer Puck,[15] Samuel H. Sternberg,[16]
Jonathan S. Weissman,[4,17]
Keith R. Yamamoto,[4,18]

POLICY

Genome engineering technology offers unparalleled potential for modifying human and nonhuman genomes. In humans, it holds the promise of curing genetic disease, while in other organisms it provides methods to reshape the biosphere for the benefit of the environment and human societies. However, with such enormous opportunities come unknown risks to human health and well-being. In January, a group of interested stakeholders met in Napa, California (1), to discuss the scientific, medical, legal, and ethical implications of these new prospects for genome biology. The goal was to initiate an informed discussion of the uses of genome engineering technology, and to identify those areas where action is essential to prepare for future developments. The meeting identified immediate steps to take toward ensuring that the application of genome engineering technology is performed safely and ethically.

The promise of so-called "precision medicine" is propelled in part by synergies between two powerful technologies: DNA sequencing and genome engineering. Advances in DNA sequencing capabilities and genome-wide association studies have provided critical information about the genetic changes that influence the development of disease. In the past, without the means to make specific and efficient modifications to a genome, the ability to act on this information was limited. However, this limitation has been upended by the rapid development and widespread adoption of a simple, inexpensive, and remarkably effective genome engineering method known as clustered regularly interspaced short palindromic repeats (CRISPR)–Cas9 (2). Building on predecessor platforms, a rapidly expanding family of CRISPR-Cas9–derived technologies is revolutionizing the fields of genetics and molecular biology as researchers employ these methods to change DNA sequences—by introducing or correcting genetic mutations—in a wide variety of cells and organisms.

CURRENT APPLICATIONS. The simplicity of the CRISPR-Cas9 system allows any researcher with knowledge of molecular biology to modify genomes, making feasible experiments that were previously difficult or impossible to conduct. For example, the CRISPR-Cas9 system enables introduction of DNA sequence changes that correct genetic defects in whole animals, such as replacing a mutated gene underlying liver-based metabolic disease in a mouse model (3). The technique also allows DNA sequence changes in pluripotent embryonic stem cells (4) that can then be cultured to produce specific tissues, such as cardiomyocytes or neurons (5). Such studies are laying the groundwork for refined approaches that could eventually treat human disease. CRISPR-Cas9 technology can also be used to replicate precisely the genetic basis for human diseases in model organisms, leading to unprecedented insights into previously enigmatic disorders.

In addition to facilitating changes in differentiated somatic cells of animals and plants, CRISPR-Cas9 technology, as well as other genome engineering methods, can be used to change the DNA in the nuclei of reproductive cells that transmit information from one generation to the next (an

organism's "germ line"). Thus, it is now possible to carry out genome modification in fertilized animal eggs or embryos, thereby altering the genetic makeup of every differentiated cell in an organism and so ensuring that the changes will be passed on to the organism's progeny. Humans are no exception—changes to the human germ line could be made using this simple and widely available technology.

MOVING FORWARD. Given these rapid developments, it would be wise to begin a discussion that bridges the research community, relevant industries, medical centers, regulatory bodies, and the public to explore responsible uses of this technology. To initiate this conversation, developers and users of the CRISPR-Cas9 technology, and experts in genetics, law, and bioethics, discussed the implications and rapid expansion of the genome engineering field (1). This group, all from the United States, and which included some of the leaders in the original 1970s discussions about recombinant DNA research at Asilomar and elsewhere, focused on the issue of human germline engineering, as the methods have already been demonstrated in mice (6) and monkeys (7). The Napa discussion did not address mitochondrial transfer (8, 9), a technique that does not use CRISPR-Cas9. Although characterized by some as another form of "germline" engineering, mitochondrial transfer raises different issues and has already been approved by the Human Fertilisation and Embryology Authority and by Parliament in the United Kingdom (10) and is being considered by the Institute of Medicine and the Food and Drug Administration in the United States (11). At the Napa meeting, "genome modification" and "germline engineering" referred to changes in the DNA of the nucleus of a germ cell.

The possibility of human germline engineering has long been a source of excitement and unease among the general public, especially in light of concerns about initiating a "slippery slope" from disease-curing applications toward uses with less compelling or even troubling implications. Assuming the safety and efficacy of the technology can be ensured, a key point of discussion is whether the treatment or cure of severe

> *"...we...discourage... germline genome modification for clinical application in humans, while... implications of such activity are discussed..."*

diseases in humans would be a responsible use of genome engineering, and if so, under what circumstances. For example, would it be appropriate to use the technology to change a disease-causing genetic mutation to a sequence more typical among healthy people? Even this seemingly straightforward scenario raises serious concerns, including the potential for unintended consequences of heritable germline modifications, because there are limits to our knowledge of human genetics, gene-environment interactions, and the pathways of disease (including the interplay between one disease and other conditions or diseases in the same patient). In the United States, such human research currently would require an Investigational New Drug exemption from the Food and Drug Administration, but value judgments about the balance between actions in the present and consequences in the future need deeper consideration of the ethical implications of human germline genome editing than the Investigational New Drug process provides.

RECOMMENDATIONS. To better inform future public conversations recommended by the Napa meeting, research is needed to understand and manage risks arising from the use of the CRISPR-Cas9 technology. Considerations include the possibility of off-target alterations, as well as on-target events that have unintended consequences. It is critical to implement appropriate and standardized benchmarking methods to determine the frequency of off-target effects and to assess the physiology of cells and tissues that have undergone genome editing. At present, the potential safety and efficacy issues arising from the use of this technology must be thoroughly investigated and understood be-

fore any attempts at human engineering are sanctioned, if ever, for clinical testing. As with any therapeutic strategy, higher risks can be tolerated when the reward of success is high, but such risks also demand higher confidence in their likely efficacy. And, for countries whose regulatory agencies focus on safety and efficacy but not on broader social and ethical concerns, another venue is needed to facilitate public conversation.

Given the speed with which the genome engineering field is evolving, the Napa meeting concluded that there is an urgent need for open discussion of the merits and risks of human genome modification by a broad cohort of scientists, clinicians, social scientists, the general public, and relevant public entities and interest groups.

In the near term, we recommend that steps be taken to:

1) Strongly discourage, even in those countries with lax jurisdictions where it might be permitted, any attempts at germline genome modification for clinical application in humans, while societal, environmental, and ethical implications of such activity are discussed among scientific and governmental organizations. (In countries with a highly developed bioscience capacity, germline genome modification in humans is currently illegal or tightly regulated.) This will enable pathways to responsible uses of this technology, if any, to be identified.

2) Create forums in which experts from the scientific and bioethics communities can provide information and education about this new era of human biology, the issues accompanying the risks and rewards of using such powerful technology for a wide variety of applications including the potential to treat or cure human genetic disease, and the attendant ethical, social, and legal implications of genome modification.

3) Encourage and support transparent research to evaluate the efficacy and specificity of CRISPR-Cas9 genome engineering technology in human and nonhuman model systems relevant to its potential applications for germline gene therapy. Such research is essential to inform deliberations about what clinical applications, if any, might in the future be deemed permissible.

4) Convene a globally representative group of developers and users of genome

[1]California Institute of Technology, Mail Code 147-75, Pasadena, CA 91125, USA. [2]Stanford University School of Medicine, 291 Campus Drive, Stanford, CA 94305, USA. [3]University of California, Berkeley, 450 Li Ka Shing no. 3370, Berkeley, CA 94720-3370, USA. [4]Innovative Genomics Initiative, University of California, Berkeley, 188 Li Ka Shing Center, Berkeley, CA 94720-3370, USA. [5]Department of Biochemistry, University of Utah School of Medicine, 15 North Medical Drive East, Room 4100, Salt Lake City, UT 84112-5650, USA. [6]Department of Medical History and Bioethics, School of Medicine and Public Health, University of Wisconsin Law School, 975 Bascom Mall, Madison, WI 53706, USA. [7]Department of Genetics, Harvard Medical School, 77 Avenue Louis Pasteur, Boston, MA 02115, USA. [8]Boston Children's Hospital, 300 Longwood Avenue, Karp Family Building, 7th Floor, Boston, MA 02115, USA. [9]Howard Hughes Medical Institute, 4000 Jones Bridge Road, Chevy Chase, MD 20815, USA. [10]Departments of Molecular and Cell Biology and Chemistry, Howard Hughes Medical Institute, 731 Stanley Hall, MS 3220, University of California, Berkeley, Berkeley, CA 94720-3220, USA. [11]Center for Law and the Biosciences, Crown Quadrangle 559 Nathan Abbott Way Stanford, CA 94305-8610, USA. [12]Department of Biochemistry, University of Zurich, Winterthurerstrasse 190, CH-8057 Zurich, Switzerland. [13]Department of Molecular and Cell Biology, College of Letters and Science, University of California, Berkeley, 210K Durant Hall, Berkeley, CA 94720-2920, USA. [14]Alta Partners, One Embarcadero Center, 37th Floor, San Francisco, CA 94111, USA. [15]Department of Pediatrics UCSF School of Medicine, 513 Parnassus Avenue, San Francisco, CA 94143, USA. [16]Department of Chemistry, 731 Stanley Hall, MS 3220, University of California, Berkeley, CA 94720-3220, USA. [17]Department of Cellular and Molecular Pharmacology, Howard Hughes Medical Institute, University of California, San Francisco, Byers Hall, 1700 4th Street, San Francisco, CA 94158-2330, USA. [18]UCSF School of Medicine, 600 16th Street, San Francisco, CA 94158, USA. *E-mail: doudna@berkeley.edu

engineering technology and experts in genetics, law, and bioethics, as well as members of the scientific community, the public, and relevant government agencies and interest groups, to further consider these important issues, and where appropriate, recommend policies.

CONCLUSIONS. At the dawn of the recombinant DNA era, the most important lesson learned was that public trust in science ultimately begins with and requires ongoing transparency and open discussion. That lesson is amplified today with the emergence of CRISPR-Cas9 technology and the imminent prospects for genome engineering. Initiating these fascinating and challenging discussions now will optimize the decisions society will make at the advent of a new era in biology and genetics. ∎

REFERENCES AND NOTES

1. IGI Forum on Bioethics, Napa, California; this meeting was sponsored by the Innovative Genomics Initiative at the University of California, Berkeley, and the University of California, San Francisco, on 24 January 2015; all the authors, except for G.C. and M.J., participated in the meeting.
2. J. A. Doudna, E. Charpentier, *Science* **346**, 1258096 (2014).
3. H. Yin *et al.*, *Nat. Biotechnol.* **32**, 551 (2014).
4. P. Mali *et al.*, *Science* **339**, 823 (2013).
5. Z. Zhu, F. González, D. Huangfu, *Methods Enzymol.* **546**, 215 (2014).
6. H. Wang *et al.*, *Cell* **153**, 910 (2013).
7. Y. Niu *et al.*, *Cell* **156**, 836 (2014).
8. www.hfea.gov.uk/8807.html
9. M. Tachibana *et al.*, *Nature* **493**, 627 (2013).
10. The Human Fertilisation and Embryology (Mitochondrial Donation) Regulations 2015; www.legislation.gov.uk/uksi/2015/572/contents/made (effective 29 October 2015).
11. U.S. Food and Drug Administration, Cellular, Tissue, and Gene Therapies Advisory Committee Meeting: Announcement, www.fda.gov/AdvisoryCommittees/Calendar/ucm380042.htm; www.iom.edu/activities/research/mitoethics.aspx.

GEOLOGY

Defining the epoch we live in

Is a formally designated "Anthropocene" a good idea?

By **William F. Ruddiman,**[1] **Erle C. Ellis,**[2] **Jed O. Kaplan,**[3] **Dorian Q. Fuller**[4]

Human alterations of Earth's environments are pervasive. Visible changes include the built environment, conversion of forests and grasslands to agriculture, algal blooms, smog, and the siltation of dams and estuaries. Less obvious transformations include increases in ozone, carbon dioxide (CO_2), and methane (CH_4) in the atmosphere, and ocean acidification. Motivated by the pervasiveness of these alterations, Crutzen and Stoermer argued in 2000 that we live in the "Anthropocene," a time in which humans have replaced nature as the dominant environmental force on Earth (*1*). Many of these wide-ranging changes first emerged during the past 200 years and accelerated rapidly in the 20th century (*2*). Yet, a focus on the most recent changes risks overlooking pervasive human transformations of Earth's surface for thousands of years, with profound effects on the atmosphere, climate, and biodiversity.

Crutzen and Stoermer originally favored placing the start of the Anthropocene in the late 1700s because of the industrial revolution initiated by James Watt's invention of the steam engine at that time. However, this choice lacked a key requirement for formal stratigraphic designation: a "golden spike" marker that is widely detectable in geologic records. Recently, a working group of the subcommission of Quaternary Stratigraphy of the Geological Society of London released a preliminary recommendation to mark the start of the Anthropocene on 16 July 1945, when the first atomic bomb test took place in Alamogordo, New Mexico (*3*). The working group chose that time because the isotopic by-products of bomb testing provide a distinctive marker horizon in ice cores, ocean and lake sediments, and soils.

This "stratigraphically optimal" choice [as it was called in (*3*)] faces intense scrutiny from scientists studying the long history of large and profound human effects on this planet (see the figure). For example, about 65% of the genera of large mammals became extinct between 50,000 and 12,500 years ago, with the two most abrupt extinction episodes in Australia and the Americas (*4*). Climate cannot be the major factor in

these episodes because most of these genera had survived some 50 previous glacial-interglacial cycles. Hunting and burning by recently arrived humans is the most plausible explanation of these dramatic and unprecedented collapses.

With the beginning of the Holocene around 11,600 years ago, an even more profound human alteration of Earth's surface had begun: the Neolithic agricultural revolution (see the figure). Subsequent millennia

> *"Does it really make sense to define the start of a human-dominated era millennia after most forests in arable regions had been cut for agriculture...?"*

saw global-scale changes that include domestication of the world's crops after 11,000 years ago and livestock after 9000 years ago, followed by the spread of agriculture across all of Earth's arable lands (*5*), clearance of forested regions with resulting carbon dioxide emissions after 7000 years ago (*6*), and the spread of methane-emitting rice agriculture and livestock after 5000 years ago (*7*). Reversals of a natural downward trend in atmospheric carbon dioxide after 7000 years ago and methane after 5000 years ago have both been attributed to gas emissions from farming (*8*). Other early changes include the transformation of Earth's natural biome vegetation to "anthromes" modified by human activities, with increasing habitat fragmentation (*9*); disturbance and erosion of soils by human activity (*10*, *11*); the onset of the Bronze Age 5000 years ago and of the Iron Age 3000 years ago; and the appearance of urban areas in Mesopotamia by 5000 years ago. Although these changes began slowly and at different times in different regions,

1Department of Environmental Sciences, University of Virginia, Charlottesville, VA 22903, USA. 2Department of Geography and Environmental Systems, University of Maryland, Baltimore County, Baltimore, MD 21250, USA. 3Institute of Earth Surface Dynamics, University of Lausanne, 1015 Lausanne, Switzerland. 4Institute of Archeology, University College London, London WC1H 0PY, UK. E-mail: wfr5c@virginia.edu

engineering technology and experts in genetics, law, and bioethics, as well as members of the scientific community, the public, and relevant government agencies and interest groups, to further consider these important issues, and where appropriate, recommend policies.

CONCLUSIONS. At the dawn of the recombinant DNA era, the most important lesson learned was that public trust in science ultimately begins with and requires ongoing transparency and open discussion. That lesson is amplified today with the emergence of CRISPR-Cas9 technology and the imminent prospects for genome engineering. Initiating these fascinating and challenging discussions now will optimize the decisions society will make at the advent of a new era in biology and genetics. ∎

REFERENCES AND NOTES

1. IGI Forum on Bioethics, Napa, California; this meeting was sponsored by the Innovative Genomics Initiative at the University of California, Berkeley, and the University of California, San Francisco, on 24 January 2015; all the authors, except for G.C. and M.J., participated in the meeting.
2. J. A. Doudna, E. Charpentier, *Science* **346**, 1258096 (2014).
3. H. Yin *et al.*, *Nat. Biotechnol.* **32**, 551 (2014).
4. P. Mali *et al.*, *Science* **339**, 823 (2013).
5. Z. Zhu, F. González, D. Huangfu, *Methods Enzymol.* **546**, 215 (2014).
6. H. Wang *et al.*, *Cell* **153**, 910 (2013).
7. Y. Niu *et al.*, *Cell* **156**, 836 (2014).
8. www.hfea.gov.uk/8807.html
9. M. Tachibana *et al.*, *Nature* **493**, 627 (2013).
10. The Human Fertilisation and Embryology (Mitochondrial Donation) Regulations 2015; www.legislation.gov.uk/uksi/2015/572/contents/made (effective 29 October 2015).
11. U.S. Food and Drug Administration, Cellular, Tissue, and Gene Therapies Advisory Committee Meeting: Announcement, www.fda.gov/AdvisoryCommittees/Calendar/ucm380042.htm; www.iom.edu/activities/research/mitoethics.aspx.

GEOLOGY

Defining the epoch we live in

Is a formally designated "Anthropocene" a good idea?

By **William F. Ruddiman**,[1] **Erle C. Ellis**,[2] **Jed O. Kaplan**,[3] **Dorian Q. Fuller**[4]

Human alterations of Earth's environments are pervasive. Visible changes include the built environment, conversion of forests and grasslands to agriculture, algal blooms, smog, and the siltation of dams and estuaries. Less obvious transformations include increases in ozone, carbon dioxide (CO_2), and methane (CH_4) in the atmosphere, and ocean acidification. Motivated by the pervasiveness of these alterations, Crutzen and Stoermer argued in 2000 that we live in the "Anthropocene," a time in which humans have replaced nature as the dominant environmental force on Earth (*1*). Many of these wide-ranging changes first emerged during the past 200 years and accelerated rapidly in the 20th century (*2*). Yet, a focus on the most recent changes risks overlooking pervasive human transformations of Earth's surface for thousands of years, with profound effects on the atmosphere, climate, and biodiversity.

Crutzen and Stoermer originally favored placing the start of the Anthropocene in the late 1700s because of the industrial revolution initiated by James Watt's invention of the steam engine at that time. However, this choice lacked a key requirement for formal stratigraphic designation: a "golden spike" marker that is widely detectable in geologic records. Recently, a working group of the subcommission of Quaternary Stratigraphy of the Geological Society of London released a preliminary recommendation to mark the start of the Anthropocene on 16 July 1945, when the first atomic bomb test took place in Alamogordo, New Mexico (*3*). The working group chose that time because the isotopic by-products of bomb testing provide a distinctive marker horizon in ice cores, ocean and lake sediments, and soils.

This "stratigraphically optimal" choice [as it was called in (*3*)] faces intense scrutiny from scientists studying the long history of large and profound human effects on this planet (see the figure). For example, about 65% of the genera of large mammals became extinct between 50,000 and 12,500 years ago, with the two most abrupt extinction episodes in Australia and the Americas (*4*). Climate cannot be the major factor in these episodes because most of these genera had survived some 50 previous glacial-interglacial cycles. Hunting and burning by recently arrived humans is the most plausible explanation of these dramatic and unprecedented collapses.

With the beginning of the Holocene around 11,600 years ago, an even more profound human alteration of Earth's surface had begun: the Neolithic agricultural revolution (see the figure). Subsequent millennia

> *"Does it really make sense to define the start of a human-dominated era millennia after most forests in arable regions had been cut for agriculture...?"*

saw global-scale changes that include domestication of the world's crops after 11,000 years ago and livestock after 9000 years ago, followed by the spread of agriculture across all of Earth's arable lands (*5*), clearance of forested regions with resulting carbon dioxide emissions after 7000 years ago (*6*), and the spread of methane-emitting rice agriculture and livestock after 5000 years ago (*7*). Reversals of a natural downward trend in atmospheric carbon dioxide after 7000 years ago and methane after 5000 years ago have both been attributed to gas emissions from farming (*8*). Other early changes include the transformation of Earth's natural biome vegetation to "anthromes" modified by human activities, with increasing habitat fragmentation (*9*); disturbance and erosion of soils by human activity (*10*, *11*); the onset of the Bronze Age 5000 years ago and of the Iron Age 3000 years ago; and the appearance of urban areas in Mesopotamia by 5000 years ago. Although these changes began slowly and at different times in different regions,

[1]Department of Environmental Sciences, University of Virginia, Charlottesville, VA 22903, USA. [2]Department of Geography and Environmental Systems, University of Maryland, Baltimore County, Baltimore, MD 21250, USA. [3]Institute of Earth Surface Dynamics, University of Lausanne, 1015 Lausanne, Switzerland. [4]Institute of Archeology, University College London, London WC1H 0PY, UK. E-mail: wfr5c@virginia.edu

Long-term anthropogenic changes
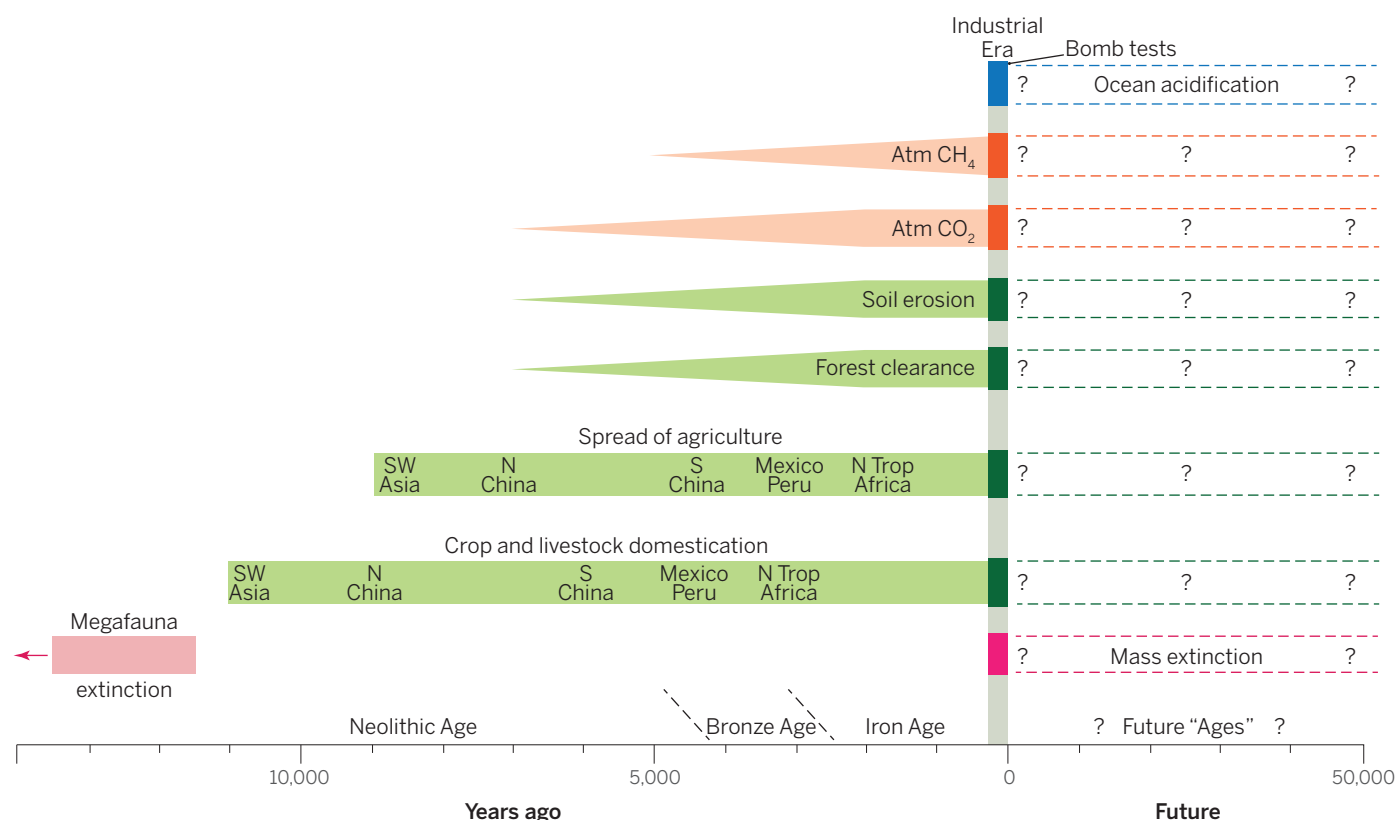
What's in a name? The industrial era has been a time of greatly accelerated environmental changes (*1, 2*), but it was preceded by large and important transformations, including massive large-mammal extinctions in the Americas and major changes associated with the spread of agriculture, including the spread of domesticated crops and livestock (*5*), land clearance, forest cutting, habitat transformations (*6, 9*), irrigated rice paddies (*7*), soil erosion (*10, 11*), and anthropogenic emissions of CO_2 and CH_4 to the atmosphere (*8*). These anthropogenic changes would not be included if the "Anthropocene" is defined by the first atomic bomb test in 1945 (*3*). Future changes, e.g., in species extinctions and ocean acidification, are projected to be much larger than those already seen, but are difficult to predict.

all reached globally significant levels millennia before the industrial era (*12*). But the timing of these changes varied from region to region, leaving no single "golden spike" to mark their onset.

Large-scale alterations of Earth's surface continued into the industrial era. Following the introduction of mechanized agriculture, most prairie and steppe grasslands had been plowed and planted with crops by 1900. Burning of fossil fuels pushed CO_2 values rapidly higher, and emissions from irrigated rice, livestock, coal mining, and landfills boosted methane levels. Two world wars introduced many new environmental upheavals, including exponential increases of lead and sulfate loadings in the atmosphere. Contrary to this increasing trend of exploitation of planet Earth, however, high northern latitude areas of Canada, the eastern United States, northern Europe, and Russia reversed millennia-long deforestation trends and began to reforest during the 1800s and 1900s as new agricultural technologies increased land-use efficiency.

Selecting 1945 as the start of the "Anthropocene" would implicitly omit these extensive agricultural and early-industrial alterations. Does it really make sense to define the start of a human-dominated era millennia after most forests in arable regions had been cut for agriculture, most rice paddies had been irrigated, and CO_2 and CH_4 concentrations had been rising because of agricultural and industrial emissions? And does it make sense to choose a time almost a century after most of Earth's prairie and steppe grasslands had been plowed and planted? Together, forest cutting and grassland conversion are by far the two largest spatial transformations of Earth's surface in human history. From this viewpoint, the "stratigraphically optimal" choice of 1945 as the start of the Anthropocene does not qualify as "environmentally optimal."

Despite differing views, the term "Anthropocene" is clearly here to stay. One way forward would be to use the term informally (with a small "a"). This approach would al-

low for modifiers appropriate to the specific interval under discussion, such as early agricultural or industrial. In this way, we could avoid the confinement imposed by a single formal designation, yet acknowledge the long and rich history of humanity's environmental transformations of this planet, both for better and for worse. ∎

REFERENCES

1. P. J. Crutzen, E. F. Stoermer, *IGBP Newsletter* **41**, 12 (2000).
2. W. Steffen, P. J. Crutzen, J. R. McNeill, *Ambio* **36**, 614 (2007).
3. J. Zalasiewicz *et al.*, *Quat. Int.* (2015). 10.1016/j.quaint.2014.11.045
4. A. D. Barnosky, P. L. Koch, R. S. Feranec, S. L. Wing, A. B. Shabel, *Science* **306**, 70 (2004).
5. G. Larson *et al.*, *Proc. Natl. Acad. Sci. U.S.A.* **111**, 6139 (2014).
6. J. O. Kaplan *et al.*, *Holocene* **21**, 775 (2011).
7. D. Q. Fuller *et al.*, *Holocene* **21**, 743 (2011).
8. W. F. Ruddiman, *Clim. Change* **61**, 261 (2003).
9. E. C. Ellis, *Philos. Trans. R. Soc. London A* **369**, 1010 (2011).
10. Y. Zhuang, T. Kidder, *Holocene* **24**, 1602 (2014).
11. T. Hoffmann *et al.*, *Earth Surf. Dynam* **1**, 45 (2013).
12. W. F. Ruddiman, *Earth Transformed* (Freeman, New York, 2013).

TRIBOLOGY

Tracking antiwear film formation

Atomic force microscopy visualizes the formation of a lubricating film

By **Udo D. Schwarz**

Lubrication has been practiced since the early days of human civilization (*1*); for example, heavy objects were moved more easily on wooden or stone floors by spreading water onto the surface. In the early 20th century, the advent of the internal combustion engine and its long periods of operation posed several lubrication challenges. Modern lubrication and antiwear schemes use base oils supplemented by chemical additives (*2*). Much of the development, however, has been empirical in nature, leaving the molecular mechanisms that eventually lead to the desired reduction in friction and wear only rudimentarily understood (*3*). On page 102 of this issue, Gosvami *et al.* (*4*) present a rare exception in visualizing the formation of an antiwear film on the molecular scale and quantifying how its growth and stability depended on important parameters such as applied temperature and pressure.

Oils and additives used to lubricate machinery may have many different purposes (*2*, *5*). Reducing the friction between the moving parts directly results in energy

Department of Mechanical Engineering and Materials Science and Center for Research on Interface Structures and Phenomena (CRISP), Yale University, New Haven, CT 06520, USA. E-mail: udo.schwarz@yale.edu

savings and lower operating costs. More indirectly, the introduction of molecular species can suppress deterioration of the moving surfaces and involved parts, either by preventing chemical reactions and transformations at surfaces or by preventing mechanical alterations that are usually referred to as wear. One of the most successful strategies to prevent degradation of the moving parts, such as pistons and cylinders in automotive engines, comprises the formation of so-called "tribochemical films," where layers up to several hundred nanometers thick form from molecular precursors under operating conditions that protect the surfaces they cover from wear and degradation.

The study by Gosvami *et al.* focuses on zinc dialkyldithiophosphates (ZDDPs) as a prototypical tribofilm former. ZDDPs are arguably the most successful class of lubricant additives ever invented (*6*). They have been in continuous use since the late 1930s and are still being used in practically all engine oils. This persistence is particularly striking because additive companies have long been looking for alternatives; modern oil formulations and environmental regulations limit the content of phosphorus (*7*). ZDDPs work not only astonishingly well under diverse operating conditions but are also very reasonably priced. A similarly

cost-effective antiwear compound with comparable performance has been impossible to identify.

This lack of success in finding a replacement for ZDDPs is, however, not a result of insufficient research. Ever since their introduction as additives, ZDDPs have been the focus of an extraordinary number of research papers (*8*, *9*). It is known that ZDDPs form layered patches on the surfaces they cover and that they also act as corrosion inhibitors and antioxidants. Even so, it remains unclear how the film functions to provide such robust protection for such a large number of applications.

Gosvami *et al.* studied tribofilms formed from ZDDP-containing lubricant base stock at elevated temperatures (80° to 140°C) with atomic force microscopy to visualize phenomena and mechanisms at the nanometer level. Nucleation, growth, and thickness saturation of patchy tribofilms was observed and quantified versus sliding time. The growth rate increased exponentially with either temperature or compressive stress (applied through gradually increasing the load on the scanning tip), which is consistent with a thermally activated, stress-assisted reaction rate model. The films grew regardless of the presence of iron on either the tip or substrate, which indicates that iron does not play an essential role in film formation.

• 170 liters of fuel per car per year
• 104 billion liters of fuel worldwide per year

Fuel energy
100%

Heat loss
(exhaust and cooling)
62%

Mechanical power
38%

Friction losses in
engine and transmission
16.5%

Energy to move the car
(rolling resistance, brakes, air drag)
21.5%
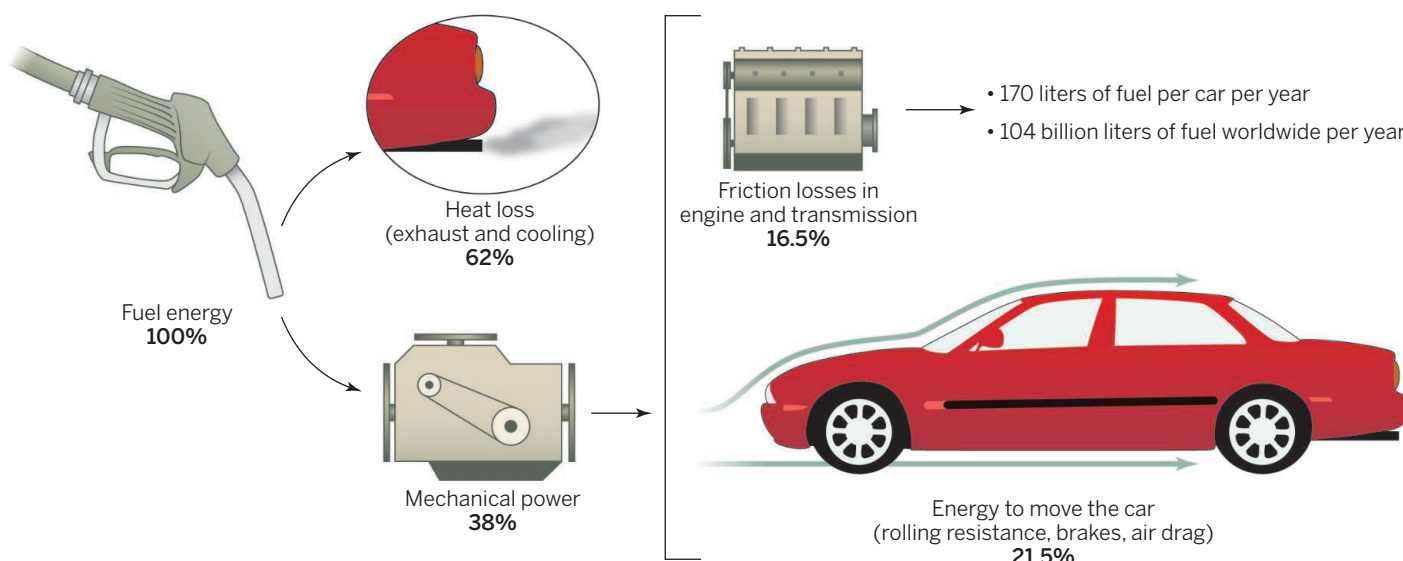
Passenger car energy consumption. Almost one-sixth of the energy provided by automotive fuel goes to overcoming friction losses. A reduction of as little as 1% in friction inside the car's engine block as a result of improved lubrication technology would result in 1 billion liters of fuel (gasoline or diesel) saved annually worldwide. The methodology of Gosvami *et al.* enables fundamental studies of lubricating films created during machine operation.

This finding is particularly important for car manufacturers attempting to replace current steel engine block materials (as is still the case for heavy-duty engines) with lighter alloys that contain considerable amounts of aluminum or magnesium.

It was previously known that the ZDDP tribofilm is not only self-limiting in thickness but also features a gradient in composition, structure, and mechanical properties that becomes stronger and stiffer nearer the substrate (6). The formation of this complex structure can now be elegantly explained with the observed contact-pressure dependence of tribofilm formation. The tribofilm has a lower modulus than the substrate, so the contact stress at constant load decreases as the tribofilm thickens, which in turn reduces the amount of stress-induced cross-linking and other reactions that produce the tribofilm. Weaker, more compliant structures form that lead to a gradually further reduction in contact pressure, which ultimately terminates any further growth.

Considering the large numbers of internal combustion engines in service, even small improvements in engine efficiency, emission levels, and durability have a major effect on the world fuel economy and the environment, with a potential to save tens of billions of liters of fuel annually (see the figure) (10). The innovative in situ approach demonstrated by Gosvami et al. has the potential to transform lubrication science if researchers can successfully apply it to the multitude of molecular-level tribochemical phenomena that still lack detailed understanding. Given a nanometer-scale understanding of the chemistry of lubricants and how additives affect the interactions between lubricants and rubbing surfaces, new lubricants could be designed that will be longer-lasting, environmentally friendly, and compatible with catalytic converters and lightweight nonferrous engine block materials alike. ■

REFERENCES AND NOTES

1. D. Dowson, *History of Tribology* (Longman, London, 1979).
2. R. M. Mortier, M. F. Fox, S. T. Orszulik, Eds., *Chemistry and Technology of Lubricants* (Springer-Verlag, Dordrecht, Netherlands, ed. 3, 2010).
3. S. M. Hsu, *Tribol. Int.* **37**, 553 (2004).
4. N. N. Gosvami et al., *Science* **348**, 102 (2015).
5. S. C. Tung, M. L. McMillan, *Tribol. Int.* **37**, 517 (2004).
6. H. Spikes, *Tribol. Lett.* **17**, 469 (2004).
7. H. Spikes, *Lubricat. Sci.* **20**, 103 (2008).
8. A. M. Barnes, K. D. Bartle, V. R. A. Thibon, *Tribol. Int.* **34**, 389 (2001).
9. M. A. Nicholls, T. Do, P. R. Norton, M. Kasrai, G. M. Bancroft, *Tribol. Int.* **38**, 15 (2005).
10. K. Holmberg, P. Andersson, A. Erdemir, *Tribol. Int.* **47**, 221 (2012).

GENE EXPRESSION

MicroRNAs silence the noisy genome

Evolution may have selected for a dampening service for genes whose noise may have otherwise been too high

By **Yonit Hoffman**[1,2] *and* **Yitzhak Pilpel**[1]

All molecular machines have imperfections, and the biological ones are no exception. One type of flaw is a quantitative one: Although all the cells within an organ are genetically identical, the concentrations of many of their proteins can be "noisy"—that is, vary and fluctuate between all the cells. Biologists decompose such noise into two sources: an intrinsic one, which results from the stochastic nature of the biochemistry operating within cells, and an extrinsic one that manifests global differences between cells, such as the number of protein production facilities (e.g., ribosomes) (1). A major question is whether organisms have evolved means to control noise, especially when imprecisions are detrimental. On page 128 in this issue, Schmiedel et al. (2) report combining mathematical modeling and a synthetic gene approach to establish a complex role for microRNAs (miRNAs) in controlling cellular protein content.

Since their discovery, miRNAs have been considered important regulators of basic cellular and organismal biology. These small noncoding RNAs base pair with complementary sequences in messenger RNAs (mRNAs), thereby degrading their mRNA targets or preventing their translation into proteins. Yet, the observation that the quantitative effect of miRNAs on their targets is often minor remains a mystery. It has thus been suggested that miRNAs provide noise filtration functions, limiting variability in protein expression across a population of cells (3, 4). But how can one reveal the potential noise-reducing effect of miRNAs on genes? A mere inspection of genes within their natural complex genomic context might not suffice because this context consists of numerous variables and it is impossible to dissect the effects of each of them. Schmiedel et al. avoid these obstacles by analyzing a reporter gene that is synthetically connected to gene parts that convey regulation by miRNA. In particular, the authors constructed a fluorescence reporter that allows measuring of gene expression noise, while varying miRNA regulatory input. In this approach, miRNAs bind to targeted mRNAs through dedicated regions—the 3′-untranslated regions (UTRs) of the mRNAs. Sequences that contain different 3′UTRs, each with one or more binding sites (of varying binding strengths) for different miRNAs, were synthesized. These sequences were each fused to the fluorescent reporter gene. Each construct was then expressed in cultured mammalian cells (including constructs with no binding site for miRNAs).

> ### "Which genes should be the prime subjects of such a noise dampening mechanism?"

Comparing single-cell fluorescence revealed an important difference between reporters that have or that do not have miRNA binding sites. In cells that happened to express the reporter at a low level, noisiness of its expression dropped if the reporter had a miRNA binding site. By contrast, in cells that expressed the reporter at a high level, the presence of a miRNA binding site was associated with elevated noisiness of its expression (see the figure). This result was recapitulated by a mathematical model that implements basic principles of gene expression, with clear predictions: Reduction in intrinsic noise should be proportional to miRNA-mediated repression, and extrinsic noise will be "inherited" from noise in the miRNAs (there is variability in the expression of miRNAs as well). To test the intrinsic noise prediction, Schmiedel et al. created another reporter, subject to the same miRNA regulation. Because mRNAs encoding both reporters "see" the same miRNAs, differences between their noise must be ascribed to the intrinsic compo-

[1]Department of Molecular Genetics, Weizmann Institute of Science, Rehovot 76100, Israel. [2]Molecular Cell Biology, Weizmann Institute of Science Rehovot, 76100 Israel. E-mail: pilpel@weizmann.ac.il
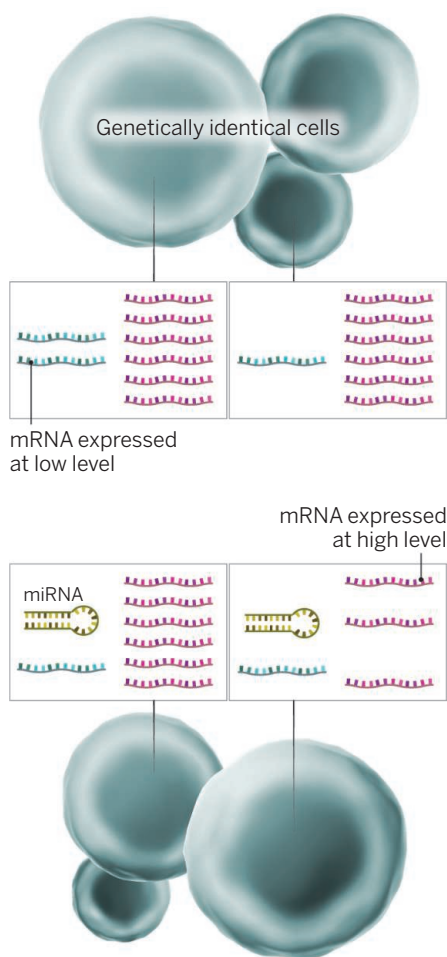
Noise-canceling RNA. The amounts of mRNA corresponding to two genes are shown in two identical cells. One gene is expressed at a low level, and there is variation (noise) of this expression between the cells. In the presence of a regulatory miRNA, the mRNA that is expressed at a lower level fluctuates less, whereas the mRNA that is present in greater amounts becomes more noisy.

nent. For each reporter, the authors synthesized a version encoding a 3'UTR with or without binding sites for miRNA. The result was clear: miRNA reduced intrinsic noise, even when the reporter was expressed at a high level. This suggests that the original observation—that there is increased noise of a gene's expression when its expression level is high—must have been due to extrinsic noise.

Indeed, as for the extrinsic noise, Schmiedel et al. suspected that modifying the noise level of the miRNAs themselves would affect the reporter's noise too. For that, the authors examined what happens if the miRNA is produced from two gene copies, rather than from one. This situation could reduce noise in the miRNA because fluctuations in the expression of one copy are counteracted by the other. They found that miRNAs encoded by

more than one gene copy in the genome presented less noise. Further, mRNAs of natural genes are often targeted by more than one type of miRNA. Schmiedel et al. determined that such combinatorial effects reduce the amount of the extrinsic noise because it decreases the total amount of miRNA-pool noise. This finding was found to hold also for native genes' 3'UTR.

A key question in any such synthetic approach is, how applicable are the conclusions to natural genes? Examining expression for the entire mouse genome, Schmiedel et al. reveal that some 90% of the genes fall within the range of expression that would subject them to such a miRNA-based noise dampening mechanism.

Which genes should be the prime subjects of such a noise dampening mechanism? Single-cell transcriptomics (5, 6) should allow noise measurement for each gene and miRNA. With such data, it will be possible to examine the connection between the extent of miRNA regulation of a gene and its noise. Means to manipulate miRNA levels (7) should allow examination of the effect of changes in miRNA expression on the noisiness in their targets. One can then ask which genes are endowed with noise filtration and whether there are genes that are deliberately noisy. Schmiedel et al. ascribed intrinsic noise reduction to enhanced transcription that presumably compensates for the mRNA degradation (which maintains a given expression level). Recent reports on the "circular" nature of gene expression—namely, that mRNA degradation feeds back to elevate transcription (8)—may thus provide an intriguing potential mechanism that explains the intrinsic noise reduction effect. And the story need not end with miRNAs. A most profound revolution in genomics is the realization that there are many additional types of RNA. For instance, "antisense" RNAs may also act in noise filtration, especially when coregulated with their corresponding sense transcript (9). Perhaps some long noncoding RNAs (10), too, contribute to fine tuning of gene expression programs. ■

REFERENCES

1. M. B. Elowitz, A. J. Levine, E. D. Siggia, P. S. Swain, *Science* **297**, 1183 (2002).
2. J. M. Schmiedel *et al.*, *Science* **348**, 128 (2015).
3. E. Hornstein, N. Shomron, *Nat. Genet.* **38** (suppl.), S20 (2006).
4. M. S. Ebert, P. A. Sharp, *Cell* **149**, 515 (2012).
5. D. A. Jaitin *et al.*, *Science* **343**, 776 (2014).
6. T. Hashimshony, F. Wagner, N. Sher, I. Yanai, *Cell Rep.* **2**, 666 (2012).
7. J. Krützfeldt *et al.*, *Nature* **438**, 685 (2005).
8. G. Haimovich *et al.*, *Cell* **153**, 1000 (2013).
9. M. Lapidot, Y. Pilpel, *EMBO Rep.* **7**, 1216 (2006).
10. M. Guttman *et al.*, *Nature* **458**, 223 (2009).

PSYCHOLOGY

Infants explore the unexpected

Infants are more likely to explore objects that behave in unexpected ways, such as passing through walls

By **Laura Schulz**

Science can delight us with new and surprising findings. Sometimes, however, a study delights us by confirming something we already believed but could not yet prove. This is the kind of pleasure occasioned by Stahl and Feigenson's report on page 91 of this issue (1). In a series of elegant experiments, the authors show that, controlling for overall attention, 11-month-old infants are more likely to learn a new sound associated with an object if the object previously violated the infants' expectations (e.g., by appearing to pass through walls or roll over gaps without falling) than if the object behaved as expected. Moreover, infants not only selectively explore objects that violate their expectations but also explore in ways specific to the violation. Thus, they bang objects that violate expectations of solidity and drop objects that violate expectations of support (see the figure).

Perhaps the most surprising thing about these observations is that they had not been made sooner. For decades, researchers have known that infants look longer at events that violate their expectations than at events consistent with their prior beliefs (2). The presumption was that such selective attention must support learning, but it was difficult to show this in a way that did not follow trivially from the fact that infants look for a long time at unexpected events. The current study solves that problem by matching infants' initial exposure to the events and then asking whether infants who observe theory-violating evidence are more likely to learn an unrelated property of the objects.

Researchers have also long assumed that children's exploratory play must support learning (3–5). Again, however, it has been difficult to demonstrate this in a way that does not follow trivially from the fact that the longer children explore an object,
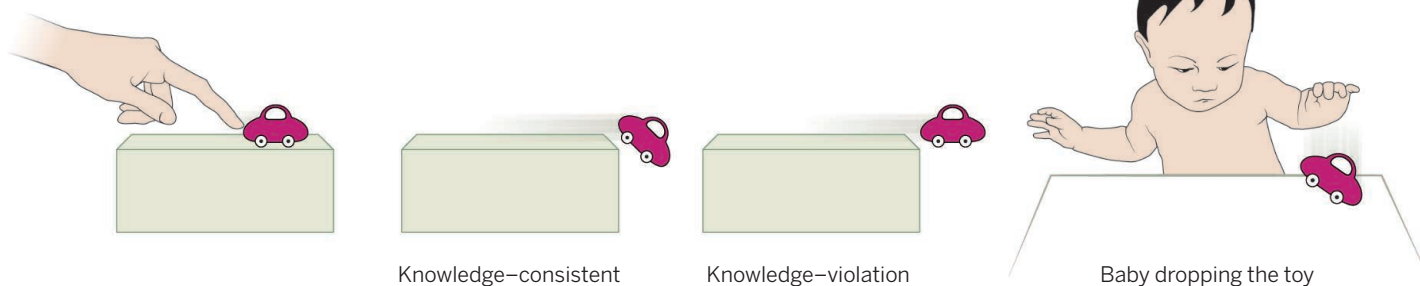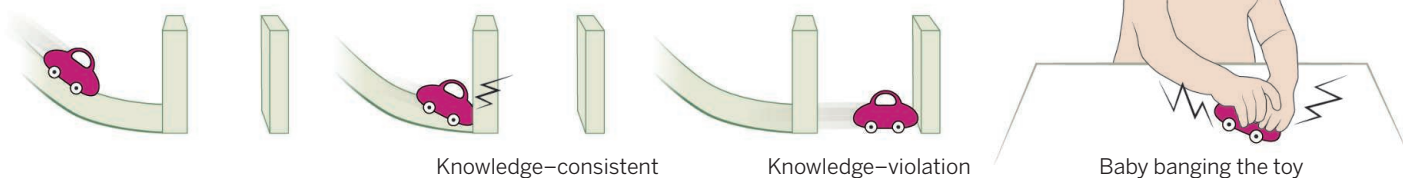
The importance of violating expectation. Stahl and Feigenson show that babies who have previously seen an object behave in an unexpected way are more likely to explore this object. The results help to understand how babies and young children learn.

the more of its properties they are likely to discover. In the past decade, research has begun to bridge the gap between formal models of learning (6) and children's play. This research has, for instance, shown that preschoolers engage in selective exploration both when evidence violates their prior beliefs (i.e., when evidence is surprising) (7) and when evidence fails to distinguish equally probable possibilities (i.e., when evidence is confounded) (8).

Moreover, children spontaneously explore in ways that tend to support information gain. They are sensitive to the degree to which exploration reduces uncertainty (9) and will isolate causal variables and test them one at a time in response to both surprising (10) and confounded (11) evidence. However, such studies have focused on preschoolers or older children. It is both gratifying and astonishing to find not only that infants less than a year old selectively explore objects that violate their prior beliefs but also that they do so in ways directly relevant to the violation they observe.

Stahl and Feigenson frame their study with respect to "core knowledge," the idea that cognitive representations of objects and agents are present at birth in humans and other species. Constraints imposed by these innate representations could support infants' ability to learn rapidly from sparse data. However, when the authors suggest that violations of core knowledge might signal "a special opportunity for learning" one has to wonder how typical of learning these opportunities really are. Core knowledge is hypothesized to be an innate component of human cognition precisely because it represents aspects of the environment that are stable across evolutionary time scales. It is thus not likely to be violated (outside of developmental laboratories). If infants were to rely on violations of core knowledge as a "wedge into the hard problems of knowing when and what to learn," they would learn very little. It seems far more likely, as the authors acknowledge in their conclusion, that violations of any expectations—whether innate or recently acquired—provide special opportunities for learning.

One might also wonder how much of a violation of expectation is a good thing. Infants do not always prefer information that is more surprising or more complex: They appear to like things that they think they can learn. Thus, for instance, infants prefer to attend to patterns of linguistic input that are predictable enough to permit learning (12) and to sequences of stimuli that are neither too predictable nor too un-predictable (13). Quantitative models may help to explore the ways in which the predictability of events affects infants' learning. Bringing together the methods and results of the present study with those of other recent exciting experimental results and computational models of infant's attention (14) could pave the way toward a more comprehensive theory of how infants learn and explore. ■

REFERENCES

1. A. E. Stahl, L. Feigenson, *Science* **348**, 91 (2015).
2. E. S. Spelke, K. Breinlinger, J. Macomber, K. Jacobson, *Psychol. Rev.* **99**, 605 (1992).
3. J. Bruner, A. Jolly, K. Sylva, *Play—Its Role in Development and Evolution* (Basic Books, New York, 1976).
4. J. Piaget, *The Child's Conception of Physical Causality* (Harcourt, Brace, New York, 1930).
5. D. G. Singer, R. M. Golinkoff, K. Hirsh-Pasek, Eds., *Play = Learning: How Play Motivates and Enhances Children's Cognitive and Social-Emotional Growth* (Oxford Univ. Press, New York, NY, 2006).
6. J. B. Tenenbaum, C. Kemp, T. L. Griffiths, N. D. Goodman, *Science* **331**, 1279 (2011).
7. C. H. Legare, *Child Dev.* **83**, 173 (2012).
8. L. E. Schulz, E. B. Bonawitz, *Dev. Psychol.* **43**, 1045 (2007).
9. D. Klahr, C. Zimmerman, J. Jirout, *Science* **333**, 971 (2011).
10. T. J. van Schijndel, I. Visser, B. M. van Bers, M. E. J. Raijmakers, *J. Exp. Child Psychol.* **131**, 104 (2015).
11. C. Cook, N. D. Goodman, L. E. Schulz, *Cognition* **120**, 341 (2011).
12. L. Gerken, F. K. Balcomb, J. L. Minton, *Dev. Sci.* **14**, 972 (2011).
13. C. Kidd, S. T. Piantadosi, R. N. Aslin, *PLOS ONE* **7**, e36399 (2012).
14. E. Téglás *et al.*, *Science* **332**, 1054 (2011).

Department of Brain and Cognitive Sciences, Massachusetts Institute of Technology, Cambridge, MA 02139, USA. E-mail: lschulz@mit.edu

ILLUSTRATION: P. HUEY/SCIENCE

ASTRONOMY

How young stars grow and become focused

Observations 18 years apart capture early changes of a massive star

By M. G. Hoare

Massive stars are the enigmatic big beasts of the stellar jungle. Although rare, they make up for this through their prodigious output of hard radiation and kinetic energy from winds, and their explosive demise as supernovae. The latter disperse heavy elements such as iron throughout interstellar space ready for incorporation in the next generations of stars and planets, and of course, ourselves. When present in large numbers in a galaxy, their combined effect can disrupt the interstellar material to such an extent as to change the very nature of the galaxy itself. These energetic outflows are present even during the birth of massive stars. Indeed, this is one of the main reasons why understanding their formation from the gravitational collapse of interstellar clouds is so challenging. However, new sensitive, high-resolution facilities are being brought to bear on the problem. On page 114 of this issue Carrasco-González et al. (1) present radio observations using the upgraded Jansky Very Large Array (JVLA). Rapid changes in the distribution of the ionized gas flowing out at high speed from a massive young star could provide new insights into the birth pangs of these astrophysical objects.

Overcoming the strong outward radiation pressure of these stars, which can be up to a million times more luminous than our Sun, is key to building up the stellar mass. In recent years, the role of accretion via a rotating disk has come to the fore as a way to transport large amounts of material past the intense radiation field onto the growing star (2). As with most astrophysical accretion disks, jets and/or bipolar outflows are expected to be driven outwards along the rotation axis. These can then punch holes in the surrounding in-falling cloud, releasing
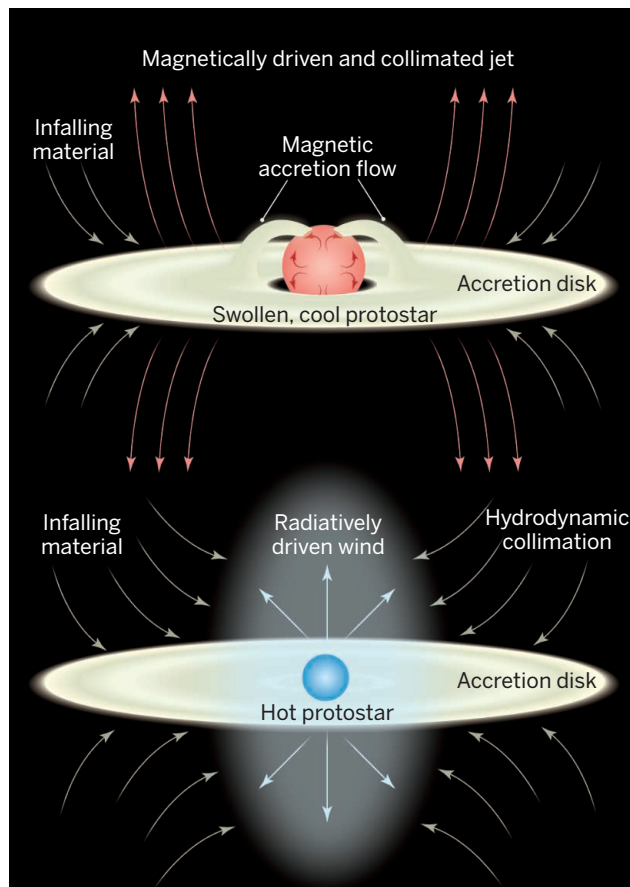
Getting focused. Illustration of the two types of mechanisms that may give rise to collimated outflows from massive protostars: magnetic and radiative.

some of the radiation pressure like a safety valve (3, 4). What drives and collimates these outflows is one of the big unsolved problems in star formation, particularly for high-mass protostars. Two classes of mechanisms present themselves: magnetic and radiative. Magneto-hydrodynamic mechanisms, often invoking a magnetic field generated by the star itself, have long been thought to be responsible for the highly collimated magnetized jets seen in low-mass protostars (5). This mechanism is potentially problematic for massive stars because once they are settled into their hydrogen-burning main-sequence phase, they do not have strong magnetic fields. Their high surface temperatures prevent convection currents occurring in their envelopes that can generate strong magnetic fields via a dynamo effect in stars like the Sun. Radiation pressure could drive the outflows, but a collimating mechanism

must then be found. Hydrodynamic collimation by the rotationally flattened circumstellar matter has been invoked for this (see the figure). Simulations and observations have shown that radiation pressure acting on an accretion disk actually generates a wind in the disk plane rather than perpendicular to it (6).

Carrasco-González et al. claim to have seen a transition from an initially isotropic outflow to a more collimated jet via changes in the morphology seen in radio continuum images taken 18 years apart. The change in the shape of the radio free-free emission from ionized gas is backed up by similar changes in the distribution of spots of water maser emission. They model the changes by assuming an initially isotropic wind that would most naturally be explained by a radiatively driven wind from the central star. This is then collimated hydrodynamically by a toroidal surrounding medium. Massive stars are known to have such radiatively driven winds once on the main sequence, but these have speeds of thousands of kilometers per second, and their density is too low to explain the outflows seen during the formation stage. Where jet speeds have been directly measured for massive protostars, they are found to be several hundreds of kilometers per second (7), similar to those seen in the low-mass, magnetically driven jets. These speeds are similar to those required in Carrasco-González et al.'s model. A jet arising from a different massive protostar has also been seen to exhibit synchrotron emission, which also implies a magnetic origin (8).

So there appear to be some contradictions here, with the outflow properties being more consistent with moderately fast, highly collimated, magnetically driven jets, whereas the star is expected to be nonmagnetic and dominated by radiation pressure. However, theoretical studies have shown that if protostars with masses in the range of 5 to 20 solar masses accrete at high rates, then the protostar swells up and is much cooler (9).

School of Physics and Astronomy, University of Leeds, Leeds LS2 9JT, UK. E-mail: m.g.hoare@leeds.ac.uk

ILLUSTRATION: P. HUEY/SCIENCE

Such an object would be convective and generate strong magnetic fields that could then drive and collimate protostellar jets. This also naturally explains why these luminous, but cool, protostellar objects do not ionize the wider surroundings. Such a scenario has been shown to match the observed distribution and lifetimes of massive protostars seen in the Milky Way (10).

The object discussed by Carrasco-González et al. is currently only about 300 times the total luminosity of the Sun (11), which corresponds to about 6 solar masses. This puts it currently in the mass range where it could be swollen, magnetic, and capable of driving a collimated jet. The observations of Carrasco-González et al. do not actually rule out the possibility that the flow was always collimated, because the first epoch observations show an unresolved point source. If so, then we may just be seeing a new blob emerge down the jet similar to the behavior that is common in other types of astrophysical jets, such as those arising from black hole sources.

The remaining questions will soon be addressed by other new high-resolution facilities. Higher-resolution radio studies of the ionized gas will come from the e-MERLIN array in the United Kingdom, while the Atacama Large Millimeter Array (ALMA) array in Chile will provide the corresponding view of the surrounding molecular material to determine if a confining torus is present, as well as the accretion disk. ALMA will also probe the kinematics, but we will have to wait for the mid-frequency element of the Square Kilometre Array in South Africa to probe the motions of the ionized gas itself. The advance of numerical simulation should also enable self-consistent three-dimensional simulations of the disk-jet system that include the effects of both radiation and magnetic fields. Hence, the coming few years promise to unmask the inner workings of the formation of these objects that play such a central role in astrophysics. ■

REFERENCES

1. C. Carrasco-González et al., Science **348**, 114 (2015).
2. M. R. Krumholz, R. I. Klein, C. F. McKee, S. S. Offner, A. J. Cunningham, Science **323**, 754 (2009).
3. A. J. Cunningham, R. I. Klein, M. R. Krumholz, C. F. McKee, Astrophys. J. **740**, 107 (2011).
4. R. Kuiper, H. W. Yorke, N. J. Turner, Astrophys. J. **800**, 86 (2015).
5. A. Frank et al., in Protostars and Planets VI, H. Beuther, R. Klessen, C. Dullemond, Th. Henning, Eds. (Univ. of Arizona Press, Tucson, 2014), p. 451.
6. M. G. Hoare, Astrophys. J. **649**, 856 (2006).
7. S. Curiel et al., Astrophys. J. **638**, 878 (2006).
8. C. Carrasco-González et al., Science **330**, 1209 (2010).
9. T. Hosokawa, K. Omukai, Astrophys. J. **691**, 823 (2009).
10. B. Davies et al., Mon. Not. R. Astron. Soc. **416**, 972 (2011).
11. P. Persi, M. Tapia, H. A. Smith, Astron. Astrophys. **445**, 971 (2006).

IMMUNOLOGY

MULT1plying cancer immunity

A soluble ligand of an innate immunoreceptor arms natural killers for tumor attack

By Alexander Steinle[1] and Adelheid Cerwenka[2]

Immunotherapy of cancer, based on natural killer (NK) cells, is an emerging field (1). Activation of these innate lymphocytes depends on signals emanating from receptors that recognize transformed cells. The extent and spectrum of receptor engagement by cognate ligands that tumors bear determines the outcome of NK cell responses, including direct cellular killing (through the release of cytolytic granules) and communication with other immune cells (through secreted cytokines). One potent activating NK cell receptor involved in the destruction of ligand-expressing transformed cells is natural-killer group 2, member D (NKG2D). Recently, however, an immunosuppressive role was attributed to persistently engaged NKG2D. On page 136 of this issue, Deng et al. (2) report that, contrary to expectations, release of a particular NKG2D ligand by tumor cells results in NK cell activation and enhanced tumor rejection in a mouse model. This remarkable result may open new treatment options for cancer patients.

NK cells of the innate immune system recognize danger by detecting stressed, transformed, or virus-infected cells through the receptor NKG2D. In 1999, NKG2D was described as expressed by almost all human cytotoxic lymphocytes, detecting cell stress–inducible molecules [called major histocompatibility complex (MHC) class I–related chain molecules (MICA/B)] on tumor cells. Upon binding to a ligand, NKG2D triggers an intracellular signaling pathway involving phosphatidylinositol 3-kinase (3, 4). Eight ligands for NKG2D have been identified in human, each bearing an MHC class I–like ectodomain that binds to NKG2D. The number of functional NKG2D ligands in mouse strains varies (5). Initial studies revealed NK cell–dependent rejection of tumor cells ectopically expressing retinoic acid early inducible-1 (RAE-1), a mouse NKG2D ligand (6, 7). These findings were extended using NKG2D-deficient mice that exhibited an impaired control of certain spontaneous tumors (8).

The concept of NKG2D as an activating receptor was challenged recently by results showing that its chronic exposure to surface-attached NKG2D ligands leads to
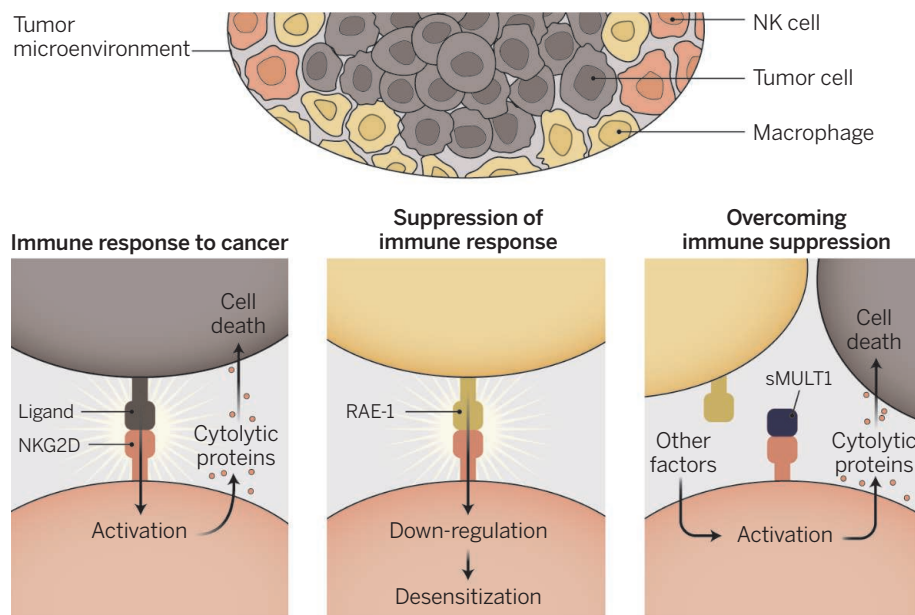
Affinity matters. Acute exposure of NKG2D receptors to ligands expressed by tumor cells leads to tumor cell death (left). Chronic exposure of RAE-1 on myeloid cells in the tumor microenvironment impairs NK cell antitumor activity (middle). sMULT1 binds with high affinity to NKG2D and blocks the desensitizing interaction with RAE-1. This restores tumoricidal activity of NK cells (right).

down-regulation of NKG2D (9) and to an NK cell desensitization in response not only to NKG2D ligands but also to other molecules that activate NK cells (global desensitization) (10). Furthermore, human tumor cells excrete soluble NKG2D ligand by means of proteolytic shedding, alternative splicing, or exosomal release, thereby reducing the NKG2D ligand surface density on tumor cells (5, 11). NKG2D ligand excretion has also been proposed to reduce NKG2D surface expression (by causing receptor internalization) and to reduce NK cell function (by perpetually binding to NKG2D, thereby desensitizing NK cells) (1, 12), consistent with an immunosuppressive role of excreted NKG2D ligands.

"Immunotherapy of cancer, based on natural killer cells, is an emerging field..."

Murine ULBP-like transcript 1 (MULT1) is a transmembrane protein expressed by tumor cells, and is a mouse ligand for NKG2D (13). Deng et al. show that soluble MULT1 (sMULT1) released from tumor cells binds with high affinity to NKG2D and prevents the immunosuppressive chronic interaction of NKG2D with another ligand, RAE-1, which is expressed by macrophages in the tumor microenvironment. By blocking RAE-1-NKG2D interaction sMULT1 reconstitutes NK cell responsiveness to other activating molecules and promotes tumor destruction. Deng et al. monitored the growth of different tumor cell lines engineered to release sMULT1. Intriguingly, in vivo growth of these sMULT1-releasing tumor cells (in mice) was not accelerated but was instead delayed and paralleled by a higher reactivity of NK cells. Similar effects were observed in mice inoculated with tumor cells that could be induced to release sMULT1 or in mice injected intratumorally with sMULT1. Moreover, in mice with tumors that secreted sMULT1, expression of NKG2D did not decrease, but rather increased. Because monovalent sMULT1 did not affect the responsiveness of purified NK cells in vitro, the authors hypothesized that other cells contribute in vivo to this phenomenon. Myeloid cells (such as macrophages) in the tumor microenvironment express RAE-1 (14), and in tumor-bearing RAE-1–deficient or NKG2D-deficient mice, higher NK cell activity was observed by Deng et al. Thus, sMULT1 enhances tumor

rejection by counteracting NK desensitization in the tumor microenvironment, and restoring NKG2D expression and NK cell activity (see the figure).

A fascinating and unresolved puzzle is why such an array of ligands evolved to bind to NKG2D. It was previously proposed that the needs for distinct cellular responses to different types of stress stimuli, for differential tissue expression, and for different cellular compartmentalization led to the evolution of several highly diverse NKG2D ligands. It was also proposed that the diversity of NKG2D ligands was shaped through the selective pressure of viruses and tumors, as a safeguarding mechanism to counteract viral or tumoral immune escape strategies (5). Deng et al. provide an additional mechanism with important implications for tumor immunity: Various NKG2D ligands bind NKG2D with different affinities. Specifically, sMULT1, a high-affinity NKG2D ligand, may compete with lower-affinity ligands in the tumor microenvironment, such as RAE-1, for NKG2D occupancy. sMULT1 may abate desensitization caused by chronic exposure to RAE-1. By blocking the immunosuppressive NKG2D-RAE-1 interaction, sMULT1 may prevent NK cell silencing and, rather, promote NK cell antitumor activity.

For successful translation of these findings into the clinic, it will be important to identify the nature of the NKG2D ligand and the nature of the cells expressing this ligand in human tumor beds, as well as molecular mechanisms causing global NK desensitization. In addition, situations where NKG2D is vital for tumor destruction need to be defined, as in the case of tumors that express high amounts of NKG2D ligand, which would mark them as direct targets for an NK cell attack. Here, alternatives to a direct interception of the desensitizing interaction between NKG2D and its ligands need to be developed to preserve tumoricidal NK activity. For example, signaling pathways downstream of NKG2D involved in NK desensitization could be defined and developed as targets for cancer therapy. ∎

REFERENCES

1. E. Ullrich et al., Oncoimmunology 2, e26097 (2013).
2. W. Deng et al., Science 348, 136 (2015).
3. S. Bauer et al., Science 285, 727 (1999).
4. J. Wu et al., Science 285, 730 (1999).
5. D. H. Raulet et al., Annu. Rev. Immunol. 31, 413 (2013).
6. A. Cerwenka, J. L. Baron, L. L. Lanier, Proc. Natl. Acad. Sci. U.S.A. 98, 11521 (2001).
7. A. Diefenbach et al., Nature 413, 165 (2001).
8. N. Guerra et al., Immunity 28, 571 (2008).
9. K. Wiemann et al., J. Immunol. 175, 720 (2005).
10. J. D. Coudert et al., Blood 111, 3571 (2008).
11. H. R. Salih et al., Front. Biosci. 13, 3448 (2008).
12. V. Groh, J. Wu, C. Yee, T. Spies, Nature 419, 734 (2002).
13. L. N. Carayannopoulos et al., J. Immunol. 15, 169 (2002).
14. N. Nausch et al., Blood 112, 4080 (2008).

¹Institute for Molecular Medicine, Goethe University, Frankfurt am Main, Germany. ²Innate Immunity Group, German Cancer Research Center (DKFZ), Heidelberg, Germany. E-mail: a.cerwenka@dkfz-heidelberg.de

10.1126/science.aaa9842

Ebola and beyond

Recent experiences in confronting the Ebola epidemic suggest principles for vaccine efficacy trials in challenging environments

By Marc Lipsitch,¹*† Nir Eyal,²
M. Elizabeth Halloran,³,⁴
Miguel A. Hernán,⁵ Ira M. Longini,⁶
Eli N. Perencevich,⁷,⁸ Rebecca F. Grais⁹*

M any epidemic-prone infectious diseases present challenges that the current West African Ebola outbreak brings into sharp relief. Specifically, the urgency to evaluate vaccines, initially limited vaccine supplies, and large and unpredictable spatial and temporal fluctuations in incidence have presented huge logistical, ethical, and statistical challenges to trial design.

In the Ebola outbreak, long and intense discussion led to broad agreement on the need to evaluate the efficacy of Ebola vaccines through an individually randomized controlled trial (iRCT) (1), with cluster-randomized designs providing supplemental information.

POLICY However, by the time an iRCT began in Liberia, the ability to estimate vaccine efficacy was threatened by the otherwise welcome declining incidence of Ebola virus infection (2). Other trials, planned to provide evidence on vaccines' direct and indirect (herd immunity) effects, might not be able to include enough Ebola cases to provide statistically robust efficacy estimates (2, 3).

Similar challenges may arise when evaluating vaccines for diseases such as meningococcal meningitis, cholera, Middle East Respiratory Syndrome and other corona-virus infections, vector-borne viral diseases such as dengue and chikungunya, and novel influenza strains. Resource-poor populations continue to be at particularly high risk for such infections (4). We suggest three principles, all well-established in the clinical trials literature and applied to varying degrees in the Ebola vaccine trials, that will be of general use in designing vaccine trials during emergencies [Trials of therapies for infected persons arguably

involve a different set of logistical and ethical challenges (5)]. Each principle is mainly responding to a challenge identified in the Ebola context: block randomization with matching is a response to heterogeneity of incidence; stepped rollout is a response to urgency; and adaptive design is a response to uncertainty.

PRINCIPLE I: BLOCK RANDOMIZATION WITHIN SMALL CENTERS, WITH ANALYSIS MATCHED BY CENTER.

For Ebola and other diseases, participants in different districts might experience a surge in cases and hence in infection risk at different times after randomization, depending on the local dynamics of the epidemic. Incidence is thus likely to be considerably more similar between intervention and control participants within a center than in the population as a whole.

To deal with very different incidence across sites, we suggest that randomization of participants to investigational vaccine or control should take place separately within each center (block randomization) and that vaccine efficacy estimates should be obtained for each center and combined statistically to obtain an overall efficacy estimate. A center would be a relatively small group of persons projected to have relatively homogeneous exposure to Ebola infection over the following months. In practice, centers could be composed of the frontline workers at a single Ebola treatment unit, burial teams in a single district, or geographic subgroups of the general population. Matching the analysis by center therefore compares individuals whose risks are more similar to one another and may thereby improve statistical efficiency (6).

Using block randomization of participants within small centers would also maintain balance (and limit loss of sample size) even if at the analysis phase, it becomes necessary to exclude centers in which data are expected to be unreliable—for example, due to expected failure of vaccine delivery or the cold chain or other overwhelming logistical challenges. Previously, such an approach was successfully used to evaluate approaches to national health insurance in Mexico and ensure that a trial design was "politically robust" (7, 8). If analysis provided evidence of interference by local politicians with the randomization scheme, matched pairs of districts could be removed.

PRINCIPLE II: STEPPED ROLLOUT.

Individual centers may become ready to commence a trial at different times because of factors that include vaccine availability, timing of identification of centers and participants in areas of continuing incidence, establishment of a reliable cold chain for vaccine delivery, setting up of information systems, and contracting available trained personnel for vaccine administration and follow-up. A standard iRCT (see Fig. 1A) would await readiness of all centers before commencing. Instead, stepped rollout initiates the trial promptly in each center as soon as that center is ready (see Fig. 1B). Stepped rollout has been used for logistical (9) or political (7, 8) purposes. A key advantage of this approach is shortening the lag between starting a trial and accruing sufficient person-time (Fig. 1B). Shortening the lag may be particularly important when incidence in an area surges over several weeks due to intense transmission.

Administering an Ebola vaccine in Guinea.

PRINCIPLE III: ADAPTIVE DESIGN.

Vaccine trials require participants who are expected to be at high risk of infection weeks to months later (after an immune response has been generated). Thus, identification of trial sites relies on predictions of future incidence, which are exceedingly difficult.

The third principle states that centers can be added adaptively, which counters the unpredictability of incidence by allowing flexibility in sample size. Adaptive designs can increase statistical power by continuing to observe participants already in the trial and/or by adding centers or participants according to prespecified rules (10). For example, in the Ebola outbreak, an early estimate of the sample size for the Liberia trial was about 27,000 persons followed for 3 to 4 months (11–13). However, because of spatiotemporal variations in incidence, the follow-up time was extended to

10 to 12 months before the trial began (14).

The design of adaptive trials requires the specification of rules by which decisions to add new centers, to continue follow-up in existing centers, or to end the trial for success or futility will be made at various stages (10). This approach also permits adaptive adjustments to shifting conditions in later centers (e.g., availability of vaccine or the need for additional trial arms), based on lessons learned in earlier centers (15).

BROADER APPLICATIONS AND A RESEARCH AGENDA.

Each design principle has been employed in other settings to resolve particular challenges of trial design. We believe this combination might find broad application in many such settings and contributes to a larger effort to define common principles and practices for such settings. For example, an Ebola vaccine trial in Guinea has just begun (16) with "ring vaccination"—vaccinating "rings" of contacts and geographic neighbors of confirmed cases, a strategy previously used for smallpox eradication. To evaluate vaccine effectiveness, rings will be randomized such that all individuals in certain rings will be offered experimental Ebola vaccine immediately upon identification of a case of infection, whereas individuals in other rings will be offered vaccine only after some delay. The differential incidence of disease between rings with immediate versus delayed vaccination will be a measure of vaccine effectiveness. Enrolling new rings as Ebola cases are detected is a form of stepped rollout that, by focusing the trial in areas of known

Strategies for vaccine trials in challenging conditions. (**A**) A classic iRCT. Randomization has occurred within the whole population, and the trial can only start when all of the centers are ready. The red line represents the maximum number of participants the trial could enroll, given increasing logistical capacity. The area of the box is the total person-time in the trial; it is the size of the trial measured in person-weeks of observation. (**B**) Illustration of stepped rollout (beginning the trial at each center when that center becomes ready to participate) and adaptive design [planning to add persons in new centers (green) and/or extend person-time of observation in existing centers (yellow), depending on incidence]. The estimated person-time required to do the trial (purple box) is the same as in (A), but because under stepped rollout the trial can start earlier, it can end earlier. Parameters are all illustrative, and (for simplicity) centers are shown as becoming ready in a linear manner with time.

Strategies for vaccine trials

A Standard design

B Adaptive design with stepped rollout

transmission, is particularly well suited to circumstances of spotty and declining incidence. The design is adaptive as well, adding rings until there is sufficient statistical evidence to stop the trial, because at that point there is either enough evidence to declare the vaccine efficacious (success) or no reasonable likelihood of garnering such evidence by continuing the trial (futility). In addition, to improve comparability of the risk between vaccinated and not-yet-vaccinated people, immediate-vaccination rings can be matched for analysis with delayed rings that are similar in certain ways (e.g., geographically proximate rings).

Limited infrastructure, unpredictable variation in incidence, and a public health imperative to provide vaccine as quickly as possible are common in vaccine efficacy trials, even outside public health emergencies. Conduct of vaccine trials in outbreak settings and in populations most likely to benefit from vaccination is fraught with difficulties
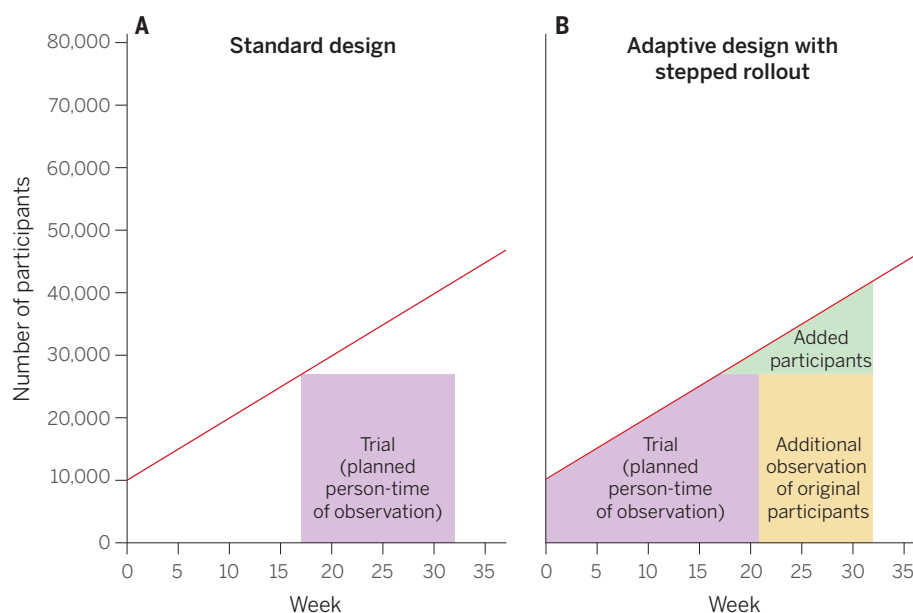
but reveals essential information about vaccine performance. Trial designs that are appropriately adapted to the most challenging settings are sorely needed, not only to improve the external validity of trial results but also to ensure that vaccine quickly reaches those most in need.

Outside the Ebola context, feasibility of particular designs will depend not only on the epidemiology of the relevant disease (time and spatial scale of transmission, ease of diagnosis, etc.) but also on the characteristics of the vaccines being tried (including number of doses required, timing of immunogenicity, and potential for post-exposure effectiveness). Ethical considerations of speeding the availability of possibly efficacious vaccines to large numbers of people will need to be balanced against the need for evaluation of vaccine efficacy so that resources can be concentrated on effective interventions. But discussions of ethical, logistical, and statistical considerations in trial design take time, and rapid implementation of studies is important for timely and reliable results before the epidemic wanes. The more such discussions can take place outside emergencies and establish general principles to inform vaccine trial designs in future outbreaks, the more effective the responses to such outbreaks will be. ∎

[1]Center for Communicable Disease Dynamics and Departments of Epidemiology and Immunology and Infectious Diseases, Harvard T. H. Chan School of Public Health, Boston, MA 02115, USA. [2]Department of Global Health and Population, Harvard T. H. Chan School of Public Health and Center for Bioethics, Harvard Medical School, Boston, MA, USA. [3]Center for Inference and Dynamics of Infectious Diseases, Vaccine and Infectious Disease Division, Fred Hutchinson Cancer Research Center, Seattle, WA, USA. [4]Department of Biostatistics, University of Washington, Seattle, WA 98105, USA. [5]Center for Communicable Disease Dynamics and Departments of Epidemiology and Biostatistics, Harvard T. H. Chan School of Public Health, and Harvard-MIT Division of Health Sciences and Technology, Boston, MA, USA. [6]Center for Inference and Dynamics of Infectious Diseases, Department of Biostatistics, College of Public Health and Health Professions, and College of Medicine, University of Florida, Gainesville, FL, USA. [7]Department of Internal Medicine, University of Iowa Carver College of Medicine, Iowa City, IA, USA. [8]Center for Comprehensive Access and Delivery Research and Evaluation, Iowa Veterans Affairs Health Care System, Iowa City, IA, USA. [9]Epicentre, Paris, France. *Corresponding author. E-mail: mlipsitc@hsph.harvard.edu (M.L.); Rebecca.grais@epicentre.msf.org (R.F.G.)†Present address: Visiting Professor, Department of Infectious Disease Epidemiology, Imperial College London, London, UK.

REFERENCES AND NOTES

1. WHO high-level meeting on Ebola vaccines access and financing, 23 October 2014; http://apps.who.int/iris/bitstream/10665/137184/1/WHO_EVD_Meet_EMP_14.2_eng.pdf?ua=1&ua=1
2. J. H. Giahyue, Liberia begins clinical trial for Ebola vaccines as outbreak ebbs. Reuters, 2 February 2015; www.reuters.com/article/2015/02/02/ health-ebola-vaccines-idUSL6N0VC2AE20150202 (2015).
3. A. Maxmen, Why we're still waiting on an Ebola vaccine. Al Jazeera America, 11 March 2015; http://america.aljazeera.com/articles/2015/3/11/why-were-still-waiting-on-an-ebola-vaccine.html
4. SAGE Working Group on Vaccination in Acute Humanitarian Emergencies, Vaccination in acute humanitarian emergencies: A framework for decision-making (WHO, Geneva, 2013; www.who.int/iris/handle/10665/92462
5. C. Adebamowo et al., Lancet **384**, 1423 (2014).
6. J. P. Matts, J. M. Lachin, Control. Clin. Trials **9**, 327 (1988).
7. G. King et al., Lancet **373**, 1447 (2009).
8. G. King et al., J. Policy Anal. Manage. **26**, 479 (2007).
9. C. C. Iwuji et al., Trials **14**, 230 (2013).
10. C. Jennison, B. Turnbull, Group sequential methods with applications to clinical trials, 2000; Chapman-Hall/CRC, Boca Raton, FL.
11. WHO, WHO high-level meeting on Ebola vaccines access and financing: Summary report, 23 October 2014; http://apps.who.int/iris/bitstream/10665/137184/1/WHO_EVD_Meet_EMP_14.2_eng.pdf?ua=1
12. H. Branswell, Improved Ebola situation in Liberia may complicate vaccine trials, Scientific American; www.scientificamerican.com/article/improved-ebola-situation-liberia-may-complicate-vaccine-trials (2014).
13. F. Fleck, A. Lesher, Bull. World Health Organ. **93**, 7 (2015).
14. NIAID, PREVAIL Phase 2/3 clinical trial of investigational Ebola vaccines, 2 February 2015; www.niaid.nih.gov/news/QA/Pages/EbolaVaxResultsQA.aspx. (2015).
15. World Health Organization, "Experimental Ebola Vaccines. Situation report, 1 October 2014; www.who.int/mediacentre/news/ebola/01-october-2014/en/" (2014).
16. WHO/MSF/NIPH, Ebola vaccine efficacy trial ready to launch in Guinea, 5 March 2015; www.who.int/mediacentre/news/releases/2015/ebola-vaccine-trial/en/

CANCER

The guardian of the genome

Inside the quest to characterize the role of p53 in cancer

By **Anna Mandinova* and Sam W. Lee**

The discovery of the tumor suppressor protein known as p53, and the process of unearthing its functions, came about as a result of the efforts of thousands of scientists around the globe. The story of this endeavor is full of exciting breakthroughs, as well as disappointing setbacks, and is sure to be compelling to those who are taking their first steps toward a career in cancer science or for those who are simply fascinated by the mysteries of biology.

In *p53: The Gene That Cracked the Cancer Code*, science writer Sue Armstrong takes a fresh look at this complicated tale. The book is well researched and features interviews with key scientists. The result is a brilliant narrative that captures the essence of the scientific challenges faced by researchers in this pursuit and the progress that has been made in our understanding of p53.

Armstrong begins in the late 1970s, when scientists in laboratories around the world were studying the ability of a virus named SV40 to induce tumor growth. During the laborious purification of the large T antigen—a protein product transcribed during SV40 infection that researchers believed was critical to transforming normal cells into cancerous ones—they noticed an unknown contaminant. The contaminant was also present in excessive amounts in SV40-transformed cells. It turned out to be a previously unknown protein, which was given the unassuming name p53.

Next, Armstrong skillfully describes the efforts that led to the transformation of p53 from an artifact into a high-profile "guardian of the human genome" (*1*). This part of the narrative is marked by unexpected results. Researchers initially believed that *TP53* (the gene that codes for p53) was an oncogene involved in the malignant transformation of cells, which caused the development of various types of solid tumors. Its true role as a tumor suppressor that safeguards cellular DNA from damage and gov-

The reviewers are at the Massachusetts General Hospital, Harvard Medical School, Building 49, 13th Street, Charlestown, MA 02129, USA. *Corresponding author. E-mail: amandinova@mgh.harvard.edu

p53
The Gene That Cracked the Cancer Code
Sue Armstrong
Bloomsbury Sigma, 2015.
287 pp.
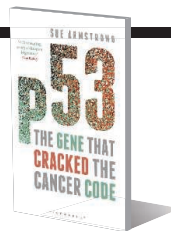
erns DNA repair and stress response was recognized in the late 1980s.

The book also addresses other cellular processes that are affected by p53 signaling, including senescence and immune response, and touches upon Li-Fraumeni syndrome, a rare hereditary disorder linked to p53 germline mutations, which is characterized by higher incidences of several types of cancer. An especially captivating part of this book is the parallel discussion of several recent fundamental discoveries in biology, including the sequencing of the human genome, the discovery of long noncoding RNAs (lncRNAs), and progress made in other oncogenic pathways. The narrative concludes with a discussion of the various therapeutic approaches inspired by discoveries in the p53 field and ends with a message of hope for future cures.
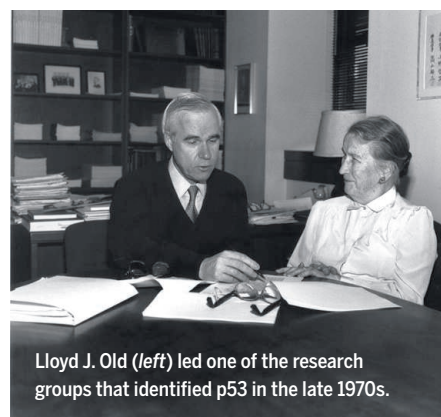
Lloyd J. Old (*left*) led one of the research groups that identified p53 in the late 1970s.

Although presented in the background, the dedication, talent, and personal sacrifices of generations of brilliant cancer researchers come across in this book. The daily struggles and challenges posed by failed experiments and controversial results are not forgotten in the narrative and are woven throughout the stories of enthusiasm and excitement. For those who have had personal brushes with cancer, this book will provide a reassuring picture of the progress of cancer research. However, its balanced portrayal of the challenges and setbacks that are common in oncology research should temper any premature enthusiasm.

More than any textbook, article, or lecture could, this book offers a sip of contagious enthusiasm and a conviction that scientists will eventually "crack the cancer code."

REFERENCES

1. T. Strachan, A. P. Read, *Human Molecular Genetics*, (Wiley, New York, ed. 2, 1999), chap. 18.

Five years later, questions remain about the ecological impact of the Deepwater Horizon oil spill.

IN BRIEF

A Sea in Flames
The Deepwater Horizon Oil Blowout
Carl Safina
Crown Publishers, 2011, 373 pp.
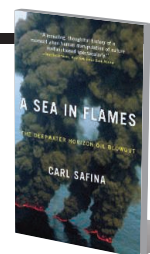
In *A Sea in Flames*, ecologist Carl Safina captures the chaos and confusion that surrounded the 2010 explosion aboard the drill rig Deepwater Horizon in clear, vivid prose. Drawing on first-hand observations, interviews, and extensive research, he recounts the events that led up to the explosion, skewers the petroleum industry and the government officials charged with overseeing the response to the resulting oil spill, and conveys the anguish and frustration felt by scientists and coastal fishermen who feared the worst for the Gulf's marine ecosystem.

EXHIBITION

Objectified

An artist's approach to materials science

By **Deborah Dixon**

Cornelia Parker
Mary Griffiths, Curator
The Whitworth, Manchester, UK
14 February 2015 to 31 May 2015

F ollowing the exhibition of her installation *Cold Dark Matter: An Exploded View* in 1991, Cornelia Parker became a key figure in a new sort of cross-disciplinary collaboration between science and art. These collaborations combine the sense of wonder and excitement experienced by scientists when new materials emerge with an artist's interpretations of the possibilities these new materials create.

Cold Dark Matter—which forms the nucleus of Parker's latest retrospective—was formed by blowing up a garden shed. The resulting fragments have been sorted and choreographed into a new formation that has an extraordinary presence. The title of the piece evokes the Big Bang, and the shadows cast by the fragments seem to reference the vast, insensible mass of dark matter thought to permeate the universe. Closer observation reveals the mundane, everyday objects that have been

VIDEO

See Cornelia Parker discuss the making of *Blakean Abstract* at http://bit.ly/Blakean

caught up in this choreography: a shredded hot water bottle, a still folded deck chair, gardening tools. Torn from their usual usage, they seem to flock with new energy.

This emphasis on material transformation is taken further in subsequent pieces. Some are playful—for example, *Measuring Niagara with a Teaspoon* (2007) stretches this dainty object into a wire the height of Niagara Falls, while *Composition with Horns (Double Flat)* (2005) consists of 16 crushed instruments

suspended inches above the floor.

However, there is no doubting Parker's preoccupation with objects that highlight the linkages between the state and violence and suffering. A filmed interview with Noam Chomsky (2007) on the banalization of violence and cruelty, for example, is followed up by a series of needlework samplers (2015) produced by inmates of Her Majesty's Prisons, each of which are inscribed with dictionary definitions of war and peace, life and death, and so on. A specially commissioned installation, *War Room* (2015), uses the perforated reams of red paper from which war memorial poppies are cut to swathe an entire gallery wing. There is no sentimentality here but rather a reference to the manner in which remembrance has become an unreflective, readily industrialized habit.

The performance that opened the exhibition was a collaboration between Parker and Konstantin Novoselov, who won the Nobel Prize for Physics in 2010 for his co-discovery of graphene. Novoselov extracted graphite from pencil traces on a drawing by the Romantic painter and poet William Blake and used these to produce a sample of graphene. The graphene was used to create a field-effect transistor that formed the basis of a humidity-sensitive sensor. When Novoselov breathed on the sensor (*Breath of a Physicist*, 2015), a firework display, choreographed by Parker, was initiated (*Blakean Abstract*, 2015). The emphasis here is on a constant material transformation that defies our efforts to fix the nature and meaning of objects. What such a bravura spectacle also celebrates is the potential not only for a meeting of minds but also for a more visceral mingling of bodies at work.

The reviewer is at the School of Geographical and Earth Sciences, University of Glasgow, East Quadrangle, University Avenue, Glasgow G12 8QQ, Scotland. E-mail: deborah.dixon@ glasgow.ac.uk
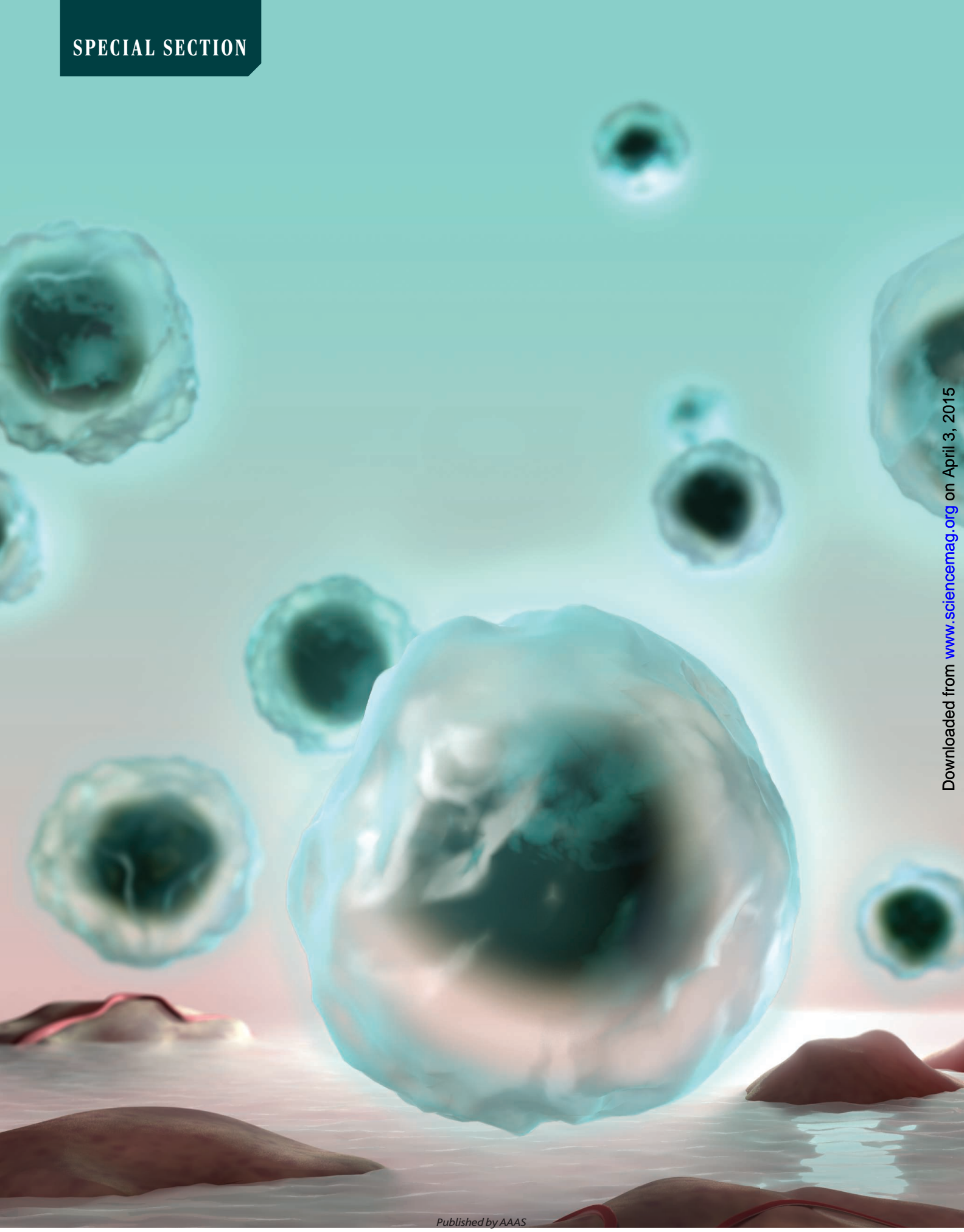
REALIZING THE
PROMISE

by **Kristen L. Mueller**

F or cancer treatment, 2011 marked the beginning of a new era. Fifteen years after *Science* published a paper showing that antibodies blocking an inhibitory receptor on the T cell surface unleash these T cells to kill tumors in mice, the U.S. Food and Drug Administration approved such an antibody for use in treating melanoma. The idea of harnessing immune cells to fight cancer isn't new, but only recently have scientists amassed enough clinical data to demonstrate what a game-changer cancer immunotherapy can be.

The underlying basis of cancer immunotherapy is to activate a patient's own T cells so that they can kill their tumors. Reports of amazing recoveries abound, where patients remain cancer-free many years after receiving the therapy.

Given this success, what is the best pathway forward? Currently, only a fraction of patients respond to immunotherapy, and immunotherapy only works in a subset of cancers. Understanding why is essential. This will require a multifaceted approach that involves designing innovative clinical trials to access important patient samples and determining which cancer therapies can be combined to give the best efficacy. Basic science is also critical: Unraveling the complex interplay of cells in the tumor microenvironment, understanding how tumor mutational load influences therapeutic efficacy, and dissecting how our resident microbes shape the development and treatment of cancer will also provide important insights that will forge the way toward improving existing therapies and developing new ones. This field is no stranger to obstacles, so the future looks very promising indeed.

ILLUSTRATION: V. ALTOUNIAN/*SCIENCE*

REVIEWS

The future of immune checkpoint therapy

Padmanee Sharma[1,2]* and James P. Allison[1]*

Immune checkpoint therapy, which targets regulatory pathways in T cells to enhance antitumor immune responses, has led to important clinical advances and provided a new weapon against cancer. This therapy has elicited durable clinical responses and, in a fraction of patients, long-term remissions where patients exhibit no clinical signs of cancer for many years. The way forward for this class of novel agents lies in our ability to understand human immune responses in the tumor microenvironment. This will provide valuable information regarding the dynamic nature of the immune response and regulation of additional pathways that will need to be targeted through combination therapies to provide survival benefit for greater numbers of patients.

The field of immune checkpoint therapy has joined the ranks of surgery, radiation, chemotherapy, and targeted therapy as a pillar of cancer therapy. Three new immune checkpoint agents have now been approved by the U.S. Food and Drug Administration (FDA) for the treatment of melanoma, and there is a high expectation that these agents, and others in this class, will also be approved over the next several years for treatment of patients with lung cancer, kidney cancer, bladder cancer, prostate cancer, lymphoma, and many other tumor types. The antibody against CTLA-4 ipilimumab was approved in 2011, and two antibodies against PD-1 (pembrolizumab and nivolumab) were approved in 2014. These drugs represent a radical and disruptive change in cancer therapy in two ways. First, they do not target the tumor cell, but target molecules involved in regulation of T cells, the soldiers of the immune system. And, perhaps in a more radical shift, the goal of the therapy is not to activate the immune system to attack particular targets on tumor cells, but rather to remove inhibitory pathways that block effective antitumor T cell responses. Immune checkpoint therapy, with anti-CTLA-4 having longer follow-up than other agents, leads to durable clinical responses that can last a decade and more, but only in a fraction of patients. There are ongoing studies to identify predictive biomarkers with which to select patients for treatment with a particular agent, but the complexity of the immune response has made this difficult.
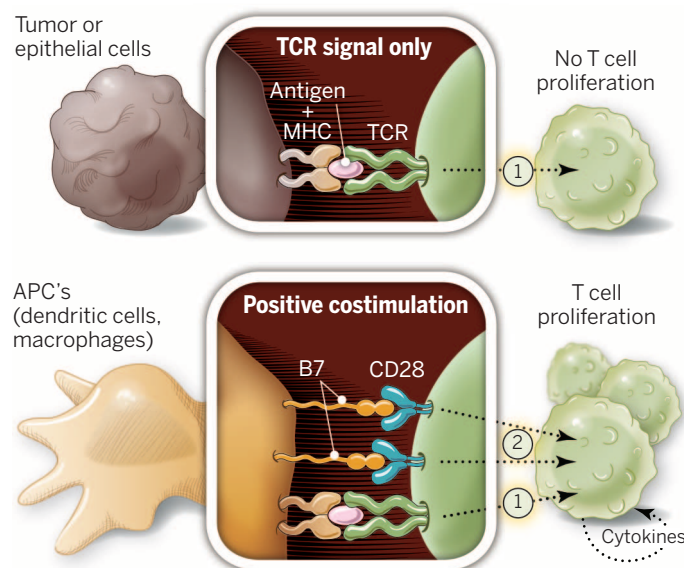
Fig. 1. Activation of T cells requires two signals. T cell activation occurs only after interaction between T cell receptor (TCR) and antigen in the context of MHC (signal 1) plus CD28 costimulation (signal 2).

In the past two decades, remarkable advances in basic science have led to new strategies for the treatment of cancer, which are justifiably generating optimism that it may soon be possible to cure a subset of patients with some types of cancer. We now have detailed knowledge of the molecular basis of cancer to allow a more "personalized" treatment based on genomic sequencing of an individual's cancer cells to identify specific mutations in genes. These mutations can then be targeted with compounds to block the downstream pathways that drive cancer development and progression. Therefore, each specific mutation serves as the predictive biomarker for selecting patients for treatment with a given agent. For example, patients with melanoma whose tumors harbor the BRAFV600E mutation, which enables constitutive activation of the BRAF signaling pathway, would be selected to receive treatment with an agent that inhibits BRAF (1, 2). These targeted therapies have led to promising clinical responses, albeit generally of short duration, in patients whose tumors express the appropriate target biomarker.

The clinical success of genomically targeted agents laid the foundation for other cancer therapies, including the prerequisite to identify predictive biomarkers for selection of patients for treatment. Eventually, as the field of cancer immunotherapy found clinical success with agents based on a greater understanding of how to unleash T cell responses by targeting immune checkpoints, it became clear that the framework used for identification of predictive biomarkers for genomically targeted agents would present a challenge. As opposed to mutated genes in tumors that permanently mark a tumor, the immune response is dynamic and changes rapidly. Therefore, the issue facing the field of cancer immunotherapy may not be the identification of a single biomarker to select a subset of patients for treatment. Instead, we must assess the effectiveness of an evolving immune response, define the immune response that contributes to clinical benefit, and then, hopefully, drive every patient's immune response in that direction through combination therapies.

Tumor microenvironment: Cancer cells and host immune responses

Tumors are composed of many cell types, including the cell of origin with genetic alterations and a myriad of other cells, such as fibroblasts, endothelial cells, and eventually, perhaps, a variety of immune cells. Initially the immune infiltrates may be scarce, but eventually may contain natural killer (NK) cells and macrophages with lytic capacity and, perhaps most importantly, T cells. T cells attack tumor cells that express tumor-specific antigens in the form of complexes of tumor-derived peptides bound to major histocompatibility complex (MHC) molecules on the cell. The tumor antigens can be derived from oncogenic viruses, differentiation antigens, epigenetically regulated molecules such as cancer testes antigens, or neoantigens derived from mutations associated with the process of carcinogenesis (3). T cells survey the microenvironment and become activated when tumor antigens are recognized. They then proliferate and differentiate, ultimately leading to the T cell's ability to attack and destroy cells that express relevant antigens. However, regulation of T cell responses is an extremely complex process consisting of both stimulatory and inhibitory cell intrinsic signaling pathways, which limit T cell responses against cancer and prevent eradication of tumors.

Recognition of antigen-MHC complexes by the T cell antigen receptor is not sufficient for

[1]Department of Immunology, M.D. Anderson Cancer Center, Houston, TX, USA. [2]Genitourinary Medical Oncology, M.D. Anderson Cancer Center, Houston, TX, USA.
*Corresponding author. E-mail: padsharma@mdanderson.org (P.S.); jallison@mdanderson.org (J.P A.)

activation of naïve T cells—additional costimulatory signals (*4*, *5*) are required that are provided by the engagement of CD28 on the T cell surface with B7 molecules (CD80 and CD86) on the antigen-presenting cell (APC) (Fig. 1). Expression of B7 molecules is limited to subsets of hematopoietic cells, especially dendritic cells, which have specialized processes for efficient antigen presentation. With the exception of certain lymphomas, cancer cells do not express B7 molecules, and hence are largely invisible to the immune system. This can be overcome by an inflammatory response, such as the killing of tumor cells, which permits APCs, such as dendritic cells, to take up antigen and present antigen bound to MHC along with B7 molecules for effective activation of T cells.

After encountering tumor antigen in the context of B7 costimulation, initially in tumor-draining lymph nodes, tumor-specific T cells may acquire effector function and traffic to the tumor site to mount an attack on the tumor. Infiltration of T cells into the tumor microenvironment is a critical hurdle that must be overcome for an effective antitumor immune response to occur. However, once T cells are in the tumor microenvironment, the success of the assault is determined by their ability to overcome additional barriers and counter-defenses they encounter from the tumor cells, stroma, regulatory T cells, myeloid-derived suppressor cells, inhibitory cytokines, and other cells in the complex tumor microenvironment that act to mitigate antitumor immune responses.

In the 1980s, tumor antigens from human melanomas were found to elicit T cell responses (*6*), which drove efforts to use vaccination strategies to mobilize the immune system to attack cancer. The vaccines generally consisted of some form of the antigen (for example, peptide or DNA vaccines), as well as additional components to enhance responses (for example, cytokines).

While there were anecdotal successes, in hundreds of trials there was scant evidence of reproducible clinical responses (*7*). This failure to induce effective immune responses by attempting to turn T cell response "on" with antigenic vaccines led many to become skeptical of the potential of immunotherapy as a strategy for cancer treatment.

Regulation of T cell responses

Further insights into the fundamental mechanisms that regulate early aspects of T cell activation may provide one of many possible explanations for the limited effectiveness of these early vaccine trials. By the mid-1990s, it was becoming clear that T cell activation was even more complex, and in addition to initiating proliferation and functional differentiation, T cell activation also induced an inhibitory pathway that could eventually attenuate and terminate T cell responses. Expression of *ctla-4*, a gene with very high homology to CD28, is initiated by T cell activation, and, like CD28, CTLA-4 binds B7 molecules, albeit with much higher affinity. Although CTLA-4 was first thought to be another costimulatory molecule (*8*), two laboratories independently showed that it opposed CD28 costimulation and down-regulated T cell responses (*9*, *10*). Thus, activation of T cells results in induction of expression of CTLA-4, which accumulates in the T cell at the T cell–APC interface, reaching a level where it eventually blocks costimulation and abrogates an activated T cell response (Fig. 2).

Based on knowledge of the function of CTLA-4, we proposed that blocking its interaction with the B7 molecules might allow T cell responses to persist sufficiently to achieve tumor eradication. We hypothesized that this could be achieved by releasing the endogenous immune responses, perhaps even without specific knowledge of the antigenic targets of those responses or even

the type of cancer. We also proposed that combination treatment with an antibody against CTLA-4 and agents that directly killed tumor cells to release antigens for presentation by APCs to T cells would improve antitumor responses. Our hypotheses were tested in many different experiments in mice (*11–15*), with data generated to support the concept, leading to the development of ipilimumab, an antibody against human CTLA-4 for clinical testing. Ipilimumab led to considerable improvement in overall survival for patients with metastatic melanoma (*16*, *17*), which led to FDA approval in 2011.

The preclinical successes of anti-CTLA-4 in achieving tumor rejection in animal models and the ultimate clinical success opened a new field of immune checkpoint therapy (*18*, *19*). It is now known that there are many additional immune checkpoints. Programmed cell death–1 (PD-1) was shown in 2000 to be another immune checkpoint that limits the responses of activated T cells (*20*). PD-1, like CTLA-4, has two ligands, PD-L1 and PD-L2, which are expressed on many cell types. The function of PD-1 is completely distinct from CTLA-4 in that PD-1 does not interfere with costimulation, but interferes with signaling mediated by the T cell antigen receptor (*4*). Also, one of its ligands, PD-L1 (B7-H1), can be expressed on many cell types (Fig. 2), including T cells, epithelial cells, endothelial cells, and tumor cells after exposure to the cytokine interferon-γ (IFN-γ), produced by activated T cells (*21*). This has led to the notion that rather than functioning early in T cell activation, the PD-1/PD-L1 pathway acts to protect cells from T cell attack.

Immune checkpoint therapy in the clinic

Ipilimumab, a fully human antibody to human CTLA-4, entered clinical trials in the late 1990s and early 2000s. As predicted, tumor regression was observed in patients with a variety of tumor types. Phase I/II trials showed clinical responses in
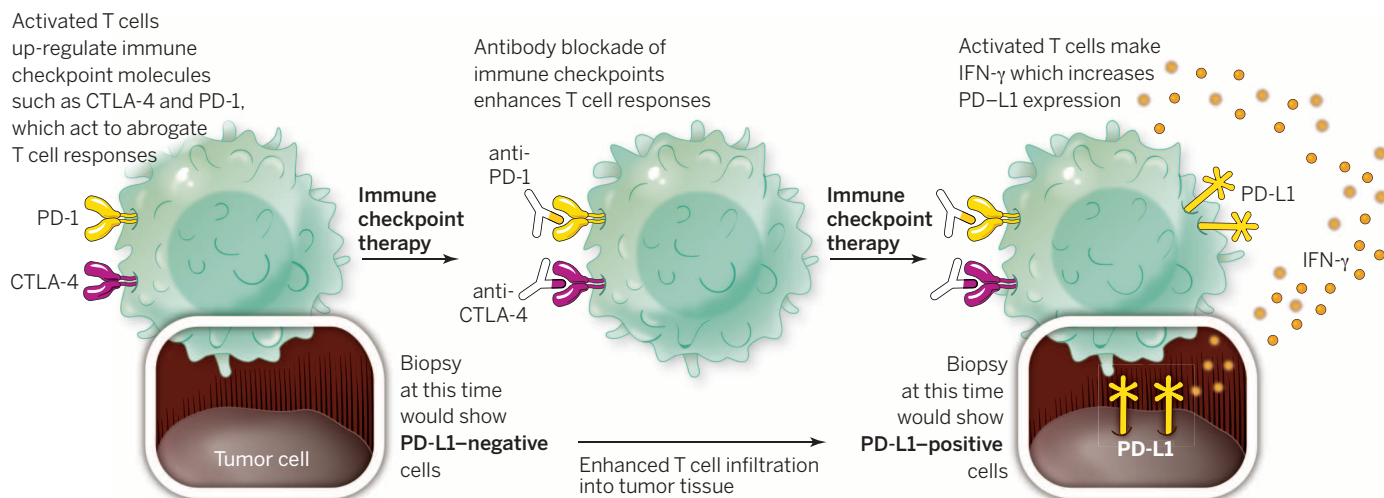
Fig. 2. Blockade of immune checkpoints to enhance T cell responses. After T cell activation, T cells express immune checkpoints such as CTLA-4 and PD-1. A biopsy of tumors taken from patients before treatment with immune checkpoint therapy (so prior to infiltration of activated T cells into tumor tissues) may indicate lack of PD-L1 expression. However, upon T cell activation, T cells can traffic to tumors, up-regulate expression of immune checkpoints such as CTLA-4 and PD-1, and produce cytokines such as IFN-γ, which leads to expression of PD-L1 on tumor cells and other cells, including T cells, within the tumor tissues.

patients with melanoma (22), renal cell carcinoma (23), prostate cancer (24), urothelial carcinoma (25), and ovarian cancer (26). Two phase III clinical trials with anti-CTLA-4 (ipilimumab) were conducted in patients with advanced melanoma and demonstrated improved overall survival for patients treated with ipilimumab (16, 17). Importantly, durable responses were observed in about 20% of patients living for more than 4 years, including a recent analysis indicating survival of 10 years or more for a subset of patients (27).

Antibodies targeting the PD-1/PD-L1 axis have also shown clinical responses in multiple tumor types. Anti-PD-L1 antibodies led to tumor regression in patients with melanoma, renal cell carcinoma, non–small cell lung cancer (28), and bladder cancer (29). Phase I clinical trials with anti-PD-1 (nivolumab) demonstrated similar clinical responses (30). Recently, a large phase I clinical trial with the anti-PD-1 antibody MK-3475 was shown to lead to response rates of ~37 to 38% in patients with advanced melanoma (31), with a subsequent study reporting an overall response rate of 26% in patients who had progressive disease after prior ipilimumab treatment (32), which led to FDA approval of MK-3475 (pembroluzimab) in September 2014. A phase III trial of a different anti-PD-1 antibody (nivolumab) also showed clinical benefit in patients with metastatic melanoma. In this trial, the objective response rate was 40% and overall survival rate was 72.9% for patients treated with nivolumab as compared to an objective response rate of 13.9% and overall survival rate of 42.1% for patients treated with dacrabazine chemotherapy (33). Nivolumab received FDA approval in December 2014 as a treatment for patients with metastatic melanoma. In addition, nivolumab was FDA-approved in March 2015 for patients with previously treated advanced or metastatic non–small cell lung cancer based on a phase III clinical trial, which reported an improvement in overall survival for patients treated with nivolumab as compared to patients treated with docetaxel chemotherapy.

That CTLA-4 and PD-1 regulate distinct inhibitory pathways and have nonoverlapping mechanisms of action suggested that concurrent combination therapy with both might be more efficacious than either alone. This was indeed shown to be the case in preclinical studies in murine models (34). In 2013, a phase I clinical trial with anti-CTLA-4 (ipilimumab) in combination with anti-PD-1 (nivolumab) demonstrated tumor regression in ~50% of treated patients with advanced melanoma, most with tumor regression of 80% or more (35). There are ongoing clinical trials with anti-CTLA-4 plus anti-PD-1, or anti-PD-L1, in other tumor types, with preliminary data indicating promising results, which highlight this novel combination as an effective immunotherapy strategy for cancer patients.

Tissue-based immune monitoring: Anti-CTLA-4 therapy

Properly designed presurgical or tissue-based trials, where treatment is administered before surgical resection of tumors, can provide valuable insight into the cellular and molecular mechanisms of immune checkpoint therapy by providing sufficient tissues to conduct a battery of analyses. Data gathered from analysis of tumor tissue can then guide rational searches for relevant markers in the blood. We designed the first presurgical clinical trial with anti-CTLA-4 (ipilimumab), which was administered to 12 patients with localized bladder cancer prior to radical cystectomy (36). The endpoints of this study were safety and access to samples for immune monitoring. We did not view this trial as a neoadjuvant study, which administers therapy prior to surgery for clinical benefit, but as a presurgical study to provide mechanistic insights regarding the impact of anti-CTLA-4 therapy on the tumor microenvironment. Unexpectedly,

> "Because of the very nature of immune checkpoint therapy, the development of pharmacodynamic, predictive, or prognostic biomarkers faces unique challenges."

the trial enabled us to detect a clinical signal for anti-CTLA-4 as a therapeutic agent for patients with bladder cancer since three patients had no residual tumors identified within the cystectomy samples. This trial was also successful in establishing the safety of anti-CTLA-4 in the presurgical setting, which would be important for future trials, and obtaining patients' matched tumor and blood samples for immune monitoring. This work laid the foundation for using presurgical trials as an important tool to evaluate human immune responses in the tumor microenvironment, which should be included in the current paradigm of phase I, II, and III clinical trials.

The collection of fresh tumor samples at the time of surgery can provide sufficient tissue for genetic, phenotypic, and functional studies, as well as material for immunohistochemical (IHC) analyses, which can provide extensive insight into the biologic impact of the immunotherapy agent on the tumor microenvironment. For example, high-quality mRNA can be obtained for gene expression studies comparing posttreatment tumor tissues to pretreatment tumor tissues or untreated samples obtained from a stage-matched control group of patients. These types of studies allow unbiased analyses of the samples to identify novel genes and pathways that are affected by therapy. In our ipilimumab trial, gene array data revealed that most of the differences between treated and untreated samples could be attributed to pathways involved in T cell signaling, which is not surprising given the large increases in T cell infiltrates in tumor tissues after

CTLA-4 blockade (25, 26). The most pronounced difference was an increase in T cells that express inducible costimulator (ICOS), a T cell surface molecule that is a closely related member of the extended CD28/CTLA-4 family. We confirmed our gene expression studies by flow cytometry. ICOS+ T cells were increased in tumor tissues from patients treated with ipilimumab (36). The increase in the frequency of ICOS+ T cells in tumor infiltrates was accompanied by similar increases in the blood. These data, coupled with other studies, showed that an increase in the frequency of ICOS+ CD4 T cells served as a pharmacodynamic biomarker of anti-CTLA-4 treatment (37).

To test our hypothesis that ICOS+ CD4 T cells might play a role in the therapeutic effect of CTLA-4 blockade, we conducted studies in mice. In wild-type C57BL/6 mice, anti-CTLA-4 treatment resulted in tumor rejection in 80 to 90% of mice, but in gene-targeted mice that were deficient for either ICOS or its ligand, the efficacy was less than 50% (38). The loss of efficacy of CTLA-4 blockade in the absence of an intact ICOS pathway indicates the critical importance of ICOS to the therapeutic effects of treatment with anti-CTLA-4 antibodies. The important role played by ICOS in the effectiveness of CLTA-4 blockade suggested that providing an agonistic stimulus for the ICOS pathway during anti-CTLA-4 therapy might increase its effectiveness. To test this notion, we conducted studies in mice to provide an agonistic signal through ICOS in combination with CTLA-4 blockade. We found that combination therapy resulted in an increase in efficacy that was about four to five times as large as that of control treatments (39). Thus, ICOS is a stimulatory checkpoint that provides a novel target for combination immunotherapy strategies. Antibodies for ICOS are being developed for clinical testing, which are expected to start within the next year.

Whereas some presurgical and tissue-based trials are focused on evaluating human immune responses in the tumor microenvironment, other studies have focused on evaluating components of the cancer cells that may contribute to clinical benefit with anti-CTLA-4. Genetic analyses of melanoma tumors revealed that higher numbers of mutations, termed "mutational load," and creation of new antigens that can be recognized by T cells as a result of these mutations, termed "neoantigens," correlated with clinical responses to anti-CTLA-4 therapy (3, 40). These studies provide a strong rationale to integrate genetic analyses of the tumor with immune profiling of the tumor microenvironment for a more comprehensive evaluation of mechanisms that contribute to clinical responses with anti-CTLA-4 therapy.

Tissue-based immune monitoring: Anti-PD-1/PD-L1 therapy

Given that immune checkpoint therapy only benefits a fraction of patients, there are ongoing efforts to identify predictive biomarkers that could be used to select patients for treatment.

Because the PD-1 ligand PD-L1 (and sometimes PD-L2) can be expressed on tumor cells and immune cells in the tumor microenvironment, there have been efforts to use expression of PD-L1 as a criterion for selecting patients for treatments with antibodies targeting the PD-1/PD-L1 pathway.

The initial phase I trial with anti-PD-1 therapy (nivolumab) reported that PD-L1 expression on tumor cells, measured on pretreatment archival samples by immunohistochemical (IHC) methods, may potentially serve as a predictive marker to indicate which patients would benefit from treatment (30). Patients with PD-L1–positive tumors (≥5% staining for PD-L1 on tumor cells) had an objective response rate of 36% (9 of 25 patients) whereas patients with PD-L1–

negative tumors did not show any objective clinical responses (0 of 17 patients). However, in subsequent trials, some patients whose tumors were deemed to be PD-L1–negative had clinical responses to anti-PD-1 and anti-PD-L1 treatments with either tumor regression or stabilization of disease. For example, on a phase I trial with anti-PD-1 (nivolumab), patients with PD-L1–positive tumors had an objective response rate of 44% (7 of 16) and patients with PD-L1–negative tumors had an objective response rate of 17% (3 of 18) (41). Although PD-L1 expression in tumor tissues does correlate with higher response rates, it is not predictive for clinical benefit. Furthermore, current data indicate that the differences in response rates do not translate to differences in survival benefit. For patients with

metastatic melanoma who received treatment with nivolumab on a phase III trial, the median overall survival had not been reached for either PD-L1 subgroup, and both subgroups had improved overall survival as compared to patients who received dacarbazine chemotherapy (33).

In a phase I study of anti-PD-L1 (MPDL3280A), patients with bladder cancer were considered to have PD-L1–positive tumors if their pretreatment archival tumor samples contained ≥5% PD-L1–positive tumor-infiltrating immune cells (29). Twenty-one patients with PD-L1–positive tumors were enrolled onto the trial prior to enrollment of patients with PD-L1–negative tumor samples. Data were reported after a minimum of 6 weeks of follow-up. An objective response rate of 43.3% (13 out of 30 patients) and stable disease rate of 26.7% (8 of 30) was reported for patients with PD-L1-positive tumors, which was compared to an objective response rate of 11.4% (4 of 35 patients) and stable disease rate of 37.1% (13 of 35) for patients with PD-L1–negative tumors. Because the patients with PD-L1–positive tumors received treatment for a longer period of time as compared to patients with PD-L1–negative tumors, it is unclear if the difference in response rates in this study was due to PD-L1 expression or time on treatment. However, for patients with metastatic bladder cancer whose disease had progressed after first-line chemotherapy and in a setting where there are no approved second-line treatments, an objective response rate of 11% and stable disease rate of 37.1% are clinically relevant.

Similarly, in another phase I study of anti-PD-L1 (MPDL3280A) in multiple tumor types, objective response rates were reported as 46% in the cohort of patients whose tumors had the highest PD-L1-expression, 17% in the cohort of patients whose tumors had moderate expression of PD-L1, 21% in the cohort of patients whose tumors had minimal PD-L1 expression, and 13% in the cohort of patients whose tumors had no detectable level of PD-L1 expression (42). Thus, this trial also showed that patients whose tumors were deemed as PD-L1–negative can have objective responses. Interestingly, the cohort of patients whose tumors were categorized as moderate expression of PD-L1, which correlates with PD-L1-positive status, had objective responses (17%) and median progression-free survival (18 weeks) that were similar to the objective responses (21%) and median progression-free survival (17 weeks) of the cohort of patients whose tumors had minimal expression of PD-L1, which correlates with PD-L1–negative status. Additional studies will be needed to determine whether PD-L1 expression in the tumor microenvironment affects survival outcomes for patients treated with anti-PD-L1.

On the basis of data reported thus far, it seems fair to conclude that expression of PD-L1 in tumor tissues should not be used as a predictive biomarker for selection or exclusion of patients for treatment with either anti-PD-1 or anti-PD-L1 antibodies. In a study of primary and
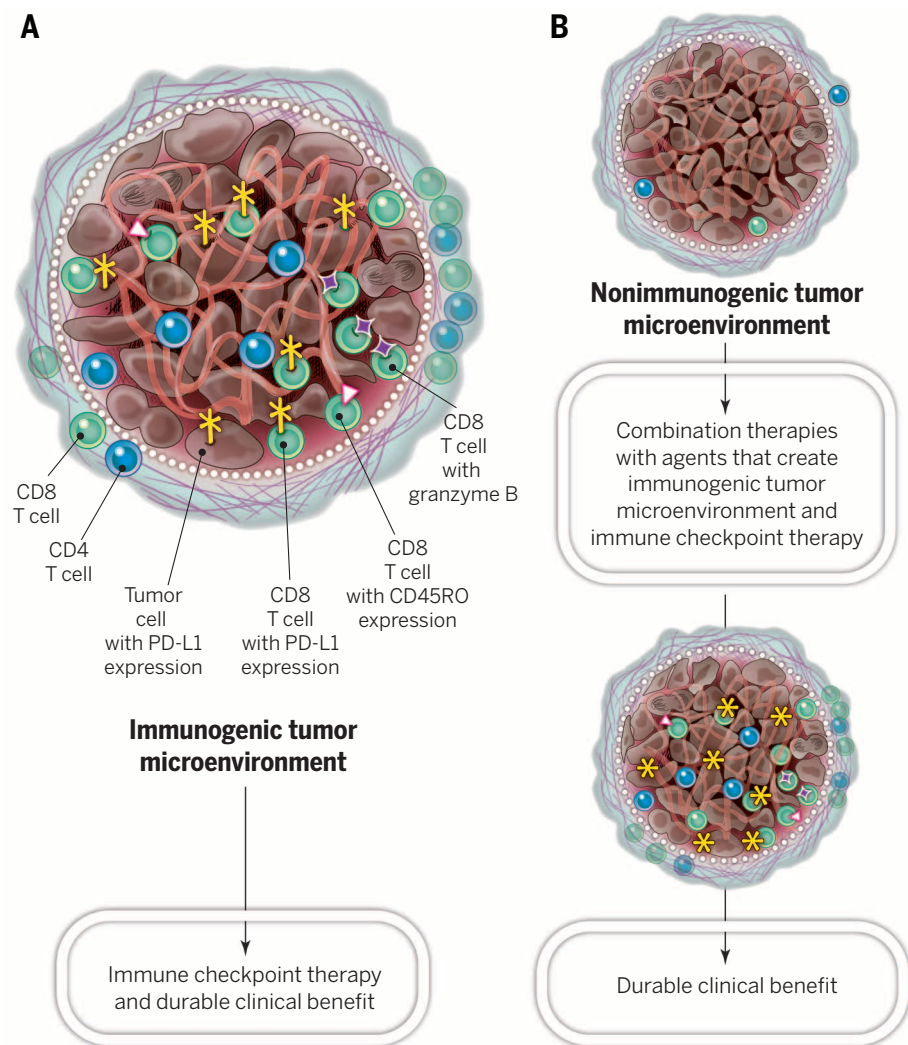
Fig. 3. Potential characteristics of immunogenic and nonimmunogenic tumors. (**A**) Tumor tissue depiction indicating tumor cells and an invasive margin (dotted line), which may delineate separation of tumor cells from stromal components. Evaluation of tumor tissues may reveal an immunogenic tumor microenvironment consisting of many immunologic markers, including CD8 T cells, CD4 T cells, PD-L1, granzyme B, and CD45RO, which may be effectively treated with immune checkpoint therapy to elicit clinical benefit. (**B**) Tumor tissues that lack expression of many immunologic markers may indicate a nonimmunogenic tumor microenvironment, which may require combination therapies consisting of an agent to create an immunogenic tumor microenvironment plus an immune checkpoint agent to further enhance the immune response for clinical benefit.

metastatic melanoma samples, many taken from the same patient, it was shown that PD-L1 expression was discordant between primary tumors and metastases and between intra-patient metastases. In addition, patients whose tumor tissues were positive for both PD-L1 expression and infiltration of T cells were found to have improved overall disease-specific survival as compared to patients who had only one of the two features or lacked both features (*43*). Similarly, in a study with anti-PD-1 (pembrolizumab), it was reported that while expression of PD-L1 in pretreatment tumor tissues correlated with clinical outcomes, the preexisting density of CD8 T cells in the invasive margin of the tumor was more predictive of clinical response to anti-PD-1 (*44*). These data suggest that PD-L1 expression in the tumor is most compelling when it is observed in the context of an active T cell response, and that the ongoing T cell response itself, not PD-L1 expression, is the key factor.

Taken together, these data indicate the complexity of determining the PD-L1 status of a patient's tumor by examination of a single pre-treatment tumor sample (Fig. 2). It also raises questions as to whether clinical decisions regarding treatment of patients who have failed conventional therapies and for whom no other treatments are available should be based on static assessment of PD-L1 expression in pretreatment tumor samples.

However, in some settings, expression of PD-L1 in tumors is constitutive and is neither associated with T cell infiltration nor induced by IFN-γ. In these settings, assessment of PD-L1 expression in tumor tissues may be very useful in guiding treatment. In Hodgkin's lymphoma, Reed-Sternberg cells are known to harbor amplification of chromosome 9p24.1, which encodes PD-L1 and PD-L2 and leads to their constitutive expression. Anti-PD-1 (nivolumab) was shown to elicit an objective response rate of 87% in a cohort of 20 patients with Hodgkin's lymphoma (*45*). Therefore, in the setting of Hodgkin's lymphoma, and possibly other malignancies that harbor amplification of chromosome 9p24 or up-regulate PD-L1 or PD-L2 in response to an oncogenic signal, the expression of these ligands may indeed serve as a predictive biomarker.

In addition to evaluation of PD-L1 expression, tumor tissues can also be studied to identify patterns of expression of multiple immunologic components, including other checkpoints and their ligands. T cells that coexpress PD-1 together with other inhibitory molecules such as LAG-3 or Tim-3 may be even more profoundly hyporesponsive than those expressing PD-1 alone and indicate the need for the blockade of multiple checkpoints (*46*, *47*). Given the complexity of regulation of T cell responses by multiple signaling pathways, both negative and positive, it will be necessary to determine the patterns of expression of the receptors, as well as the ligands on T cells, tumor cells, myeloid cells, and other components of the tumor microenvironment, for development of combination strategies with greater clinical benefit.

Additional biomarkers that play a role in antitumor responses elicited by anti-PD-1 therapy and anti-PD-L1 therapies may also be identified through genetic analyses of tumor cells. Similar to previous reports with anti-CTLA-4 therapy, higher numbers of mutations, including mutations in DNA repair pathways, with subsequent increase in numbers of neoantigens, was found to correlate with clinical responses in patients with non–small cell lung cancer who received treatment with anti-PD-1 (pembrolizumab) (*48*). These data highlight the complex interplay between cancer cells and the immune system, which will need further elucidation, to guide rational development of combination therapies.

Combination therapy to increase clinical benefit

Given the dynamic nature of immune responses to tumors and the complexity of regulation of expression of multiple immune checkpoints and their ligands, it may be difficult to rely on any single immunologic biomarker to select patients for treatment. It may be necessary to evaluate multiple components within the tumor microenvironment, which may enable us to distinguish between an immunogenic (hot) tumor microenvironment (Fig. 3A) that is comprised of infiltrating T cells, cytokines such as granzyme B, memory T cell markers such as CD45RO and PD-L1 expression versus a non-immunogenic (cold) tumor microenvironment that lacks these components (Fig. 3B). Patients whose tumors

ronment, with subsequent inhibition of antitumor T cell responses, but also increase the chance of benefit from anti-PD-1 and anti-PD-L1 therapies. Therefore, combination treatment with anti-CTLA-4 plus anti-PD-1 or anti-PD-L1 should enable the creation of an immunogenic tumor microenvironment with subsequent clinical benefit for patients regardless of whether their pretreatment tumor tissues have infiltrating T cells or express PD-L1. Data from a recent phase I clinical trial with anti-CTLA-4 (ipilimumab) plus anti-PD-1 (nivolumab) demonstrated that patients with metastatic melanoma had similar response rates in the setting of concurrent therapy regardless of PD-L1 expression in pretreatment tumor tissues (*35*). For patients with PD-L1–positive tumors, the objective response rate was 46% (6 of 13 patients), which was similar to the objective response rate of 41% (9 of 22 patients) for those patients with PD-L1–negative tumors. Similar data were reported for a combination study with anti-PD-1 (nivolumab) plus anti-CTLA-4 (ipilimumab) in patients with metastatic renal cell carcinoma (mRCC) (*49*).

Conventional cancer therapies (Table 1) may also lead to tumor cell death and release of antigens to initiate activation of T cells, which may then migrate into tumor tissues. Therefore, combination studies with these conventional agents and immune checkpoint therapies should create an "immunogenic" tumor microenvironment with subsequent clinical benefit for patients.

Table 1. Potential agents for combination therapy. List of some conventional cancer therapies, inhibitory immune signals and stimulatory immune signals that can be considered for combination strategies to improve antitumor responses and durable clinical benefit.

CONVENTIONAL THERAPIES	INHIBITORY IMMUNE SIGNALS	STIMULATORY IMMUNE SIGNALS
Chemotherapy	CTLA-4	ICOS
Radiation	PD-1/PD-L1	OX40
Surgery	LAG-3	41BB
Genomically targeted	TIM-3	Vaccines
Anti-angiogenic	VISTA	Cytokines
Hormonal	BTLA	Oncolytic virus

are immunogenic would be treated with immune checkpoint therapy to elicit durable clinical benefit but, patients whose tumors are non-immunogenic would receive combination therapies designed to create an immunogenic tumor microenvironment that would respond to treatment with subsequent durable clinical benefit (Fig. 3).

Substantial data already exist to indicate that certain combination therapies may overcome the limitations of anti-CTLA-4 and anti-PD-1/PD-L1 monotherapies. For example, anti-CTLA-4 seems to drive T cells into tumors, resulting in an increase in the number of T cells and a concomitant increase in IFN-γ. This, in turn, can induce expression of PD-L1 in the tumor microenvi-

There are multiple ongoing trials with radiation therapy in combination with anti-CTLA-4 or anti-PD-1/PD-L1 antibodies, which will provide valuable information regarding schedule, safety, and efficacy of these combinations for future studies (*50*, *51*). In addition, combination treatment with anti-PD-1 (nivolumab) plus pazopanib or sunitib in patients with mRCC resulted in promising clinical responses, with response rates that were similar across all patients regardless of PD-L1 expression in pretreatment tumor tissues (*52*).

Other combination strategies, such as vaccines plus anti-CTLA-4 (ipilimumab), are also being developed and have shown promising results in patients with pancreatic cancer, which has

been consistently viewed as a nonimmunogenic tumor type (*53*). Combination treatments are also being developed to enable blockade of multiple inhibitory pathways, such as LAG-3 (*54*, *55*), TIM-3 (*56*, *57*), VISTA (*58*, *59*), and BTLA (*60*, *61*), or blockade of an inhibitory pathway while providing an agonistic signal through a stimulatory pathway, such as ICOS (*39*), OX40 (*62*), 41BB (*63*), vaccines (*24*, *53*), cytokines (*64*), and oncolytic virus (*65*). The development of these combinations and others are critical for driving antitumor immune responses in many cancer patients, even those who are deemed to have nonimmunogenic or PD-L1–negative tumors.

Discussion

Because of the very nature of immune checkpoint therapy, the development of pharmacodynamic, predictive, or prognostic biomarkers faces unique challenges. Agents that block immune checkpoints unleash dynamic and complex immune responses. Anti-CTLA-4 antibody overcomes a block in essential costimulatory signals that are required for activation of both naïve T cells and resting clones, whereas PD-1/PD-L1 blockade seems to remove a barrier to the function of T cells later in the response and in the tumor tissue. Therefore, there is a fundamental difference in the predictive value of preexisting tumor inflammation for PD-1/PD-L1 and CTLA-4 blockade. The existence of a T cell infiltrate and select biomarkers, such as expression of PD-L1, which indicate a "hot" tumor microenvironment, does correlate with clinical benefit for patients treated with anti-PD-1 or anti-PD-L1. However, in the setting of a "cold" tumor microenvironment, it seems that anti-CTLA-4 therapy can drive T cells into the tumor and induce expression of PD-L1, thus creating a tumor microenvironment that may be responsive to anti-PD-1 or anti-PD-L1 therapy, which provides a strong rationale for combination therapy.

There are many ongoing efforts to identify predictive biomarkers of immune checkpoint therapy. It may be that germline differences in immune genes and pathways or host microbiome may affect host immune responses and clinical outcomes in the setting of immune checkpoint therapy. Also, the nature of the tumor itself can also affect the outcome of immune checkpoint therapy. Tumor types differ considerably in their mutational load, which may affect the number of neoantigens that can serve as targets of antitumor T cell responses (*66*). Patients with tumors at the high end of the mutational spectrum may be more likely to respond to immune checkpoint therapy. For example, anti-PD-1 therapy was thought to be ineffective against colon cancer, but it appears that colon cancer with microsatellite instability, and consequently a higher overall mutational load, may be responsive to treatment with anti-PD-1 (*67*). However, this concept may not hold true for all tumor types, because patients with kidney cancer, which has relatively low numbers of mutations, have had notable clinical responses to immune checkpoint therapy (*28*, *30*).

There are multiple immunologic pathways, both positive and negative, with new checkpoints and ligands that emerge as an immune response develops. Because of the constant evolution of an immune response, it is unlikely that a single immunologic biomarker can be identified at baseline that can predict responses to any agent. It will probably be necessary to develop panels of markers based on patterns of expression of relevant markers, and use these to guide development of combination therapies that will increase the response rate. These combinations will not be limited to agents that target immune checkpoints, because it is apparent that small molecules that target signaling pathways involved in cancer can affect antitumor immune responses (*68*). This can occur at the level of the T cells by enhancing activation signals, but also at the level of the tumor by inducing tumor antigen expression and presentation, thus making the tumors more susceptible to T cell killing. The goal then should be to use panels of markers to guide development of combination therapies, and then examine tumor tissues for changes in markers elicited by the combinations to guide decisions about additional treatment to further increase efficacy, and, hopefully, durable clinical responses.

Immune checkpoint therapies and combination strategies with immunotherapy have provided cancer patients with novel treatments that have the potential to elicit durable control of disease and even cures. The specificity, adaptability, and memory response that are inherent to the immune system give us the opportunity to measure multiple components, not just a single biomarker, that can be targeted over time to provide curative treatments for many patients. The ability of an activated immune response to generate a diverse T cell repertoire that adapts to heterogeneous and genetically unstable tumors and the persistence of memory T cells with specificity for tumor antigens, which provide efficient recall responses against recurrent disease, make it absolutely essential to expand our efforts to find rational combinations to unleash antitumor immune responses for the benefit of cancer patients. Properly done, it seems likely that cures for many types of cancer will soon become reality.

REFERENCES AND NOTES

1. J. A. Curtin et al., *N. Engl. J. Med.* **353**, 2135–2147 (2005).
2. H. Davies et al., *Nature* **417**, 949–954 (2002).
3. T. Schumacher, R. Schreiber, *Science* **348**, 69–74 (2015).
4. R. J. Greenwald, G. J. Freeman, A. H. Sharpe, *Annu. Rev. Immunol.* **23**, 515–548 (2005).
5. S. E. Townsend, J. P. Allison, *Science* **259**, 368–370 (1993).
6. P. van der Bruggen et al., *Science* **254**, 1643–1647 (1991).
7. S. A. Rosenberg, J. C. Yang, N. P. Restifo, *Nat. Med.* **10**, 909–915 (2004).
8. P. S. Linsley et al., *J. Exp. Med.* **176**, 1595–1604 (1992).
9. T. L. Walunas et al., *Immunity* **1**, 405–413 (1994).
10. M. F. Krummel, J. P. Allison, *J. Exp. Med.* **182**, 459–465 (1995).
11. D. R. Leach, M. F. Krummel, J. P. Allison, *Science* **271**, 1734–1736 (1996).
12. A. A. Hurwitz, T. F. Yu, D. R. Leach, J. P. Allison, *Proc. Natl. Acad. Sci. U.S.A.* **95**, 10067–10071 (1998).
13. A. van Elsas, A. A. Hurwitz, J. P. Allison, *J. Exp. Med.* **190**, 355–366 (1999).
14. R. Waitz, M. Fassò, J. P. Allison, *OncoImmunology* **1**, 544–546 (2012).
15. D. Zamarin et al., *Sci. Transl. Med.* **6**, 226ra32 (2014).
16. F. S. Hodi et al., *N. Engl. J. Med.* **363**, 711–723 (2010).
17. C. Robert et al., *N. Engl. J. Med.* **364**, 2517–2526 (2011).
18. P. Sharma, K. Wagner, J. D. Wolchok, J. P. Allison, *Nat. Rev. Cancer* **11**, 805–812 (2011).
19. D. M. Pardoll, *Nat. Rev. Cancer* **12**, 252–264 (2012).
20. G. J. Freeman et al., *J. Exp. Med.* **192**, 1027–1034 (2000).
21. H. Dong et al., *Nat. Med.* **8**, 793–800 (2002).
22. J. S. Weber et al., *J. Clin. Oncol.* **26**, 5950–5956 (2008).
23. J. C. Yang et al., *J. Immunother.* **30**, 825–830 (2007).
24. A. J. van den Eertwegh et al., *Lancet Oncol.* **13**, 509–517 (2012).
25. B. C. Carthon et al., *Clin. Cancer Res.* **16**, 2861–2871 (2010).
26. F. S. Hodi et al., *Proc. Natl. Acad. Sci. U.S.A.* **105**, 3005–3010 (2008).
27. D. Schadendorf et al., *J. Clin. Oncol.* 10.1200/JCO.2014.56.2736 (2015).
28. J. R. Brahmer et al., *N. Engl. J. Med.* **366**, 2455–2465 (2012).
29. T. Powles et al., *Nature* **515**, 558–562 (2014).
30. S. L. Topalian et al., *N. Engl. J. Med.* **366**, 2443–2454 (2012).
31. O. Hamid et al., *N. Engl. J. Med.* **369**, 134–144 (2013).
32. C. Robert et al., *Lancet* **384**, 1109–1117 (2014).
33. C. Robert et al., *N. Engl. J. Med.* **372**, 320–330 (2015).
34. M. A. Curran, W. Montalvo, H. Yagita, J. P. Allison, *Proc. Natl. Acad. Sci. U.S.A.* **107**, 4275–4280 (2010).
35. J. D. Wolchok et al., *N. Engl. J. Med.* **369**, 122–133 (2013).
36. C. I. Liakou et al., *Proc. Natl. Acad. Sci. U.S.A.* **105**, 14987–14992 (2008).
37. D. Ng Tang et al., *Cancer Immunol. Res.* **1**, 229–234 (2013).
38. T. Fu, Q. He, P. Sharma, *Cancer Res.* **71**, 5445–5454 (2011).
39. X. Fan, S. A. Quezada, M. A. Sepulveda, P. Sharma, J. P. Allison, *J. Exp. Med.* **211**, 715–725 (2014).
40. A. Snyder et al., *N. Engl. J. Med.* **371**, 2189–2199 (2014).
41. J. Grosso et al., *J. Clin. Oncol.* **31** (suppl.), 3016 (2013).
42. R. S. Herbst et al., *Nature* **515**, 563–567 (2014).
43. J. Madore et al., *Pigment Cell Melanoma Res.* 10.1111/pcmr.12340 (2014).
44. P. C. Tumeh et al., *Nature* **515**, 568–571 (2014).
45. S. M. Ansell et al., *N. Engl. J. Med.* **372**, 311–319 (2015).
46. S. R. Woo et al., *Cancer Res.* **72**, 917–927 (2012).
47. K. Sakuishi et al., *J. Exp. Med.* **207**, 2187–2194 (2010).
48. N. Rizvi et al., *Science* **348**, 124–128 (2015).
49. J. H. Hammers et al., *J. Clin. Oncol.* **32** (suppl.), 4504 (2014).
50. M. Crittenden et al., *Semin. Radiat. Oncol.* **25**, 54–64 (2015).
51. C. Tang et al., *Cancer Immunol Res* **2**, 831–838 (2014).
52. A. Amin et al., *J. Clin. Oncol.* **32** (suppl.), 4010 (2014).
53. D. T. Le et al., *J. Immunother.* **36**, 382–389 (2013).
54. F. Triebel et al., *J. Exp. Med.* **171**, 1393–1405 (1990).
55. M. V. Goldberg, C. G. Drake, *Curr. Top Microbiol Immunol* **344**, 269–278 (2011).
56. J. Fourcade et al., *J. Exp. Med.* **207**, 2175–2186 (2010).
57. V. K. Kuchroo, D. T. Umetsu, R. H. DeKruyff, G. J. Freeman, *Nat. Rev. Immunol.* **3**, 454–462 (2003).
58. L. Wang et al., *J. Exp. Med.* **208**, 577–592 (2011).
59. I. Le Mercier et al., *Cancer Res.* **74**, 1933–1944 (2014).
60. L. Derré et al., *J. Clin. Invest.* **120**, 157–167 (2010).
61. J. Fourcade et al., *Cancer Res.* **72**, 887–896 (2012).
62. W. L. Redmond, S. N. Linch, M. J. Kasiewicz, *Cancer Immunol Res* **2**, 142–153 (2014).
63. H. E. Kohrt et al., *J. Clin. Invest.* **124**, 2668–2682 (2014).
64. F. S. Hodi et al., *J. Am. Med. Assoc.* **312**, 1744–1753 (2014).
65. C. E. Engeland et al., *Mol. Ther.* **22**, 1949–1959 (2014).
66. L. B. Alexandrov et al., *Nature* **500**, 415–421 (2013).
67. N. J. Llosa et al., *Cancer Discov* **5**, 43–51 (2015).
68. D. T. Frederick et al., *Clin. Cancer Res.* **19**, 1225–1231 (2013).

REVIEWS

Adoptive cell transfer as personalized immunotherapy for human cancer

Steven A. Rosenberg* and Nicholas P. Restifo*

Adoptive cell therapy (ACT) is a highly personalized cancer therapy that involves administration to the cancer-bearing host of immune cells with direct anticancer activity. ACT using naturally occurring tumor-reactive lymphocytes has mediated durable, complete regressions in patients with melanoma, probably by targeting somatic mutations exclusive to each cancer. These results have expanded the reach of ACT to the treatment of common epithelial cancers. In addition, the ability to genetically engineer lymphocytes to express conventional T cell receptors or chimeric antigen receptors has further extended the successful application of ACT for cancer treatment.

Adoptive cell therapy (ACT) has multiple advantages compared with other forms of cancer immunotherapy that rely on the active in vivo development of sufficient numbers of antitumor T cells with the functions necessary to mediate cancer regression. For use in ACT, large numbers of antitumor lymphocytes (up to 10^{11}) can be readily grown in vitro and selected for high-avidity recognition of the tumor, as well as for the effector functions required to mediate cancer regression. In vitro activation allows such cells to be released from the inhibitory factors that exist in vivo. Perhaps most importantly, ACT enables the manipulation of the host before cell transfer to provide a favorable microenvironment that better supports antitumor immunity. ACT is a "living" treatment because the administered cells can proliferate in vivo and maintain their antitumor effector functions.

A major factor limiting the successful use of ACT in humans is the identification of cells that can target antigens selectively expressed on the cancer and not on essential normal tissues. ACT has used either natural host cells that exhibit antitumor reactivity or host cells that have been genetically engineered with antitumor T cell receptors (TCRs) or chimeric antigen receptors (CARs). With the use of these approaches, ACT has mediated dramatic regressions in a variety of cancer histologies, including melanoma, cervical cancer, lymphoma, leukemia, bile duct cancer, and neuroblastoma. This Review will discuss the current state of ACT for the treatment of human cancer, as well as the principles of effective treatment that point toward improvements in this approach.

A brief history of ACT

Very little was known about the function of T lymphocytes until the 1960s, when it was shown that lymphocytes were the mediators of allograft rejection in experimental animals. Attempts to use T cells to treat transplanted murine tumors were limited by the inability to expand and manipulate T cells in culture. Thus, ACT used transfer of syngeneic lymphocytes from rodents heavily immunized against the tumor, and modest growth inhibition of small established tumors was observed (1, 2). In early preclinical studies, the importance of host inhibitory factors was suggested by findings that lymphodepletion using either chemotherapy or radiation before cell transfer enhanced the ability of transferred lymphocytes to treat established tumors (3, 4).

The ability to use ACT was facilitated by the description of T cell growth factor [interleukin-2 (IL-2)] in 1976, which provided a means to grow T lymphocytes ex vivo, often without loss of effector functions (5). The direct administration of high doses of IL-2 could inhibit tumor growth in mice (6), and studies in 1982 demonstrated that the intravenous injection of immune lymphocytes expanded in IL-2 could effectively treat bulky subcutaneous FBL3 lymphomas (7). In addition, administration of IL-2 after cell transfer could enhance the therapeutic potential of these adoptively transferred lymphocytes (8). The demonstration in 1985 that IL-2 administration could result in complete durable tumor regressions in some patients with metastatic melanoma (9) provided a stimulus to identify the specific T cells and their cognate antigens involved in this cancer immunotherapy. Lymphocytes infiltrating into the stroma of growing, transplantable tumors were shown to represent a concentrated source of lymphocytes capable of recognizing tumor in vitro, and studies in murine tumor models demonstrated that the adoptive transfer of these syngeneic tumor-infiltrating lymphocytes (TILs) expanded in IL-2 could mediate regression of established lung and liver tumors (10). In vitro studies in 1986 showed that human TILs obtained from resected melanomas contained cells capable of specific recognition of autologous tumors (11), and these studies led in 1988 to the first demonstration that ACT using autologous TILs could mediate objective regression of cancer in patients with metastatic melanoma (12).

Populations of TILs that grow from tumors are generally mixtures of CD8+ and CD4+ T cells with few if any major contaminating cells in mature cultures. The ability of pure populations of T lymphocytes to mediate cancer regression in patients provided the first direct evidence that T cells played a vital role in human cancer immunotherapy. However, responses were often of short
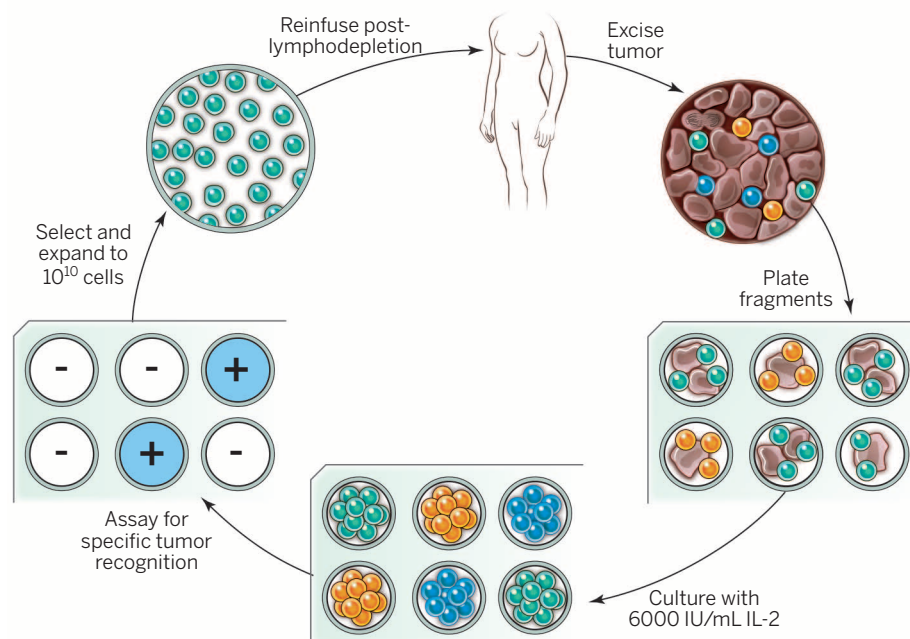
Fig. 1. General schema for using the adoptive cell transfer of naturally occurring autologous TILs. The resected melanoma specimen is digested into a single-cell suspension or divided into multiple tumor fragments that are individually grown in IL-2. Lymphocytes overgrow, destroy tumors within 2 to 3 weeks, and generate pure cultures of lymphocytes that can be tested for reactivity in coculture assays. Individual cultures are then rapidly expanded in the presence of excess irradiated feeder lymphocytes, OKT3, and IL-2. By approximately 5 to 6 weeks after resecting the tumor, up to 10^{11} lymphocytes can be obtained for infusion into patients.

Labels in figure: Reinfuse post-lymphodepletion · Excise tumor · Select and expand to 10^{10} cells · Plate fragments · Assay for specific tumor recognition · Culture with 6000 IU/mL IL-2

Surgery Branch, National Cancer Institute, Center for Cancer Research, National Institutes of Health, 9000 Rockville Pike, CRC Building, Room 3W-3940, Bethesda, MD 20892, USA.
*Corresponding author. E-mail: sar@nih.gov (S.A.R.); restifo@nih.gov (N.P.R.)

duration, and the transferred cells could rarely be found in the circulation just days after administration. A critical improvement in the application of ACT to the treatment of human cancer was reported in 2002, when it was shown that lymphodepletion using a nonmyeloablative chemotherapy regimen administered immediately before TIL transfer could lead to increased cancer regression, as well as the persistent oligoclonal repopulation of the host with the transferred antitumor lymphocytes (13). In some patients, the administered antitumor cells represented up to 80% of the CD8+ T cells in the circulation months after the infusion.

Lymphocyte cultures can be grown from many tumor histologies; however, melanoma appeared to be the only cancer that reproducibly gave rise to TIL cultures capable of specific antitumor recognition. The stimulus to more widely apply ACT to treat multiple human cancers led to studies of the genetic engineering of lymphocytes to express antitumor receptors. Following mouse models (14), it was shown for the first time in humans in 2006 that administration of normal circulating lymphocytes transduced with a retrovirus encoding a TCR that recognized the MART-1 melanoma-melanocyte antigen could mediate tumor regression (15). Administration of lymphocytes genetically engineered to express a chimeric antigen receptor (CAR) against the B cell antigen CD19 was shown in 2010 to mediate regression of an advanced B cell lymphoma (16). These findings of the use of either naturally occurring or genetically engineered antitumor T cells set the stage for the extended development of ACT for the treatment of human cancer.

ACT using TILs is an effective immunotherapy for patients with metastatic melanoma
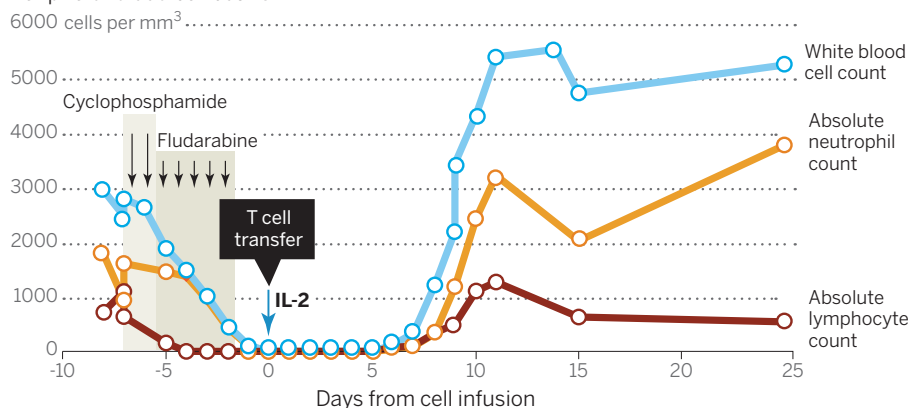
Adoptive cell therapy using autologous TILs is the most effective approach to induce complete durable regressions in patients with metastatic melanoma (Table 1). The general approach for growing and administering human TILs is shown in Fig. 1. The resected melanoma specimen is digested into a single-cell suspension or divided into multiple tumor fragments that are individually grown in IL-2. Lymphocytes overgrow, destroy tumors within 2 to 3 weeks, and give rise to pure cultures of lymphocytes that can be tested for reactivity against tumors, if available, in coculture assays. Individual cultures are then rapidly expanded in the presence of excess irradiated feeder lymphocytes, an antibody targeting the epsilon subunit within the human CD3 complex of the TCR, and IL-2. By ~5 to 6 weeks after resecting the tumor, up to 10^11 lymphocytes can be obtained for infusion into patients. A substantial increase in cell persistence and the incidence and duration of clinical responses was seen when patients received a lymphodepleting preparative regimen before the cell infusion (13). It might be possible to optimize the intensity or duration of the lymphodepletion that is employed, but the most frequently used lymphodepleting preparative regimen consists of 60 mg/kg cyclophosphamide for 2 days and 25 mg/m^2 fludarabine adminis-

tered for 5 days followed by cells and IL-2 given at 720,000 IU/kg to tolerance (Fig. 2). In a pilot study in the Surgery Branch, National Cancer Institute (NCI), objective cancer regressions by RECIST criteria (Response Evaluation Criteria in Solid Tumors) were seen in 21 of 43 patients (49%), including 5 patients (12%) who underwent complete cancer regression (13). When 200 or 1200 centigray (cGy; 1 Gy = 100 rads) total-body irradiation (TBI) was added to the preparative regimen in pilot trials of 25 patients each, objective response (OR) rates

of 52 and 72% were seen, including 20 and 40% complete regressions. However, there were no statistically significant differences in the OR rates between preparative regimens (13, 17). Twenty of the 93 patients (22%) in these trials had complete regressions, and 19 (20%) have not experienced recurrences at follow-up times of 5 to 10 years and are probably cured. A prospective randomized study comparing the chemotherapy preparative regimen alone versus chemotherapy plus the addition of 1200 cGy TBI in 101 patients was recently concluded at the NCI, National Institutes of Health (NIH), and results are pending.

In the combined experience of the treatment of 194 patients using TILs grown from individual melanoma fragments at the NCI (Bethesda, Maryland), 107 patients (55%) have shown ORs. Similar OR rates to TIL therapy have been reported by multiple groups, including those from the Moffitt Cancer Center (Tampa, Florida) (38% OR rate) (18), the MD Anderson Cancer Center (Houston, Texas) (48% OR rate) (19), and the Ella Cancer Institute (Ramat Gan, Israel) (40% OR rate) (20) (Table 1).

There is no relation between the bulk of disease or the site of metastases and the likelihood of achieving a complete cancer regression (17). Of the

34 complete responders thus far seen in the two trials at the NCI, only one has recurred, and only one patient with complete regression received more than one treatment. The brain is not a sanctuary site, and regression of brain metastases has been observed (21). Prior treatment with targeted therapy using the Braf inhibitor vemurafenib (Zelboraf) does not appear to affect the likelihood of having an OR to ACT treatment in patients with melanoma. ACT can also be effective after other immunotherapies have failed. Of the 194 patients treated in the NCI trials, OR rates in patients who had no prior therapy or who progressed through IL-2, antibody to cytotoxic T lymphocyte–associated protein 4 (anti–CTLA-4), anti-PD1, or Braf inhibitors were 48, 63, 42, 50, and 43%, respectively.

Lymphodepletion appears to be an important component of ACT, and mouse models have shown that lymphodepletion given before cell transfer can increase the effectiveness of treatment more than 10-fold. In the clinic, the persistence of T cells was once a rarity (22), but in trials conducted after the initiation of lymphodepleting therapy, adoptively transferred T cells could comprise the majority of the peripheral blood CD8+ cells 1 month after transfer (13). The cellular basis of the effect of lymphodepletion is complex and still not completely understood. In mouse models, myeloid-derived suppressor cells and CD4+ FoxP3 regulatory T cells can be found at high levels in tumors in vivo and can depress immune responses in the mouse tumor microenvironment (23). In accord with these preclinical findings, preparative chemotherapy in humans severely depletes lymphocytes and myeloid cells from the circulation at the time of cell infusion, although the rate of reappearance of FoxP3 inhibitory T cells after lymphodepletion was inversely correlated with clinical response (24).

Lymphodepletion prior to T cell transfer is followed by immune reconstitution

Fig. 2. A substantial increase in cell persistence and the incidence and duration of clinical responses is observed when patients received a lymphodepleting preparative regimen before the cell infusion. The most frequently used lymphodepleting preparative regimen consists of 60 mg/kg cyclophosphamide given for 2 days and 25 mg/m^2 fludarabine administered over 5 days, followed by T cells and IL-2 administration.

Table 1. Selected clinical trials of ACT for the treatment of human cancer. CLL, chronic lymphocytic leukemia; ALL, acute lymphocytic leukemia; CR, complete response; HPC, human papillomavirus; allo-HSCT, allogeneic hematopoietic stem cell transplantation; DLBCL, diffuse large B cell lymphoma; EBV, Epstein-Barr virus. Dashes indicate not applicable.

CELLS USED FOR ACT	YEAR	CANCER HISTOLOGY	MOLECULAR TARGET	PATIENTS	NUMBER OF ORS	COMMENTS
Tumor-inflitrating lymphocytes*	1998	Melanoma (12)		20	55%	Original use TIL ACT
	1994	Melanoma (88)		86	34%	
	2002	Melanoma (13)		13	46%	Lymphodepletion before cell transfer
	2011	Melanoma (17)		93	56%	20% CR beyond 5 years
	2012	Melanoma (19)		31	48%	
	2012	Melanoma (18)		13	38%	Intention to treat: 26% OR rate
	2013	Melanoma (20)		57	40%	Intention to treat: 29% OR rate
	2014	Cervical cancer (89)		9	33%	Probably targeting HPV antigens
	2014	Bile duct (44)	Mutated ERB2	1	–	Selected to target a somatic mutation
In vitro sensitization	2008	Melanoma (90)	NY-ESO-1	9	33%	Clones reactive against cancer-testes antigens
	2014	Leukemia (91)	WT-1	11	–	Many treated at high risk for relapse
Genetically engineered with CARs	2010	Lymphoma (16)	CD19	1	100%	First use of anti-CD19 CAR
	2011	CLL (68)	CD19	3	100%	Lentivirus used for transduction
	2013	ALL (70)	CD19	5	100%	Four of five then underwent allo-HSCT
	2014	ALL (92)	CD19	30	90%	CR in 90%
	2014	Lymphoma (71)	CD19	15	80%	Four of seven CR in DLBCL
	2014	ALL (93)	CD19	16	88%	Many moved to allo-HSCT
	2014	ALL (94)	CD19	21	67%	Dose-escalation study
	2011	Neuroblastoma (78)	GD2	11	27%	CR2 CARs into EBV-reactive cells
Genetically engineered with TCRs	2011	Synovial sarcoma (81)	NY-ESO-1	6	67%	First report targeting nonmelanoma solid tumor
	2006	Melanoma (15, 32)	MART-1	11	45%	

*Molecular targets of TIL in melanoma appear to be exomic mutations expressed by the cancer (39, 40, 44)

Levels of homeostatic cytokines, which promote T cell proliferation and survival, are dramatically induced upon lymphodepletion (25) in mouse models. In humans, lymphodepletion leads to the appearance in the circulation of the T cell growth factor IL-15, which serves to promote the expansion of the transferred cells in the absence of competing endogenous lymphocytes (26). Further, lymphodepletion can enhance the translocation of commensal microflora across mucosal barriers in the mouse, and this can enhance the effect of ACT by stimulating Toll-like receptors (27) to activate antigen-presenting cells (APCs). These preclinical results have highly affected clinical translation, and it seems likely that immune ablation will be a part of future cell-based treatments in patients with cancer.

Adoptive cell therapy is a "living" treatment, and administered lymphocytes can expand more than 1000-fold after administration. Studies in mouse models, including those involving the injection of human cells into immunodeficient animals, have emphasized the importance of the differentiation state of the infused cells (28, 29). The phenotypic and functional status of less differentiated murine cells is highly positively correlated with their ability to eliminate vascularized tumor in vivo. These findings are in accordance with the high positive correlation between the persistence of the transferred TILs in the circulation of patients at 1 month and with the induction of partial and complete clinical responses (17). Further, one clinical study showed a strong correlation between expression of the phenotypic marker CD27, which is associated with cells early in their differentiation pathway, and clinical response (17). The presence of longer telomeres as a correlate of clinical response was seen in one study (17) but not in another (18).

The observation that melanoma TILs can mediate durable, complete, and probably curative cancer regression in patients with metastatic melanoma has raised considerable interest in the possible use of TILs for the treatment of multiple cancer types. Although TILs can be grown in vitro from virtually all tumors, only melanomas consistently give rise to TILs with antitumor reactivity. In an attempt to gain insight into the possible extension of ACT to the treatment of other common cancers, extensive studies of the antigens recognized by TILs have been pursued.

Melanoma TILs recognize the products of cancer mutations

Early studies identified two nonmutated melanoma-melanocyte differentiation proteins, MART-1 and gp100, that were often recognized by melanoma TILs (30, 31). Melanocytes in the skin, eye, and ear express the MART-1 and gp100 proteins, and yet toxicity targeting these proteins was not seen in the majority of patients treated with TILs who underwent complete cancer regression. In contrast, when a high-affinity TCR against MART-1 or gp100 was inserted into lymphocytes used for ACT, profound eye and ear toxicity was often seen in the absence of antitumor activity, which suggests that the reactivity against melanoma-melanocyte antigens was not the decisive target resulting in the in vivo antitumor activity of melanoma TILs (32).

A study of exomic mutation rates in more than 3000 tumor-normal pairs revealed that the frequency of nonsynonymous mutations varied more than 1000-fold across different cancer types (33). Pediatric cancers exhibited mutation frequencies as low as 0.1/Mb, whereas melanomas and lung cancers often exceeded 100 mutations/Mb.

The suggestion that mutations might be targets of immune recognition of tumor cells has been around for some time (34). The responsiveness of melanoma to a variety of immunotherapy approaches such as ACT, IL-2, anti–CTLA-4, and anti–PD-1 suggested that peptide epitopes encoded by the large number of mutations in melanoma might be the targets of TIL therapy (35). Support for this hypothesis comes from recent observations that anti–PD-1 can mediate ORs not only in patients with melanoma but also in patients with lung and bladder cancer, the two tumor types closest to melanoma with a high frequency of mutations (36). A patient successfully treated with anti–CTLA-4 generated circulating T cells that recognized a distinct mutation in the melanoma (37). Another study suggested that increased numbers of exomic mutations in a cancer correlated with better outcomes (38).

New approaches using whole-exomic sequencing of tumor-normal pairs in patients with melanoma have consistently identified nonsynonymous cancer mutations recognized by autologous TILs that mediated complete cancer regressions (39, 40). However, not all expressed mutations can be recognized by T cells. Proteins incorporating the mutations must be processed to short peptides of ~9 amino acids for major histocompatibility complex (MHC) class 1 and a bit longer for MHC class 2; these peptides are then presented on the cell surface. One approach to identify the immunogenic

mutations that we have taken is to identify 21– to 25–amino acid polypeptides, each one containing a mutated amino acid flanked by 10 to 12 normal residues. Using peptide-MHC binding algorithms, these polypeptides can then be scanned to identify peptides with high binding to individual MHC molecules of the patient. The top-predicted binding peptides are then synthesized and tested for recognition by coculture with TILs that mediated cancer regression. This method depends on the accuracy of peptide-MHC binding algorithms, which are often inadequate for many of the less frequent MHC molecules (39).

An alternate method eliminates the need for predicted peptide binding to MHC and enables the screening of all candidate peptides on all MHC loci in a single test (40) (Fig. 3). As above, minigenes, rather than polypeptides, are constructed that encode each mutated amino acid flanked by 10 to 12 amino acids. Strings of 6 to 20 minigenes are then linked into tandem minigenes, and these DNA constructs are subsequently cloned into an expression plasmid and in vitro transcribed to RNA, which is electroporated into the patient's autologous APCs. These APCs present all mutated peptides capable of being processed and binding to any of the patient's class 1 or class 2 MHC molecules. Culture of the patient's TILs with these APCs can identify the tandem minigene as well as the individual minigene responsible for tumor recognition. Using these approaches, TILs from 21 patients with mela-

noma that responded to ACT identified 45 mutations presented on a variety of class 1 and class 2 MHC molecules. Thus far, every mutation recognized by TILs was distinct (i.e., each from a different expressed protein), with none shared by another melanoma in the set studied. These findings provide suggestive evidence that melanoma TILs capable of mediating antitumor responses were recognizing random somatic mutations in the cancer. In many cases, multiple mutations were recognized by an individual TIL population. The concept that cancer regressions after immunotherapy are the result of targeting mutations explains why patients can experience tumor regression without autoimmune sequelae. Conversely, the ineffectiveness of the vast number of therapeutic cancer vaccines that targeted nonmutated self-proteins can also be explained (41, 42). Whereas strong reactivity to self-antigens causes autoimmune toxicity, vaccines against self-antigens trigger the expansion of low-affinity TCRs against self-proteins that escaped negative selection in the thymus. This raises the possibility that vaccines targeting mutated immunogenic epitopes may be much more effective. The specific targeting of individual mutated antigens in a patient's cancer presents a daunting problem for widespread therapeutic application of ACT but also presents an opportunity to develop treatments for multiple cancer types. Schumacher and Schreiber discuss additional aspects for targeting mutated antigens in this issue (43).
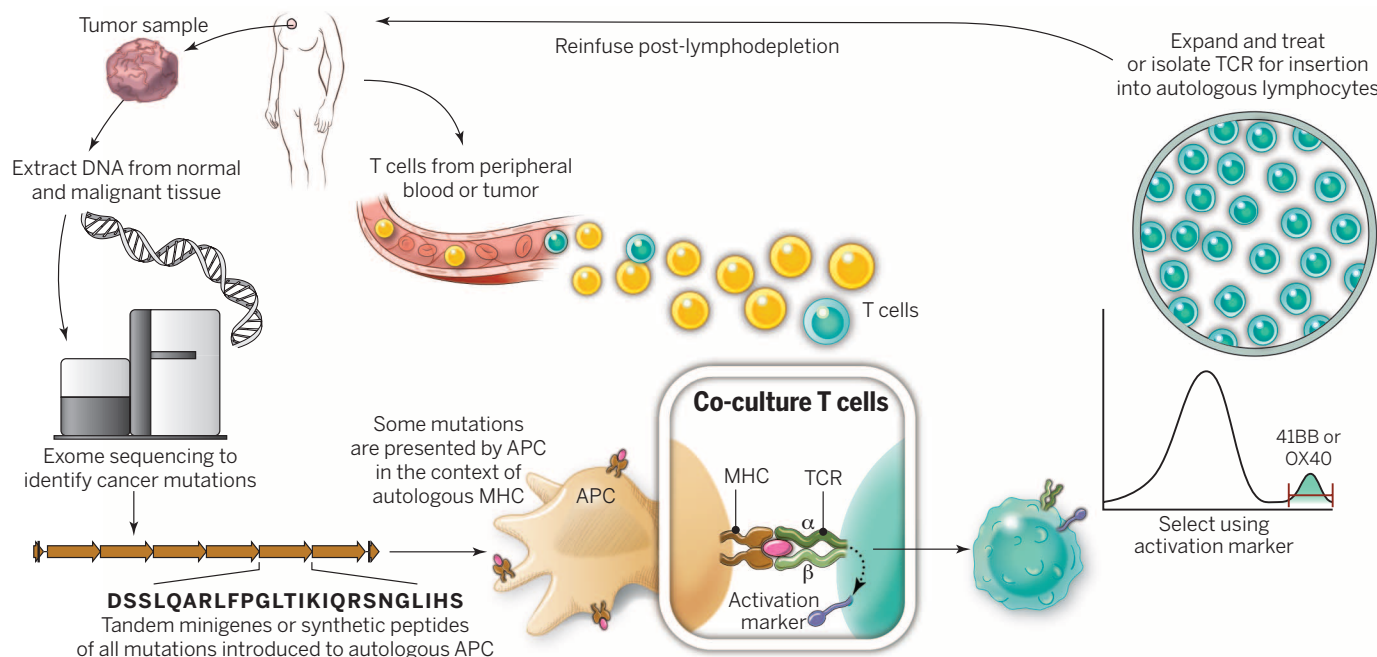
Fig. 3. A "blueprint" for the treatment of patients with T cells recognizing tumor-specific mutations. The sequences of exomic DNA from tumor cells and normal cells from the same patient are compared to identify tumor-specific mutations. Knowledge of these mutations can then be used to synthesize either minigenes or polypeptides encoding each mutated amino acid flanked by 10 to 12 amino acids. These peptides or minigenes can be expressed by a patient's autologous APCs, where they are processed and presented in the context of a patient's MHC. Coculture of the patient's T cells with these APCs can be used to identify all mutations processed and presented in the context of all of a patient's MHC class I and class II molecules. The identification of individual mutations responsible for tumor recognition is possible because T cells express activation markers, such as 41BB (CD8+ T cells) and OX40 (CD4+ T cells), when they recognize their cognate target antigen. T cells expressing the activation marker can then by purified using flow cytometry before their expansion and reinfusion into the tumor-bearing patient.

TILs from common epithelial cancers can also recognize cancer mutations

A recent report has shown that the mutated antigens in a nonmelanoma epithelial cancer can give rise to immune responses, despite the low number of mutations in these cancers (*44*). Exomic sequencing of a metastatic cholangio-carcinoma in a patient who had progressed through multiple chemotherapies revealed 26 nonsynonymous mutations. Tandem minigenes that encoded each mutated amino acid and its flanking sequences were constructed and electroporated into the patient's APCs. CD4 cells from TIL cultures from this patient's tumor recognized the ERBB2IP mutation restricted by the MHC class 2 antigen HLA-DQ O6. ERBB2IP is a tumor suppressor that binds to ERBB2 and attenuates downstream RAS/ERK signaling. Despite the lack of an objective clinical response to the administration of bulk autologous TILs in this patient, administration of TILs that were selected to contain more than 95% ERBB2IP mutation-reactive TILs mediated a dramatic regression of liver and lung metastases ongoing beyond 1 year. This result provides compelling evidence that mutation-reactive T cells are capable of mediating in vivo tumor regression in patients with this epithelial cancer. Further, the findings suggest that this treatment approach may be suitable for patients with other common epithelial cancers that are not normally considered to be immunogenic.

Mutations that are targeted may be driver mutations essential for the malignant phenotype of the cell, or alternatively, the TILs may contain reactivity against multiple immunogenic passenger mutations, which would decrease the likelihood that the loss of any individual antigen would subvert the clinical antitumor response. TIL populations can be highly polyclonal and thus are likely to be capable of potentially recognizing multiple antigens simultaneously. Given their curative potential, it seems likely that TILs are able to recognize antigens expressed by cancer stem cells. Although some of the mutations are probably driver mutations because they are found in expressed genes associated with known oncogenic pathways (e.g., mutated β-catenin), many of the targets of TILs may well be passenger mutations.

Genetic engineering of lymphocytes for use in ACT

In an attempt to broaden the reach of ACT to other cancers, techniques were developed to introduce antitumor receptors into normal T cells that could be used for therapy (Fig. 4). The specificity of T cells can be redirected by the integration of genes encoding either conventional alpha-beta TCRs or CARs. CARs were pioneered by Gross and colleagues in the late 1980s (*45*) and can be constructed by linking the variable regions of the antibody heavy and light chains to intracellular signaling chains such as CD3-zeta, often in-cluding costimulatory domains encoding CD28 (*46*) or CD137 to fully activate T cells (*47, 48*). CARs can provide non-MHC–restricted recognition of cell surface components and can be introduced into T cells with high efficiency using viral vectors.

An important question confronting the use of genetically engineered cells in the ACT of cancer involves selection of the ideal human T cell subpopulation into which the gene should be introduced, as well as the selection of appropriate antigenic targets of the introduced TCRs or CARs. Preclinical studies in mouse models strongly suggest that improved antitumor responses are seen when T cells in early stages of differentiation (such as naïve or central memory cells) are transduced (*49*), a result supported by studies in monkeys showing improved in vivo persistence of infused central memory compared with effector memory cells (*50*). CD8+ T cells can be categorized into distinct memory subsets based on their differentiation states. We and others have found that CD8+ T cells follow a progressive pathway of differentiation from naïve T cells into central memory and effector memory T cell populations [summarized in (*51*)]. CD8+ T cells paradoxically lose antitumor T cell functionality as they acquire the ability to lyse target cells and to produce the cytokine interferon-γ, qualities thought to be important in their antitumor efficacy (*52*). The differentiation state of CD8+ T cells is inversely related to their capacity to proliferate and persist (*52–54*). These
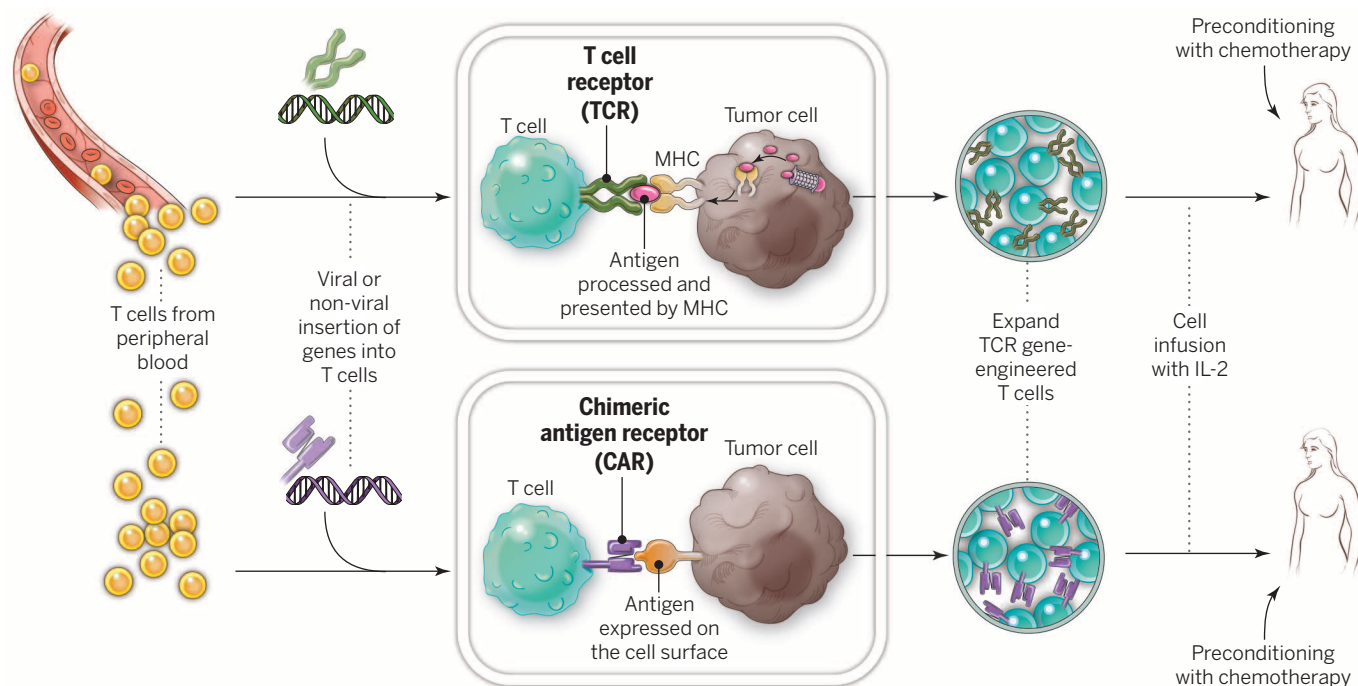
Fig. 4. Gene-modification of peripheral blood lymphocytes. In an attempt to broaden the reach of ACT to other cancers, techniques are being developed to introduce antitumor receptors into normal T cells that could be used for therapy. The top panel shows the insertion of a conventional TCR into a patient's T lymphocytes, followed by the expansion and infusion back into the patient. The bottom panel shows the insertion of a CAR into a patient's T cell, followed by the expansion of these cells and their re-infusion. TCRs and CARs are fundamentally different in their structures and in the structures that they recognize. TCRs are composed of one α chain and one β chain, and they recognize antigens that have been processed and presented by one of the patient's own MHC molecules. CARs are artificial receptors that can be constructed by linking the variable regions of the antibody heavy and light chains to intracellular signaling chains (such as CD3-zeta, CD28, 41BB) alone or in combination with other signaling moieties. CARs recognize antigens that do not need to be MHC-restricted, but they must be presented on the tumor cell surface.

findings may be clinically relevant, and younger T cells are statistically positively correlated with clinical effectiveness in ACT trials (17). It seems clear that, like many organ systems in the body, CD8+ T cells can exist in a stem cell–like state, capable of clonal repopulation. Human T memory stem cells express a gene program that enables them to proliferate extensively and can further differentiate into other T cell populations (29).

Much of the existing work in cancer immunotherapy has focused on CD8+ T cells. However, CD4+ T cells can also efficiently promote tumor rejection. CD4+ T cells do not merely enhance CD8+ T cell function, but they also play a more direct role in tumor elimination. This notion has been validated recently in humans (44). The roles that CD4+ T cells play in the antitumor immune response crucially depend on their polarization, which is determined by their expression of key transcription factors. CD4+ cells can destroy tumor cells, and recent evidence suggests that adoptively transferred T helper 17 cells can promote long-lived antitumor immunity (55).

Toxicity of ACT when targeting antigens shared by tumors and normal tissue

The marked potency of T cells enables the recognition of minute levels of antigen expressed on normal cells. Thus, targeting normal, nonmutated antigenic targets that are expressed on normal tissues but overexpressed on tumors has led to severe on-target, off-tumor toxicity in patients. Suitable antigens to target are those presented exclusively on the cancer or, alternatively, on normal cells that are not essential for survival.

The first successful application of ACT using genetically engineered lymphocytes treated 17 patients with metastatic melanoma using autologous T cells transduced with a weakly avid human TCR recognizing the MART-1 melanoma-melanocyte differentiation antigen (15). Two patients experienced objective partial regressions of metastatic melanoma, and in both patients the transferred cells could be found in the peripheral blood 1 year after cell infusion. This approach was expanded to 36 patients with metastatic melanoma who received high-avidity TCRs that recognized either the MART-1 or gp100 melanoma-melanocyte antigens (32). Although objective cancer regressions were observed in 30 and 19% of patients who received the MART-1 or gp100 TCR, respectively, severe off-tumor, on-target toxicity was seen in the skin, eyes, and ears of patients due to the expression of melanocytes in these organs. These findings coincided with severe eye toxicity seen in mice when targeting melanocyte antigens and provided an early demonstration of the power of T cell therapy (56). The treatment of patients with renal cancer using T cells encoding a CAR against carbonic anhydrase 9, which is overexpressed in renal cancer, led to severe liver toxicity due to expression of this antigen in biliary duct epithelium (57). A high-affinity TCR against the carcinoembryonic antigen was used to treat patients with metastatic colorectal cancer that expressed high levels of this antigen (58). All three patients experienced life-threatening coli-

tis and colonic hemorrhage that precluded further use of this TCR, even though one patient exhibited a partial response of liver metastases. Unexpected toxicities can also result when previously unknown cross-reactivities are seen that target normal self-proteins expressed in vital organs. MAGE-A3, a cancer-testes antigen to be discussed in more detail below, is not known to be expressed in any normal tissues. However, targeting an HLA-A*0201–restricted peptide in MAGE-A3 caused severe damage to gray matter in the brain, resulting in two deaths because this TCR recognized a different but related epitope expressed by MAGE-A12, expressed at very low levels in the brain (59). It should also be noted that CARs are capable of toxicity against self-antigens as well. Acute pulmonary toxicity resulting in death was observed after infusion of CAR T cells specific for ERBB2, which seemed likely due to the recognition of low levels of this antigen on pulmonary epithelium (60).

Several groups have attempted to affinity-enhance TCRs by altering amino acids in the antigen-combining sites of the TCR (61, 62). By removing the protective effects of negative thymic selection that eliminate high-affinity TCRs against normal proteins, these modified TCRs could potentially recognize new and unrelated determinants. Two patients (one with multiple myeloma and one with melanoma) were treated with an HLA-A1–restricted MAGE-A3–specific TCR whose affinity was enhanced by this site-specific mutagenesis, and both experienced fatal cardiogenic shock due to the recognition of an HLA-A1–restricted peptide derived from an unrelated protein, titin, present in cardiac muscle (63). Thus, methods aimed at enhancing the affinities of TCRs can be fraught with problems of unexpected toxicities, which remain difficult to predict. Of course, the same pitfalls of unexpected toxicities may apply to the use of novel CARs.

Targeting antigens expressed on cancers and nonessential human tissues

Cancers that express target molecules shared with nonessential normal organs represent potential targets for human cancer immunotherapy using ACT. A prominent example of such an antigen is the CD19 molecule expressed on more than 90% of B cell malignancies and on B cells at all stages of differentiation, excluding plasma cells. Following preclinical work by many groups [summarized in (64–67)], the first successful clinical application of anti-CD19 CAR gene therapy in humans was reported in 2010 (16). Administration of autologous cells expressing the anti-CD19 CAR to a patient with refractory lymphoma resulted in cancer regression in a patient who remains progression-free after two cycles of treatment ongoing 4 years after treatment. Multiple groups have now shown the effectiveness of ACT targeting CD19 in patients with follicular lymphoma, large-cell lymphomas, chronic lymphocytic leukemia, and acute lymphocytic leukemia (68–72). On-target toxicity against CD19 results in B cell loss in the circulation and in the bone marrow and can be overcome by the periodic administration of immunoglobulin infusions. Sub-

stantial toxicity can be seen by the excessive release of cytokines by CAR-expressing cells, and thus, careful selection of the lymphodepleting preparative regimen and the cell dose is required to safely apply ACT targeting CD19, as well as many other antigens now under experimental study (72).

Dramatic regressions of lymphomas and leukemias with ACT have elicited considerable enthusiasm, although most reports contain fewer than 20 patients, and fewer than 200 patients have been treated worldwide. The introduction of CARs into lymphocytes has mainly used gammaretroviruses and lentiviruses, although nonviral approaches such as transposon-transposase systems (73) and CRISPR-cas (CRISPR, clustered regularly interspaced palindromic repeat) technology to introduce genes are also being explored (74). The single-chain antibody governs recognition of the antigen to be targeted, although the T cell is activated via the CD3-zeta chain signaling domain. In addition to the zeta chain, a variety of costimulatory molecules have been employed in retroviral constructs such as CD27, CD28, CD134, CD137, or ICOS that can profoundly influence the function of the CAR [reviewed in (64–66)]. Optimization of these costimulatory domains is a subject of active study. The results of CAR therapy for B cell malignancies might be confounded by the sensitivity of lymphomas and leukemias to the preparative chemotherapy regimen. Thus, delineation between the effects of the preparative therapy and those of the CAR T cells needs to be considered.

Multiple other B cell antigens are being studied as targets, including CD22, CD23, ROR-1, and the immunoglobulin light-chain idiotype expressed by the individual cancer (65). CARs targeting either CD33 or CD123 have been studied as a therapy for patients with acute myeloid leukemia, though the expression of these molecules on normal precursors can lead to prolonged myeloablation (75). BCMA is a tumor necrosis factor receptor family protein expressed on mature B cells and plasma cells and can be targeted on multiple myeloma (65). The Reed-Sternberg cell expresses CD30, and this target is being explored as a treatment for patients with refractory Hodgkin lymphoma (75–77).

Although CARs are being successfully applied to the treatment of hematologic malignancies, the lack of shared antigens on the surface of solid tumors that are not also expressed on essential normal tissues has severely limited the application of CARs to the treatment of solid tumors. Thyroglobulin is a potential target for some patients with thyroid cancers because thyroglobulin is present only in the thyroid gland and not on solid tissues. Neuroblastomas express GD2, which has been targeted by CARs (78). Mesothelin has also been forwarded as a potential target, although it is also expressed on normal tissues, including cells in the pericardium and pleural and peritoneal linings (79). A search is ongoing for other tissue-specific surface antigens expressed on tissues that are not essential for survival.

Cancer-testis antigens are a family of intracellular proteins that are expressed during fetal development but have highly restricted expression in adult normal tissues (80). There are more than

100 different members of this family of molecules whose expression is epigenetically up-regulated from 10 to 80% of cancer types using highly sensitive techniques. However, initial enthusiasm for targeting cancer-testes antigens has been tempered by the lack of high levels of protein expression of these antigens. Approximately 10% of common cancers appear to express enough protein to be suitable targets for antitumor T cells. There are low levels of some cancer-testes antigens expressed on normal tissues, and this can lead to untoward toxicities. The NYESO-1 cancer-testes antigen has been targeted via a human TCR transduced into autologous cells (*81*). ORs were seen in 5 of 11 patients with metastatic melanoma and 4 of 6 patients with highly refractory synovial cell sarcoma.

Looking to the future of ACT for the treatment of cancer

The continued development of ACT, as well as other immunologic approaches to the treatment of cancer, depends on the identification of suitable targets for immunologic attack. Although CARs have been successful in the treatment of hematologic malignancies and are likely to soon join the mainstream of oncologic treatment, the ability to treat common epithelial solid cancers, which account for ~90% of all cancer fatalities, is severely limited by the lack of suitable targets exclusive to cancer. Extensive searches for monoclonal antibodies that can recognize distinct determinants on the surface of solid cancers but not normal tissues have been in progress for more than 30 years, but few suitable determinants have been found. The EGFRvIII mutation on ~40% of high-grade glioblastomas is a rare example of a shared-surface mutation, and attempts to target this molecule using CARs are in progress (*82*). Shared mutations in intracellular proteins involved in oncogenesis—such as Braf in melanomas and Kras in pancreatic and other solid cancers—would be ideal ACT targets using conventional alpha-beta TCRs, though immunogenic epitopes have not yet been identified in these molecules. Driver and random somatic mutations occurring in many solid cancers may represent excellent targets for the treatment of solid tumors.

Opportunities to improve ACT involve the identification and development of specific antitumor T cells with the functional properties optimal for tumor destruction (*83*). One approach under active evaluation is the growth of cells under conditions that enable in vitro proliferation while limiting differentiation, such as the use of IL-21 or inhibitors that target the kinase AKT (*84, 85*). Improved specific lymphodepleting preparative regimens and better design of the transducing vectors, including the incorporation of optimal costimulatory molecules, are likely to improve clinical results. Introduction of genes encoding other molecules such as the cytokine IL-12, which can profoundly alter the tumor microenvironment to favor antitumor immunity, has shown substantial promise in animal models (*86*). Enhanced methods for regulating the expression of these highly potent cytokine genes would be an important part of incorporating them into clinical treatment. The incorporation of "suicide" genes that can enable destruction of the transferred cells could add an extra level of safety when exploring genetic changes in lymphocytes (*87*).

Adoptive cell therapy is a more complex approach to the delivery of cancer treatment than many other types of immunotherapy and has often been criticized as impractical and too costly for widespread application. The need to develop highly personalized treatments for each patient does not fit into the paradigm of major pharmaceutical companies that depend on "off-the-shelf" reagents that can be widely distributed. However, curative immunotherapies for patients with common epithelial cancers will probably dictate the need for more personalized approaches. Several new biotechnology companies have arisen to meet the need to expand a patient's lymphocytes, and detailed genetic analysis of individual tumors is already commonplace at large academically affiliated medical centers. Although multiple commercial models have been proposed, widespread application of ACT will probably depend on the development of centralized facilities for producing tumor-reactive TILs or genetically modified lymphocytes that can then be delivered to the treating institution. The effectiveness of treatment will need to trump convenience of administration in the application of new effective approaches to cancer immunotherapy.

REFERENCES AND NOTES

1. E. J. Delorme, P. Alexander, *Lancet* **284**, 117–120 (1964).
2. A. Fefer, *Cancer Res.* **29**, 2177–2183 (1969).
3. E. Fernandez-Cruz, B. A. Woda, J. D. Feldman, *J. Exp. Med.* **152**, 823–841 (1980).
4. M. J. Berendt, R. J. North, *J. Exp. Med.* **151**, 69–80 (1980).
5. D. A. Morgan, F. W. Ruscetti, R. Gallo, *Science* **193**, 1007–1008 (1976).
6. S. A. Rosenberg, J. J. Mulé, P. J. Spiess, C. M. Reichert, S. L. Schwarz, *J. Exp. Med.* **161**, 1169–1188 (1985).
7. T. J. Eberlein, M. Rosenstein, S. A. Rosenberg, *J. Exp. Med.* **156**, 385–397 (1982).
8. J. H. Donohue et al., *J. Immunol.* **132**, 2123–2128 (1984).
9. S. A. Rosenberg et al., *N. Engl. J. Med.* **313**, 1485–1492 (1985).
10. S. A. Rosenberg, P. Spiess, R. Lafreniere, *Science* **233**, 1318–1321 (1986).
11. L. M. Muul, P. J. Spiess, E. P. Director, S. A. Rosenberg, *J. Immunol.* **138**, 989–995 (1987).
12. S. A. Rosenberg et al., *N. Engl. J. Med.* **319**, 1676–1680 (1988).
13. M. E. Dudley et al., *Science* **298**, 850–854 (2002).
14. H. W. H. G. Kessels, M. C. Wolkers, M. D. van den Boom, M. A. van den Valk, T. N. M. Schumacher, *Nat. Immunol.* **2**, 957–961 (2001).
15. R. A. Morgan et al., *Science* **314**, 126–129 (2006).
16. J. N. Kochenderfer et al., *Blood* **116**, 4099–4102 (2010).
17. S. A. Rosenberg et al., *Clin. Cancer Res.* **17**, 4550–4557 (2011).
18. S. Pilon-Thomas et al., *J. Immunother.* **35**, 615–620 (2012).
19. L. G. Radvanyi et al., *Clin. Cancer Res.* **18**, 6758–6770 (2012).
20. M. J. Besser et al., *Clin. Cancer Res.* **19**, 4792–4800 (2013).
21. J. J. Hong et al., *Clin. Cancer Res.* **16**, 4892–4898 (2010).
22. S. A. Rosenberg et al., *N. Engl. J. Med.* **323**, 570–578 (1990).
23. V. Bronte et al., *J. Immunol.* **161**, 5313–5320 (1998).
24. X. Yao et al., *Blood* **119**, 5688–5696 (2012).
25. L. Gattinoni et al., *J. Exp. Med.* **202**, 907–912 (2005).
26. M. E. Dudley et al., *J. Clin. Oncol.* **26**, 5233–5239 (2008).
27. C. M. Paulos et al., *J. Clin. Invest.* **117**, 2197–2204 (2007).
28. N. P. Restifo, M. E. Dudley, S. A. Rosenberg, *Nat. Rev. Immunol.* **12**, 269–281 (2012).
29. L. Gattinoni et al., *Nat. Med.* **17**, 1290–1297 (2011).
30. Y. Kawakami et al., *Proc. Natl. Acad. Sci. U.S.A.* **91**, 6458–6462 (1994).
31. Y. Kawakami et al., *Proc. Natl. Acad. Sci. U.S.A.* **91**, 3515–3519 (1994).
32. L. A. Johnson et al., *Blood* **114**, 535–546 (2009).
33. M. S. Lawrence et al., *Nature* **499**, 214–218 (2013).
34. T. Wölfel et al., *Science* **269**, 1281–1284 (1995).
35. M. M. Gubin et al., *Nature* **515**, 577–581 (2014).
36. S. L. Topalian et al., *N. Engl. J. Med.* **366**, 2443–2454 (2012).
37. R. N. van Rooij et al., *J. Clin. Oncol.* **31**, e439–e442 (2013).
38. S. D. Brown et al., *Genome Res.* **24**, 743–750 (2014).
39. P. F. Robbins et al., *Nat. Med.* **19**, 747–752 (2013).
40. Y. C. Lu et al., *Clin. Cancer Res.* **20**, 3401–3410 (2014).
41. S. A. Rosenberg, J. C. Yang, N. P. Restifo, *Nat. Med.* **10**, 909–915 (2004).
42. C. A. Klebanoff, N. Acquavella, Z. Yu, N. P. Restifo, *Immunol. Rev.* **239**, 27–44 (2011).
43. T. N. Schumacher, R. D. Schreiber, *Science* **348**, 69–74 (2015).
44. E. Tran et al., *Science* **344**, 641–645 (2014).
45. G. Gross, T. Waks, Z. Eshhar, *Proc. Natl. Acad. Sci. U.S.A.* **86**, 10024–10028 (1989).
46. J. Maher, R. J. Brentjens, G. Gunset, I. Rivière, M. Sadelain, *Nat. Biotechnol.* **20**, 70–75 (2002).
47. C. Imai et al., *Leukemia* **18**, 676–684 (2004).
48. D. G. Song et al.., *Cancer Res.* **71**, 4617–4627 (2011).
49. C. A. Klebanoff et al., *Proc. Natl. Acad. Sci. U.S.A.* **102**, 9571–9576 (2005).
50. C. Berger et al., *J. Clin. Invest.* **118**, 294–305 (2008).
51. L. Gattinoni, D. J. Powell Jr., S. A. Rosenberg, N. P. Restifo, *Nat. Rev. Immunol.* **6**, 383–393 (2006).
52. L. Gattinoni et al., *J. Clin. Invest.* **115**, 1616–1626 (2005).
53. V. R. Buchholz et al., *Science* **340**, 630–635 (2013).
54. C. Gerlach et al., *Science* **340**, 635–639 (2013).
55. P. Muranski et al., *Immunity* **35**, 972–985 (2011).
56. D. C. Palmer et al., *Proc. Natl. Acad. Sci. U.S.A.* **105**, 8061–8066 (2008).
57. C. H. Lamers et al., *Mol. Ther.* **21**, 904–912 (2013).
58. M. R. Parkhurst et al., *Mol. Ther.* **19**, 620–626 (2011).
59. R. A. Morgan et al., *J. Immunother.* **36**, 133–151 (2013).
60. R. A. Morgan et al., *Mol. Ther.* **18**, 843–851 (2010).
61. Y. Li et al., *Nat. Biotechnol.* **23**, 349–354 (2005).
62. P. F. Robbins et al., *J. Immunol.* **180**, 6116–6131 (2008).
63. G. P. Linette et al., *Blood* **122**, 863–871 (2013).
64. R. A. Gardner, M. C. Jensen, *Cancer J.* **20**, 107–111 (2014).
65. S. Gill, C. H. June, *Immunol. Rev.* **263**, 68–89 (2015).
66. M. Sadelain, R. Brentjens, I. Rivière, *Cancer Discov.* **3**, 388–398 (2013).
67. J. N. Kochenderfer, S. A. Rosenberg, *Nat. Rev. Clin. Oncol.* **10**, 267–276 (2013).
68. M. Kalos et al., *Sci. Transl. Med.* **3**, 95ra73 (2011).
69. S. A. Grupp et al., *N. Engl. J. Med.* **368**, 1509–1518 (2013).
70. R. J. Brentjens et al., *Sci. Transl. Med.* **5**, 177ra38 (2013).
71. J. N. Kochenderfer et al., *J. Clin. Oncol.* **33**, 540–549 (2015).
72. D. W. Lee et al., *Blood* **124**, 188–195 (2014).
73. H. Singh, H. Huls, P. Kebriaei, L. J. Cooper, *Immunol. Rev.* **257**, 181–190 (2014).
74. J. A. Doudna, E. Charpentier, *Science* **346**, 1258096 (2014).
75. I. Pizzitola et al., *Leukemia* **28**, 1596–1605 (2014).
76. B. Savoldo et al., *Blood* **110**, 2620–2630 (2007).
77. A. K. Gopal et al., *Blood* **125**, 1236–1243 (2015).
78. C. U. Louis et al., *Blood* **118**, 6050–6056 (2011).
79. Y. Zhao et al., *Cancer Res.* **70**, 9053–9061 (2010).
80. M. J. Scanlan, A. O. Gure, A. A. Jungbluth, L. J. Old, Y. T. Chen, *Immunol. Rev.* **188**, 22–32 (2002).
81. P. F. Robbins et al., *J. Clin. Oncol.* **29**, 917–924 (2011).
82. R. A. Morgan et al., *Hum. Gene Ther.* **23**, 1043–1053 (2012).
83. A. Gros et al., *J. Clin. Invest.* **124**, 2246–2259 (2014).
84. Y. Li, M. Bleakley, C. Yee, *J. Immunol.* **175**, 2261–2269 (2005).
85. J. G. Crompton et al., *Cancer Res.* **75**, 296–305 (2015).
86. S. P. Kerkar et al., *J. Clin. Invest.* **121**, 4746–4757 (2011).
87. A. Di Stasi et al., *N. Engl. J. Med.* **365**, 1673–1683 (2011).
88. S. A. Rosenberg et al., *J. Natl. Cancer Inst.* **86**, 1159–1166 (1994).
89. C. S. Hinrichs et al., 2014 American Society of Clinical Oncology (ASCO) Annual Meeting, Chicago, IL, 30 May to 3 June 1014 (ASCO, Alexandria, VA, 2014), abstract LBA3008; http://meetinglibrary.asco.org/content/129263-144.
90. N. N. Hunder et al., *N. Engl. J. Med.* **358**, 2698–2703 (2008).
91. A. G. Chapuis et al., *Sci. Transl. Med.* **5**, 174ra27 (2013).
92. S. L. Maude et al., *N. Engl. J. Med.* **371**, 1507–1517 (2014).
93. M. L. Davila et al., *Sci. Transl. Med.* **6**, 224ra25 (2014).
94. D. W. Lee et al., *Lancet* **385**, 517–528 (2015).

Neoantigens in cancer immunotherapy

Ton N. Schumacher[1]* and Robert D. Schreiber[2]*

The clinical relevance of T cells in the control of a diverse set of human cancers is now beyond doubt. However, the nature of the antigens that allow the immune system to distinguish cancer cells from noncancer cells has long remained obscure. Recent technological innovations have made it possible to dissect the immune response to patient-specific neoantigens that arise as a consequence of tumor-specific mutations, and emerging data suggest that recognition of such neoantigens is a major factor in the activity of clinical immunotherapies. These observations indicate that neoantigen load may form a biomarker in cancer immunotherapy and provide an incentive for the development of novel therapeutic approaches that selectively enhance T cell reactivity against this class of antigens.

Immunotherapies that boost the ability of endogenous T cells to destroy cancer cells have demonstrated therapeutic efficacy in a variety of human malignancies. Until recently, evidence that the endogenous T cell compartment could help control tumor growth was in large part restricted to preclinical mouse tumor models and to human melanoma. Specifically, mice lacking an intact immune system were shown to be more susceptible to carcinogen-induced and spontaneous cancers compared with their immunocompetent counterparts (1). With respect to human studies, the effects of the T cell cytokine interleukin-2 in a small subset of melanoma patients provided early clinical evidence of the potential of immunotherapy in this disease. In 2010, the field was revitalized by a landmark randomized clinical trial that demonstrated that treatment with ipilimumab, an antibody that targets the T cell checkpoint protein CTLA-4, improved overall survival of patients with metastatic melanoma (2). As a direct test of the tumoricidal potential of the endogenous T cell compartment, work by Rosenberg and colleagues demonstrated that infusion of autologous ex vivo expanded tumor-infiltrating lymphocytes can induce objective clinical responses in metastatic melanoma (3), and at least part of this clinical activity is due to cytotoxic T cells (4). Importantly, recent studies demonstrate that T cell–based immunotherapies are also effective in a range of other human malignancies. In particular, early-phase trials of antibodies that interfere with the T cell checkpoint molecule PD-1 have shown clinical activity in tumor types as diverse as melanoma, lung cancer, bladder cancer, stomach cancer, renal cell cancer, head and neck cancer, and Hodgkin's lymph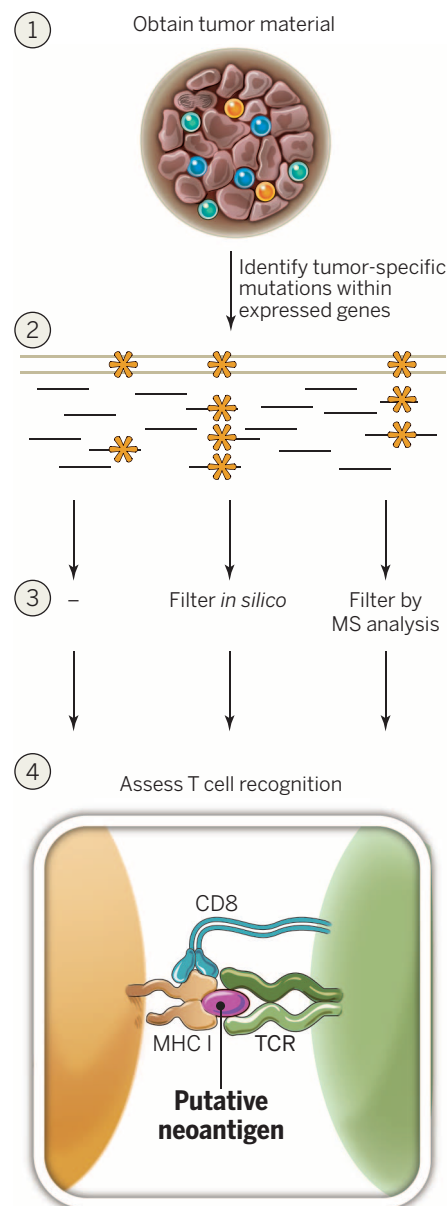oma (5). Based on the relationship between pretherapy CD8+ T cell infiltrates and response to PD-1 blockade in melanoma, cytotoxic T cell activity also appears to play a central role in this form of cancer immunotherapy (6).

An implicit conclusion from these clinical data is that in a substantial fraction of patients, the endogenous T cell compartment is able to recognize peptide epitopes that are displayed on major histocompatibility complexes (MHCs) on the surface of the malignant cells. On theoretical grounds, such cancer rejection epitopes may be derived from two classes of antigens. A first class of potential cancer rejection antigens is formed by nonmutated proteins to which T cell tolerance is incomplete—for instance, because of their restricted tissue expression pattern. A second class of potential cancer rejection antigens is formed by peptides that are entirely absent from the normal human genome, so-called neoantigens. For the large group of human tumors without a viral etiology, such neo-epitopes are solely created by tumor-specific DNA alterations that result in the formation of novel protein sequences. For virus-associated tumors, such as cervical cancer and a subset of head and neck cancers, epitopes derived from viral open reading frames also contribute to the pool of neoantigens.

As compared with nonmutated self-antigens, neoantigens have been postulated to be of particular relevance to tumor control, as the quality of the T cell pool that is available for these antigens is not affected by central T cell tolerance (7). Although a number of heroic studies provided early evidence for the immunogenicity of mutation-derived neoantigens [reviewed in (8)], technology to systemically analyze T cell reactivity against these antigens only became available recently. Here, we review our emerging understanding of the role of patient-specific neoantigens in current cancer immunotherapies and the implications of these data for the development of next-generation immunotherapies.

Exome-guided neoantigen identification: Process considerations

A large fraction of the mutations in human tumors is not shared between patients at

[1]Division of Immunology, Netherlands Cancer Institute, Plesmanlaan 121, 1066 CX, Amsterdam, Netherlands. [2]Department of Pathology and Immunology, Washington University School of Medicine, 660 South Euclid Avenue, St. Louis, MO 63110, USA.
*Corresponding author. E-mail: t.schumacher@nki.nl (T.N.S.); schreiber@immunology.wustl.edu (R.D.S.)

Fig. 1. Cancer exome–based identification of neoantigens. Tumor material is analyzed for nonsynonymous somatic mutations. When available, RNA sequencing data are used to focus on mutations in expressed genes. Peptide stretches containing any of the identified nonsynonymous mutations are generated in silico and are either left unfiltered (16, 17), filtered through the use of prediction algorithms [e.g., (10–13)], or used to identify MHC-associated neoantigens in mass spectrometry data (15, 20). Modeling of the effect of mutations on the resulting peptide-MHC complex may be used as an additional filter (20). Resulting epitope sets are used to identify physiologically occurring neoantigen-specific T cell responses by MHC multimer-based screens (13, 22) or functional assays [e.g., (11, 12)], within both CD8+ [e.g., (11–13, 19, 39)] and CD4+ (16, 18) T cell populations. Alternatively, T cell induction strategies are used to validate predicted neoantigens [e.g., (10, 20)].

meaningful frequencies and may therefore be considered patient-specific. Because of this, technologies to interrogate T cell reactivity against putative mutation-derived neoantigens need to be based on the genome of an individual tumor. With the development of deep-sequencing technologies, it has become feasible to identify the mutations present within the protein-encoding part of the genome (the exome) of an individual tumor with relative ease and thereby predict potential neoantigens (*9*). Two studies in mouse models provided the first direct evidence that such a cancer exome–based approach can be used to identify neoantigens that can be recognized by T cells (*10*, *11*). In brief, for all mutations that resulted in the formation of novel protein sequence, potential MHC binding peptides were predicted, and the resulting set of potential neoantigens was used to query T cell reactivity. Subsequent studies have demonstrated that cancer exome–based analyses can also be exploited in a clinical setting, to dissect T cell reactivity in patients who are treated by either tumor-infiltrating lymphocyte (TIL) cell therapy or checkpoint blockade (*12*, *13*). Furthermore, following this early work, the identification of neoantigens on the basis of cancer exome data has been documented in a variety of experimental model systems and human malignancies (*10–22*).

The technological pipeline used to identify neoantigens in these different studies has varied substantially, and further optimization is likely possible (Fig. 1). Accepting the limitations of probing the mutational profile of a tumor in a single biopsy (*23*), the genetic analysis of the tumor itself can be considered a robust process. Specifically, based on the analysis of neoantigens previously identified by other means, the false-negative rate of cancer

exome sequencing is low—i.e., the vast majority of neoantigens occur within exonic sequence for which coverage is sufficient (*24*). At the same time, it is apparent from unbiased screening efforts—in which the entire collection of identified mutations was used to query T cell reactivity—that the vast majority of mutations within expressed genes do not lead to the formation of neoantigens that are recognized by autologous T cells (*16*, *17*). Because of this, a robust pipeline that can be used for the filtering of cancer exome data is essential, in particular for tumors with high mutational loads.

How can such filtering be performed? With the set of mutations within expressed genes as a starting point, two additional requirements can be formulated. First, a mutated protein needs to be processed and then presented as a mutant peptide by MHC molecules. Second, T cells need to be present that can recognize this peptide-MHC complex. In two recent preclinical studies, presentation of a handful of predicted neoantigens by MHC molecules was experimentally demonstrated by mass spectrometry (*15*, *20*), and this approach may form a valuable strategy to further optimize MHC presentation algorithms. At the same time, the sensitivity of mass spectrometry is presently still limited, thereby likely resulting in a substantial fraction of false negatives. For this reason, but also because of logistical issues, implementation of this approach in a clinical setting is unlikely to happen soon. Lacking direct evidence for MHC presentation, as can be provided by mass spectrometry, presentation of neoantigens by MHC class I molecules may be predicted using previously established algorithms that analyze aspects such as the likelihood of proteasomal processing, transport into the endoplasmic reticulum, and affinity for the relevant MHC class I alleles. In addition,

gene expression levels (or perhaps preferably protein translation levels) may potentially also be used to help predict epitope abundance (*25*).

Although most neoantigen identification studies have successfully used criteria for epitope prediction that are similar to those previously established for the identification of pathogen-derived epitopes [e.g., (*12*, *13*)], Srivastava and colleagues have argued that neoantigens in a transplantable mouse tumor model display very different properties from viral antigens and generally have a very low affinity for MHC class I (*14*). Although lacking a satisfactory explanation to reconcile these findings, we do note that the vast majority of human neoantigens that have been identified in unbiased screens do display a high predicted MHC binding affinity (*24*, *26*). Likewise, minor histocompatibility antigens, an antigen class that is conceptually similar to neoantigens, are correctly identified by classical MHC binding algorithms (*27*). Moreover, the mutations that were identified in a recent preclinical study as forming tumor-specific mutant antigens that could induce therapeutic tumor rejection when used in tumor vaccines (*15*) were not predicted to be significant using the Srivastava approach. Another potential filter step that has been suggested examines whether the mutation is expected to improve MHC binding, rather than solely alter the T cell receptor (TCR)–exposed surface of the mutant peptide. However, with examples of both categories in both mouse models and human data, the added value of such a filter may be relatively modest (*11*, *15*, *20*, *26*). For MHC class I restricted neoantigens, conceivably the biggest gain in prediction algorithms can be made with respect to identification of the subset of MHC binding peptides that can successfully be recognized
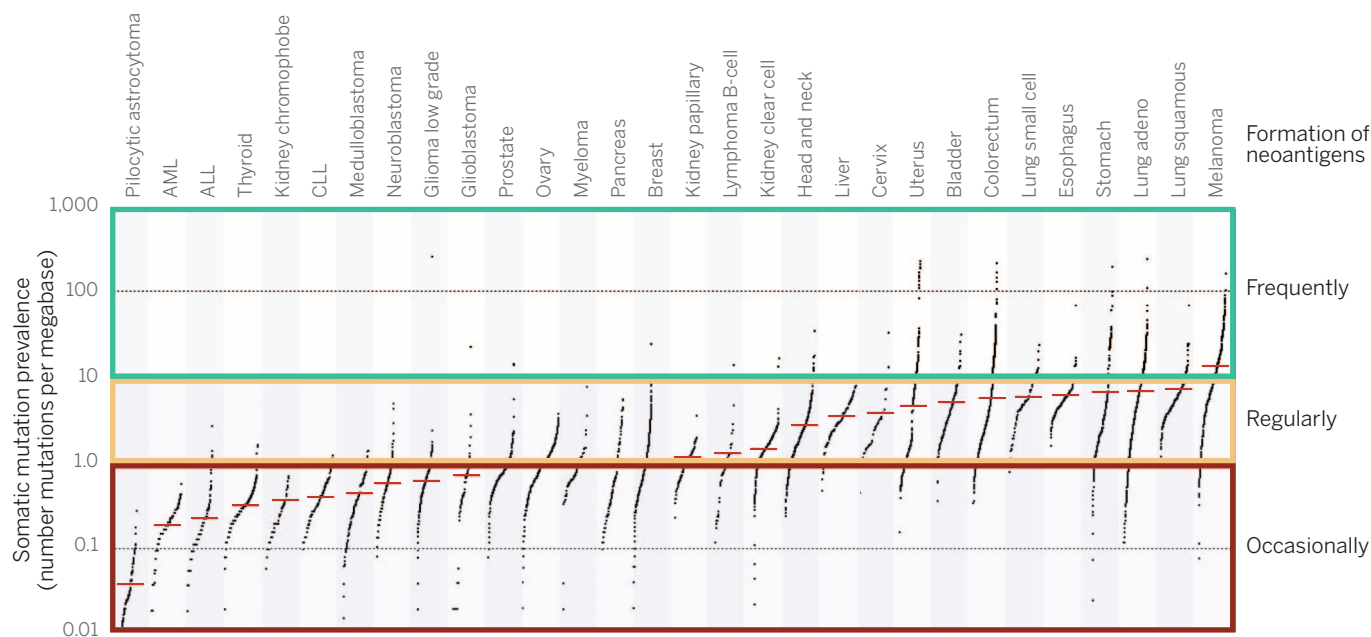
Fig. 2. Estimate of the neoantigen repertoire in human cancer. Data depict the number of somatic mutations in individual tumors. Categories on the right indicate current estimates of the likelihood of neoantigen formation in different tumor types. Adapted from (*50*). It is possible that the immune system in melanoma patients picks up on only a fraction of the available neoantigen repertoire, in which case the current analysis will be an underestimate. A value of 10 somatic mutations per Mb of coding DNA corresponds to ~150 nonsynonymous mutations within expressed genes.

by the TCR repertoire. With respect to this, the nature of the central TCR-exposed residues of MHC-bound peptides has been shown to be associated with peptide immunogenicity (*28*). By the same token, alterations at these sites may potentially be picked up by the immune system more readily (*20*). However, a substantial further experimental effort is required to evaluate to what extent algorithms that predict immunogenicity can facilitate the identification of MHC class I–restricted neoantigens. For MHC class II–restricted neoantigens, it will be important to obtain a better understanding not only of peptide immunogenicity but also of the basic factors that determine the efficiency of epitope presentation.

Size and nature of the neoantigen repertoire

Large-scale analyses of neoantigen-specific T cell reactivity have now been carried out for a substantial number of patients, mostly in melanoma (*12*, *13*, *16*, *17*). With the caveat of a potential selection bias toward patients with a clinical benefit upon immunotherapeutic intervention, these analyses provide a first estimate of the frequency with which the immune system recognizes the neoantigens that are formed as a consequence of mutations. The first and arguably most important conclusion that can be drawn from these analyses is that the T cell–based immune system reacts to both MHC class I–restricted (*12*, *13*, *17*) and MHC class II–restricted neoantigens (*16*) in a large fraction of melanoma patients. The second conclusion that can be drawn from these analyses is that only a very small fraction of the nonsynonymous mutations in expressed genes in these tumors leads to the formation of a neoantigen for which CD4+ or CD8+ T cell reactivity can be detected within tumor-infiltrating lymphocytes.

What do these observations mean for the potential formation of neoantigen repertoires in other human malignancies? Most human melanomas have a mutational load above 10 somatic mutations per megabase (Mb) of coding DNA, and this is apparently sufficient to lead to the frequent formation of neoantigens that can be seen by T cells. Based on these data, formation of neoantigens that can potentially be recognized by autologous T cells is expected to also be common for other tumors with a mutational load above 10 somatic mutations per Mb (corresponding to approximately 150 non-synonymous mutations within expressed genes) (Fig. 2). This group contains a sizable fraction of high-prevalence tumor types such as lung cancer and colorectal cancer. If formation of neoantigens is a frequent event in tumors with mutational loads above 10 somatic mutations per Mb, many tumors with a mutational load of 1 to 10 per Mb may still be expected to carry neoantigens that

can be recognized by T cells. However, as based on the fact that even for melanomas with a mutational load around 10 mutations per Mb, T cell reactivity is not always observed (*16*), tumor types with a mutational load below 1 mutation per Mb appear less likely to commonly express neoantigens that can be recognized by autologous T cells.

Although this analysis provides a useful first sketch of the expected relevance of neoantigens

Fig. 3. Characteristics of melanoma neoantigens. (**Top**) For a group of CD4+ T cell neoantigens (8 epitopes) and CD8+ T cell neoantigens (13 epitopes) identified by cancer exome–based screens, the frequency of mutation of that residue in a cohort of ~20,000 human tumor samples (*51*) is depicted. (**Bottom**) For the same group of CD4+ T cell and CD8+ T cell neoantigens, the fraction of encoding mutations that occurs within known oncogenes (*52*) is depicted.

in different tumor types, three important factors should be taken into account. First, by relying on the presence of preexisting T cell reactivity as a readout, the human studies carried out to date will only detect neoantigens that were immunogenic during in vivo tumor outgrowth (either spontaneously or boosted by therapy). It is conceivable that not all tumor-expressed neoantigens induce an autologous T cell response—for instance, because they are not efficiently cross presented. In addition, at least in preclinical models, there is evidence for immunodominance of tumor antigens, where the immune system becomes so fixated on particular antigens that it ignores other antigens that are both present and detectable in the tumor (*29*). If only a fraction of the available neoantigens would normally elicit T cell reactivity, the analyses carried out to date may underestimate the actual neoantigen repertoire. As a second consideration, it is important to realize that the formation of neoantigens is a probabilistic process in which each additional mutation increases the odds that a relevant neoantigen is created. Thus, in this "neoantigen lottery," there will be cases in which despite a

high mutational load, neoantigen-specific T cell reactivity is lacking or, vice versa, in which a tumor with only a handful of mutations will express an MHC class I– or class II–restricted neoantigen. Third, although we here make a prediction with regard to the frequency with which neoantigens that can potentially be recognized by the TCR repertoire are formed, it should be kept in mind that the presence of a neoantigen does not equal the induction of T cell reactivity. Human tumors vary substantially in the composition of their microenvironment, and this is likely to influence the ability of the T cell pool to respond to mutated antigens. Related to this, from a conceptual point of view, therapeutic manipulation of T cell reactivity would seem particularly attractive for tumor types that do express large numbers of antigens but in which the tumor microenvironment hinders the activation of the T cells that recognize them.
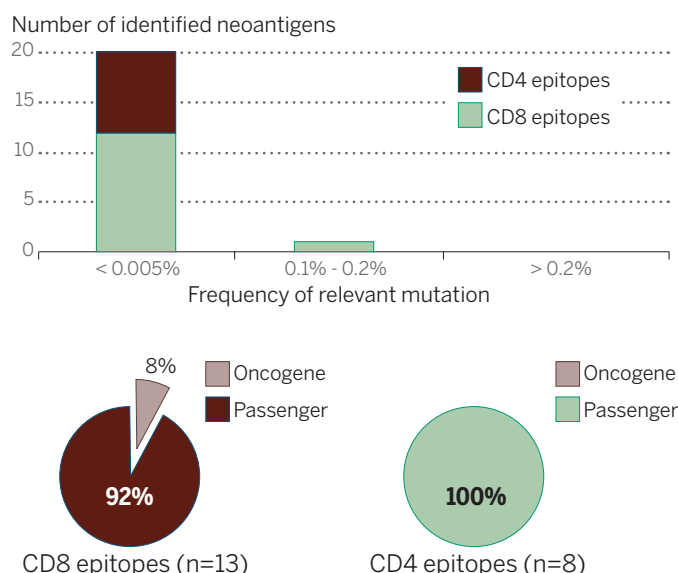
What are the characteristics of mutation-derived neoantigens in human cancer, both with respect to the genes from which they are derived and the frequency with which they occur within the patient population? In an ideal world, neoantigens would be derived from essential oncogenes and occur in large patient groups, to both reduce the likelihood of escape and facilitate clinical interventions that enhance T cell reactivity against them. Clearly, T cell responses do sometimes occur against MHC class I–restricted (*30*) and MHC class II–restricted neoantigens in validated oncogenes that are shared between subgroups of patients (*31*). At the same time, it is apparent that, at least in melanoma, the bulk of the neoantigen-specific T cell response is directed toward mutated proteins that are essentially unique to that tumor and that are unlikely to play a key role in cellular transformation (Fig. 3, top and bottom) (*16*). A direct implication of this bias in neoantigen-specific T cell reactivity toward patient-specific passenger mutations is that the targeting of defined neoantigens will likely require the development of personalized immunotherapies.

Extrinsic influences on the tumor antigenic landscape

The neoantigen repertoire expressed in a clinically apparent cancer may have been substantially influenced by the developing tumor's interaction with the immune system that occurs even before it becomes clinically apparent. This is the process of "cancer immunoediting" that has been well documented in preclinical cancer models (*1*, *32*, *33*). In its most complex form, cancer immunoediting may occur in three phases: elimination, in which the innate and adaptive immune systems work

together to recognize a developing tumor and destroy it before it becomes clinically apparent; equilibrium, in which residual occult tumor cells not destroyed in the elimination phase are held in a state of tumor dormancy as a consequence of adaptive immune system activity and undergo "editing"; and escape, in which edited tumor cells are no longer recognized or controlled by immune processes, begin to grow progressively, induce an immunosuppressive tumor microenvironment, and then emerge as clinically apparent cancers. Recent work has demonstrated that T cells play a major role in shaping the immunogenicity of developing cancers—i.e., "edit" tumor immunogenicity—and exert this effect by at least two mechanisms. First, T cells can shape tumor antigenicity/immunogenicity through an immunoselection process by destroying tumor cells that express strong tumor-specific mutant antigens, leaving behind tumor cells that either express weaker antigens (some of which may still be mutant tumor antigens) or are incapable of expressing antigens (e.g., those that have developed mutations in antigen processing or presentation) (11). Second, chronic T cell attack on a tumor has been shown to silence expression of certain tumor-specific antigens through epigenetic mechanisms in a preclinical model (34). Strikingly, a recent study, based on analysis of thousands of the Cancer Genome Atlas solid tumor samples, showed that, in particular in colorectal cancer, mutated peptides predicted to bind to autologous MHC class I molecules are less frequent than expected by chance, an observation that is consistent with immune-based selection (35). By extension, the combination of cell-extrinsic forces such as cancer immunoediting and the stochastic nature of epitopes arising from tumor-specific mutations may help drive the heterogeneous mutational—and by inference, antigenic—landscapes that have been noted in certain tumors (23). As such, the antigenic heterogeneity of tumors might explain some of the differences in response that individual patients display to checkpoint blockade therapy. Individuals who develop durable responses to checkpoint blockade may be those whose tumors retain sufficient antigenicity to render them sensitive to the heightened immune function that accompanies cancer immunotherapy, despite not being controlled by naturally occurring antitumor immune responses.

Role of neoantigens in cancer immunotherapy

On theoretical grounds, two factors should determine the relative importance of neoantigens and nonmutated self-antigens in the effects of cancer immunotherapies such as checkpoint blockade and TIL therapy: first, the frequency with which T cell responses against the two antigen classes occur; second, the relative potency of T cell responses specific for the two antigen classes. Recent work in mouse models using transplantable carcinogen-induced cancers has demonstrated that checkpoint blockade alters both the quality of the neoantigen-specific intratumoral T cell response (as reflected by common- and

treatment-specific changes in gene expression in CD8+ TILs isolated from tumor-bearing mice treated with antibodies to CTLA-4 and/or PD-1) and the magnitude of this T cell response (seen with CTLA-4 or combined CTLA-4/PD-1 blockade but not with PD-1 blockade only) (15). Because the neoantigens identified in this model serve as cancer rejection antigens, these data provide compelling evidence that checkpoint blockade acts at least in part through neoantigen-specific T cell reactivity in this setting. However, in the case of human melanoma, where autochthonous tumors may be in contact with the immune system for years, the situation is more complicated. As discussed above, T cell reactivity against neoantigens is common in melanoma. Furthermore, a case report has shown that such reactivity can be enhanced by anti–CTLA-4 treatment (13). However, T cell reactivity against nonmutated shared antigens is also observed in the majority of melanoma patients, and broadening of this T cell response has been documented following both TIL therapy and anti–CTLA-4 treatment (36, 37). Thus, although the murine data show that neoantigen-specific T cell reactivity can be critical to the effects of checkpoint blockade, the human data are presently only consistent with this possibility.

What other data are available with respect to this issue? If recognition of neoantigens is an important component of cancer immunotherapy, one would expect tumor types with high numbers of mutations to be characterized by strong T cell

> *"The genetic damage that on the one hand leads to oncogenic outgrowth can also be targeted by the immune system to control malignancies."*

responses and to be particularly sensitive to immunotherapy. Furthermore, also within a given tumor type, response rate should correlate with mutational load. Evidence for a role of neoantigens in driving the strength of the intratumoral T cell response is provided by the observation that the presence of CD8+ T cells in cancer lesions, as read out using RNA sequencing data, is higher in tumors with a high mutational burden (38). Furthermore, an extensive analysis by Hacohen and colleagues has demonstrated that the level of transcripts associated with cytolytic activity of natural killer cells and T cells correlates with mutational load in a large series of human tumors (35). With respect to the effects of immunotherapy in tumors with different mutational loads, in non–small cell lung cancer patients treated with anti–PD-1, mutational load shows a strong correlation with clinical response (22). Likewise, in melanoma patients treated with ipilimumab, an antibody to CTLA-4, long-term benefit is also associated with a higher

mutational load, although the effect appears less profound in this setting (39). A striking observation in the latter study has been that the predicted MHC binding neoantigens in patients with a long-term clinical benefit were enriched for a large series of tetrapeptide motifs that were not found in tumors of patients with no or minimal clinical benefit. An appealing interpretation of these data is that the neoantigen-specific T cell response is preferentially directed toward a subset of mutant sequences, something that could facilitate bioinformatic identification of neoantigens for therapeutic targeting. However, analysis of the sequence properties of human neoantigens identified in other studies does not show the profound bias toward these tetrapeptide signatures that would be predicted if their role were central in the tumor-specific T cell response (40), and conceivably the identified tetrapeptide motifs play a different role.

It will be valuable to extend the analysis of genomic determinants of tumor cell sensitivity to cancer immunotherapeutics to other malignancies. However, because of the probabilistic nature of neoantigen generation, mutational load will by itself always remain an imperfect biomarker, even in a situation in which neoantigen reactivity is the sole tumor-specific T cell reactivity that is relevant to tumor control. Furthermore, the formation of tumor-specific antigens is only one of a number of essential conditions for a successful immune attack on cancer cells, a concept that is well described by the cancer-immunity cycle introduced by Chen and Mellman (41). As an example, genetic inactivation of the β_2-microglobulin subunit of MHC class I molecules is a relatively frequent event in some tumor types (42). In addition, a recent analysis of genetic alterations that are present in tumors with high immune activity provides evidence for a series of other escape mechanisms (35). In such cases, in which the cancer-immunity cycle is disrupted at another site, the number of neoantigens produced is unlikely to still be of much relevance. Because of this interdependence of different phases of the cancer-immunity cycle, the combined use of assay systems that report on these different phases appears warranted.

Arguably the most direct data on the relevance of neoantigen-specific T cells in human tumor control comes from a small number of clinical studies that involve infusion of defined T cell populations or infusion of TCR-transduced T cells. Encouragingly, a recent case report demonstrated regression of a metastatic cholangiocarcinoma by infusion of a CD4+ T cell product that was highly enriched for reactivity against an MHC class II–restricted neoantigen (18). Combined with the observation that, at least in melanoma, CD4+ T cell recognition of neoantigens is a frequent event (16), these data underscore the potential clinical relevance of MHC class II–restricted neoantigens. Comparison of the clinical effects of TIL therapy with that of T cells modified with TCRs recognizing different shared antigens can also be considered informative. Infusion of T cells modified with TCRs directed against the gp100 and MART-I
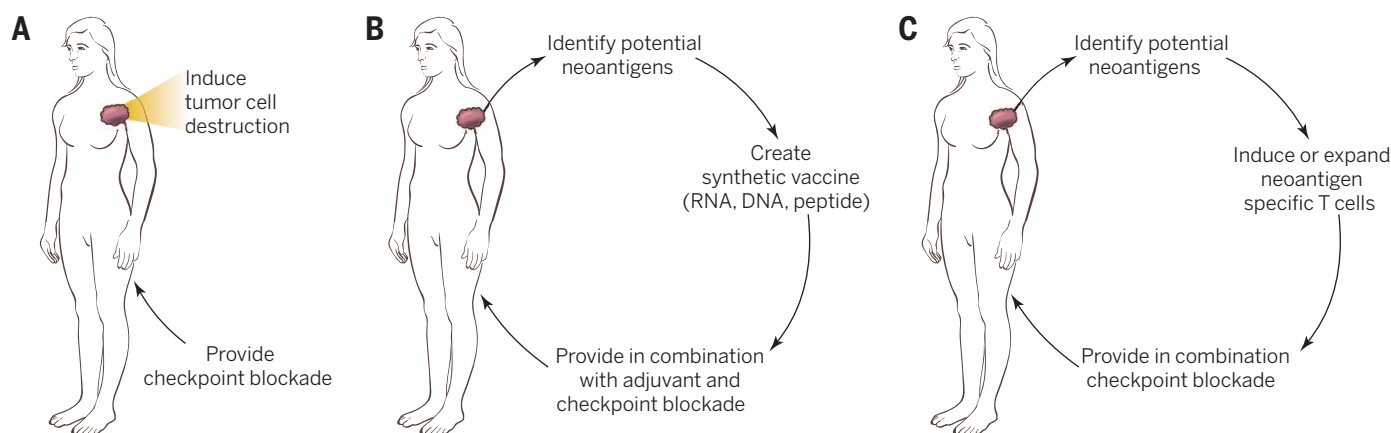
Fig. 4. Strategies to target the patient-specific neoantigen repertoire. (**A**) Immunotherapy is given in combination with interventions such as radiotherapy that enhance exposure to autologous neoantigens. (**B**) Potential neoantigens are identified as in Fig. 1 steps 1 to 3, a patient-specific vaccine is produced, and this vaccine is given together with adjuvant and T cell checkpoint-blocking antibodies. (**C**) Potential neoantigens are identified as in Fig. 1 steps 1 to 3, T cells that are specific for these neoantigens are induced or expanded in vitro, and the resulting T cell product is given together with T cell checkpoint-blocking antibodies.

melanocyte differentiation antigens, a prominent class of self-antigens in melanoma, shows a relatively modest clinical effect that is accompanied by substantial on-target toxicity against healthy melanocytes (43). Because this toxicity is relatively infrequent in TIL therapy, these data strongly suggest that T cell reactivity against the melanocyte differentiation antigens is not a major driver of the antitumor activity of this therapy. At the same time, there is data showing that T cell products directed against NY-eso-1, one of the nonmutant self-antigens from the family of cancer/germline antigens that show very limited expression in healthy tissue, can display substantial antitumor activity (44, 45). Thus, although the available data support the notion that T cell recognition of neoantigens contributes substantially to the effects of the currently used immunotherapies, it would not be justified to dismiss a potential contribution of T cell responses against a subset of nonmutant antigens. A direct comparison of the antitumor activity of neoantigen-specific and self-antigen–specific T cells obtained from individual patients would be useful to further address this issue.

Therapeutic use of the patient-specific neoantigen repertoire

Based on the fact that, at least in tumors with high mutational loads, the amount of DNA damage is sufficient for the immune system to see one or multiple epitopes as foreign, it becomes of interest to stimulate neoantigen-specific T cell responses in cancer patients. Such stimulation can obviously only be of value if the strength of the neoantigen-specific T cell response is otherwise a limiting factor in tumor control. Human data on this important issue are lacking. However, in mouse models, vaccination with defined neoantigens has been shown to result in increased tumor control (10, 14, 15, 20), providing sufficient rationale for the clinical development of neoantigen-directed therapeutics. Because the majority of possible neoantigens are specific to the individual being

treated (Fig. 3), such therapeutic approaches will in most cases entail personalized immunotherapies that exploit either the antigen repertoire in the tumor cells themselves or information on that repertoire, as obtained by tumor sequencing (Fig. 4). As a first approach, a combination of checkpoint-blocking antibodies with therapeutic interventions—such as tumor radiotherapy, oncolytic viruses, or autologous tumor cell vaccines—that can increase neoantigen exposure to the T cell–based immune system may be synergistic (Fig. 4A). As a downside, as compared to molecularly defined vaccines, the neoantigens released by such strategies will be diluted by the large amount of nonmutant peptides that are also present. In addition, control over the maturation signals received by antigen-presenting cells is relatively limited. Nevertheless, because of the relative ease of clinical development of some of these combination therapies, extensive testing of such therapies is warranted.

To allow a more defined targeting of the neoantigen repertoire in human tumors, two alternative approaches should be considered, in both cases relying on sets of potential neoantigens as identified by sequencing of tumor material (Fig. 4, B and C). First, synthetic vaccines may be produced that contain or encode a set of predicted neoantigens. Although still a substantial departure from the classical pharmaceutical model, clinical development of such personalized vaccines is within reach (46–48). Mouse model data support the clinical translation of this approach, and the two most pressing questions appear to be (i) whether our ability to predict the most relevant neoantigens is already sufficiently advanced and (ii) how such vaccines may best be administered. Second, the information obtained from tumor sequencing may be used to create neoantigen-specific T cell products in vitro. This may involve either the expansion of neoantigen-specific T cell populations that can already be detected within tumor tissue or in blood or the de novo induction of such cells.

Regardless of the strategy used to enhance neoantigen-specific T cell reactivity, it will likely prove important to target multiple neoantigens simultaneously in order to prevent tumor escape by editing of the mutated epitope concerned (1). In addition, it may be prudent to avoid the targeting of mutations in gene products that are seen by the immune system in autoimmune disease to avoid induction of or exacerbation of cancer-associated autoimmune disease (49).

Concluding remarks

Based on data obtained over the past few years, it is plausible that neoantigen-specific T cell reactivity forms a major "active ingredient" of successful cancer immunotherapies. In other words, the genetic damage that on the one hand leads to oncogenic outgrowth can also be targeted by the immune system to control malignancies. Based on this finding, it will be important to engineer therapeutic interventions by which neoantigen-specific T cell reactivity is selectively enhanced. Because of the tumor-restricted expression of the antigens that are being targeted, these personalized cancer immunotherapies offer the promise of high specificity and safety. Conceivably, the boosting of neoantigen-specific T cell reactivity that can be achieved with such personalized immunotherapies will further increase the spectrum of human malignancies that respond to cancer immunotherapy.

REFERENCES AND NOTES

1. R. D. Schreiber, L. J. Old, M. J. Smyth, *Science* **331**, 1565–1570 (2011).
2. F. S. Hodi *et al.*, *N. Engl. J. Med.* **363**, 711–723 (2010).
3. C. S. Hinrichs, S. A. Rosenberg, *Immunol. Rev.* **257**, 56–71 (2014).
4. M. E. Dudley *et al.*, *J. Clin. Oncol.* **31**, 2152–2159 (2013).
5. P. Sharma, J. P. Allison, *Science* **348**, 56–61 (2015).
6. P. C. Tumeh *et al.*, *Nature* **515**, 568–571 (2014).
7. E. Gilboa, *Immunity* **11**, 263–270 (1999).
8. B. Heemskerk, P. Kvistborg, T. N. Schumacher, *EMBO J.* **32**, 194–203 (2013).

9.   N. H. Segal et al., Cancer Res. **68**, 889–892 (2008).
10. J. C. Castle et al., Cancer Res. **72**, 1081–1091 (2012).
11. H. Matsushita et al., Nature **482**, 400–404 (2012).
12. P. F. Robbins et al., Nat. Med. **19**, 747–752 (2013).
13. N. van Rooij et al., J. Clin. Oncol. **31**, e439–e442 (2013).
14. F. Duan et al., J. Exp. Med. **211**, 2231–2248 (2014).
15. M. M. Gubin et al., Nature **515**, 577–581 (2014).
16. C. Linnemann et al., Nat. Med. **21**, 81–85 (2015).
17. Y. C. Lu et al., Clin. Cancer Res. **20**, 3401–3410 (2014).
18. E. Tran et al., Science **344**, 641–645 (2014).
19. D. A. Wick et al., Clin. Cancer Res. **20**, 1125–1134 (2014).
20. M. Yadav et al., Nature **515**, 572–576 (2014).
21. M. Rajasagi et al., Blood **124**, 453–462 (2014).
22. N. A. Rizvi et al., Science **348**, 124–128 (2015).
23. M. Gerlinger et al., N. Engl. J. Med. **366**, 883–892 (2012).
24. M. M. van Buuren, J. J. Calis, T. N. Schumacher, OncoImmunology **3**, e28836 (2014).
25. M. H. Fortier et al., J. Exp. Med. **205**, 595–610 (2008).
26. E. F. Fritsch et al., Cancer Immunol Res **2**, 522–529 (2014).
27. C. A. Van Bergen et al., Cancer Res. **70**, 9073–9083 (2010).
28. J. J. A. Calis et al., PLOS Comput. Biol. **9**, e1003266 (2013).
29. M. E. Dudley, D. C. Roopenian, J. Exp. Med. **184**, 441–447 (1996).
30. T. Wölfel et al., Science **269**, 1281–1284 (1995).
31. T. Schumacher et al., Nature **512**, 324–327 (2014).
32. C. M. Koebel et al., Nature **450**, 903–907 (2007).
33. V. Shankaran et al., Nature **410**, 1107–1111 (2001).
34. M. DuPage, C. Mazumdar, L. M. Schmidt, A. F. Cheung, T. Jacks, Nature **482**, 405–409 (2012).
35. M. S. Rooney, S. A. Shukla, C. J. Wu, G. Getz, N. Hacohen, Cell **160**, 48–61 (2015).
36. P. Kvistborg et al., Sci. Transl. Med. **6**, 254ra128 (2014).
37. P. Kvistborg et al., OncoImmunology **1**, 409–418 (2012).
38. S. D. Brown et al., Genome Res. **24**, 743–750 (2014).
39. A. Snyder et al., N. Engl. J. Med. **371**, 2189–2199 (2014).
40. T. N. Schumacher, C. Kesmir, M. M. van Buuren, Cancer Cell **27**, 12–14 (2015).
41. D. S. Chen, I. Mellman, Immunity **39**, 1–10 (2013).
42. C. M. Cabrera et al., Tissue Antigens **61**, 211–219 (2003).
43. L. A. Johnson et al., Blood **114**, 535–546 (2009).
44. N. N. Hunder et al., N. Engl. J. Med. **358**, 2698–2703 (2008).
45. P. F. Robbins et al., Clin. Cancer Res. **21**, 1019–1027 (2015).
46. V. Boisguérin et al., Br. J. Cancer **111**, 1469–1475 (2014).
47. E. F. Fritsch, N. Hacohen, C. J. Wu, OncoImmunology **3**, e29311 (2014).
48. R. H. Vonderheide, K. L. Nathanson, Nat. Med. **19**, 1098–1100 (2013).
49. C. G. Joseph et al., Science **343**, 152–157 (2014).
50. L. B. Alexandrov et al., Nature **500**, 415–421 (2013).
51. S. A. Forbes et al., Nucleic Acids Res. **43**, D805–D811 (2015).
52. P. A. Futreal et al., Nature Rev. Cancer **4**, 177 (2004).

REVIEWS

T cell exclusion, immune privilege, and the tumor microenvironment

Johanna A. Joyce[1]* and Douglas T. Fearon[2,3]*

Effective immunotherapy promotes the killing of cancer cells by cytotoxic T cells. This requires not only that cancer-specific T cells be generated, but also that these T cells physically contact cancer cells. The coexistence in some patients of cancer cells and T cells that recognize them indicates that tumors may exhibit the phenomenon of immune privilege, in which immunogenic tissue is protected from immune attack. Here, we review the evidence that stromal cells of the tumor microenvironment mediate this restriction by excluding T cells from the vicinity of cancer cells. Overcoming this T cell checkpoint may thus enable optimal immunotherapy.

The microenvironment of tumors contains numerous cell types in addition to cancer cells, which include bone marrow–derived inflammatory cells, lymphocytes, blood vessels, fibroblastic cells, and the extracellular matrix composed of collagen and proteoglycans (1, 2). The importance of a stromal microenvironment, especially one that has characteristics of a "wound" or regenerating tissue, has been recognized for at least a century (3), but its possible role in blunting an immune attack of cancer cells awaited the discovery of adaptive cellular immunity. In 1960, Klein and colleagues found that when mice developed primary methylcholanthrene-induced sarcomas, they also developed an antitumor immune response mediated by lymph node cells to a secondary challenge comprising cancer cells derived from the primary tumor (4). The paradoxical and critical finding of the study was that this anticancer immune response did not control the growth of the primary tumor, despite its ability to prevent the establishment of a secondary tumor comprising cancer cells derived from the primary tumor. In traditional immunological terminology, the primary tumor evaded immune control by establishing an immune-privileged microenvironment that is functionally analogous to that of certain normal tissues, such as the eye (5).

Unambiguous evidence for the inability in humans of a systemic immune response to eliminate immunogenic cancer cells was provided by Boon's studies 30 years later of the antigens that elicit specific CD8^{+} T cell responses in melanoma patients (6). Cloned CD8^{+} T cells from a melanoma patient were used to identify the antigen expressed by that patient's cancer: MAGE-A1. The explicit demonstration of the coexistence of a progressing melanoma with melanoma-specific T cells in this patient implicitly raised the question of why the T cells did not control the growth of the cancer. Immunoediting, or the elimination of immunogenic cancer cells (7), could be excluded, which left the possibility of immune suppression by the tumor microenvironment (TME). Despite this evidence that the presence of antigen-specific CD8^{+} T cells alone may not be sufficient for the control of cancer, a major pharmaceutical company recently conducted phase III trials in patients with non–small cell lung cancer (NSCLC) of the clinical efficacy of vaccination with the MAGE-A3 antigen (MAGRIT, NCT00480025). The study did not meet its primary end point of extending disease-free survival and was discontinued in 2014. Moreover, Rosenberg and colleagues reported evidence of disease recurrence in melanoma patients despite very high levels of vaccine-induced circulating T cells and no evidence of antigen loss by the cancer cells (8).

The discovery of melanoma-specific T cells in patients led to another strategy to increase the frequency of cancer-specific T cells in patients, that of adoptively transferring large numbers of in vitro expanded tumor-infiltrating lymphocytes (TILs). As discussed elsewhere in this issue of Science (9), this approach has shown some efficacy, which has been of major importance to the field by serving as proof that the immune system has the potential to control cancer (10). However, adoptive T cell therapy (ACT) with TILs has not had the dramatic success of ACT with virus-specific CD8^{+} T cells to immunodeficient bone marrow transplant recipients with cytomegalovirus infection (11) or Epstein-Barr virus–associated lymphoproliferative disorders (12). Differences in the microenvironments of virally infected tissues and cancers may account for these distinct outcomes, with the latter being immune-suppressive. Another important point of comparison is that the TME of solid cancers is likely to be fundamentally different to that of the leukemias, in which clinical trials of ACT with T cells expressing chimeric antigen receptors, so-called CAR T cells, have demonstrable efficacy (9). These findings raise the possibility that increasing the frequency of cancer-specific T cells, by whatever means, may be more effective if combined with an approach that alters the immune-suppressive TME.

[1]Cancer Biology and Genetics Program, Memorial Sloan Kettering Cancer Center, New York, NY 10065, USA. [2]Cold Spring Harbor Laboratory, New York, NY 11724, USA. [3]Department of Microbiology and Immunology, Joan and Sanford I. Weill Department of Medicine, Weill Cornell Medical School, New York, NY 10065, USA.
*Corresponding author. E-mail: joycej@mskcc.org (J.A.J.); dfearon@cshl.edu (D.T.F.)
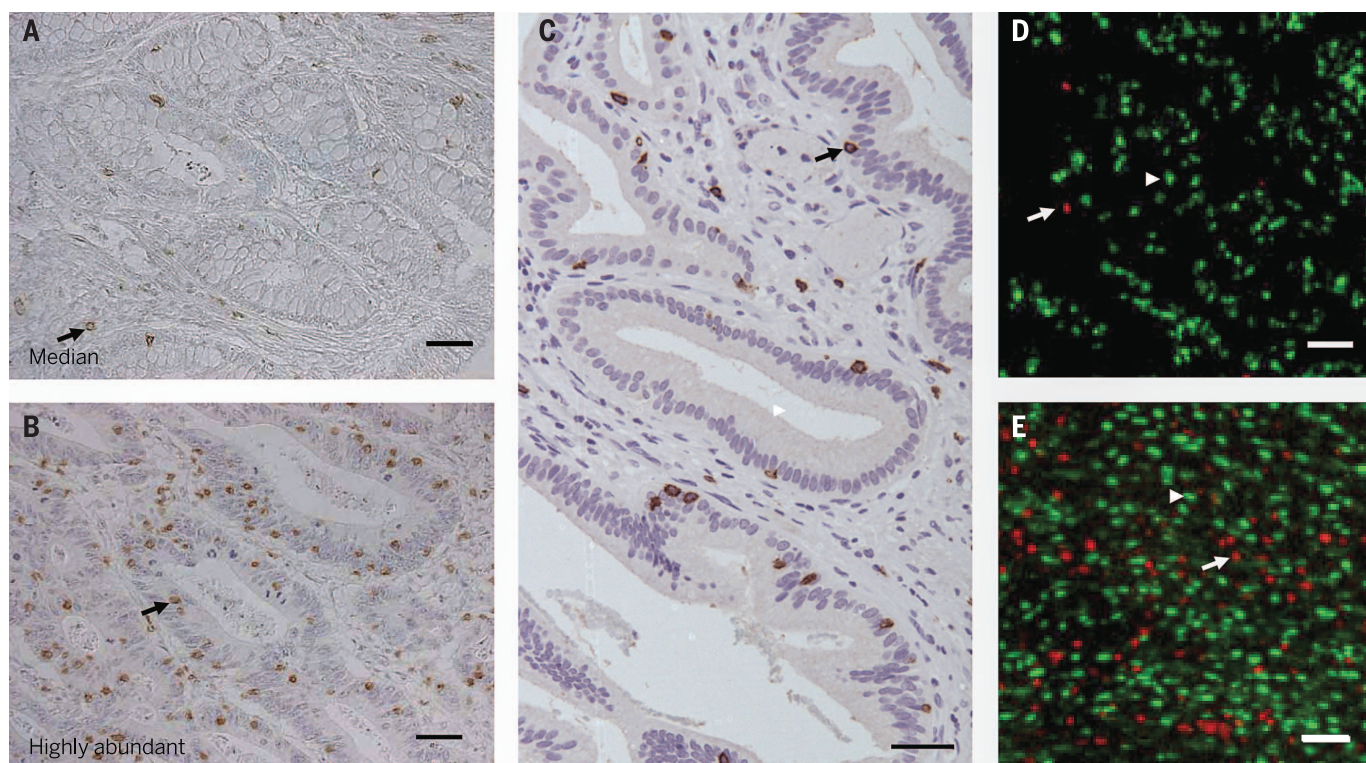
Fig. 1. Exclusion of T cells from human and mouse adenocarcinomas. (**A** to **C**) CD3$^+$ T cells are identified by immunoperoxidase stains of [(A) and (B)] human colorectal (*82*) and (C) human pancreatic ductal adenocarcinomas, demonstrating the presence of few [(A) and (C)] and many (B) intraductal T cells. (**D** and **E**) CD3$^+$ T cells and p53$^+$ cancer cells are identified by use of immunofluorescent stains of pancreatic ductal adenocarcinomas taken from (D) untreated mice and (E) mice that have been treated for 24 hours with the CXCR4 antagonist, AMD3100, demonstrating that T cell exclusion can be regulated by CXCR4 signaling (*29*). Scale bars, 50 μm. Arrows indicate examples of CD3$^+$ T cells, and arrowheads indicate examples of p53$^+$ cancer cells.

The more recent strategy of enhancing the function of effector T cells by targeting immuno-regulatory membrane receptors has been successful in subsets of patients with melanoma, NSCLC, urothelial bladder cancer, and renal cell cancer (*13–18*). The therapeutic effect of blocking antibodies to the immune checkpoint regulators cytotoxic T-lymphocyte–associated protein 4 (CTLA-4) and the programmed cell death protein 1 (PD-1)/PD-L1 receptor-ligand pair is covered in detail elsewhere in this issue of *Science* (*19*), and we briefly discuss them here because these therapies relate to the TME. For example, in the mice, anti-CTLA-4 therapy leads to clearance from the tumor of Foxp3$^+$ regulatory T cells (T$_{reg}$ cells) (*20*), which may impair the functions of effector T cells at that site (*21*). Cancer cells—as well as infiltrating monocytic cells, including dendritic cells (DCs) and macrophages—express PD-L1 (*16, 17, 22, 23*), which suppresses the proliferative and effector responses of T cells by engaging the inhibitory PD-1 receptor on these cells. Nevertheless, it has become apparent that even if these T cell checkpoint antagonists overcome some of the immune-suppressive effects of the TME, there may be other, more fundamental inhibitory reactions in the TME to explain why most patients—especially those with microsatellite stable colorectal cancer (CRC), ovarian cancer, prostate cancer, and pancreatic ductal adenocarcinoma (PDA)—rarely exhibit objective responses to these therapies (*14, 15, 24*).

A clue to the nature of this dominant immune suppression mediated by the TME comes from studies that have examined the spatial relationship of CD8$^+$ effector T cells to cancer cells in three of the tumors that did not respond to anti-PD-1/anti-PD-L1: CRC, ovarian cancer, and PDA (Fig. 1). In 1998, the exclusion of CD8$^+$ T cells from the vicinity of cancer cells in CRC was shown to correlate with a poor long-term clinical outcome (*25*), an observation that was confirmed and extended by Galon and colleagues in 2006 (*26*). Exclusion of T cells from the vicinity of cancer cells was also found in ovarian cancer (*27, 28*) and PDA (*29*). Thus, the tumor immunology field provided evidence more than 10 years ago that the

TME can limit the capacity of T cells to accumulate among cancer cells. It is reasonable to conclude that until this problem is circumvented, the full potential of other approaches to T cell–mediated tumor immunotherapy, such as augmenting the numbers and function of cancer-specific T cells, may not be realized.

Fortunately, studies over the past several years have begun to explain how this form of immune suppression is mediated. Preclinical studies in mouse models of cancer now implicate the major stromal cell types of the TME, cancer-associated fibroblasts (CAFs) and myelomonocytic cells, including several subsets of cells within the general designation of myeloid-derived suppressor

Table 1. Myelomonocytic cells and CAFs control the accumulation of T cells.

TUMOR	TARGET	CELL TYPE AFFECTED BY THERAPEUTIC INTERVENTION	REFERENCE
B16 melanoma-GM-CSF	CCR2	Monocytes	(*30*)
PDA	GM-CSF	MDSCs	(*31*)
PDA	GM-CSF	MDSCs	(*32*)
Cervical, Breast	CSF-1R	Monocytes, TAMs	(*33, 36*)
PDA	CXCR4	Likely T cells (CXCL12 is produced by CAFs)	(*29*)
PDA	CSF-1R	Monocytes, TAMs	(*34*)
Prostate	CSF-1R	Monocytes, TAMs	(*35*)

cells (MDSCs) and tumor-associated macrophages (TAMs), as being responsible for restricting the accumulation of T cells in the vicinity of cancer cells (*29–36*) (Table 1). As would be predicted, overcoming this restriction revealed the antitumor effects of a T cell checkpoint antagonist that had been ineffective when administered as monotherapy. Moreover, as will be discussed, the tumor vasculature also plays an active role in restricting T cell entry into the TME. Fortunately, for each immune suppressive element of the TME there are therapeutic entities that are potentially suitable for administration to patients.

Control by the TME of the extravasation of T cells from the circulatory system into tumors

After the priming of cancer-specific T cells in the lymph nodes that drain the tumor, these T cells traffic via the circulatory system to the tumor. Studies have shown that the TME may regulate the accumulation of T cells in tumors at the initial step of their interaction with local blood vessels. Given that many other immune cells that compose the TME are nonetheless able to extravasate from the circulation (*1*), there must be means by which these distinct cell types are differentially recruited into the tumor. One mechanism for cellular discrimination comes from the release of chemokines that preferentially recruit certain immune cell types over others. Another is the capacity of the TME to posttranslationally alter chemokines. For example, the production of reactive nitrogen species by MDSCs within the TME induces nitration of CCL2 (N-CCL2), which
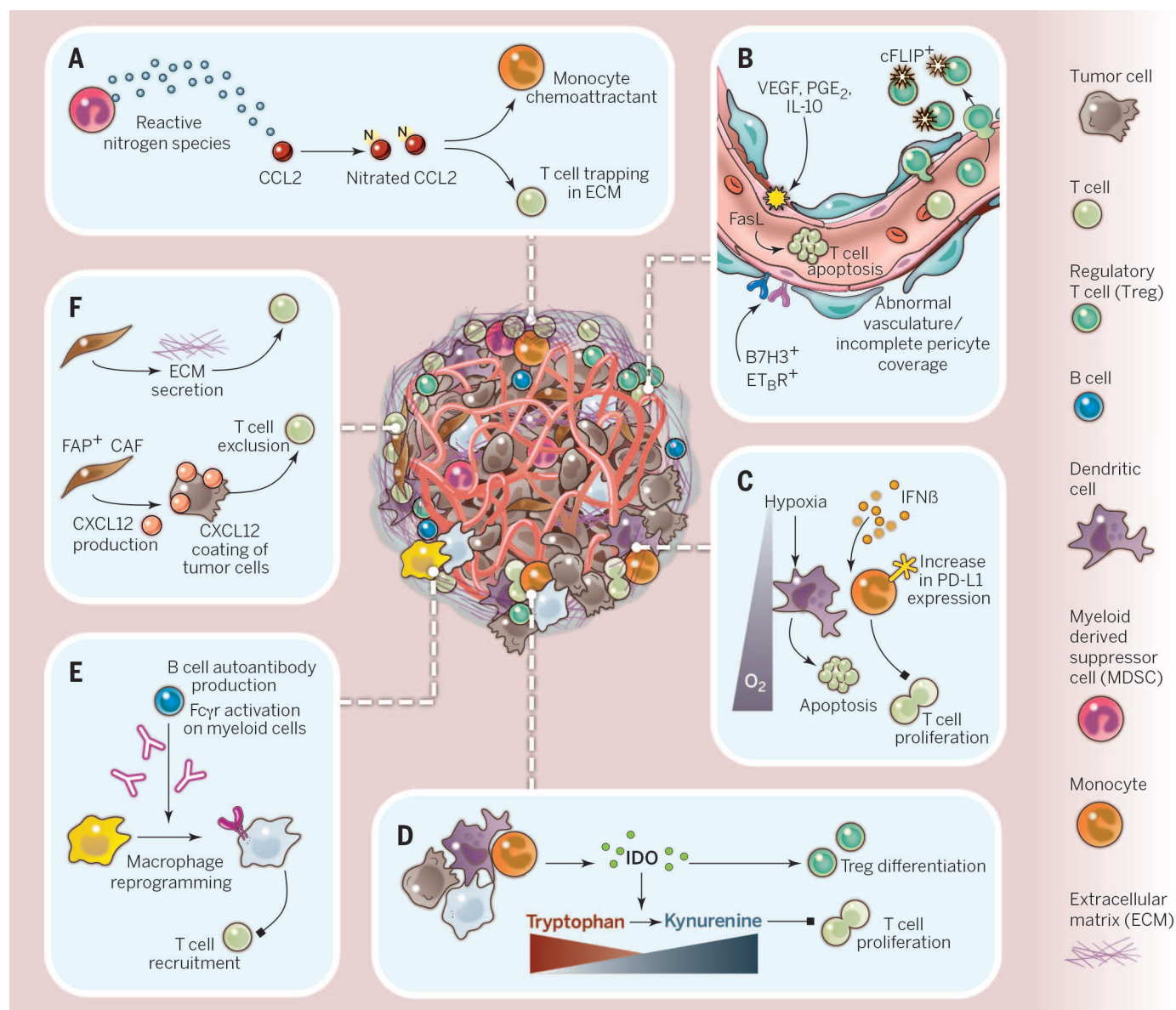
Fig. 2. Mechanisms of TME-driven immune suppression. A plethora of noncancerous cells in the TME regulate the infiltration, accumulation, and proliferation of T cells in tumors, with representative examples shown here. (**A**) T cell recruitment can be blocked by nitration of the chemokine CCL2, resulting in T cell trapping in the stroma. (**B**) The tumor vasculature plays a complex role in preferential recruitment of other immune cells over T cells, in part through endothelial cell (EC)–specific expression of FasL, ET_BR, and B7H3. (**C**) PD-L1 expression can be up-regulated in myelomonocytic cells, in addition to tumor cells, and is driven in part by hypoxic conditions in the TME and the production of cytokines, such as IFNβ. (**D**) The aberrant production of metabolites in the TME, such as the pathway regulated by IDO, can result in a multitude of effects directly on T cell functions and indirectly via other cells such as T_{reg} cells. (**E**) B cells can regulate the phenotype of TAMs resulting in suppression of CD8 cells. (**F**) Cancer-associated fibroblasts (CAFs) have multiple functions in the TME, in part through extracellular matrix (ECM)–mediated T cell trapping and CXCL12-regulated T cell exclusion.

results in the trapping of T cells in the stroma that surrounds tumor cells of human colon and prostate cancers (Fig. 2A) (37). In contrast, N-CCL2 still attracts monocytes, potentially contributing to the differential recruitment of these distinct immune cell types in vivo. Inhibitors of CCL2 nitration enhanced the accumulation of TILs in the corresponding animal models and resulted in improved efficacy of ACT.

Even if the appropriate chemotactic signals for the extravasation and recruitment to the tumor of T cells are present, the vasculature can override their effects and actively exclude T cells (Fig. 2B), a function that may distinguish between the effector T cells and other leukocyte populations, such as T_{reg} cells and myeloid cells. Insights into the mechanism of how this might occur have come from studies comparing T cell–rich and T cell–poor tumors. These studies revealed that the apoptosis inducer Fas ligand (FasL) is expressed in the tumor vasculature of multiple tumor types, including ovarian, colon, prostate, breast, bladder, and renal cancer (38). In tumors with high levels of endothelial FasL, there are few CD8$^+$ T cells but abundant T_{reg} cells, which may be protected against FasL-mediated killing by their relatively high expression of the apoptosis inhibitor, c-FLIP. Accordingly, in preclinical models FasL inhibition resulted in a substantial increase in the influx of tumor-rejecting T cells relative to T_{reg} cells, which led to T cell–dependent tumor suppression. FasL expression itself is induced by the TME-derived immunosuppressive factors vascular endothelial growth factor (VEGF), prostaglandin E_2 (PGE_2), and interleukin-10 (IL-10), suggesting that multiple
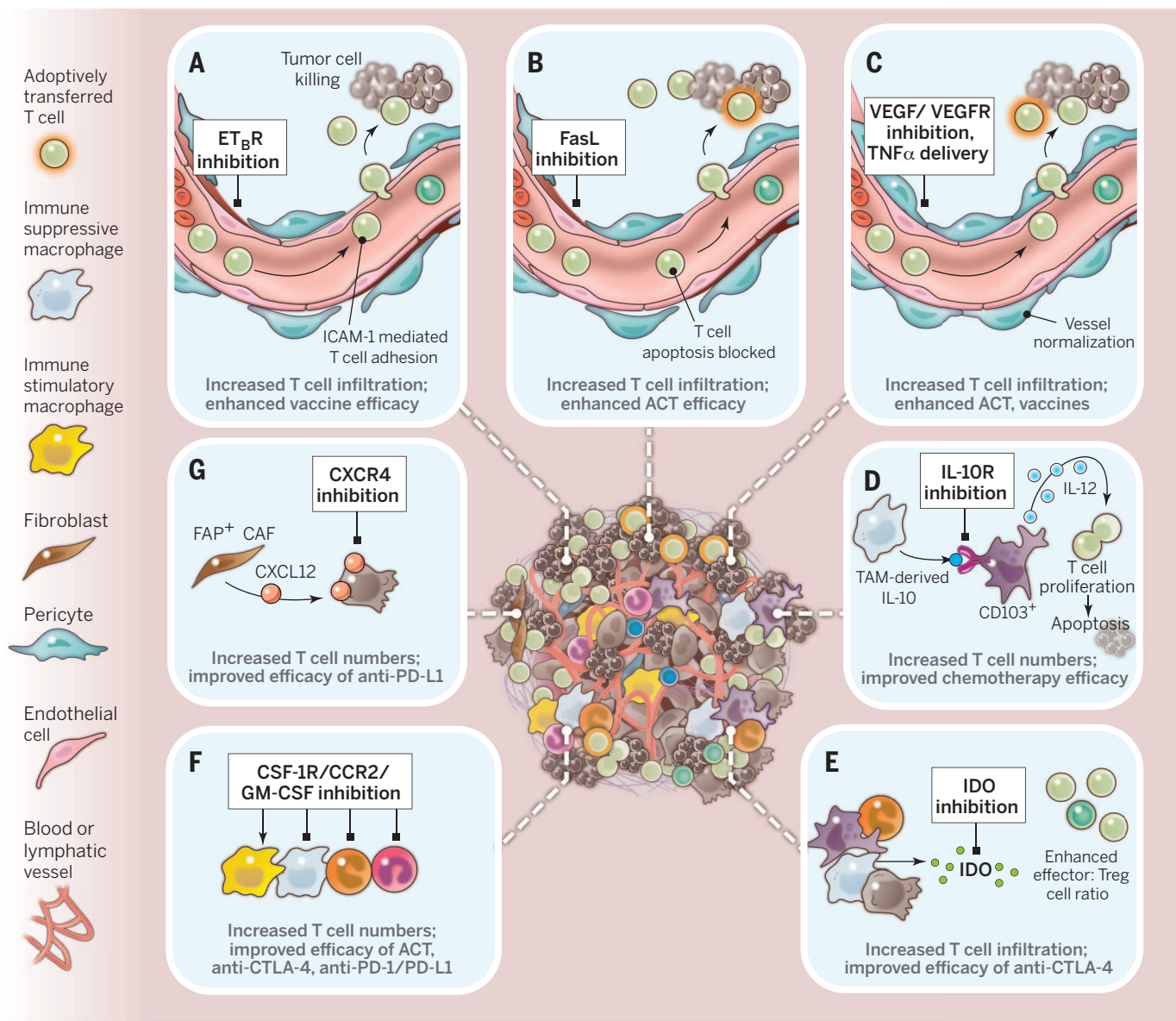
Fig. 3. Therapeutic strategies to overcome immune suppression in the TME. A number of vascular-targeted therapies result in increased T cell infiltration and improved efficacy of different immunotherapies such as adoptive cell therapy and anticancer vaccines. These include (**A**) ET_BR inhibition, (**B**) FasL inhibition, and (**C**) VEGF/VEGFR/TNFα inhibition. (**D**) Dendritic cells (DCs) can have opposing functions in the TME, either supporting or suppressing tumor development. CD103$^+$ DCs have an immune stimulatory function, resulting in IL-12 secretion and T cell replication when the immune-suppressive cytokine receptor IL-10R is inhibited. (**E**) IDO inhibition has multiple effects on TILs, including augmenting T cell expansion and preventing their differentiation into T_{reg} cells. (**F**) Various myelomonocytic cells suppress T cell numbers and/or functions; this suppression can be relieved by inhibition of a number of cytokine signaling pathways indicated here, resulting in depletion or reeducation of these cells in the TME. Further information is provided in Table 1. (**G**) Inhibition of CXCL12/ CXCR4 downstream of FAP$^+$ CAFs in the TME leads to T cell accumulation and increased efficacy of anti-PD-L1 therapy.

networks of cellular interactions may converge to establish immune tolerance. In ovarian cancer elevated VEGF levels, and expression of the immune regulatory ligand B7H3 (CD276), or the endothelin B receptor (ET_BR) on tumor vessels correlates with decreased T cell infiltration and worse clinical outcome (27, 39, 40). Pharmacological inhibition of ET_BR increased T cell adhesion to endothelial cells in an intercellular adhesion molecule-1 (ICAM-1)–dependent manner, resulting in significantly enhanced TIL numbers in mice and a corresponding tumor response to an otherwise ineffective anticancer vaccine (Fig. 3A) (40). Similarly, FasL inhibition also improves the efficacy of ACT (Fig. 3B) (38). The improved efficacy of these distinct TME-directed immunotherapies was not as a consequence of a more effective systemic antitumor immune response but could be attributed to increased effector T cell infiltration into tumors.

Attention has also been focused on anti-angiogenic therapies as a potential means to enhance the efficacy of immunotherapy (41). Anti-angiogenic inhibitors targeting VEGF and its receptor VEGFR2, which are approved for clinical use in multiple cancers (42), induce vascular normalization. This, in turn, increases TILs and improves the efficacy of ACT and cancer vaccines in preclinical models (Fig. 3C) (43, 44). In relation to the next section of this Review, VEGF impairs the maturation of DCs (45), so that anti-VEGF therapy has an additional means by which it could enhance intratumoral immune responses. Further support for the importance of vascular normalization has come from the finding that deleting the regulator of G-protein signaling, Rgs5 (46), reduced vessel leakiness and hypoxia, enhanced T cell infiltration into mouse pancreatic neuroendocrine tumors, and prolonged animal survival. Therefore, from an immunotherapeutic perspective, vascular normalization is likely to be more efficacious than anti-angiogenic therapies that result in vessel destruction, as exemplified by the differential effects of delivering the pro-inflammatory cytokines interferon-γ (IFN-γ) versus tumor necrosis factor-α (TNF-α). Only targeted delivery of the latter, which was reported to normalize tumor blood vessels and increase CD8+ T cell infiltration, enhanced vaccine and ACT therapies (Fig. 3C) (47, 48).

TME-mediated regulation of the local replication of T cells within tumors

The extravasation of cancer-specific T cells into the tumor is a necessary, but not sufficient, step in the immune control of cancer. For effective immune killing of cancer cells, these T cells must also locally replicate to further increase their frequency, avoid being killed themselves by hostile elements of the TME, and overcome barriers that restrict their distribution to the stroma and away from cancer cells. The TME affects all three of these intratumoral T cell responses.

Although the site of the self-renewing T cells that are clonally expanding in response to cancer cell–associated antigens is likely to be the draining lymph nodes, the enrichment of cancer-specific ef-

fector T cells within the tumor relative to their frequency in the periphery indicates that replication of effector T cells within the tumor also occurs. Findings in preclinical models suggest that the TME may be the major site of clonal expansion of cancer-specific T cells (49, 50), and that the CD8+ T cell replicative response at this site is orchestrated by the CD103+, Baft3-dependent DC, which can efficiently cross-present cancer cell antigens (51, 52). The dependence of T cell–mediated tumor regression on the intratumoral presence of CD103+ DCs suggests that therapeutic interventions that enhance their numbers or capacity for driving T cell replication in the TME may contribute to tumor control. Among such strategies are antibodies to the IL-10R, which in a mouse model of mammary carcinoma neutralized the effects of IL-10 produced by TAMs, relieved the suppression of IL-12 production by intratumoral DCs, and improved the CD8+ T cell–dependent antitumor effects of chemotherapy (Fig. 3D) (53). A similar outcome was achieved by neutralizing CSF-1, which impaired the intratumoral accumulation of TAMs (32, 33). Yet another strategy is the administration of antibody–IFN-β complexes, targeted against oncogenic receptors, such as EGFR, that activate intratumoral DCs for cross-presentation of antigen to CD8+ T cells (54). Tumor eradication resulted when PD-L1, which also was induced by IFN-β acting on DCs, was neutralized, demonstrating the recurring theme in the immune system that activating stimuli prompt compensatory inhibitory responses. DC function also may be adversely affected by the hypoxic conditions characteristic of the TME, which induces PD-L1 expression on DCs and other myelomonocytic cells (Fig. 2C) as a result of HIF-1α binding directly to a hypoxia-responsive element in the PD-L1 promoter (55). Even the aerobic glycolysis of cancer cells may antagonize local immune reactions via its increased production of lactate, which induces the M2 polarization of TAMs (56). An M1 to M2 phenotypic transition of intratumoral macrophages has also been reported after the induction of cancer cell apoptosis in human and mouse gastrointestinal stromal tumors by the administration of the KIT oncoprotein inhibitor, imatinib (57). It should be noted that the designation of M1 and M2 polarization states undoubtedly represent an oversimplification of the complexity of macrophage biology (58) and that at least six different TAM subpopulations have been reported (59). Therefore, descriptors of TAM phenotypes in the TME are likely to be most informative in investigating and therapeutically targeting these cells.

In addition to altering T cell replication indirectly via effects on myeloid cells, the TME may directly impair intratumoral T cell proliferation. Indole 2,3-dioxygenase (IDO)—which can be expressed by DCs, MDSCs, and cancer cells—catabolizes tryptophan and generates kynurenine (Fig. 2D). Both the deprivation of tryptophan and the generation of its metabolic product inhibit clonal expansion (60, 61). IDO also promotes the conversion of naïve T cells to T_{reg} cells and increases IL-6 expression, which augments MDSC functions (62). Accordingly, IDO1 genetic deficiency is asso-

ciated with reduced tumor burden and metastasis and enhanced survival in mouse models of lung and breast cancer (62). The therapeutic potential of inhibiting IDO, in combination with the T cell checkpoint antagonist anti-CTLA-4, has been demonstrated in the B16 melanoma model and was associated with increased accumulation of intratumoral T cells (Fig. 3E) (63). Last, the capacity of IDO to block the reprogramming of T_{reg} cells to helperlike cells by suppressing the loss of the transcription factor Eos, and the corresponding transcriptional program it regulates, exemplifies another means by which this enzyme promotes immune suppression within the TME (64).

Control by the TME of the viability of T cells within tumors

The TME can also limit the viability of T cells. Both IDO and PD-L1 not only may impair the intratumoral proliferation of effector T cells but may also induce apoptosis of these cells. Products of myelomonocytic cells that cause the apoptosis of T cells include FasL, TNF-α, and TNF-related apoptosis inducing ligand (TRAIL). In addition to these known effectors of death, previously unidentified pathways that control the viability of intratumoral T cells may be discovered by innovative, unbiased approaches. For example, an in vivo, pooled short hairpin RNA screen identified Ppp2r2d as a key regulator promoting T cell apoptosis and suppressing T cell proliferation within the TME (65).

Interventions that target intratumoral TAMs and MDSCs can also lead to reduced tumor burdens in preclinical models, in both T cell–dependent and T cell–independent ways. For instance, inhibiting chemokine receptor type 2 (CCR2) (30), colony-stimulating factor-1 receptor (CSF-1R) (33, 34, 36), and granulocyte macrophage colony-stimulating factor (GM-CSF) (31, 32) in preclinical models of melanoma, pancreatic, breast, and prostatic carcinoma increased intratumoral T cells and controlled tumor growth, especially when combined with anti-CTLA-4 or anti-PD-1/PD-L1 (Table 1 and Fig. 3F). Although these studies did not determine whether the increases in T cells were a consequence of enhanced viability or replication, they emphasize again how elements of the TME regulate the accumulation of effector T cells. Inhibition of CSF-1R in a preclinical model of proneural glioblastoma multiforme and in patient-derived glioma xenografts increased survival and caused regression of established tumors in an apparent T cell–independent manner that correlated with the reprogramming of macrophages away from an M2 phenotype (66). Similarly, an activator of TAMs, an agonistic antibody to CD40, when administered in combination with the chemotherapeutic drug gemcitabine, suppressed the growth of mouse PDA in a T cell–independent manner (67), suggesting that macrophages alone, when appropriately stimulated, may have potent anticancer functions. B cells have also been shown to regulate the phenotype of TAMs in the squamous cell carcinoma TME (Fig. 2E) (68). Correspondingly, B cell depletion reprogrammed TAMs, thus relieving their suppression of CD8 cells and enhancing chemotherapy efficacy. Another example

of how the antitumor effects of macrophages can be used therapeutically is an autochthonous mouse model of melanoma in which the melanoma-killing capability of these cells was revealed by depleting T_{reg} cells and neutralizing IL-10 (69). TAMs would also be the mediators of the anti-tumor effects of antibodies (70) and genetically engineered ligands (71) that interact with CD47 on cancer cells to prevent the CD47/signal regulatory protein–α (SIRPα) signaling system from suppressing the phagocytosis of antibody-coated cancer cells.

The TME regulates spatial distribution of T cells within tumors

Increased numbers of intratumoral, cancer-specific T cells will be of little import if T cells are restricted to the stroma and prevented from accumulating in the vicinity of cancer cells. CAFs, which may be identified by their expression of the membrane protein fibroblast activation protein-α (FAP), have been shown to have two means by which they can mediate this restriction, the first of which is a physical exclusion mediated by the extracellular matrix that they produce (Fig. 2F). Live cell imaging of lung tumor tissue slices from patients revealed active T cell motility in regions of loose fibronectin and collagen, whereas T cells migrated poorly in dense matrix areas surrounding tumor nests (72). When either collagenase was added to reduce matrix rigidity, or the chemokine CCL5 was experimentally produced by tumor cells, there was increased T cell movement out of the stromal regions and into contact with cancer cells.

The second means by which FAP$^+$ CAFs exclude T cells involves their biosynthesis of CXCL12 (Fig. 2F). Conditionally depleting these cells from the stroma of an ectopic, transplanted tumor (73) and of an autochthonous PDA (29) allowed pre-existing cancer-specific T cells to rapidly control tumor growth and revealed the antitumor effects of anti-PD-L1. However, depleting FAP$^+$ stromal cells is not a reasonable therapeutic option unless the depletion can be limited to the TME because these cells carry out essential functions in several normal tissues (74). The recent report of "reprogramming" these cells in the TME by administration of a vitamin D analog (75) may be one means of circumventing this problem. Another may be to block their immune suppressive mechanism. In a preclinical mouse model of PDA, FAP$^+$ CAFs produce the chemokine CXCL12, which is bound by the PDA cancer cells, which had been previously reported for cancer cells in human PDA, CRC, and ovarian cancer (76–78). Because FAP$^+$ stromal cells also accumulate in nontransformed, inflammatory lesions, this "coating" of cancer cells may reflect a means by which "injured" epithelial cells protect themselves from adaptive immune attack. Administering an inhibitor of CXCR4, the receptor for CXCL12, to the PDA-bearing mice caused the rapid accumulation of T cells among cancer cells, arrest of tumor growth, and tumor sensitivity to anti-PD-L1 (Fig. 3G) (29). How the cancer cell–bound CXCL12 excludes T cells has not yet been shown, although the mechanism must involve either T cells or myelomonocytic cells because they, and not cancer cells or FAP$^+$ CAFs, express CXCR4 in this model.

Conceptual challenges and therapeutic opportunities

Among the challenges that remain for understanding the immune suppressive roles of the TME, three are foremost: comprehending the mechanisms by which the TME excludes T cells, determining whether the TME of primary and metastatic tumor sites differ, and assessing the potential clinical efficacy of interventions that affect the TME. The preclinical studies in mice that showed that inhibiting CCR2, CSF-1/CSF-1R, GM-CSF, or CXCR4 improved immune control of tumor growth also showed that these interventions shared a capacity for increasing the frequency of T cells among cancer cells (Fig. 3). Because targeting CCR2 and CSF-1/CSF-1R diminishes the accumulation of CCR2-expressing cell types, including bone marrow–derived TAMs and DCs, one must conclude that at least one function of these cells is to suppress the accumulation of intratumoral T cells. However, given that these cells are distributed in both the stromal and cancer cell regions of tumors, it is not readily apparent how they can selectively exclude T cells only from the vicinity of the cancer cells. On the other hand, the distribution of intratumoral CXCL12, which is associated with cancer cells, does correlate, albeit inversely, with that of T cells, so that the hypothesis that CXCL12 is involved with T cell exclusion would be reasonable and is supported by the antitumor outcome of inhibiting CXCR4. Even here a mechanism that may account for this effect of CXCR4, other than T cell "repulsion" (79), is not apparent. For the moment, then, one may only suggest that because CSF1R- and CCR2-dependent cells and CXCR4 signaling are both required for the exclusion of T cells, they are elements of a single pathway that mediates this dominant immune suppressive process.

Regarding the TME of metastatic sites, most preclinical and clinical analyses to date have been restricted to primary tumors. It has been noted earlier that mice in which an immune response has been induced by growth of a primary methycholanthrene-induced sarcoma prevent the establishment of a secondary tumor by these sarcoma cells (4). In a preclinical model of spontaneous melanoma, cancer cells were found to disseminate early but to remain in a dormant state that was mediated, at least in part, by CD8$^+$ T cells (81). Consistent with this report of immune-induced metastatic dormancy is a study that found metastases in another mouse model that grew rapidly in association with the exclusion of CD8$^+$ T cells (81). A challenge will be to determine whether the immune-suppressive intensity of the TMEs of metastatic lesions may vary, with dormant metastases being dominated by immune control and growing lesions exhibiting immune suppression.

With respect to clinically assessing the effects of altering the TME for the purpose of increasing the frequency of intratumoral effector T cells, the academic oncologist already has several agents available that are specific for the same targets in humans that have regulated this process in mouse cancers: IDO inhibitors, CSF-1R inhibitors, CCR2-specific antibodies, and an inhibitor of CXCR4. Examples of each are already in clinical trials in human cancer patients, usually as monotherapies. There is an obvious rationale to combine those agents that are found to augment the intratumoral accumulation of effector T cells with therapies that improve the response of T cells to TCR ligation, such as antibodies to PD-1 and PD-L1, or increase the overall frequency of cancer-specific T cells, such as vaccines and ACT.

Last, recognition of the function of the TME in excluding T cells prompts an interest in the identity of the normal biological circumstance that is responsible for the development of this phenomenon. Tumor immunologists currently consider mutated genes to be the major source of antigens in cancer cells that T cells respond to, but some cancers that have a low mutational burden may elicit cancer-specific CD8$^+$ T cells, as exemplified by the mouse model of PDA (29). Is it possible that nontransformed epithelial cells in regenerating tissues also express immunogenic neoantigens, a circumstance that would select for an immune suppressive microenvironment? The frequent occurrence of the immune suppressive elements of the TME, myelomonocytic cells, and FAP$^+$ stromal fibroblasts in regenerating tissues is consistent with this conjecture and merits further investigation.

REFERENCES AND NOTES

1. D. F. Quail, J. A. Joyce, Nat. Med. 19, 1423–1437 (2013).
2. D. Hanahan, L. M. Coussens, Cancer Cell 21, 309–322 (2012).
3. F. S. Jones, P. Rous, J. Exp. Med. 20, 404–412 (1914).
4. G. Klein, H. O. Sjogren, E. Klein, K. E. Hellstrom, Cancer Res. 20, 1561–1572 (1960).
5. P. B. Medawar, Br. J. Exp. Pathol. 29, 58–69 (1948).
6. P. van der Bruggen et al., Science 254, 1643–1647 (1991).
7. R. D. Schreiber, L. J. Old, M. J. Smyth, Science 331, 1565–1570 (2011).
8. S. A. Rosenberg et al., J. Immunol. 175, 6169–6176 (2005).
9. S. A. Rosenberg, N. P. Restifo, Science 348, 62–68 (2015).
10. S. A. Rosenberg et al., Clin. Cancer Res. 17, 4550–4557 (2011).
11. S. R. Riddell et al., Science 257, 238–241 (1992).
12. E. B. Papadopoulos et al., N. Engl. J. Med. 330, 1185–1191 (1994).
13. F. S. Hodi et al., N. Engl. J. Med. 363, 711–723 (2010).
14. J. R. Brahmer et al., N. Engl. J. Med. 366, 2455–2465 (2012).
15. S. L. Topalian et al., N. Engl. J. Med. 366, 2443–2454 (2012).
16. T. Powles et al., Nature 515, 558–562 (2014).
17. R. S. Herbst et al., Nature 515, 563–567 (2014).
18. P. C. Tumeh et al., Nature 515, 568–571 (2014).
19. P. Sharma, J. P. Allison, Science 348, 56–61 (2015).
20. T. R. Simpson et al., J. Exp. Med. 210, 1695–1710 (2013).
21. S. Z. Josefowicz, L. F. Lu, A. Y. Rudensky, Annu. Rev. Immunol. 30, 531–564 (2012).
22. T. Okazaki, S. Chikuma, Y. Iwai, S. Fagarasan, T. Honjo, Nat. Immunol. 14, 1212–1218 (2013).
23. F. Wei et al., Proc. Natl. Acad. Sci. U.S.A. 110, E2480–E2489 (2013).
24. R. E. Royal et al., J. Immunother. 33, 828–833 (2010).
25. Y. Naito et al., Cancer Res. 58, 3491–3494 (1998).
26. J. Galon et al., Science 313, 1960–1964 (2006).
27. L. Zhang et al., N. Engl. J. Med. 348, 203–213 (2003).
28. E. Sato et al., Proc. Natl. Acad. Sci. U.S.A. 102, 18538–18543 (2005).
29. C. Feig et al., Proc. Natl. Acad. Sci. U.S.A. 110, 20212–20217 (2013).
30. A. M. Lesokhin et al., Cancer Res. 72, 876–886 (2012).

31. L. J. Bayne et al., Cancer Cell 21, 822–835 (2012).
32. Y. Pylayeva-Gupta, K. E. Lee, C. H. Hajdu, G. Miller, D. Bar-Sagi, Cancer Cell 21, 836–847 (2012).
33. D. C. Strachan et al., OncoImmunology 2, e26968 (2013).
34. Y. Zhu et al., Cancer Res. 74, 5057–5069 (2014).
35. A. J. Garcia et al., Mol. Cell. Biol. 34, 2017–2028 (2014).
36. D. G. DeNardo et al., Cancer Discov. 1, 54–67 (2011).
37. B. Molon et al., J. Exp. Med. 208, 1949–1962 (2011).
38. G. T. Motz et al., Nat. Med. 20, 607–615 (2014).
39. X. Zang et al., Mod. Pathol. 23, 1104–1112 (2010).
40. R. J. Buckanovich et al., Nat. Med. 14, 28–36 (2008).
41. Y. Huang, S. Goel, D. G. Duda, D. Fukumura, R. K. Jain, Cancer Res. 73, 2943–2948 (2013).
42. G. C. Jayson, D. J. Hicklin, L. M. Ellis, Nat. Rev. Clin. Oncol. 9, 297–303 (2012).
43. R. K. Shrimali et al., Cancer Res. 70, 6171–6180 (2010).
44. Y. Huang et al., Proc. Natl. Acad. Sci. U.S.A. 109, 17561–17566 (2012).
45. D. I. Gabrilovich et al., Nat. Med. 2, 1096–1103 (1996).
46. J. Hamzah et al., Nature 453, 410–414 (2008).
47. A. Johansson, J. Hamzah, C. J. Payne, R. Ganss, Proc. Natl. Acad. Sci. U.S.A. 109, 7841–7846 (2012).
48. A. Calcinotto et al., J. Immunol. 188, 2687–2694 (2012).
49. E. D. Thompson, H. L. Enriquez, Y. X. Fu, V. H. Engelhard, J. Exp. Med. 207, 1791–1804 (2010).
50. Y. Ma et al., Cancer Res. 74, 436–445 (2014).
51. M. L. Broz et al., Cancer Cell 26, 638–652 (2014).
52. K. Hildner et al., Science 322, 1097–1100 (2008).
53. B. Ruffell et al., Cancer Cell 26, 623–637 (2014).
54. X. Yang et al., Cancer Cell 25, 37–48 (2014).
55. M. Z. Noman et al., J. Exp. Med. 211, 781–790 (2014).
56. O. R. Colegio et al., Nature 513, 559–563 (2014).
57. M. J. Cavnar et al., J. Exp. Med. 210, 2873–2886 (2013).
58. P. J. Murray et al., Immunity 41, 14–20 (2014).
59. B. Z. Qian, J. W. Pollard, Cell 141, 39–51 (2010).
60. D. H. Munn, A. L. Mellor, Trends Immunol. 34, 137–143 (2013).
61. M. Platten, W. Wick, B. J. Van den Eynde, Cancer Res. 72, 5435–5440 (2012).
62. C. Smith et al., Cancer Discov. 2, 722–735 (2012).
63. R. B. Holmgaard, D. Zamarin, D. H. Munn, J. D. Wolchok, J. P. Allison, J. Exp. Med. 210, 1389–1402 (2013).
64. M. D. Sharma et al., Immunity 38, 998–1012 (2013).
65. P. Zhou et al., Nature 506, 52–57 (2014).
66. S. M. Pyonteck et al., Nat. Med. 19, 1264–1272 (2013).
67. G. L. Beatty et al., Science 331, 1612–1616 (2011).
68. N. I. Affara et al., Cancer Cell 25, 809–821 (2014).
69. A. Pommier et al., Proc. Natl. Acad. Sci. U.S.A. 110, 13085–13090 (2013).
70. Y. Murata, T. Kotani, H. Ohnishi, T. Matozaki, J. Biochem. 155, 335–344 (2014).
71. K. Weiskopf et al., Science 341, 88–91 (2013).
72. H. Salmon et al., J. Clin. Invest. 122, 899–910 (2012).
73. M. Kraman et al., Science 330, 827–830 (2010).
74. E. W. Roberts et al., J. Exp. Med. 210, 1137–1151 (2013).
75. M. H. Sherman et al., Cell 159, 80–93 (2014).
76. C. J. Scotton et al., Cancer Res. 62, 5930–5938 (2002).
77. J. J. Liang et al., Cancer Epidemiol. Biomarkers Prev. 19, 2598–2604 (2010).
78. Y. Akishima-Fukasawa et al., Am. J. Clin. Pathol. 132, 202–210, quiz 307 (2009).
79. M. C. Poznansky et al., Nat. Med. 6, 543–548 (2000).
80. J. Eyles et al., J. Clin. Invest. 120, 2030–2039 (2010).
81. J. Predina et al., Proc. Natl. Acad. Sci. U.S.A. 110, E415–E424 (2013).
82. T. Chiba et al., Br. J. Cancer 91, 1711–1717 (2004).

REVIEWS

Cancer and the microbiota

Wendy S. Garrett[1,2,3,4]

A host's microbiota may increase, diminish, or have no effect at all on cancer susceptibility. Assigning causal roles in cancer to specific microbes and microbiotas, unraveling host-microbiota interactions with environmental factors in carcinogenesis, and exploiting such knowledge for cancer diagnosis and treatment are areas of intensive interest. This Review considers how microbes and the microbiota may amplify or mitigate carcinogenesis, responsiveness to cancer therapeutics, and cancer-associated complications.

The relationship between cancer and microbes is complex. Although cancer is generally considered to be a disease of host genetics and environmental factors, microorganisms are implicated in ~20% of human malignancies (1). Microbes present at mucosal sites can become part of the tumor microenvironment of aerodigestive tract malignancies, and intratumoral microbes can affect cancer growth and spread in many ways (2–6). In counterpoise, the gut microbiota also functions in detoxification of dietary components, reducing inflammation, and maintaining a balance in host cell growth and proliferation. The possibility of microbe-based cancer therapeutics has attracted interest for more than 100 years, from Coley's toxins (one of the earliest forms of cancer bacteriotherapy) to the current era of synthetic biology's designer microbes and microbiota transplants. Thus, interrogation of the roles of microbes and the microbiota in cancer requires a holistic perspective.

The ways in which microbes and the microbiota contribute to carcinogenesis, whether by enhancing or diminishing a host's risk, fall into three broad categories: (i) altering the balance of host cell proliferation and death, (ii) guiding immune system function, and (iii) influencing metabolism of host-produced factors, ingested foodstuffs, and pharmaceuticals (Fig. 1). Assigning microbial communities, their members, and aggregate biomolecular activities into these categories will require a substantial research commitment. This Review discusses how microbes and the microbiota may contribute to cancer development and progression, responsiveness to cancer therapeutics, and cancer-associated complications.

Microbial contributions to carcinogenesis

Of the estimated 3.7×10^{30} microbes living on Earth (7), only 10 are designated by the International Agency for Cancer Research (IACR)

[1]Department of Immunology and Infectious Diseases and Department of Genetics and Complex Diseases, Harvard T. H. Chan School of Public Health, Boston, MA 02115, USA. [2]Department of Medical Oncology, Dana-Farber Cancer Institute, Boston, MA 02115, USA. [3]Department of Medicine, Harvard Medical School, Boston, MA 02115, USA. [4]Broad Institute of Harvard and MIT, Cambridge, MA 02142, USA.
Corresponding author. E-mail: wendy_garrett@dfci.harvard.edu

as carcinogenic to humans (1). Although most of these carcinogenic microbes colonize large percentages of the human population, only a subset of affected individuals develop cancer, because host and microbial genotypes influence cancer susceptibility.

Tumors arising at boundary surfaces, such as the skin, oropharynx, and respiratory, digestive, and urogenital tracts, harbor a microbiota, which complicates cancer-microbe causality. Enrichment of a microbe at a tumor site does not connote that a microbe is directly associated, let alone causal, in disease. Rather, microbes may find a tumor's oxygen tension or carbon sources permissive and take advantage of an underused nutritional niche. Decreased abundances of specific microbes may also place a host at enhanced risk for cancer development at sites local or distant from this microbial shift. Thus, rigorous frameworks for interpreting tumor-associated microbiota data are essential (2).

Oncomicrobes, shifting the balance of when to die and when to grow

Bona fide oncomicrobes—microbes that trigger transformation events in host cells—are rare. Beyond the 10 IACR-designated microbes, there are a handful of other microorganisms with robust but fewer aggregate data supporting their role in human carcinogenesis. As many of these and their carcinogenic mechanisms have been recently reviewed (2–6, 8), select activities representing common pathways by which microbes influence cancer will be highlighted.

Human oncoviruses can drive carcinogenesis by integrating oncogenes into host genomes. Human papillomaviruses (HPV) express oncoproteins such as E6 and E7. Data from recent genomic analyses of HPV⁺ cervical cancers suggest that viral integration also selectively triggers amplification of host genes in pathways with established roles in cancer (9).

Microbes also drive transformation by affecting genomic stability, resistance to cell death, and proliferative signaling. Many bacteria have evolved mechanisms to damage DNA, so as to kill competitors and survive in the microbial world. Unfortunately, these bacterial defensive factors can lead to mutational events that contribute to carcinogenesis (Fig. 2). Examples include colibactin encoded by the pks locus [expressed by B2

Healthy tissue

Aerodigestive tract lumen

MUCOSAL BARRIER

Infection, trauma, dietary factors, germline mutations

Barrier breach

Impaired host and microbial resiliency

Persistent barrier breach

Failure to re-attain healthy host and microbial homeostasis

Microbiota

Altered balance of host cell proliferation and death

Altered immune system function

Altered host and microbial metabolism

Carcinogenesis

Fig. 1. The path from health to solid tumor malignancies at mucosal sites and the microbiota's contribution. Human body surfaces are subject to constant environmental insult and injury. Infections, trauma, dietary factors, and germline mutations can contribute to breach of the body's mucosal barriers. In most individuals, barrier breaches are rapidly repaired and tissue homeostasis is restored. Impaired host or microbial resiliency contributes to persistent barrier breach and a failure to restore homeostasis. In these settings, the microbiota may influence carcinogenesis by (i) altering host cell proliferation and death, (ii) perturbing immune system function, and (iii) influencing metabolism within a host.

group *Escherichia coli* (*10*) as well as by other Enterobacteriaceae (*11*)], *Bacteroides fragilis* toxin (Bft) produced by enterotoxigenic *B. fragilis*, and cytolethal distending toxin (CDT) produced by several ε- and γ-proteobacteria. Colibactin has emerged as a molecule of interest in colorectal carcinogenesis, given the detection of pks⁺ *E. coli* in human colorectal cancers and the ability of colibactin-expressing *E. coli* to potentiate intestinal tumorigenesis in mice (*12, 13*). Accumulating data also support a role for enterotoxigenic *B. fragilis* in both human and animal models of colon tumors (*14–17*). Both colibactin and CDT can cause double-stranded DNA damage in mammalian cells (*18*). In contrast, Bft acts indirectly by eliciting high levels of reactive oxygen species (ROS), which in turn damage host DNA (*19*). Chronically high ROS levels can outpace a host's DNA repair mechanisms, leading to DNA damage and mutations (Fig. 2).

Beyond damaging DNA, several microbes possess proteins that engage host pathways involved in carcinogenesis. The Wnt/β-catenin signaling pathway, which regulates cell stemness, polarity, and growth (*20*), is one example and is altered in many malignancies. Several cancer-associated bacteria also can influence β-catenin signaling (Fig. 2). Oncogenic type 1 strains of *Helicobacter pylori* express a protein called CagA, which is injected directly into the cytoplasm of host cells and aberrantly modulates β-catenin to drive gastric cancer (*8*). CagA-mediated β-catenin activation leads to up-regulation of genes involved in cellular proliferation, survival, and migration, as well as angiogenesis—all processes central to carcinogenesis. *Fusobacterium nucleatum* is a member of the oral microbiota and is associated with human colorectal adenomas and adenocarcinomas and amplified intestinal tumorigenesis in mice (*21–24*). *F. nucleatum* expresses FadA, a bacterial cell surface adhesion component that binds host E-cadherin, leading to β-catenin activation (*25*). Enterotoxigenic *B. fragilis*, which is enriched in some human colorectal cancers (*14*), can stimulate E-cadherin cleavage via Btf, leading to β-catenin activation (*26*). *Salmonella typhi* strains that maintain chronic infections secrete AvrA, which can activate epithelial β-catenin signaling (*27, 28*), and are associated with hepatobiliary cancers (*29–31*).

This phenomenon of activating β-catenin signaling reflects an interesting convergence of evolution, as several of these bacteria are normal constituents of the human microbiota. Although microbial engagement of β-catenin signaling may reflect a drive to establish a niche in a new tissue site, the presence of these cancer-potentiating microbes and their access to E-cadherin in evolving tumors demonstrate that a loss of appropriate boundaries and barrier maintenance between host and microbe is a critical step in the development of some tumors (Figs. 1 and 2).

The immune system, microbes, microbiota, and cancer

Mucosal surface barriers permit host-microbial symbiosis (*32*); they are susceptible to constant environmental insult and must rapidly repair to reestablish homeostasis. Compromised resiliency of the host or microbiota can place tissues on a path to malignancy. Cancer and inflammatory disorders can arise when barriers break down and microbes and immune systems find themselves in geographies and assemblages for which they have not coevolved. Once barriers are breached, microbes can further influence immune responses in evolving tumor microenvironments by eliciting proinflammatory or immunosuppressive programs (Fig. 2).

Proinflammatory responses can be procarcinogenic

Both the chronic, high-grade inflammation of inflammatory disorders (e.g., inflammatory bowel disease) and the lower-grade smoldering inflammation of malignancies and obesity drive a tumor-permissive milieu. Inflammatory factors such as reactive oxygen and nitrogen species, cytokines, and chemokines can contribute to tumor growth and spread (Fig. 2). Data from human tissues and animal models show that tumors can up-regulate and activate many pattern recognition receptors, including Toll-like receptors (*3, 8*). Activation of these receptors results in feedforward loops of activation of NF-κB, a master regulator of cancer-associated inflammation (*33*) (Fig. 2). Numerous cancer-associated microbes appear to activate NF-κB signaling within the tumor microenvironment [e.g., the colon cancer–associated *F. nucleatum* (*23*)]. The activation of NF-κB by *F. nucleatum* may be the result of pattern recognition receptor engagement (*10, 34–37*) or FadA engagement of E-cadherin (*25*). Other pattern recognition receptors, such as the nucleotide-binding oligomerization domain–like receptor (NLR) family members NOD-2, NLRP3, NLRP6, and NLRP12, may play a role in mediating colorectal cancer; mice deficient in these NLRs display an enhanced susceptibility to colitis-associated colorectal cancer (caCRC) (*38–44*).

Engagement of the immune system within the tumor microenvironment is not restricted to the innate immune system. Once barriers are breached and the innate immune system is activated, subsequent adaptive immune responses ensue, often with deleterious consequence for

tumor progression. The interleukin-23 (IL-23)–IL-17 axis (*45*), tumor necrosis factor–α (TNF-α)–TNF receptor signaling (*3, 5, 6, 46*), IL-6–IL-6 family member signaling (*46, 47*), and STAT3 activation (*48, 49*)—an output of these cytokine-mediated signaling pathways—all represent innate and adaptive pathways contributing to tumor progression and growth (Fig. 2).

The microbiota is responsive and adapts to changes in its host, such as inflammation. Adaptation to new selective pressures may result in a microbiota at a tissue site that is not well suited for barrier repair, immune homeostasis, or maintenance of traditional host and microbe boundaries. Mouse models of caCRC furnish insight in this regard. One such model uses azoxymethane, a genotoxin, and dextran sodium sulfate, a colon barrier–disrupting agent. Either agent alone results in colon tumors in susceptible mouse strains; using them together accelerates tumorigenesis. Although this model does not recapitulate the molecular and environmental events that lead to caCRC, it provides an opportunity to study the convergence of an environmental genotoxin, barrier disruption, and severe chronic inflammation on cancer development.

Microbiota transfer studies in caCRC models support the idea that perturbations to a host immune system, either by genetic deletion or genotoxin coupled with inflammatory stimulus, may select for microbiotas enriched for bacterial clades adept at attaching to host surfaces, invading host tissue, or triggering host inflammatory mediators (*21, 22, 40, 50, 51*). Fecal microbiota from *Nod2-* or *Nlrp6*-deficient mice acquire features that enhance the susceptibility of wild-type mice to caCRC (*40, 44*). In mice, the gut microbiota modulate colon tumorigenesis, independent of genetic deficiencies. When germ-free mice were colonized with microbes

Fig. 2. Mechanisms by which microbes influence cancer development and progression. (**A**) Bacterial toxins can directly damage host DNA. Bacteria also damage DNA indirectly via host-produced reactive oxygen and nitrogen species. When DNA damage exceeds host cell repair capacity, cell death or cancer-enabling mutations occur. (**B**) β-Catenin signaling alterations are a frequent target of cancer-associated microbes. Some microbes bind E-cadherin on colonic epithelial cells, with altered polarity or within a disrupted barrier, and trigger β-catenin activation. Other microbes inject effectors (e.g., CagA or AvrA) that activate β-catenin signaling, resulting in dysregulated cell growth, acquisition of stem cell–like qualities, and loss of cell polarity. (**C**) Pro-inflammatory pathways are engaged upon mucosal barrier breach in an evolving tumor. Loss of boundaries between host and microbe engages pattern recognition receptors and their signaling cascades. Feedforward loops of chronic inflammation mediated by NF-κB and STAT3 signaling fuel carcinogenesis within both transforming and non-neoplastic cells within the tumors.

CANCER DEVELOPMENT & PROGRESSION
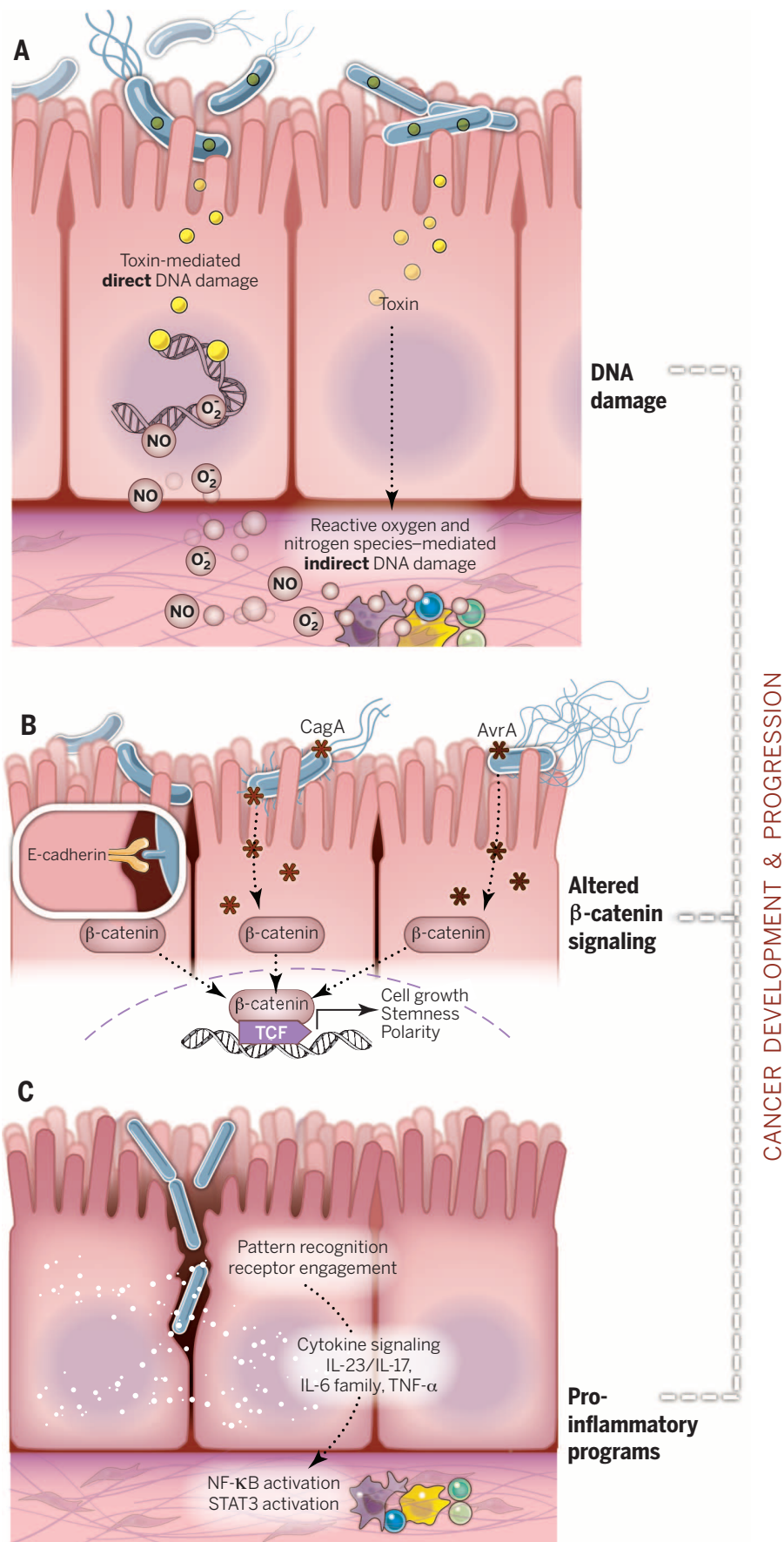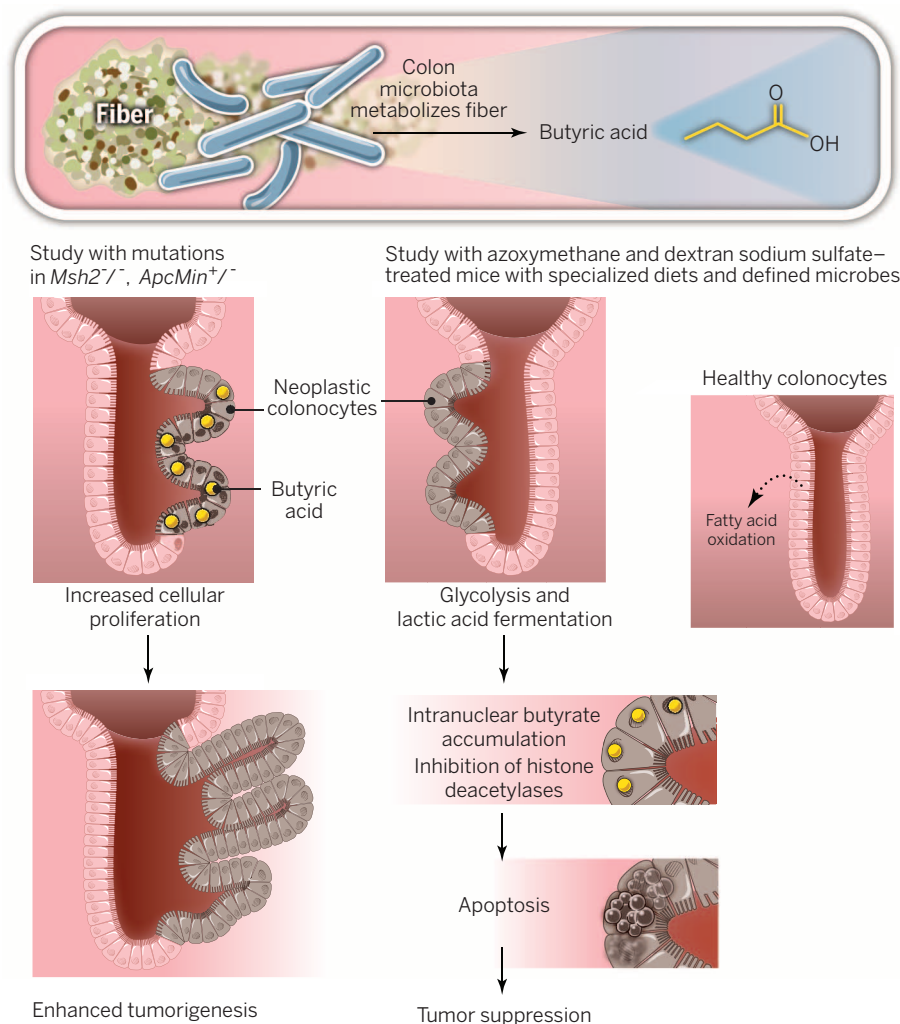
Fig. 3. Dietary fiber, microbiota, butyrate, and tumorigenesis. Metabolism of fiber by colonic microbes results in generation of butyric acid. When genetic mutations in *Msh2* and *Apc* are present, butyrate increases cell proliferation and enhances tumorigenesis. Data from another model of colorectal carcinogenesis indicate the opposite outcome: Neoplastic colonocytes engage in glycolysis for cellular energy, unlike healthy colonocytes (which favor fatty acid oxidation). As a result, butyrate accumulates in the nucleus of neoplastic cells, engaging tumor-suppressive pathways and apoptosis.

directly inhibit antitumor immunity by engaging TIGIT, a receptor with immunoglobulin and ITIM domains expressed on some T cells and natural killer cells, and blocking its ability to kill tumor cells (*61*). Whether microbes contribute to immunotherapeutic resistance in other cancers remains to be investigated.

Interrogating the role of microbes and microbiotas in cancer with new and old technologies

Microbiota studies in cancer remain at an early stage. Information gathering and descriptive studies are still necessary, and many critical questions remain. What other mechanisms might microbes use to influence tumorigenesis? If single microbes can compromise antitumor immunity or enhance susceptibility to oncomicrobes, are there configurations of the microbiota that do this, too (or are protective)? Are there microbes or microbiotas that enhance responsiveness to immunotherapies or other therapeutic interventions? To answer these questions, it is important to identify the key next steps in understanding how the human microbiota affects tumor growth and spread.

Sequencing-based technologies are a boon to both cancer biology and microbiology. Cancer genomes and their functional analyses have led to the implementation of precision medicine approaches to cancer care. Efforts to sequence individual microbes and human microbiomes are providing insight into how they influence human health and disease. Computational tools that identify microbial data within human sequencing data sets are welcome new additions to the armamentarium of cancer microbe hunters (*62*, *63*).

Despite the affordable price of sequencing, advances in culture techniques (*64–66*), and high-throughput analysis pipelines, the path of cancer microbiome discovery is fraught with pitfalls. Cancers may develop over decades, and different microbes and microbiotas may participate at distinct stages of the neoplastic process. For many malignancies, by the time a cancer is detected, the window of opportunity for identifying the inciting microbial agent(s) may have passed, allowing these organisms to remain elusive. However, the microbiota should remain a focus of study in locally advanced and metastatic cancer, as microbes may contribute to an established cancer's continued growth and spread.

Beyond sequencing, microscopy and flow cytometry–based approaches are useful tools to detect and study tumor-associated microbiotas. Human colon tumors may harbor specific consortia of bacteria that assemble themselves into biofilms (*17*). These biofilms appear to be specific to certain biogeographies within the gastrointestinal tract and have members that have been associated with colorectal adenomas and adenocarcinomas in human and mouse studies (e.g., enterotoxigenic *B. fragilis* and *F. nucleatum*). Microbiological studies of the oral cavity have shed light on microbial biofilms and their roles in human health and disease (*67*, *68*).

from donors with or without caCRC, followed by treatments that induced caCRC, those recipients that received gut microbiomes from caCRC-bearing mice developed more tumors (*51*). Similar mouse experiments using fecal transfers from humans with colon cancer suggest that there are microbiome structures, both protective and risk-elevating, that influence tumorigenesis (*52*).

Inflammation also results in the generation of respiratory electron acceptors such as nitrate, ethanolamine, and tetrathionate, which some bacterial clades can use for their own fitness advantage (*53–59*). Several bacteria (e.g., *E. coli* and *Salmonella* spp.) can use these electron acceptors and also possess the key features that reinforce the chronic inflammatory programs that can enhance cancer growth and spread. However, it remains to be determined whether bacterial use of these electron acceptors enhances cancer growth.

Immune-dampening responses can be cancer-permissive

Microbes not only trigger and reinforce proinflammatory immune circuits but also exploit or elicit immunosuppressive responses. A microbe may take advantage of preexisting immunosuppression or elicit immune-dampening responses to avoid destruction. Chronic systemic immunosuppression, as seen with advanced HIV infection, increases the risk for many cancers, especially virally associated malignancies. Microbial-elicited immunosuppression can also contribute to impaired antitumor immunity. Most current cancer-directed immunotherapies are focused on rousing immune responsiveness to tumors (*60*). The colon cancer–associated bacterium *F. nucleatum* may

Within biofilms, microbial cross-feeding and co-metabolism occur (69). Consortia of tumor-associated microbes have the potential to generate metabolites that require collective microbial metabolism, and these co-metabolites may contribute to or halt carcinogenesis. The role of microbial metabolism in host physiology is an exciting area, with several recent studies re-examining the role of microbial metabolites in cancer (4, 70).

Microbes, metabolism, and cancer

In 1956, Warburg put forth the hypothesis that altered cellular metabolism is the root cause of carcinogenesis (71), and cancer cell metabolism is currently a promising therapeutic target (72). Microbes participate in a range of host metabolic activities. Microbial metabolites or co-metabolites (generated with contributions from both host and microbe) can contribute to inflammatory tone and can influence the balance of proliferation and cell death in tissues (4). Consideration of the effects of a microbiota's metabolism, and specifically microbial metabolites generated within the tumor microenvironment, on cancer growth and spread adds another therapeutic and diagnostic angle for targeting cancers through metabolic alterations.

A meal fit/unfit for a tumor: Fiber and fats

What defines a microbial oncometabolite (73), and how are such metabolites generated? Both the host and its microbes affect the metabolism of dietary fiber, fats, ethanol, and phytoestrogens. As with microbes, metabolites can affect immune cell function, barrier function, and cell proliferation and death. Metabolites generated from dietary fiber and fats that have an established effect on cancer are considered below, along with recent insights.

Intestinal fermentation of dietary fiber by members of the colonic microbiota results in the generation of several short-chain fatty acids (SCFAs) including acetic, propionic, and butyric acids. These SCFAs have a range of effects on many cell types, including anti-inflammatory effects on myeloid cells (74) and colonic regulatory T cells (75–77), with consequences for intratumoral inflammation. SCFA's effects may be tuned by the receptors that they bind (e.g., Niacr1/Gpr109a, Gpr43, Gpr41, or Olfr78). Gpr109a is a receptor for niacin and butyrate. It plays an important role in mediating the effects of dietary fiber and the microbiota in the colon, where it is expressed by both colonic epithelial cells and intestinal myeloid cells. Activation of Gpr109a by butyrate results in anti-inflammatory host responses in myeloid cells that lead to regulatory T cell generation, and loss of Gpr109a increases susceptibility to caCRC (78).

SCFAs also affect host gene expression patterns, cell proliferation, and cell death via both receptor-mediated and receptor-independent mechanisms. SCFAs and their activation of Gpr43 reduce the proliferation rate of leukemia cells (79). In a study of ~70 human colon adenocarci-nomas, *GPR43* expression was reduced in cancer versus healthy tissue; restoration of *GPR43* in a human colon cancer line increased apoptotic cell death upon SCFA exposure (80).

SCFAs' effects on host cellular processes vary according to concentration and host genotype. Two recent mouse studies, which arrived at different conclusions regarding the relationship of dietary fiber, the microbiota, and butyrate to colorectal tumorigenesis, reflect this heterogeneous response to SCFAs (Fig. 3). Dietary fiber and butyrate-producing bacteria suppressed tumors in mice that harbored strictly defined microbial communities, received specialized diets, and were treated with azoxymethane and dextran sodium sulfate (81). This study's data supported a model wherein the glycolytic metabolism of cancer cells resulted in reduced metabolism of butyrate and enhanced butyrate nuclear accumulation. High intranuclear butyrate levels increased histone acetylation and led to increased apoptosis and reduced cellular proliferation. In a mouse model of intestinal tumorigenesis driven by mutations in both the *Apc* gene and the mismatch repair gene *Msh2*, the microbiota and butyrate had tumor-promoting effects (82). Butyrate's principal effect in this model system was to drive a hyperproliferative response in *Msh2*-deficient epithelial cells. Cancer genetics and butyrate concentrations were critical factors in SCFAs' disparate effects on tumorigenesis between these studies. These studies underscore the challenges of translating microbiome, diet, and cancer basic science data into consensus guidelines for dietary interventions to reduce cancer risk. Given that a single microbial metabolite can mediate a range of effects in tumor models, investigators will require additional experimental systems to unravel the effects of the human-microbial meta-metabolome for health and cancer susceptibility.

In contrast with the conflicting basic science and epidemiological data surrounding dietary fiber (83), there is consensus that high saturated fat intake heightens cancer risk. Debate surrounding a high-fat diet (HFD) focuses on several mechanisms that may act alone or in combination, involving obesity, the microbiome, bile acids, and inflammation. There are a myriad of studies exploring the interconnection between obesity and malignancy (84–86). Obesity is now regarded as an inflammatory state (87), and we are learning more about the gut microbiome's contribution to obese and lean states (88, 89). Data support the idea that inflammation, the microbiota, and obesity constitute an inseparable trio that fuels cancer. However, a recent study suggests otherwise. In a mouse model of duodenal hyperplasia, adenomas, and invasive cancer driven by *k-ras* mutation, HFD and microbial dysbiosis amplified tumor growth and spread in the absence of obesity or the development of a robust proinflammatory response (90); mutated *k-ras* modulated Paneth
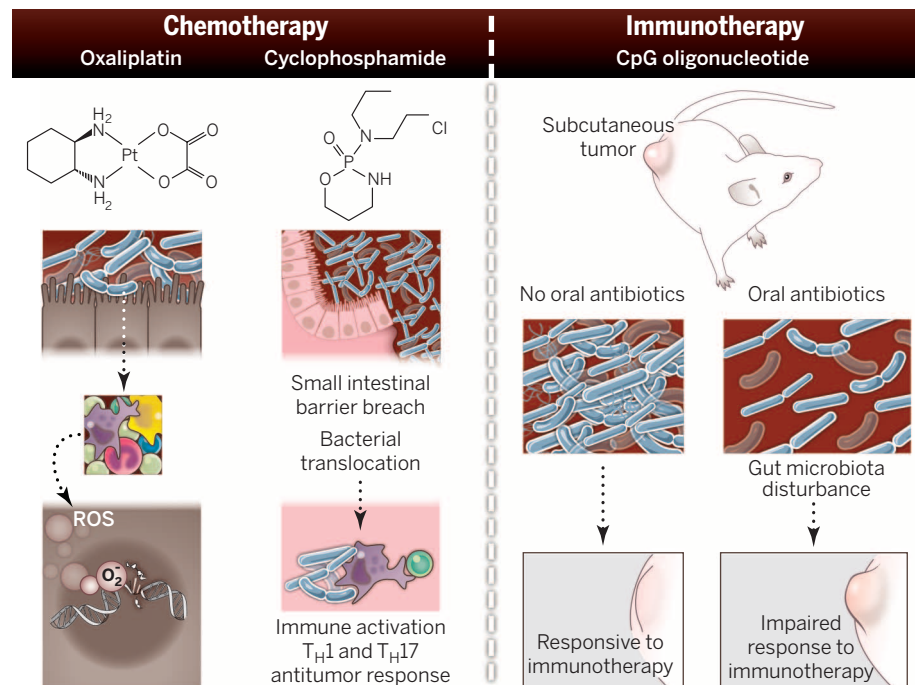
Fig. 4. How the microbiota modulate chemotherapy and immunotherapy efficacy in mouse models. The gut microbiota stimulate immune cells to produce reactive oxygen species (ROS). ROS enhance DNA damage caused by oxaliplatin, blocking DNA replication and transcription and resulting in cell death. Cyclophosphamide can cause small intestinal barrier breach. This barrier disruption results in bacterial translocation that potentiates antitumor T_H1 and T_H17 responses. CpG oligonucleotides are a microbial-associated molecular pattern and are used in immunotherapy. Antibiotic disruption of the gut microbiota in mice compromised the efficacy of CpG in a mouse subcutaneous tumor model.

cell antimicrobial expression and HFD affected intestinal mucin expression, thereby altering the intestinal microbiota. The fecal microbiota of HFD *k-ras* mutant mice was sufficient to transmit the cancer-potentiating effects of the HFD when transferred to antibiotic-treated *k-ras* mutant mice.

Another mechanism by which HFD influences cancer risk is via bile acids that are produced to solubilize and digest the consumed fats—specifically, the microbially generated secondary bile acids. The role of secondary bile acids in increased or decreased cancer risk has been studied for decades (*2*). One recent study provided new insight into deoxycholic acid's pro-oncogenic mechanisms in liver cancer: HFD or genetic susceptibility to obesity can increase deoxycholic acid–mediated activation of a mitogenic and proinflammatory response program in hepatic stellate cells, thereby potentiating liver cancer in mice (*91*). These studies reinforce the importance of gene-environment interactions in carcinogenesis and underscore the need to consider how dietary patterns influence the genomes and genomic outputs of both host and microbiome in mitigating or amplifying cancer risk.

Drugs, bugs, and cancer

The gut microbiota function in drug metabolism, influencing toxicity and efficacy (*92, 93*). Because chemotherapeutic agents have a narrow therapeutic window, there is interest in the microbiota's modulation of chemotherapy toxicity and efficacy (Fig. 4). Irinotecan is a topoisomerase-1 inhibitor that is used in combination with other chemotherapies to treat several cancers. A common side effect is diarrhea. For some patients, the severity of the diarrhea requires hospitalization. Microbial-produced β-glucuronidases regulate levels of irinotecan's bioactive form within the intestinal lumen and thus influence irinotecan's toxicity (*94*). Oral bacterial β-glucuronidase inhibitors blunt the dose-limiting toxicities of irinotecan in mice and do not harm host cells or kill bacteria, which suggests that microbial metabolism is a plausible target in cancer care (*95*).

The gut microbiota also affect the efficacy of chemotherapy. Oxaliplatin is a platinum-based chemotherapy used to treat several gastrointestinal malignancies. Together, the microbiota and immune system contribute to oxaliplatin's efficacy (*96*). The gut microbiota prime myeloid cells for high-level ROS production. The resultant intratumoral oxidative stress augments oxaliplatin-associated DNA damage, triggering cancer cell death (*96*). Cyclophosphamide, an alkylating agent used in hematologic malignancies and solid tumors, can injure the small intestinal epithelium. The ensuing barrier breach results in gut microbiota–dependent, T helper (T$_H$) cell–mediated antitumor responses (*97*). Delineating the roles of gut microbiota in response to chemotherapy in model systems and undertaking epidemiologic studies with microbiome analysis in patients with and at risk for cancer will be critical for realizing the microbiota as an adjuvant therapy that enhances efficacy or attenuates toxicity of chemotherapies.

The microbiota and immunotherapy: Friend or foe?

The success of immunotherapy (in the form of cytokine therapy, targeting immune checkpoint blockade, and vaccine therapy) has been one of the most exciting developments in cancer care over the past decade (*98*). Given the intertwined nature of the microbiota and the immune system, it is plausible that the microbiota influence a host's responsiveness to immunotherapy. In support of this idea, antibiotic-mediated disruption of the microbiota in mice bearing subcutaneous tumors impaired the effectiveness of CpG oligonucleotide immunotherapy (Fig. 4) (*96*). Observations that immunotherapies are showing efficacy in melanoma and bladder, renal, and lung cancer but not in cancer of the colon (which is densely populated by bacteria) fuel interest in how the microbiota contributes to immunotherapy's efficacy. Furthermore, given the severe colitis observed in some patients receiving immunotherapies (*99*) (e.g., antibodies to CTLA4 and PD-L1) and the role of gut microbes in colitis, it is possible that the gut microbiota influences this toxicity. As patient populations expand, investigators will hopefully interrogate whether there are microbiota that are predictive for colitis and other toxicities. Examining the microbiota and its effects on immunotherapy efficacy and toxicity in preclinical models and patients is a critical next step.

Hematopoietic transplants, complications, and the microbiota

Allogeneic hematopoietic stem cell transplant (allo-HSCT), a mainstay in hematologic malignancy treatment, is a challenge to both host and microbiota. An individual's microbiota is confronted with a new host within its host as well as chemotherapy, radiation, oral and gastrointestinal barrier breach, and broad-spectrum antibiotics. Studies have begun to examine perturbations to the gut microbiota and clinical outcomes during allo-HSCT (*100*).

Bacteremia, *Clostridium difficile* infection, and graft-versus-host disease (GVHD) are common events in allo-HSCT patients. Bacteremias with vancomycin-resistant *Enterococcus* (VRE) are a grave concern. Two preclinical studies examining how antibiotics perturb the gut microbiota to enable VRE displacement of a healthy microbiota (*101*) and how the anaerobic bacteria *Barnesiella* spp. may confer resistance to VRE (*102*) have provided mechanistic insight into these bloodstream infections. These studies set the stage for a clinical study showing that enterococcal gut microbiota domination was associated with a factor of 9 higher risk of VRE bacteremia in allo-HSCT patients (*103*). Hospitalized patients and allo-HSCT patients both confront toxigenic *C. difficile* infection. Using mouse models, microbiome analysis, and allo-HSCT patient populations, researchers identified a microbe that can restore bile acid–mediated resistance to *C. difficile* (*104*). The workflows of this precision medicine–based study are applicable to many diseases associated with altered microbiotas.

Allo-HSCT patients can experience gastrointestinal, pulmonary, and skin complications after transplant; some of these are idiopathic clinical syndromes while others are GVHD manifestations. Using shotgun DNA sequencing of colon tissue and the PathSeq pipeline, investigators found that *Bradyrhizobium enterica* was enriched in affected colonic tissue from patients with idiopathic colitis after receiving a cord blood transplant (*105*), providing insight and a potential treatment. Using samples from mice and humans that had undergone allogeneic bone marrow transplants, investigators characterized the gut microbiota changes in active intestinal GVHD (*106*). In mice, depletion of lactobacilli exacerbated GVHD-associated intestinal inflammation and their reintroduction attenuated inflammation (*106*). The challenge intrinsic to these studies, and realized in (*104*), is to use our evolving knowledge of the microbiome and microbes to identify bacteriotherapy for cancer and its complications.

Back to the future: Perspectives and directions for cancer bacteriotherapy

The genesis of immunotherapy came from an appreciation for the co-adaptation between host and microbe. Exploiting this knowledge and using bacteria to trigger the immune system to attack and destroy cancers dates back to the 1850s, when several German physicians noticed that some cancer patients with active infections showed signs of tumor regression. This led Coley to test bacterial extracts in patients with bone cancers around 1900. Heat-killed cultures of *Streptococcus pyogenes* and *Serratia marcescens*, or Coley's toxins, were one of earliest forms of immunotherapy (*60*). Since this seminal work, one bacterium has entered the mainstream of cancer treatment. For the past three to four decades, Bacillus Calmette-Guerin (BCG) has been used to treat non–muscle-invasive bladder cancer. The live bacteria, which are delivered directly into the bladder, elicit inflammation that triggers an antitumor immune response (*107*). Much still remains to be learned about the immune response to BCG and antitumor immunity, and why BCG loses efficacy once the cancer is more invasive (*108*).

Over the past 30 years, several bacterial-based approaches to cancer therapy have emerged. Bacterial-based vaccines that express tumor antigens have shown efficacy in preclinical studies, and recombinant *Listeria monocytogenes*–based vaccines showed tremendous promise in mice (*109*). Interest remains in using bacteria as a delivery vehicle for plant toxins, such as ricin and saporin, or pseudomonal exotoxins that can block protein synthesis and induce apoptosis in cancer cells (*110*). Bacteria have evolved elegant systems to communicate with each other, to kill one another (*111*), and to deliver their

effectors into host cells (*112*). The extension and application of these secretion systems, which have been honed by millennia of evolution, seems like a therapeutic slam dunk but has been challenging in practice. A recent study in dogs (*113*) has breathed new life into the concept of bacteriotherapy with *Clostridium novyii*, which emerged as a promising concept in preclinical models almost 15 years ago (*114*); however, balancing toxicity with efficacy remains difficult.

Synthetic biology approaches to cancer care hold enormous potential, especially those that make use of bacteria. These efforts involve the reengineering of bacterial cells for the delivery of biomolecules under tunable networks and on/off toggle switches triggered by host responses (*115*). The goals are simple: to target cancers and minimize damage to healthy tissues via genetic network designs informed by engineering principles. Proof of concept that designer microbes can invade cancer cells (*116*) to target and perturb key cancer pathways has been established (*117*). Evaluation in robust preclinical models will be the next step. Application and design for cancer care will need to focus on maximizing anticancer responses while minimizing toxicities and infectious complications.

Like synthetic biology, microbiome studies have emerged as a promising area of investigation for cancer care over the past decade. The microbiome may afford many answers to several looming questions in cancer biology: What are the critical gene-environmental interactions in cancer susceptibility? Why do certain foods or dietary patterns confer increased or decreased risk in certain populations and individuals? Why do chemotherapies, immunotherapies, and preventive agents fail or succeed for patients, irrespective of host germline or cancer genotype? The microbiome seems to provide many potential answers in the forms of select clades, consortia, metabolites, and enzymatic activities, but it remains unclear whether and how these will translate from preclinical models to humans. One opportunity for the microbiota in the near term is as a biomarker for diagnosis (*118*), prognostication, or identifying those most at risk for treatment-related complications. Although there may be dissent about the best next steps, there is consensus that therapeutic consideration of cancer and the microbiota requires a multidisciplinary approach and more intensive investigation.

REFERENCES AND NOTES

1. C. de Martel et al., *Lancet Oncol.* **13**, 607–615 (2012).
2. C. L. Sears, W. S. Garrett, *Cell Host Microbe* **15**, 317–328 (2014).
3. R. F. Schwabe, C. Jobin, *Nat. Rev. Cancer* **13**, 800–812 (2013).
4. P. Louis, G. L. Hold, H. J. Flint, *Nat. Rev. Microbiol.* **12**, 661–672 (2014).
5. E. Elinav et al., *Nat. Rev. Cancer* **13**, 759–771 (2013).
6. T. Irrazábal, A. Belcheva, S. E. Girardin, A. Martin, D. J. Philpott, *Mol. Cell* **54**, 309–320 (2014).
7. J. Kallmeyer, R. Pockalny, R. R. Adhikari, D. C. Smith, S. D'Hondt, *Proc. Natl. Acad. Sci. U.S.A.* **109**, 16213–16216 (2012).
8. M. T. Abreu, R. M. Peek Jr., *Gastroenterology* **146**, 1534–1546.e3 (2014).
9. A. I. Ojesina et al., *Nature* **506**, 371–375 (2014).
10. J.-P. Nougayrède et al., *Science* **313**, 848–851 (2006).
11. J. Putze et al., *Infect. Immun.* **77**, 4696–4703 (2009).
12. J. C. Arthur et al., *Nat. Commun.* **5**, 4724 (2014).
13. J. C. Arthur et al., *Science* **338**, 120–123 (2012).
14. A. Boleij et al., *Clin. Infect. Dis.* **60**, 208–215 (2015).
15. C. L. Sears et al., *Clin. Infect. Dis.* **47**, 797–803 (2008).
16. S. Wu et al., *Nat. Med.* **15**, 1016–1022 (2009).
17. C. M. Dejea et al., *Proc. Natl. Acad. Sci. U.S.A.* **111**, 18321–18326 (2014).
18. L. Guerra, R. Guidi, T. Frisan, *FEBS J.* **278**, 4577–4588 (2011).
19. A. C. Goodwin et al., *Proc. Natl. Acad. Sci. U.S.A.* **108**, 15354–15359 (2011).
20. H. Clevers, R. Nusse, *Cell* **149**, 1192–1205 (2012).
21. M. Castellarin et al., *Genome Res.* **22**, 299–306 (2012).
22. A. D. Kostic et al., *Genome Res.* **22**, 292–298 (2012).
23. A. D. Kostic et al., *Cell Host Microbe* **14**, 207–215 (2013).
24. A. N. McCoy et al., *PLOS ONE* **8**, e53653 (2013).
25. M. R. Rubinstein et al., *Cell Host Microbe* **14**, 195–206 (2013).
26. C. L. Sears, *Clin. Microbiol. Rev.* **22**, 349–369 (2009).
27. R. Lu et al., *Oncogenesis* **3**, e105 (2014).
28. R. Lu et al., *Am. J. Physiol. Gastrointest. Liver Physiol.* **303**, G1113–G1125 (2012).
29. U. Dutta, P. K. Garg, R. Kumar, R. K. Tandon, *Am. J. Gastroenterol.* **95**, 784–787 (2000).
30. E. C. Lazcano-Ponce et al., *CA Cancer J. Clin.* **51**, 349–364 (2001).
31. I. I. Wistuba, A. F. Gazdar, *Nat. Rev. Cancer* **4**, 695–706 (2004).
32. L. V. Hooper, D. R. Littman, A. J. Macpherson, *Science* **336**, 1268–1273 (2012).
33. J. A. DiDonato, F. Mercurio, M. Karin, *Immunol. Rev.* **246**, 379–400 (2012).
34. G. Zhang, R. Chen, J. D. Rudney, *J. Periodontal Res.* **46**, 558–567 (2011).
35. M. R. Milward et al., *Clin. Exp. Immunol.* **148**, 307–324 (2007).
36. E. Allen-Vercoe, J. Strauss, K. Chadee, *Gut Microbes* **2**, 294–298 (2011).
37. S.-R. Park et al., *Infect. Immun.* **82**, 1914–1920 (2014).
38. I. C. Allen et al., *J. Exp. Med.* **207**, 1045–1056 (2010).
39. G. Y. Chen, M. Liu, F. Wang, J. Bertin, G. Núñez, *J. Immunol.* **186**, 7187–7194 (2011).
40. B. Hu et al., *Proc. Natl. Acad. Sci. U.S.A.* **110**, 9862–9867 (2013).
41. B. Hu et al., *Proc. Natl. Acad. Sci. U.S.A.* **107**, 21635–21640 (2010).
42. M. H. Zaki, P. Vogel, M. Body-Malapel, M. Lamkanfi, T.-D. Kanneganti, *J. Immunol.* **185**, 4912–4920 (2010).
43. M. H. Zaki et al., *Cancer Cell* **20**, 649–660 (2011).
44. A. Couturier-Maillard et al., *J. Clin. Invest.* **123**, 700–711 (2013).
45. S. I. Grivennikov et al., *Nature* **491**, 254–258 (2012).
46. S. I. Grivennikov, M. Karin, *Ann. Rheum. Dis.* **70** (suppl. 1), i104–i108 (2011).
47. S. I. Grivennikov, *Cancer Cell* **24**, 145–147 (2013).
48. H. Yu, D. Pardoll, R. Jove, *Nat. Rev. Cancer* **9**, 798–809 (2009).
49. N. Li, S. I. Grivennikov, M. Karin, *Cancer Cell* **19**, 429–431 (2011).
50. R. L. Warren et al., *Microbiome* **1**, 16 (2013).
51. J. P. Zackular et al., *MBio* **4**, e00692-13 (2013).
52. N. T. Baxter, J. P. Zackular, G. Y. Chen, P. D. Schloss, *Microbiome* **2**, 20 (2014).
53. F. Faber, A. J. Bäumler, *Immunol. Lett.* **162**, 48–53 (2014).
54. F. Rivera-Chávez et al., *PLOS Pathog.* **9**, e1003267 (2013).
55. S. E. Winter, A. J. Bäumler, *Gut Microbes* **5**, 71–73 (2014).
56. S.-P. Nuccio, A. J. Bäumler, *MBio* **5**, e00929-14 (2014).
57. S. E. Winter et al., *Science* **339**, 708–711 (2013).
58. P. Thiennimitr et al., *Proc. Natl. Acad. Sci. U.S.A.* **108**, 17480–17485 (2011).
59. S. E. Winter et al., *Nature* **467**, 426–429 (2010).
60. I. Mellman, G. Coukos, G. Dranoff, *Nature* **480**, 480–489 (2011).
61. C. Gur et al., *Immunity* **42**, 344–355 (2015).
62. A. D. Kostic et al., *Nat. Biotechnol.* **29**, 393–396 (2011).
63. D. R. Riley et al., *PLOS Comput. Biol.* **9**, e1003107 (2013).
64. A. L. Goodman et al., *Proc. Natl. Acad. Sci. U.S.A.* **108**, 6252–6257 (2011).
65. I. Vanwonterghem, P. D. Jensen, D. P. Ho, D. J. Batstone, G. W. Tyson, *Curr. Opin. Biotechnol.* **27**, 55–64 (2014).
66. M. V. Sizova et al., *Appl. Environ. Microbiol.* **78**, 194–203 (2012).
67. C. J. Wright et al., *Mol. Oral Microbiol.* **28**, 83–101 (2013).
68. M. A. Curtis, C. Zenobia, R. P. Darveau, *Cell Host Microbe* **10**, 302–306 (2011).
69. K. E. Boyle, S. Heilmann, D. van Ditmarsch, J. B. Xavier, *Curr. Opin. Microbiol.* **16**, 207–212 (2013).
70. R. Medzhitov, D. S. Schneider, M. P. Soares, *Science* **335**, 936–941 (2012).
71. O. Warburg, *Science* **123**, 309–314 (1956).
72. M. G. Vander Heiden, *Nat. Rev. Drug Discov.* **10**, 671–684 (2011).
73. S. J. Bultman, C. Jobin, *Cell Host Microbe* **16**, 143–145 (2014).
74. K. M. Maslowski et al., *Nature* **461**, 1282–1286 (2009).
75. P. M. Smith et al., *Science* **341**, 569–573 (2013).
76. N. Arpaia et al., *Nature* **504**, 451–455 (2013).
77. Y. Furusawa et al., *Nature* **504**, 446–450 (2013).
78. N. Singh et al., *Immunity* **40**, 128–139 (2014).
79. L. B. Bindels et al., *Br. J. Cancer* **107**, 1337–1344 (2012).
80. Y. Tang, Y. Chen, H. Jiang, G. T. Robbins, D. Nie, *Int. J. Cancer* **128**, 847–856 (2011).
81. D. R. Donohoe et al., *Cancer Discov.* 10.1158/2159-8290.CD-14-0501 (2014).
82. A. Belcheva et al., *Cell* **158**, 288–299 (2014).
83. M. Song, W. S. Garrett, A. T. Chan, *Gastroenterology* 10.1053/j.gastro.2014.12.035 (2015).
84. R. W. O'Rourke, *Surg. Obes. Relat. Dis.* **10**, 1208–1219 (2014).
85. J. Park, T. S. Morley, M. Kim, D. J. Clegg, P. E. Scherer, *Nat. Rev. Endocrinol.* **10**, 455–465 (2014).
86. N. A. Berger, *Ann. N.Y. Acad. Sci.* **1311**, 57–76 (2014).
87. M. F. Gregor, G. S. Hotamisligil, *Annu. Rev. Immunol.* **29**, 415–445 (2011).
88. R. E. Ley, *Curr. Opin. Gastroenterol.* **26**, 5–11 (2010).
89. P. J. Turnbaugh et al., *Nature* **457**, 480–484 (2009).
90. M. D. Schulz et al., *Nature* **514**, 508–512 (2014).
91. S. Yoshimoto et al., *Nature* **499**, 97–101 (2013).
92. A. D. Patterson, P. J. Turnbaugh, *Cell Metab.* **20**, 761–768 (2014).
93. R. N. Carmody, P. J. Turnbaugh, *J. Clin. Invest.* **124**, 4173–4181 (2014).
94. A. B. Roberts, B. D. Wallace, M. K. Venkatesh, S. Mani, M. R. Redinbo, *Mol. Pharmacol.* **84**, 208–217 (2013).
95. B. D. Wallace et al., *Science* **330**, 831–835 (2010).
96. N. Iida et al., *Science* **342**, 967–970 (2013).
97. S. Viaud et al., *Science* **342**, 971–976 (2013).
98. J. Couzin-Frankel, *Science* **342**, 1432–1433 (2013).
99. C. Gedye, A. van der Westhuizen, T. John, *Intern. Med. J.* 10.1111/imj.12653 (2014).
100. Y. Taur et al., *Blood* **124**, 1174–1182 (2014).
101. C. Ubeda et al., *J. Clin. Invest.* **120**, 4332–4341 (2010).
102. C. Ubeda et al., *Infect. Immun.* **81**, 965–973 (2013).
103. Y. Taur et al., *Clin. Infect. Dis.* **55**, 905–914 (2012).
104. C. G. Buffie et al., *Nature* **517**, 205–208 (2015).
105. A. S. Bhatt et al., *N. Engl. J. Med.* **369**, 517–528 (2013).
106. R. R. Jenq et al., *J. Exp. Med.* **209**, 903–911 (2012).
107. M. A. Ingersoll, M. L. Albert, *Mucosal Immunol.* **6**, 1041–1053 (2013).
108. G. Redelman-Sidi, M. S. Glickman, B. H. Bochner, *Nat. Rev. Urol.* **11**, 153–162 (2014).
109. Z. K. Pan, G. Ikonomidis, A. Lazenby, D. Pardoll, Y. Paterson, *Nat. Med.* **1**, 471–477 (1995).
110. N. Nair, T. Kasai, M. Seno, *Anticancer Res.* **34**, 6289–6296 (2014).
111. B. T. Ho, T. G. Dong, J. J. Mekalanos, *Cell Host Microbe* **15**, 9–21 (2014).
112. J. E. Galán, H. Wolf-Watz, *Nature* **444**, 567–573 (2006).
113. N. J. Roberts et al., *Sci. Transl. Med.* **6**, 249ra111 (2014).
114. L. H. Dang, C. Bettegowda, D. L. Huso, K. W. Kinzler, B. Vogelstein, *Proc. Natl. Acad. Sci. U.S.A.* **98**, 15155–15160 (2001).
115. W. C. Ruder, T. Lu, J. J. Collins, *Science* **333**, 1248–1252 (2011).
116. J. C. Anderson, E. J. Clarke, A. P. Arkin, C. A. Voigt, *J. Mol. Biol.* **355**, 619–627 (2006).
117. S. Xiang, J. Fruehauf, C. J. Li, *Nat. Biotechnol.* **24**, 697–702 (2006).
118. J. P. Zackular, M. A. M. Rogers, M. T. Ruffin 4th, P. D. Schloss, *Cancer Prev. Res.* **7**, 1112–1121 (2014).

Enhanced thermoelectric
performance of bulk
bismuth telluride
Kim et al., *p. 109*
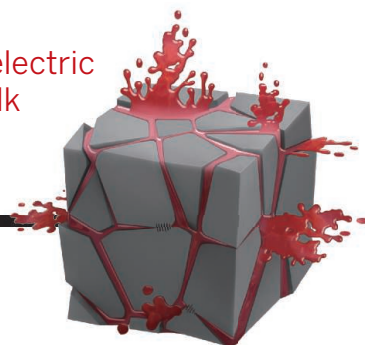
Edited by **Stella Hurtley**

Evolution of ionized
wind during star formation

IMAGES: (TOP TO BOTTOM) KIM *ET AL.*; WOLFGANG STEFFEN/INSTITUTO DE ASTRONOMÍA/UNAM; DAVID M. PHILLIPS/SCIENCE SOURCE

STELLAR PHYSICS

Young stars grow up and narrow their focus

Stars are thought to grow by gathering spirals of material from a disk. If this is the case, to balance angular momentum, gas should flow out rapidly along the disk's rotation axis. Carrasco-Gonzalez *et al.* now seem to have glimpsed the "before" and "after" stages of the onset of such an outflow, over the course of just 18 years (see the Perspective by Hoare). Radio monitoring of the massive protostar W75N(B)-VLA2 reveals a transition from a spherical wind to a collimated one, giving critical insight into what happens as a massive star forms. — MMM

Science, this issue p. 114; see also p. 44

COGNITIVE DEVELOPMENT

Learning when and what to learn

Infants use "unexpectedness" as a cue for learning. Stahl and Feigenson studied how babies reacted when objects behaved in surprising ways (see the Perspective by Schulz). Babies who saw apparently solid and weighty objects moving through a wall or past the edge of a table without falling looked intently at them. When given the opportunity to explore these peculiar objects, they did so by banging them on the floor—as if to test their solidity—or dropping them—as if to test their weightiness. — GJC

Science, this issue p. 91;
see also p. 42

RIBOSOME

The whole mitoribosome at high resolution

Mitochondria are thought to be the descendents of a prokaryotic cell that took up residence in a protoeukaryotic cell. Mitochondria retain a few genes involved in oxidative phosphorylation. To translate these genes, mitochondria contain highly divergent mitochondrial ribosomes, or mitoribosomes. Amunts *et al.* determined the high-resolution structures of complete mammalian mitoribosomes using cryoelectron microscopy. Mitoribosomes include an unusual mRNA binding channel. The findings elucidate how aminoglycoside antibiotics can inadvertently inhibit mitoribosomes and how mutations in mitoribosomes can lead to disease. — GR

Science, this issue p. 95

MICROBIOLOGY

CRISPRing *Candida* for health's sake

Candida albicans is a significant cause of mortality in immunocompromised individuals and a major health concern in hospital-acquired infections. The lack of facile molecular genetic tools has been a major obstacle for a better understanding of this pathogen. Vyas *et al* developed a CRISPR system that allows precise gene manipulation in *Candida*. Their approach could revolutionize our ability to manipulate the *Candida* genome for a better understanding of the biology of

Pseudohyphae of *Candida albicans*, an opportunistic fungal pathogen

this pathogen and the development of targeted therapeutics. — ASH

Sci. Adv. 10.1126/sciadv.1500248 (2015).

MOLECULAR PHYSICS
Making a molecular fossil lookalike

Atoms are generally compact objects. However, if one of the electrons orbiting the nucleus is given an extra boost of energy so that it's barely still attached, you get a much larger Rydberg atom. Booth *et al.* created an even more exotic species: a giant molecule consisting of a regular cesium atom bound within a Rydberg atom of the same element. The molecules are named "trilobites" because their electronic density visually resembles fossils of these extinct marine creatures. — JS

Science, this issue p. 99

PLANT BIOLOGY
Protecting against runaway defense systems

RNA interference defends cells against invading genetic elements, such as viruses or transgenes. But while the invasive RNAs are under attack, what protects the normal endogenous RNAs? Zhang *et al.* identified, in the small plant *Arabidopsis*, a surveillance system to do just that: Preserve the normal transcriptome and keep the attack focused on invasive transcripts. — PJH

Science, this issue p. 120

TRIBOLOGY
Additive explanation for anti-wear

Additives in oil are vital for protecting engines from wear by forming films at sliding interfaces. Zinc dialkydithiophosphate (ZDDP) has been used for decades to reduce engine wear. Now there is a strong incentive for finding a replacement for ZDDP: Its breakdown products shorten catalytic converter lifetime. Gosvami *et al.* examined exactly how ZDDP produces an anti-wear film under high stress or elevated temperature (see the Perspective by Schwarz). Understanding these mechanisms will help in the development of higher-performance and more effective additives. — BG

Science, this issue p. 102; see also p. 40

VIROLOGY
Evolution in the Ebola virus outbreak

Has rapid mutation produced alarming new virus characteristics in the 2013–2015 Ebola virus outbreak in West Africa? Hoenen *et al.* sequenced isolates obtained 9 months into the epidemic from cases in Mali. The nucleotide substitution rate was consistent with rates estimated from past Central African outbreaks. In contrast, analysis of sequence data from early in the outbreak indicated rapid mutation. This more recent finding offers confidence that diagnostic methods, vaccines, and other treatment interventions will remain effective. Nevertheless, vigilance must be maintained: A few mutations can radically change the biological properties of other RNA viruses. — CA

Science, this issue p. 117

CANCER IMMUNOLOGY
More mutations predict better efficacy

Despite the remarkable success of cancer immunotherapies, many patients do not respond to treatment. Rizvi *et al.* studied the tumors of patients with non–small-cell lung cancer undergoing immunotherapy. In two independent cohorts, treatment efficacy was associated with a higher number of mutations in the tumors. In one patient, a tumor-specific T cell response paralleled tumor regression. — KLM

Science, this issue p. 124

Unique prions cause chronic wasting disease in North American elk and deer

PHOTO: © ROBERT HARDING WORLD IMAGERY RF/ALAMY

PRION TRANSMISSION
Prion-caused wasting

Chronic wasting disease (CWD) is killing deer and elk in the United States and Canada. CWD is caused by an infectious protein, or prion, that is found in meat and blood from infected animals. But is there a risk to humans who eat these animals? Kurt *et al.* found that mice expressing human prion protein (PrP) resisted CWD, whereas mice expressing human PrP with four elk residue substitutions were susceptible. Only two elk residue substitutions in human PrP were needed for efficient conversion of the protein to the prion conformation. The amyloid-forming propensity of the PrP was important in this conversion, which may explain why some species are highly susceptible to prions from other species. — SMH

J. Clin. Invest. 10.1172/JCI79408 (2015).

WATER QUALITY
More contaminants entering waterways

Modern wastewater treatment processes still leave behind trace amounts of pharmaceuticals, personal care products, and other potentially harmful or toxic compounds. For example, over 10 metric tons of the antimicrobial compound triclosan are released from wastewater treatment plants into U.S. waterways each year. Hensley et al. detected trace contaminants in the effluent from four U.S. wastewater treatment plants, including triclosan, chlorinated triclosan derivatives, and hydroxylated by-products of polybrominated diphenyl ethers (PBDEs)—recalcitrant compounds used as flame retardants. Chlorinated triclosan derivatives were present at the same low but appreciable levels as PBDE by-products, both of which produce toxic dioxins during photodegradation. — NW

Environ. Sci. Water Res. Technol. 10.1039/c4ew00102h (2015).

COMPLEX SYSTEMS
Finding communities in interacting systems

Understanding the underlying behavior of complex interacting systems is a challenging problem affecting the social, life, and physical sciences. Representing components of a system as nodes and assigning weights to the interactions between components can provide a graphical picture of the interacting system. Trying to map out real-life systems that are large, consist of multiple layers, and are dynamic can result in oversimplification, though. De Domenico et al. propose a method based on network flow analysis that can reveal clusters or communities of nodes that are closely connected within and across the various layers of a system. Identifying key communities in a complex interacting system could be crucial in revealing the functional structure underlying the system. — ISO

Phys. Rev. X **5**, 11027 (2015).

HISTORY OF SCIENCE
Industry influence and tooth decay

The most common chronic disease among children and adolescents in the United States is tooth decay. Without concerted efforts by the sugar industry, we might be a lot closer to eradication. Industry papers from 1959–1971 reveal a pattern of diverting the National Institute of Dental Research (NIDR) toward strategies to make sugar less harmful and away from reducing sweets. Kearne et al., who analyzed these papers, also found that 78% of an industry-established statement by the International Sugar Research Foundation was directly incorporated into the text of the NIDR request for research proposals for the National Caries Program in 1971. — BJ

PLOS Med. 10.1371/journal.pmed.1001798 (2015).

PLANT SCIENCE
Fish oil from plants

Human heart health benefits from a diet rich in the polyunsaturated fatty acids found in oily fish such as salmon and anchovies. Unfortunately, marine fisheries are increasingly fragile, and farm-raised salmon require expensive supplements to generate the desirable fatty acids. Ruiz-Lopez et al. engineered the oilseed crop plant

Widely grown *Camelina sativa* can be engineered to produce fish oil

Camelina into a source of the key fatty acids by plucking enzymes from sources as diverse as phytoplankton, microalgae, and oomycetes. *Camelina* expressing the transgenes made as much as a quarter of their seed lipids into replacements for fish oil, surpassing salmon, pound for pound, as a source of the right fatty acids. — PJH

Plant Biotechnol. J. 10.1111/pbi.12328 (2015).

GEOMORPHOLOGY
Shaping landscapes with large floods

Extreme flood events can wreak havoc on landscapes by carving out features such as large canyons. Baynes et al. consider the multimillennial impact of extreme flood events on the erosion rate of a canyon in Iceland. By dating the canyon surfaces with cosmic rays, they find that three extreme flood events dominated background erosion processes over the past 9000 years. This is due to a transition from an erosion regime driven by abrasion to one in which basalt lava columns were toppled during the large floods. High-impact, short lived events clearly play an overriding role in this locality and may be an underappreciated force for landscape evolution. — BG

Proc. Natl. Acad. Sci. U.S.A. 10.1073/pnas.1415443112 (2015).

PSYCHOLOGY
Upending our physical theories

Learning involves defining and classification, especially when the entities in question might be actual objects, such as a glass of milk or a dove, but could also have an innate property, such as animacy. Griffiths uses the scenario of a magician transforming one type of object into another to elicit judgments about which transformations are more interesting. He finds that the direction of transformation affects these judgments, with greater interest expressed in those that move from less animacy to more; that is, changing a glass of milk into a dove rather than vice versa. This asymmetry may be due to a need to adjust our prior ideas. — GJC

Cognition **136**, 43 (2015).

A large canyon in Iceland formed by an extreme flooding event

ALSO IN *SCIENCE* JOURNALS

Edited by **Stella Hurtley**

FRUSTRATED MAGNETISM
Probing the nature of an exotic magnet

To minimize their energy, materials with magnetic interactions tend to become ordered at low temperatures. However, if the magnetism is frustrated (for example, if the geometry of the crystal lattice gets in the way of minimizing the energy), the material may not reach an ordered state even at very low temperatures. Hirschberger *et al.* studied the excitations of such a system—the pyrochlore compound $Tb_2Ti_2O_7$—using thermal transport measurements. Thermal conductivity at very low temperatures resembled that of a disordered metal; a puzzling finding in an electrically insulating transparent material. — JS

Science, this issue p. 106

THERMOELECTRICS
Squeezing out efficient thermoelectrics

Thermoelectric materials hold the promise of converting waste heat into electricity. The challenge is to develop high-efficiency materials that are not too expensive. Kim *et al.* suggest a pathway for developing inexpensive thermoelectrics. They show a dramatic improvement of efficiency in bismuth telluride samples by quickly squeezing out excess liquid during compaction. This method introduces grain boundary dislocations in a way that avoids degrading electrical conductivity, which makes a better thermoelectric material. With the potential for scale-up and application to cheaper materials, this discovery presents an attractive path forward for thermoelectrics. — BG

Science, this issue p. 109

GENE EXPRESSION
Expression variability under miRNA control

MicroRNAs (miRNAs) repress gene expression by inhibiting translation and increasing mRNA degradation. Schmiedel *et al.* used single-cell reporter experiments and mathematical modeling to show that miRNAs can reduce not just expression but the expression variability of target genes (see the Perspective by Hoffman and Pilpel). Combinatorial targeting principles ensured reduced variability for most miRNA gene targets. Thus, miRNAs may provide safeguards for the precision of gene expression during development or cellular homeostasis. — BAP

Science, this issue p. 128; see also p. 41

ANTITUMOR IMMUNITY
Natural born killers for tumors

Cancer immunotherapies work by activating cytotoxic lymphocytes, usually CD8^{+} T cells, to kill tumors. But adding new approaches to the arsenal might boost these therapies. Deng *et al.* now report that natural killer (NK) cells, another type of lymphocyte, can also kill tumors (see the Perspective by Steinle and Cerwenka). Mouse tumors secrete a protein called MULT1 that binds to a protein called NKG2D on the surface of NK cells. This activates NK cells and signals them to kill the tumor cells. Treating tumor-bearing mice with soluble MULT1 caused their NK cells to reject the tumors. — KLM

Science, this issue p. 136; see also p. 45

GEOLOGY
Should we define the start of the Anthropocene?

Human activities influence environmental processes on Earth's surface to such an extent that scientist have coined the term "Anthropocene" to describe the time we live in. But when did the Anthropocene start? In a Perspective, Ruddiman *et al*. argue against trying to define a specific start date based on a "golden spike" in the geological record, such as traces from the first atomic tests in 1945. Giving this epoch such a recent start risks neglecting earlier human impacts, such as the megafauna extinctions tens of thousands of years ago and the impacts of early agriculture. — JFU

Science, this issue p. 38

EPIGENETICS
Inheritance of a covalent histone modification

Genomic DNA is the repository of all genetic information and is packaged into chromatin. Chromatin is also a repository of regulatory information in the form of covalent marks added to the histones that package the DNA. These marks can determine tissue- and organ-specific gene expression patterns, which must be transmitted to daughter cells to maintain their identity. Ragunathan *et al*. and Audergon *et al.* show that in fission yeast, a chromatin mark, like genetic information, can be inherited across many cell generations. The mark can be inherited independently of DNA sequence, DNA methylation, or RNA interference. Thus, histone marks constitute true epigenetic information. — GR

Science, this issue p. 90; see also p. 132

CANCER
Turning the tables on an inhibitor

Loss-of-function mutations are commonly detected in the tumor suppressor PTEN in various cancers. PTEN is inhibited by PREX2, a protein that promotes cell migration. Mense *et al.* found that the inhibition was reciprocal: Independently from its activity as a lipid phosphatase, PTEN suppressed the activity of PREX2. Forms of PREX2 with cancer-associated mutations were not inhibited by PTEN, reduced the lipid phosphatase activity of PTEN, and enhanced cancer cell invasion. Analysis of human tumors revealed a correlation between PREX2 mutation and high PTEN expression, suggesting that tumors select for PREX2 mutants that are not inhibited by PTEN. — WW

Sci. Signal. **8**, ra32 (2015).

INFECTIOUS DISEASE
CMV boosts immune response in the young

Cytomegalovirus (CMV) has long been thought of as a sleeper agent—present in a latent form in most people but dangerous when activated in immunosuppressed individuals. Furman *et al.* looked more closely at the effects of CMV infection in young healthy people. In contrast to older people, in whom CMV infection decreased response to flu vaccine, CMV infection actually enhanced flu vaccine responses in young adults. This beneficial effect was also seen in mice. Thus, latent CMV infection may be beneficial to the host, which may explain the prevalence of CMV infection worldwide. — ACC

Sci. Transl. Med. **7**, 281ra44 (2015).

RESEARCH ARTICLE SUMMARY

EPIGENETICS

Epigenetic inheritance uncoupled from sequence-specific recruitment

Kaushik Ragunathan, Gloria Jih, Danesh Moazed*

INTRODUCTION: Changes in histone post-translational modifications are associated with epigenetic states that define distinct patterns of gene expression. Whereas sequence-specific DNA binding proteins play essential roles in establishing an epigenetic state, their contributions to maintenance remain unclear. Previous attempts to separate the inheritance of epigenetic states from sequence-specific establishment suggest that specific DNA sequences and DNA binding proteins are continuously required for epigenetic inheritance. Moreover, in addition to DNA binding proteins, the establishment and maintenance of epigenetic states involves self-reinforcing interactions between histone modifications and RNA interference (RNAi) or DNA methylation. Therefore, whether histone-based mechanisms can transmit epigenetic memory independently of specific DNA sequences remains unknown.

RATIONALE: The fission yeast *Schizosaccharomyces pombe* contains chromosomal domains that share many features with heterochromatin in multicellular eukaryotes, such as methylation of histone H3 lysine 9 (H3K9), catalysis by the human Suv39h homolog Clr4, association with HP1 proteins (Swi6 and Chp2), and histone hypoacetylation. We developed an inducible system for heterochromatin establishment in *S. pombe* by fusion of the Clr4 methyltransferase catalytic domain to the bacterial tetracycline repressor (TetR) protein. To generate a reporter locus, we introduced 10 tetracycline operators upstream of the normally expressed *ade6+* gene (*10XtetO-ade6+*). The silencing of *ade6+* results in the formation of red or pink colonies upon growth on medium with limiting adenine concentrations. This system allowed us to determine whether heterochromatin, once established, could be maintained after tetracycline-mediated release of the TetR-Clr4 initiator (TetR-Clr4-I) from DNA.

RESULTS: Cells containing the reporter gene in combination with the expression of TetR-Clr4-I formed pink colonies on low-adenine medium lacking tetracycline, indicating *ade6+* silencing. The establishment of heterochromatin resulted in high levels of H3K9 methylation (H3K9me), which was subsequently lost upon tetracycline-induced release of TetR-Clr4-I within ~10 cell divisions, resulting in the appearance of white colonies. Whereas perturbations to pathways that altered the rate of histone exchange or eliminating competition from endogenous heterochromatic loci had subtle effects on epigenetic inheritance of *ade6+* silencing, deletion of the putative JmjC domain–containing demethylase Epe1 resulted in cells that retained *ade6+* silencing for >50 generations after tetracycline-induced release of TetR-Clr4-I or deletion of the TetR module. Furthermore, the chromodomain of Clr4, which is involved in recognition of the H3K9me mark, was indispensable for maintenance, suggesting that a direct "read-write" mechanism mediated by Clr4 propagates histone modifications and allows histones to act as carriers of epigenetic information. This mechanism allows epigenetic states to be inherited during mitosis and meiosis and is also critical for maintaining low levels of H3K9me at native pericentromeric repeats.

CONCLUSION: Our findings indicate that even in the absence of any coupling to other positive-feedback loops, or in the absence of sequence-dependent initiation signals, H3K9me defines a silent state that can be epigenetically inherited. Maintenance of the OFF state is determined by the balance between the rate of H3K9me by the Clr4 reader-writer module and the loss rate due to demethylation by an Epe1-dependent mechanism, transcription-coupled nucleosome exchange, and dilution of histones during DNA replication. The regulation of histone demethylation activity may play a broad role in determining the reversibility of epigenetic states. ∎

red colony = silent, white colony = expressed

H3K9me defines a silent state that can be epigenetically inherited. A direct read-write mechanism involving the Clr4 H3K9 methyltransferase propagates histone modifications and allows histones to act as carriers of epigenetic information in the absence of any input from the DNA sequence, DNA methylation, or RNAi. Epe1, a putative demethylase, and other transcription-associated histone turnover pathways modulate the rate of decay of the epigenetic state.

EPIGENETICS

Epigenetic inheritance uncoupled from sequence-specific recruitment

Kaushik Ragunathan, Gloria Jih, Danesh Moazed*

Changes in histone posttranslational modifications are associated with epigenetic states that define distinct patterns of gene expression. It remains unclear whether epigenetic information can be transmitted through histone modifications independently of specific DNA sequence, DNA methylation, or RNA interference. Here we show that, in the fission yeast *Schizosaccharomyces pombe*, ectopically induced domains of histone H3 lysine 9 methylation (H3K9me), a conserved marker of heterochromatin, are inherited through several mitotic and meiotic cell divisions after removal of the sequence-specific initiator. The putative JmjC domain H3K9 demethylase, Epe1, and the chromodomain of the H3K9 methyltransferase, Clr4/Suv39h, play opposing roles in maintaining silent H3K9me domains. These results demonstrate how a direct "read-write" mechanism involving Clr4 propagates histone modifications and allows histones to act as carriers of epigenetic information.

An individual cell can give rise to progeny with distinct patterns of gene expression and phenotypes without change in its DNA sequence. In eukaryotic cells, a major mechanism that gives rise to such phenotypic or epigenetic states involves changes in histone posttranslational modifications and chromatin structure (*1, 2*). The basic unit of chromatin is the nucleosome, which is composed of 147 base pairs (bp) of DNA wrapped twice around an octamer composed of histones H2A, H2B, H3, and H4 (*3*). The highly conserved basic N termini and, to a lesser extent, the globular domains of histones contain a variety of posttranslational modifications that affect nucleosome stability or provide binding sites for effectors that activate or repress transcription (*4–8*).

It has been established for nearly four decades that parental histones are retained and randomly distributed to newly synthesized daughter DNA strands during DNA replication (*9–12*). It was therefore logical to propose that combinations of histone modifications, sometimes referred to as a "histone code," are responsible for epigenetic memory of gene expression patterns (*13, 14*). However, previous attempts to separate sequence-specific establishment from maintenance have failed to provide unambiguous support for a purely histone-based inheritance mechanism in systems that display stable epigenetic expression states (*2, 15, 16*). Most notably, silencers (i.e., DNA sequences that mediate the establishment of hypoacetylated domains of silent chromatin in the budding yeast *Saccharomyces cerevisiae*) are continuously required for maintenance of the silent state (*17, 18*). Similarly, the *Drosophila* Polycomb

response element, which acts analogously to the yeast silencer, is continuously required for maintenance of domains of histone H3 lysine 27 (H3K27) methylation and reporter gene silencing (*19, 20*). The question therefore remains as to whether histones can act as carriers of epigenetic information in the absence of any input from the underlying DNA sequence.

The fission yeast *Schizosaccharomyces pombe* contains extensive domains of heterochromatin at its pericentromeric DNA repeats, subtelomeric regions, and the silent mating type loci (*21*). These domains share many features of heterochromatin in multicellular eukaryotes, such as H3K9 methylation (H3K9me), which is catalyzed by the human Suv39h homolog Clr4; association with HP1 proteins (Swi6 and Chp2); and histone hypoacetylation. Furthermore, *S. pombe* heterochromatin displays epigenetic inheritance properties in which cells containing a reporter gene inserted within heterochromatin display variegating reporter gene expression (*22*). The ON and OFF states of such reporter genes can be stably transmitted in cis through both mitotic and meiotic cell divisions (*23, 24*). However, because these observations of epigenetic inheritance were made at native sequences, contributions arising from sequence-specific elements that stabilize heterochromatin could not be ruled out (*2*). To determine whether heterochromatin maintenance can be separated from the sequences that initiate its establishment, we developed a system for inducible heterochromatin establishment in *S. pombe* by fusion of the Clr4 methyltransferase catalytic domain to the bacterial tetracycline repressor (TetR) protein. This allowed us to establish an extended heterochromatic domain and study its initiator-independent maintenance either by tetracycline-mediated release of TetR-Clr4 from DNA or after deletion of the TetR module. Our results indicate

that domains of H3K9me can be inherited for >50 generations in the absence of sequence-specific recruitment and define central roles for the putative demethylase, Epe1, in the erasure of H3K9me and the chromodomain of the Clr4 methyltransferase in its maintenance.

Inducible establishment of heterochromatin

Silent chromatin domains can be established by ectopic recruitment of histone-modifying enzymes to chromatin via fusion with heterologous DNA binding proteins (*25, 26*). To create an inducible system for heterochromatin formation, we fused a Clr4 protein lacking its N-terminal chromodomain (required for binding to methylated histone H3K9) while retaining its enzymatic methyltransferase activity to the bacterial TetR protein (designated "TetR-Clr4-I" for TetR-Clr4 initiator) (Fig. 1A). The TetR DNA binding domain facilitates protein targeting to a locus that harbors its cognate DNA binding sequence, and this recruitment activity is abrogated by the addition of tetracycline (TetR_{off} system) (*27*). We generated cells in which TetR-Clr4-I replaced the wild-type (WT) Clr4 (*TetR-clr4-I*) or in which WT Clr4 was intact and TetR-Clr4-I was inserted at another locus (*TetR-clr4-I, clr4⁺*). Comparisons between strains with or without *clr4⁺* allowed us to evaluate the contribution of the Clr4 chromodomain to establishment and/or maintenance. To generate a reporter locus, we replaced the euchromatic *ura4⁺* locus with an *ade6⁺* gene containing 10 tetracycline operators immediately upstream of the promoter (*10XtetO-ade6⁺*) (Fig. 1A). *ade6⁺* provides a convenient visual reporter, as its silencing results in formation of red or pink colonies upon growth on medium with limiting adenine concentrations (*22*).

As shown in Fig. 1B, cells containing the *10XtetO-ade6⁺* reporter in combination with the expression of the TetR-Clr4-I fusion protein, but not those containing the fusion protein alone or the reporter alone, formed pink colonies on low-adenine medium lacking tetracycline (–tet). Consistent with previous observations (*26*), silencing did not require *clr4⁺*—suggesting that the chromodomain of Clr4 was not required for de novo heterochromatin establishment (Fig. 1B)—but depended on HP1 proteins (Swi6 and Chp2) and histone deacetylases (Clr3 and Sir2), which act downstream of H3K9me (fig. S1A). Colonies grown in the absence of tetracycline were then plated on medium containing tetracycline (+tet) to determine whether the silent state could be maintained upon release of TetR-Clr4-I from DNA. Tetracycline-dependent release of TetR-Clr4-I from *tetO* sites resulted in the loss of silencing, as indicated by the formation of white colonies (Fig. 1B, +tet). Chromatin immunoprecipitation (ChIP) experiments verified that tetracycline addition resulted in release of TetR-Clr4-I from the *10XtetO* sites, as the TetR ChIP signal in the presence of tetracycline was near background levels similar to that observed for cells lacking TetR-Clr4-I (Fig. 1C). Furthermore, ChIP combined with high-throughput sequencing (ChIP-seq) and ChIP

Department of Cell Biology, Howard Hughes Medical Institute, Harvard Medical School, 240 Longwood Avenue, Boston, MA 02115, USA.
*Corresponding author: danesh@hms.harvard.edu

quantitative polymerase chain reaction (qPCR) experiments showed that a 40- to 50-kb domain of H3K9 di- and trimethylation (H3K9me2 and -me3) encompassing the *10XtetO-ade6*+ region was completely lost 24 hours (~10 cell divisions) after the addition of tetracycline to the growth medium (Fig. 1D and fig. S1, B to D). We obtained similar results with cells that carried a WT copy of *clr4*+ in addition to *TetR-clr4-I* (Fig. 1D and fig. S1D, lower two rows). These results demonstrate that a domain of H3K9me and the associated silent state are reversed within 10 cell divisions after release of the sequence-specific initiator from DNA.

Inheritance uncoupled from sequence-specific initiation

A minimal mechanistic requirement for inheritance of a domain containing H3K9me marks involves the recognition of preexisting H3K9 methylated histones coupled to the modification of newly deposited histones. The loss of a ~45-kb domain of H3K9 dimethylation after release of TetR-Clr4-I (Fig. 1D) may either be due to nucleosome exchange processes associated with transcription and chromatin remodeling or erasure of the methyl mark by a demethylase. Alternatively, the rapid decay of methylation in this domain may be facilitated by competition between the ectopic locus and native heterochromatic domains for a limiting pool of proteins that play critical roles in maintenance.

To test these different scenarios, we constructed *TetR-clr4-I, 10XtetO-ade6*+ cells (with or without *clr4*+) that carried deletions for genes involved in various chromatin-maintenance pathways (*28–30*). The deletion of *epe1*+, which encodes a putative histone H3K9 demethylase (*30*), did not affect the establishment of silencing, as indicated by the appearance of red colonies on –tet medium for both *TetR-clr4-I, epe1Δ* cells and *TetR-clr4-I, clr4*+, *epe1Δ* cells (Fig. 2A, left side). In contrast to *epe1*+ cells, *epe1Δ* cells formed red, white, and sectored colonies in the presence of tetracycline, indicating that the silent state was maintained after release of the initiator and that this phenotype was observed only in the case of cells that also contained a WT copy of *clr4*+ (Fig. 2A, right side; compare last two rows with first two rows). ChIP experiments verified that tetracycline addition promoted the release of TetR-Clr4-I from *tetO* sites (Fig. 2B). Consistent with the colony color–silencing assays, ChIP-seq and ChIP-qPCR experiments also indicated that the large domain of H3K9 di- and trimethylation surrounding the *10XtetO-ade6*+ locus was lost in *TetR-clr4-I, epe1Δ* cells but was maintained in *TetR-clr4-I, clr4*+, *epe1Δ* cells (Fig. 2C and fig. S2, A to C) 24 hours after the addition of tetracycline. Within this domain, the expression of several other transcription units was silenced on –tet medium, and this silencing was maintained for several hours after tetracycline addition (fig. S3).

Maintenance of the silent state in *epe1Δ* cells required the HP1 proteins (Swi6 and Chp2) and the Clr3 and Sir2 histone deacetylases (Fig. 3A)

but not the Dicer ribonuclease (Dcr1) or the Argonaute protein (Ago1) (Fig. 3, B and C). Thus, maintenance requires the machinery that acts downstream of H3K9me but occurs independently of an RNA interference (RNAi)–based mechanism. Consistent with the idea that Epe1 acts as a demethylase, the replacement of *epe1*+ with alleles containing active-site mutations (*epe1-K314A* and *epe1-H297A*) (*30, 31*) displayed a maintenance phenotype similar to its deletion (*epe1Δ*) (Fig. 3D). Furthermore, consistent with a requirement for the chromodomain of *clr4*+ in maintenance (Fig. 2A), the replacement of *clr4*+ with a *clr4-IΔ* allele (which lacks the chromodomain)

resulted in the formation of only white colonies on +tet medium (Fig. 3E). Therefore, rather than differences in *clr4*+ dosage, the appearance of red or sectored colonies depends on the presence of Clr4 with an intact chromodomain.

In an attempt to identify other features of chromatin that could be important for maintenance, we deleted two genes that are associated with transcription: *mst2*+, which encodes a histone acetyltransferase (*32*), and *set1*+, which encodes a histone H3K4 methyltransferase (*33*). In both cases, we observed establishment that was stronger than that of the wild type (–tet), as well as weak maintenance (+tet) effects (fig. S4, A and
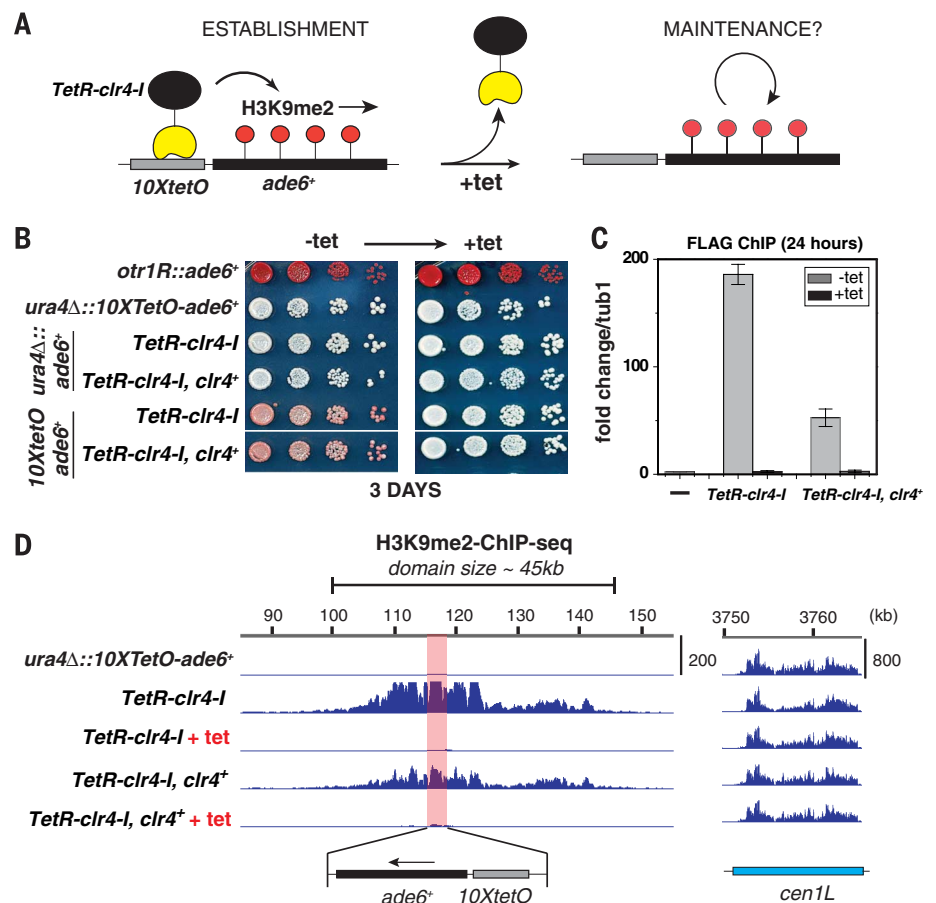
Fig. 1. Ectopic heterochromatin is lost after sequence-specific establishment upon tetracycline addition. (**A**) Diagram of experimental scheme for TetR-Clr4-I (TetR-Clr4-I)–mediated H3K9me at the *ura4Δ::10XtetO-ade6*+ locus. Tetracycline (tet) promotes the release of TetR-Clr4-I from *tetO* sites so that initiator-independent maintenance could be tested. (**B**) Test of *ade6*+ silencing on low-adenine medium in the absence (-tet) and presence (+tet) of tetracycline. Silencing of *ade6*+ results in formation of red colonies. Centromeric *ade6*+ (*otr1R::ade6*) served as a positive control; the target locus alone (*ura4Δ::10XtetO-ade6*+) and *ura4Δ::10XtetO-ade6*+) cells served as negative controls. (**C**) ChIP-qPCR experiments assess the association of FLAG-tagged TetR-Clr4-I with the *10XtetO-ade6*+ locus in the presence and absence of tetracycline. The dash on the x axis indicates background ChIP signal from cells that did not express TetR-Clr4-I. In the presence of tetracycline, TetR-Clr4-I occupancy is close to background levels. Error bars indicate SD. (**D**) ChIP-seq experiments show that TetR-Clr4-I induces a de novo H3K9me2 domain that surrounds the *tetO-ade6*+ locus (highlighted in red) for ~20 kb on either side, in cells with or without *clr4*+, which is lost 24 hours after tetracycline addition. H3K9me2 ChIP-qPCR data and H3K9me3 for samples in (D) are presented in fig. S1. Chromosome 3 (site of insertion of *10XtetO-ade6*+) and chromosome 1 [centromere 1 left (*cen1L*)] coordinates are shown above the tracks, and read numbers (per million) are indicated on the right. H3K9me2 at DNA repeats of *cen1L* serves as an internal control for the ChIP-seq data.

D). Although there were no obvious effects on colony color after 3 days of growth on tetracycline-containing medium, we observed clear persistence of H3K9me coupled with the release of TerR-Clr4-I in *mst2Δ* cells 24 hours after the addition of tetracycline (fig. S4, B and C). We then tested whether destabilizing endogenous heterochromatic regions could release factors that affect maintenance by deleting *poz1+*, a DNA binding protein required for heterochromatin formation at telomeres (*34*), or *dcr1+*, which is required for RNAi-dependent heterochromatin formation at centromeres (*35*) (fig. S5). In these mutants, effects on colony color were absent (*dcr1Δ*, fig. S5A) or subtle (*poz1Δ*, fig. S5D), but we clearly observed persistence of H3K9me 24 hours after release of TetR-Clr4-I in both deletion backgrounds (fig. S5, B, C, E, and F).

These results indicate that a domain of H3K9 methylation and its associated silent state can be maintained through mitotic cell divisions in the absence of sequence-specific initiation. The decay rate of this epigenetic state is primarily influenced by the erasure of the methyl mark by the putative demethylase Epe1 and, to a lesser extent, by pathways that promote transcription or heterochromatin assembly at endogenous loci. We note that the efficiency of maintenance does not correlate with the strength of the initial silenced state (establishment), indicating that perturbations to each pathway results in the release or recruitment of subsets of proteins that make different contributions to the establishment and/or maintenance of heterochromatin.

Because the different deletions essentially altered the rate of decay of ectopic H3K9me, we hypothesized that epigenetic maintenance at the ectopic locus might also exist in WT cells over the time scales of a few cell divisions. To observe the decay of silent chromatin with higher time resolution, we generated cells in which a green fluorescent protein (GFP) reporter was silenced by TetR-Clr4-I. We modified the endogenous *ura4+* gene to encode a Ura4-GFP fusion protein. In addition, we inserted the same *10XtetO* sites used in the earlier experiments immediately upstream of a 114-bp fragment of the *ura4+* promoter (Fig. 4A). As determined by fluorescence-activated cell sorting (FACS) analysis, *10XtetO-ura4-GFP* was silenced in a TetR-Clr4-I–dependent manner in the presence or absence of *clr4+*. To assess decay rates, we transferred cells that were grown in medium lacking tetracycline (GFP OFF cells) to medium containing tetracycline and harvested samples at 0, 3, 6, 9, 12, 15, 23, 26, 32, 36, 39, 50, 60, 77, and 100 hours for FACS analysis. FACS data for a subset of these time points are presented in Fig. 4, B to E, and the results for all time points are plotted in Fig. 4F. In general, upon tetracycline addition, the pattern of silencing of the *10XtetO-ura4-GFP* reporter in either *epe1+* or *epe1Δ* over ~2 days was consistent with the *10XtetO-ade6+* silencing results (Fig. 4, B and C). With the higher time resolution and sensitivity of detecting phenotypic expression states, we found that the OFF state persists in ~10% of the *TetR-clr4-I, clr4+, epe1+* cells for up to 40 hours (~20 cell divisions) after transfer to tetracycline-containing medium (Fig. 4, D and F), whereas cells containing *TetR-clr4-I, clr4+, epe1Δ* displayed the most stable maintenance patterns with ~60% of the cells maintaining the OFF state, even after 100 hours of growth (~50 cell divisions) in tetracycline-containing medium (Fig. 4E). These observations indicate that epigenetic maintenance was not unique to *epe1Δ* cells and that its detection was normally masked by the rapid erasure of H3K9me marks by Epe1. Although the decay rate for cells containing *TetR-clr4-I, epe1+* was rapid (<6 hours), the deletion of Epe1, even in this background, resulted in a slower decay rate (Fig. 4E). We observed the GFP OFF state in *TetR-clr4-I, epe1Δ* cells lacking *clr4+*, 6 hours after transfer to tetracycline medium with a complete shift to the ON state occurring only at ~23 hours after transfer (Fig. 4C). In these cells, upon elimination of Epe1, the decay rate is probably defined primarily by the dilution of modified histones, which may maintain epigenetic states for a few generations in the absence of Clr4-mediated reestablishment.

It may be argued that maintenance of H3K9me and the silent state in the initiator-based experiments might arise from low-affinity binding of TetR-Clr4-I to DNA in the presence of tetracycline (*27*). We sought to unequivocally rule out any role for sequence-dependent initiation in the inheritance we observed by using homologous recombination to replace *TetR-clr4-I* with *clr4-IΔ*, which harbors a deletion of the TetR DNA binding domain (Fig. 5A). After transformation to replace *TetR-clr4-I* with *clr4-IΔ* and plating on selective low-adenine medium (Fig. 5A), we obtained red, sectored, and white colonies, which were tested and confirmed for the replacement event by allele-specific PCR (fig. S6). The isolation of red *clr4-IΔ, epe1Δ* cells confirmed that the silent state could be maintained in the complete absence of sequence-dependent Clr4 recruitment to DNA. Furthermore, the plating of red *clr4-IΔ, epe1Δ* cells on low-adenine medium produced red, sectored, and white colonies (Fig. 5B), whereas plating of white *clr4-IΔ, epe1Δ* isolates produced only white colonies (Fig. 5C). In the absence of the initiator and no other means of reestablishment, the loss of the silent state was an irreversible event (Fig. 5C). Consistent with the deletion of the TetR domain, ChIP experiments showed a complete loss of the TetR occupancy signal at the *10XtetO-ade6+* locus (Fig. 5D). On the other hand, we detected high levels of H3K9 dimethylation at the *10XtetO-ade6+* locus in red but not white isolates (Fig. 5E). We conclude that, once
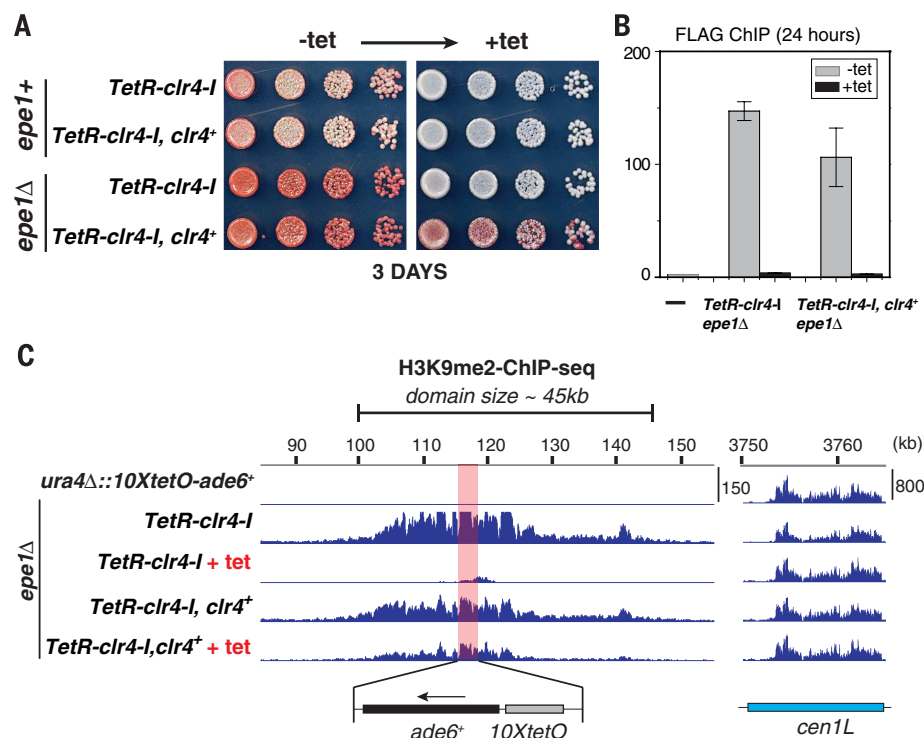
Fig. 2. Deletion of *epe1+* allows maintenance of heterochromatin after release of TetR-Clr4-I. (**A**) Color-silencing assays showing that in *TetR-clr4-I, clr4+, epe1Δ* cells, silencing is maintained on +tet medium. (**B**) ChIP experiments showing that TetR-Clr4-I is released from *tetO* sites in +tet medium. Error bars indicate SD. (**C**) ChIP-seq experiments showing that in *epe1Δ* cells, H3K9me2 is maintained 24 hours after tetracycline addition in a *clr4+*-dependent manner. H3K9me2 ChIP-qPCR and H3K9me3 ChIP-seq data for samples shown here are presented in fig. S2. Chromosome 3 (site of insertion of *10XtetO-ade6+*) and chromosome 1 (*cen1L*) coordinates are shown above the tracks, and read numbers (per million) are indicated on the right. H3K9me2 at DNA repeats of *cen1L* serves as an internal control for the ChIP-seq data.

assembled, silent chromatin and histone H3K9me at the *10XtetO-ade6+* locus can be maintained in the complete absence of the sequence-specific recruitment. To determine whether the initiator-independent silent state could also be inherited through meiosis, we crossed red haploid cells of opposite mating type, which lacked the TetR DNA binding domain (*clr4-IΔ, clr4+, epe1Δ*), to obtain diploid cells (Fig. 6A). These diploid cells were then sporulated, and after tetrad dissection, the resulting haploid progeny were plated on low-adenine medium. As shown in Fig. 6B, the resulting haploid cells formed mostly red or sectored colonies, indicating that the silent state was also inherited through meiotic cell divisions.

Inheritance of H3K9me at native heterochromatin

We next determined the extent to which epigenetic maintenance mechanisms akin to what is observed for the ectopic locus might also operate at native *S. pombe* pericentromeric repeats. Although RNAi is required for silencing of reporter genes that are inserted within pericentromeric repeat regions, deletion of RNAi components does not entirely eliminate H3K9me and silencing (*36, 37*) (Fig. 7A). Residual H3K9me in RNAi deletions might arise from either epigenetic maintenance mechanisms or weak RNAi-independent establishment signals within centromeres (*38*). To test for the presence of RNAi-independent signals that may operate at pericentromeric repeats, we determined whether H3K9me could be established de novo at the repeats in cells with deletions of RNAi factors *dcr1+* or *ago1+*. To perform this experiment, we reintroduced *clr4+* into *clr4Δ*, *clr4Δ ago1Δ*, or *clr4Δ dcr1Δ* cells (Fig. 7B) and used ChIP-seq and ChIP-qPCR to quantify H3K9 dimethylation levels. As shown in Fig. 7C, the reintroduction of *clr4+* into *clr4Δ* cells fully restored H3K9 dimethylation at the pericentromeric *dg* and *dh* repeats of chromosome 1. In contrast, *clr4+* reintroduction into *clr4Δ ago1Δ* or *clr4Δ dcr1Δ* double-mutant cells failed to promote any H3K9 dimethylation (Fig. 7, C and D). These results show that RNAi is the primary mechanism for sequence-specific establishment of pericentromeric H3K9me domains and suggest that the H3K9me observed at these repeats after deletion of RNAi components results from epigenetic maintenance.

Our ectopic heterochromatin experiments established a role for the chromodomain of Clr4 in epigenetic inheritance of H3K9me (Figs. 2 to 5). Consistent with the hypothesis that RNAi-independent H3K9me at pericentromeric repeats is maintained by epigenetic mechanisms, residual H3K9me at the centromeric *dg* repeats was abolished in *ago1Δ clr4-W31G* double-mutant cells (Fig. 7E). Clr4-W31G contains a mutation in the chromodomain that attenuates binding to H3K9me (*39*). The complete loss of H3K9me in *ago1Δ clr4-W31G* double mutant cells therefore suggests that the residual H3K9me marks are maintained by a mechanism that involves direct chromodomain-dependent recruitment of Clr4 to preexisting marks. In further support of this

hypothesis, the introduction of an additional copy of WT *clr4+*, but not the *clr4-W31G* mutant, into *ago1Δ* cells boosted the residual H3K9me levels approximately threefold (Fig. 5F). Together, these results support a direct "read-write" mechanism in which Clr4 binds to preexisting H3K9-methylated nucleosomes and catalyzes the methylation of H3K9 on newly deposited nucleosomes to maintain heterochromatin independently of the initial signals that induced methylation. It is noteworthy that, in RNAi mutant cells, deletions of *epe1+*, *mst2+*, and *poz1+* boost H3K9me levels and restore silencing to varying degrees at the pericentromeric repeats (*28–30*). Furthermore, consistent with its role in H3K9me inheritance, the chromodomain of Clr4 is also required for the RNAi-independent spreading of H3K9me at the mating type locus (*40*). Our results suggest that the epigenetic maintenance of H3K9me, rather than alternative establishment pathways, is primarily responsible for RNAi-independent silencing in these deletion backgrounds.

Discussion

Our findings on mitotic and meiotic inheritance of H3K9me and silent chromatin in the absence of sequence-specific recruitment—and without requirement for a small RNA (sRNA) positive-feedback loop associated with RNAi, or other known modification systems such as DNA CpG methylation—strongly suggest that histones modified by H3K9me can act as carriers of epigenetic information. This conclusion is supported by (i) our demonstration that deletion of the fission yeast putative histone H3K9 demethylase, *epe1+*, stabilizes the epigenetic OFF state and allows its transmission through >50 cell divisions and (ii) the requirement for the Clr4 methyltransferase chromodomain, a domain that recognizes
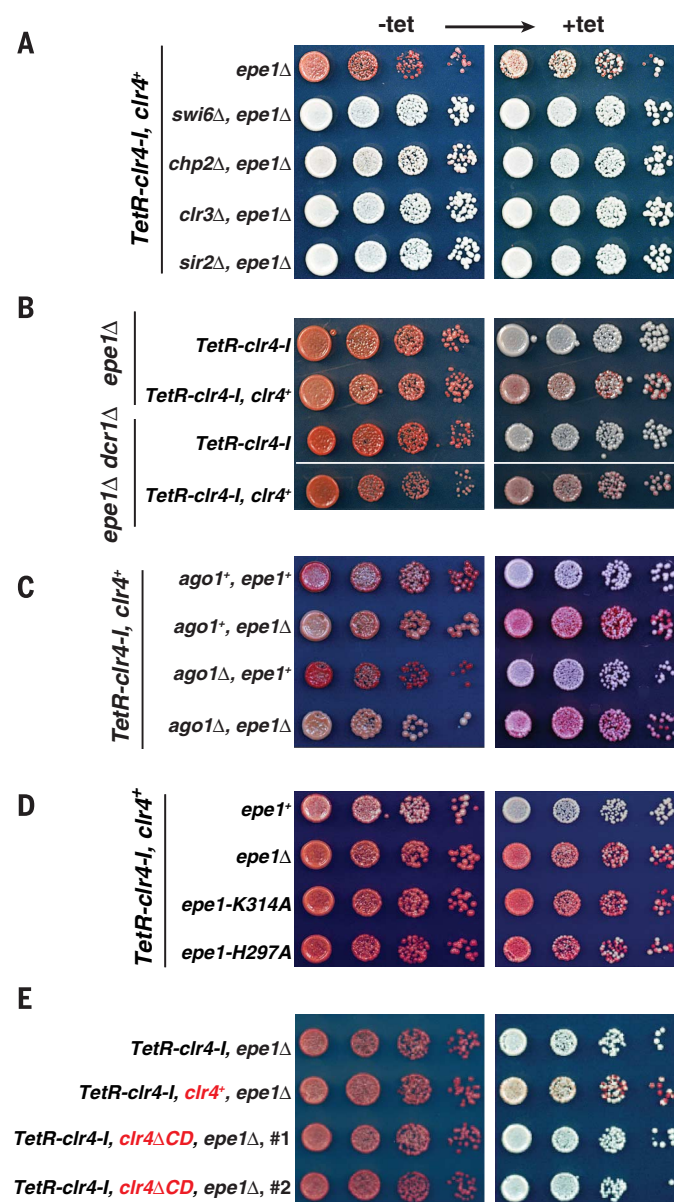
Fig. 3. Requirements for maintenance of the initiator-independent silent state. (**A**) Establishment and maintenance require HP1 proteins (Swi6 and Chp2) and histone deacetylases (Clr3 and Sir2). (**B**) Maintenance of ectopic silencing in *epe1Δ* cells does not require Dicer (Dcr1), as indicated by the growth of red *dcr1Δ* cells on +tet medium. (**C**) Maintenance of ectopic silencing in *epe1Δ* cells does not require Argonaute (Ago1), as indicated by the growth of red *ago1Δ* cells on +tet medium. (**D**) Either deleting *epe1* (*epe1Δ*) or mutations in its active site (*epe1-K314A* or *epe1-H297A*) allow maintenance of the off state after release of the TetR-Clr4-I initiator. (**E**) Replacement of *clr4+* with *clr4ΔCD*, encoding Clr4 lacking the chromodomain, abolishes initiator-independent silencing.

di- and trimethylated H3K9, suggesting a direct read-write mechanism for this mode of epigenetic inheritance.

Several recent studies have described the transgenerational inheritance of environmentally induced changes in gene expression from parent to offspring (*41*). The mechanism of this transgenerational inheritance has not been fully defined but appears to occur via both sRNA-dependent and -independent pathways. In *Caenorhabditis elegans*, plants, fission yeast, and possibly other systems, the transmission of histone modification patterns is often coupled to sRNA generation and/or CpG DNA methylation (*42–44*). The latter pathways can form positive-feedback loops that help maintain histone modification patterns (*2, 45*). This coupling of positive-feedback loops would increase the rate of reestablishment of silent domains and thus counteract the erasure activity of enzymes such as Epe1 or mechanisms that increase the rate of histone turnover.

A previous study used a small-molecule dimerization strategy to show that ectopically induced domains of H3K9me at the Oct4 locus in murine fibroblasts can be maintained after the removal of the small-molecule inducer by a mechanism that is reinforced by CpG DNA methylation (*46*). However, unlike the experiments presented here, the use of the Oct4 locus, which is normally packaged into heterochromatin in fibroblasts (*46*), precludes any conclusions about sequence-independent inheritance, as contributions from locus-specific sequence elements that normally silence Oct4 in differentiated cells cannot be ruled out. It therefore remains to be determined whether H3K9me can be inherited independently of specific DNA

sequences or modulation of H3K9 demethylase activity in mammalian cells. Also, in fission yeast, a previous study reported that ectopic heterochromatin-dependent silencing of an *ade6+* allele induced by a centromeric DNA fragment is maintained in an RNAi-dependent manner after excision of the centromeric DNA fragment (*47*), suggesting that a sRNA amplification loop may somehow be established at the *ade6+* locus, which helps to maintain the silent state. However, these findings contradict other studies, which have demonstrated that silencing of *ura4+* alleles by the generation of sRNA from a hairpin could not be maintained in the absence of the inducing hairpin (*48, 49*). Our findings indicate that even in the absence of coupling to other positive-feedback loops, or in the absence of sequence-dependent initiation signals, H3K9me defines a silent state that can be epigenetically inherited (fig. S7). Maintenance of the OFF state is probably determined by the balance between the rate of H3K9me by the Clr4 reader-writer module and the loss rate due to demethylation by an Epe1-dependent mechanism, transcription-coupled nucleosome exchange, and dilution of histones during DNA replication.

Although demethylase activity for the *S. pombe* Epe1 protein has not yet been demonstrated in vitro, key residues required for demethylase activity in other Jumonji domain proteins are conserved in Epe1 and required for its in vivo effects on silencing (*30, 50*) and its effect on initiator-independent inheritance of heterochromatin (this study, Fig. 4C). In addition, a recent study showed that the activity of human PHF2, another member of the Jumonji domain protein family, is regulated by phosphorylation (*51*),

raising the possibility that a posttranslational modification or cofactor may be required for reconstitution of Epe1 demethylase activity. Regulation of histone demethylation activity may play a broad role in determining the reversibility of epigenetic states. Although it is unknown whether Epe1 activity or levels regulate epigenetic transitions in *S. pombe*, regulation of histone demethylase activity has been implicated in control of developmental transitions in multicellular eukaryotes. In mouse embryonic stem cells, the pluripotency transcription factor Oct4 activates the expression of Jumonji domain Jmjd1a and Jmjd2c H3K9 demethylases, and this activation appears to be important for stem cell self-renewal (*52*). An attractive possibility is that as epigenetic states become established during transition from pluripotency to the differentiated state, reduction in the expression of H3K9 demethylases helps to stabilize the differentiated state (*52*). In another example, down-regulation of the amine oxidase family histone demethylase LSD1 during activation of individual olfactory receptor (OR) genes in the mammalian nose has been suggested to create an epigenetic "trap" that prevents the activation of additional OR genes (*53*). More generally, H3K9 demethylases may act as surveillance enzymes that prevent the formation of spurious H3K9 methylated domains, which may lead to epigenetic mutations and gene inactivation.

Materials and methods

Plasmids

Plasmids containing *10XtetO* binding sites upstream of *ade6+* and *ura4-GFP* reporter genes were constructed by first synthesizing a plasmid
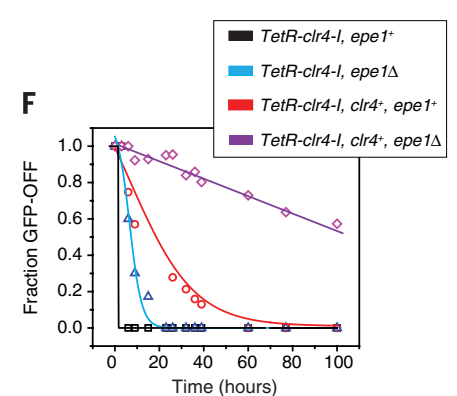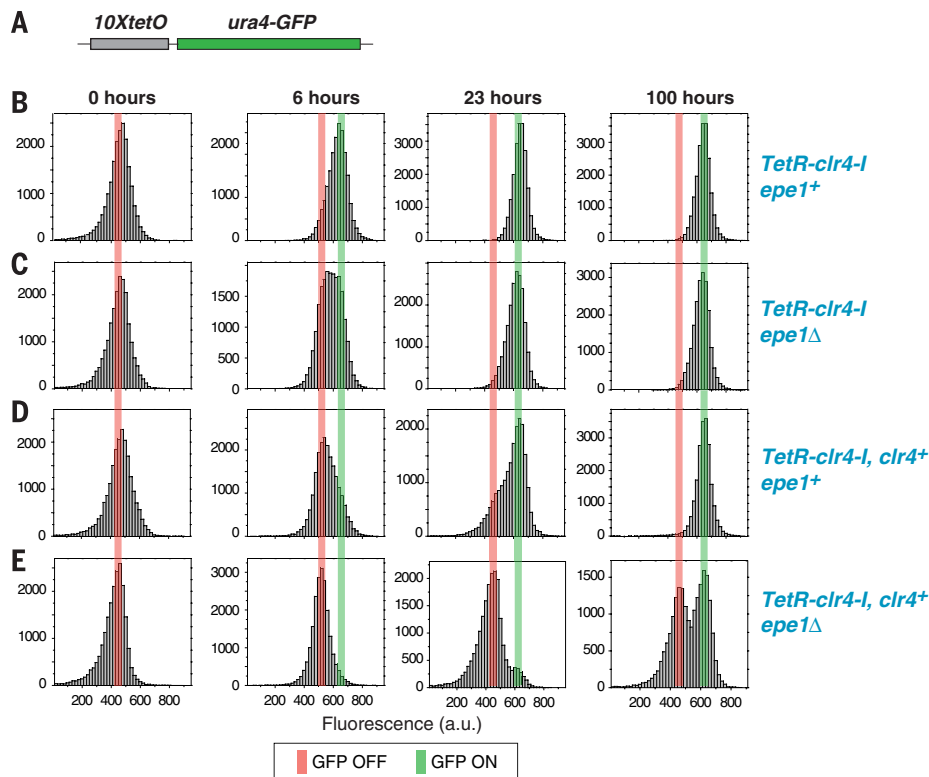
Fig. 4. Kinetics of decay of the silent state after release of TetR-Clr4-I using a GFP reporter gene reveals epigenetic maintenance in *epe1+* cells. (**A**) Schematic diagram of the *10XtetO-ura4-GFP* locus. (**B** to **E**) FACS analysis of GFP expression in the indicated strains at 0, 6, 23, and 100 hours after tetracycline addition shows the time evolution of the distribution of GFP-OFF cells. a.u., arbitrary units. (**F**) Data for time points between 0 and 100 hours after addition of tetracycline were plotted to display the fraction of GFP-OFF cells as a function of time. Dose-response curve fitting was used as a guide.

containing 10 *tetO* sites flanked by 200-bp homology sequences to facilitate reporter insertion at the *ura4* locus. The reporter genes were cloned downstream of the *tetO* binding sites using *PacI* and *AscI* restriction sites that were incorporated during the initial synthesis of the plasmid. The *ade6*+ reporter construct consists of the full-length WT *ade6*+ gene with endogenous upstream promoter and downstream terminator sequences. The *ura4-GFP* reporter consists of the full-length *ura4*+ gene fused at the C terminus with a monomeric yeast codon–optimized GFP using Gibson assembly (*54*). This construct was subsequently cloned downstream of the 10 *tetO* sites and appended with a 114-bp *ura4* promoter element and the corresponding endogenous *ura4* downstream terminator sequence. The plasmid containing *TetR-clr4-I* was constructed by modifying a pFA6a-natMX6-P*nmt1* plasmid. The promoter elements in the original plasmid were replaced with the endogenous *clr4*+ promoter (using *BglII* and *PacI* restriction sites). The TetR construct consists of an N-terminal SV40 nuclear localization sequence followed immediately by a 2X-FLAG tag. The *clr4*+ chromodomain deletion construct consists of a *clr4* allele lacking amino acids 7 to 59. The synthesis of the *TetR-clr4-I* fusion with the upstream endogenous clr4 promoter elements was achieved by Gibson assembly. The deletion of the TetR DNA binding element was achieved after modifying a pFA6a-hphMX6-P*nmt1* plasmid by insertion of the endogenous *clr4*+ promoter and a *clr4* allele lacking the chromodomain.

Strains

A strain containing the 10 *tetO* sites was first made by insertion of the reporter gene at the *ura4*+ locus. The subsequent introduction of the TetR-Clr4-I fusion protein was achieved with the use of a PCR-based gene-targeting approach (*55*). Strains with the designation TetR-Clr4-I are those in which the endogenous copy of *clr4* is replaced with the TetR-Clr4-I fusion, making it the only source of Clr4 expression in the cells. In strains where the WT copy of *clr4*+ is intact (i.e., *TetR-clr4-I,clr4*+), the fusion protein is inserted at the *trp1*+ locus. The deletions of the various RNAi and chromatin components were achieved either by PCR-based gene-targeting approaches or by a cross followed by random spore analysis and PCR-based screening to select for colonies that harbored the reporter gene, the TetR fusion protein, and the appropriate deletion. Strains containing deletions of the TetR DNA binding domain (*clr4-I∆*) were constructed by both PCR-based targeting approaches and crosses followed by random spore analysis. The resulting colonies were tested using allele specific primers. To isolate red colonies that harbor a deletion of the TetR DNA binding domain, sectored colonies, which tested positive for the deletion in the allele-specific PCR screen, were replated to isolate single red colonies on plates containing limiting adenine. All strains used in this study are listed in table S1.

Crosses were performed between red isolates of haploid cells of opposite mating type that harbored a deletion of the TetR DNA binding
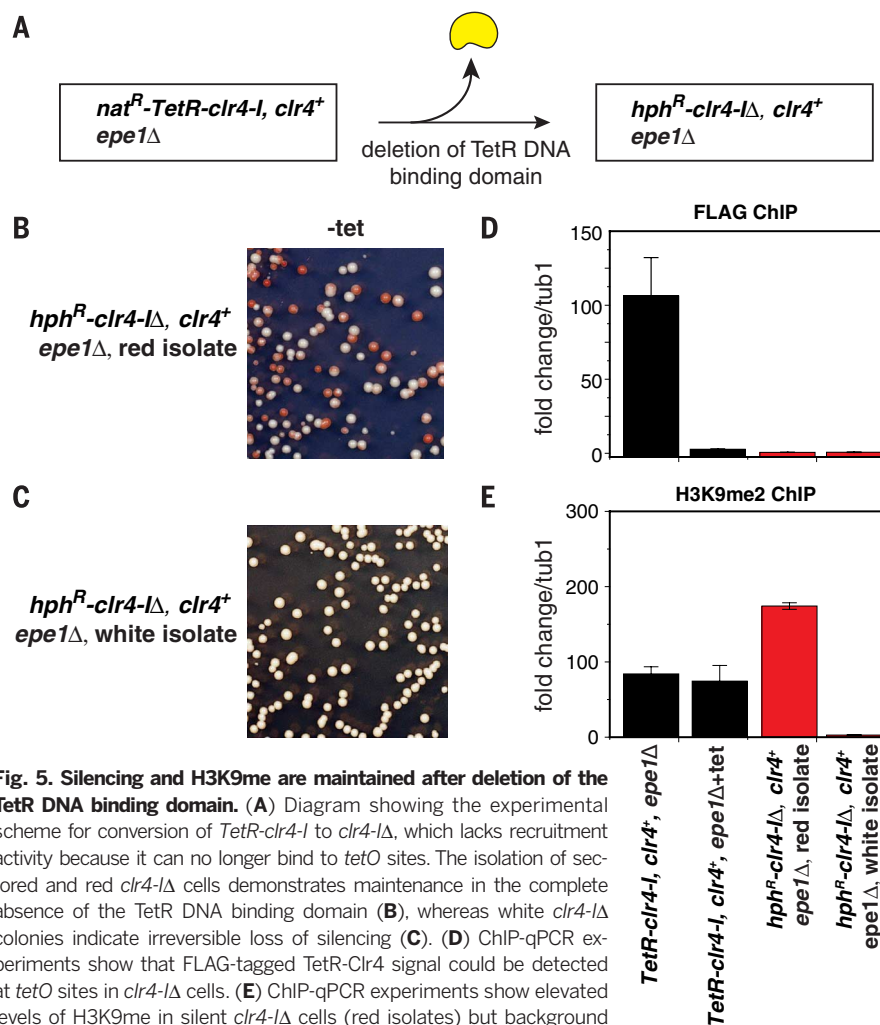
Fig. 5. Silencing and H3K9me are maintained after deletion of the TetR DNA binding domain. (**A**) Diagram showing the experimental scheme for conversion of *TetR-clr4-I* to *clr4-I∆*, which lacks recruitment activity because it can no longer bind to *tetO* sites. The isolation of sectored and red *clr4-I∆* cells demonstrates maintenance in the complete absence of the TetR DNA binding domain (**B**), whereas white *clr4-I∆* colonies indicate irreversible loss of silencing (**C**). (**D**) ChIP-qPCR experiments show that FLAG-tagged TetR-Clr4 signal could be detected at *tetO* sites in *clr4-I∆* cells. (**E**) ChIP-qPCR experiments show elevated levels of H3K9me in silent *clr4-I∆* cells (red isolates) but background levels of methylation in *ade6*+-expressing (white) *clr4-I∆* cells. Error bars in (D) and (E) represent SD.

Fig. 6. Inheritance of initiator-independent silencing through meiotic cell divisions. (**A**) Scheme for mating of silent (red) *ade6*+ haploid cells of the indicated genotypes in which the TetR-Clr4-I was deleted. After sporulation of the resulting diploid cells, tetrads were dissected, and the haploid meiotic progeny were plated on low-adenine medium (**B**). Results of four tetrad dissections are presented and show inheritance and variegation of the silent state.
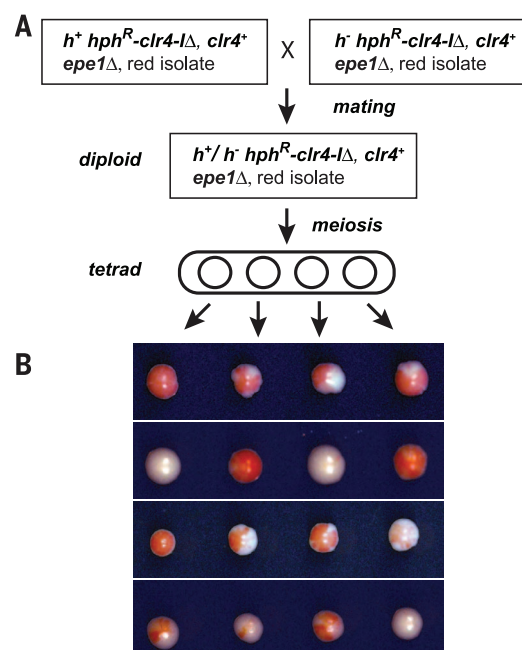
module. The resulting diploid, which lacks any sequence-specific establishment factors, was then allowed to sporulate. After tetrad dissection, spores were plated on low-adenine medium and allowed to grow at 32°C for 3 days.

Chromatin immunoprecipitation

Cells were grown to a density of 2.5×10^7 cells/ml at 32°C in yeast extract supplemented with adenine (YEA) or YEA containing tetracycline (2.5 µg/ml). Cells were cross-linked with 1% formaldehyde for 30 min at room temperature before quenching with 125 mM glycine for 5 min. The subsequent steps for sample processing were performed as previously described (56). Immunoprecipitation was performed using the following antibodies: 2.5 µl α-H3K9me2 (ab1220, Abcam) for quantifying H3K9me2 levels, 2 µg α-H3K9me3 (57) for quantifying H3K9me3 levels, and 2.5 µl α-FLAG (M2, Sigma) for quantifying TetR-Clr4-I occupancy at the ectopic locus before and after addition of tetracycline. DNA purified from the ChIP experiments was analyzed by quantitative PCR using an Applied Biosystems 7900HT Fast Real-Time PCR system. See table S2 for primer sequences. ChIP-seq libraries were constructed, sequenced using an Illumina HiSeq platform, and processed as described previously (49).

Silencing assays

Strains containing the *ade6*+ reporter construct were grown overnight, after which fivefold dilutions of each culture were spotted on plates containing only yeast extract and glucose without any additional adenine supplements with (+tet) or without (–tet) tetracycline (2.5 µg/ml). Each silencing assay also included centromeric silencing reporter strains that are unresponsive to tetracycline (*otr1R:ade6*+ and *ura4::10XtetO- ade6*+) as controls to ensure that the addition of tetracycline does not induce any changes in reporter gene expression.

FACS analysis

Cells containing *TetR-clr4-I* and *10XtetO- ura4-GFP* reporter were maintained in log phase (~2.5 × 10^7 cells/ml) through the course of sample preparation at various time points after addition of tetracycline (2.5µg/ml). Approximately 2.5×10^7 cells were harvested and fixed by addition of 70% ethanol for 20 min. The cells were then washed twice with 1X tris-buffered saline (TBS) (200 mM Tris pH 7.5, 150 mM NaCl) and resuspended in 1 ml of 1X TBS in a FACS tube (BD Falcon). GFP fluorescence was then measured using a FACScalibur instrument (Becton Dickinson), and excitation was achieved by using an argon laser emission of 488 nm. Data collection was performed using Cellquest software (Becton Dickinson), and a primary gate based on physical parameters (forward and side light scatter) was set to exclude dead cells or debris. Typically, 20,000 cells were analyzed for each sample and time point. The resulting GFP fluorescence profiles were fit using Gaussian curves (Origin 8.0), assuming a model in which cells exhibit two expression states: either GFP-ON or GFP-OFF. The fraction of cells in each state was calculated by measuring the area under the curve for each Gaussian fit.

Fig. 7. RNAi-independent H3K9me at pericentromeric repeats is epigenetically inherited. (**A**) ChIP-seq experiments showing the persistence of residual histone H3K9me2 at the pericentromeric *dg* and *dh* repeats of chromosome 1 in *ago1*Δ and *dcr1*Δ cells. Libraries were sequenced on the Illumina HiSeq2500 platform and normalized to reads per million (*y* axis). Chromosome coordinates are indicated above the plots. (**B**) Scheme for the reintroduction of *clr4*+ into *RNAi*Δ, *clr4*Δ cells to test the requirement for RNAi in H3K9me establishment. *clr4*+ was reintroduced to the native locus to avoid overexpression. (**C**) ChIP-seq experiments showing that the reintroduction of *clr4*+ into *clr4*Δ cells, but not *clr4*Δ *ago1*Δ or *clr4*Δ *dcr1*Δ cells, restores H3K9me2 at the pericentromeric repeats of chromosome 1 (left). Reads for H3K9me2 at the telomeres of chromosome 1 (*telL1*) on the right side show that, unlike the centromeres, establishment of telomeric H3K9me does not require RNAi. (**D**) ChIP-qPCR experiments verify that RNAi is required for the reestablishment of H3K9me2 at the pericentromeric *dg* repeats. (**E**) ChIP-qPCR experiments show that a mutation in the chromodomain of Clr4 (*clr4W31G*) abolishes the maintenance of H3K9me2 at *dg* repeats. (**F**) ChIP-qPCR experiments show that an additional copy of WT *clr4*+, but not *clr4W31G*, boosts residual H3K9me2 levels at *dg*. Error bars in (D) to (F) represent SD.

REFERENCES AND NOTES

1. L. Ringrose, R. Paro, Epigenetic regulation of cellular memory by the Polycomb and Trithorax group proteins. *Annu. Rev. Genet.* **38**, 413–443 (2004). doi: 10.1146/annurev.genet.38. 072902.091907; pmid: 15568982
2. D. Moazed, Mechanisms for the inheritance of chromatin states. *Cell* **146**, 510–518 (2011). doi: 10.1016/j.cell.2011.07.013; pmid: 21854979
3. K. Luger, A. W. Mäder, R. K. Richmond, D. F. Sargent, T. J. Richmond, Crystal structure of the nucleosome core

particle at 2.8 A resolution. *Nature* **389**, 251–260 (1997). doi: 10.1038/38444; pmid: 9305837

4. T. Jenuwein, C. D. Allis, Translating the histone code. *Science* **293**, 1074–1080 (2001). doi: 10.1126/science.1063127; pmid: 11498575

5. B. Li, M. Carey, J. L. Workman, The role of chromatin during transcription. *Cell* **128**, 707–719 (2007). doi: 10.1016/j.cell.2007.01.015; pmid: 17320508

6. T. Kouzarides, Chromatin modifications and their function. *Cell* **128**, 693–705 (2007). doi: 10.1016/j.cell.2007.02.005; pmid: 17320507

7. S. L. Schreiber, B. E. Bernstein, Signaling network model of chromatin. *Cell* **111**, 771–778 (2002). doi: 10.1016/S0092-8674(02)01196-0; pmid: 12526804

8. O. J. Rando, Combinatorial complexity in chromatin structure and function: Revisiting the histone code. *Curr. Opin. Genet. Dev.* **22**, 148–155 (2012). doi: 10.1016/j.gde.2012.02.013; pmid: 22440480

9. V. Jackson, R. Chalkley, Separation of newly synthesized nucleohistone by equilibrium centrifugation in cesium chloride. *Biochemistry* **13**, 3952–3956 (1974). doi: 10.1021/bi00716a021; pmid: 4370363

10. J. M. Sogo, H. Stahl, T. Koller, R. Knippers, Structure of replicating simian virus 40 minichromosomes. The replication fork, core histone segregation and terminal structures. *J. Mol. Biol.* **189**, 189–204 (1986). doi: 10.1016/0022-2836(86)90390-6; pmid: 3023620

11. M. Radman-Livaja et al., Patterns and mechanisms of ancestral histone protein inheritance in budding yeast. *PLOS Biol.* **9**, e1001075 (2011). doi: 10.1371/journal.pbio.1001075; pmid: 21666805

12. A. V. Probst, E. Dunleavy, G. Almouzni, Epigenetic inheritance during the cell cycle. *Nat. Rev. Mol. Cell Biol.* **10**, 192–206 (2009). doi: 10.1038/nrm2640; pmid: 19234478

13. B. D. Strahl, C. D. Allis, The language of covalent histone modifications. *Nature* **403**, 41–45 (2000). doi: 10.1038/47412; pmid: 10638745

14. B. M. Turner, Histone acetylation and an epigenetic code. *BioEssays* **22**, 836–845 (2000). doi: 10.1002/1521-1878(200009)22:9<836::AID-BIES9>3.0.CO;2-X; pmid: 10944586

15. M. Ptashne, On the use of the word 'epigenetic'. *Curr. Biol.* **17**, R233–R236 (2007). doi: 10.1016/j.cub.2007.02.030; pmid: 17407749

16. R. Margueron, D. Reinberg, Chromatin structure and the inheritance of epigenetic information. *Nat. Rev. Genet.* **11**, 285–296 (2010). doi: 10.1038/nrg2752; pmid: 20300089

17. T. H. Cheng, M. R. Gartenberg, Yeast heterochromatin is a dynamic structure that requires silencers continuously. *Genes Dev.* **14**, 452–463 (2000). pmid: 10691737

18. S. G. Holmes, J. R. Broach, Silencers are required for inheritance of the repressed state in yeast. *Genes Dev.* **10**, 1021–1032 (1996). doi: 10.1101/gad.10.8.1021; pmid: 8608937

19. A. K. Sengupta, A. Kuhrs, J. Müller, General transcriptional silencing by a Polycomb response element in *Drosophila*. *Development* **131**, 1959–1965 (2004). doi: 10.1242/dev.01084; pmid: 15056613

20. A. Busturia, C. D. Wightman, S. Sakonju, A silencer is required for maintenance of transcriptional repression throughout *Drosophila* development. *Development* **124**, 4343–4350 (1997). pmid: 9334282

21. M. Bühler, S. M. Gasser, Silent chromatin at the middle and ends: Lessons from yeasts. *EMBO J.* **28**, 2149–2161 (2009). doi: 10.1038/emboj.2009.185; pmid: 19629038

22. R. C. Allshire, J. P. Javerzat, N. J. Redhead, G. Cranston, Position effect variegation at fission yeast centromeres. *Cell* **76**, 157–169 (1994). doi: 10.1016/0092-8674(94)90180-5; pmid: 8287474

23. S. I. Grewal, A. J. Klar, Chromosomal inheritance of epigenetic states in fission yeast during mitosis and meiosis. *Cell* **86**, 95–101 (1996). doi: 10.1016/S0092-8674(00)80080-X; pmid: 8689692

24. J. Nakayama, A. J. Klar, S. I. Grewal, A chromodomain protein, Swi6, performs imprinting functions in fission yeast during mitosis and meiosis. *Cell* **101**, 307–317 (2000). doi: 10.1016/S0092-8674(00)80840-5; pmid: 10847685

25. C. T. Chien, S. Buck, R. Sternglanz, D. Shore, Targeting of SIR1 protein establishes transcriptional silencing at HM loci and

telomeres in yeast. *Cell* **75**, 531–541 (1993). doi: 10.1016/0092-8674(93)90387-6; pmid: 8221892

26. A. Kagansky et al., Synthetic heterochromatin bypasses RNAi and centromeric repeats to establish functional centromeres. *Science* **324**, 1716–1719 (2009). doi: 10.1126/science.1172026; pmid: 19556509

27. M. Gossen, H. Bujard, Tight control of gene expression in mammalian cells by tetracycline-responsive promoters. *Proc. Natl. Acad. Sci. U.S.A.* **89**, 5547–5551 (1992). doi: 10.1073/pnas.89.12.5547; pmid: 1319065

28. B. D. Reddy et al., Elimination of a specific histone H3K14 acetyltransferase complex bypasses the RNAi pathway to regulate pericentric heterochromatin functions. *Genes Dev.* **25**, 214–219 (2011). doi: 10.1101/gad.1993611; pmid: 21289066

29. X. Tadeo et al., Elimination of shelterin components bypasses RNAi for pericentric heterochromatin assembly. *Genes Dev.* **27**, 2489–2499 (2013). doi: 10.1101/gad.226118.113; pmid: 24240238

30. S. C. Trewick, E. Minc, R. Antonelli, T. Urano, R. C. Allshire, The JmjC domain protein Epe1 prevents unregulated assembly and disassembly of heterochromatin. *EMBO J.* **26**, 4670–4682 (2007). doi: 10.1038/sj.emboj.7601892; pmid: 17948055

31. Y. Tsukada et al., Histone demethylation by a family of JmjC domain-containing proteins. *Nature* **439**, 811–816 (2006). doi: 10.1038/nature04433; pmid: 16362057

32. E. B. Gómez, J. M. Espinosa, S. L. Forsburg, *Schizosaccharomyces pombe mst2*+ encodes a MYST family histone acetyltransferase that negatively regulates telomere silencing. *Mol. Cell. Biol.* **25**, 8887–8903 (2005). doi: 10.1128/MCB.25.20.8887-8903.2005; pmid: 16199868

33. A. Roguev et al., High conservation of the Set1/Rad6 axis of histone 3 lysine 4 methylation in budding and fission yeasts. *J. Biol. Chem.* **278**, 8487–8493 (2003). doi: 10.1074/jbc.M209562200; pmid: 12488447

34. T. Miyoshi, J. Kanoh, M. Saito, F. Ishikawa, Fission yeast Pot1-Tpp1 protects telomeres and regulates telomere length. *Science* **320**, 1341–1344 (2008). doi: 10.1126/science.1154819; pmid: 18535244

35. T. A. Volpe et al., Regulation of heterochromatic silencing and histone H3 lysine-9 methylation by RNAi. *Science* **297**, 1833–1837 (2002). doi: 10.1126/science.1074973; pmid: 12193640

36. M. Sadaie, T. Iida, T. Urano, J. Nakayama, A chromodomain protein, Chp1, is required for the establishment of heterochromatin in fission yeast. *EMBO J.* **23**, 3825–3835 (2004). doi: 10.1038/sj.emboj.7600401; pmid: 15372076

37. M. Halic, D. Moazed, Dicer-independent primal RNAs trigger RNAi and heterochromatin formation. *Cell* **140**, 504–516 (2010). doi: 10.1016/j.cell.2010.01.019; pmid: 20178743

38. F. E. Reyes-Turcu, K. Zhang, M. Zofall, E. Chen, S. I. Grewal, Defects in RNA quality control factors reveal RNAi-independent nucleation of heterochromatin. *Nat. Struct. Mol. Biol.* **18**, 1132–1138 (2011). doi: 10.1038/nsmb.2122; pmid: 21892171

39. J. Nakayama, J. C. Rice, B. D. Strahl, C. D. Allis, S. I. Grewal, Role of histone H3 lysine 9 methylation in epigenetic control of heterochromatin assembly. *Science* **292**, 110–113 (2001). doi: 10.1126/science.1060118; pmid: 11283354

40. K. Zhang, K. Mosch, W. Fischle, S. I. Grewal, Roles of the Clr4 methyltransferase complex in nucleation, spreading and maintenance of heterochromatin. *Nat. Struct. Mol. Biol.* **15**, 381–388 (2008). doi: 10.1038/nsmb.1406; pmid: 18345014

41. E. Heard, R. A. Martienssen, Transgenerational epigenetic inheritance: Myths and mechanisms. *Cell* **157**, 95–109 (2014). doi: 10.1016/j.cell.2014.02.045; pmid: 24679529

42. S. G. Gu et al., Amplification of siRNA in *Caenorhabditis elegans* generates a transgenerational sequence-targeted histone H3 lysine 9 methylation footprint. *Nat. Genet.* **44**, 157–164 (2012). doi: 10.1038/ng.1039; pmid: 22231482

43. X. Zhong et al., Molecular mechanism of action of plant DRM de novo DNA methyltransferases. *Cell* **157**, 1050–1060 (2014). doi: 10.1016/j.cell.2014.03.056; pmid: 24855943

44. M. R. Motamedi et al., Two RNAi complexes, RITS and RDRC, physically interact and localize to noncoding centromeric RNAs. *Cell* **119**, 789–802 (2004). doi: 10.1016/j.cell.2004.11.034; pmid: 15607976

45. J. A. Law, S. E. Jacobsen, Establishing, maintaining and modifying DNA methylation patterns in plants and animals.

Nat. Rev. Genet. **11**, 204–220 (2010). doi: 10.1038/nrg2719; pmid: 20142834

46. N. A. Hathaway et al., Dynamics and memory of heterochromatin in living cells. *Cell* **149**, 1447–1460 (2012). doi: 10.1016/j.cell.2012.03.052; pmid: 22704655

47. B. S. Wheeler, B. T. Ruderman, H. F. Willard, K. C. Scott, Uncoupling of genomic and epigenetic signals in the maintenance and inheritance of heterochromatin domains in fission yeast. *Genetics* **190**, 549–557 (2012). doi: 10.1534/genetics.111.137083; pmid: 22143918

48. T. Iida, J. Nakayama, D. Moazed, siRNA-mediated heterochromatin establishment requires HP1 and is associated with antisense transcription. *Mol. Cell* **31**, 178–189 (2008). doi: 10.1016/j.molcel.2008.07.003; pmid: 18657501

49. R. Yu, G. Jih, N. Iglesias, D. Moazed, Determinants of heterochromatic siRNA biogenesis and function. *Mol. Cell* **53**, 262–276 (2014). doi: 10.1016/j.molcel.2013.11.014; pmid: 24374313

50. Y. Shi, J. R. Whetstine, Dynamic regulation of histone lysine methylation by demethylases. *Mol. Cell* **25**, 1–14 (2007). doi: 10.1016/j.molcel.2006.12.010; pmid: 17218267

51. A. Baba et al., PKA-dependent regulation of the histone lysine demethylase complex PHF2-ARID5B. *Nat. Cell Biol.* **13**, 668–675 (2011). doi: 10.1038/ncb2228; pmid: 21532585

52. Y. H. Loh, W. Zhang, X. Chen, J. George, H. H. Ng, Jmjd1a and Jmjd2c histone H3 Lys 9 demethylases regulate self-renewal in embryonic stem cells. *Genes Dev.* **21**, 2545–2557 (2007). doi: 10.1101/gad.1588207; pmid: 17938240

53. D. B. Lyons et al., An epigenetic trap stabilizes singular olfactory receptor expression. *Cell* **154**, 325–336 (2013). doi: 10.1016/j.cell.2013.06.039; pmid: 23870122

54. D. G. Gibson et al., Enzymatic assembly of DNA molecules up to several hundred kilobases. *Nat. Methods* **6**, 343–345 (2009). doi: 10.1038/nmeth.1318; pmid: 19363495

55. J. Bähler et al., Heterologous modules for efficient and versatile PCR-based gene targeting in *Schizosaccharomyces pombe*. *Yeast* **14**, 943–951 (1998). doi: 10.1002/(SICI)1097-0061(199807)14:10<943::AID-YEA292>3.0.CO;2-Y; pmid: 9717240

56. E. D. Egan, C. R. Braun, S. P. Gygi, D. Moazed, Post-transcriptional regulation of meiotic genes by a nuclear RNA silencing complex. *RNA* **20**, 867–881 (2014). doi: 10.1261/rna.044479.114; pmid: 24713849

57. T. Hattori et al., Recombinant antibodies to histone post-translational modifications. *Nat. Methods* **10**, 992–995 (2013). doi: 10.1038/nmeth.2605; pmid: 23955773

COGNITIVE DEVELOPMENT

Observing the unexpected enhances infants' learning and exploration

Aimee E. Stahl* and Lisa Feigenson

Given the overwhelming quantity of information available from the environment, how do young learners know what to learn about and what to ignore? We found that 11-month-old infants (N = 110) used violations of prior expectations as special opportunities for learning. The infants were shown events that violated expectations about object behavior or events that were nearly identical but did not violate expectations. The sight of an object that violated expectations enhanced learning and promoted information-seeking behaviors; specifically, infants learned more effectively about objects that committed violations, explored those objects more, and engaged in hypothesis-testing behaviors that reflected the particular kind of violation seen. Thus, early in life, expectancy violations offer a wedge into the problem of what to learn.

Humans are capable of remarkable achievements, from learning a language to designing skyscrapers and mastering calculus. These achievements would be impossible without learning. Yet, as many theorists have noted, the problems of when learning should occur, and what should be learned at all, are highly underdetermined (1, 2). In an environment that is dynamic and complex, how can a learner know which aspects of the world to attend to and learn from, and which to ignore? Without a filter for determining when and what to learn, or a teacher to provide guidance (3), information overload can, in practice, make learning impossible.

At the same time, some aspects of the world appear to be represented even prior to learning. These cognitive primitives, sometimes collectively called "core knowledge," can be observed in newborn creatures (4, 5) and emerge across diverse rearing conditions (6) and cultures (7). But far from obviating the need for learning, core knowledge may be a foundational understanding from which learning begins. One way this could be so is if core knowledge offers a wedge into the hard problems of knowing when and what to learn. If a learner has a basic repertoire of core expectations about the world, then detecting a violation of these expectations—a conflict between what was predicted and what is observed—might signal a special opportunity for learning.

A clue that core knowledge may in fact guide early learning comes from infants' behavior in tests of preverbal cognition. Across hundreds of studies, infants respond when basic expectations are violated, including expectations generated by core knowledge (8). For example, infants look longer when a ball appears to pass through a wall than when it is stopped by the wall, suggesting a core understanding of object solidity (9), and they look longer when an object hidden in one location is revealed in a different location, suggesting a core understanding of object continuity (10). Seeing surprising events like these can trigger increases in infants' looking, as well as alterations in facial expression (11), pupil dilation (12), and changes in cerebral blood flow or brain electrical activity (13, 14). These various responses have been taken to indicate the detection of a discrepancy between what was expected and what is observed, and have been documented across many knowledge domains. Infants detect violations when, for example, a hidden object vanishes (15), when $5 + 5 = 5$ (16), and when a social entity approaches someone mean rather than someone nice (17). Responses to such surprising physical, numerical, and social events have been invaluable in efforts to characterize the roots of human cognition. Yet it remains unknown what purpose these surprise responses serve and what the cognitive consequences of experiencing an expectancy violation might be.

Here we tested the hypothesis that, early in life, violations of core expectations signal a special opportunity for learning. First we asked whether infants more effectively learn new information about objects that violate expectations than about objects that accord with expectations (experiments 1 to 3). Then we asked whether infants preferentially seek information from objects that violated expectations, and whether their exploratory actions test plausible explanations for an observed violation (experiment 4).

Infants' learning about objects that violated expectations

In experiments 1 to 3, we showed infants an event whose outcome either was expected because it accorded with core knowledge of object behavior or was surprising because it violated core knowledge, using events modeled on those in many previous studies. Then we taught infants something new about the object that had participated in the event, and finally we measured how well they learned this new information.

Three aspects of our design were crucial. First, we ensured that events that violated core knowledge differed minimally from events that accorded with core knowledge, by perceptually matching the events in all respects except for their outcomes. Second, we ensured that any observed learning enhancement was caused by experiencing a violation of core expectations, rather than by longer perceptual exposure to objects that violated expectations, by matching the duration of infants' looking across outcome types. Third, we ensured that infants were learning something genuinely new by teaching them information that could not have been known beforehand and that could not have been acquired just by seeing the objects themselves (i.e., we taught infants an object's hidden property).

In experiment 1, 11-month-old infants saw an event that either accorded with or violated object solidity or spatiotemporal continuity, two core physical principles to which young infants have consistently shown sensitivity (18–20) (N = 40; movies S1 to S4). In the solidity event (Fig. 1A), infants saw an object (a toy car for half the infants; a ball for the other half) roll down a ramp and pass behind a screen. A solid wall, partially visible above the screen, clearly blocked the object's path. Infants then saw the screen removed to reveal either that the object had been stopped by the wall, thereby according with expectations about solidity (Knowledge-Consistent outcome, n = 10), or that the object appeared to have passed through the wall, thereby violating expectations about solidity (Knowledge-Violation outcome, n = 10). In the spatiotemporal continuity event (Fig. 1B), a separate group of infants saw two screens placed on an empty stage. The experimenter hid an object (a ball for half the infants; a block for the other half) behind the left screen, then lifted both screens to reveal either that the object was still behind the left screen, thereby according with expectations about continuity (Knowledge-Consistent outcome, n = 10), or that the object was now behind the right screen, thereby violating expectations about continuity (Knowledge-Violation outcome, n = 10).

Unlike previous studies designed to measure differences in infants' looking to expected versus

Department of Psychological & Brain Sciences, Johns Hopkins University, Baltimore, MD 21218, USA.
*Corresponding author. E-mail: astahl4@jhu.edu

violation events, here we gave all infants the same limited visual exposure to the Knowledge-Consistent and Knowledge-Violation outcomes; all infants had just 10 s to encode the event outcome. A univariate analysis of variance (ANOVA), with looking time to the event outcome as the dependent variable and event type (Solidity or Continuity) and outcome type (Knowledge-Consistent or Knowledge-Violation) as fixed factors, showed no main effect of outcome type [$F(1,36) = 0.002$, $P = 0.96$] (18) (table S1), which was as predicted given the short encoding window in our design. Thus, any subsequent differences in learning cannot be attributed to longer perceptual exposure to the object in the Knowledge-Violation events.

Immediately after this 10-s exposure to the outcome of the Knowledge-Consistent or the Knowledge-Violation event, we taught all infants new information about the object in the event. The experimenter demonstrated that the object had a hidden auditory property (e.g., it squeaked) by moving it up and down while the sound played synchronously from a hidden central location for 12 s. Our dependent measure was infants' learning of this object-sound mapping. In the test trial, infants saw the target object from the preceding event and a new distractor object resting silently on the stage (baseline; 5 s). For half the infants, the ball was the target and either the car or the block was the distractor; this was reversed for the other half. Then the experimenter moved both objects up and down simultaneously while the previously taught sound (e.g., squeaking) played from a hidden central location (mapping test; 10 s). For each infant we calculated a learning score by determining the proportion of time that infants looked at the target object (relative to the new distractor object) during the baseline, then subtracting this value from the proportion of time they looked at the target object during the mapping test, when the taught sound played (table S1). If infants had successfully learned the object-sound mapping, they should increase the proportion of time they looked at the target object when the sound played;

such auditory-visual "matching" is the pattern typically observed in studies of infants' mapping abilities (21).

We found that infants' learning of the object-sound mapping depended on whether they had just seen a Knowledge-Consistent or a Knowledge-Violation event. A univariate ANOVA, with learning score as the dependent variable and event type (Solidity or Continuity) and outcome type (Knowledge-Consistent or Knowledge-Violation) as fixed factors, yielded only a significant main effect of outcome type [$F(1,36) = 10.691$, $P = 0.002$, partial $\eta^2 = 0.229$]. Infants' learning scores were significantly greater after Knowledge-Violation events than after Knowledge-Consistent events (Fig. 2A). We then compared infants' learning scores to chance (zero). Infants showed no evidence of learning after events consistent with object solidity [$t(9) = -1.088$, $P = 0.31$] or continuity [$t(9) = 1.62$, $P = 0.14$] but showed significant learning after violations to object solidity [$t(9) = 3.092$, $P = 0.01$] and spatiotemporal continuity [$t(9) = 3.715$, $P = 0.005$] (18) (Fig. 2A and table S1).

In experiment 2, we asked whether this pattern reflected actual learning or simply indicated greater attention to objects that had violated expectations. As in experiment 1, infants saw an object violate the core principle of solidity ($n = 10$) or continuity ($n = 10$) and were then taught that the object had a hidden auditory property (e.g., it squeaked). However, during the mapping test, we played an entirely novel sound (e.g., rattling). This time, infants did not increase their proportion of looking to the target object when the novel sound played after violations of either solidity [$t(9) = 1.453$, $P = 0.18$] or continuity [$t(9) = 0.036$, $P = 0.97$] (table S1). A univariate ANOVA, with learning score as the dependent variable and event type (Solidity or Continuity) and sound type (taught sound from the Knowledge-Violation condition of experiment 1 or novel sound from experiment 2) as fixed factors, yielded only a significant main effect of sound type. Infants' learning scores were significantly greater when the taught sound played in the mapping test (experiment 1) than

when the novel sound played (experiment 2) [$F(1,36) = 5.349$, $P = 0.03$, partial $\eta^2 = 0.129$] (18). This confirms that infants' performance in experiment 1 reflected successful learning of an object property, rather than heightened visual preference for an object that had violated expectations.

In experiment 3, we asked whether violations of expectation enhance learning specifically about objects that violated expectations, rather than about anything that might follow a violation. We showed infants ($n = 10$) the continuity violation from experiment 1, with an object (i.e., ball) hidden behind the left screen but revealed behind the right. After the object was revealed in the surprising location, the experimenter reached in with a new object (i.e., a block) and demonstrated that it had a hidden auditory property (e.g., it squeaked). We then measured infants' learning about this new object. As in experiment 1, we calculated learning scores by determining the proportion of time that infants looked at this new object (relative to a distractor object) during the silent baseline, then subtracting this value from the proportion of time they looked at it during the mapping test, when the taught sound played. We found that infants did not map the sound to the new object in the mapping test; their learning scores did not differ from chance [$t(9) = 0.074$, $P = 0.94$] (table S1). An independent-samples t test confirmed that this pattern differed significantly from that of experiment 1, in which infants were taught about the very object that had violated continuity [$t(18) = 2.126$, $P = 0.048$] (18). Hence, violations of expectation enhanced learning only for the object involved in the violation event, not for unrelated objects. Further, infants' failure to learn about the new object shows that the enhanced learning in experiment 1 was not due to general arousal or novelty. When taught about an object that was completely perceptually novel (because it had never been seen before) but did not violate any expectations, infants showed no evidence of learning.
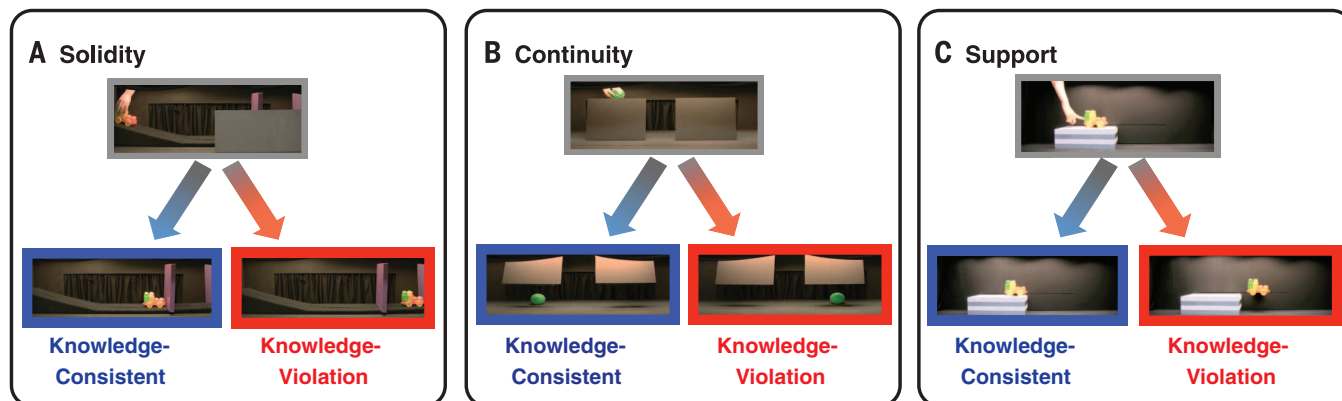
Fig. 1. Knowledge-Consistent and Knowledge-Violation outcomes in experiments 1 to 4. (A) Solidity events (movies S1 and S2). **(B)** Continuity events (movies S3 and S4). **(C)** Support events (movies S5 and S6).

Infants' exploration and hypothesis testing after violations of expectation

Our finding that violations shaped infants' learning in a targeted way, enhancing learning only about objects relevant to the observed violation, raises a further question about the nature of the new information learned. In experiments 1 to 3, the new information taught to infants was arbitrary, in the sense that it did not clearly causally relate to the surprising violations (because the sound made by an object does not offer a direct explanation for its behavior). Besides enhancing learning for such arbitrary mappings [like those acquired by nonhuman animals (22)], do violations of expectation privilege the learning of particular kinds of information that are relevant to the nature of the surprising event? When an observation conflicts with prior knowledge, an effective learning strategy would be to seek evidence that could explain the discrepancy between what was predicted and what is observed. Older children engage in this kind of hypothesis testing, performing targeted actions to support or rule out possible explanations for an event (23, 24). But it is unknown whether preverbal infants actively test hypotheses about events, especially events involving violations of core knowledge.

In experiment 4, we first asked whether infants (N = 40) preferentially seek information from an object that violated expectations over an object that did not. Infants saw an event that either accorded with or violated the principles of object solidity or (extending our inquiry to another principle) object support (18) (movies S5 and S6). The solidity events were identical to those in experiment 1 (Knowledge-Consistent outcome, n = 10; Knowledge-Violation outcome, n = 10) (Fig. 1A). In the support event (Fig. 1C), infants saw an object (e.g., car) either pushed along a surface while remaining completely supported, thereby according with expectations about support (Knowledge-Consistent outcome, n = 10), or pushed over the surface edge without falling, thereby violating expectations about support (Knowledge-Violation outcome, n = 10) (25). As before, we limited infants' visual exposure to the event outcomes; a univariate ANOVA, with looking time to the event outcome as the dependent variable and event type (Solidity or Support) and outcome type (Knowledge-Consistent or Knowledge-Violation) as fixed factors, showed no main effect of outcome type [$F(1,36)$ = 0.794, P = 0.379] (18) (table S2).

After infants saw the outcome of the solidity or support event, we gave them two objects to freely explore for 60 s: the target object from the preceding event (e.g., car) and a new distractor object (e.g., ball; for half the infants the car was the target and the ball was the distractor, and for the other half this was reversed). We calculated infants' exploration preference scores by subtracting the amount of time they explored the new distractor object from the amount of time they explored the target object (table S2). We predicted that infants who had seen a Knowledge-Consistent event would show no preference, whereas infants who had seen a Knowledge-Violation event would prefer to explore the object that had just violated their expectations. A univariate ANOVA, with infants' exploration preference score as the dependent variable and event type (Solidity or Support) and outcome type (Knowledge-Consistent or Knowledge-Violation) as fixed factors, yielded a significant main effect of outcome type [$F(1,36)$ = 5.933, P = 0.02, partial η^2 = 0.14]: Infants who had seen the Knowledge-Violation event explored the target object more than infants who had seen the Knowledge-Consistent event. We then compared infants'
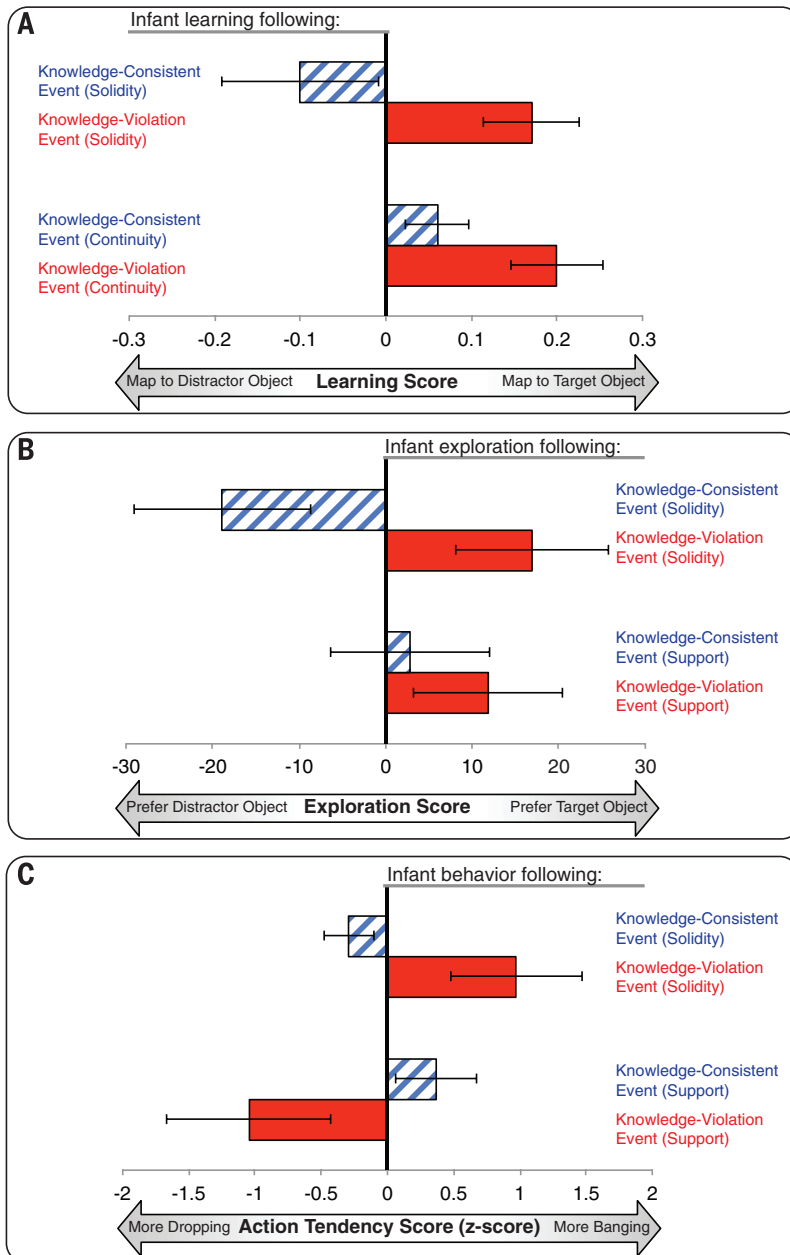
Fig. 2. Results from experiments 1 and 4. (**A**) Infants' learning after Knowledge-Consistent and Knowledge-Violation events in experiment 1. Bars represent average learning scores (proportion of looking at target object during mapping test minus proportion of looking at target object during baseline). (**B**) Infants' exploration after Knowledge-Consistent and Knowledge-Violation events in experiment 4. Bars represent looking at and/or touching the target object minus looking at and/or touching the new distractor object. (**C**) Infants' exploratory behaviors on the target object after Knowledge-Consistent and Knowledge-Violation events in experiment 4. Bars represent infants' z-scored object-banging behaviors minus z-scored object-dropping behaviors. All error bars represent SEM.

exploration preference scores to chance (zero). Collapsed across the solidity and support events, infants who had seen a Knowledge-Consistent event explored the target and distractor objects equally [$t(19) = -1.128$, $P = 0.27$], whereas infants who had seen a Knowledge-Violation event preferred to explore the target object [$t(19) = 2.395$, $P = 0.027$] (18) (Fig. 2B and table S2).

Infants who saw a violation event showed enhanced interest in the violation object, preferring to explore it over a new object. Because details of infants' exploratory behaviors might reveal an even richer interplay between knowledge and exploration, we next asked whether infants explored the target object qualitatively differently depending on which violation they had seen. We analyzed two common exploratory behaviors, each relevant to one of the presented events: banging an object (relevant to testing object solidity) and dropping an object onto the table or floor (relevant to testing object support). Because dropping an object takes longer than banging an object, we converted the frequency of these behaviors into z scores to enable direct comparison (table S2). To calculate infants' tendency to bang versus drop objects, we subtracted each infant's z-scored dropping frequency from their z-scored banging frequency. A univariate ANOVA, with action tendency score on the target object as the dependent variable and event type (Solidity or Support) and outcome type (Knowledge-Consistent or Knowledge-Violation) as fixed factors, yielded a significant interaction between event type and outcome type [$F(1,36) = 9.43$, $P = 0.004$, partial $\eta^2 = 0.208$] (Fig. 2C). An independent-samples t test revealed that infants who had seen an object appear to pass through a wall (Knowledge-Violation solidity event) banged that object more than they dropped it, relative to infants who had seen the same object stopped by the wall (Knowledge-Consistent solidity event) [$t(18) = 2.378$, $P = 0.029$]. By contrast, infants who had seen an object appear to hover in mid-air (Knowledge-Violation support event) did the reverse: They dropped the object more than they banged it, relative to infants who had seen the same object fully supported (Knowledge-Consistent support event) [$t(18) = -2.045$, $P = 0.056$] (18) (Fig. 2C and table S2). This double dissociation in infants' behavior—wherein infants who saw a solidity violation tended to actively bang the target object, whereas infants who saw a support violation tended to drop it—shows that infants tailored their exploratory actions to the type of violation seen.

The infants' banging and dropping of the new distractor object that had not participated in the solidity or support event did not differ across event types or outcomes. A univariate ANOVA, with action tendency score on the distractor object as the dependent variable and event type (Solidity or Support) and outcome type (Knowledge-Consistent or Knowledge-Violation) as fixed factors, yielded no significant interaction [$F(1,36) = 0.062$, $P = 0.80$]. Critically, a repeated-measures ANOVA that examined action tendency scores across object type (target or distractor), event type (Solidity or Support), and outcome type (Knowledge-Consistent or Knowledge-Violation) yielded a significant interaction among these three factors [$F(1,36) = 4.95$, $P = 0.032$, partial $\eta^2 = 0.12$] (18); infants performed differential actions only after Knowledge-Violation events and only on the objects that had committed the violation. This dissociation in infants' actions on just the target object reveals two senses in which infants' behaviors were highly directed: They focused on the entity that had violated expectations, and they were relevant to the nature of the observed violation. Thus, infants' behaviors are not merely reflexive responses to the novelty of surprising outcomes but instead reflect deeper attempts to learn about aspects of the world that failed to accord with expectations.

Conclusions

Our findings show that infants' learning is changed when their expectations are violated. Much as scientists faced with unexpected patterns of data are propelled to think harder, run further experiments, or change their methods of inquiry, untutored preverbal minds are sensitive to conflict between the predicted and the observed, and use this conflict as a scaffold for new learning.

In our experiments, we tested learning after violations of expectations drawn from core knowledge of object behavior—knowledge that is available from early in life, is universal across human cultures, and is present in other species. The existence of these foundational expectations has been used to argue for the presence of rich innate knowledge in infants; given our finding that violations of these expectations lead to enhanced learning, early knowledge and early learning are mutually reinforcing. In addition, expectancy violations involving other types of knowledge are also likely to be important in learning. Children form new expectations by tracking experienced contingencies (26), by receiving others' testimony (27), and by using abstract knowledge to form probabilistic predictions about events they have never observed (28). Some of these sophisticated behaviors have been interpreted in terms of Bayesian inferences that generate knowledge by weighing new evidence against prior beliefs (29, 30). Our findings accord well with such a framework and suggest avenues to explore how violations detected in different domains of prior knowledge, or using different kinds of new evidence, shape exploration and learning throughout the life span and across species.

Together, our experiments reveal that when infants see an object defy their expectations, they learn about that object better, explore that object more, and test relevant hypotheses for that object's behavior. Seen through this lens, the decades of findings that infants look longer at surprising events suggest not only that infants are equipped with core knowledge about fundamental aspects of the world but also that this knowledge is harnessed to empower new learning even in infancy. Thus, core knowledge is not an alternative to learning but is instead a key ingredient in driving learning forward.

REFERENCES AND NOTES

1. N. Chomsky, in *Language and Learning: The Debate Between Jean Piaget and Noam Chomsky*, M. Piatelli-Palmarini, Ed. (Routledge and Kegan Paul, London, 1980), pp. 393–396.
2. J. B. Tenenbaum, C. Kemp, T. L. Griffiths, N. D. Goodman, *Science* 331, 1279–1285 (2011).
3. G. Csibra, G. Gergely, *Trends Cognit. Sci.* 13, 148–153 (2009).
4. V. Izard, C. Sann, E. S. Spelke, A. Streri, *Proc. Natl. Acad. Sci. U.S.A.* 106, 10382–10385 (2009).
5. L. Regolin, G. Vallortigara, *Percept. Psychophys.* 57, 971–976 (1995).
6. C. Chiandetti, G. Vallortigara, *Anim. Cognit.* 13, 463–470 (2010).
7. S. Dehaene, V. Izard, P. Pica, E. Spelke, *Science* 311, 381–384 (2006).
8. E. S. Spelke, K. D. Kinzler, *Dev. Sci.* 10, 89–96 (2007).
9. E. S. Spelke, K. Breinlinger, J. Macomber, K. Jacobson, *Psychol. Rev.* 99, 605–632 (1992).
10. T. Wilcox, L. Nadel, R. Rosser, *Infant Behav. Dev.* 19, 309–323 (1996).
11. L. A. Camras et al., *Emotion* 2, 179–193 (2002).
12. G. Gredebäck, A. Melinder, *Cognition* 114, 197–206 (2010).
13. T. Wilcox, H. Bortfeld, R. Woods, E. Wruck, D. A. Boas, *J. Biomed. Opt.* 10, 011010–011019 (2005).
14. A. Berger, G. Tzur, M. I. Posner, *Proc. Natl. Acad. Sci. U.S.A.* 103, 12649–12653 (2006).
15. R. Baillargeon, E. S. Spelke, S. Wasserman, *Cognition* 20, 191–208 (1985).
16. K. McCrink, K. Wynn, *Psychol. Sci.* 15, 776–781 (2004).
17. V. Kuhlmeier, K. Wynn, P. Bloom, *Psychol. Sci.* 14, 402–408 (2003).
18. See supplementary materials on *Science* Online.
19. R. Baillargeon, *Cognition* 23, 21–41 (1986).
20. E. S. Spelke, R. Kestenbaum, D. Simons, D. Wein, *Br. J. Dev. Psychol.* 13, 113–142 (1995).
21. P. K. Kuhl, A. N. Meltzoff, *Infant Behav. Dev.* 7, 361–381 (1984).
22. J. M. Pearce, G. Hall, *Psychol. Rev.* 87, 532–552 (1980).
23. E. B. Bonawitz, T. J. P. van Schijndel, D. Friel, L. Schulz, *Cognit. Psychol.* 64, 215–234 (2012).
24. C. H. Legare, *Child Dev.* 83, 173–185 (2012).
25. A. Needham, R. Baillargeon, *Cognition* 47, 121–148 (1993).
26. J. R. Saffran, R. N. Aslin, E. L. Newport, *Science* 274, 1926–1928 (1996).
27. V. K. Jaswal, *Cognit. Psychol.* 61, 248–272 (2010).
28. E. Téglás et al., *Science* 332, 1054–1059 (2011).
29. J. B. Tenenbaum, T. L. Griffiths, C. Kemp, *Trends Cognit. Sci.* 10, 309–318 (2006).
30. L. Schulz, *Trends Cognit. Sci.* 16, 382–389 (2012).

RIBOSOME

The structure of the human mitochondrial ribosome

Alexey Amunts,* Alan Brown,* Jaan Toots, Sjors H. W. Scheres, V. Ramakrishnan†

The highly divergent ribosomes of human mitochondria (mitoribosomes) synthesize 13 essential proteins of oxidative phosphorylation complexes. We have determined the structure of the intact mitoribosome to 3.5 angstrom resolution by means of single-particle electron cryogenic microscopy. It reveals 80 extensively interconnected proteins, 36 of which are specific to mitochondria, and three ribosomal RNA molecules. The head domain of the small subunit, particularly the messenger (mRNA) channel, is highly remodeled. Many intersubunit bridges are specific to the mitoribosome, which adopts conformations involving ratcheting or rolling of the small subunit that are distinct from those seen in bacteria or eukaryotes. An intrinsic guanosine triphosphatase mediates a contact between the head and central protuberance. The structure provides a reference for analysis of mutations that cause severe pathologies and for future drug design.

M itoribosomes have substantially diverged from bacterial ribosomes, with which they share a common ancestor. They have a reversal in their protein-to-RNA ratio, as a result of a contraction of ribosomal RNA (rRNA) and acquisition of many additional proteins, which facilitate specific requirements of protein synthesis in mitochondria, such as synthesis of hydrophobic proteins and their co-translational delivery to the membrane (1–3). The atomic structure of the mitoribosomal large subunit (mt-LSU) is known (1–3). However, obtaining a similar high-resolution structure of the entire mitoribosome has been hindered by the conformational variability of the small subunit (mt-SSU). The mt-SSU binds messenger (mRNA), is involved in accurate initiation and decoding, and undergoes large-scale conformational changes during the elongation cycle (4). Here, we report

Medical Research Council (MRC) Laboratory of Molecular Biology, Francis Crick Avenue, Cambridge CB2 0QH, UK.
*These authors contributed equally to this work. †Corresponding author. E-mail: ramak@mrc-lmb.cam.ac.uk

the structure of the intact human mitoribosome at 3.5 Å resolution by means of electron cryogenic microscopy (cryo-EM), revealing an atomic model for the mt-SSU, the unusual dynamics of the mitoribosome, and the molecular details of mitochondria-specific bridges between the two subunits.

Structure determination

To overcome the conformational flexibility of the mt-SSU, we collected 7528 micrographs from a total of four data sets, including the data set used to solve the structure of the human mt-LSU (2). Each data set was initially processed independently, with two-dimensional (2D) and 3D classification used to remove particles that aligned poorly or corresponded to "free" mt-LSU. The resultant 884,122 particles were classified further, revealing three distinct subpopulations, each resolved to better than 5 Å resolution, in which the mt-SSU adopts different orientational states (fig. S1).

To improve the quality of the maps further to permit accurate model building, we applied

masks during refinement. Rather than use all particles, we combined the data sets that extended to 4.0 Å or better with additional views of the mitoribosome extracted from the remaining data sets, giving a total of 449,823 particles (fig. S2A). As the mitoribosome displays preferential orientation on the EM grid, the inclusion of a wider variety of views improved the angular sampling of the reconstructions (fig. S2B) and resulted in a higher overall resolution than that obtained by using all data. Refinement with masks applied over the mt-LSU, mt-SSU, and the head domain improved the resolution to 3.3, 3.5, and 3.9 Å, respectively (Fig. 1 and figs. S2 and S3). Although local resolution varies within the maps, even at the periphery the density is sufficient for de novo model building (Fig. 1).

Overall structure

The model of the human mitoribosome contains three rRNA molecules (16S mt-LSU rRNA, 12S mt-SSU rRNA, and mt-tRNA^Val) and 80 proteins, of which 36 are specific to mitochondria. Additionally, most proteins with homologs in bacteria have substantial extensions. The increased protein mass results in a ribosome with a distinct morphology (Fig. 2A), a more extensive protein-protein network of more than 200 contacts (fig. S5), and an rRNA core better shielded from reactive oxygen species.

For the mt-SSU, we are able to locate all reported constituent proteins (30, with 14 specific to mitochondria), with the exception of MRPS36, confirming the recent observation that it is not a mitoribosomal protein (table S2) (5). Additionally, mS30 is shown to be present as a single copy in the mt-LSU and renamed to mL65 (3), and two further homologs of bS18 to that observed in the mt-LSU are identified (fig. S6). For the mt-LSU, we located two additional proteins, bL31m and mL54, which were previously identified in the porcine mt-LSU (3) and further improved the model at the central protuberance and subunit interface (6).

The mt-SSU lacks homologs of uS4, uS8, uS13, uS19, and bS20. With the exception of uS4, these proteins have not been substituted by
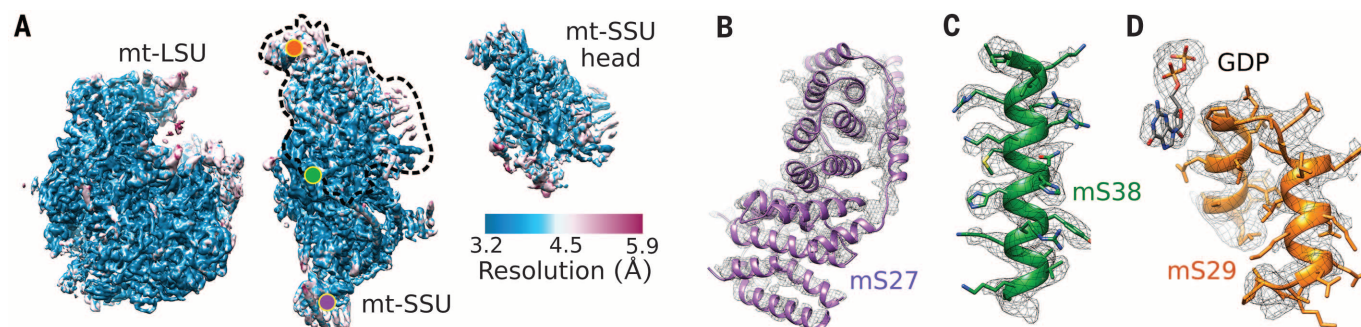
Fig. 1. Map quality. (**A**) Maps generated by using masked refinement colored by means of local resolution. The outline of the mask applied to the head is shown as a dashed line. Colored circles pinpoint the location on the mt-SSU of the density examples shown in (B) to (D). (**B**) Density for mS27 at the bottom of the mt-SSU. (**C**) Well-resolved density for mS38 in the core of the mt-SSU. (**D**) Density for mS29, including the bound GDP at the head.

mitochondria-specific elements (Fig. 2B). In bacteria, uS13 and uS19 from the head form bridges with the central protuberance and interact with the anticodon stem loop of tRNAs in the pretranslocation state (7). Alternative bridges have been formed by mitochondria-specific elements, whereas contacts with tRNA are lost. The mt-SSU is elongated as a result of mitochondria-specific proteins at both extremities (mS29 at the head and mS27 at the bottom). mS26 forms a distinctive 170 Å helix that wraps around the body.

The mt-rRNA is about half the size of the bacterial one (Fig. S7). As observed for the mt-LSU, deletion of mt-SSU rRNA segments occurs at sites that can be bridged by short (two to three nucleotides) sections of rRNA (2) (fig. S8). The remaining rRNA adopts conformations consistent with those in bacteria, except for h44. This helix is a universal element of ribosomes that forms several inter-subunit bridges as well as part of the decoding center. In bacteria, the lower part of the helix is rigid and anchored by bS20, whereas the middle part forms major intersubunit bridges (B2a, B3, B5, and B6a), and the upper part is flexible, being involved in tRNA translocation (8).

In the human mitoribosome, the conformation, coordination, and flexibility of the lower part of h44 have diverged extensively. In part, this may be a response to the loss of constraints of maintaining a bridge (B6) with mt-LSU rRNA H62, which is absent. The decreased rigidity (as observed through high B-factors) is due to loss of stabilizing interactions with bS20 and base pair rearrangements. In contrast, the movement of the upper part of h44 is likely restricted by the presence of mS38.

Conformational heterogeneity

Ribosomes are highly dynamic, with a ratchet-like rotation of the SSU correlated with mRNA-tRNA translocation. We compared the three distinct subpopulations in our sample with the classical, nonrotated bacterial ribosome (9) and with each other (table S3). The majority of human mitoribosomes (class 1, 60%) adopt an orientation that is different from the nonrotated state in bacteria. The small subunits are related by a 7.4° rotation around an axis that runs through h44 and h3 (fig. S9A). Class 2 (22%) closely resembles the fully ratcheted state observed for the bacterial ribosome (Fig. 3A) (10). It is related to class 1 by a 9.2° counterclockwise rotation (as viewed from the solvent face of the mt-SSU), with bridge B3 acting as a pivot, as seen in bacteria (11). Class 3 (12%) is related to class 1 by a rotation of 9.5° around the long axis of the mt-SSU (Fig. 3B). This conformational mode is observed in eukaryotic, but not bacterial, ribosomes during the elongation cycle and termed "subunit rolling" (12). The remaining 6% of particles aligned poorly and potentially represent a continuum of less well-populated states.

In bacterial ribosomes alongside the ratchet-like subunit rearrangement, the head domain

can swivel by a further 6° to 7° (13). We observed only slight rotational movement of the head domain of the mt-SSU rRNA (1° to 2°), which may result from additional protein elements connecting the head and body, particularly mS37 and uS5m. mS29, which forms mitochondria-specific bridges with the central protuberance of the mt-LSU, is displaced by up to 3.4 Å between the three classes in a movement independent of the rRNA head orientation (fig. S9B).

Intersubunit bridges

The two ribosomal subunits are connected by a number of intersubunit bridges, although their composition was unclear at lower resolution (14, 15). The movement of the two subunits relative to one another, and rearrangement of the bridges, is an intrinsic part of the mechanism of the ribosome. In bacteria and eukaryotes, these

bridges consist mainly of conserved RNA-RNA interactions (16). In contrast, the interface of the mitoribosome has a far greater ratio of protein-mediated contacts, with three protein-protein and six protein-RNA bridges. The effect of the extensively remodeled bridges is an mt-SSU that can sample more conformational space than the bacterial ribosome.

Intersubunit bridges B1, B1b/c, B4, B6, and B8 that are found in bacterial and cytoplasmic ribosomes are absent from human mitoribosomes (Fig. 4 and fig. S10). Based on class 1, which forms the largest interface between subunits, we define seven additional mitochondria-specific bridges (designated with the prefix "m") (Fig. 4, fig. S11, and table S4). The bridges occur along the long axis of the mt-SSU from the head to the lower body, although they are primarily centered on the central region of the

Fig. 2. Overview of the human mitoribosome. (**A**) Proteins conserved with bacteria (blue), extensions of homologous proteins (yellow), and mitochondria-specific proteins (red). rRNA is shown in gray. (**B**) Location of proteins in the human mt-SSU.
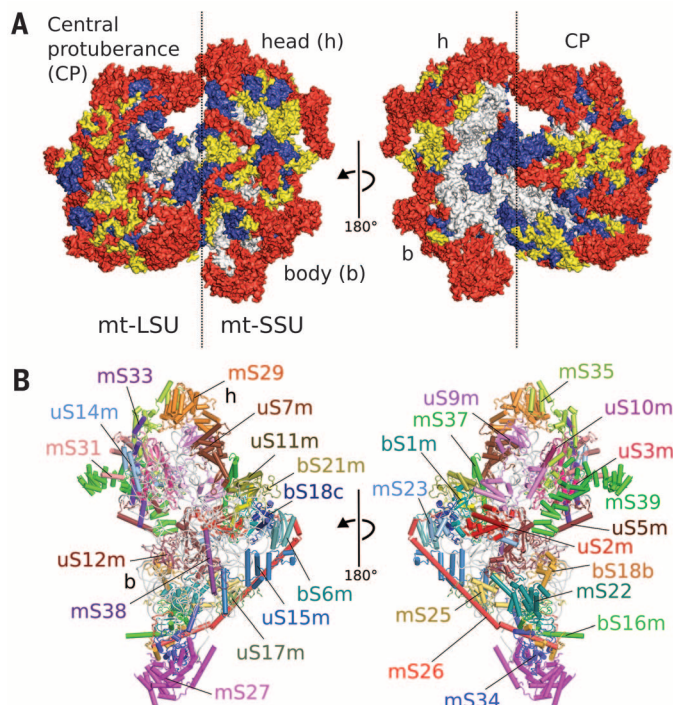
Fig. 3. Dynamics of intersubunit orientations. (**A** and **B**) Comparison of mt-SSU orientations based on common superposition of the mt-LSU. Shifts between equivalent rRNA phosphorus atoms and protein Cα atoms in the different states are color-coded (0 to 20 Å). (A) Intersubunit rotation resembling the ratchetlike mechanism common to all ribosomes. (B) Rotation of the small subunit around its long axis. (**C**) Schematic of mitoribosomal conformational changes.
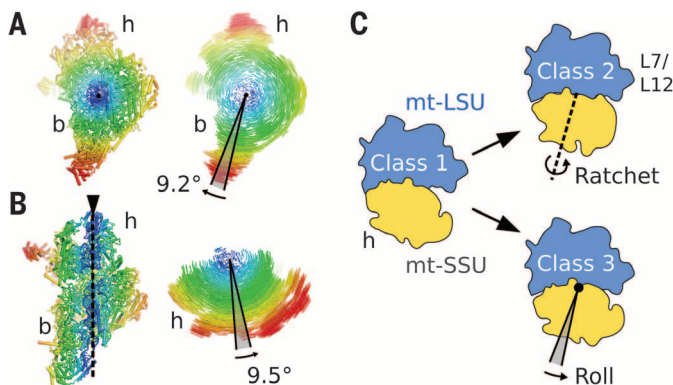
body. Bridges mB1a and mB1b at the head of the mt-SSU are analogous to bacterial bridges B1a and B1b because they mediate interactions with the central protuberance of the LSU through mitochondria-specific proteins. At the lower body, mB6 is formed between the N-terminal extension of bL19m and mS27.

Of the mitochondria-specific bridges, mB4 buries the largest surface area and is formed by an interaction between mS38 and mt-LSU rRNA H71. At the interface, a helical element of mS38 runs parallel to the upper part of h44 before a 90° kink, with the N terminus protruding into the mt-SSU rRNA (Fig. 5, A and B). Its location and structure resemble those of eL41, a short basic α-helix that forms a eukaryotic-specific bridge (eB14) in the cytoplasmic ribosome (*17*), suggesting that mS38 and eL41 are the products of convergent evolution. Although the length of eL41 and the contacts it makes with the two subunits vary among species (*18*), mS38 is substan-

tially longer, and the helix that runs parallel to the interface is specific to mitoribosomes because it fills a space generated by the absence of mt-LSU rRNA H62.

With the exception of the pivot bridge B3 that maintains nearly identical contacts in all observed classes, the other bridges form dynamic communication pathways (table S5). The bridges at the head and bottom of the mt-SSU are particularly dynamic and are therefore poorly resolved. In the ratcheted state, a new bridge (mB7) is formed between uL2m and the phosphate backbone of h23. The rolling movement preserves the upper part of h44 and therefore its bridges with the mt-LSU.

A GTPase mediates intersubunit bridges with the central protuberance

In all domains of life, guanosine triphosphatase (GTPase) factors act on the ribosome at every stage of translation. However, mitoribosomes

are the only ribosomes that have acquired an intrinsic GTPase activity through the guanosine 5′-triphosphate (GTP)–binding protein, mS29 (*19*). In mice, mS29 deficiency is lethal in utero with abnormal, shrunken mitochondria (*20*). We located mS29 to the mt-SSU head close to the subunit interface (Fig. 5, D and E), with density for a bound nucleoside diphosphate (fig. S12). mS29 is involved in coordinating two mitochondria-specific bridges (mB1a and mB1b) with elements of the remodeled central protuberance (fig. S11 and table S4). Structurally, mS29 is similar to P loop–containing nucleoside triphosphate hydrolases and possesses both Walker A and B motifs (residues 128 to 135 and 249 to 263, respectively) that are necessary for catalysis (*21*), suggesting that mS29 is catalytically active. The structure also reveals that a hydrogen bond between the carbonyl group of GTP and the main chain amide of Met100 (fig. S12B) is responsible for the specificity of the mitoribosome for guanosine over adenosine (*19*).

The presence of guanosine diphosphate (GDP) bound to mS29 at the subunit interface suggests that GTPase activity is linked to subunit association, which is compatible with the observation that although the mt-SSU readily binds GTP, the intact mitoribosome does not (*19*) because the γ-phosphate would clash with Thr313.

The mRNA channel

During translation, the mRNA occupies an RNA-rich groove that encircles the neck of the SSU (*22*). The human mitoribosome has substantial differences in both the entry and exit sites of this channel compared with other ribosomes (Fig. 6). In bacterial ribosomes, incoming mRNA passes through a ring-shaped entrance formed by uS3, uS4, and uS5 that is located between the head and shoulder of the SSU. Basic residues from uS3 and uS4 confer helicase-like activity on the ribosome that unwinds secondary structure present in the mRNA (*23*). In the human mitoribosome, the entry site has been remodeled because of the
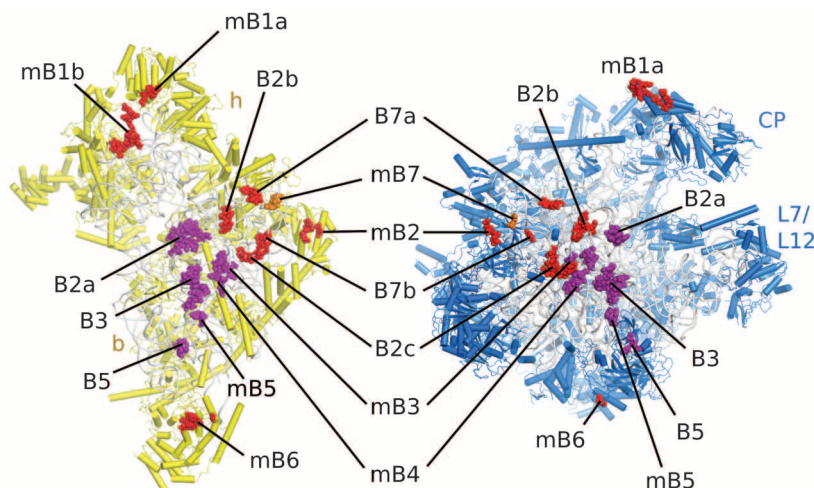
Fig. 4. Distribution of intersubunit bridges. View showing subunit interfaces. Residues that form bridges are shown as spheres. Bridges invariant in all classes are shown in purple, and dynamic bridges are in red. mB7 is specific to class 2 and shown in teal.
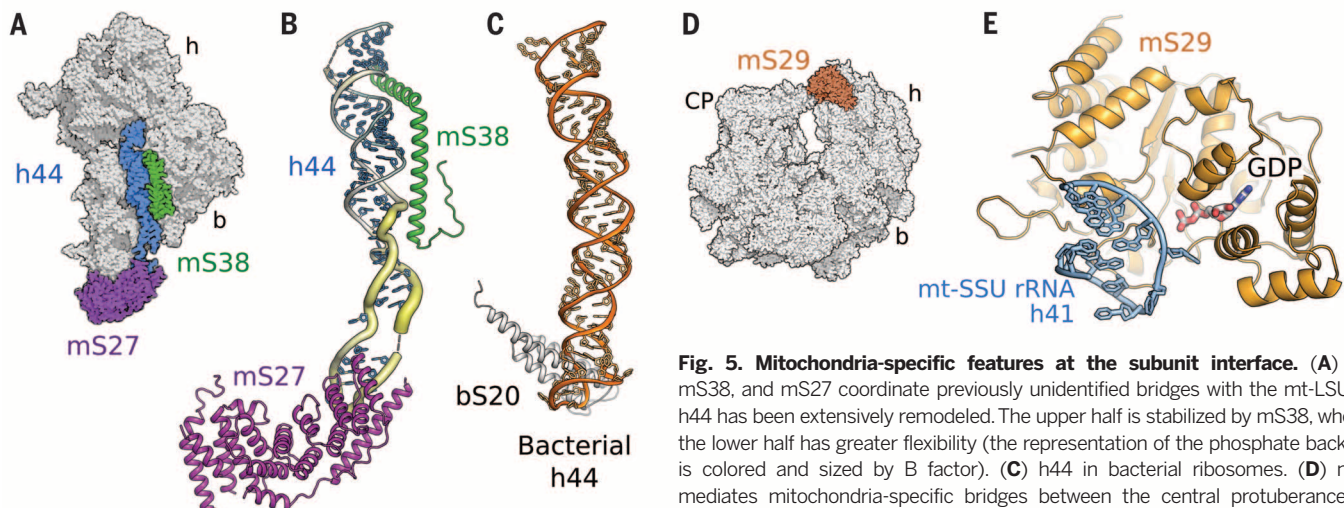
Fig. 5. Mitochondria-specific features at the subunit interface. (**A**) h44, mS38, and mS27 coordinate previously unidentified bridges with the mt-LSU. (**B**) h44 has been extensively remodeled. The upper half is stabilized by mS38, whereas the lower half has greater flexibility (the representation of the phosphate backbone is colored and sized by B factor). (**C**) h44 in bacterial ribosomes. (**D**) mS29 mediates mitochondria-specific bridges between the central protuberance and head. (**E**) In monosomes, mS29 is bound to GDP.
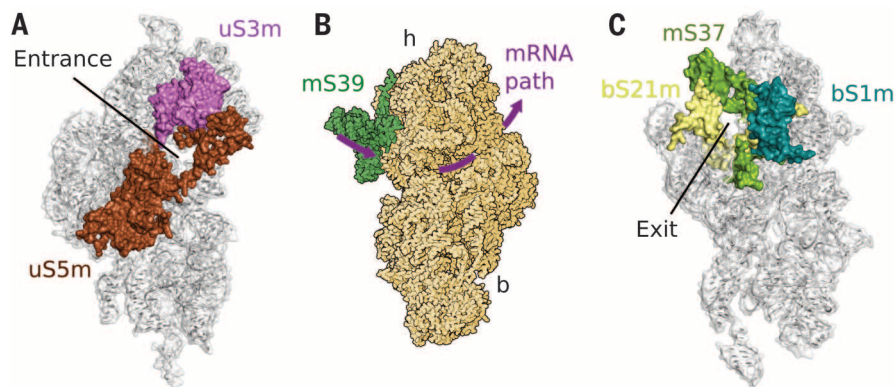
Fig. 6. Remodeling of the mRNA channel. (**A**) A wide entrance to the mRNA channel is formed by uS3m and uS5m. (**B**) Overall path taken by mRNA in the human mitoribosome, with mS39 located near the channel entrance. (**C**) mRNA emerges through an exit formed by bS1m, bS21m, and mS37.

absence of uS4 and deletion of the C-terminal domain of uS3. The new entry site is dominated by an extension to uS5m that partially compensates for the lack of uS4 and interacts with uS3m (Fig. 6A). As a result, the entrance has shifted, and its diameter expanded from 9 to 15 Å (fig. S13, A and B). The interior of the channel is lined with basic (Arg^{189}, Lys^{239}, and Arg^{264}) and aromatic (Phe^{229}) residues from uS5m, which might be involved in direct interactions with mRNA (fig. S13C).

Although the entrance has widened, the average diameter of the channel is still less than that of an RNA duplex. Therefore, mRNAs must enter as a single strand. In the proximity of the channel entrance is a pentatricopeptide repeat (PPR) protein (mS39) bound to the solvent side of the head (Fig. 6B). This is the largest protein of the mt-SSU and comprises a helix-turn-helix array stretching over 110 Å. Its knockdown results in a substantial overall decrease in mitochondrial protein synthesis (24). A conserved property of PPR proteins is the ability to bind single-stranded RNA (25), including the 5′ ends of mRNA (26). In our structure, the RNA binding motifs closest to the channel entrance are solvent-exposed and remain unoccupied.

The exit from the channel between the head and platform is important for bacterial translation initiation. In bacteria, the Shine-Dalgarno sequence base pairs with the otherwise flexible 3′ end of SSU rRNA to specify the position of the start codon (22). Human mt-mRNAs lack a Shine-Delgarno sequence and are mostly leaderless (27); therefore, the 3′ end of rRNA is not expected to be involved in initiation. Indeed, in the mitoribosome this region is deleted, and the 3′ end of rRNA is stably associated with mS37. This represents an example of convergent evolution with the eukaryotic ribosome, which also does not require a Shine-Dalgarno for initiation, in which the function of locking the 3′ end of rRNA is performed by eS26 (28).

At the channel exit, there is a protein with a single oligonucleotide-binding (OB) fold that is consistent with a low-resolution EM reconstruction (EMD-5693) and biochemical data

(29) for a homolog of the N-terminal domain of bS1 (fig. S14). Unlike bacterial bS1, bS1m is tightly associated with the ribosome through extensive interactions with uS2m and bS21m (Fig. 6B). In bacteria, bS1 is composed of six OB folds that work in a concerted manner to unfold mRNAs for active translation (30). We can exclude the possibility that bS1m forms a platform for bS1-like assembly because it lacks the essential solvent-exposed helix that forms the interaction with the following OB domain (fig. S14D) (31). However, the structural and positional conservation of bS1m with bS1 and a large electropositive patch that faces the emerging mRNA suggest a role in binding RNA (fig. S14, E and F).

Antibiotic sensitivity and effect of ribosomal mutations

Aminoglycosides are potent antibiotics for combating severe bacterial infections (32) and are also used for treatment of genetic disorders (33). Mutations in the mt-SSU rRNA gene, particularly A1555G and C1494T, have been reported to predispose carriers to aminoglycoside hypersensitivity linked to increased ototoxicity and nephrotoxicity (34). The structure reveals that these two mutations would reintroduce base pairs to limit the increased flexibility of the decoding center and resemble more closely the aminoglycoside-binding site in bacterial ribosomes (fig. S15A) (35). Because the clinical use of aminoglycosides and oxazolidinones (fig. S15B) is limited by toxicity owing to inhibition of mitoribosomes (34, 36), the structure will aid the rational design of more selective compounds. Similarly, the structure provides a reference for the analysis of mitoribosomal mutations that cause severe pathologies (table S6 and fig. S16).

REFERENCES AND NOTES

1. A. Amunts et al., Science 343, 1485–1489 (2014).
2. A. Brown et al., Science 346, 718–722 (2014).
3. B. J. Greber et al., Nature 515, 283–286 (2014).
4. W. Zhang, J. A. Dunkle, J. H. Cate, Science 325, 1014–1017 (2009).
5. M. Heublein et al., Mol. Biol. Cell 25, 3342–3349 (2014).
6. Materials and methods are available as supplementary materials on Science Online.
7. Y. Chen, S. Feng, V. Kumar, R. Ero, Y. G. Gao, Nat. Struct. Mol. Biol. 20, 1077–1084 (2013).
8. M. S. VanLoock et al., J. Mol. Biol. 304, 507–515 (2000).
9. M. Selmer et al., Science 313, 1935–1942 (2006).
10. D. S. Tourigny, I. S. Fernández, A. C. Kelley, V. Ramakrishnan, Science 340, 1235490 (2013).
11. J. A. Dunkle et al., Science 332, 981–984 (2011).
12. T. V. Budkevich et al., Cell 158, 121–131 (2014).
13. S. Mohan, J. P. Donohue, H. F. Noller, Proc. Natl. Acad. Sci. U.S.A. 111, 13325–13330 (2014).
14. M. R. Sharma et al., Cell 115, 97–108 (2003).
15. P. S. Kaushal et al., Proc. Natl. Acad. Sci. U.S.A. 111, 7284–7289 (2014).
16. J. Chen, A. Tsai, S. E. O'Leary, A. Petrov, J. D. Puglisi, Curr. Opin. Struct. Biol. 22, 804–814 (2012).
17. A. Ben-Shem et al., Science 334, 1524–1529 (2011).
18. W. Wong et al., eLife 3, 03080 (2014).
19. N. D. Denslow, J. C. Anders, T. W. O'Brien, J. Biol. Chem. 266, 9586–9590 (1991).
20. H. R. Kim et al., FASEB J. 21, 188–196 (2007).
21. J. E. Walker, M. Saraste, M. J. Runswick, N. J. Gay, EMBO J. 1, 945–951 (1982).
22. G. Z. Yusupova, M. M. Yusupov, J. H. Cate, H. F. Noller, Cell 106, 233–241 (2001).
23. S. Takyar, R. P. Hickerson, H. F. Noller, Cell 120, 49–58 (2005).
24. S. M. Davies et al., FEBS Lett. 583, 1853–1858 (2009).
25. P. Yin et al., Nature 504, 168–171 (2013).
26. N. Manavski, V. Guyon, J. Meurer, U. Wienand, R. Brettschneider, Plant Cell 24, 3087–3105 (2012).
27. J. Montoya, D. Ojala, G. Attardi, Nature 290, 465–470 (1981).
28. J. Rabl, M. Leibundgut, S. F. Ataide, A. Haag, N. Ban, Science 331, 730–736 (2011).
29. K. Byrgazov, S. Manoharadas, A. C. Kaberdina, O. Vesper I. Moll, PLOS ONE 7, e32702 (2012).
30. X. Qu, L. Lancaster, H. F. Noller, C. Bustamante, I. Tinoco Jr., Proc. Natl. Acad. Sci. U.S.A. 109, 14458–14463 (2012).
31. D. Takeshita, S. Yamashita, K. Tomita, Nucleic Acids Res. 42, 10809–10822 (2014).
32. J. A. Caminero, G. Sotgiu, A. Zumla, G. B. Migliori, Lancet Infect. Dis. 10, 621–629 (2010).
33. K. M. Keeling, D. Wang, S. E. Conard, D. M. Bedwell, Crit. Rev. Biochem. Mol. Biol. 47, 444–463 (2012).
34. E. Selimoglu, Curr. Pharm. Des. 13, 119–126 (2007).
35. Y. Qian, M. X. Guan, Antimicrob. Agents Chemother. 53, 4612–4618 (2009).
36. A. Soriano, O. Miró, J. Mensa, N. Engl. J. Med. 353, 2305–2306 (2005).

SUPPLEMENTARY MATERIALS

www.sciencemag.org/content/348/6230/95/suppl/DC1
Materials and Methods
Supplementary Text
Figs. S1 to S16
Tables S1 to S6
References (37–63)

REPORTS

MOLECULAR PHYSICS

Production of trilobite Rydberg molecule dimers with kilo-Debye permanent electric dipole moments

D. Booth,[1] S. T. Rittenhouse,[2] J. Yang,[1] H. R. Sadeghpour,[3]* J. P. Shaffer[1]

Permanent electric dipole moments are important for understanding symmetry breaking in molecular physics, control of chemical reactions, and realization of strongly correlated many-body quantum systems. However, large molecular permanent electric dipole moments are challenging to realize experimentally. We report the observation of ultralong-range Rydberg molecules with bond lengths of ~100 nanometers and kilo-Debye permanent electric dipole moments that form when an ultracold ground-state cesium (Cs) atom becomes bound within the electronic cloud of an extended Cs electronic orbit. The electronic character of this hybrid class of "trilobite" molecules is dominated by degenerate Rydberg manifolds, making them difficult to produce by conventional photoassociation. We used detailed coupled-channel calculations to reproduce their properties quantitatively. Our findings may lead to progress in ultracold chemistry and strongly correlated many-body physics.

Electric dipole moments of molecules are fundamentally important for the control of chemical reactions (*1, 2*), precision spectroscopy, realization of certain strongly correlated many-body gases (*3*), quantum information processing (*4*), and tests of fundamental symmetries (*2*). Permanent electric dipole moments (PEDMs) in molecules are a manifestation of symmetry breaking. They form in quantum states by charge separation and mixing of opposite-parity eigenstates. Homonuclear molecules are therefore not expected to possess PEDMs (*5*).

Ultralong-range rubidium (Rb) Rydberg dimers correlating to $nS + 5S$ molecular asymptotes, where n is the Rydberg atom's principal quantum number, possess sizable PEDMs (~1 Debye) and a linear Stark map (*6*). Because of the smaller noninteger component of the Cs S-state quantum defect μ_S [μ_S(Cs) = 4.05, whereas μ_S(Rb) = 3.13], Cs Rydberg molecules correlating to $nS + 6S$ asymptotes are predicted to have a PEDM as large as ~15 Debye (*6*). The quantum defect is the amount by which the principal quantum number of an atomic state is shifted—that is, $n^* = n - \mu_l$. In contrast to states with angular momentum quantum numbers $l \leq 2$ (*7–13*), which are most easily addressed by laser excitation, the original theory of ultralong-range Rydberg molecules (*14*) predicted that huge kilo-Debye PEDMs would form in the excitation of a completely l-degenerate Rydberg manifold. An ultralong-range Rydberg molecule that is a hybrid of the low and high l-type molecules would possess a giant PEDM but still be accessible via conventional two-photon laser excitation. Because of their energy level structure and ground-state electron scattering properties, Cs atoms are an ideal system for observing such a hybrid species.

We found that for Cs atoms, the peculiarly small noninteger fraction of the S-state quantum defect strongly admixes the $(n - 4)l > 2$ degenerate electronic manifold with spherically symmetric nondegenerate nS states to form ultralong-range Rydberg molecules with kilo-Debye PEDMs, which are spectroscopically accessible. The Rydberg electron probability distributions for the observed Cs($nS + 6S$) $^3\Sigma^+$ Rydberg molecules are predominantly of the "trilobite" type (Fig. 1A). Here, the label in parentheses denotes the separated atom limit and the superscripts refer to the total electronic spin (triplet) and the homonuclear molecule reflection symmetry (+) through a plane containing the internuclear axis. The fractional mixing of states with high angular momentum can be as large as 90%. This contrasts with the 0.01% admixture of hydrogenic state character that occurs in Rb(nS) Rydberg molecules as studied in (*6*). The large admixture of a nearly degenerate electronic manifold localizes the electron density on the Cs(6S) perturber (Fig. 1A). We measured the PEDM by monitoring how the molecular Rydberg lines broaden when subjected to an external electric field of strength $F \approx 30$ mV/cm (Fig. 1C). Quantitative calculations of potential energy curves (PECs) with complicated nonadiabatic avoided crossings, vibrational energy levels, and PEDMs corroborated the observations (Fig. 1B, Fig. 2A, and Fig. 3A).

Excitation into Rydberg states in a quantum gas has the potential for probing many-body effects with high precision and creating exotic states of matter. A recent observation of Rydberg electron orbital excitation to sizes comparable to or exceeding the extent of a Bose-Einstein condensate heralds possibilities for charged impurity research with extremely low mass ratios (*15*). Because of Rydberg blockade (*16*), only one Rydberg atom is excited in the condensate and single-impurity studies can be conducted. The formation of ultralong-range Rydberg molecules can be likened to localization in solids (*17*): Ultralong-range Rydberg molecules are formed through multiple scattering of electrons from perturbers, leading to the localization of the electronic wave packet. The Cs states produced in this work are precursors to states where the electron is strongly localized at the position of several ground-state atoms. Such states will have exotic properties; they can involve dipolar and spin degrees of freedom, as well as interactions between Rydberg atoms if more than one Rydberg atom is present.

The interaction between a Rydberg electron and a ground-state perturber located within the Rydberg atom can be described by a Fermi contact interaction with energy-dependent scattering lengths (*18, 19*). For Cs, there is a large p-wave spin-orbit splitting, manifested in the ^3P_J electron-cesium scattering phase shifts that must be considered. To calculate the molecular states for the Cs dimer, we diagonalized the electronic Hamiltonian that results from the electron-atom interaction for a range of internuclear distance R, using a large basis set of Rydberg electron orbital wave functions (*20*). The calculation yielded a set of Born-Oppenheimer (BO) PECs, $U(R)$, and their corresponding Rydberg electron wave functions, $\Psi(R;\mathbf{r})$. Examples of these PECs and electron density distributions calculated from the $\Psi(R;\mathbf{r})$ are shown in Fig. 1, A and B. The resulting set of coupled Schrödinger equations were solved directly to extract the vibrational states and the full spectrum of Rydberg molecular states.

The depth of the BO PECs with respect to the $nS + 6S$ molecular asymptotes shows extreme sensitivity to the value of the zero-energy s-wave scattering length. This is because the depth of the PECs with respect to the hydrogenic manifold is approximately proportional to the scattering length. Because the hydrogenic manifold lies several GHz above the Cs Rydberg S state, a 1% variation in the electron ground-state atom s-wave scattering length results in a change of ~100 MHz in the PEC depth. We used this sensitivity to adjust the value of the s-wave scattering length so that the lowest vibrational level in the outer well of the PEC correlating to $40S + 6S$ was in agreement with the experimentally observed resonance peak. The s-wave scattering length obtained was $-21.3 \pm 0.1\ a_0$, where a_0 is the Bohr radius. This value is 2% smaller than the theoretically calculated value of $-21.7 a_0$ used in (*9, 21*). The error bars are set conservatively to correspond to an energy level shift approximately equal to the spectral width of the observed vibrational states.

The p-wave electron-perturber scattering creates a set of narrow avoided crossings in the BO PECs,

[1]Homer L. Dodge Department of Physics and Astronomy, University of Oklahoma, Norman, OK 73019, USA. [2]Department of Physics and Astronomy, Western Washington University, Bellingham, WA 98225, USA. [3]ITAMP, Harvard-Smithsonian Center for Astrophysics, Cambridge, MA 02138, USA.
*Corresponding author. E-mail: hrs@cfa.harvard.edu

evident in Fig. 1B. These features correspond to metastable p-wave Cs$^-$ states (22). The PEC crossings can have a large impact on the overall behavior of the molecular PECs and the resulting vibrational states, particularly for those states lying nearby in energy. Far from the crossings, the PECs are dominated by s-wave scattering. We focus on states in the outermost PEC wells (Fig. 1B), where the p-wave scattering produces only a small energy shift and the spin-orbit splitting between the $M_J = \pm 1$ and $M_J = 0$ bound-state energies is smaller than the experimental spectral resolution of 3 MHz.

The experiment was performed in a far-off resonance trap (FORT). The crossed FORT was loaded to a peak density of 5×10^{13} cm^{-3} at a temperature of 40 μK. A two-photon excitation was used to photoassociate the molecules (Fig. 2B). The molecules were ionized using the FORT beams. The ions were detected with a microchannel plate detector. The molecular spectra were acquired by counting Cs$^+$ and Cs$_2^+$ ions arriving at the detector as a function of excitation laser frequency. No Cs$_2^+$ ions were detected.

Molecular spectra were acquired red-detuned from the $n = 37$, 39, and 40$S_{1/2}$ atomic states. Three spectral absorption lines were selected for Stark shift measurements: the excited vibrational level at ~ -277 MHz, $v = 4$, in the PEC correlating to the 37S + 6S limit, and the ground vibrational levels, $v = 0$, in the PECs correlating to the 39S + 6S and 40S + 6S limits. These states are indicated in Fig. 1B with arrows, and their ion yield spectra are shown in Fig. 2A and Fig. 3A. For the Stark shift measurements, external electric field (F_a) scans were performed on the spectral lines to determine their positions and widths. Because the electric field plates can only apply electric fields normal to the plates in our apparatus, a constant horizontal background electric field of $F_h \approx 15$ mV cm^{-1} was present for all the measurements.

At electric fields of $F_a \approx 15$ to 30 mV cm^{-1}, the Stark shift appeared as a broadening of the spectral line that increases linearly as a function of F_a (Fig. 1C) (20). The broadening increased nonlinearly at very small $F_a \approx 10$ mV cm^{-1} because of the presence of $F_h \approx 15$ mV cm^{-1}. From the

broadenings shown in Fig. 1C, we determined dipole moments for the measured molecular states. For the -277 MHz vibrational peak near the 37S + 6S asymptote, the measured electric dipole moment was $D = 2330 \pm 400$ Debye, whereas we obtained $D = 2310 \pm 250$ Debye and $D = 1910 \pm 150$ Debye for the $v = 0$ level in the outer wells shown in Fig. 1B near the 39S + 6S and 40S + 6S asymptotes, respectively. The observed PEDMs are 100 to 1000 times those measured in previous experiments (6, 9), primarily because of the greater degenerate admixture present in the states observed here. Electron density distributions for each molecular state, $|\Psi(R_e; \mathbf{r})|^2$, whose PEDM was measured are shown in Fig. 1A. In contrast to the Rb results (6), it was not necessary to subtract the Cs nS-state contributions from $\Psi(R; \mathbf{r})$ to observe the "trilobite."

The highly localized electron density shown in Fig. 1A combined with the large internuclear separation (~120 nm) yields an extremely large PEDM, $d = \langle \chi_v(R) | d(R) | \chi_v(R) \rangle$, where $d(R) = \langle \Psi(R; \mathbf{r}) | z | \Psi(R; \mathbf{r}) \rangle$ is the R-dependent dipole moment, and $| \chi_v(R) \rangle$ is the vth vibrational wave
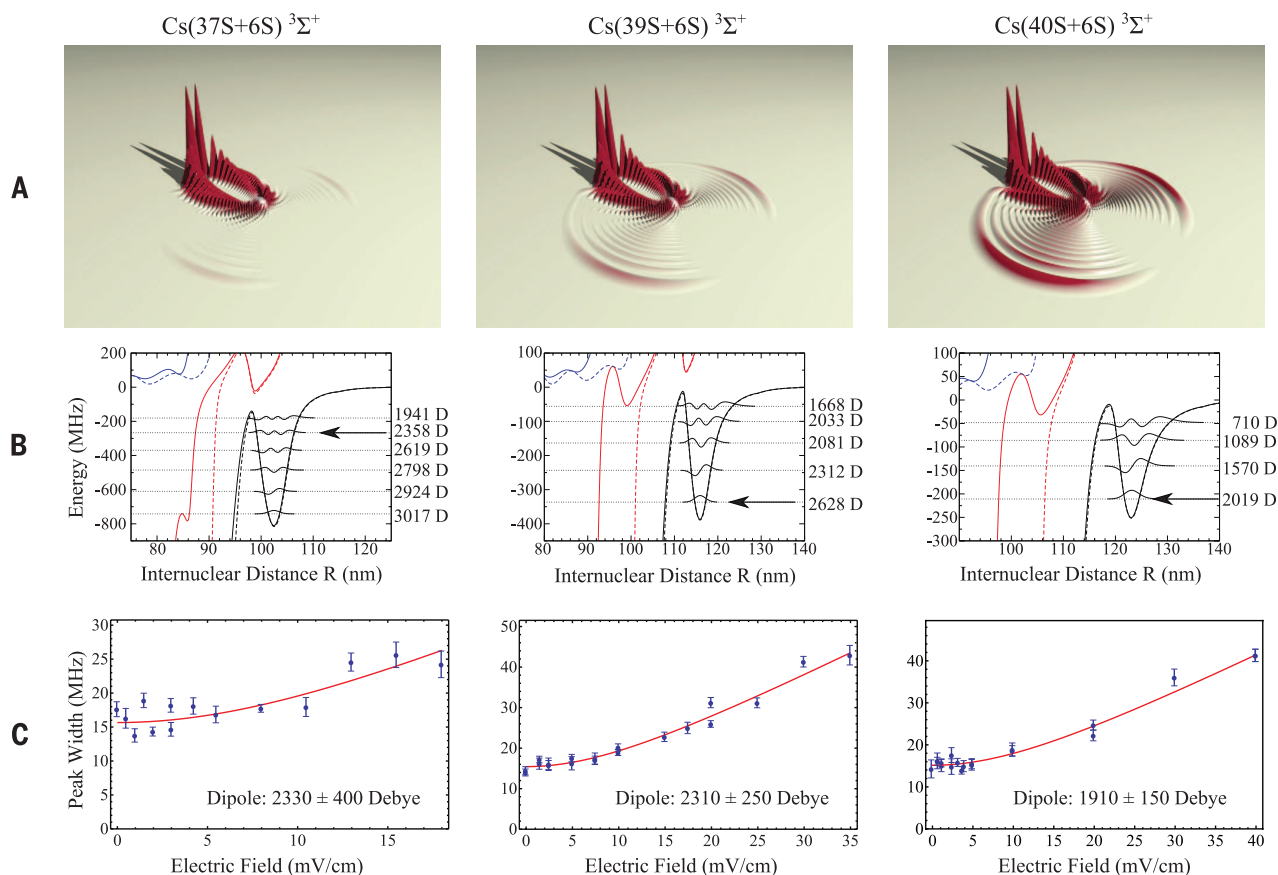
Fig. 1. Trilobite states in Cs molecules. (**A**) The electron probability distribution $|\Psi(R_e; \mathbf{r})|^2$ (Eq. 1) for the molecular states red-detuned from Cs($n = $ 37S, 39S, and 40S) Rydberg lines, each marked in (B) with an arrow, in cylindrical coordinates. The Rydberg ion is located near the center of each plot, and the Rydberg electron is localized near the location of the ground-state perturber. The distributions are shown at the equilibrium separations at $R_e = $ 102.4, 115.9, and 123.0 nm for the corresponding BO PECs, given in (B). (**B**) The BO PECs (black, red, and blue curves) correlate asymptotically to the nS + 6S, ($n - 4$)F + 6S, and ($n - 4$)G + 6S states, respectively. The dashed and solid PECs have $M_J = 0$ and $M_J = \pm 1$ projection symmetry, respectively. The vibrational wave functions in the outermost wells are indicated in black. The vibrationally averaged PEDMs are listed on the right for each value of v. (**C**) Linewidths as a function of F_a for the arrow-marked states in (B). The error bars for the PEDM are determined as the background field and two-photon laser linewidth are varied within the measurement error. The error bars on the linewidth data are the statistical error of the linewidth fit.

function. The R-dependent dipole moment $d(R)$ is almost entirely a consequence of the hybridization by the high-l degenerate Rydberg manifold. $\Psi(R;\mathbf{r})$ can be written as

$$\Psi(R;\mathbf{r}) = c_S(R)\psi_{nS}(\mathbf{r}) + c_T(R)\psi_{(n-4)T}(R;\mathbf{r}) \quad (1)$$

where the $\psi_{(n-4)T}(R;\mathbf{r})$ trilobite state is a linear combination of $l > 2$ states that maximally localizes the Rydberg electron near the ground-state perturber. Here, $c_S(R)$ and $c_T(R)$ are the probability amplitudes for finding the electron in an nS state or a trilobite state, respectively. The R-dependent dipole moment is $d(R) \approx |c_T(R)|^2 d_T(R)$, where $d_T(R) \propto (n-4)^2 R$ is the dipole moment of the bare trilobite molecule. Far from the avoided crossings, $c_S(R)$ is approximately proportional to $[E_{(n-4)l>2} - E_{nS}]/U(R)$, where E_{nl} is the atomic Rydberg energy. Therefore, the PEDM becomes monotonically smaller with increasing v as the higher-lying vibrational wave functions progressively maximize their probability amplitude at the outer turning points. The calculated PEDMs (Fig. 1B) are within 13% of the corresponding experimental values (Fig. 1C). The main source of error in the theoretical PEDMs is the uncertainty in the position of the vibrational state energy levels. For example, a shift in the binding energy of 40 MHz in $v = 0$ for Cs(37S + 6S) $^3\Sigma$ results in an 80 Debye change in the PEDM. Taking this uncertainty into account, the experimental and theoretical values agree to within one standard deviation.

Figure 2A shows a comparison between the experimental spectrum and the PEC correlating to the 37S + 6S dissociation limit, with $F_h = 15$ mV cm^{-1}. By applying the same functional form employed for fitting the Stark shifts, we calculated the theoretical spectra shown in Fig. 3A. There is sizable modulation in the peak strength between even and odd v. The modulation of the vibrational state amplitude is most clearly observed for the molecular states correlating to the 37S + 6S asymptote, as well as near the minima of each of the different PEC wells. The modulation is a consequence of odd-parity cancellation in the Franck-Condon factors, akin to the Cooper minima in atomic ionization spectra (23). The de Broglie wavelength of the Cs atoms is $\lambda_{dB}(T = 40~\mu K) \approx 35$ nm, whereas the width of the potential wells is $w \approx 5$ nm. Over this span, the ground-state wave function is effectively flat.

The observed lifetimes of each state are shown in Fig. 3B. The lifetimes are shorter than the Cs(nS) states. For example, the lifetime of the 40S state limited by radiative and blackbody decay at 300 K is 37 μs (24). The shorter lifetimes are indicative of mixing states, other than the nS states, such as $(n-4)F$ Rydberg state, which
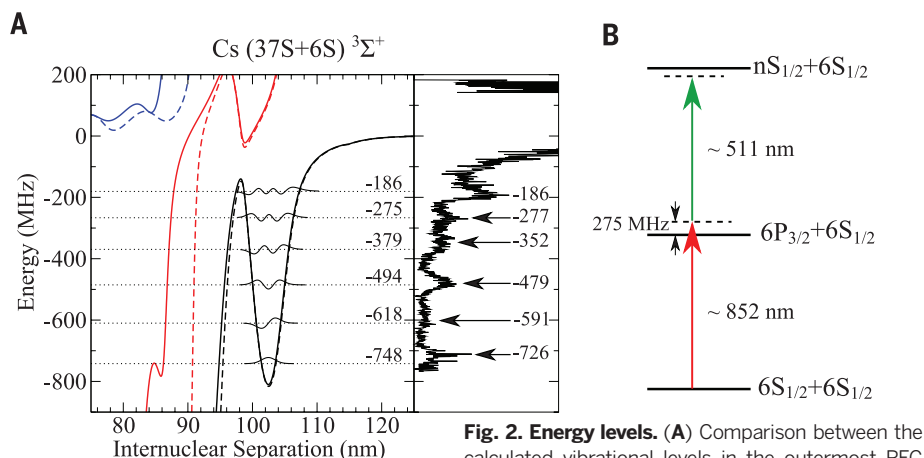
Fig. 2. Energy levels. (**A**) Comparison between the calculated vibrational levels in the outermost PEC well superposed with the associated wave functions (left) and observed spectra (right) for states correlating to the 37S + 6S limit. Even-parity ($v = 0, 2, ...$) vibrational levels have stronger signals because the de Broglie wavelength of the ground-state wave function, $\lambda_{dB} \approx 35$ nm, is much longer than the width of the outermost potential well. (**B**) Level diagram for the two-photon excitation scheme.
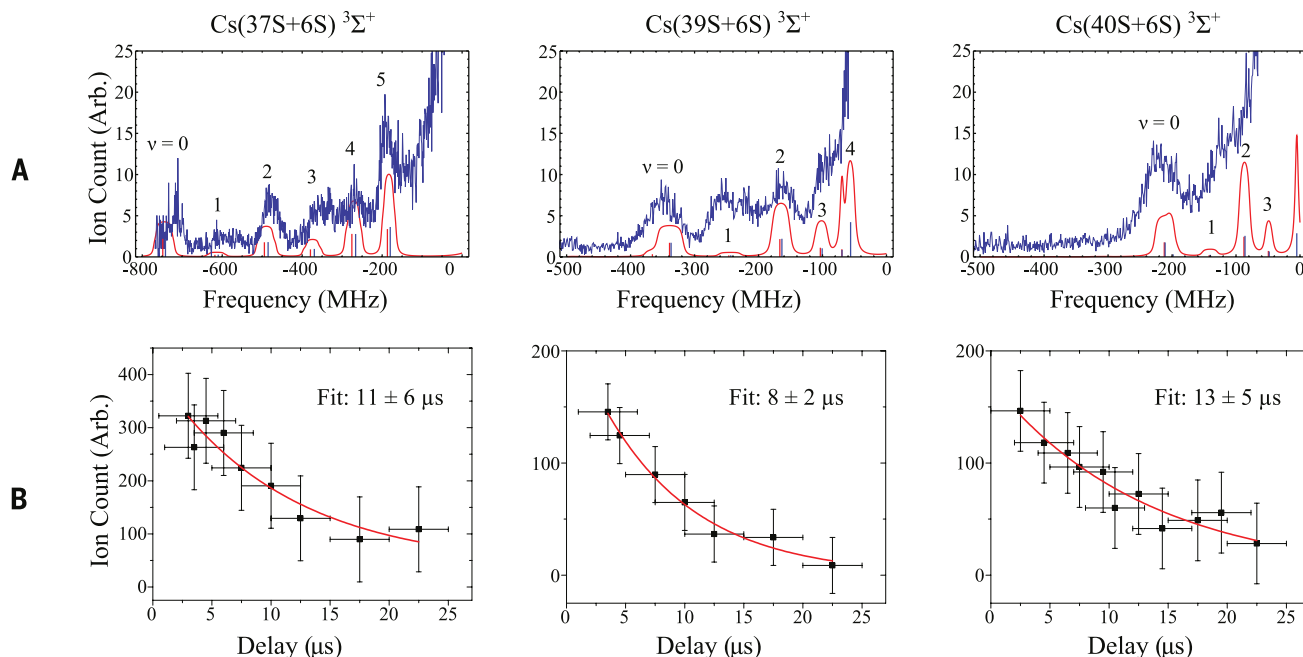
Fig. 3. Molecular spectra. (**A**) Comparison between calculated spectra (red) and experimental spectra (blue) for the states correlating to the 37S + 6S, 39S + 6S, and 40S + 6S dissociation limits. The centroids of the vibrational levels are shown as sticks underneath the calculated spectra. Bound states corresponding to the $M_J = 0$ and $M_J = \pm 1$ projections are indicated with red and blue sticks, respectively. (**B**) Ion counts for the $v = 4$ level in the PEC correlating to the 37S + 6S limit, and for the $v = 0$ level in PECs correlating to the 39S + 6S and 40S + 6S limits, as a function of the delay between excitation and ionization. The uncertainties in the delay time are due to the width of the 5-μs laser pulses used. The vertical error bars are the statistical error in the ion counts.

has a small, yet nonzero, quantum defect. The corresponding lifetime of Cs(36F) is $\tau_{36F} \approx 18$ μs (25). The fact that the decay of the molecular state is different from the purely radiative decay of the Cs(nS) Rydberg state, and closer to the nearby $(n-4)F$ state, is another indication of the degenerate mixing involved in the formation of the hybrid trilobite molecules.

The class of ultralong-range molecule observed here is an advantageous cross between a traditional "trilobite" molecule and a low-l ultralong-range Rydberg molecule (7–12). The discovery of the trilobite ultralong-range Rydberg molecule could open opportunities in ultracold chemistry and strongly correlated many-body physics, as these exotic states require engineered mesoscopic localization and kilo-Debye permanent electric dipole moments.

REFERENCES AND NOTES

1. S. Ospelkaus et al., Science 327, 853–857 (2010).
2. L. Carr, D. DeMille, R. V. Krems, J. Ye, New J. Phys. 11, 055049 (2009).
3. H. Weimer, M. Müller, I. Lesanovsky, P. Zoller, H. P. Büchler, Nat. Phys. 6, 382–388 (2010).
4. M. D. Lukin et al., Phys. Rev. Lett. 87, 037901 (2001).
5. W. Klemperer, K. K. Lehmann, J. K. G. Watson, S. C. Wofsy, J. Phys. Chem. 97, 2413–2416 (1993).
6. W. Li et al., Science 334, 1110 (2011).
7. C. H. Greene, E. L. Hamilton, H. Crowell, C. Vadla, K. Niemax, Phys. Rev. Lett. 97, 233002 (2006).
8. V. Bendkowsky et al., Nature 458, 1005–1008 (2009).
9. J. Tallant, S. T. Rittenhouse, D. Booth, H. R. Sadeghpour, J. P. Shaffer, Phys. Rev. Lett. 109, 173202 (2012).
10. M. A. Bellos et al., Phys. Rev. Lett. 111, 053001 (2013).
11. A. T. Krupp et al., Phys. Rev. Lett. 112, 143008 (2014).
12. D. A. Anderson, S. A. Miller, G. Raithel, Phys. Rev. Lett. 112, 163201 (2014).
13. H. Saßmannshausen, F. Merkt, J. Deiglmayr, http://arxiv.org/abs/1412.0846 (2014).
14. C. H. Greene, A. S. Dickinson, H. R. Sadeghpour, Phys. Rev. Lett. 85, 2458–2461 (2000).
15. J. B. Balewski et al., Nature 502, 664–667 (2013).
16. M. D. Lukin, P. R. Hemmer, Phys. Rev. Lett. 84, 2818–2821 (2000).
17. P. W. Anderson, Phys. Rev. 109, 1492–1505 (1958).
18. E. Fermi, Nuovo Cim. 11, 157–166 (1934).
19. A. Omont, J. Phys. 38, 1343–1359 (1977).
20. See supplementary materials on Science Online.
21. C. Bahrim, U. Thumm, I. I. Fabrikant, J. Phys. B 34, L195–L201 (2001).
22. E. L. Hamilton, C. H. Greene, H. R. Sadeghpour, J. Phys. B 35, L199 (2002).
23. J. W. Cooper, Phys. Rev. 128, 681–693 (1962).
24. I. I. Beterov, I. I. Ryabtsev, D. B. Tretyakov, V. M. Entin, Phys. Rev. A 79, 052504 (2009).
25. T. F. Gallagher, Rydberg Atoms (Cambridge Univ. Press, Cambridge, 1994).

TRIBOLOGY

Mechanisms of antiwear tribofilm growth revealed in situ by single-asperity sliding contacts

N. N. Gosvami,[1] J. A. Bares,[1]* F. Mangolini,[2] A. R. Konicek,[3] D. G. Yablon,[3]† R. W. Carpick[1]‡

Zinc dialkyldithiophosphates (ZDDPs) form antiwear tribofilms at sliding interfaces and are widely used as additives in automotive lubricants. The mechanisms governing the tribofilm growth are not well understood, which limits the development of replacements that offer better performance and are less likely to degrade automobile catalytic converters over time. Using atomic force microscopy in ZDDP-containing lubricant base stock at elevated temperatures, we monitored the growth and properties of the tribofilms in situ in well-defined single-asperity sliding nanocontacts. Surface-based nucleation, growth, and thickness saturation of patchy tribofilms were observed. The growth rate increased exponentially with either applied compressive stress or temperature, consistent with a thermally activated, stress-assisted reaction rate model. Although some models rely on the presence of iron to catalyze tribofilm growth, the films grew regardless of the presence of iron on either the tip or substrate, highlighting the critical role of stress and thermal activation.

Additives are crucial components of lubricants used in a wide range of tribological applications, including vehicles, turbines, and manufacturing equipment (1). Antiwear additives and friction modifiers can extend many industrial and automotive application lifetimes by orders of magnitude, resulting in considerable energy and material savings. One of the most crucial modern antiwear additives is zinc dialkyldithiophosphate (ZDDP), chemical formula $Zn[S_2P(OR)_2]_2$, where R is an alkyl or aryl group (2, 3) (fig. S2). Extensive macroscopic studies have shown that ZDDP molecules decompose at rubbing interfaces (4, 5) and form protective surface-bonded tribofilms that reduce wear by minimizing metal-to-metal contact of steel and iron (3) and other material pairs (6, 7). ZDDP-derived tribofilms consist of rough, patchy, pad-like features that are composed of pyro- or orthophosphate glasses in the bulk, with an outer nanoscale layer of zinc polyphosphates and a sulfur-rich layer near the metal surface (3). However, the tribochemical film growth pathways are not established, and the factors that determine the film morphology and thickness (generally 50 to 150 nm) are unknown (3). Furthermore, ZDDP's effectiveness as an antiwear additive for advanced engine materials is not yet clear. For low-weight

materials such as Al- and Mg-based alloys, ZDDP forms robust tribofilms primarily on load-bearing inclusions but not on surrounding softer matrices (6, 8). Although ZDDP tribofilms can be formed between other nonferrous material pairs [e.g., low-friction diamond-like carbon (DLC) films], they are often less durable than those formed when steel or iron is present, for reasons not yet understood (9, 10). ZDDP often increases frictional losses (3) and produces Zn-, P-, and S-containing compounds in automobile engine exhaust, thus reducing catalytic converter efficiency and lifetime (1, 3, 11, 12). However, despite decades of research, no suitable substitute for ZDDP has yet been found (12), and research efforts have sought to identify the beneficial mechanisms underlying the growth and antiwear properties of ZDDP-derived tribofilms.

Various macroscopic methods have been developed to produce ZDDP tribofilms (13, 14), and the resulting films have been studied by many ex situ mechanical and chemical approaches (3, 15) and atomistic simulations (8). It is widely assumed that the tribofilm acts as a protective layer that is continually replenished, reducing metal-to-metal contact (3). Some studies indicate that antiwear properties result from ZDDP's ability to reduce peroxides in the base stock, thereby preventing corrosion (16, 17). One model explaining ZDDP tribofilm formation on steel is based on hard and soft acid-base (HSAB) reactions (18), which require the exchange of Zn^{2+} and Fe^{3+} cations between the ZDDP and iron oxide wear

[1]Department of Mechanical Engineering and Applied Mechanics, University of Pennsylvania, Philadelphia, PA 19104, USA. [2]Department of Materials Science and Engineering, University of Pennsylvania, Philadelphia, PA 19104, USA. [3]Corporate Strategic Research, ExxonMobil Research and Engineering, Annandale, NJ 08801, USA.
*Present address: BorgWarner Powertrain Technical Center, Auburn Hills, MI 48326, USA. †Present address: SurfaceChar LLC, Sharon, MA 02067, USA. ‡Corresponding author. E-mail: carpick@seas.upenn.edu
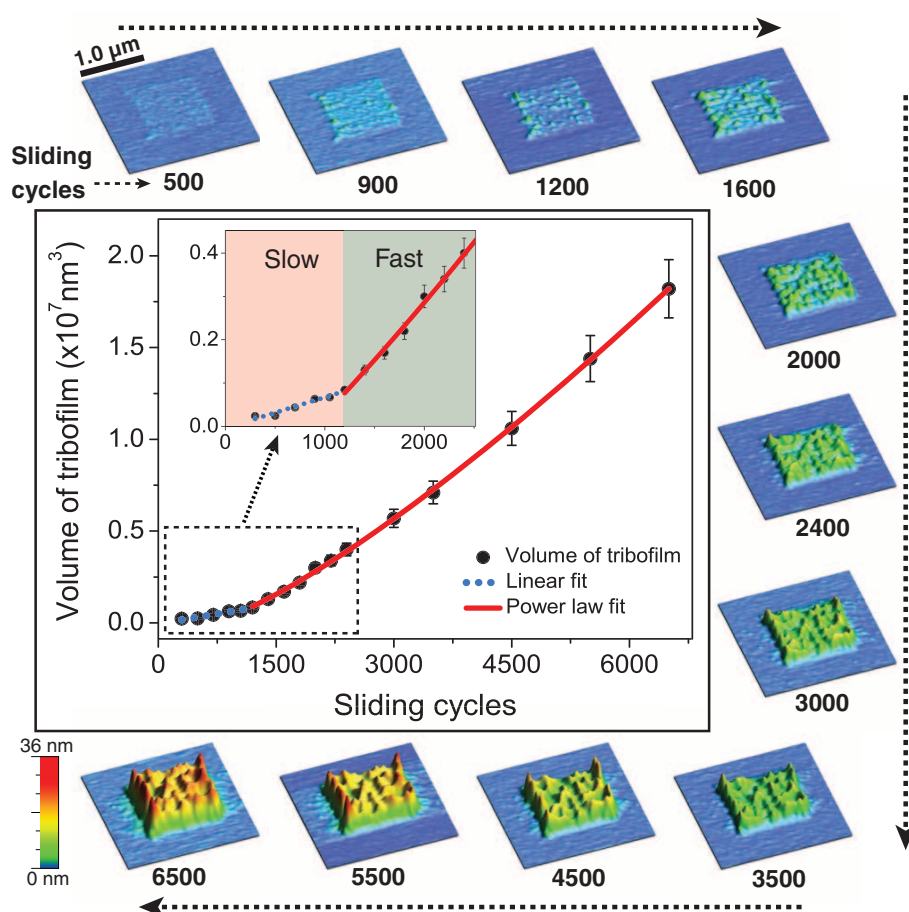
Fig. 1. Morphology and volumetric growth of tribofilm. Tribofilm volume (mean ± SD) versus sliding cycles, with linear and power-law fits to the initial and subsequent growth regimes, respectively. Inset shows a zoom-in of the initial growth period. Around the perimeter, clockwise from upper left: periodically acquired 2 μm × 2 μm AFM images of an iron oxide surface using a DLC-coated silicon AFM tip immersed in ZDDP-containing base stock, acquired at a nonperturbative load of 20.0 ± 0.1 nN. Below each image is the number of previously acquired 1 μm × 1 μm scans ("sliding cycles") at a load of 340 ± 2 nN (4.2 ± 0.5 GPa). The images demonstrate progressive tribofilm growth where the higher load was applied.

Fig. 2. Tribofilm volumetric growth rate dependence on contact pressure. Tribofilm growth rate is exponential at low contact pressures (data are means ± SD). Further growth is inhibited above ~5 GPa as the tip wears away newly deposited material. The 2 μm × 2 μm topographic contact-mode AFM images shown were acquired at a nonperturbative load after generating tribofilms in the central 1.0 μm × 0.5 μm regions at various contact pressures.
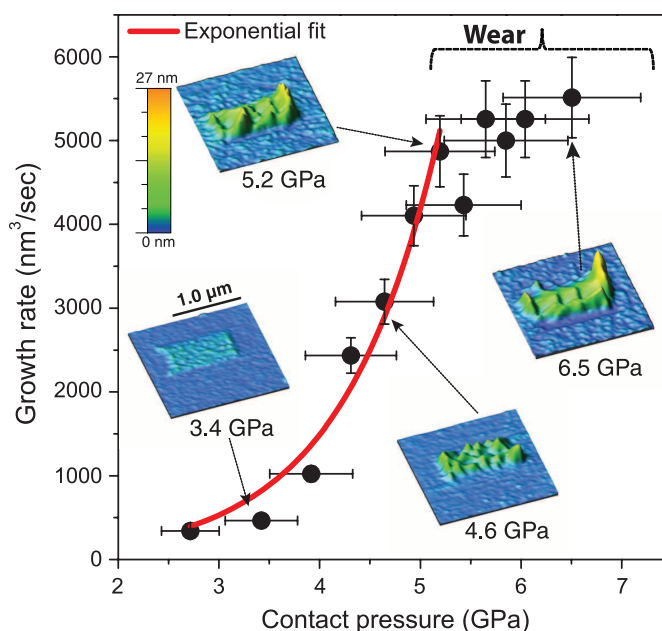
particles, respectively, where the latter are digested within the tribofilm (19). Direct experimental evidence for this model is lacking (3), nor does the model explain tribofilm formation on nonferrous surfaces (6, 7). In contrast, Mosey et al.'s first-principles atomistic simulations proposed that tribofilm formation results from contact pressure–induced cross-linking of zinc phosphate molecules (8), which are a thermal or catalytic decomposition product of ZDDP (11, 15).

There is no general consensus on the growth mechanism, and no models conclusively explain either the tribofilm patchiness or why the film thickness is limited. All prior experiments have been conducted for macroscopic, multi-asperity contacts (specific asperity contact areas and pressures thus being unknown) that are then analyzed post mortem and ex situ, often after extracting the sample from base stock, which may alter the tribofilm (20). Although macroscopic in situ studies of zinc polyphosphates under static compression (21, 22) have shown irreversible loss of crystallinity and little increase in polymerization with increased pressure, these studies do not involve dynamic sliding. In situ single-asperity sliding studies have several advantages: Contact loads and geometries can be controlled and quantified; local tribofilm properties such as morphological evolution with nanometer resolution, tribofilm volume, friction, adhesion, and wear can be measured concurrently; and results can be compared with atomistic simulations (8).

We conducted in situ single-asperity studies with an atomic force microscope (AFM). The AFM tip was slid against an Fe-coated or uncoated Si substrate at temperatures up to 140°C while immersed in ZDDP-containing base stock (23) to dynamically generate the tribofilm (fig. S3). Low-load (10 to 20 nN) contact-mode imaging revealed a soft, weakly bound thermal film, formed without prior sliding, that was easily removed by sliding with a load of 100 nN (fig. S4). This well-known "thermal film" is formed from adsorbed decomposition products of ZDDP (15, 24). Typical thermal film thicknesses of ~10 nm were obtained after ~1 hour of heating the base stock bath, but the thickness can vary with the age of the oil and heating time (24). After removing the thermal film with the tip, sliding was continued within the same region with a higher normal load to induce the growth of the tribofilm.

The morphological evolution of the tribochemical products with increasing sliding cycles (one sliding cycle = one 1 μm × 1 μm image) revealed randomly located nucleation sites and subsequent growth of the sliding-induced tribofilm (Fig. 1). The tribofilm grew vertically and laterally (only within the region scanned at higher normal load) with further sliding, leading to a rough surface (movie S1). The total film volume increased linearly with sliding time during the first ~1200 cycles (Fig. 1, inset), indicating a zero-order reaction (23). The growth rate then increased rapidly, fitting well to a power-law function corresponding to an nth-order reaction with n = 0.22 (fig. S7), which indicates a complex reaction pathway. The observed growth of a patchy film

matches well with macroscopic results (25, 26). Such macroscopic studies cannot make clear whether the patchiness resulted from multiple asperities applying a range of pressures at different contact points, or by other means. Because the loads and contact geometry are well controlled in our single-asperity experiments, the heterogeneity is apparently intrinsic to the growth mechanism. This may indicate that nucleation is sensitively dependent on surface heterogeneities such as defects or roughness and/or that there are instabilities in the growth (perhaps affected by atomic-level stress variations within the single-asperity contact) immediately after randomly occurring nucleation events.

At these stresses (~4 GPa), the tribofilm growth rate was low, and the volume rarely reached a limiting value within the time frame of our experiments (~10 hours), whereas growth typically saturates within a few hours in macroscopic experiments (27). This discrepancy may be due to differences in sliding speeds (~80 μm/s for these AFM experiments versus millimeters to meters per second for macroscopic tests) or contact areas (on the order of 10 to 100 nm^2 in AFM versus ~10^9 nm^2 for macroscopic tests), both of which reduce the area per unit time covered by AFM. The far larger amount of fluid exchange and the multi-asperity nature of the macroscopic contacts will also affect growth. Fortunately, AFM experiments performed at higher normal stresses (~6.5 GPa) enhanced the growth rate, and films reached a limiting height after prolonged sliding. We observed tribofilm wear once it reached a thickness of ~30 to 40 nm, preventing further growth (fig. S5). At this thickness, there was no observable contrast in friction between the tribofilm and the surrounding substrate. However, before the tribofilm growth had saturated, a transient increase in friction was observed (fig. S10). Further study is required to determine whether this effect is due to changes in tribofilm adhesion, modulus, roughness, or interfacial shear strength. However, the increase seen is consistent with macroscopic studies that report transient increases in friction for ZDDP-infused base stocks (28).

Within the subnanometer vertical resolution limits of our instrument, the tribofilms formed without any observable wear of the iron oxide substrate. The proposed HSAB mechanism requires substantial plastic deformation and wear of the substrate (18). Considering the nanoscale dimensions of the nucleation centers observed in our experiments, the possibilities of cation exchange and digestion of atomic-scale debris via molecular-level mechanical mixing cannot be excluded. However, such a mechanism does not explain observations of similar macroscopic ZDDP tribofilms on other substrates such as DLC and silicon (6, 7, 10, 29). We also observed formation of tribofilms in AFM experiments using Si substrates with no Fe present (fig. S6); the growth rate and morphology of these films were indistinguishable from those we formed on Fe substrates.

Our results also provide direct evidence that the tribofilm is not a product of sliding-induced transformation of the adsorbed thermal film, because growth occurred in regions where the thermal film was completely removed (fig. S4). Rather, these results indicate that tribofilm growth is fed by molecular species from solution into the contact zone, where tribochemical reactions occur.

Tribofilm growth rate and morphology were investigated as a function of normal load, which is directly related to the initial contact pressure (contact pressure at a fixed load will decrease as the compliant tribofilm's thickness increases). Multiple tribofilms were generated by sliding the AFM probe for 2000 sliding cycles at 100°C for a range of fixed loads (i.e., different initial contact pressures) (Fig. 2). Tribofilm morphologies and volumes clearly reveal that growth is strongly affected by contact pressure. Beyond 5.2 ± 0.6 GPa, tribofilm deformation and pile-up was observed and the growth rate was stabilized, indicating concurrent tribofilm generation and removal. This agrees with macroscopic observations and directly demonstrates the sacrificial property of ZDDP tribofilms beyond a critical thickness and contact pressure at the nanoscale (30).

The stress-dependent growth rate $\Gamma_{\text{growth rate}}$ (nm^3/s) fits well to a stress-activated Arrhenius model (Fig. 2):

$$\Gamma_{\text{growth rate}} = \Gamma_0 \, \exp\left(-\frac{\Delta G_{\text{act}}}{k_B T}\right) \qquad (1)$$

where the prefactor Γ_0 depends on the effective attempt frequency and the molar volume of the growth species (23), ΔG_{act} is the free activation energy of the rate-limiting reaction in the growth process, k_B is Boltzmann's constant, and T is absolute temperature. The fit assumes that ΔG_{act} is influenced by stress according to

$$\Delta G_{\text{act}} = \Delta U_{\text{act}} - \sigma \Delta V_{\text{act}} \qquad (2)$$

where ΔU_{act} is the internal activation energy (i.e., the energy barrier in the absence of stress), σ is the mean value of the stress component affecting the activation barrier (assumed to be the compressive contact pressure), and ΔV_{act} is the activation volume (31). The good fit suggests that tribofilm formation is an activated process (31). We find $\Delta U_{\text{act}} = 0.8 \pm 0.2$ eV and $\Delta V_{\text{act}} = 3.8 \pm 1.2$ Å^3, consistent with parameters for single atomic bond breaking or formation processes. The stress dependence suggests that the observed heterogeneous nucleation (Fig. 1) could result from atomic-scale surface roughness, which would lead to varying contact areas and stresses for a given normal load; thus, the energy barrier for the relevant tribochemical reaction would be lower where the local stress is higher.

Experiments performed as a function of temperature provide further support for an activated tribochemical reaction mechanism (Fig. 3). The volumetric growth rate of tribofilms generated by 5000 sliding cycles at ~4.4 GPa depended exponentially upon temperature. From fitting Eq. 1, we obtain $\Delta G_{\text{act}} = 0.62 \pm 0.10$ eV. Using the initial contact pressure determined from AFM force-distance data and using ΔV_{act} from data in Fig. 2, we obtain $\Delta U_{\text{act}} = 0.74 \pm 0.10$ eV using Eq. 2, in excellent agreement with the value obtained from the stress-dependent data. This confirms the applicability of reaction rate theory by using independent stress- and temperature-dependent measurements. Our results provide a robust basis to support the idea that tribofilm growth occurs via stress-activated and thermally activated tribochemical reactions, in contrast to previous empirical approaches (25). Our data do not provide any direct support for the HSAB model (18), which asserts that tribofilms can form even at contact pressures as low as 1 MPa, where the entropy of mixing, not stress and temperature, drives the
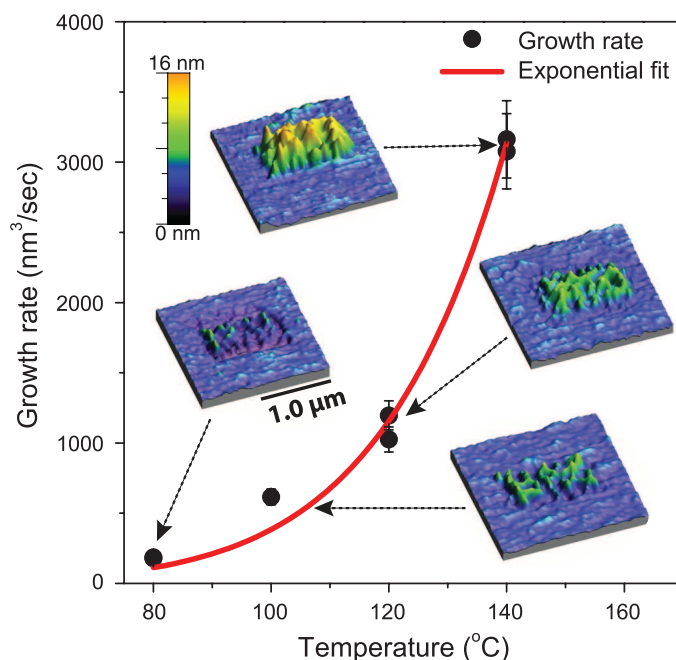
Fig. 3. Tribofilm volumetric growth rate dependence on temperature. Growth rate (mean ± SD) versus temperature data fitted with an exponential function (Eq. 1). The 2 μm × 2 μm topographic contact-mode AFM images shown were acquired at a nonperturbative load after generating tribofilms in the central 1.0 μm × 0.5 μm regions at 80°, 100°, 120°, and 140°C at an initial contact pressure of ~4.4 GPa.

reaction (19). The data are consistent with molecular dynamics simulations showing that tribofilm formation can be driven by contact pressure (8). However, we note that the simulation studies were performed on simpler zinc phosphate systems (with no sulfur), and effects of sliding were not investigated. Here, we used sliding experiments to show directly the role of pressure and temperature in forming tribofilms from ZDDP itself.

Ex situ chemical analysis using energy-dispersive spectroscopy (EDS) and Auger electron spectroscopy (AES) identified the tribofilms' elemental composition. Point spectroscopy and elemental mapping by EDS (Fig. 4A) revealed clear signatures of Zn, S, and P inside the tribofilm, as expected from ZDDP-derived products (32). Much smaller peaks corresponding to P, S, and Zn were observed outside the tribofilm region; these are attributable to the thin (~10 nm), weakly bound thermal film (a large fraction of which is likely dissolved during solvent rinsing before the EDS measurements). Elemental maps (Fig. 4A) reveal uniform distributions of P, S, and Zn inside the tribofilm. The distribution of Fe was uniform and indistinguishable between regions inside and outside the tribofilm, further showing that

no measurable wear or displacement of Fe was involved in tribofilm formation. AES, more surface-sensitive than EDS, revealed Zn, S, and P in the tribofilm region only (Fig. 4B). Far more Fe was seen outside the tribofilm, indicating that little or no Fe is mixed into the outermost regions of the tribofilm.

The observed reduction of tribofilm robustness with increased thickness is consistent with reports that the modulus and hardness of macroscopic ZDDP tribofilms decrease with thickness (20). Furthermore, the contact pressure dependence of tribofilm formation reported here (Fig. 2) can explain the reported gradient in composition, structure, and mechanical properties of ZDDP tribofilms. Specifically, because the tribofilm has a lower modulus than the substrate, the contact stress at constant load decreases as the tribofilm thickens. This in turn reduces the amount of stress-induced polymerization and other reactions that produce the tribofilm, resulting in a weaker, more compliant, graded structure and a further reduction in contact pressure. This feedback-driven self-limiting growth mechanism hinges on the stress dependence of the thermally activated growth that we have uncovered (Fig. 2).

Our results show that the ZDDP tribofilm growth rate increases exponentially with applied pressure and temperature under single-asperity contact, in very good agreement with stress-assisted reaction rate theory; the kinetic parameters are consistent with a covalent bond reaction pathway. Repeated sliding at sufficiently high loads leads to abundant tribochemical reactions and the associated nucleation and growth of robust tribofilms with a pad-like structure similar to macroscopically generated films. The tribofilm is not a product of the weakly adsorbed thermal film, but instead is generated from molecular species fed continuously into the contact zone. We confirmed the sacrificial nature of the tribofilm beyond a threshold thickness, indicating that layers grown at lower applied pressures are weaker. The observations imply that ZDDP's antiwear behavior derives from mechanical protection provided by the tribofilm, as opposed to corrosion inhibition. We suggest that this in situ approach can be directly applied to understand further molecular-level tribochemical phenomena and functionality, such as the behavior of other important lubricant additives (e.g., friction modifiers) or films formed in vapor-phase lubrication (33).
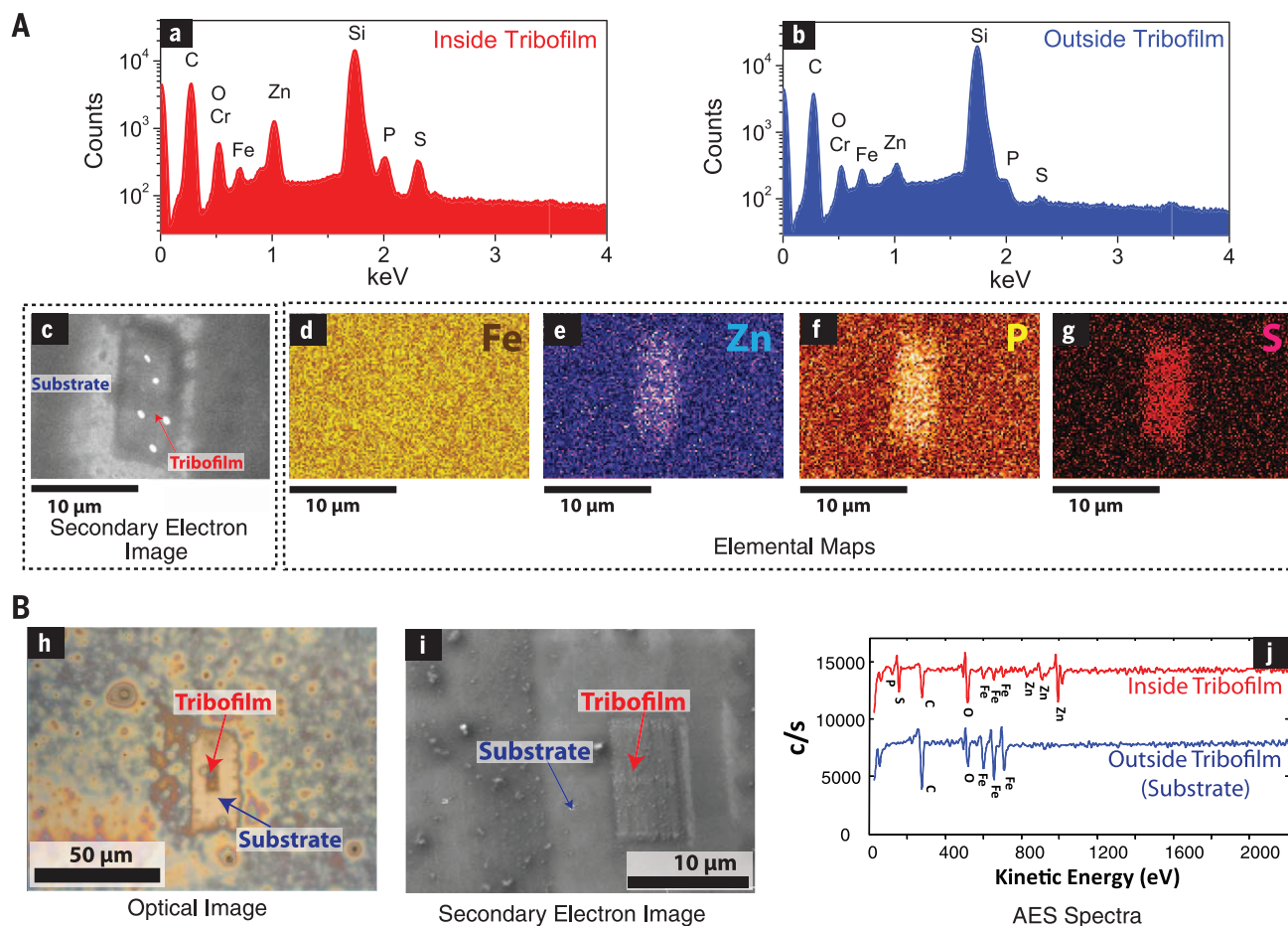
Fig. 4. Ex situ chemical characterization. (**A**) EDS point spectra (estimated sampling depth of ~1 μm) acquired for regions (a) inside and (b) outside the tribofilm (i.e., for the portion of the substrate covered with the thermal film). (c) Secondary electron image of the 10 μm × 5.0 μm tribofilm. Corresponding elemental maps are shown for (d) Fe, (e) Zn, (f) P, and (g) S. (**B**) (h) Optical and (i) secondary electron image of a 10 μm × 5.0 μm tribofilm obtained by scanning AES. (j) AES spectra for the tribofilm and the substrate (estimated sampling depth ~3 nm).

REFERENCES AND NOTES

1. R. I. Taylor, *Faraday Discuss.* **156**, 361–382 (2012).
2. A. M. Barnes, K. D. Bartle, V. R. A. Thibon, *Tribol. Int.* **34**, 389–395 (2001).
3. H. Spikes, *Tribol. Lett.* **17**, 469–489 (2004).
4. E. S. Ferrari, K. J. Roberts, M. Sansone, D. Adams, *Wear* **236**, 259–275 (1999).
5. M. L. S. Fuller, M. Kasrai, G. M. Bancroft, K. Fyfe, K. H. Tan, *Tribol. Int.* **31**, 627–644 (1998).
6. M. A. Nicholls *et al.*, *Tribol. Lett.* **18**, 261–278 (2005).
7. B. Vengudusamy, J. H. Green, G. D. Lamb, H. A. Spikes, *Tribol. Int.* **44**, 165–174 (2011).
8. N. J. Mosey, M. H. Müser, T. K. Woo, *Science* **307**, 1612–1615 (2005).
9. B. Vengudusamy, J. H. Green, G. D. Lamb, H. A. Spikes, *Tribol. Lett.* **51**, 469–478 (2013).
10. S. Equey *et al.*, *Tribol. Int.* **41**, 1090–1096 (2008).
11. G. C. Smith, *J. Phys. D* **33**, R187–R197 (2000).
12. H. Spikes, *Lubr. Sci.* **20**, 103–136 (2008).
13. K. T. Miklozic, J. Graham, H. Spikes, *Tribol. Lett.* **11**, 71–81 (2001).
14. K. T. Miklozic, T. R. Forbus, H. A. Spikes, *Tribol. Trans.* **50**, 328–335 (2007).
15. M. A. Nicholls, T. Do, P. R. Norton, M. Kasrai, G. M. Bancroft, *Tribol. Int.* **38**, 15–39 (2005).
16. J. J. Habeeb, W. H. Stover, *ASLE Trans.* **30**, 419–426 (1986).
17. F. Rounds, *Tribol. Trans.* **36**, 297–303 (1993).
18. J. M. Martin, *Tribol. Lett.* **6**, 1–8 (1999).
19. J. M. Martin, T. Onodera, C. Minfray, F. Dassenoy, A. Miyamoto, *Faraday Discuss.* **156**, 311–323 (2012).
20. S. Bec *et al.*, *Proc. R. Soc. London Ser. A* **455**, 4181–4203 (1999).
21. S. Berkani *et al.*, *Tribol. Lett.* **51**, 489–498 (2013).
22. D. Shakhvorostov *et al.*, *J. Chem. Phys.* **128**, 074706 (2008).
23. See supplementary materials on *Science* Online.
24. M. Aktary, M. T. McDermott, J. Torkelson, *Wear* **247**, 172–179 (2001).
25. H. Fujita, H. A. Spikes, *Tribol. Trans.* **48**, 567–575 (2005).
26. M. Aktary, M. T. McDermott, G. A. McAlpine, *Tribol. Lett.* **12**, 155–162 (2002).
27. H. Fujita, R. P. Glovnea, H. A. Spikes, *Tribol. Trans.* **48**, 558–566 (2005).
28. B. Kim, R. Mourhatch, P. B. Aswath, *Wear* **268**, 579–591 (2010).
29. M. Burkinshaw, A. Neville, A. Morina, M. Sutton, *Tribol. Int.* **46**, 41–51 (2012).
30. Y. R. Li, G. Pereira, M. Kasrai, P. R. Norton, *Tribol. Lett.* **29**, 201–211 (2008).
31. T. D. B. Jacobs, R. W. Carpick, *Nat. Nanotechnol.* **8**, 108–112 (2013).
32. A. Morina, A. Neville, *J. Phys. D* **40**, 5476–5487 (2007).
33. A. L. Barnette, D. B. Asay, J. A. Ohlhausen, M. T. Dugger, S. H. Kim, *Langmuir* **26**, 16299–16304 (2010).

FRUSTRATED MAGNETISM

Large thermal Hall conductivity of neutral spin excitations in a frustrated quantum magnet

Max Hirschberger,[1] Jason W. Krizan,[2] R. J. Cava,[2] N. P. Ong[1]*

In frustrated quantum magnets, long-range magnetic order fails to develop despite a large exchange coupling between the spins. In contrast to the magnons in conventional magnets, their spin excitations are poorly understood. Here, we show that the thermal Hall conductivity κ_{xy} provides a powerful probe of spin excitations in the "quantum spin ice" pyrochlore $Tb_2Ti_2O_7$. The thermal Hall response is large, even though the material is transparent. The Hall response arises from spin excitations with specific characteristics that distinguish them from magnons. At low temperature (<1 kelvin), the thermal conductivity resembles that of a dirty metal. Using the Hall angle, we construct a phase diagram showing how the excitations are suppressed by a magnetic field.

Spin waves or magnons, the elementary excitations in a magnet, can transport heat when a thermal gradient $-\nabla T$ is applied. Because magnons are not charged, the thermal current is expected to be symmetric with respect to the sign-reversal of a magnetic field H, resulting in a zero thermal Hall conductivity κ_{xy}. However, recent findings based on the Berry curvature have overturned this semiclassical result. Following a prediction by Katsura, Nagaosa, and Lee (*1*), Onose *et al.* recently observed a weak κ_{xy} signal in the ferromagnetic insulator $Lu_2V_2O_7$ (*2*). Subsequently, it was pointed out (*3*) that κ_{xy} should include a contribution from the magnetization current (*4–6*).

In frustrated magnets, long-range magnetic order fails to develop even at millikelvin temperatures T because of strong quantum fluctuations. The low-lying excitations are currently of great interest (*7–9*). The pyrochlore $Tb_2Ti_2O_7$ is an insulator in which Tb and Ti define interpenetrating networks of tetrahedra (*10*). Each Tb^{3+} ion has a large local moment [9.4 bohr magnetons (μ_B)], but the lowest lying level is a crystal-field induced spin-1/2 doublet. The spin-spin interaction is of the antiferromagnetic Ising-type, with easy axis along the local (111) axis. Susceptibility experiments report a Curie-Weiss temperature $\theta = -19$ K (*10, 11*). However, long-range order is not detected down to 50 mK (*11, 12*). Neutron scattering observed diffuse scattering in zero H, which condensed to a Bragg peak at (002) when $H = 2$ T (*13*). Recently, neutron diffraction at 50 mK and H = 0 has detected elastic diffusive peaks at (1/2, 1/2, 1/2), with short correlation length ($\xi \sim 8$ Å) (*14*) and "pinch points" (*15*), which is suggestive of incipient spin-ice order subject to strong quantum fluctuations. Distinct from classical spin-ice pyrochlores (such as $Dy_2Ti_2O_7$) (*16*), the ground state of $Tb_2Ti_2O_7$ and $Yb_2Ti_2O_7$—

broadly termed "quantum spin ice" (*7, 8, 17*)—is predicted to host the quantum spin liquid (at $T = 0$) and the thermal spin-liquid (when entropy dominates at finite T), as well as a still unidentified Coulomb ferromagnetic state (*17–19*). All three states harbor exotic excitations.

In spite of the extensive experimental literature, nearly nothing is known about the transport properties of the spin excitations. Here, we show that κ_{xy} provides a powerful way to detect the excitations and determine their properties.

We investigated two crystals, cut with the x-y plane (largest face) normal to (110) in sample 1 and normal to (111) in sample 2. With **H** || **z** and thermal current density $\mathbf{J}_q$ || **x** (Fig. 1), we measured the longitudinal gradient $-\partial_x T$ and the transverse gradient $-\partial_y T$ to obtain the thermal resistivity tensor W_{ij} (defined by $-\partial_i T = W_{ij} J_{qj}$) and the thermal conductivity tensor $\kappa_{ij} = W_{ij}^{-1}$. Throughout, we plot κ_{ij} divided by T in order to remove the entropy factor. The thermal Hall angle is defined by $\tan\theta_H = \kappa_{xy}/\kappa_{xx} = W_{yx}/W_{xx}$. For measurements of $-\partial_y T$, three types of thermometers were used: ruthenium oxide ($T < 15$ K), Cernox ($10 \le T \le 40$ K), and chromel-constantan thermocouples ($T \ge 25$ K). The magnetoresistances of the thermometers were extensively calibrated. At 1 K, we resolve 0.5 mK in the Hall signal for a longitudinal $\delta_x T \sim 100$ mK. The fragility of the crystals above 5 T and the unusually large magneto-caloric effect in $Tb_2Ti_2O_7$ below 5 K posed challenges that required specially designed mounts and measurement protocols (*20*).

The observed Hall response in $Tb_2Ti_2O_7$ becomes quite large below 15 K. Seeing a large thermal Hall signal in an orange, transparent crystal is strongly counterintuitive (because transparency implies the complete absence of charge carriers, the usual source of a Hall current). Hence, we have performed several tests in order to verify that it is intrinsic (*20*). The Hall signal (always "holelike") should be independently antisymmetric in **H** and in $\mathbf{J}_q$. To reverse $\mathbf{J}_q$, we warmed up the sample and reconfigured the Au wires. The

[1]Department of Physics, Princeton University, Princeton, NJ 08544, USA. [2]Department of Chemistry, Princeton University, Princeton, NJ 08544, USA.
*Corresponding author. E-mail: npo@princeton.edu
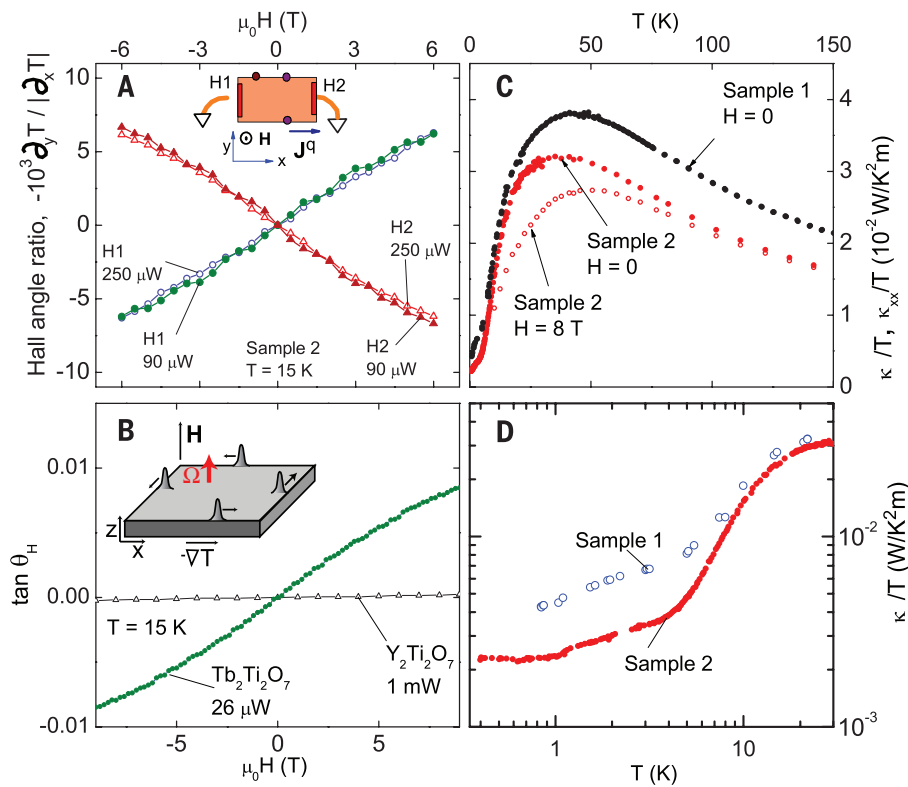
Fig. 1. The thermal Hall effect in the pyrochlore Tb$_2$Ti$_2$O$_7$. (**A**) Hall angle ratio $-\partial_y T/|\partial_x T|$ measured at 15 K with thermal current density $\mathbf{J}_q$ flowing to the right (green circles). (Inset) Current was applied to heater H1, and the right edge was grounded to the bath. When $\mathbf{J}_q$ points to the left, the Hall angle ratio is inverted in sign (solid triangles) but unchanged in magnitude (to 2%). When the power is increased threefold (90 → 270 μW), $-\partial_y T/|\partial_x T|$ is nearly unchanged, confirming linear response (open symbols). (**B**) Comparison between the thermal Hall signal in sample 1 (solid circles, with applied heater power 26 μW at 15 K) with the null signal in the nonmagnetic analog Y$_2$Ti$_2$O$_7$, with heater power 38× larger (1 mW at 15 K) (open triangles). (Inset) Wave-packet model proposed in (3) for κ_{xy} in a ferromagnetic insulator. (**C**) T dependence of κ/T ($\equiv \kappa_{xx}/T$ at $H = 0$) for samples 1 and 2 (solid symbols). In sample 2, κ_{xx}/T at $H = 8$ T is also plotted as open circles. (**D**) The low-T behavior of κ/T. In sample 2, κ/T becomes T- independent below 1 K, which is similar to the case of a dirty metal.
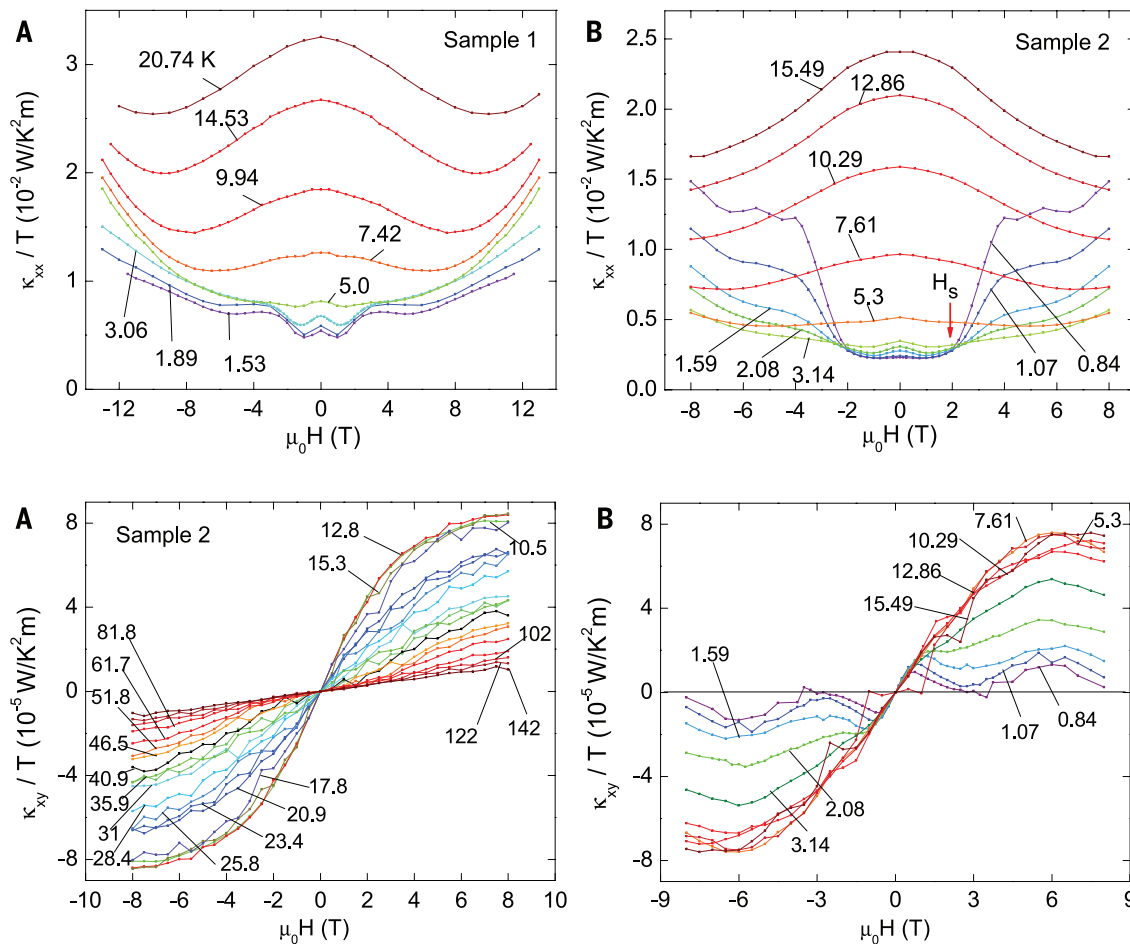
Fig. 2. κ_{xx}/T vs. H in Tb$_2$Ti$_2$O$_7$ at various temperatures. (**A**) For sample 1, in the interval 5 to 21 K, the thermal conductivity initially decreases as H increases but then goes through a broad minimum, before increasing steeply at larger H. (**B**) For sample 2, a new feature becomes apparent in low H and below 5K: At the step-field $H_s \simeq 2$ T (red arrow), κ_{xx} undergoes a step increase (by a factor of 4.5 at 0.84 K).
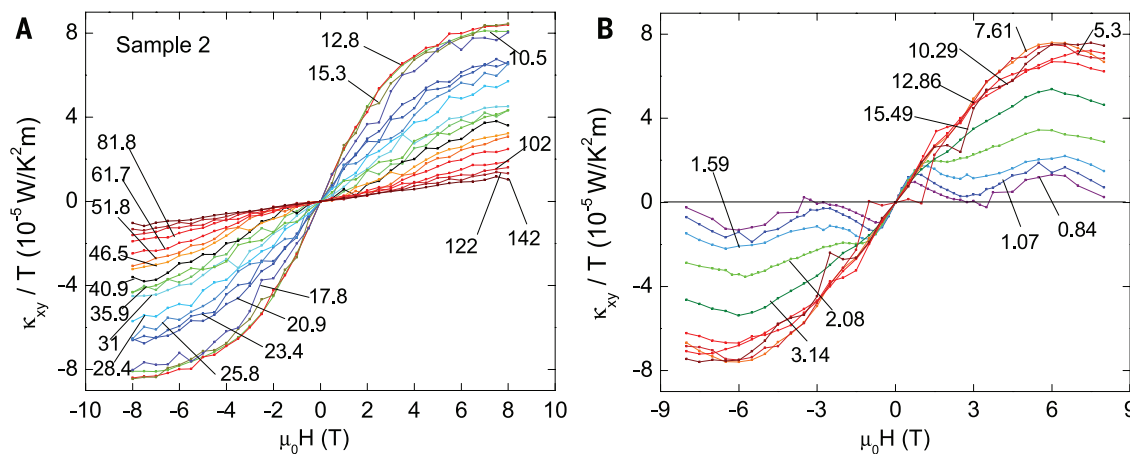
Fig. 3. Thermal Hall conductivity κ_{xy}/T versus H in Tb$_2$Ti$_2$O$_7$ for sample 2. (**A**) From 140 to 50 K, κ_{xy}/T is H-linear. Below 45 K, it develops pronounced curvature at large H, reaching its largest value near 12 K. The sign is always holelike. (**B**) Below 15 K, the weak-field slope $[\kappa_{xy}/TB]_0$ is nearly T-independent. Below 3 K, the field profile shows additional features that become prominent as $T \to 0$—namely, the sharp peak near 1 T and the broad maximum at 6 T.

data in Fig. 1A confirm that the Hall-angle ratio $-\partial_y T/|\partial_x T|$ at 15 K is indeed antisymmetric in both $\mathbf{H}$ and $\mathbf{J}_q$. The ratio remains virtually the same when the applied heater power is increased (open symbols in Fig. 1A), indicating a linear response. In addition, we performed thermal Hall measurements on the nonmagnetic analog $Y_2Ti_2O_7$ (Fig. 1B) and verified that it displays a null result (unresolved from our background signal, which is 1700× weaker than in $Tb_2Ti_2O_7$).

The T dependence of the thermal conductivity κ ($\equiv \kappa_{xx}$ in $H = 0$) (Fig. 1C) reveals an interesting feature at very low T. Initially, as we cool below 150 K, κ/T attains a broad peak at 40 K and then decreases steeply, reflecting freezing out of the phonons. Below 1 K, κ/T settles to a constant value (Fig. 1D). The constancy in κ/T—incompatible with phonon or magnon conduction—is reminiscent of a dirty metal. Despite the complete absence of itinerant electrons, the heat current is conveyed by neutral excitations that seem to behave like fermions.

In finite $\mathbf{H}$, κ_{xx} displays a rich pattern of behavior (Fig. 2) [previous measurements of κ_{xx} versus H are available in (21)]. Above ~80 K, κ_{xx}/T is nearly insensitive to H, which is consistent with heat conduction dominated by phonons (fig. S6). Below 80 K, a fairly large H dependence is observed (Fig. 2A). An 8-T field suppresses κ_{xx} by 25 to 30% over a broad T interval 7 to 80 K. In

sample 2, with $\mathbf{H} \parallel (111)$, the field profile is nearly flat for $3 < T < 5$ K (Fig. 2B). Below 3 K, the profile is dominated by a step-increase (by a factor of 4.5 at 0.84 K) that onsets at the step-field H_s (arrow). H_s (~2 T from 0.84 to 2 K) agrees well with the field H_2 detected by susceptibility (22). In neutron scattering (13), the checkerboard diffuse scattering condenses to a sharp Bragg spot at (002) at 2 T. As seen here, κ_{xx} undergoes a fourfold increase partly from spin waves stiffened by H and from phonon lifetime enhancement (12).

The thermal Hall conductivity (as κ_{xy}/T) in sample 2 (the curves for sample 1 are similar) is plotted in Fig. 3. The Hall signal is positive (holelike) at all T. Above 35 K, κ_{xy}/T is H-linear with a slope that decreases nominally as $1/T$ (Fig. 3A). The thermal Hall response becomes large and generally nonlinear in H below 15 K. Cooling below 3 K reveals several features (Fig. 3B). Close to 1 T, κ_{xy}/T displays a shoulder that evolves to a peak feature at 0.84 K. We discuss this important peak in relation to the Hall angle below. Above 1 T, κ_{xy}/T goes through a shallow minimum followed by a broad maximum at 6 T.

A striking feature of the Hall curves in Fig. 3B is that the initial (weak-field) slope $[\kappa_{xy}/TB]_0$ is nominally T-independent below 10 K (where $[\cdots]_0 \equiv \lim_{B\to 0} \cdots$, with $B = \mu_0 H$). To bring this out, we show the full T dependence of $[\kappa_{xy}/TB]_0$ in Fig. 4C for both samples. As T is lowered from 140 K,

the rapid increase of $[\kappa_{xy}/TB]_0$ saturates abruptly below 15 K to a constant, within our uncertainties. The thermal Hall effect becomes large below this crossover temperature. In contrast, the Hall angle in weak H does not saturate (Fig. 4A). The initial slope $[\tan\theta_H/B]_0$ continues to increase as T falls from $15 \to 0.84$ K, a behavior also reminiscent of metals, in which $[\tan\theta_H/B]_0 \sim \lambda$ (the mean free path). As mentioned, $\tan\theta_H$ displays a prominent peak at the "peak field" $H_p(T)$ (blue arrow). For $H > H_p$, the Hall response is strongly suppressed (curves at 1 K and 0.84 K). We plot H_p versus T as solid circles in Fig. 4B and find that it nearly coincides with the low field-scale H_1 (dashed curve) recently reported in (22).

Further information on the crossover field comes from the Hall-angle slope $\tan\theta_H/B$. It is useful to regard $\tan\theta_H/B$ as a "susceptibility" that measures the strength of the off-diagonal (Hall) response. If we fix H and vary T, we obtain the curves shown in Fig. 4D. At zero H, $\tan\theta_H/B$ rises monotonically as $T \to 0.84$ K. At finite H, however, each curve displays a distinct maximum that defines the field scale $H_p'(T)$. Plotted in Fig. 4B, the curves of H_p' (open circles) and H_p (solid circles) demarcate the region in which the Hall susceptibility $\tan\theta_H/B$ is largest (darkest shading). The "phase diagram" highlights a crucial feature of the Hall excitations and its host quantum state. As noted (Fig. 4, A and D), the Hall susceptibility $\tan\theta_H/B$ peaks at H_p then falls steadily, reaching nearly zero at the step field H_s. To us, this suggests that the host state, subject to strong quantum fluctuations, is readily suppressed by a large H. At low T, it is confined to the narrow wedge defined by the field H_p (and H_p'). We discuss next why κ_{xy} cannot be caused by phonons or magnons.

A weak phonon Hall effect was observed (23) in the garnet $Tb_3Ga_5O_{12}$. We already mentioned that the constancy of κ/T below 1 K in our samples (Fig. 1C) is incompatible with phonon conduction. Despite the small κ, $\tan\theta_H$ (at 1 T) is 90× larger than in the garnet. More importantly, the curve of $\tan\theta_H$ versus H provides a sharp test. In the phonon scenario, skew scattering from local moments in the disordered state yields a weak Hall signal at low H. As H increases, alignment of the moments should lead to an increasing $\tan\theta_H$, especially above H_s, where the magnetization is ~ 3 μ_B per Tb ion (22). Instead, the opposite is observed; $\tan\theta_H$ rapidly falls to nearly zero when the host quantum state is suppressed above H_p. This strong contradiction persuades us that phonons are not the origin of κ_{xy}.

The true ground state of $Tb_2Ti_2O_7$ is still elusive (9, 24). The incipient two-in, two-out correlation measured at 70 mK (14) has a very short ξ (~ 8 Å). At our T (> 0.84 K), ξ should be even shorter, so that the spin excitations responsible for κ_{xy} cannot be conventional magnons. Indeed, the constancy of $[\kappa_{xy}/T]_0$ below 15 K in Fig. 3C violates the power-law dependence (with $a > 2$) predicted by the magnon model (3).

Instead, our results point to neutral excitations subject to a Lorentz-like force $\mathbf{F}_L = e_s \mathbf{v} \times \mathbf{B}$, with e_s an effective charge and $\mathbf{v}$ the drift velocity
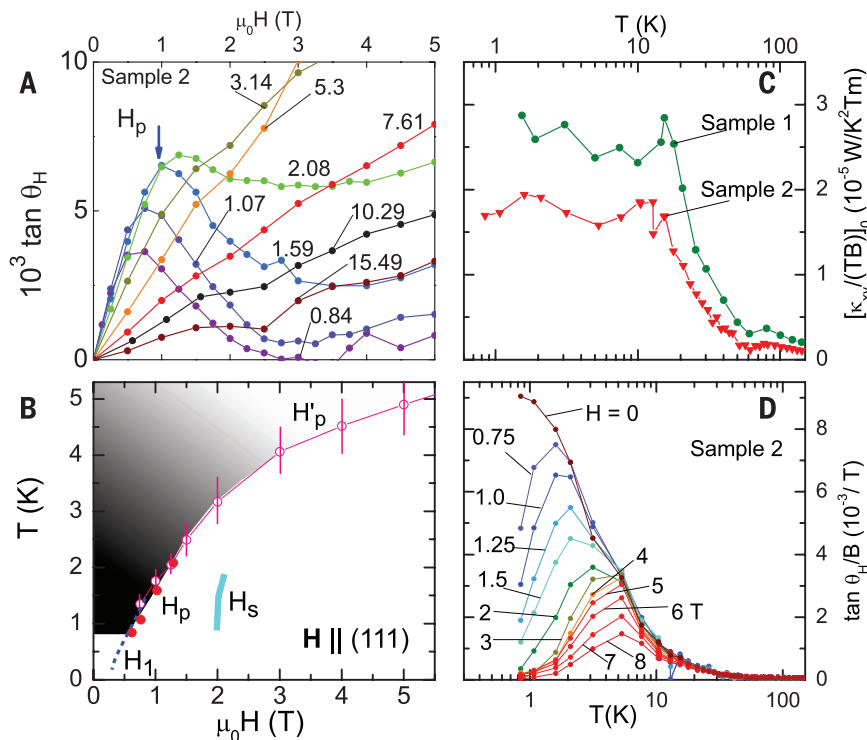
Fig. 4. The Hall angle and its temperature dependence. (A) Hall angle θ_H in weak H and low T (sample 2). Below 3 K, $\tan\theta_H$ shows a prominent peak at the peak field $H_p(T)$ (arrow). The Hall response is strongly suppressed when $H > H_p$ (most evident at 0.84 K). (B) T-dependence of H_p [from (A), solid circles] and H_p' [from (D), open circles] in sample 2 [$\mathbf{H} \parallel (111)$]. The dashed curve is H_1 from (22). The thick solid curve is H_s. The region in which the Hall-angle slope $\tan\theta_H/B$ is large is shown shaded (darkest hue represents largest $\tan\theta_H$). (C) Initial slope $[\kappa_{xy}/TB]_0$ is nearly T-independent below 15 K in samples 1 and 2. (D) $\tan\theta_H/B$ versus T in fixed H. At low T, θ_H/B reaches 9×10^{-3} rad/T. The positions of the broad maxima in $\tan\theta_H/B$ define H_p' (T) [open circles in (B)].

driven by $-\nabla T$ (Fig. 1A). As noted in (1), if the spin excitations are fermionic, the Wiedemann-Franz law requires κ/T to be T-independent at low T. Hence, the constancy of κ/T seems consistent with neutral fermionic excitations below 1 K, where λ is no longer T-dependent. The sign of κ_{xy} implies e_s is positive, and a crude estimate gives $e_s = 70$ to $540\times$ the elemental charge e (20).

REFERENCES AND NOTES

1. H. Katsura, N. Nagaosa, P. A. Lee, Phys. Rev. Lett. **104**, 066403 (2010).
2. Y. Onose et al., Science **329**, 297–299 (2010).
3. R. Matsumoto, S. Murakami, Phys. Rev. Lett. **106**, 197202 (2011).
4. J. M. Luttinger, Phys. Rev. **135** (6A), A1505–A1514 (1964).
5. Y. N. Obraztsov, Sov. Phys. Solid State **6**, 331–336 (1964).
6. H. Oji, P. Streda, Phys. Rev. B **31**, 7291–7295 (1985).
7. H. R. Molavian, M. J. P. Gingras, B. Canals, Phys. Rev. Lett. **98**, 157204 (2007).
8. L. Balents, Nature **464**, 199–208 (2010).
9. M. J. P. Gingras, P. A. McClarty, Rep. Prog. Phys. **77**, 056501 (2014).
10. J. S. Gardner, M. J. P. Gingras, J. E. Greedan, Rev. Mod. Phys. **82**, 53–107 (2010).
11. J. S. Gardner et al., Phys. Rev. Lett. **82**, 1012–1015 (1999).
12. J. S. Gardner et al., Phys. Rev. B **68**, 180401 (2003).
13. K. C. Rule et al., Phys. Rev. Lett. **96**, 177201 (2006).
14. K. Fritsch et al., Phys. Rev. B **87**, 094410 (2013).
15. T. Fennell, M. Kenzelmann, B. Roessli, M. K. Haas, R. J. Cava, Phys. Rev. Lett. **109**, 017201 (2012).
16. C. Castelnovo, R. Moessner, S. L. Sondhi, Annual Rev. Cond. Matter Phys. **3**, 35–55 (2012).
17. K. A. Ross, L. Savary, B. D. Gaulin, L. Balents, Phys. Rev. X **1**, 021002 (2011).
18. L. Savary, L. Balents, Phys. Rev. Lett. **108**, 037202 (2012).
19. L. Savary, L. Balents, Phys. Rev. B **87**, 205130 (2013).
20. Methods and materials are available as supplementary materials on Science Online.
21. Q. J. Li et al., Phys. Rev. B **87**, 214408 (2013).
22. S. Legl et al., Phys. Rev. Lett. **109**, 047201 (2012).
23. C. Strohm, G. L. J. A. Rikken, P. Wyder, Phys. Rev. Lett. **95**, 155901 (2005).
24. M. J. P. Gingras et al., Phys. Rev. B **62**, 6496–6511 (2000).

THERMOELECTRICS

Dense dislocation arrays embedded in grain boundaries for high-performance bulk thermoelectrics

Sang Il Kim,[1]*† Kyu Hyoung Lee,[2]* Hyeon A Mun,[3,4]* Hyun Sik Kim,[1,5]
Sung Woo Hwang,[1] Jong Wook Roh,[1] Dae Jin Yang,[1] Weon Ho Shin,[1] Xiang Shu Li,[1]
Young Hee Lee,[3,4] G. Jeffrey Snyder,[3,5] Sung Wng Kim[3,4]†

The widespread use of thermoelectric technology is constrained by a relatively low conversion efficiency of the bulk alloys, which is evaluated in terms of a dimensionless figure of merit (zT). The zT of bulk alloys can be improved by reducing lattice thermal conductivity through grain boundary and point-defect scattering, which target low- and high-frequency phonons. Dense dislocation arrays formed at low-energy grain boundaries by liquid-phase compaction in $Bi_{0.5}Sb_{1.5}Te_3$ (bismuth antimony telluride) effectively scatter midfrequency phonons, leading to a substantially lower lattice thermal conductivity. Full-spectrum phonon scattering with minimal charge-carrier scattering dramatically improved the zT to 1.86 ± 0.15 at 320 kelvin (K). Further, a thermoelectric cooler confirmed the performance with a maximum temperature difference of 81 K, which is much higher than current commercial Peltier cooling devices.

Thermoelectric (TE) Peltier devices enable solid-state cooling to replace cumbersome vapor-compression cycle technologies as well as electricity generation from a variety of waste heat sources such as industries and vehicles. Next-generation distributed cooling systems enabled by small Peltier devices promise zonal and personal temperature control to provide enhanced comfort with reduced overall energy use (1). Widespread use of TE devices requires improvements in performance of TE materials but also

[1]Materials Research Center, Samsung Advanced Institute of Technology, Samsung Electronics, Suwon 443-803, South Korea. [2]Department of Nano Applied Engineering, Kangwon National University, Chuncheon 200-701, South Korea. [3]Department of Energy Science, Sungkyunkwan University, 300 Cheoncheon-dong, Jangan-gu, Suwon 440-746, South Korea. [4]IBS Center for Integrated Nanostructure Physics, Institute for Basic Science, Sungkyunkwan University, Suwon 440-746, South Korea. [5]Materials Science, California Institute of Technology, Pasadena, California 91125, USA.
*These authors contributed equally to this work. †Corresponding author. E-mail: sang.il.kim@samsung.com; kimsungwng@skku.edu

the realization of improved performance in actual devices (1). The performance of TE materials is evaluated with a dimensionless figure of merit [$zT = S^2 \times \sigma \times T/(\kappa_{ele} + \kappa_{lat})$] dependent on the Seebeck coefficient (S), electrical conductivity (σ), electronic (κ_{ele}) and lattice (phonon, κ_{lat}) thermal conductivity, and absolute temperature (T). Introducing dislocation arrays at grain boundaries has the potential to improve zT by decreasing thermal conductivity, but dislocation arrays formed by traditional sintering techniques also decrease electrical conductivity. By modifying a traditional liquid-phase sintering technique, we avoid this pitfall and provide a different pathway for fabricating bulk alloys with high zT.

Bismuth antimony telluride alloys are the most widely used TE bulk material developed in the 1960s for Peltier cooling with p-type composition close to $Bi_{0.5}Sb_{1.5}Te_3$ and peak zT of 1.1 near 300 K (2). The Bi-Sb atomic disorder in $Bi_{0.5}Sb_{1.5}Te_3$ scatters the heat-carrying phonons, reducing κ_{lat} that permits such high zT values. Matched

with Bi_2Te_3–based n-type alloys, devices are commercially produced that provide a maximum temperature drop (ΔT_{max}) of 64 to 72 K with 300 K hot side (T_h) (3, 4). Recent measured improvements in zT of $Bi_{0.5}Sb_{1.5}Te_3$ bulk alloys have been reported using strategies primarily based on nanometer-scale microstructures to add boundary scattering of phonons at the composite interface or grain boundaries (5–8). However, improvements in the performance (ΔT_{max}) of Peltier cooling devices have not been realized since the development of bismuth antimony telluride (4).

Heat-carrying phonons cover a broad spectrum of frequencies (ω), and the lattice thermal conductivity (κ_{lat}) can be expressed as a sum of contributions from different frequencies (4, 9): $\kappa_{lat} = \int\kappa_s(\omega)d\omega$. The spectral lattice thermal conductivity ($\kappa_s(\omega)$) can be expressed as arising from the spectral heat capacity of phonons $C_p(\omega)$, their velocity $v(\omega)$, and their scattering time $\tau(\omega)$, such that $\kappa_s(\omega) = C_p(\omega) \times v^2(\omega) \times \tau(\omega)$. Phonons in all crystalline materials are scattered by other phonons by Umklapp scattering, which generally has a $\tau_U^{-1} \sim \omega^2$ dependence. Combining this with the Debye approximation for heat-carrying phonons [$C_p(\omega) \sim \omega^2$] gives $\kappa_s(\omega)$ = constant. This leaves a wide range of phonon frequencies where all frequencies contribute to the thermal conductivity (Fig. 1A).

The κ_{lat} can be further reduced with additional scattering mechanisms. Traditional mechanisms are only effective at the high- or low-frequency ends (4). Point-defect scattering of phonons from the Bi-Sb disorder in $Bi_{0.5}Sb_{1.5}Te_3$ targets high-frequency phonons with a scattering time depending on frequency as $\tau_{PD}^{-1} \sim \omega^4$ (4), similar to Rayleigh scattering. However, boundary scattering of phonons targets low-frequency phonons, as it is frequency independent ($\tau_B^{-1} \sim$ constant) (10). Even the scattering of nanometer-sized particles can be well described with these two models as the small-size Rayleigh regime rapidly crosses over to the boundary regime as the particle size increases (11). A full-spectrum strategy targeting the wide spectrum of phonons, including midfrequency phonon scattering, is necessary for further reduction in κ_{lat}. However, at the same time the high

Fig. 1. Full-spectrum phonon scattering in high-performance bulk thermoelectrics. (**A**) The inclusion of dislocation scattering (DC + DS) is effective across the full frequency spectrum. Boundary (B) and point defect (PD) are effective only at low and high frequencies. The acoustic mode Debye frequency is f_a. (**B**) Lattice thermal conductivity (κ_{lat}) for $Bi_{0.5}Sb_{1.5}Te_3$ alloys produced by melt-solidification (ingot), solid-phase compaction (BM and S-MS), and liquid-phase compaction (Te-MS). The lowest κ_{lat} of Te-MS can be explained by the midfrequency phonon scattering due to dislocation arrays embedded in grain boundaries (inset, fig. S15C) (17). (**C**) The figure of merit (zT) as a function of temperature for $Bi_{0.5}Sb_{1.5}Te_3$ alloys. The data points (red) give the average (±SD) of all 30 Te-MS samples (inset, fig. S9F) (17), which shows excellent reproducibility. (**D**) A Peltier cooling module (bottom) with 127 couples made from p-type $Bi_{0.5}Sb_{1.5}Te_3$ Te-MS pellet (top) and n-type 1 weight percent (wt %) SbI_3 doped $Bi_2Te_{2.7}Se_{0.3}$ ingot. (**E**) The maximum coefficient of performance (COP_{max}) measured on modules of (D) where the high performance is confirmed with notably high ΔT_{max} of 81 K with 300 K hot side (17).

Fig. 2. Comparison of thermoelectric properties of $Bi_{0.5}Sb_{1.5}Te_3$ between different fabrication methods. Introduction of dislocation arrays has a large effect on thermal conductivity but a small effect on electronic conductivity. (**A**) Temperature dependence of electrical conductivity (σ). Charge-carrier mobilities of S-MS (190 cm^2 V^{-1} s^{-1}) are lower than for Te-MS (280 cm^2 V^{-1} s^{-1}) materials (inset). (**B**) Temperature dependence of Seebeck coefficient (S) and power factor (σS^2) (inset). Temperature dependences of total (**C**) and lattice (**D**) thermal conductivity (κ_{tot} and κ_{lat}) for all samples. The error bars of Te-MS in all panels are the standard deviations from the measurements of 30 samples (fig. S9).
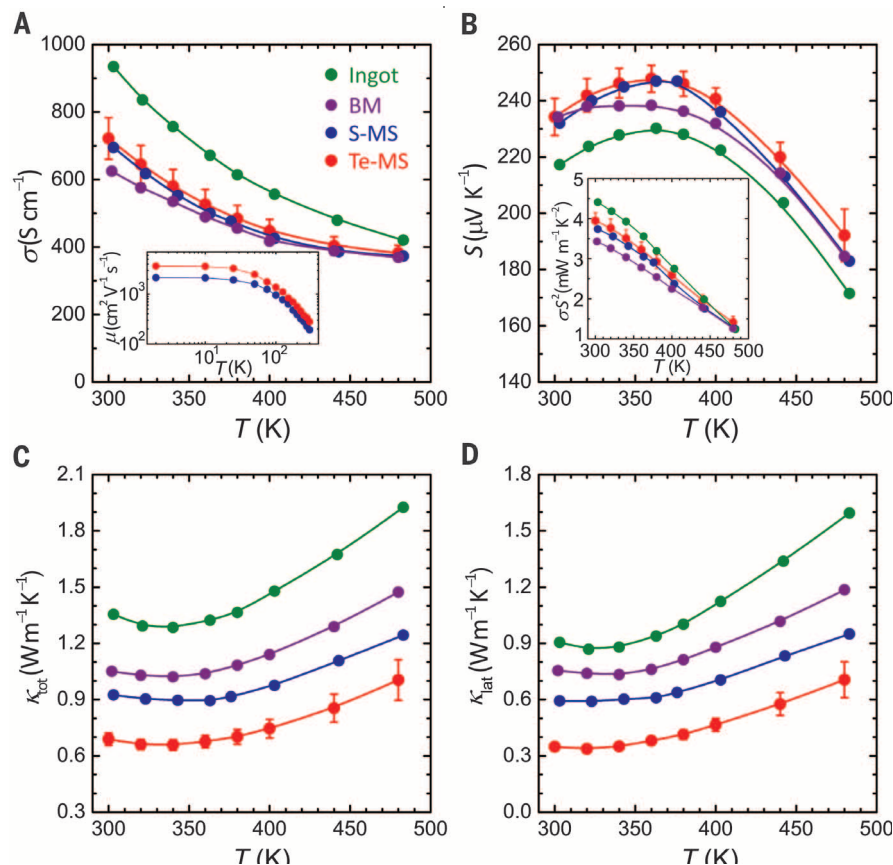
carrier mobility (μ) must be maintained because the maximum zT of a material is determined by the ratio μ/κ_{lat} (quality factor) (4). Thus, any reduction in κ_{lat} by phonon scattering must not be compensated by a similar reduction in μ due to electron scattering for there to be a net benefit (12).

Liquid-phase sintering produces low-energy, semicoherent grain boundaries that one can expect to have a minimal effect on electron scattering. The techniques to engineer and characterize grain boundaries have been well established in materials science due to their importance in engineering the mechanical strength (13), magnetism (14), and other material properties (15). Most importantly, the periodic dislocations that can arise from such low-energy grain boundaries add a new mechanism that targets the midfrequency phonons with both $\tau^{-1} \sim \omega$ and $\tau^{-1} \sim \omega^3$ dependence that is between those for point-defect and boundary scattering (4, 9). To produce the periodic dislocations at low-energy grain boundaries in Bi0.5Sb1.5Te3 alloys, we applied a simple liquid-phase compacting process. The process differed from typical liquid-phase sintering because it included applied pressure and transient flow of the liquid phase during compaction. The process greatly reduced κ_{lat} to

0.33 W m^{-1} K^{-1} at 320 K (Figs. 1B and 2D) and resulted in an exceptionally high zT of 1.86 ± 0.15 at 320 K for dozens of independently measured Bi0.5Sb1.5Te3 samples (Fig. 1C) used to make a Peltier cooling module with 127 couples (Fig. 1D). The module outperforms all known single-stage Peltier cooling modules (4, 16), demonstrating a ΔT_{max} of 81 K with T_h of 300 K (Fig. 1E). We compare ingot, ball-milled (BM), and stoichiometric melt-spun (S-MS) Bi0.5Sb1.5Te3 materials (Figs. 1 and 2) (17). The latter two types of samples were fabricated by using spark plasma sintering (SPS). Two different melt-spun materials were synthesized, stoichiometric (S-MS) and with excess Te (Te-MS) (Fig. 3A, red arrow).

Melt-spun samples have plate-like microstructure of S-MS and Te-MS ribbons with platelets several micrometers wide and several hundred nanometers thick (Fig. 3B and fig. S1, B to D) (17). The Te excess composition has an eutectic microstructure over the entire ribbon that forms between the Bi0.5Sb1.5Te3 platelets (Fig. 3B and fig. S1, C and D) (17). The eutectic phase consists mostly of elemental Te and a small amount of Bi0.5Sb1.5Te3 nanoparticles. During the high temperature (480°C) and pressure (70 MPa) process of SPS, above the melting point of Te (450°C), the

excess Te in the eutectic phase was liquidified and expelled to the outer surface of the graphite die (Fig. 3C and fig. S3) (17).

The morphology of the grain boundary structure in the Te-MS material is remarkably different than the typical grain boundaries as found in the S-MS material. Transmission electron microscopy (TEM) images (Fig. 4, B to J) reveal a Moiré pattern (up to 50 nm wide) at the grain boundaries between the Bi0.5Sb1.5Te3 grains in the Te-MS material (Fig. 4B), compared to the few nanometer width as observed in the S-MS material (Fig. 4A). Moiré patterns can be observed when the grain boundary plane is oblique to the TEM zone axis, so the two crystals overlap along the viewing direction. The Moiré patterns indicate that the grains are highly crystalline with clean grain boundaries in which the obscured dislocations exist. From the elemental mapping (TEM–energy-dispersive x-ray spectroscopy) in the Te-MS material, we confirmed no presence of excess Te at the grain boundaries (fig. S19), suggesting that the abnormal contrast is not due to a secondary phase.

The clean grain boundary structure observed in Te-MS material requires the presence of periodic arrays of dislocations that form at low-energy grain boundaries. Figure 4C shows a
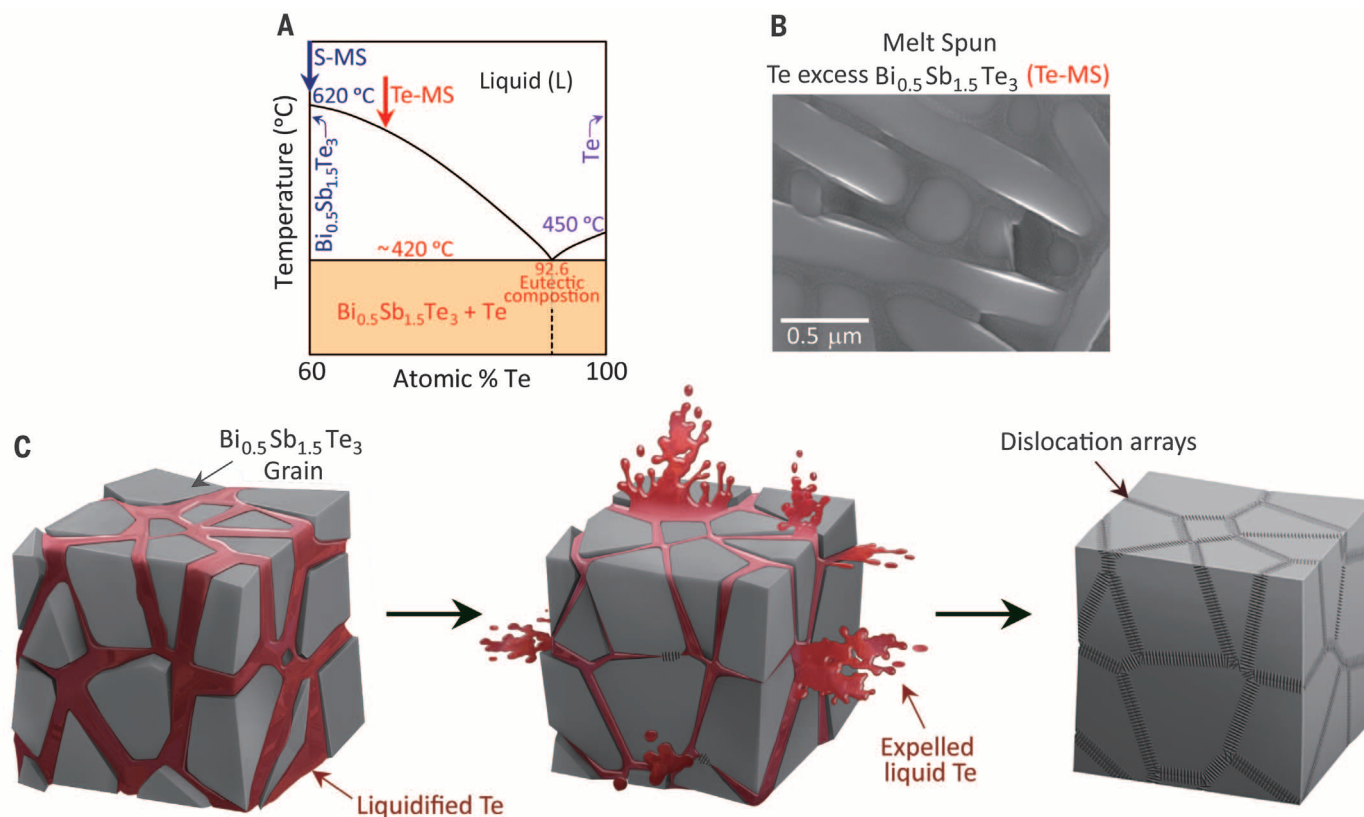
Fig. 3. Generation of dislocation arrays at grain boundaries in Bi0.5Sb1.5Te3. (A) Phase diagram of Bi0.5Sb1.5Te3–Te system showing an eutectic composition at 92.6 at % Te. Blue and red arrows indicate the nominal composition of melt-spun stoichiometric Bi0.5Sb1.5Te3 (S-MS) and 25 wt % Te excess Bi0.5Sb1.5Te3 (Te-MS) material. (B) The scanning electron microscope (SEM) image of melt-spun ribbon of Te-MS material showing the Bi0.5Sb1.5Te3 platelets surrounded by the eutectic phase of Bi0.5Sb1.5Te3–Te mixture, in which the Bi0.5Sb1.5Te3 particles (white spots) have the size of 10 to 20 nm. The SEM image of melt-spun ribbons of S-MS is shown in fig. S1B. (C) Schematic illustration showing the generation of dislocation arrays during the liquid-phase compaction process. The Te liquid (red) between the Bi0.5Sb1.5Te3 grains flows out during the compacting process and facilitates the formation of dislocation arrays embedded in low-energy grain boundaries.
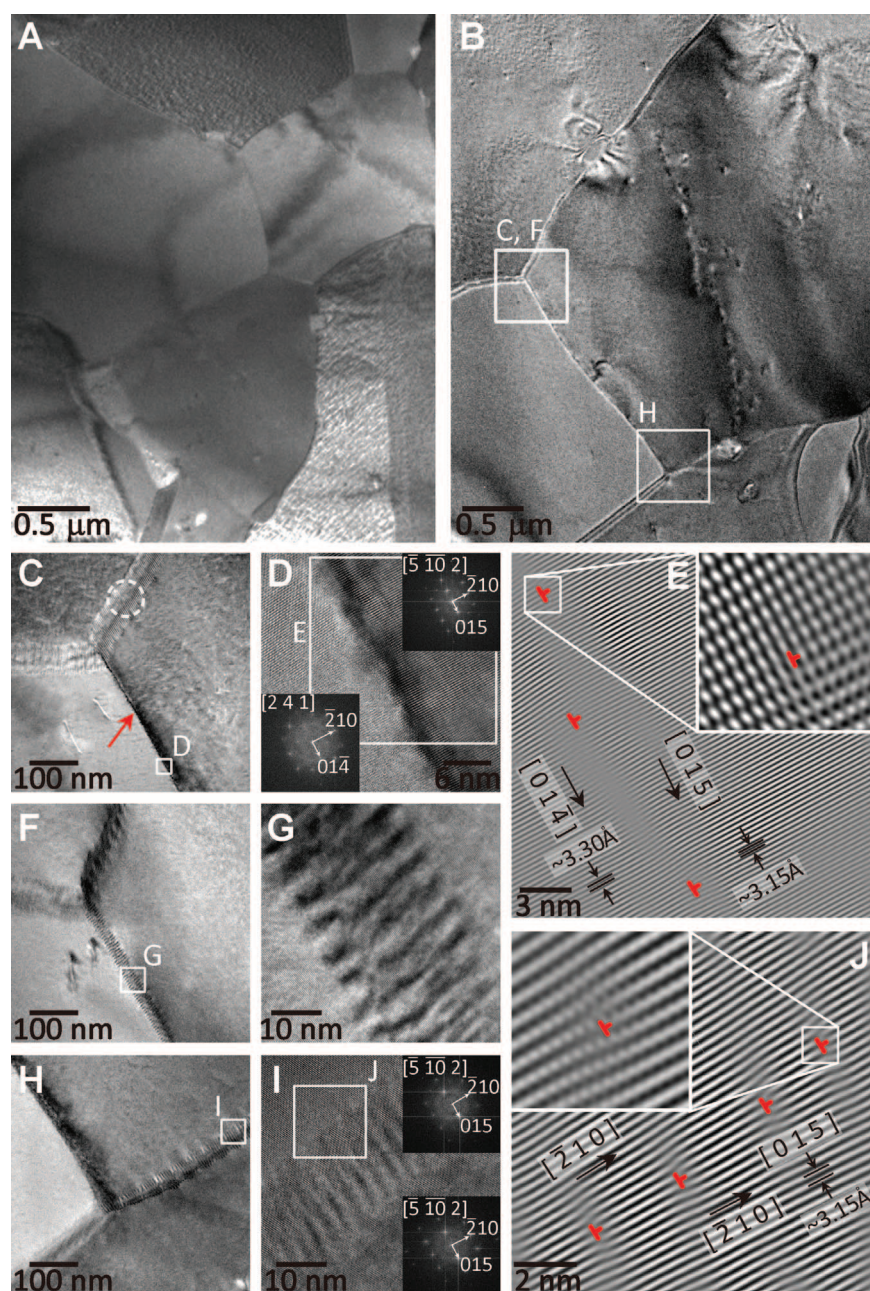
Fig. 4. Dislocation arrays embedded in grain boundaries. (**A**) Low-magnification TEM image of S-MS material. (**B**) Low-magnification TEM image of a Te-MS material. (**C**) Enlarged view of boxed region in (B). The grain boundary indicated by the red arrow is aligned along the zone axis showing only strain effects, whereas the two grain boundaries in the upper part show Moiré patterns. The high-magnification TEM image of circled area is shown in fig. S15. (**D**) Enlarged view of boxed region in (C). The insets are FFT images of adjacent grains crossing a twist-type grain boundary (GB). (**E**) IFFT image of (0 1 5) and (0 1 $\bar{4}$) atomic planes of left and right grains in the inset (D). Along the boundary, edge dislocations, indicated as red symbols, are clearly shown. Burgers vectors of each dislocation is $\mathbf{B_D}$ = <0 1 5>, parallel to the boundary. The misfit between the two planes is ~0.15 Å (~ 4.5%), which compensates the misfit spacing of ~6 nm and is identical to the periodic patterns (~6 nm spacing) in (F) and (G). (**F**) Enlarged view of boxed region in (B). A view of tilted zone axis from (C), showing periodic Moiré patterns along GBs. (**G**) Enlarged views of boxed region in (F). (**H**) Enlarged view of boxed region in (B). (**I**) Enlarged view of boxed region in (H). The insets are FFT images of adjacent grains crossing a tilt-type GB. Enlarged high-resolution TEM image of boxed region dislocation arrays is shown in fig. S18C. (**J**) FFT image of (0 1 5) atomic planes in the inset of (I). Burgers vectors of the each dislocation is $\mathbf{B_D}$ = <$\bar{2}$ 1 0>, perpendicular to the boundary. The misfit spacing of ~2.5 nm was obtained. Insets of (E) and (J) are the IFFT images of boxed areas, respectively, clearly identifying the dislocations. Other arrays of dislocations embedded in the low-angle grain boundary are shown in figs. S17 and S18.

grain boundary (indicated by red arrow) aligned along the zone axis showing only strain effects. The indexing of fast Fourier transform (FFT) images confirmed the coincidence of (0 1 $\bar{4}$) and (0 1 5) atomic planes along the two adjacent grains at the twist-type grain boundary with lattice spacing of 3.30 and 3.15 Å, respectively. Edge dislocation arrays are found in inverse FFT (IFFT) images of Fig. 4D (Fig. 4E, red symbols). The dislocations compensate for the d-spacing mismatch between the crystallographic planes of adjacent grains, which is ~0.15 Å (4.5%) between (0 1 5) and (0 1 $\bar{4}$) atomic planes, introducing misfit spacing of ~6 nm. This mismatch is identical, as expected (18) to the periodicity in the translational Moiré patterns of the grain boundary observed in Figs. 4, F and G, which were taken by slightly tilting the zone axis from that of Figs. 4, C and D. Dislocation arrays with the periodic spacing of ~2 nm were observed together with Moiré fringes at the circled area of the upper grain boundary in Fig. 4C (fig. S15). Another array of dislocations was observed in tilt-type boundary in Fig. 4H. The FFT images in the inset of Fig. 4I revealed the 5° misorientation between two adjacent grains and an inverse IFFT image of (0 1 5) atomic planes in Fig. 4J and dislocation arrays with the misfit spacing of ~2.5 nm (fig. S16C). Such dislocation arrays are expected to be present in low-angle grain boundaries or between grains with small d-spacing mismatch to lower the interfacial energy (19). The dislocation arrays observed here have a close spacing between cores of ~2.5 and 6 nm, which, considering the size of the grains, corresponds to an areal dislocation density of ~2×10^{11} cm^{-2} that is 100 times higher than that observed in grains of Bi$_2$Te$_3$ (20).

In a typical solid-phase sintering, the grain boundaries have random alignment due to a limited diffusion length of atoms/dislocations, and so the chance of low-angle boundary (<11°) is very low (19). In contrast, in liquid-phase sintering, the wetting liquid penetrates into the grain boundaries (21). Atoms in a liquid have much higher diffusivities and also dislocations at the grain boundaries have much higher diffusion lengths (22). The high solubility of Bi and Sb in the Te liquid and insignificant solubility of Te in the solid phase contributes to the very rapid mass transport (over 100 times faster than in solids) and rapid rearrangement of the grains (21). In addition, the capillary force of the liquid at the grain boundary exerts a force facilitating grain rearrangement (21, 23).

However, the liquid phase becomes absorbed in the matrix of the grain in a typical transient liquid-phase sintering, leading to compositional variation of the matrix. This prohibits the application of traditional liquid-phase sintering for thermoelectric Bi-Sb-Te because compositional variation will degrade the TE properties. In contrast, the liquidified excess Te in the eutectic phase is expelled during the high-pressure–assisted liquid-phase compacting processing. Any slight amount of Te remaining is nearly insoluble in Bi$_{0.5}$Sb$_{1.5}$Te$_3$ and does not as dramatically affect the carrier concentration. Furthermore, the applied pressure

induces additional stresses, which helps create dislocations (23) and accelerate grain rearrangement (21). As a result, the grain interfaces rearrange to allow low-energy grain boundaries, which results in dislocation arrays within much of the grain boundary.

From the thermal and electrical transport properties, it appears that the semicoherent grain boundaries of Te-MS material do maintain high charge-carrier mobility (17) but provide sufficient atomic strain to scatter heat-carrying phonons. The small increase in the Seebeck coefficient is due to a slight decrease in carrier concentration for S-MS and Te-MS materials compared with the ingot material (Fig. 2B). The reduced grain size of the S-MS and Te-MS materials leads to lower carrier mobility. This decrease is less dramatic for Te-MS indicating that the semicoherent grain boundaries in Te-MS are less disruptive to charge carriers than those in the S-MS material (Fig. 2A). Low-energy grain boundaries in Bi-Sb-Te are likely formed when atomic displacements are primarily in the Te-Te van der Waals layer, which have been observed experimentally (24). Displacements in this layer are also likely to be least disruptive to the charge carriers and maintain high mobility.

Although the dense dislocation arrays embedded in grain boundaries do little to scatter charge carriers, they are remarkably efficient at scattering phonons and greatly reducing thermal conductivity in the Te-MS material (Fig. 2D). The κ_{lat} values were extracted from κ_{tot} by subtracting the electronic thermal conductivity (κ_{ele}), which was estimated using the Wiedemann-Franz relation. We calculated the Lorenz number (L_0) using the reduced Fermi energy obtained from measured S values at different temperatures (17). The calculations indicate that dislocation arrays embedded in grain boundaries cause the reduction of κ_{lat}. The κ_{lat} value at 320 K (0.33 W m^{-1} K^{-1}) of the Te-MS sample is comparable to the reported value (0.29 W m^{-1} K^{-1}) in highly deformed Bi$_{0.2}$Sb$_{1.8}$Te$_3$ with high-density lattice defects (25), indicating that dense dislocation arrays at grain boundaries are effective to reduce the κ_{lat}.

We have modeled the temperature-dependent κ_{lat} of BM, S-MS and Te-MS materials based on the Debye-Callaway model (26) using parameters derived from independently measured physical properties (Fig. 1B) (17). The total phonon relaxation time (τ_{tot}) was estimated by including scattering from Umklapp processes (τ_U) and point defects (τ_{PD}) using parameters based on bulk alloys (9, 27, 28). We used microscopy to determine the parameter of average grain size (d) for the grain boundary scattering (τ_B) (17, 18). The calculated κ_{lat} (0.66 W m^{-1} K^{-1} at 300 K) for BM matches the measured data well, verifying the values used for Umklapp processes (τ_U) and point defects (τ_{PD}) of Bi$_{0.5}$Sb$_{1.5}$Te$_3$ alloys. The 18% reduction in κ_{lat} observed in S-MS material relative to BM material at 300 K is explained by a grain size reduction from 50 μm to 300 nm. The additional 29% reduction in κ_{lat} for Te-MS material is explained by introducing phonon relaxation times associated with additional scattering from dislocation cores (τ_{DC}) and strain (τ_{DS}) (29–31), using the experimentally

determined dislocation density (~2 × 10^{11} cm^{-2}) and the effective Burgers vector (B_D of ~12.7 Å).

This analysis shows that the periodic spacing of dislocation arrays plays a vital role for reducing κ_{lat}. When the spacing between dislocation cores is small, as observed in Te-MS material, the scattering from dislocation strain is reinforced (32). This effect was experimentally observed in Ag-Cd alloys with the large scattering effect as due to the dislocation pile-up (10). When dislocations are closely spaced, the effective Burgers vector (B_D) is the sum of the individual Burgers vectors involved (33). As the scattering rate is proportional to $B_D{}^2$ (17), this pile-up of dislocation strain leads to a nonlinear increase in scattering. The exact amount of reinforcement is not precisely specified in the theory and leads to the only adjustable parameter in the model. Nevertheless, the Burgers vector that precisely fits the data is well within the range observed experimentally (24).

The dislocation scattering mechanism is particularly effective because it targets phonons not scattered sufficiently by the other mechanisms providing a full-spectrum solution to scatter phonons. Compared with Umklapp scattering (Fig. 1A), boundary scattering from grain boundaries ($\tau_B{}^{-1} \sim \omega^0$) is efficient at scattering low-frequency phonons but quickly becomes ineffective at higher frequencies. Conversely, point defects scatter mostly high-frequency phonons ($\tau_{PD}{}^{-1} \sim \omega^4$). However, most of the remaining heat-carrying phonons have intermediate frequency around 0.63 THz (Fig. 1A). The 0.63 THz phonons still carry 74% of the heat that they would have carried without any scattering from boundaries or point defects in the S-MS material. Including the dislocation scattering as found in the Te-MS material, the κ_s of 0.63 THz phonons drops to less than 45% of the heat that they would have carried with only Umklapp scattering (Fig. 1A).

The low thermal conductivity while maintaining high mobility results in a dimensionless figure of merit (zT) for Te-MS that reaches a maximum value of 2.01 at 320 K within the range of 1.86 ± 0.15 at 320 K for 30 samples (Fig. 1C and fig. S9F), a much higher value than for S-MS or ingot materials. Most importantly, for cooling applications, the zT at 300 K is high (1.72 ± 0.12), suggesting that it should provide superior refrigeration than other materials. For example, the zT is higher than that of nanograined Bi$_{0.5}$Sb$_{1.5}$Te$_3$ alloy (dotted line in Fig. 1C) (7) near room temperature. This results from the ability of dislocation arrays to enable a full-spectrum scattering of phonons due to a compounding effect not found in randomly dispersed dislocations inside grains. The present liquid-phase compaction method assisted with a transient liquid flow is highly scalable for commercial use and generally applicable to other thermoelectric systems such as PbTe, CoSb$_3$, and Si-Ge alloys, and even engineer thermal properties of other thermal materials such as thermal barrier coatings (34). This may accelerate practical applications of thermoelectric systems in refrigeration and beyond to waste heat recovery and power generation.

The ultimate verification of the exceptional zT comes from testing the performance of a Peltier cooler (Fig. 1D) made using Te-MS materials. A state-of-the-art Peltier device using the Te-MS as the p-type material and an n-type ingot material made cutting-edge commercial methods (17). The device not only greatly outperforms a similar device made with the p- and n-type ingot materials (Fig. 1E) but also outperforms all commercial Peltier devices (16). We determined the coefficient of performance (COP) (cooling power divided by input power) to assess the cooling performance of both Peltier devices. A key characteristic performance metric of a Peltier cooler is ΔT_{max}, which is directly related to the zT of materials. The ΔT_{max} values are easily extracted from the COP measurements as the temperature difference reached when the cooling power vanishes. Although the ΔT_{max} of the Peltier cooler made from the ingot materials falls within the range of current commercial devices, 64 K < ΔT_{max} < 72 K for T_h of 300 K, the Peltier cooler made with the Te-MS p-type material exhibits a ΔT_{max} of 81 K for T_h of 300 K (Fig. 1E) (17).

REFERENCES AND NOTES

1. L. E. Bell, *Science* **321**, 1457–1461 (2008).
2. H. Scherrer, S. Scherrer, in *Thermoelectrics Handbook Macro to Nano*, D. M. Rowe, Ed. (CRC, Boca Raton, FL, 2006), chap. 27.
3. R. J. Buist, in *3rd International Conference on Thermoelectric Energy Conversion*, Arlington, Texas, 12 to 14 May 1980 (IEEE, New York, 1980), pp. 130–134.
4. H. J. Goldsmid, in *Electronic Refrigeration* (Pion, London, 1986), chaps. 2 and 7.
5. M. S. Dresselhaus *et al.*, *Adv. Mater.* **19**, 1043–1053 (2007).
6. D. L. Medlin, G. J. Snyder, *Curr. Opin. Colloid Interface Sci.* **14**, 226–235 (2009).
7. B. Poudel *et al.*, *Science* **320**, 634–638 (2008).
8. S. Fan *et al.*, *Appl. Phys. Lett.* **96**, 182104 (2010).
9. E. S. Toberer, A. Zevalkink, G. J. Snyder, *J. Mater. Chem.* **21**, 15843–15852 (2011).
10. P. G. Klemens, *Proc. Phys. Soc. A* **68**, 1113–1128 (1955).
11. P. Kim, L. Shi, A. Majumdar, P. L. McEuen, *Phys. Rev. Lett.* **87**, 215502 (2001).
12. H. Wang, A. D. LaLonde, Y. Pei, G. J. Snyder, *Adv. Funct. Mater.* **23**, 1586–1596 (2013).
13. M. Nader, F. Aldinger, M. J. Hoffmann, *J. Mater. Sci.* **34**, 1197–1204 (1999).
14. P. J. Jorgensen, R. W. Bartlett, *J. Appl. Phys.* **44**, 2876–2880 (1973).
15. S. Nazaré, G. Ondracek, F. Thümmler, in *Relations Between Stereometric Microstructure and Properties of Cermets and Porous Materials*, H. H. Hausner, Ed. (Springer, New York, 1971), pp. 171–186.
16. D. Zhao, G. Tan, *Appl. Therm. Eng.* **66**, 15–24 (2014).
17. Materials and methods are available as supplementary materials on *Science* Online.
18. D. B. Williams, C. B. Carter, *Transmission Electron Microscopy* (Springer, New York, 1996).
19. F. J. Humphreys, M. Hatherly, *Recrystallization and Related Annealing Phenomena* (Elsevier, Oxford, ed. 2, 2004).
20. N. Peranio, O. Eibl, *Phys. Status Solidi A* **206**, 42–49 (2009).
21. R. M. German, P. Suri, S. J. Park, *J. Mater. Sci.* **44**, 1–39 (2009).
22. C. Herzig, Y. Mishin, in *Diffusion in Condensed Matter*, P. Heitjans, J. Kärger, Eds. (Springer, Berlin, Heidelberg, 2005), chap. 8.
23. J. W. Cahn, Y. Mishin, A. Suzuki, *Acta Mater.* **54**, 4953–4975 (2006).
24. D. L. Medlin, K. J. Erickson, S. J. Limmer, W. G. Yelton, M. P. Siegal, *J. Mater. Sci.* **49**, 3970–3979 (2014).
25. L. P. Hu *et al.*, *NPG Asia Mater.* **6**, e88 (2014).
26. J. Callaway, H. C. von Baeyer, *Phys. Rev.* **120**, 1149–1154 (1960).

27. G. A. Slack, S. Galginaitis, *Phys. Rev.* **133** (1A), A253–A268 (1964).
28. M. Roufosse, P. G. Klemens, *Phys. Rev. B* **7**, 5379–5386 (1973).
29. J. He, S. N. Girard, M. G. Kanatzidis, V. P. Dravid, *Adv. Funct. Mater.* **20**, 764–772 (2010).
30. B. Abeles, *Phys. Rev.* **131**, 1906–1911 (1963).
31. D. T. Morelli, J. P. Heremans, G. A. Slack, *Phys. Rev. B* **66**, 195304 (2002).
32. D. J. H. Cockayne, I. L. F. Ray, M. J. Whelan, *Philos. Mag.* **20**, 1265–1270 (1969).
33. N. F. Mott, *Philos. Mag.* **43**, 1151–1178 (1952).
34. D. R. Clarke, S. R. Phillpot, *Mater. Today* **8**, 22–29 (2005).

STELLAR PHYSICS

Observing the onset of outflow collimation in a massive protostar

C. Carrasco-González,[1]* J. M. Torrelles,[2] J. Cantó,[3] S. Curiel,[3] G. Surcis,[4] W. H. T. Vlemmings,[5] H. J. van Langevelde,[4,6] C. Goddi,[4,7] G. Anglada,[8] S.-W. Kim,[9,10] J.-S. Kim,[11] J. F. Gómez[8]

The current paradigm of star formation through accretion disks, and magnetohydrodynamically driven gas ejections, predicts the development of collimated outflows, rather than expansion without any preferential direction. We present radio continuum observations of the massive protostar W75N(B)-VLA 2, showing that it is a thermal, collimated ionized wind and that it has evolved in 18 years from a compact source into an elongated one. This is consistent with the evolution of the associated expanding water-vapor maser shell, which changed from a nearly circular morphology, tracing an almost isotropic outflow, to an elliptical one outlining collimated motions. We model this behavior in terms of an episodic, short-lived, originally isotropic ionized wind whose morphology evolves as it moves within a toroidal density stratification.

W ater-vapor masers at 22 GHz are commonly found in star-forming regions, arising in the shocked regions created by powerful outflows from protostars in their earliest phases of evolution (*1*). Observations of these masers with very long baseline interferometry (VLBI) indicate that at the early life of massive stars, there may exist episodic, short-lived (tens of years) events associated with very poorly collimated outflows (*2*–*5*). These results are surprising because, according to the core-accretion model for the formation of massive stars ($\geq 8 M_\odot$), which is a scaled-up version of low-mass star formation, collimated outflows are already expected at their very early phases (*6*–*8*).

[1]Centro de Radioastronomía y Astrofísica UNAM, Apartado Postal 3-72 (Xangari), 58089 Morelia, Michoacán, Mexico. [2]Institut de Ciències de l'Espai (CSIC) and Institut de Ciències del Cosmos (UB)/Institut d'Estudis Espacials de Catalunya, Calle Martí i Franquès 1, 08028 Barcelona, Spain. [3]Instituto de Astronomía (UNAM), Apartado 70-264, 04510 Mexico D.F., Mexico. [4]Joint Institute for VLBI in Europe, Postbus 2, 79990 AA Dwingeloo, Netherlands. [5]Chalmers University of Technology, Onsala Space Observatory, SE-439 92 Onsala, Sweden. [6]Sterrewacht Leiden, Leiden University, Postbus 9513, 2300 RA Leiden, Netherlands. [7]Department of Astrophysics, Institute for Mathematics, Astrophysics and Particle Physics, Radboud University, Post Office Box 9010, 6500 GL Nijmegen, Netherlands. [8]Instituto de Astrofísica de Andalucía (CSIC), Apartado 3004, 18080 Granada, Spain. [9]Korea Astronomy and Space Science Institute, 776 Daedeokdaero, Yuseong, Daejeon 305-348, Republic of Korea. [10]Korea University of Science and Technology, 217 Gajeong-ro Yuseong-gu, Daejeon 305-350, Republic of Korea. [11]National Astronomical Observatory of Japan, 2-21-1 Osawa, Mitaka, Tokyo 181-8588, Japan.
*Corresponding author: E-mail: carrasco@crya.unam.mx

A unique case of a short-lived, poorly collimated outflow is the one found in the high-mass star-forming region W75N(B). This region contains two massive protostars, VLA 1 and VLA 2, separated by ≤ 0.7 arc sec [projected separation of ≤ 910 astronomical units (AU) at the source distance of 1.3 kpc; (*9*)], both associated with strong water-vapor maser emission at 22 GHz (*10*, *11*), and with a markedly different outflow geometry. At epoch 1996, VLA 1 shows an elongated radio continuum emission consistent with a thermal radio jet, as well as water maser emission tracing a collimated outflow of ~1300 AU along its major axis. In contrast, in VLA 2, the water masers traced a shock-excited shell of ~185 AU diameter radially expanding with respect to a central, compact radio continuum source (≤ 0.12 arc sec, ≤ 160 AU) of unknown nature (*12*). A monitoring of the water masers toward these two objects from 1996 to 2012 shows that the masers in VLA 1 display a persistent linear distribution along the major axis of the radio jet. In the case of VLA 2, we observe that the water maser shell continues its expansion at ~30 km s^{-1} 16 years after its first detection. More important, the shell has evolved from an almost circular structure (~185 AU) to an elliptical one (~354 × 190 AU) oriented northeast-southwest, along a direction similar to that of the nearby VLA 1 radio jet (*13*, *14*) (fig. S1) and of the ordered large-scale (2000 AU) magnetic field observed in the region (*15*). The estimated kinematic age for the expanding shell is ~25 years, indicating that it is driven by a short-lived, episodic outflow

event. Moreover, our polarization measurements of the water maser emission show that whereas the magnetic field around VLA 1 has not changed over time, the magnetic field around VLA 2 changed its orientation, following the direction of the major axis of the water maser elliptical structure. That is, it now shares a similar northeast-southwest orientation with those of both the magnetic field around VLA 1 and the large-scale magnetic field in the region (*14*, *15*) (fig. S1).

All these observations suggest that we are observing in "real time" the transition from an uncollimated outflow to a collimated outflow during the early life of a massive star. This scenario predicts that, within the same time span of the evolution of the shell, VLA 2 must have also evolved from a compact radio continuum source to an extended elongated source along the major axis of the water maser shell. Furthermore, the radio continuum emission of VLA 2 should have physical properties (e.g., spectral energy distribution, size of the source as a function of frequency) characteristic of free-free emission from a thermal, collimated ionized wind (*16*, *17*). This can be tested through continuum observations at centimeter wavelengths that usually trace the emission from collimated, ionized winds (*17*, *18*).

Taking advantage of the high sensitivity and high angular resolution of the Jansky Very Large Array (VLA) at centimeter wavelengths, we obtained new observations in 2014 at several bands in the frequency range from 4 to 48 GHz (*19*). These highly sensitive observations confirmed the expected scenario proposed above. The source VLA 2 is detected at all bands. In the images of higher-frequency bands [U (~15 GHz), K (~23 GHz), and Q (~44 GHz)], which have higher angular resolutions (~0.1 to 0.2 arc sec), the source VLA 2 appears clearly elongated in the northeast-southwest direction (Fig. 1). Water maser emission was also observed simultaneously with the K band continuum emission (*19*), allowing a very accurate alignment (better than ~1 milli–arc sec) between the masers and the continuum emission. We find that the elongation of the continuum emission is in good agreement with that of the water maser distribution (Fig. 1).

Comparison of the radio continuum emission of VLA 2 at K band between epochs 1996 (*10*) and 2014 is shown in Fig. 2. Whereas in 1996 the emission was compact, in 2014 we observed extended emission in the northeast-southwest direction. In particular, the core of the radio continuum emission of VLA 2 has evolved from a compact source in 1996 (≤ 160 AU) to an elongated core with a full width at half-maximum (FWHM) of

~220 AU × ≲160 AU (position angle ≅ 65°) in 2014. This evolution is consistent with those of the expanding water maser shell and of the magnetic field over the same time span (fig. S1) (14). This core elongation is clearly seen in all the images that we have made by weighting the interferometer uv data in different ways, from natural to uniform (19) (fig. S2). In addition, we also found that the VLA 2 source exhibits weak extended emission at distances of ~390 AU southwest from the peak position, which was not detected in 1996. Because the sensitivity attained in our 2014 observations (~10 μJy beam^{-1}) is a factor of ~15 better than in 1996 (~150 μJy beam^{-1}), it is plausible that the weak extended emission was already present in 1996 but not detected because of the lower sensitivity in those observations. That the peak intensity of VLA 2 has significantly decreased from 1996 to 2014, while total flux densities in both epochs have remained similar (table S3), rather suggests that the radio continuum emission from VLA 2 arises from a larger, more elongated structure in the 2014 epoch (see model below). In addition, the distribution of the water masers follows the observed morphology of the continuum emission at both epochs (Fig. 2), indicating that they trace a molecular shell surrounding the radio continuum source. We also considered the possibility that the extended radio continuum emission in 2014 is actually the signature of a new variable protostar. Nevertheless, this hypothesis is rendered unlikely by the spatial coincidence of this new radio continuum emission with VLA 2.

As a result of the wide bandwidths provided by the VLA, we performed an analysis of the behavior of the flux density and of the size of the major axis of VLA 2 with frequency (19) (table S3 and fig. S4). This analysis was carried out only at U, K, and Q bands, whose high angular resolution allows us to completely isolate the emission of VLA 2 from the other sources in the field. We find that the flux density (S_ν) at the lowest observed frequencies (U and K bands) is dominated by free-free emission with a spectral index $\alpha_{ff} \cong 0.61$ ($S_\nu \propto \nu^{\alpha_{ff}}$). Moreover, we also find that the size of the major axis of VLA 2 (θ) decreases with frequency as a power law (θ ∝ ν^β), with an exponent β ≅ −0.7. The behavior of both the flux density and the size of the major axis of VLA 2 is in good agreement with what is expected from a thermal, collimated, and ionized wind (16, 17). The presence of water maser emission and the detection of shock-excited SiO emission highly concentrated toward this source (20) further support a very fast wind interaction region rather than an HII region. The VLA 2 wind could contribute, together with the winds from the other young stellar objects (YSOs) in the region, to the large-scale (~2 pc) molecular outflow observed in the W75N(B) star-forming region (21).

At the highest observed frequencies (Q band), the emission deviates by ~30% from the expected flux densities of the ionized wind at these frequencies, showing in addition a steeper spectral index that can be easily explained by the presence of thermal dust emission. The presence of thermal dust emission at frequencies higher than 40 GHz is commonly found in protostars and is related to the presence of a dusty circumstellar disk around the protostar and/or to a dusty envelope. Our data suggest that the spectral index of the dust component in the observed wavelength range is $\alpha_{dust} \cong 3$ to 4 (fig. S4), a value similar to what is commonly found in massive protostars (22, 23).

In summary, our observations reveal that the radio continuum source VLA 2 has evolved in only 18 years from being a compact source to become an elongated source in the same direction as that of the water maser shell and the magnetic field. Moreover, the characteristics of the continuum emission and the distribution of the water masers in VLA 2 are now consistent with a thermal, collimated ionized wind, surrounded by a dusty disk or envelope. We interpret these results in terms of the evolution of an episodic, short-lived, originally isotropic ionized wind interacting with a toroidal environmental density stratification.

The interaction of a wind with the surrounding environment produces a two-shock structure that travels away from the star. The outer shock accelerates the environment, whereas the inner shock decelerates the wind. For young stars with moderate wind velocities (a few hundred km s^{-1}), both the inner and outer shocks are, in general, radiative and result in the formation of a thin expanding shell bounded by the two shocks. In (24), we model this scenario for the case of a steady isotropic wind with mass loss rate $\dot{M}_w$ and terminal velocity V_w, surrounded by a torus of dense material with a density distribution of the form $\rho(R,\theta) = \rho_0/(1+[R/R_c(\theta)]^2)$. R is the distance from the star; $R_c(\theta) = R_0(1 + p\sin^2\theta)$ is the latitude-dependent radial size of the core, with θ the polar angle measured from the symmetry axis of the torus; ρ_0 is the density of the molecular core; and p is related to the density contrast between the equator (θ = π/2) and the pole (θ = 0) of the toroidal environment. This density distribution implies that for $R \ll R_c$ the density is nearly uniform, that is, independent of direction and radial size, whereas for $R \gg R_c$ the density decreases as $1/R^2$, which is the behavior of the density of self-gravitating isothermal spheres at large distances.

Our model (24) shows that at small radii ($R \ll R_c$), the shell grows isotropically (with no angular dependence), the initial velocity of the expanding shell is the velocity of the wind, and the shell decelerates owing to the incorporation of environmental material with zero velocity. The expansion at large radii ($R \gg R_c$) has two important
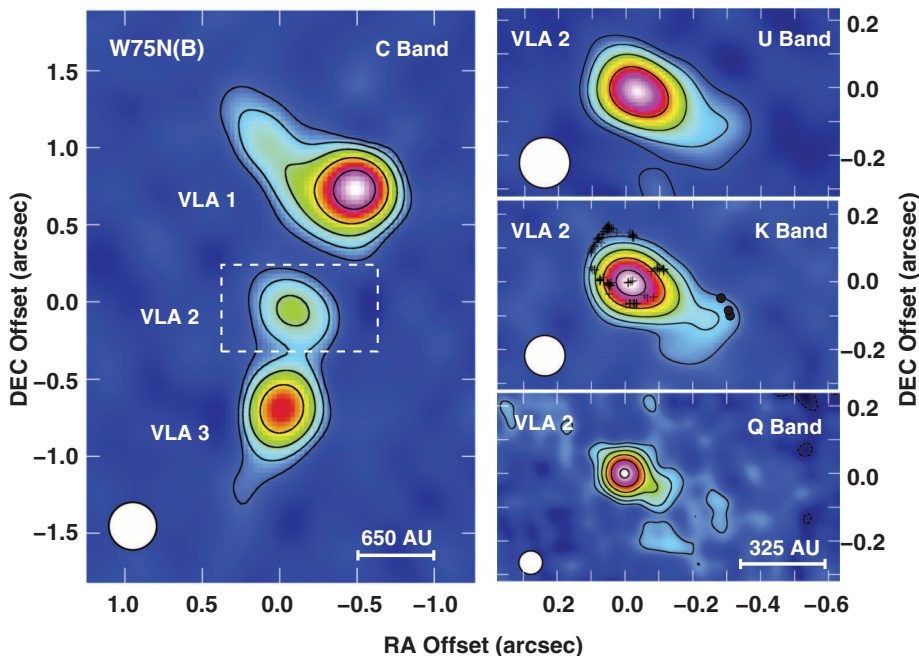
Fig. 1. Radio continuum maps of the core of W75N(B) star-forming region obtained with the VLA in 2014 at several bands (C, U, K, and Q). Left panel shows the C band (5 GHz) image of the region enclosing the sources VLA 1, 2, and 3. Right panels show close-ups to the VLA 2 source at U (15 GHz), K (23 GHz), and Q (43 GHz) bands. In the K band panel, we also show the positions of the water masers (plus symbols) observed simultaneously to the K band continuum, as well as the methanol masers (black dots). As seen in the right panels, VLA 2 appears elongated at all frequencies. This elongation is similar to that of the maser distribution. Contours are 4, 8, 16, 32, 64, and 128 times the root mean square (RMS) of each map: 30 μJy beam^{-1} (C band), 11 μJy beam^{-1} (U band), 10 μJy beam^{-1} (K band), and 12 μJy beam^{-1} (Q band). The restoring circular beam of each map (shown in the bottom left corner) is 0.31″, 0.15″, 0.12″, and 0.07″ for C, U, K, and Q band, respectively (0.1″ ≅ 130 AU at the source distance of 1.3 kpc). In all panels, the absolute position of the (0,0) is at right ascension RA(J2000) = 20^{h}38^{m}36.486^s and declination DEC (J2000) = +42°37′34.09″ (±0.03″), the peak position of VLA 2 at Q band, where the massive protostar is expected to be located. The accuracy in the relative positions of the water and methanol masers with respect to the K band continuum is better than ~1 and ~ 30 milli–arc sec, respectively (19).

Fig. 2. Comparison of the K band continuum emission of VLA 2 in epochs 1996 (top) and 2014 (bottom). The (0,0) position is the same as in Fig. 1. Contours are 30, 40, 50, 60, 70, 80, and 90% of the peak intensity in 1996 (1.42 mJy beam^{-1}) (RMS = 150 μJy beam^{-1}), and 5, 10, 20, 30, 40, 50, 60, 70, 80, and 90% of the peak intensity in 2014 (0.82 mJy beam^{-1}) (RMS = 10 μJy beam^{-1}). Both maps were obtained with the same restoring circular beam of 0.12″ (shown in the bottom left corner of each panel). In both panels, the half-power level is shown as a dashed line. We also show the water maser positions (plus symbols) for epochs 1996 and 2014 as observed with the VLA by (10) and this work, respectively. The position of the methanol masers for epoch 2014 (black dots; this work) are also indicated. The FWHM size of the radio continuum emission has evolved from a compact source into an elongated source in the northeast-southwest direction, in a direction similar to that of the observed evolution of the water maser shell and magnetic field in VLA 2 (14) (fig. S1).

Fig. 3. Evolution of an isotropic ionized wind driving the shock-excited water maser shell and that interacts with a toroidal environmental density stratification (24). The model predicts an initial round shell, evolving into an elongated shell that expands faster along the symmetry axis of the torus. Here we represent density isocontours of the toroidal environment (blue contours) for values ρ/ρ$_0$ = 0.1, 0.3, 0.5, 0.7, and 0.9 [Eqs. E1 and E2 with p = 5; see (24)]. The spatial evolution of the shell as a function of time t after the initial ejection of the wind (red contours) is shown for values t/t_0 = 1, 5, 10, 20, 30, and 40 with t_0 = 0.5 years [adopting V_w = 250 km s^{-1} and R_0 = 28 AU from (24)].
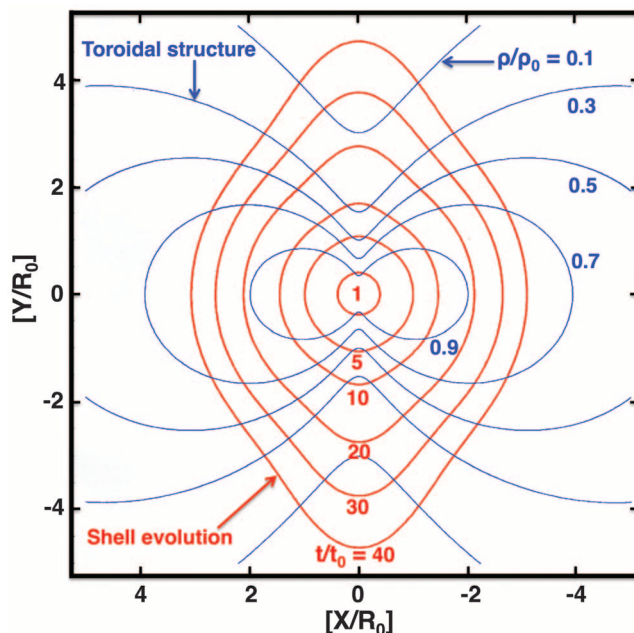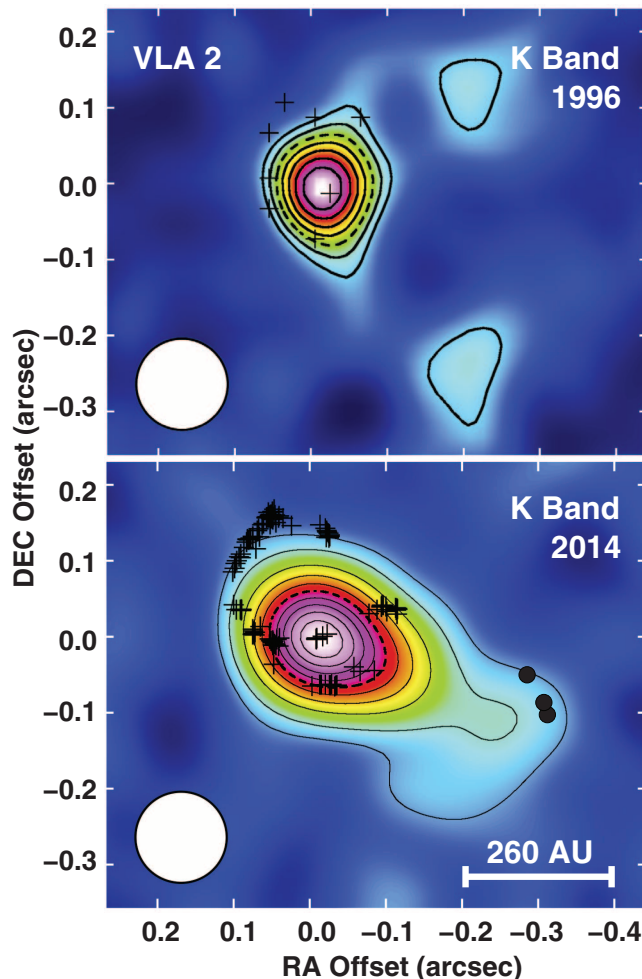
physical characteristics. First, there is a strong angular dependence of the expansion velocity of the shell, being much larger along the symmetry axis of the torus than along its equator; and second, this expansion velocity asymptotically tends to an angular-dependent constant value. Thus, this isotropic wind + torus model can explain the distinctive characteristics of our radio continuum and water maser observations (the transition from a nearly spherical outflow to a collimated, elongated one over a short period of time and the expansion of the masers at constant velocity), because the shell tends to expand faster along the symmetry axis of the surrounding torus (Fig. 3).

In our model (24) (Fig. 3), we identify the semi-major axis of the water maser shell reported at different epochs by (14) with the evolution of the shell radius along the symmetry axis of the surrounding torus (θ = 0), and the semi-minor axis of the water maser shell with the shell size along the equator (θ = π/2). Taking this into account, and assuming that the radio continuum source VLA 2 traces the emission of the ionized wind that drives the shell, we can find a range of possible physical values to fit the observations. In particular, we obtain values for the mass loss rate and terminal wind velocity of $\dot{M}_w \cong (4 \text{ to } 11) \times 10^{-7} M_\odot$ year^{-1} and $V_w \cong 110$ to 350 km s^{-1}, respectively. In addition, for the initial epoch of ejection of the wind, we found $t_i \cong 1984$ to 1985, with uniform density core radial size $R_0 \cong 26$ to 29 AU and particle density $n_0 \cong (4 \text{ to } 6) \times 10^7$ cm^{-3}.

All the parameters estimated by our model match those expected for a massive protostar embedded in a high-density environment. Furthermore, from the thermal dust emission at 7 mm (after removal of the free-free contamination), we roughly estimate a total (dust + gas) mass of $\gtrsim 0.001 M_\odot$ (19). This mass corresponds to an average particle density of $\gtrsim 2 \times 10^7$ cm^{-3} in a region of ~0.2 arc sec (the maximum size of the region where we detect 7-mm continuum emission; Fig. 1). Within the uncertainties of the estimates (19), we find that these values are consistent with the parameters of the toroidal gas structure.

Our data do not allow us to determine what the morphology of the radio continuum emission was like at scales ≲0.1 arc sec in 1996. In particular, we cannot rule out that the source was already slightly elongated, with a size smaller than the beam, in 1996. However, 1996 corresponds to an epoch ~10 years after the estimated launch time (1983 to 1984). According to our model, with that time interval, some deviation from an originally spherical wind should already be expected (Fig. 3). The combination of all our radio continuum results, together with other important available data, can provide a coherent scenario for this source. Our scenario proposes a change in the collimation of the wind, from a poorly collimated outflow (maybe initially spherical) to a highly collimated wind, and this is consistent with all the available data: a compact continuum source and water masers poorly collimated in 1996, an elongated radio continuum source, and collimated water masers in 2014. We can then affirm that a change in the collimation of the wind has taken place in this

time span. We also find that the ionized wind, the water maser shell, and the magnetic field in VLA 2 (at scales of a few hundred AU) have all evolved spatially in the same sense, sharing now a similar northeast-southwest orientation. This is similar to the orientation of the magnetic field in the neighboring radio jet VLA 1 and of the "large-scale" (~2000 AU) magnetic field in the region (*14*, *15*). Therefore, the magnetic field at these "large scales" might control the formation of both objects (VLA 1 and VLA 2). In particular, we think that the magnetic field could have favored the formation of the toroidal gas structure around VLA 2, with its symmetry axis also oriented northeast-southwest, as in our model.

The proposed scenario can thus explain the singular evolution of an episodic, short-lived (~30 years), originally noncollimated outflow, traced by the water masers, into a collimated outflow by its interaction with the ambient medium. Our observations and modeling reveal that the collimation of these short-lived outflow events from massive protostars occurs at relatively large distances from the central star, at radii between ~30 AU (the radial size obtained from our model for the initial expansion of the shell) and ~100 AU (the radius where the expanding shell turned out from a round to an elliptical shape; fig. S1) [see also (*25*, *26*)]. These scales are on the order of those predicted for poorly collimated outflows in magnetized, massive collapsing cores during the very early stages (~10^3 to 10^4 years), according to the magnetohydrodynamic simulations developed by (*27*). However, these simulations can only produce relatively low-velocity (~10 km s^{-1}), poorly collimated outflows, which seem still insufficient to explain the larger wind velocities (≥100 kms^{-1}) needed to drive the expanding motions of the shock-excited water maser shell in VLA 2. We also considered the scenario in which a very young spherical compact HII region embedded in an accretion disk begins to expand, following the model in (*28*). In this model, the HII region evolves to a bipolar morphology along the symmetry axis of the accretion disk, producing a wind driven by the thermal pressure of the ionized gas. However, the relatively low velocity of that wind (≲30 km s^{-1}) (*26*) seems also insufficient to shock excite and drive the expanding water maser shell.

In summary, although episodic, short-lived outflows in massive protostars are probably related to episodic increases in the accretion rates, as observed in low-mass star formation (*29*), the origin of poorly collimated outflows with relatively high velocities, as observed in VLA 2, deserves further theoretical research. Our observations show the "real time" evolution of such an originally poorly collimated outflow into a collimated one. This opens a new, exciting window of opportunity to study how the basic ingredients of star formation (e.g., molecular outflow, ionized wind, magnetic field) evolve over the next few years, providing insights that may have important implications for our knowledge of the early stages of high-mass star formation. We may be on the brink of describing and modeling in "real time" all of these rapid changes.

REFERENCES AND NOTES

1. D. Hollenbach, M. Elitzur, C. F. McKee, *Astrophys. J.* **773**, 70 (2013).
2. J. M. Torrelles *et al.*, *Nature* **411**, 277–280 (2001).
3. G. Surcis *et al.*, *Astron. Astrophys.* **527**, A48 (2011).
4. J. M. Torrelles *et al.*, *Mon. Not. R. Astron. Soc.* **410**, 627–640 (2011).
5. L. Moscadelli, C. Goddi, R. Cesaroni, M. T. Beltrán, R. S. Furuya, *Astron. Astrophys.* **472**, 867–879 (2007).
6. G. Garay, S. Lizano, *Publ. Astron. Soc. Pac.* **111**, 1049–1087 (1999).
7. C. F. McKee, J. C. Tan, *Astrophys. J.* **585**, 850–871 (2003).
8. J. M. Girart, M. T. Beltrán, Q. Zhang, R. Rao, R. Estalella, *Science* **324**, 1408–1411 (2009).
9. K. L. J. Rygl *et al.*, *Astron. Astrophys.* **539**, A79 (2012).
10. J. M. Torrelles *et al.*, *Astrophys. J.* **489**, 744–752 (1997).
11. D. S. Shepherd, S. E. Kurtz, L. Testi, *Astrophys. J.* **601**, 952–961 (2004).
12. J. M. Torrelles *et al.*, *Astrophys. J.* **598**, L115–L119 (2003).
13. J.-S. Kim *et al.*, *Astrophys. J.* **767**, 86 (2013).
14. G. Surcis *et al.*, *Astron. Astrophys.* **565**, L8 (2014).
15. G. Surcis, W. H. T. Vlemmings, R. Dodson, H. J. van Langevelde, *Astron. Astrophys.* **506**, 757–761 (2009).
16. S. P. Reynolds, *Astrophys. J.* **304**, 713 (1986).
17. L. F. Rodríguez *et al.*, *Astrophys. J.* **430**, L65 (1994).
18. G. Anglada *et al.*, *Astron. J.* **116**, 2953–2964 (1998).
19. See supplementary materials on *Science* Online
20. Y. C. Minh *et al.*, *Astrophys. J.* **723**, 1231–1240 (2010).
21. D. S. Shepherd, L. Testi, D. P. Stark, *Astrophys. J.* **584**, 882–894 (2003).
22. M. Osorio, S. Lizano, P. D'Alessio, *Astrophys. J.* **525**, 808–820 (1999).
23. L. T. Maud, M. G. Hoare, A. G. Gibb, D. Shepherd, R. Indebetouw, *Mon. Not. R. Astron. Soc.* **428**, 609–624 (2013).
24. See section E in supplementary materials on *Science* Online
25. L. D. Matthews *et al.*, *Astrophys. J.* **708**, 80–92 (2010).
26. L. J. Greenhill, C. Goddi, C. J. Chandler, L. D. Matthews, E. M. L. Humphreys, *Astrophys. J.* **770**, L32 (2013).
27. D. Seifried, R. E. Pudritz, R. Banerjee, D. Duffin, R. S. Klessen, *Mon. Not. R. Astron. Soc.* **422**, 347–366 (2012).
28. E. Keto, *Astrophys. J.* **666**, 976–981 (2007).
29. J. M. Torrelles *et al.*, *Mon. Not. R. Astron. Soc.* **442**, 148–159 (2014).

VIROLOGY

Mutation rate and genotype variation of Ebola virus from Mali case sequences

T. Hoenen,[1]* D. Safronetz,[1]* A. Groseth,[1]* K. R. Wollenberg,[2]* O. A. Koita,[3] B. Diarra,[3] I. S. Fall,[4] F. C. Haidara,[5] F. Diallo,[5] M. Sanogo,[3] Y. S. Sarro,[3] A. Kone,[3] A. C. G. Togo,[3] A. Traore,[5] M. Kodio,[5] A. Dosseh,[6] K. Rosenke,[1] E. de Wit,[1] F. Feldmann,[7] H. Ebihara,[1] V. J. Munster,[1] K. C. Zoon,[8] H. Feldmann,[1]†‡ S. Sow[5]†‡

The occurrence of Ebola virus (EBOV) in West Africa during 2013–2015 is unprecedented. Early reports suggested that in this outbreak EBOV is mutating twice as fast as previously observed, which indicates the potential for changes in transmissibility and virulence and could render current molecular diagnostics and countermeasures ineffective. We have determined additional full-length sequences from two clusters of imported EBOV infections into Mali, and we show that the nucleotide substitution rate (9.6 × 10^{-4} substitutions per site per year) is consistent with rates observed in Central African outbreaks. In addition, overall variation among all genotypes observed remains low. Thus, our data indicate that EBOV is not undergoing rapid evolution in humans during the current outbreak. This finding has important implications for outbreak response and public health decisions and should alleviate several previously raised concerns.

I n December 2013, an outbreak of Ebola virus (EBOV) started in Guinea with a single index case, resulting in widespread human-to-human transmission in this country, as well as in neighboring regions of Sierra Leone and Liberia. Despite being by far the largest and longest-lasting outbreak, there has been limited information regarding the evolution of EBOV. To date, the only sequences published have been from virus isolates derived from three patient samples in Guinea from March 2014 (*1*) and from a cluster of sequences derived from samples from Sierra Leone from June 2014 (*2*). However, no new information has been available during the intervening 6 months of large-scale virus circulation, and thus these virus sequences may no longer adequately inform us about the nature of currently circulating strains. This is of particular importance because diagnostics

are based predominantly on reverse transcription polymerase chain reaction (3) and are thus sequence-dependent, as are some of the therapeutic options currently being considered for deployment (i.e., small interfering RNA–based treatments, such as TKM-Ebola). Further, mutations in the glycoprotein (GP) could affect the efficacy of vaccines or antibody treatments (e.g., ZMapp). Analyses based on the limited available sequence information have also been used to suggest that EBOV is mutating more rapidly during this outbreak than during previous outbreaks (2), potentially as a result of sustained and large-scale human-to-human transmission, which has, in turn, raised concerns about increased virulence or transmissibility (4).

Although the outbreak has been mostly limited to Guinea, Sierra Leone, and Liberia until now, there have been imported cases in Nigeria, Senegal, Spain, and the United States, without substantial subsequent spread of the virus. Recently, two independent introductions of EBOV into Mali also occurred: The first introduction in October 2014, from Kissidougou, Guinea, resulted in a single fatal case with no further transmission; the second introduction in November 2014, from Kouremale-Guinee, Guinea, resulted in six primary transmissions (five fatal, one nonfatal) and a single secondary transmission (nonfatal). We obtained patient samples from both introductions and determined the full-length sequences of the corresponding EBOV genomes [see (5) for materials and methods]. Surprisingly, the virus from the first introduction (hereafter referred to as "Mali-DPR1," sampled 23 October 2014) showed only nine nucleotide differences from the most closely related virus (Makona-EM106, accession number KM233036), which was sampled in Sierra Leone almost 6 months earlier (2 June 2014). Additionally, Mali-DPR1 showed only 15 nucleotide differences from the most distantly related EBOV from the West African outbreak (Gueckedou-C05, accession number KJ660348.2) (fig. S1). In terms of amino acids, only one change had been acquired in comparison to the Makona-EM106 virus [g16514a:S>N (6) at position 1645 in the polymerase (L) gene] (fig. S1). The viruses isolated from the second introduction into Mali (hereafter referred to as "Mali-DPR2, -3, and -4," sampled 12 to 21 November) were closely related

to Mali-DPR1, although they remained clearly distinct from that sequence, with seven to nine nucleotide differences. However, in terms of amino acid sequence, only a single change (t15560c:F>S at position 1327 in the L gene) was observed in

Mali-DPR4, and no amino acid changes were observed in Mali-DPR2 and -3.

Phylogenetic analysis (5) of all published sequences showed that the West African sequences group into several well-supported clades that
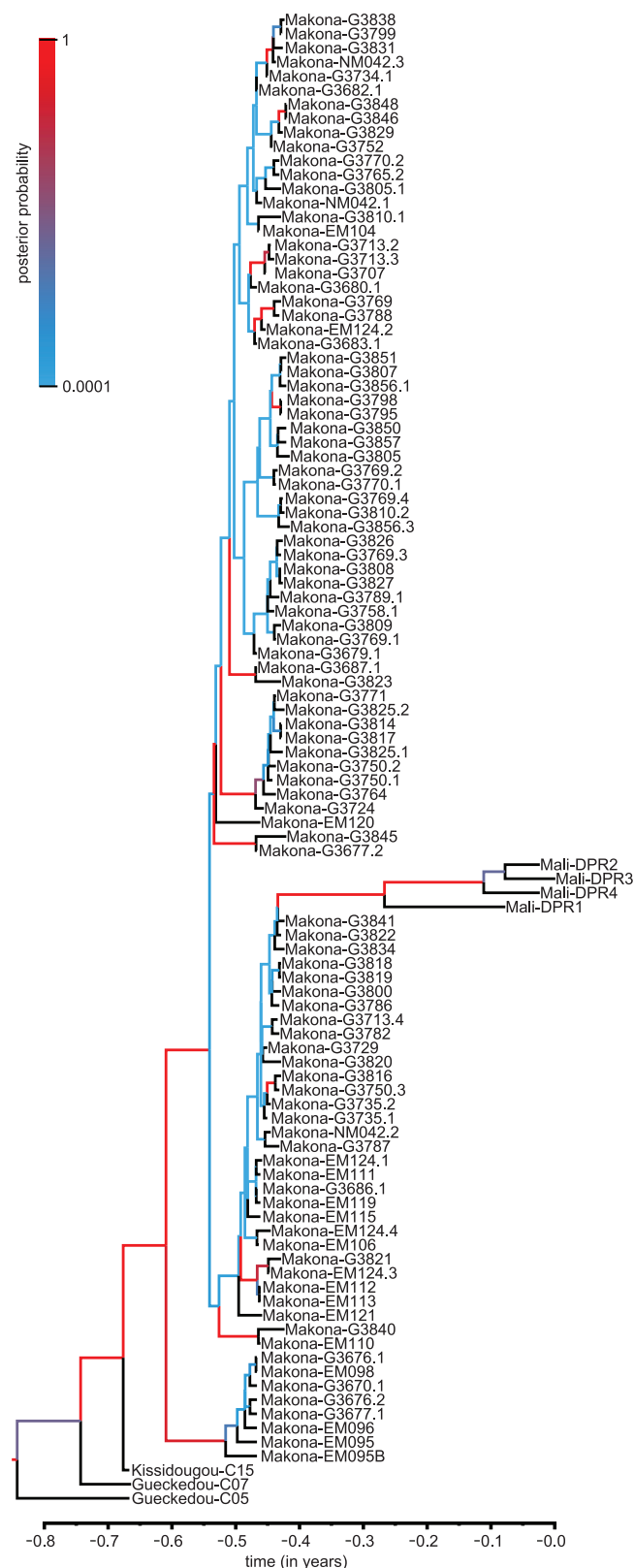
Fig. 1. Phylogenetic relationship among viruses from the ongoing outbreak. A Bayesian tree of all currently published sequences from the ongoing outbreak is shown. Branch colors indicate posterior probability, with terminal branches shown in black. The x axis indicates time in years before acquisition of the last sample (21 November 2014). Although clade structure in the analysis is ambivalent for some of the Sierra Leone viruses, there is strong support for the placement of the Malian viruses as a distinct lineage originating from the main group of Sierra Leone sequences and distinct from both the Guinean viruses, as well as another well-supported clade of Sierra Leone viruses.

[1]Laboratory of Virology, Division of Intramural Research, National Institute of Allergy and Infectious Diseases (NIAID), National Institutes of Health (NIH), Hamilton, MT 59840, USA. [2]Bioinformatics and Computational Biosciences Branch, NIAID, NIH, Bethesda, MD 20892, USA. [3]Center of Research and Training for HIV and Tuberculosis, University of Science, Technique and Technologies of Bamako, Mali. [4]World Health Organization Office, Bamako, Mali. [5]Centre des Operations d'Urgence, Centre pour le Développement des Vaccins (CVD-Mali), Centre National d'Appui à la lutte contre la Maladie, Ministère de la Sante et de l'Hygiène Publique, Bamako, Mali. [6]World Health Organization Inter-Country Support Team, Ouagadougou, Burkina Faso. [7]Rocky Mountain Veterinary Branch, Division of Intramural Research, NIAID, NIH, Hamilton, MT 59840, USA. [8]Office of the Scientific Director, NIAID, NIH, Bethesda, MD 20895, USA.
*These authors contributed equally to this work. †These authors contributed equally to this work. ‡Corresponding author. E-mail: feldmannh@niaid.nih.gov (H.F.); ssow@medicine.umaryland.edu (S.S.)

are consistently identified using Bayesian analysis (Fig. 1), as well as maximum-likelihood and neighbor-joining analyses (fig. S2), producing trees with comparable internal structure. The Malian sequences all form a discrete and well-supported branch derived from the second cluster of Sierra Leone sequences, despite being derived from two independent introduction events originating ~400 km from each other. This result is surprising, given the genetic diversity that had been shown to exist among viruses within the outbreak region during the sampling in Sierra Leone. Although we cannot completely exclude serendipitous introduction of two such closely related isolates, the strong support for coalescence of the Mali viruses to a common ancestor suggests that this genotype may be highly prevalent in this region at present and may thus represent a reasonable proxy for testing the efficacy of diagnostic, therapeutic, and vaccination approaches.

Based on these additional data, we recalculated the nucleotide substitution rate for the West African outbreak [see (5) for a full list of virus genomes]. By including the newly determined sequences from Mali, we obtained a mean substitution rate of 9.6×10^{-4} substitutions per site per year (Fig. 2). This matches previously reported nucleotide substitution rates of 6.2×10^{-4} to 9.5×10^{-4} for other EBOV sample sets (7–9) but differs from the substitution rate of ~1.9×10^{-3} that had been reported for this outbreak (2). Further analysis of this expanded data set also generated a comparable value (6.9×10^{-4} substitutions per site per year) when analysis parameters previously used to obtain these higher estimates (2) were employed. Surprisingly, reanalysis of the previously available data set from Gire et al. (2) using the model developed for this study also produced a similar value (8.2×10^{-4} substitutions per site per year). These findings appear to suggest that the strict clock used in the current analysis may be more suitable and robust for this data set and that the expanded time frame over which samples in our data sets were obtained adds additional robustness to the analysis.

Detailed analysis of the individual mutations observed among all currently known genotypes showed that the majority of mutations were synonymous or occurred in noncoding regions [particularly at the virion protein 30 (VP30)/VP24 gene border, which contains a long intergenic region] (fig. S3). Although up to four nonsynonymous nucleotide changes from the consensus sequence were observed for early sequences (i.e., those from March 2014), almost no nonsynonymous changes were observed in later sequences. Most nucleotide changes occurred only sporadically in a single genotype; however, a few changes were observed in several genotypes and might represent changes that remained conserved in later viruses. Early changes included two nonsynonymous changes, one each in the nucleoprotein (t800c:C>R) and GP (t6283c:V>A); three synonymous changes, one in VP30 (c8928a:P>P) and two in L (a15963g:K>K, c17142t:F>F); and one change in the VP24 noncoding region (g10219a). Later changes conserved among the Malian sequences were one nonsynonymous change in L (g16514a:S>N); four synonymous changes in GP (a6056c:I>I), VP30 (c8928a:P>P), and L (c14253t:G>G, a15963g:K>K); and an additional change in the VP24 noncoding region (c10315t). However, none of these nonsynonymous changes coincide with known functional domains or motifs within the affected proteins, and overall the genotypes observed have remained stable since June 2014, which is consistent with reports from earlier outbreaks of both EBOV and Marburg virus (10, 11).

In the past, EBOVs have been reported to undergo only limited genetic changes during outbreaks (10, 11), a phenomenon that also seems to be true in the current outbreak, despite prolonged human-to-human transmission. Thus, the potential for acquisition of virulence or increased transmissibility of EBOVs is constrained. Although the size and nature of the mutational targets associated with the acquisition of virulence clearly vary between viruses, and there are cases in which just a few mutations can substantially affect virus properties, there are also many limitations. These include the need for multiple mutations in some cases, as for mammalian transmission of H5N1 influenza (12), and these mutations may need to occur simultaneously or in a defined order (13). Studies aimed at identifying the virulence factors of EBOVs already indicate that virulence is a complex, multifactorial trait for these viruses, although further studies are required to better define these factors (14, 15). Furthermore, epidemiological and case management data do not support increased virulence in humans during the current outbreak (16). Thus, whereas from a public health perspective the current EBOV outbreak in West Africa continues to be an extremely pressing emergency, it is doubtful that either virulence or transmissibility has increased in the circulating EBOV strains. We have also shown that, despite the extensive and prolonged human-to-human transmission in this outbreak, the virus is not mutating at a rate beyond what is expected. Moreover, although it is certainly possible for different virus lineages to exhibit different evolutionary rates, those predicted using samples from various Ebola outbreaks have remained consistent. Similarly, on the basis of our data, it is unlikely that the types of genetic changes observed thus far would impair diagnostic measures or affect the efficacy of vaccines or potential virus-specific treatments. Nevertheless, monitoring of the situation remains paramount to ensure that this continues to be the case as this outbreak progresses and if further outbreaks arise.

REFERENCES AND NOTES

1. S. Baize et al., N. Engl. J. Med. 371, 1418–1425 (2014).
2. S. K. Gire et al., Science 345, 1369–1372 (2014).
3. A. Grolla et al., Zoonoses Public Health 59 (suppl. 2), 151–157 (2012).
4. S. D. Dowall et al., Genome Biol. 15, 540 (2014).
5. Materials and methods are available as supplementary materials on Science Online.
6. Single-letter abbreviations for the amino acid residues are as follows: A, Ala; C, Cys; D, Asp; E, Glu; F, Phe; G, Gly; H, His; I, Ile; K, Lys; L, Leu; M, Met; N, Asn; P, Pro; Q, Gln; R, Arg; S, Ser; T, Thr; V, Val; W, Trp; and Y, Tyr.
7. R. Biek, P. D. Walsh, E. M. Leroy, L. A. Real, PLOS Pathog. 2, e90 (2006).
8. S. A. Carroll et al., J. Virol. 87, 2608–2616 (2013).
9. P. D. Walsh, R. Biek, L. A. Real, PLOS Biol. 3, e371 (2005).
10. L. L. Rodriguez et al., J. Infect. Dis. 179 (suppl. 1), S170–S176 (1999).
11. J. S. Towner et al., J. Virol. 80, 6497–6516 (2006).
12. S. Herfst et al., Science 336, 1534–1541 (2012).
13. K. A. Tsetsarkin et al., Proc. Natl. Acad. Sci. U.S.A. 108, 7872–7877 (2011).
14. A. Groseth et al., PLOS Pathog. 8, e1002847 (2012).
15. A. Groseth, H. Feldmann, S. Theriault, G. Mehmetoglu, R. Flick, J. Virol. 79, 4425–4433 (2005).
16. WHO Ebola Response Team, N. Engl. J. Med. 371, 1481–1495 (2014).

Fig. 2. Nucleotide substitution rate in the current outbreak. The probability distribution of substitution rates in the current EBOV outbreak in West Africa based on all currently published sequences from this outbreak, including those from Mali, is shown as a gray shaded area. Previously reported substitution rates for EBOVs from four different publications (2, 7–9) are indicated by dotted lines (further qualifying information is provided in brackets if several rates were reported in those publications).

West Africa: 9.6x10^{-4}
Biek 2006: 6.2x10^{-4}
Carroll 2013 (EBOV): 7.1x10^{-4}
Gire 2014 (all EBOV): ~9.3x10^{-4}
Walsh 2005: 9.5x10^{-4}
Gire 2014 (West Africa): ~1.9x10^{-3}

marginal posterior probability — substitution rate (substitutions/site/year)
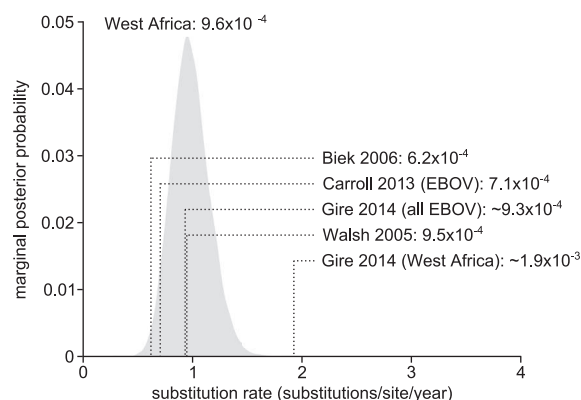
PLANT BIOLOGY

Suppression of endogenous gene silencing by bidirectional cytoplasmic RNA decay in *Arabidopsis*

Xinyan Zhang,[1] Ying Zhu,[1] Xiaodan Liu,[1] Xinyu Hong,[1] Yang Xu,[2] Ping Zhu,[2] Yang Shen,[3] Huihui Wu,[1] Yusi Ji,[1] Xing Wen,[1] Chen Zhang,[1] Qiong Zhao,[1] Yichuan Wang,[1] Jian Lu,[1,3] Hongwei Guo[1,3]*

Plant immunity against foreign gene invasion takes advantage of posttranscriptional gene silencing (PTGS). How plants elaborately avert inappropriate PTGS of endogenous coding genes remains unclear. We demonstrate in *Arabidopsis* that both 5′-3′ and 3′-5′ cytoplasmic RNA decay pathways act as repressors of transgene and endogenous PTGS. Disruption of bidirectional cytoplasmic RNA decay leads to pleiotropic developmental defects and drastic transcriptomic alterations, which are substantially rescued by PTGS mutants. Upon dysfunction of bidirectional RNA decay, a large number of 21- to 22-nucleotide endogenous small interfering RNAs are produced from coding transcripts, including multiple microRNA targets, which could interfere with their cognate gene expression and functions. This study highlights the risk of unwanted PTGS and identifies cytoplasmic RNA decay pathways as safeguards of plant transcriptome and development.

G ene expression and silencing establish the proper transcriptome of eukaryotic cells. Posttranscriptional gene silencing (PTGS), also known as RNA interference, serves as an RNA-based immune system against foreign gene invasion and is engaged in silencing a subset of endogenous genes, mainly transposons (*1, 2*). PTGS is triggered by cellular double-stranded RNAs, which are subsequently cleaved into 20- to 24-nucleotide (nt) small RNA duplexes by Dicer family proteins (*2*). One strand of the small RNA duplex can be loaded into an Argonaute (AGO)–containing silencing complex, which targets homologous RNAs for degradation and/or translation inhibition (*2*). Plants, fungi, and worms possess RNA-dependent RNA polymerases (RDRPs) that could produce secondary small interfering RNA (siRNA) molecules after the primary siRNA targeting, thus amplifying the effects of PTGS (*3*).

PTGS is an elaborately regulated process. Various plant viruses carry repressors of PTGS, combating plant immunity against infection (*4, 5*). Several components that participate in mRNA quality control and processing function as repressors of transgene PTGS (*6, 7*). In this work, we use the model plant *Arabidopsis* to investigate how endogenous protein-coding transcripts avoid being targeted by PTGS machineries that efficiently silence the expression of viral genomes or transgenes.

In *Arabidopsis*, overexpression of ETHYLENE-INSENSITIVE3 (EIN3), a transcriptional activator of ethylene signaling (*8*), resulted in a small-cotyledon phenotype characteristic of enhanced ethylene response (*9*) (Fig. 1A) (see also supplementary materials and methods). In a genetic screen searching for suppressors of this stock, we isolated four large-cotyledon mutants that phenocopied the *ein3* loss-of-function mutant (*8*) (Fig. 1A and fig. S1A). One mutant affected *ETHYLENE-INSENSITIVE5* (*EIN5*), encoding a cytoplasmic 5′-3′ exoribonuclease known in transgene PTGS repression (*7, 10*) (fig. S1). The other three mutants (*s28*, *s37*, and *s40*) showed reduced expression of *EIN3* and one of its targets, *ETHYLENE-RESPONSE-FACTOR1* (*ERF1*) (*11*) (Fig. 1B). *s28* carried a mutation in the coding sequence of a DExH-box RNA helicase (AT3G46960) of the SKI2 (Super-Killer2) type (*12*) (Fig. 1C and fig. S2A). Green fluorescent protein (GFP)–tagged AtSKI2, expressed exclusively in the cytoplasm (Fig. 1D), restored normal cotyledon development and expression of the *EIN3* transgene in the *s28* line (fig. S3). Two additional *Arabidopsis* insertional *ski2* alleles, *ski2-2* and *ski2-3* (figs. S2A and S4), displayed normal responses to ethylene (fig. S5), excluding AtSKI2 functions in the ethylene signaling pathway. *s37* and *s40*, allelic to each other, both carried nonsense mutations in AtSKI3 (AT1G76630) (*12*) (Fig. 1C and fig. S2A). In yeast, ScSki2, ScSki3, and ScSki8 function as a cytoplasmic SKI complex to unwind and thread RNAs into the 3′-5′ exoribonuclease complex (exosome) for decay (*13*) (fig. S2B). In *Arabidopsis*, we found peptides characteristic of AtSKI3, AtSKI8, and AtSKI7 and several other proteins associated with AtSKI2 (fig. S6). Pull-down experiments confirmed the direct interaction between AtSKI2 and AtSKI3 (Fig. 1E).

Evidence that AtSKI2 is a general repressor of transgene PTGS came from two experiments: (i) When we introduced an unrelated transgene [*ADENINE PHOSPHORIBOSYLTRANSFERASE 1* (*APT1*)] to the *ski2-2* line, the phenotype mimicked the *apt1* mutant (*14*) (fig. S7), suggesting cosuppression of both the *APT1* transgene and endogenous *APT1*. (ii) Mutation of *RDR6*, an RDRP essential for transgene PTGS in plants (*15*), caused the small-cotyledon phenotype and reactivated expression of the *EIN3* transgene in *s28* (Fig. 1, A and G). Furthermore, the marked accumulation of *EIN3* transgene–derived siRNAs in *s28* was eliminated by *rdr6* mutation (Fig. 1F). Thus, the cytoplasmic 3′-5′ and 5′-3′ RNA decay pathways mediated by the SKI complex and EIN5, respectively, are required for suppressing transgene PTGS.

Neither cytoplasmic RNA decay pathway alone was essential for plant development, as the *ein5* and *ski2* single mutants were morphologically normal except for mild leaf serrations in *ein5* (*10*) (Fig. 2A). However, disruption of both pathways (*ein5-1 ski2-2*) proved to be lethal at the embryonic stage (fig. S8A). Hypomorphic *ein5-1 ski2-3* homozygotes (figs. S2A and S4B) were viable but arrested at the early vegetative stage with growth disorders, including defects in meristem, rosette leaves, and leaf coloration (Fig. 2A). *rdr6* rescued the *ein5 ski2* double mutants, and the resultant triple mutants showed normal vegetative growth and fertility (Fig. 2A and fig. S8). Thus, the defects caused by *ein5 ski2* are RDR6-dependent.

We profiled the transcriptomes in the various genotypes. The profile of *rdr6-11 ein5-1 ski2-3* resembled that of *rdr6-11* but differed from that of *ein5-1 ski2-3* (Fig. 2B). We identified 596 differentially expressed genes (111 upregulated and 485 down-regulated) when both *EIN5* and *AtSKI2* were mutated (fig. S9A). Of the up- and down-regulated genes, 85.6 and 73.0%, respectively, were restored by *rdr6* mutation (fig. S9B), indicating that most of the transcriptomic changes in *ein5-1 ski2-3* are dependent on RDR6.

The genes regulated by the combination of *EIN5* and *AtSKI2* are enriched in functional categories such as flavonoid biosynthesis, ribosome, and photosynthesis (table S1). For instance, expression of several anthocyanin biosynthesis enzymes (DFR, TT8) and their regulatory transcription factors (PAP1, PAP2) (*16*) was upregulated in *ein5-1 ski2-3* but reduced in *rdr6-11 ein5-1 ski2-3* (Fig. 2C). Accordingly, anthocyanin highly accumulated in *ein5-1 ski2-3* but not in *rdr6-11 ein5-1 ski2-3* (Fig. 2D), manifesting as purple pigmentation in rosette leaves of *ein5-1 ski2-3* plants (Fig. 2A).

The defects of *ein5 ski2* were rescued by other mutations that affect the 21- to 22-nt siRNA pathway, such as *ago1*, *suppressor of gene silencing3* (*sgs3*), and the *dicer-like4* (*dcl4*) *dcl2* double mutant (*17*) (Fig. 3, A and B, and figs. S10 and S11). In *Arabidopsis*, DCL4 generates 21-nt

[1]State Key Laboratory of Protein and Plant Gene Research, College of Life Sciences, Peking University, Beijing 100871, China. [2]Biodynamic Optical Imaging Center, School of Life Sciences, Peking University, Beijing 100871, China. [3]Peking-Tsinghua Center for Life Sciences, Peking University, Beijing 100871, China.
*Corresponding author. E-mail: hongweig@pku.edu.cn
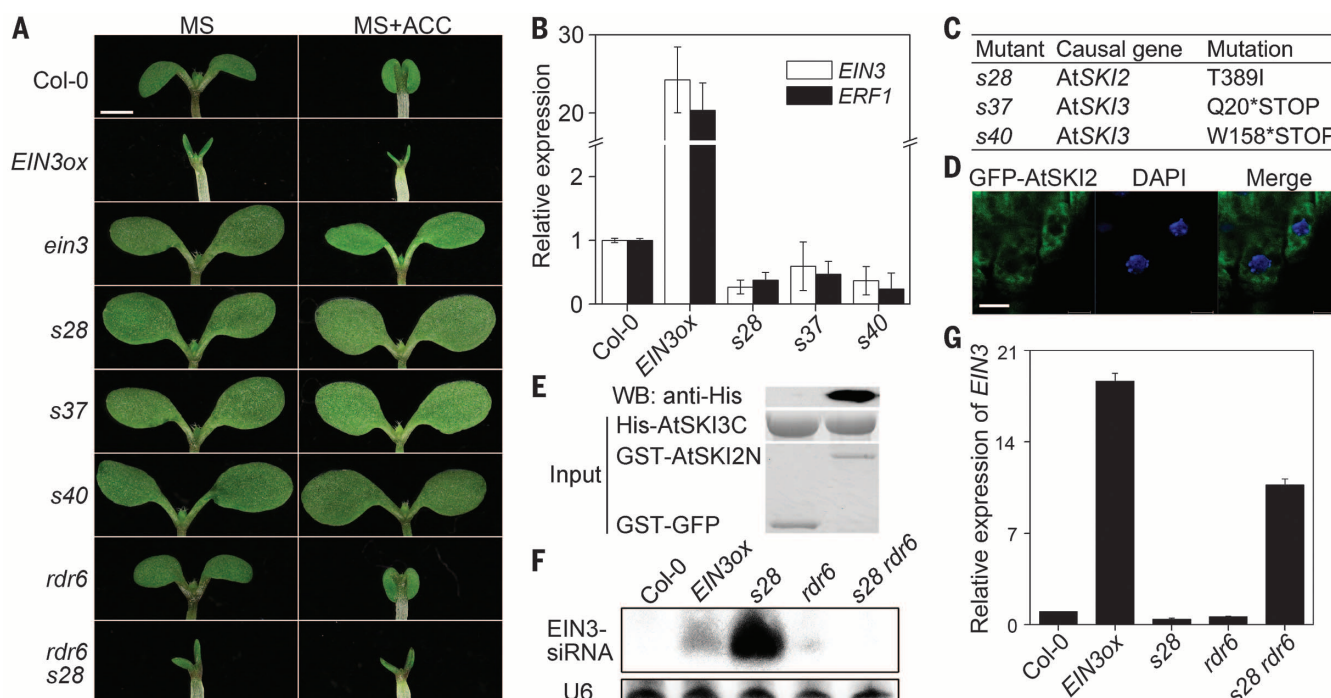
Fig. 1. RDR6-dependent transgene PTGS upon the dysfunction of 3′-5′ RNA decay. (**A**) Cotyledon phenotype of 6-day-old seedlings grown on Murashige and Skoog (MS) medium supplemented with or without 10 μM ACC, an ethylene biosynthetic precursor. *s28*, *s37*, and *s40* mutants were generated in the *EIN3ox* (EIN3-overexpressor) background. The *s28 rdr6* double mutant was generated by crossing. Scale bar, 1 mm. (**B**) Relative expression levels of *EIN3* and its target gene *ERF1* in 6-day-old seedlings. Error bars indicate SD; number of replicates (*n*) = 3. (**C**) Identification of the causal genes in the mutants by positional cloning. Mutations of amino acid (aa) residues are indicated. T, Thr; I, Ile; Q, Gln; W, Trp. (**D**) Subcellular localization of AtSKI2 fused with GFP. 4′,6-diamidino-2-phenylindole (DAPI) staining indicates the nuclei. Scale bar, 5 μm. (**E**) In vitro glutathione *S*-transferase (GST) pull-down assay between the C terminus of AtSKI3 (AtSKI3C, aa 930 to 1169) and the N terminus of AtSKI2 (AtSKI2N, aa 1 to 344). WB, Western blotting. (**F**) Northern blot detection of small RNAs derived from *EIN3*. (**G**) Relative expression levels of *EIN3* in 6-day-old seedlings. Error bars indicate SD; *n* = 3.
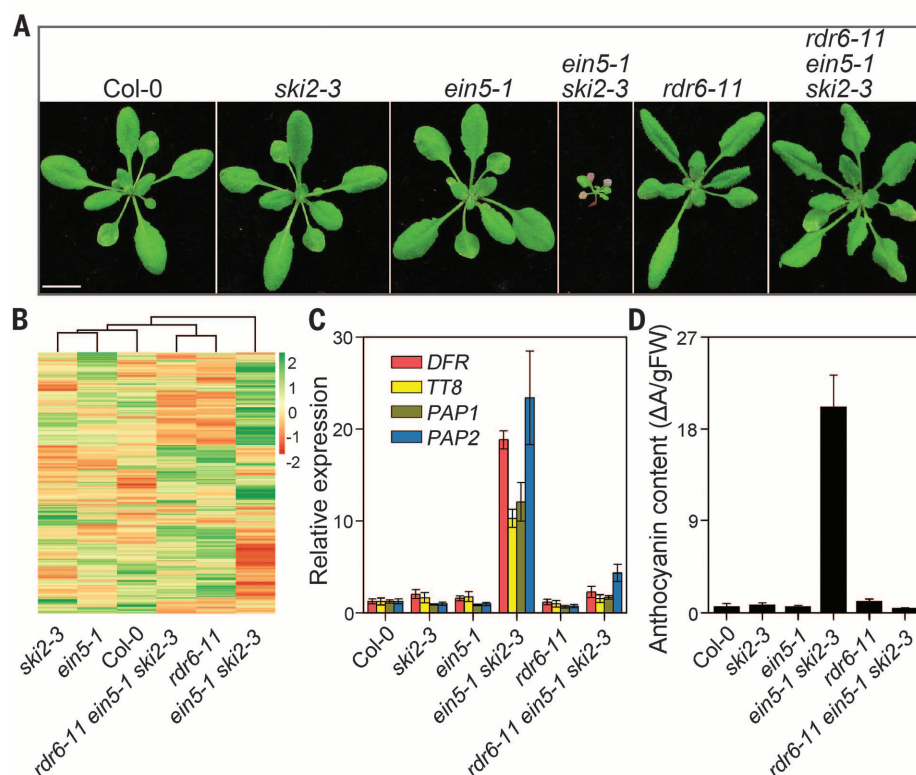
Fig. 2. Disruption of bidirectional RNA decay exhibits RDR6-dependent developmental defects and transcriptomic alterations. (**A**) Rosette morphology of 3-week-old plants of indicated genotypes. Scale bar, 1 cm. (**B**) Clustering of transcriptome profiles of *ein5-1*, *ski2-3*, *rdr6-11*, and their combinations. The clustering results are based on expression levels of 15,663 genes that have the expression levels with reads per kilobase per million > 1 in the Col-0 background. (**C**) Relative expression of genes that regulate anthocyanin biosynthesis in 16-day-old plants. Error bars indicate SD; *n* = 3. (**D**) Quantification of anthocyanin accumulation in 16-day-old plants. Error bars indicate SD, *n* = 6.
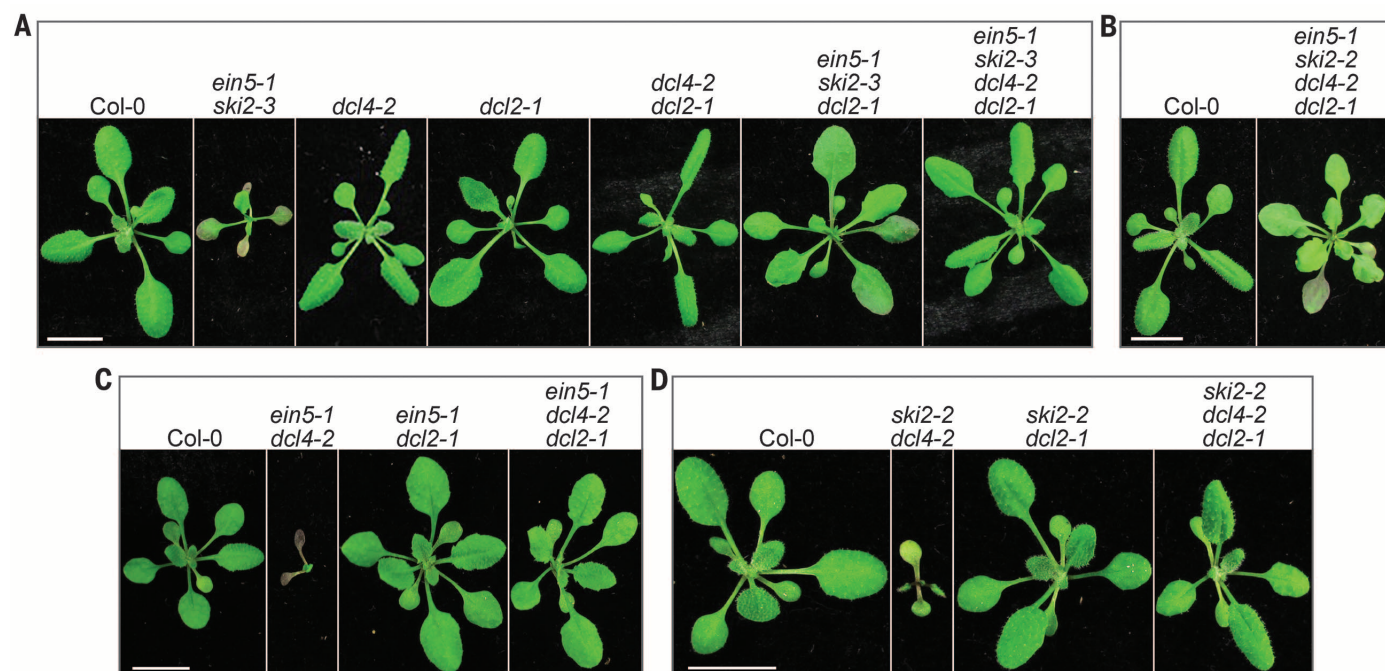
Fig. 3. Genetic interaction between the PTGS and RNA decay pathways. (**A** to **D**) Rosette morphology of 19-day-old plants was shown. No *ein5-1 ski2-3 dcl4-2* plant was viable based on genotyping the segregating population derived from the *ein5-1 ski2-3* hemizygote and *dcl4-2 dcl2-1* cross (A). Similarly, the *ein5-1 ski2-2* double mutants were not viable, and by genotyping the F₂ and F₃ plants propagated from the *ein5-1 ski2-2* hemizygote and *dcl4-2 dcl2-1* cross, no *ein5-1 ski2-2 dcl2-1* or *ein5-1 ski2-2 dcl4-2* triple mutants were viable (B). Scale bars, 1 cm.
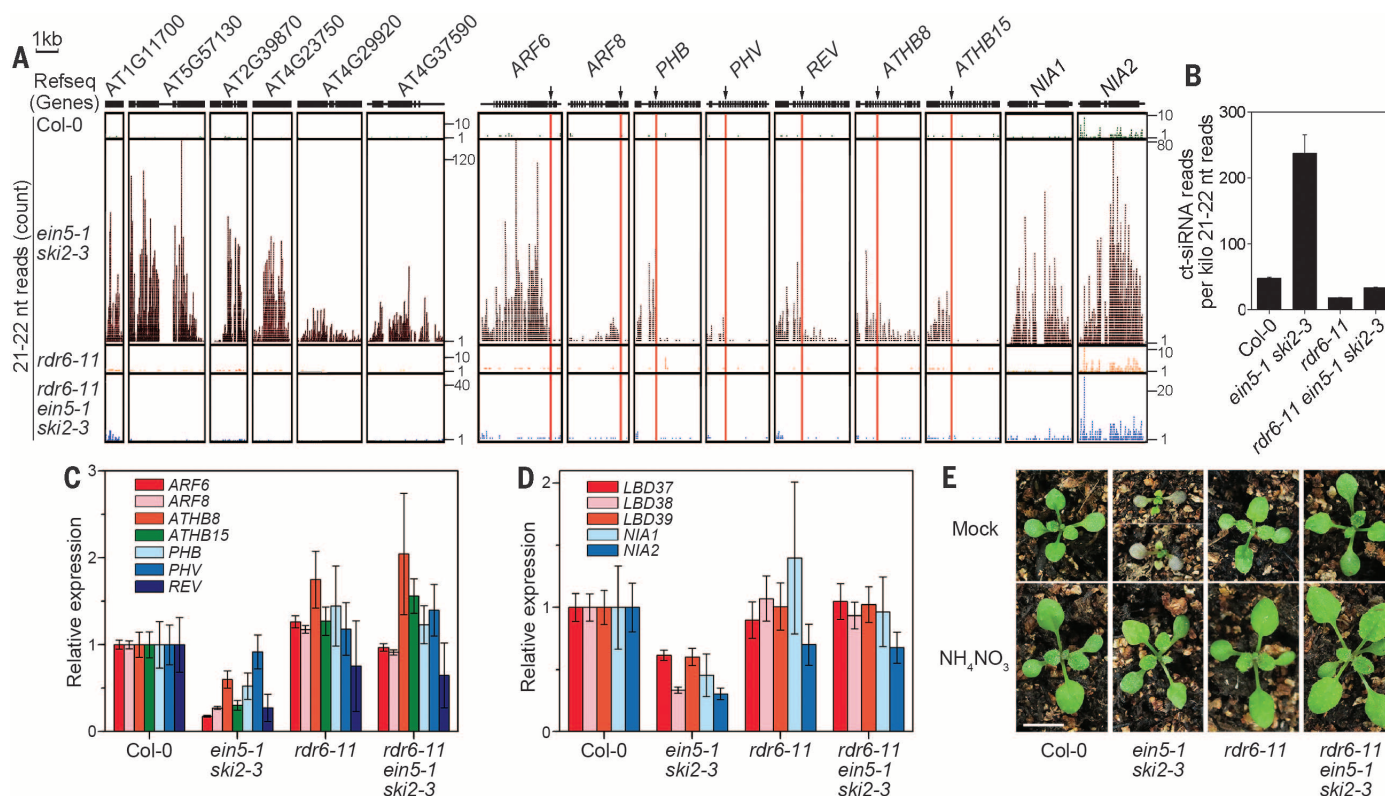
Fig. 4. Identification and functional analysis of a class of siRNAs accumulated in *ein5 ski2*. (**A**) Accumulation of 21- to 22-nt siRNAs derived from representative coding genes in *ein5 ski2*, but barely in other genotypes. Arrows indicate the miRNA cleavage sites in the selected miRNA-target genes. (**B**) Overall abundance of ct-siRNAs generated from 441 protein-coding loci in each genotype. Error bars indicate SD; *n* = 3. (**C**) Relative expression levels of select miRNA target genes (*ARF* and *HD-ZIPIII* family genes). Error bars indicate SD; *n* = 3. (**D**) Relative expression levels of *NIA1/2* and three nitrogen-responsive genes (*LBD37*, *-38*, and *-39*). Error bars indicate SD; *n* = 3. (**E**) Two-week-old plants grown in soil irrigated with water (Mock) or 1.65 g/liter ammonium nitrate solution (NH_4NO_3). Scale bar, 1 cm.

siRNAs, whereas DCL2 generates 22-nt siRNAs, which could efficiently trigger secondary siRNA biogenesis (18). Neither *dcl2* nor *dcl4* rescued the lethality of *ein5-1 ski2-2* (Fig. 3B); however, *dcl2* evidently recovered the developmental disorders of the hypomorphic *ein5-1 ski2-3* (Fig. 3A). Thus, both 21- and 22-nt siRNA pathways are deleterious to plant survival, and the 22-nt siRNA pathway is particularly detrimental to plant development when bidirectional RNA decay is disrupted. In contrast to normal morphology of *ein5 dcl2* and *ski2 dcl2*, both *ein5 dcl4* and *ski2 dcl4* plants displayed defects in rosette growth, meristem function, and leaf pigmentation. Further loss of DCL2 function rescued these defects (Fig. 3, C and D). Thus, upon deficiency of either 5′ (EIN5) or 3′ (AtSKI2) RNA decay, the DCL4-mediated pathway could compete with the DCL2-mediated pathway to minimize the risk that 22-nt siRNAs might trigger amplified PTGS harmful to plant development.

We used small RNA sequencing to profile small RNA production in wild-type (Col-0), *rdr6-11*, *ein5-1 ski2-3*, and *rdr6-11 ein5-1 ski2-3* (fig. S12A). We found that few reads mapped to all eight *Arabidopsis TAS* genes in *rdr6-11* and *rdr6-11 ein5-1 ski2-3*, consistent with the requirement of RDR6 for trans-acting siRNA (tasiRNA) biogenesis (19). Abundant and comparable levels of tasiRNA were detected in Col and *ein5-1 ski2-3* for 7 *TAS* genes (fig. S12, B and C), except for *TAS4* tasiRNAs, which may have accumulated due to the elevated expression of *TAS4* in *ein5-1 ski2-3* (fig. S13). Therefore, defects in cytoplasmic RNA decay do not affect tasiRNA biogenesis.

To further explore the genetic cause of detrimental PTGS, we filtered the genes that generate 21- to 22-nt siRNAs using two criteria: (i) loci with more mapping reads of siRNAs in *ein5-1 ski2-3* than in Col [twofold cutoff, $P < 0.005$, false discovery rate (FDR) < 0.1], and (ii) loci with fewer mapping reads of siRNAs in *rdr6-11 ein5-1 ski2-3* than in *ein5-1 ski2-3* (twofold cutoff, $P < 0.005$, FDR < 0.1). Of 456 genes that met these criteria, 441 encoded proteins (Fig. 4, A and B, and table S2). We named the siRNAs derived from the 441 loci as coding transcript–derived siRNAs (ct-siRNAs). Among these 441 loci were 39 microRNA (miRNA)–targeted protein-coding genes (table S3), including miR167 targets (*ARF6*, *ARF8*) and miR165/166 targets (five *HD-ZIPIII* genes) (Fig. 4A and fig. S14). ct-siRNAs arise from either 5′ miRNA-cleavage fragments or 5′ plus 3′ fragments of these miRNA targets (Fig. 4A and fig. S15), distinct from the biogenesis of most tasiRNAs within 3′ fragments of *TAS* loci (20).

The ct-siRNA loci were overrepresented in the down-regulated genes of *ein5-1 ski2-3* (fig. S16). For instance, expression of the above-mentioned *ARF6/8* and *HD-ZIP III* genes was reduced in *ein5-1 ski2-3* but not in *rdr6-11 ein5-1 ski2-3* (Fig. 4C), suggesting that the RDR6-dependent ct-siRNA biogenesis intensifies the repression of gene expression triggered by miRNAs. We identified *NIA1* and *NIA2*, which encode two

nitrate reductases required for nitrate assimilation in *Arabidopsis* (21), from the top 20 loci that show the most notable ct-siRNA production in *ein5 ski2* (Fig. 4A and fig. S17). Expression of *NIA1* and *NIA2*, as well as three nitrogen-responsive genes (*LBD37, -38*, and *-39*) (22), was reduced in *ein5-1 ski2-3* and was restored in *rdr6-11 ein5-1 ski2-3* (Fig. 4D). Thus, ct-siRNA–mediated silencing of *NIA1* and *NIA2* genes disturbed nitrogen metabolism, which activates anthocyanin biosynthesis (23). In agreement, the purple pigmentation of *ein5-1 ski2-3* leaves at the early stage was normalized when the plants were irrigated with ammonium nitrate, which compensates for the compromised nitrate assimilation (Fig. 4E). Thus, biogenesis of ct-siRNAs in many cases could reduce the expression of their cognate genes and compromise gene functions.

The ct-siRNA loci were also overrepresented in the up-regulated genes of *ein5-1 ski2-3* (fig. S16). Furthermore, the ct-siRNA loci, on average, were expressed at markedly higher levels than the rest of the genome (fig. S18). Transgenes expressed at higher levels are more likely to undergo PTGS to produce siRNA (24). It is thus likely that accumulation of a subset of ct-siRNAs reflects the disturbed expression of their cognate genes upon dysfunction of RNA decay pathways. In line with this, *TAS4*-tasiRNA accumulated to high levels due to elevated expression of the *TAS4* gene in *ein5 ski2* (figs. S12C and S13).

Here we describe a class of endogenous siRNAs (ct-siRNAs) with these characteristics: (i) 21 or 22 nt in length; (ii) derived from coding transcripts; (iii) produced upon the dysfunction of EIN5- and AtSKI-mediated RNA decay; (iv) dependent on RDR6, SGS3, DCL2, and DCL4 for biogenesis; and (v) partially dependent on AGO1 for action (fig. S19). Our study reveals that both transgene and endogenous PTGS occurs upon dysfunction of bidirectional cytoplasmic RNA decay, which normally eliminates aberrant transcripts arising from RNA degradation, end processing, or endo-cleavage (25). When RNA decay pathways are disrupted by genetic mutation or overloaded by overexpression of foreign genes, aberrant transcripts are selected and channeled into PTGS pathways to produce 21- to 22-nt ct-siRNAs. The DCL4-mediated pathway could serve as a decoy to antagonize the more destructive DCL2-mediated pathway, protecting endogenous mRNAs from undesirable clearance (fig. S19). Thus, cytoplasmic RNA decay sets a silencing threshold such that those invading or vastly expressed genes with high levels of aberrant RNA production probably undergo PTGS, whereas the majority of endogenous genes hardly do. As such, the siRNA-based defense system in plants that originally evolved against genome invasion carries risks of triggering adverse endogenous PTGS not typical of the protein-based immune systems found in vertebrates (3). We also propose that cytoplasmic RNA decay and siRNA pathways act as crucial components in the miRNA regulatory network. After an initial miRNA-directed cleavage, cytoplasmic RNA decay could preclude sustained or exacerbated siRNA-triggered silencing of target gene expression. Notably, miRNA-triggered tasiRNA biogenesis seems not to be affected by cytoplasmic RNA decay, raising the question as to how aberrant transcripts are sorted and targeted between cytoplasmic RNA decay and PTGS pathways.

REFERENCES AND NOTES

1. C. Cogoni, G. Macino, *Curr. Opin. Genet. Dev.* **10**, 638–643 (2000).
2. R. C. Wilson, J. A. Doudna, *Annu. Rev. Biophys.* **42**, 217–239 (2013).
3. M. Ghildiyal, P. D. Zamore, *Nat. Rev. Genet.* **10**, 94–108 (2009).
4. M. Incarbone, P. Dunoyer, *Trends Plant Sci.* **18**, 382–392 (2013).
5. N. Pumplin, O. Voinnet, *Nat. Rev. Microbiol.* **11**, 745–760 (2013).
6. A. B. Moreno *et al.*, *Nucleic Acids Res.* **41**, 4699–4708 (2013).
7. S. Gazzani, T. Lawrenson, C. Woodward, D. Headon, R. Sablowski, *Science* **306**, 1046–1048 (2004).
8. Q. Chao *et al.*, *Cell* **89**, 1133–1144 (1997).
9. H. Guo, J. R. Ecker, *Cell* **115**, 667–677 (2003).
10. G. Olmedo *et al.*, *Proc. Natl. Acad. Sci. U.S.A.* **103**, 13286–13293 (2006).
11. R. Solano, A. Stepanova, Q. Chao, J. R. Ecker, *Genes Dev.* **12**, 3703–3714 (1998).
12. E. Dorcey *et al.*, *PLOS Genet.* **8**, e1002652 (2012).
13. J. T. Brown, X. Bai, A. W. Johnson, *RNA* **6**, 449–457 (2000).
14. X. Zhang *et al.*, *Mol. Plant* **6**, 1661–1672 (2013).
15. T. Dalmay, A. Hamilton, S. Rudd, S. Angell, D. C. Baulcombe, *Cell* **101**, 543–553 (2000).
16. E. Grotewold, *Annu. Rev. Plant Biol.* **57**, 761–780 (2006).
17. N. G. Bologna, O. Voinnet, *Annu. Rev. Plant Biol.* **65**, 473–503 (2014).
18. F. Vazquez, T. Hohn, *Scientifica* **2013**, 783253 (2013).
19. A. Peragine, M. Yoshikawa, G. Wu, H. L. Albrecht, R. S. Poethig, *Genes Dev.* **18**, 2368–2379 (2004).
20. E. Allen, Z. Xie, A. M. Gustafson, J. C. Carrington, *Cell* **121**, 207–221 (2005).
21. C. F. Hwang, Y. Lin, T. D'Souza, C. L. Cheng, *Plant Physiol.* **113**, 853–862 (1997).
22. G. Rubin, T. Tohge, F. Matsuda, K. Saito, W. R. Scheible, *Plant Cell* **21**, 3567–3584 (2009).
23. C. Diaz *et al.*, *Plant Cell Physiol.* **47**, 74–83 (2006).
24. D. Schubert *et al.*, *Plant Cell* **16**, 2561–2572 (2004).
25. C. A. Beelman, R. Parker, *Cell* **81**, 179–183 (1995).

CANCER IMMUNOLOGY

Mutational landscape determines sensitivity to PD-1 blockade in non-small cell lung cancer

Naiyer A. Rizvi,[1,2]*† Matthew D. Hellmann,[1,2]* Alexandra Snyder,[1,2,3]* Pia Kvistborg,[4] Vladimir Makarov,[3] Jonathan J. Havel,[3] William Lee,[5] Jianda Yuan,[6] Phillip Wong,[6] Teresa S. Ho,[6] Martin L. Miller,[7] Natasha Rekhtman,[8] Andre L. Moreira,[8] Fawzia Ibrahim,[1] Cameron Bruggeman,[9] Billel Gasmi,[10] Roberta Zappasodi,[10] Yuka Maeda,[10] Chris Sander,[7] Edward B. Garon,[11] Taha Merghoub,[1,10] Jedd D. Wolchok,[1,2,10] Ton N. Schumacher,[4] Timothy A. Chan[2,3,5]‡

Immune checkpoint inhibitors, which unleash a patient's own T cells to kill tumors, are revolutionizing cancer treatment. To unravel the genomic determinants of response to this therapy, we used whole-exome sequencing of non–small cell lung cancers treated with pembrolizumab, an antibody targeting programmed cell death-1 (PD-1). In two independent cohorts, higher nonsynonymous mutation burden in tumors was associated with improved objective response, durable clinical benefit, and progression-free survival. Efficacy also correlated with the molecular smoking signature, higher neoantigen burden, and DNA repair pathway mutations; each factor was also associated with mutation burden. In one responder, neoantigen-specific CD8+ T cell responses paralleled tumor regression, suggesting that anti–PD-1 therapy enhances neoantigen-specific T cell reactivity. Our results suggest that the genomic landscape of lung cancers shapes response to anti–PD-1 therapy.

Today, more than a century since the initial observation that the immune system can reject human cancers (1), immune checkpoint inhibitors are demonstrating that adaptive immunity can be harnessed for the treatment of cancer (2–7). In advanced non–small cell lung cancer (NSCLC), therapies with an antibody targeting programmed cell death-1 (anti–PD-1) demonstrated response rates of 17 to 21%, with some responses being remarkably durable (3, 8).

Understanding the molecular determinants of response to immunotherapies such as anti–PD-1 therapy is one of the critical challenges in oncology. Among the best responses have been in melanomas and NSCLCs, cancers largely caused by chronic exposure to mutagens [ultraviolet light

(9) and carcinogens in cigarette smoke (10), respectively]. However, there is a large variability in mutation burden within tumor types, ranging from 10s to 1000s of mutations (11–13). This range is particularly broad in NSCLCs because tumors in never-smokers generally have few somatic mutations compared with tumors in smokers (14). We hypothesized that the mutational landscape of NSCLCs may influence response to anti–PD-1 therapy. To examine this hypothesis, we sequenced the exomes of NSCLCs from two independent cohorts of patients treated with pembrolizumab, a humanized immunoglobulin G (IgG) 4-kappa isotype antibody to PD-1 (n = 16 and n = 18, respectively), and their matched normal DNA (fig. S1 and table S1) (15).

Overall, tumor DNA sequencing generated mean target coverage of 164x, and a mean of 94.5% of the target sequence was covered to a depth of at least 10x; coverage and depth were similar between cohorts, as well as between those with or without clinical benefit (fig. S2). We identified a median of 200 nonsynonymous mutations per sample (range 11 to 1192). The median number of exonic mutations per sample was 327 (range 45 to 1732). The quantity and range of mutations were similar to published series of NSCLCs (16, 17) (fig. S3). The transition/transversion ratio (Ti/Tv) was 0.74 (fig. S4), also similar to previously described NSCLCs (16–18). To ensure accuracy of our sequencing data, targeted resequencing with an orthogonal method (Ampliseq) was performed using 376 randomly selected variants, and mutations were confirmed in 357 of those variants (95%).

Higher somatic nonsynonymous mutation burden was associated with clinical efficacy of

pembrolizumab. In the discovery cohort (n = 16), the median number of nonsynonymous mutations was 302 in patients with durable clinical benefit (DCB) (partial or stable response lasting >6 months) versus 148 with no durable benefit (NDB) (Mann-Whitney P = 0.02) (Fig. 1A). Seventy-three percent of patients with high nonsynonymous burden (defined as above the median burden of the cohort, 209) experienced DCB, compared with 13% of those with low mutation burden (below median) (Fisher's exact P = 0.04). Both confirmed objective response rate (ORR) and progression-free survival (PFS) were higher in patients with high nonsynonymous burden [ORR 63% versus 0%, Fisher's exact P = 0.03; median PFS 14.5 versus 3.7 months, log-rank P = 0.01; hazard ratio (HR) 0.19, 95% confidence interval (CI) 0.05 to 0.70] (Fig. 1B and table S2).

The validation cohort included an independent set of 18 NSCLC samples from patients treated with pembrolizumab. The clinical characteristics were similar in both cohorts. The median nonsynonymous mutation burden was 244 in tumors from patients with DCB compared to 125 in those with NDB (Mann-Whitney P = 0.04) (Fig. 1C). The rates of DCB and PFS were again significantly greater in patients with a nonsynonymous mutation burden above 200, the median of the validation cohort (DCB 83% versus 22%, Fisher's exact P = 0.04; median PFS not reached versus 3.4 months, log-rank P = 0.006; HR 0.15, 95% CI 0.04 to 0.59) (Fig. 1D and table S2).

In the discovery cohort, there was high concordance between nonsynonymous mutation burden and DCB, with an area under the receiver operator characteristic (ROC) curve (AUC) of 87% (Fig. 1E). Patients with nonsynonymous mutation burden ≥178, the cut point that combined maximal sensitivity with best specificity, had a likelihood ratio for DCB of 3.0; the sensitivity and specificity of DCB using this cut point was 100% (95% CI 59 to 100%) and 67% (29 to 93%), respectively. Applying this cut point to the validation cohort, the rate of DCB in patients with tumors harboring ≥178 mutations was 75% compared to 14% in those with <178, corresponding to a sensitivity of 86% and a specificity of 75%.

There were few but important exceptions. Five of 18 tumors with ≥178 nonsynonymous mutations had NDB, and one tumor with a very low burden (56 nonsynonymous mutations) responded to pembrolizumab. However, this response was transient, lasting 8 months. Across both cohorts, this was the only patient with a tumor mutation burden <178 and confirmed objective response. Notably, although higher nonsynonymous mutation burden correlated with improved ORR, DCB, and PFS (Fig. 1, F and G), this correlation was less evident when examining total exonic mutation burden (table S2).

We next examined all 34 exomes collectively to determine how patterns of mutational changes were associated with clinical benefit to pembrolizumab (tables S4 and S5). C-to-A transversions were more frequent, and C-to-T transitions were less frequent, in patients with DCB compared to

[1]Department of Medicine, Memorial Sloan Kettering Cancer Center, New York, NY 10065, USA. [2]Weill Cornell Medical College, New York, NY, 10065, USA. [3]Human Oncology and Pathogenesis Program, Memorial Sloan Kettering Cancer Center, New York, NY 10065, USA. [4]Division of Immunology, Netherlands Cancer Institute, 1066 CX Amsterdam, Netherlands. [5]Department of Radiation Oncology, Memorial Sloan Kettering Cancer Center, New York, NY 10065, USA. [6]Immune Monitoring Core, Ludwig Center for Cancer Immunotherapy, Memorial Sloan Kettering Cancer Center, New York, NY 10065, USA. [7]Computation Biology Program, Memorial Sloan Kettering Cancer Center, New York, NY 10065, USA. [8]Department of Pathology, Memorial Sloan Kettering Cancer Center, New York, NY 10065, USA. [9]Department of Mathematics, Columbia University, New York, NY, 10027, USA. [10]Ludwig Collaborative Laboratory, Memorial Sloan Kettering Cancer Center, New York, NY 10065, USA. [11]David Geffen School of Medicine at UCLA, 2825 Santa Monica Boulevard, Suite 200, Santa Monica, CA 90404, USA.
*These authors contributed equally to this work. †Present address: Division of Hematology/Oncology, New York-Presbyterian/Columbia University, New York, NY, USA. ‡Corresponding author. E-mail: chant@mskcc.org

NDB (Mann-Whitney P = 0.01 for both) (fig. S5). A previously validated binary classifier to identify the molecular signature of smoking (17) was applied to differentiate transversion-high (TH, smoking signature) from transversion-low (TL, never-smoking signature) tumors. Efficacy was greatest in patients with tumors harboring the smoking signature. The ORR in TH tumors was 56% versus 17% in TL tumors (Fisher's exact P = 0.03); the rate of DCB was 77% versus 22% (Fisher's exact P = 0.004); the PFS was also significantly longer in TH tumors (median not reached versus 3.5 months, log-rank P = 0.0001) (Fig. 2A). Self-reported smoking history did not significantly discriminate those most likely to benefit from pembrolizumab. The rates of neither DCB nor PFS were significantly different in ever-smokers versus never-smokers (Fisher's exact P = 0.66 and log-rank P = 0.29, respectively) or heavy smokers (median pack-years >25) versus light/never smokers (pack-years ≤25) (Fisher's exact P = 0.08 and log-rank P = 0.15, respectively). The molecular smoking signature correlated more significantly with non-synonymous mutation burden than smoking history (fig. S6, A and B).

Although carcinogens in tobacco smoke are largely responsible for the mutagenesis in lung cancers (19), the wide range of mutation burden within both smokers and never-smokers implicates additional pathways contributing to the accumulation of somatic mutations. We found deleterious mutations in a number of genes that are important in DNA repair and replication. For example, in three responders with the highest mutation burden, we identified deleterious mutations in *POLD1*, *POLE*, and *MSH2* (Fig. 3). Of particular interest, a *POLD1* E374K mutation was identified in a never-smoker with DCB whose tumor harbored the greatest nonsynonymous mutation burden (n = 507) of all never-smokers in our series. POLD1 Glu374 lies in the exonuclease proofreading domain of Pol δ (20), and mutation of this residue may contribute to low-fidelity replication of the lagging DNA strand. Consistent with this hypothesis, this tumor exome had a relatively low proportion of C-to-A transversions (20%) and

predominance of C-to-T transitions (51%), similar to other *POLD1* mutant, hypermutated tumors (21) and distinct from smoking-related lung cancers. Another responder, with the greatest mutation burden in our series, had a C284Y mutation in *POLD1*, which is also located in the exonuclease proofreading domain. We observed nonsense mutations in *PRKDC*, the catalytic subunit of DNA-dependent protein kinase (DNA-PK), and *RAD17*. Both genes are required for proper DNA repair and maintenance of genomic integrity (22, 23).

Genes harboring deleterious mutations common to four or more DCB patients and not present in NDB patients included *POLR2A*, *KEAP1*, *PAPPA2*, *PXDNL*, *RYR1*, *SCN8A*, and *SLIT3*. Mutations in *KRAS* were found in 7 of 14 tumors from patients with DCB compared to 1 of 17 in the NDB group, a finding that may be explained by the association between smoking and the presence of *KRAS* mutations in NSCLC (24). There were no mutations or copy-number alterations in antigen-presentation pathway–associated genes or *CD274*
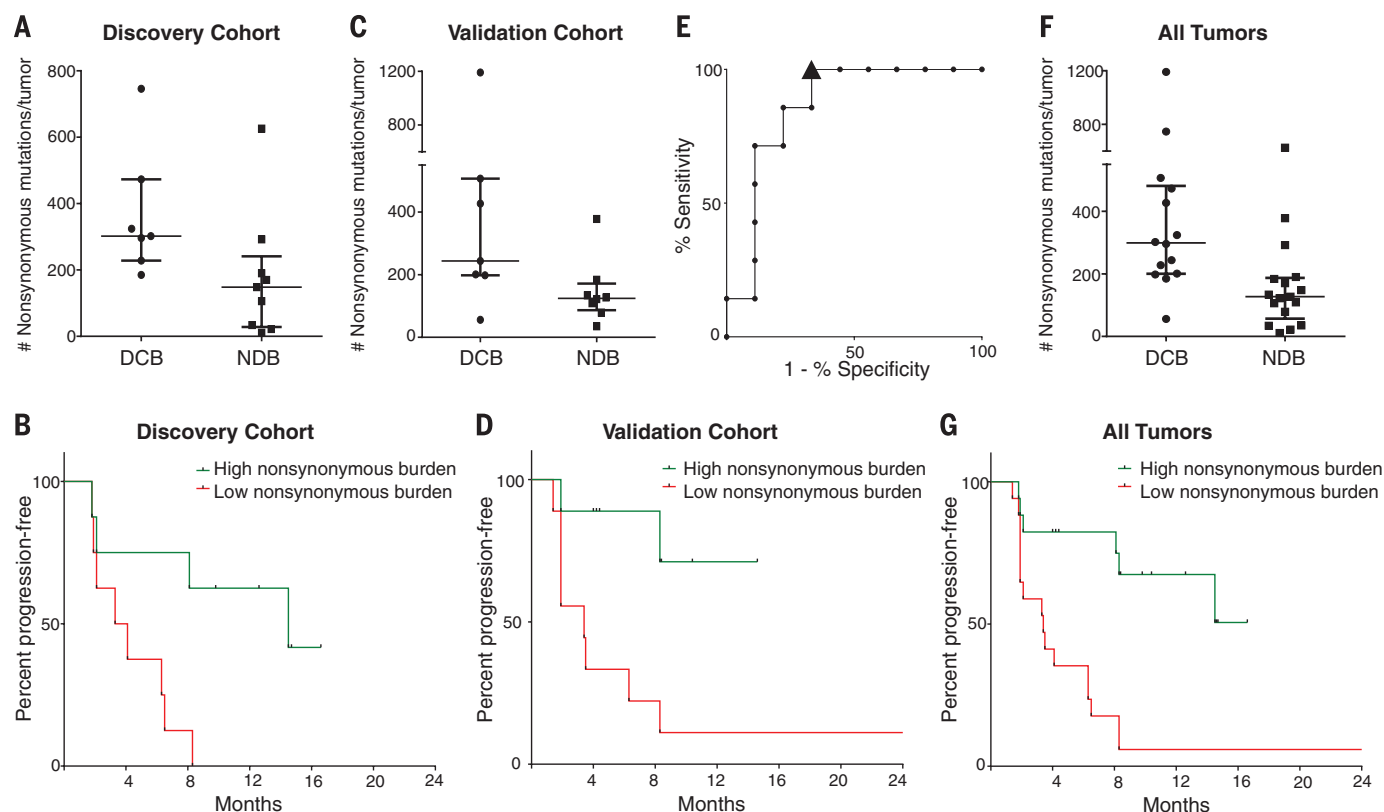
Fig. 1. Nonsynonymous mutation burden associated with clinical benefit of anti–PD-1 therapy. (A) Nonsynonymous mutation burden in tumors from patients with DCB (n = 7) or with NDB (n = 9) (median 302 versus 148, Mann-Whitney P = 0.02). **(B)** PFS in tumors with higher nonsynonymous mutation burden (n = 8) compared to tumors with lower nonsynonymous mutation burden (n = 8) in patients in the discovery cohort (HR 0.19, 95% CI 0.05 to 0.70, log-rank P = 0.01). **(C)** Nonsynonymous mutation burden in tumors with DCB (n = 7) compared to those with NDB (n = 8) in patients in the validation cohort (median 244 versus 125, Mann-Whitney P = 0.04). **(D)** PFS in tumors with higher nonsynonymous mutation burden (n = 9) compared to those with lower nonsynonymous mutation burden (n = 9) in patients in the validation cohort (HR 0.15, 95% CI 0.04 to 0.59,

log-rank P = 0.006). **(E)** ROC curve for the correlation of nonsynonymous mutation burden with DCB in discovery cohort. AUC is 0.86 (95% CI 0.66 to 1.05, null hypothesis test P = 0.02). Cut-off of ≥178 nonsynonymous mutations is designated by triangle. **(F)** Nonsynonymous mutation burden in patients with DCB (n = 14) compared to those with NDB (n = 17) for the entire set of sequenced tumors (median 299 versus 127, Mann-Whitney P = 0.0008). **(G)** PFS in those with higher nonsynonymous mutation burden (n = 17) compared to those with lower nonsynonymous mutation burden (n = 17) in the entire set of sequenced tumors (HR 0.19, 95% CI 0.08-0.47, log-rank P = 0.0004). In (A), (C), and (F), median and interquartile ranges of total nonsynonymous mutations are shown, with individual values for each tumor shown with dots.

[encoding programmed cell death ligand-1 (PD-L1)] that were associated with response or resistance.
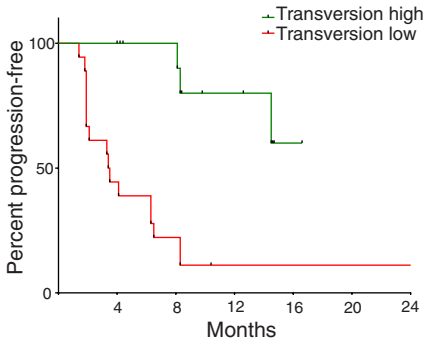
Fig. 2. Molecular smoking signature is significantly associated with improved PFS in NSCLC patients treated with pembrolizumab. PFS in tumors characterized as TH by molecular smoking signature classifier (n = 16) compared to TL tumors (n = 18) (HR 0.15, 95% 0.06 to 0.39, log-rank P = 0.0001).

How does increased mutation burden affect tumor immunogenicity? The observation that nonsynonymous mutation burden is associated with pembrolizumab efficacy is consistent with the hypothesis that recognition of neoantigens, formed as a consequence of somatic mutations, is important for the activity of anti–PD-1 therapy. We examined the landscape of neoantigens using our previously described methods (25) (fig. S7). Briefly, this approach identifies mutant nonamers with ≤500 nM binding affinity for patient-specific class I human lymphocyte antigen (HLA) alleles (26, 27), which are considered candidate neoantigens (table S6). We identified a median of 112 candidate neoantigens per tumor (range 8 to 610), and the quantity of neoantigens per tumor correlated with mutation burden (Spearman ρ 0.91, P < 0.0001), similar to the correlation recently reported across cancers (28). Tumors from patients with DCB had significantly higher candidate neoantigen burden compared to those with NDB (Fig. 4A), and high candidate neoantigen burden was associated with improved PFS (median 14.5 versus 3.5 months, log-rank P = 0.002) (Fig. 4B). The presence of sp-

ecific HLA alleles did not correlate with efficacy (fig. S8). The absolute burden of candidate neoantigens, but not the frequency per nonsynonymous mutation, correlated with response (fig. S9).

We next sought to assess whether anti–PD-1 therapy can alter neoantigen-specific T cell reactivity. To directly test this, identified candidate neoantigens were examined in a patient (Study ID no. 9 in Fig. 3 and table S3) with exceptional response to pembrolizumab and available peripheral blood lymphocytes (PBLs). Predicted HLA-A–restricted peptides were synthesized to screen for ex vivo autologous T cell reactivity in serially collected PBLs (days 0, 21, 44, 63, 256, and 297, where day 0 is the first date of treatment) using a validated high-throughput major histocompatibility complex (MHC) multimer screening strategy (29, 30). This analysis revealed a CD8+ T cell response against a neoantigen resulting from a *HERC1* P3278S mutation (ASNA**S**SAAK) (Fig. 4C). Notably, this T cell response could only be detected upon the start of therapy (level of detection 0.005%). Three weeks after therapy initiation, the magnitude of response was 0.040%
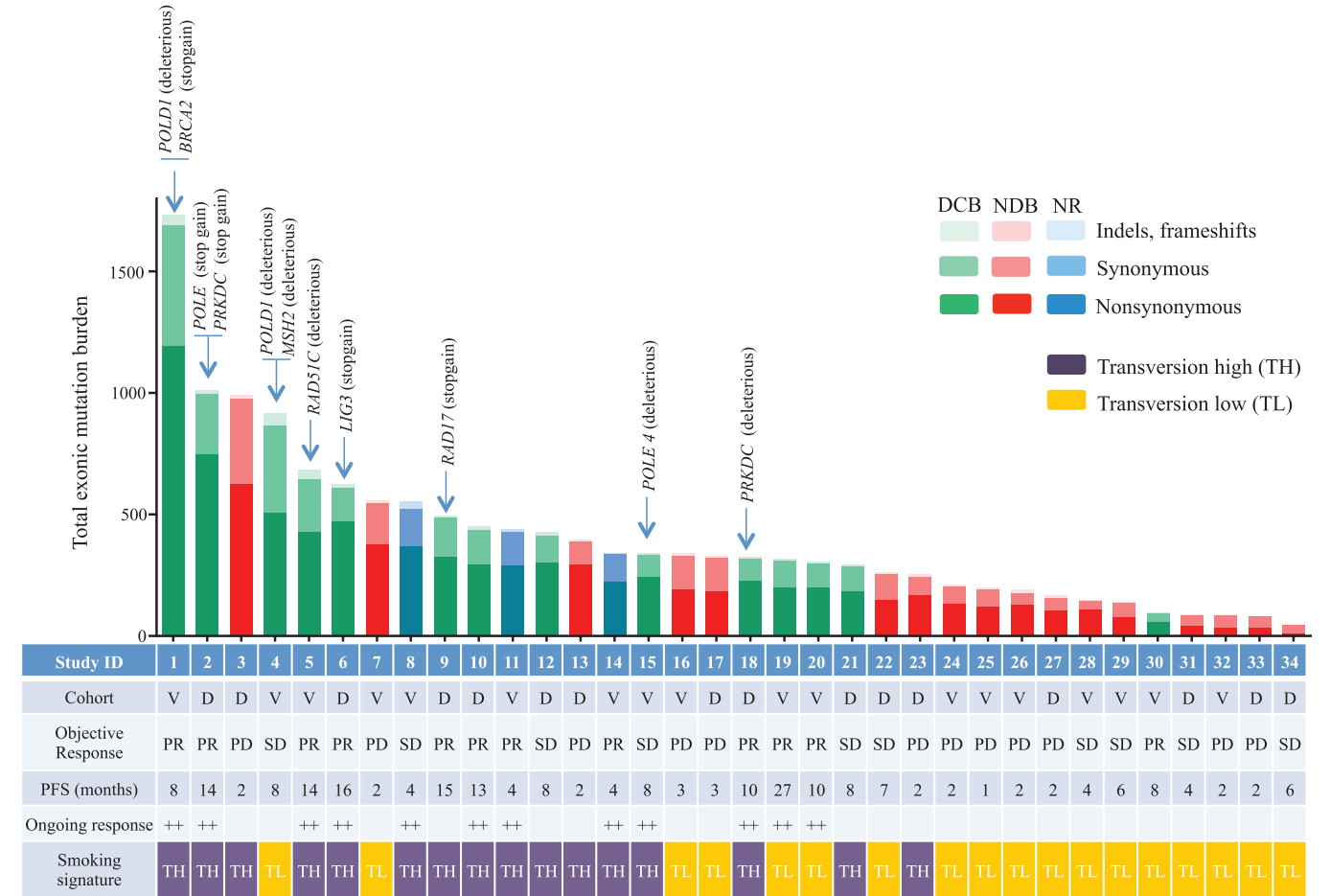
Fig. 3. Mutation burden, clinical response, and factors contributing to mutation burden. Total exonic mutation burden for each sequenced tumor with nonsynonymous (dark shading), synonymous (medium shading), and indels/frameshift mutations (light shading) displayed in the histogram. Columns are shaded to indicate clinical benefit status: DCB, green; NDB, red; not reached 6 months follow-up (NR), blue. The cohort identification (D, discovery; V, valida-

tion), best objective response (PR, partial response; SD, stable disease; PD, progression of disease), and PFS (censored at the time of data lock) are reported in the table. Those with ongoing progression-free survival are labeled with ++. The presence of the molecular smoking signature is displayed in the table with TH cases (purple) and TL cases (orange). The presence of deleterious mutations in specific DNA repair/replication genes is indicated by the arrows.

of CD8+ T cells, and this response was maintained at Day 44. This rapid induction of T cell reactivity correlated with tumor regression, and this T cell response returned to levels just above background in the subsequent months as tumor regression plateaued (Fig. 4D). HERC1 P3278S–multimer–reactive T cells from PBLs collected on day 44 were characterized by a CD45RA-CCR7-HLA-DR+LAG-3 phenotype, consistent with an activated effector population (fig. S10). These data reveal autologous T cell responses against cancer neoantigens in the context of a clinical response to anti–PD-1 therapy.

To validate the specificity of the neoantigen-reactive T cells, PBLs from days 63 and 297 were expanded in vitro in the presence of mutant peptide and subsequently restimulated with either mutant or wild-type peptide (ASNA*S*SAAK versus

ASNA*P*SAAK), and intracellular cytokines were analyzed. At both time points, a substantial population of polyfunctional CD8+ T cells [characterized by production of the cytokines interferon (IFN) γ and tumor necrosis factor (TNF) α, the marker of cytotoxic activity CD107a, and the chemokine CCL4] was detected in response to mutant but not wild-type peptide (Fig. 4E and fig. S11).

In the current study, we show that in NSCLCs treated with pembrolizumab, elevated nonsynonymous mutation burden strongly associates with clinical efficacy. Additionally, clinical efficacy correlates with a molecular signature characteristic of tobacco carcinogen–related mutagenesis, certain DNA repair mutations, and the burden of neoantigens. The molecular smoking signature correlated with efficacy, whereas self-reported smoking status did not, highlighting the power

of this classifier to identify molecularly related tumors within a heterogeneous group.

Previous studies have reported that pretreatment PD-L1 expression enriches for response to anti–PD-1 therapies (3, 8, 31), but many tumors deemed PD-L1 positive do not respond, and some responses occur in PD-L1–negative tumors (8, 31). Semiquantitative PD-L1 staining results were available for 30 of 34 patients, where strong staining represented ≥50% PD-L1 expression, weak represented 1 to 49%, and negative represented <1% [clone 22C3, Merck (8)]. As this trial largely enrolled patients with PD-L1 tumor expression, most samples had some degree of PD-L1 expression (24 of 30, 80%) (table S3), limiting the capacity to determine relationships between mutation burden and PD-L1 expression. Among those with high nonsynonymous mutation burden
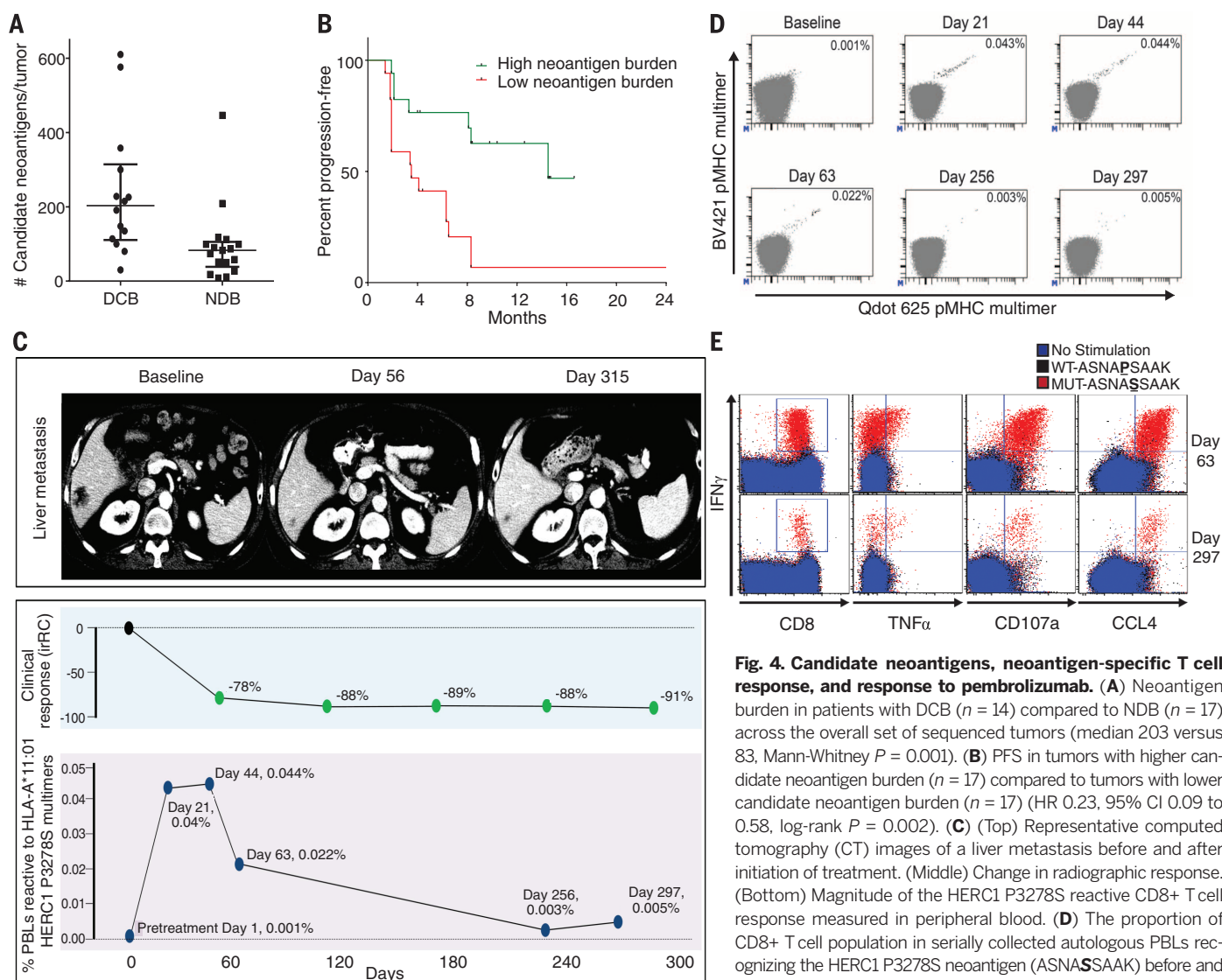
Fig. 4. Candidate neoantigens, neoantigen-specific T cell response, and response to pembrolizumab. (**A**) Neoantigen burden in patients with DCB (n = 14) compared to NDB (n = 17) across the overall set of sequenced tumors (median 203 versus 83, Mann-Whitney P = 0.001). (**B**) PFS in tumors with higher candidate neoantigen burden (n = 17) compared to tumors with lower candidate neoantigen burden (n = 17) (HR 0.23, 95% CI 0.09 to 0.58, log-rank P = 0.002). (**C**) (Top) Representative computed tomography (CT) images of a liver metastasis before and after initiation of treatment. (Middle) Change in radiographic response. (Bottom) Magnitude of the HERC1 P3278S reactive CD8+ T cell response measured in peripheral blood. (**D**) The proportion of CD8+ T cell population in serially collected autologous PBLs recognizing the HERC1 P3278S neoantigen (ASNA*S*SAAK) before and during pembrolizumab treatment. Each neoantigen is encoded by a unique combination of two fluorescently labeled peptide-MHC complexes (represented individually on each axis); neoantigen-specific T cells are represented by the events in the double positive position indicated with black dots. Percentages indicate the number of CD8+ MHC multimer+ cells out of total CD8 cells. (**E**) Autologous T cell response to wild-type HERC1 peptide (black), mutant HERC1 P3278S neoantigen (red), or no stimulation (blue), as detected by intracellular cytokine staining. T cell costains for IFNγ and CD8, TNFα, CD107a, and CCL4, respectively, are displayed for the Day 63 and Day 297 time points.

(>200, above median of overall cohort) and some degree of PD-L1 expression (weak/strong), the rate of DCB was 91% (10 of 11, 95% CI 59 to 99%). In contrast, in those with low mutation burden and some degree of PD-L1 expression, the rate of DCB was only 10% (1 of 10, 95% CI 0 to 44%). When exclusively examining patients with weak PD-L1 expression, high nonsynonymous mutation burden was associated with DCB in 75% (3 of 4, 95% CI 19 to 99%), and low mutation burden was associated with DCB in 11% (1 of 9, 0 to 48%). Large-scale studies are needed to determine the relationship between PD-L1 intensity and mutation burden. Additionally, recent data have demonstrated that the localization of PD-L1 expression within the tumor microenvironment [on infiltrating immune cells (*32*), at the invasive margin, tumor core, and so forth (*33*)] may affect the use of PD-L1 as a biomarker.

T cell recognition of cancers relies upon presentation of tumor-specific antigens on MHC molecules (*34*). A few preclinical (*35–41*) and clinical reports have demonstrated that neoantigen-specific effector T cell response can recognize (*25*, *42–45*) and shrink established tumors (*46*). Our finding that nonsynonymous mutation burden more closely associates with pembrolizumab clinical benefit than total exonic mutation burden suggests the importance of neoantigens in dictating response.

The observation that anti–PD-1–induced neoantigen-specific T cell reactivity can be observed within the peripheral blood compartment may open the door to development of blood-based assays to monitor response during anti–PD-1 therapy. We believe that our findings have an important impact on our understanding of response to anti–PD-1 therapy and on the application of these agents in the clinic.

REFERENCES AND NOTES

1. W. B. Coley, *Clin. Orthop. Relat. Res.* **1991**(262), 3–11 (1991).
2. F. S. Hodi *et al.*, *N. Engl. J. Med.* **363**, 711–723 (2010).
3. S. L. Topalian *et al.*, *N. Engl. J. Med.* **366**, 2443–2454 (2012).
4. J. D. Wolchok *et al.*, *N. Engl. J. Med.* **369**, 122–133 (2013).
5. C. Robert *et al.*, *Lancet* **384**, 1109–1117 (2014).
6. T. Powles *et al.*, *Nature* **515**, 558–562 (2014).
7. S. M. Ansell *et al.*, *N. Engl. J. Med.* **372**, 311–319 (2015).
8. E. B. Garon *et al.*, *Ann. Oncol.* **25**, LBA43 (2014).
9. G. P. Pfeifer, Y. H. You, A. Besaratinia, *Mutat. Res.* **571**, 19–31 (2005).
10. G. P. Pfeifer *et al.*, *Oncogene* **21**, 7435–7451 (2002).
11. M. S. Lawrence *et al.*, *Nature* **499**, 214–218 (2013).
12. L. B. Alexandrov *et al.*, *Nature* **500**, 415–421 (2013).
13. B. Vogelstein *et al.*, *Science* **339**, 1546–1558 (2013).
14. R. Govindan *et al.*, *Cell* **150**, 1121–1134 (2012).
15. See supplementary text available on *Science* Online.
16. P. S. Hammerman *et al.*, *Nature* **489**, 519–525 (2012).
17. Cancer Genome Atlas Research Network, *Nature* **511**, 543–550 (2014).
18. O. D. Abaan *et al.*, *Cancer Res.* **73**, 4372–4382 (2013).
19. D. Hoffmann, I. Hoffmann, K. El-Bayoumy, *Chem. Res. Toxicol.* **14**, 767–790 (2001).
20. R. Hindges, U. Hübscher, *Biol. Chem.* **378**, 345–362 (1997).
21. C. Palles *et al.*, *Nat. Genet.* **45**, 136–144 (2013).
22. J. F. Goodwin, K. E. Knudsen, *Cancer Discov.* **4**, 1126–1139 (2014).
23. X. Wang *et al.*, *Genes Dev.* **17**, 965–970 (2003).
24. S. Dogan *et al.*, *Clin. Cancer Res.* **18**, 6169–6177 (2012).
25. A. Snyder *et al.*, *N. Engl. J. Med.* **371**, 2189–2199 (2014).
26. M. Nielsen *et al.*, *Protein Sci.* **12**, 1007–1017 (2003).
27. C. Lundegaard *et al.*, *Nucleic Acids Res.* **36** (Web Server), W509–W512 (2008).
28. M. S. Rooney, S. A. Shukla, C. J. Wu, G. Getz, N. Hacohen, *Cell* **160**, 48–61 (2015).
29. B. Rodenko *et al.*, *Nat. Protoc.* **1**, 1120–1132 (2006).
30. R. S. Andersen *et al.*, *Nat. Protoc.* **7**, 891–902 (2012).
31. J. M. Taube *et al.*, *Clin. Cancer Res.* **20**, 5064–5074 (2014).
32. R. S. Herbst *et al.*, *Nature* **515**, 563–567 (2014).
33. P. C. Tumeh *et al.*, *Nature* **515**, 568–571 (2014).
34. R. D. Schreiber, L. J. Old, M. J. Smyth, *Science* **331**, 1565–1570 (2011).
35. T. Matsutake, P. K. Srivastava, *Proc. Natl. Acad. Sci. U.S.A.* **98**, 3992–3997 (2001).
36. H. Matsushita *et al.*, *Nature* **482**, 400–404 (2012).
37. J. C. Castle *et al.*, *Cancer Res.* **72**, 1081–1091 (2012).
38. T. Schumacher *et al.*, *Nature* **512**, 324–327 (2014).
39. M. M. Gubin *et al.*, *Nature* **515**, 577–581 (2014).
40. M. Yadav *et al.*, *Nature* **515**, 572–576 (2014).
41. F. Duan *et al.*, *J. Exp. Med.* **211**, 2231–2248 (2014).
42. N. van Rooij *et al.*, *J. Clin. Oncol.* **31**, e439–e442 (2013).
43. P. F. Robbins *et al.*, *Nat. Med.* **19**, 747–752 (2013).
44. M. Rajasagi *et al.*, *Blood* **124**, 453–462 (2014).
45. C. Linnemann *et al.*, *Nat. Med.* **21**, 81–85 (2015).
46. E. Tran *et al.*, *Science* **344**, 641–645 (2014).

GENE EXPRESSION

MicroRNA control of protein expression noise

Jörn M. Schmiedel,[1,2,3] **Sandy L. Klemm,**[4] **Yannan Zheng,**[3] **Apratim Sahay,**[3] **Nils Blüthgen,**[1,2]*† **Debora S. Marks,**[5]*† **Alexander van Oudenaarden**[3,6,7]*†

MicroRNAs (miRNAs) repress the expression of many genes in metazoans by accelerating messenger RNA degradation and inhibiting translation, thereby reducing the level of protein. However, miRNAs only slightly reduce the mean expression of most targeted proteins, leading to speculation about their role in the variability, or noise, of protein expression. We used mathematical modeling and single-cell reporter assays to show that miRNAs, in conjunction with increased transcription, decrease protein expression noise for lowly expressed genes but increase noise for highly expressed genes. Genes that are regulated by multiple miRNAs show more-pronounced noise reduction. We estimate that hundreds of (lowly expressed) genes in mouse embryonic stem cells have reduced noise due to substantial miRNA regulation. Our findings suggest that miRNAs confer precision to protein expression and thus offer plausible explanations for the commonly observed combinatorial targeting of endogenous genes by multiple miRNAs, as well as the preferential targeting of lowly expressed genes.

MicroRNAs (miRNAs) regulate numerous genes in metazoan organisms (*1–5*) by accelerating mRNA degradation and inhibiting translation (*6*, *7*). Although the physiological function of some miRNAs is known in detail (*1*, *2*, *8*, *9*), it is unclear why miRNA regulation is so ubiquitous and conserved, because individual miRNAs only weakly repress the vast majority of their target genes (*10*, *11*), and knockouts rarely show phenotypes (*12*). One proposed reason for this widespread regulation is the ability of miRNAs to provide precision to gene expression (*13*). Previous work has hypothesized that miRNAs could reduce protein expression variability (noise) when their repressive posttranscriptional effects are antagonized by accelerated transcriptional dynamics (*14*, *15*). However, because miRNA levels are themselves variable, one should expect the propagation of their fluctuations to introduce additional noise (Fig. 1A).

To test the effects of endogenous miRNAs, we quantified protein levels and fluctuations in mouse embryonic stem cells (mESCs) using a dual fluorescent reporter system (*16*), in which two different reporters (ZsGreen and mCherry) are transcribed from a common bidirectional promoter (Fig. 1B). One of the reporters (mCherry) contained several variants and numbers of miRNA binding sites in its 3′ untranslated region (3′UTR),

and we quantified single-cell fluorescence using a flow cytometer (Fig. 1C).

We used ZsGreen fluorescence intensity to bin cells with similar transcriptional activity (mostly due to varying plasmid copy numbers) and calculated mean and noise (standard deviation divided by mean) of mCherry intensity distributions in each bin (Fig. 1D).

We first assessed the effects of endogenous miR-20a in mESCs, on a designed target site in

[1]Integrative Research Institute for the Life Sciences and Institute for Theoretical Biology, Humboldt Universität, 10115 Berlin, Germany. [2]Institute of Pathology, Charité-Universitätsmedizin, 10117 Berlin, Germany. [3]Department of Physics, Massachusetts Institute of Technology (MIT), Cambridge MA 02139, USA. [4]Department of Electrical Engineering and Computer Science, MIT, Cambridge, MA 02139, USA. [5]Department of Systems Biology, Harvard Medical School, Longwood Avenue, Boston, MA 02115, USA. [6]Department of Biology, MIT, Cambridge, MA 02139, USA. [7]Hubrecht Institute, Royal Netherlands Academy of Arts and Sciences, and University Medical Center Utrecht, Uppsalalaan 8, 3584 CT, Utrecht, Netherlands.
*Corresponding author. E-mail: nils.bluethgen@charite.de (N.B.); debbie@hms.harvard.edu (D.S.M.); a.vanoudenaarden@hubrecht.eu (A.v.O.) †These authors contributed equally to this work.

the reporter. In cells with low expression of a reporter (mCherry) containing a miR-20a site, noise was reduced (compared to an unregulated control at equal mCherry expression), in contrast to increased noise at high reporter expression (Fig. 1E). These changes in mCherry noise were more pronounced when the miR-20a sites in the reporter were perfect targets or when there were multiple sites in the 3′ UTR (Fig. 1, F and G, and fig. S1).

In order to explore the mechanism for these seemingly opposing effects on protein expression noise, we built a mathematical model where we decomposed total noise into intrinsic noise and extrinsic noise $\eta_{tot}^2 = \eta_{int}^2 + \eta_{ext}^2$ (17, 18) (see the supplementary materials). Intrinsic noise η_{int} results from the stochasticity of transcription, translation, and decay, but is mostly dominated by transcriptional dynamics (19, 20) and low mRNA copy numbers (21, 22). Extrinsic noise η_{ext} stems from fluctuations propagating from external factors to the gene (23). The modeling predicted opposing effects of miRNA regulation on intrinsic and extrinsic noise. On the one hand, the model predicted that a miRNA-regulated gene

(reg) has reduced intrinsic noise as compared to an unregulated gene (unreg) at equal protein expression levels; intrinsic noise is approximately reduced by the square root of miRNA-mediated fold repression r, $\frac{\eta_{int}^{unreg}}{\eta_{int}^{reg}} \cong \sqrt{r}$ (Fig. 2A). Noise reduction results from miRNA-mediated accelerated mRNA turnover and increased transcriptional activity needed to produce the same amount of protein (14). The model predicts that the effect occurs independently of the mode of miRNA-mediated repression (supplementary note 1). On the other hand, the model predicted that miRNA regulation acts as an additional extrinsic noise source $\eta_{ext} = \tilde{\eta}_\mu \times \varphi$ (Fig. 2B). The magnitude of η_{ext} depends on the noise in the pool of regulating miRNAs ($\tilde{\eta}_\mu$) and on how strongly miRNAs repress the target (φ) (fig. S2). Therefore, the model predicted that the combined net effects of decreased intrinsic and additional extrinsic noise would result in decreased total noise at low expression, but increased total noise at high expression (Fig. 2C); model fits, with the miRNA pool noise $\tilde{\eta}_\mu$ as the only free parameter, yield accurate agreement
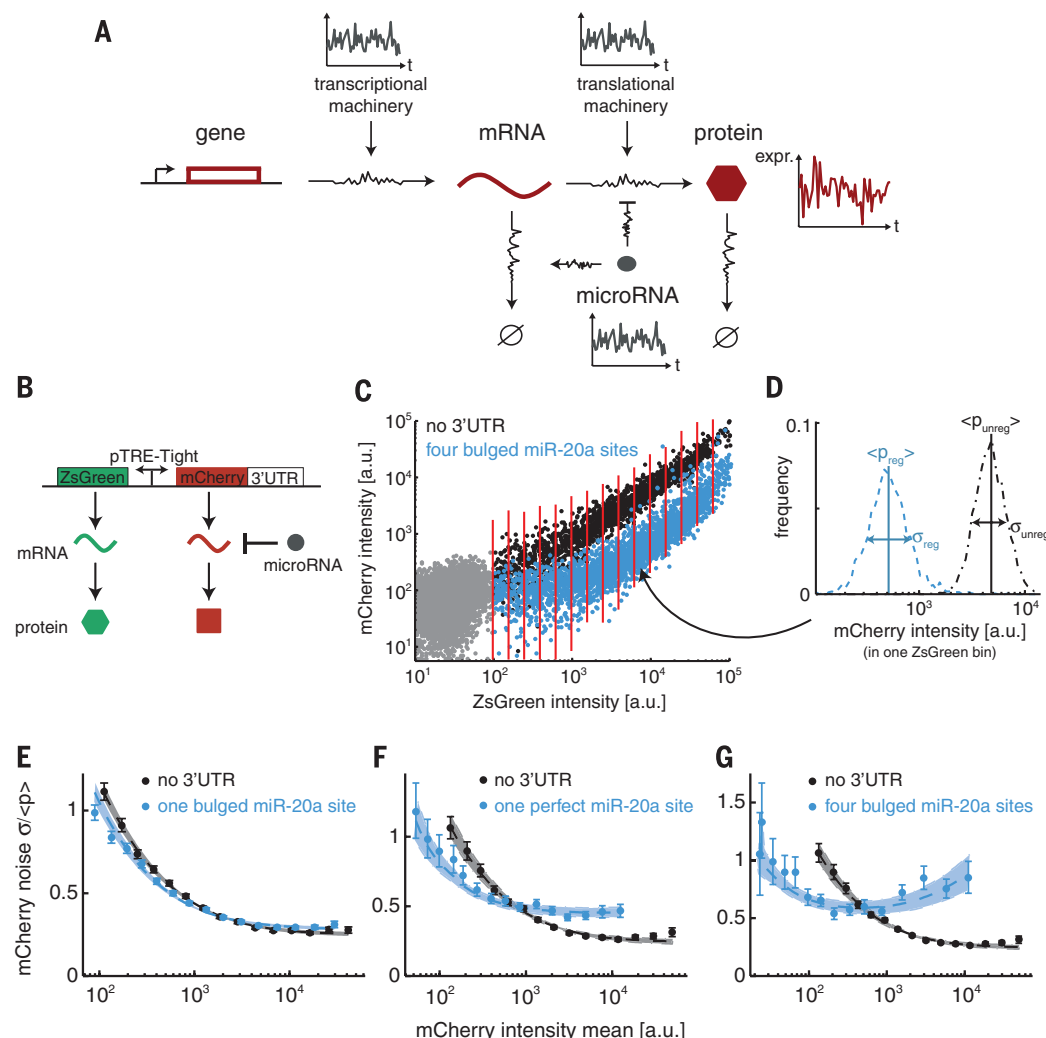
Fig. 1. miRNA regulation has opposing effects on noise at low and high protein expression. (**A**) The expression of a miRNA-regulated gene. Noise in protein expression originates from stochastic molecular reactions in the production of the protein (intrinsic noise; jagged arrows) or fluctuations propagating from external factors (extrinsic noise). (**B**) Plasmid reporter system coding for two fluorescent proteins ZsGreen and mCherry, transcribed from a common bidirectional promoter. The mCherry 3′UTR can be modified to contain miRNA binding sites. (**C**) Overlay of two flow cytometry measurements of mESC populations transiently transfected with different variants of the plasmid system: empty mCherry 3′UTR (black) and mCherry 3′UTR containing four bulged miR-20a binding sites (blue). For further processing, cells are binned according to ZsGreen intensity (red lines), and cells below ZsGreen background are discarded (gray) (supplementary materials). a.u., arbitrary units. (**D**) Mean and noise (standard deviation divided by mean σ/<p>) of mCherry intensities are calculated from marginal distributions in each bin. (**E** to **G**) Noise of mCherry intensity as a function of mean mCherry intensity in each bin for three different miR-20a–regulated constructs

(blue), as compared to respective unregulated constructs (black). Panels are ordered from left to right according to increasing repression of constructs by miR-20a (fig. S1). Dots, data; lines and shaded area, model fit.

with the experimentally observed total noise profiles (Fig. 1, E to G).

To distinguish between miRNA-mediated intrinsic and extrinsic noise effects experimentally, we modified the plasmid reporter system so that both reporters contained identical 3′UTRs (Fig. 3A and fig. S3A). Now intracellular differences in their expression can only result from processes individual to each gene (i.e., intrinsic noise). Comparing identical reporters both with and without miR-20a sites, we showed that miR-20a regulation reduced intrinsic noise, as compared to an unregulated construct (Fig. 3B), by the square root of fold repression, as predicted by modeling (Fig. 3C and fig. S3D). These results also show that the observed increase in total noise at high mCherry expression must be due to additional extrinsic noise (fig. S3C).

The model and the experiments suggest that the reduction of intrinsic noise is a generic property of miRNAs and should occur irrespective of the specific miRNAs or the molecular details of the mRNA-miRNA interaction. To test the generality of these conclusions, we constructed eight additional reporters with mCherry 3′UTRs containing a perfect binding site for a variety of miRNAs that are endogenously expressed in mESCs (fig. S4). For all constructs, the intrinsic noise reduction was approximately the square root of fold repression (using model fit to total noise, figs. S3E and S5). This was also confirmed by direct measurement for miR-291a target sites (Fig. 3C and fig. S3B) and reporters containing AU-rich elements (24) (figs. S3F and S6), the latter further supporting the plausibility that the

reduction of intrinsic noise is a generic property of posttranscriptional repressors.

Additional extrinsic noise stems from the variability of the miRNA pool, and consistent with this, we find that miRNA pool noise indeed differs between miRNAs (Fig. 3D). The validity of these results is supported by the observation that different constructs assaying the same miRNA yield similar pool noise estimates (fig. S7). Although miRNA pool noise decreases for miRNAs conferring stronger repression, it is still substantial for the most potent and highly expressed miRNAs in mESCs [miR-290 cluster (25)] (Fig. 3D). The miRNAs with two independent gene copies, producing the identical mature miRNA (Fig. 3D, red), tend to have lower miRNA pool noise than to single-gene miRNAs. This suggested to us that

Fig. 2. Predictions of the noise model for a miRNA-regulated gene. (**A**) Intrinsic noise due to low molecule numbers declines with increasing expression. miRNA regulation reduces intrinsic noise as a function of repression due to higher mRNA turnover. (**B**) Noise in miRNA pool propagating to a target gene results in additional extrinsic noise that is dependent on conferred repression and saturation of the miRNA pool (fig. S2). (**C**) Net influence of miRNA regulation results in decreased total noise at low expression levels and increased total noise at high expression levels.

Fig. 3. Exploration of intrinsic and extrinsic noise effects. (**A**) Plasmid reporter system with identical 3′UTRs for ZsGreen and mCherry, to quantify expression-dependent intrinsic noise. (**B**) Intrinsic noise as a function of expression for three different miR-20a biregulated constructs. Dots, data; lines and shaded area, model fit. (**C**) Measured intrinsic noise reduction for biregulated constructs compared to fold repression, as measured independently by mCherry-regulated constructs (fig.

S1). *n* = 3 biological replicates. (**D**) miRNA pool noise estimates for nine different miRNAs endogenously expressed in mESCs. A subset of miRNAs with two instead of one gene copies is indicated in red; *n* ≥ 3 biological replicates. (**E**) miRNA pool noise estimates for individual and mixed pools, using data from reporters with two perfect binding sites behind mCherry as indicated. Red bars, expectation for mixed pool noise when subpools were fully correlated. *n* = 3 biological replicates.

miRNA pools could have lower noise if they consist of independently transcribed miRNAs, and thus uncorrelated fluctuations can average out. To test this hypothesis, we constructed reporters with perfect target sites for miR-20a and either miR-16 or miR-290 in the mCherry 3′UTR and compared them to reporters with two perfect target sites for miR-16, miR-20a, or miR-290, respectively. We found that the noise levels in the mixed pools were lower than expected if the individual miRNA pools were fully correlated and could be lower than the noise in the individual miRNA pools (Fig. 3E and fig. S8). Therefore, our data show that, if noise between different miRNAs is not correlated, combinatorial regulation can result in lower noise of the target protein.

In contrast to our artificial 3′UTRs, endogenous mRNAs often contain many binding sites to different miRNAs and with less complementarity (3, 26). To test whether our findings are likely to be applicable in vivo, we constructed mCherry reporters with the 3′UTRs from *Wee1*, *Lats2, Casp2*, and *Rbl2*, all predicted to be com-binatorial regulated by mESC miRNAs (table S1). This multiple-miRNAs regulation resulted in 3- to 5.5-fold repression as compared to the control 3′UTRs containing mutated sites (fig. S9A) and reduced total noise except when reporter expression levels were high (Fig. 4A and fig. S9A). Model fits estimate intrinsic noise reduction for the wild-type 3′UTRs as large as the square root of fold repression (fig. S3G), consistent with our findings for the artificial 3′UTRs. Furthermore, little additional noise at high expression levels results from low noise in the mixed miRNA pools regulating the wild-type 3′UTRs (fig. S9B), corroborating the idea that combinatorial miRNA regulation is a potent way to optimize overall noise reduction.

To determine whether the reporter assay covers expression levels relevant to endogenous genes, we used fluorescence-activated cell sorting (FACS) and RNA sequencing (fig. S10A). The reporter assay covers the range of 25 to 99% of expressed genes in mESCs (Fig. 4B). Model-based extrapolation shows that the reduction of total noise for the endogenous 3′UTRs extends in a graded fashion up to the top 10% of the transcriptome expression distribution (Fig. 4C). Although most miRNAs individually repress genes only to a small extent (10, 11), hundreds of genes are substantially repressed (>twofold) by the combinatorial action of miRNAs in mESCs (fig. S11), as determined from transcriptome expression data for wild-type and miRNA-deficient Dicer knockout mESCs (27). Furthermore, most of the highly repressed genes have low expression levels [fig. S11, consistent with (28, 29)], suggesting that these genes should have reduced protein expression noise as a consequence of miRNA regulation in vivo.

Our integrated theoretical and experimental analyses show that the reduction of intrinsic noise is a generic property of miRNA regulation (and more generally posttranscriptional regulation) that is linked to the repression of protein expression. miRNAs preferentially target lowly expressed genes, for which noise reduction will be strongest, while selectively avoiding ubiquitous and highly expressed genes (28, 29). Combinatorial miRNA regulation, a widely observed phenomenon in vivo (3, 26), enhances overall noise reduction by providing strong repression to endogenous genes with only little additional noise from miRNA pools. Combinatorial miRNA regulation may thus be a potent mechanism to reinforce cellular identity by reducing gene expression fluctuations that are undesirable for the cell.

REFERENCES AND NOTES

1. R. C. Lee, R. L. Feinbaum, V. Ambros, *Cell* **75**, 843–854 (1993).
2. B. Wightman, I. Ha, G. Ruvkun, *Cell* **75**, 855–862 (1993).
3. A. J. Enright et al., *Genome Biol.* **5**, R1 (2003).
4. B. John et al., *PLOS Biol.* **2**, e363 (2004).
5. B. P. Lewis, C. B. Burge, D. P. Bartel, *Cell* **120**, 15–20 (2005).
6. H. Guo, N. T. Ingolia, J. S. Weissman, D. P. Bartel, *Nature* **466**, 835–840 (2010).
7. L. P. Lim et al., *Nature* **433**, 769–773 (2005).
8. J. Brennecke, D. R. Hipfner, A. Stark, R. B. Russell, S. M. Cohen, *Cell* **113**, 25–36 (2003).
9. R. J. Johnston Jr., O. Hobert, *Nature* **426**, 845–849 (2003).
10. D. Baek et al., *Nature* **455**, 64–71 (2008).
11. M. Selbach et al., *Nature* **455**, 58–63 (2008).
12. E. A. Miska et al., *PLOS Genet.* **3**, e215 (2007).
13. D. P. Bartel, C.-Z. Chen, *Nat. Rev. Genet.* **5**, 396–400 (2004).
14. M. S. Ebert, P. A. Sharp, *Cell* **149**, 515–524 (2012).
15. J. Noorbakhsh, A. H. Lang, P. Mehta, *PLOS ONE* **8**, e72676 (2013).
16. S. Mukherji et al., *Nat. Genet.* **43**, 854–859 (2011).
17. M. B. Elowitz, A. J. Levine, E. D. Siggia, P. S. Swain, *Science* **297**, 1183–1186 (2002).
18. P. S. Swain, M. B. Elowitz, E. D. Siggia, *Proc. Natl. Acad. Sci. U.S.A.* **99**, 12795–12800 (2002).
19. W. J. Blake, M. KÆrn, C. R. Cantor, J. J. Collins, *Nature* **422**, 633–637 (2003).
20. A. Raj, C. S. Peskin, D. Tranchina, D. Y. Vargas, S. Tyagi, *PLOS Biol.* **4**, e309 (2006).
21. E. M. Ozbudak, M. Thattai, I. Kurtser, A. D. Grossman, A. van Oudenaarden, *Nat. Genet.* **31**, 69–73 (2002).
22. A. Bar-Even et al., *Nat. Genet.* **38**, 636–643 (2006).
23. J. M. Pedraza, A. van Oudenaarden, *Science* **307**, 1965–1969 (2005).
24. C. Barreau, L. Paillard, H. B. Osborne, *Nucleic Acids Res.* **33**, 7138–7150 (2005).
25. A. Marson et al., *Cell* **134**, 521–533 (2008).
26. A. Krek et al., *Nat. Genet.* **37**, 495–500 (2005).
27. A. K. L. Leung et al., *Nat. Struct. Mol. Biol.* **18**, 237–244 (2011).
28. P. Sood, A. Krek, M. Zavolan, G. Macino, N. Rajewsky, *Proc. Natl. Acad. Sci. U.S.A.* **103**, 2746–2751 (2006).
29. K. K.-H. Farh et al., *Science* **310**, 1817–1821 (2005).
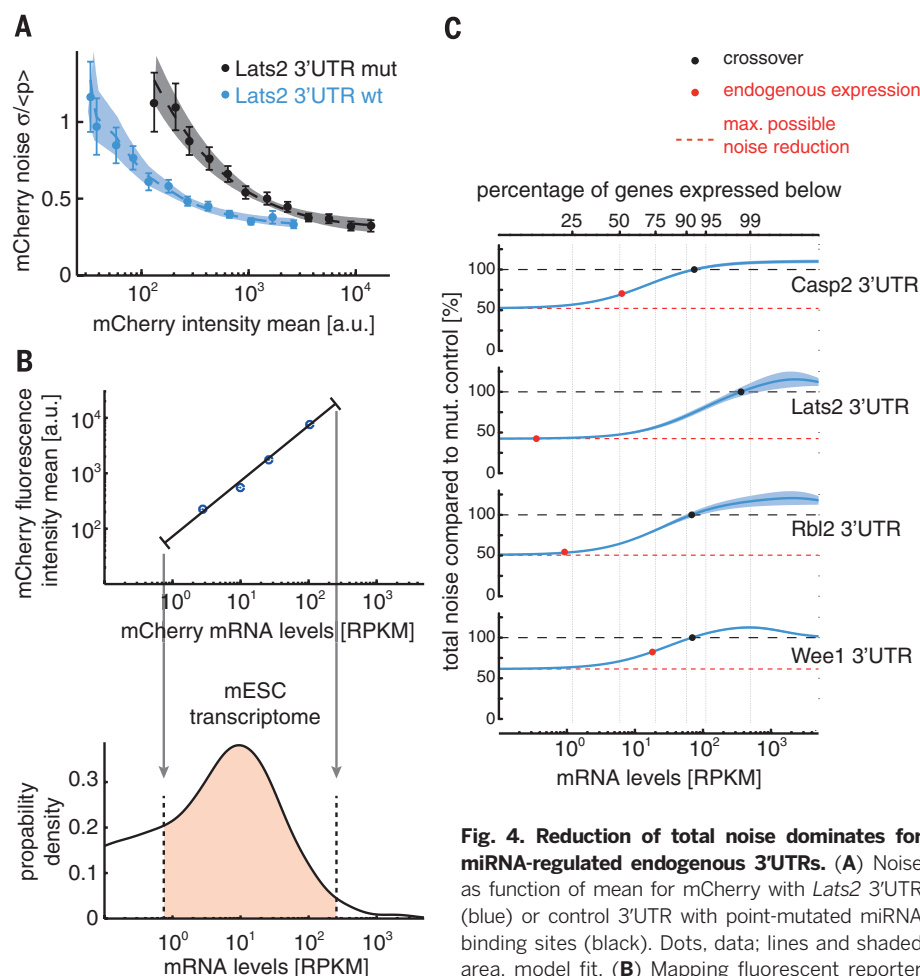
Fig. 4. Reduction of total noise dominates for miRNA-regulated endogenous 3′UTRs. (**A**) Noise as function of mean for mCherry with *Lats2* 3′UTR (blue) or control 3′UTR with point-mutated miRNA binding sites (black). Dots, data; lines and shaded area, model fit. (**B**) Mapping fluorescent reporter range to mESC transcriptome. (Upper panel) FACS and least-squares regression were used to determine conversion between mean mCherry fluorescent intensities and mCherry mRNA levels (as measured by RNA-seq). (Lower panel) Range covered by mCherry in relation to transcriptome expression in mESCs (~25 to ~99%). FPKM, fragments per kilobase of exon model per million mapped reads. (**C**) Model-based extrapolation of total noise in assayed endogenous 3′UTRs relative to control 3′UTRs as a function of transcriptome expression (blue line and area, mean and 95% confidence interval based on parameter estimates of three biological replicates).

EPIGENETICS

Restricted epigenetic inheritance of H3K9 methylation

Pauline N. C. B. Audergon, Sandra Catania,* Alexander Kagansky,† Pin Tong, Manu Shukla, Alison L. Pidoux, Robin C. Allshire‡

Posttranslational histone modifications are believed to allow the epigenetic transmission of distinct chromatin states, independently of associated DNA sequences. Histone H3 lysine 9 (H3K9) methylation is essential for heterochromatin formation; however, a demonstration of its epigenetic heritability is lacking. Fission yeast has a single H3K9 methyltransferase, Clr4, that directs all H3K9 methylation and heterochromatin. Using releasable tethered Clr4 reveals that an active process rapidly erases H3K9 methylation from tethering sites in wild-type cells. However, inactivation of the putative histone demethylase Epe1 allows H3K9 methylation and silent chromatin maintenance at the tethering site through many mitotic divisions, and transgenerationally through meiosis, after release of tethered Clr4. Thus, H3K9 methylation is a heritable epigenetic mark whose transmission is usually countered by its active removal, which prevents the unauthorized inheritance of heterochromatin.

n most eukaryotes, the methylation of nucleosomal histone H3 on lysine 9 (H3K9me) is required for the assembly of constitutive heterochromatin (1). H3K9me2/3 is bound by HP1/Swi6 proteins and Suv39/Clr4 H3K9 methyltransferases to form heterochromatic regions (2–6). Because Suv39 and Clr4 can bind the H3K9me2/3 marks that they generate, and because HP1 proteins may also facilitate recruitment of these methyltransferases (7), it is thought that H3K9 methylation and heterochromatin can be maintained by self-propagation, even when the initiator is withdrawn (8, 9). However, in eukaryotic systems that exhibit overtly heritable chromatin states, there is often a tight relationship between DNA methylation, H3K9 methylation, and heterochromatin, confounding analyses of the heritability of H3K9 methylation (10, 11). Fission yeast lacks DNA methylation and a single nonessential methyltransferase, Clr4 (Suv39 ortholog), is responsible for all H3K9me-dependent heterochromatin (12). Thus, fission yeast is an ideal system in which to determine whether H3K9me-dependent heterochromatin is truly heritable. Clr4 normally requires sequence-directed targeting to particular chromosomal regions via RNA interference (RNAi) in a process involving

Wellcome Trust Centre for Cell Biology and Institute of Cell Biology, School of Biological Sciences, The University of Edinburgh, Max Born Crescent, Edinburgh EH9 3BF, Scotland, UK.
*Present address: Department of Biochemistry and Biophysics, University of California, San Francisco, CA 94158, USA. †Present address: Medical Research Council (MRC) Human Genetics Unit, MRC Institute of Genetics and Molecular Medicine, The University of Edinburgh, Edinburgh EH4 2XU, Scotland, UK. ‡Corresponding author. E-mail: robin.allshire@ed.ac.uk

Fig. 1. H3K9 methylation is rapidly lost upon release of tethered TetR-Clr4*. (**A**) Positions of *4xtetO*, tethered TetR-Clr4* beside *ade6+* at *ura4*, and surrounding *Schizosaccharomyces pombe* chromosome III genes. Dumbbells indicate primer pairs. ncRNA, noncoding RNA. (**B** and **C**) Quantitative chromatin immunoprecipitation (qChIP) time course of FLAG-TetR-Clr4* (B) and H3K9me2 (C) levels on *4xtetO-ade6+* after AHT addition using the indicated primers. Data are mean ± SD (error bars) (n = 3 experimental replicates). P < 0.05 (t test).

heterochromatin nucleation, spreading, and maintenance (13–15). The inheritance of heterochromatin on centromere repeat DNA inserted at ectopic locations also requires RNAi, but at the mating-type locus heterochromatin is dependent on DNA binding factors in the absence of RNAi (13–17). However, constitutive tethering of Clr4 to a euchromatic locus via the Gal4 DNA binding domain (GBD) allows the assembly of an extensive domain of H3K9me-heterochromatin, independently of RNAi (18). In this study, we tethered a regulatable TetR^{off}-Clr4 fusion protein to determine whether H3K9me is a persistent histone modification that can be stably copied through mitotic cell divisions and meiosis after release or loss of the TetR^{off}-Clr4 initiator.

TetR^{off}-2xFLAG-Clr4-cdd fusion protein (abbreviated TetR-Clr4*), lacking the Clr4 chromo-domain, was stably expressed in cells with an *ade6*$^+$ gene downstream of *4xtetO* binding sites at the *ura4* locus (*4xtetO-ade6*$^+$) (Fig. 1A) (19). TetR-Clr4* silences *4xtetO-ade6*$^+$ independently of RNAi (*ago1Δ*, *dcr1Δ*), similar to GBD-Clr4 (18), resulting in reduced RNA polymerase II association and high H3K9me2 levels and silencing over a broad region (Fig. 1C and figs. S1 and S9, C to E). TetR-Clr4* is released within 5 min from *tetO* sites by addition of anhydrotetracycline (AHT) (Fig. 1B). All strains used in these experiments also express wild-type (WT) Clr4, which can interact via its chromodomain with TetR-Clr4–directed H3K9me and thus potentially use its read-write capabilities to methylate newly incorporated H3 and allow heterochromatin transmission to daughter cells after TetR-Clr4* release. However, in a time course, H3K9me2 rapidly declines over

4xtetO-ade6$^+$ after AHT addition; >90% is lost within 6 hours (Fig. 1C and fig. S2A). AHT itself does not affect endogenous heterochromatin integrity (fig. S2B). H3 levels do not decline on *4xtetO-ade6*$^+$ over this period (fig. S2A). Swi6^{HP1} is also lost from *4xtetO-ade6*$^+$ when cells are grown with AHT (fig. S1F).

We also tethered TetR-Clr4* within two non-essential genes with long open reading frames, which are less likely to contain unannotated features that might interfere with heterochromatin integrity. Moreover, both *sib1*$^+$ (15,005 base pairs) and *vps1302*$^+$ (9200 base pairs) exhibit expression levels and rates of H3 turnover that are ~three times lower than those of *ade6*$^+$ (Fig. 2, A to C, and fig. S3). *4xtetO* and *1xtetO* sites were placed within *sib1* and *vps1203*, respectively (Fig. 2, D and E). *sib1:4xtetO* and *vps1302:1xtetO* were
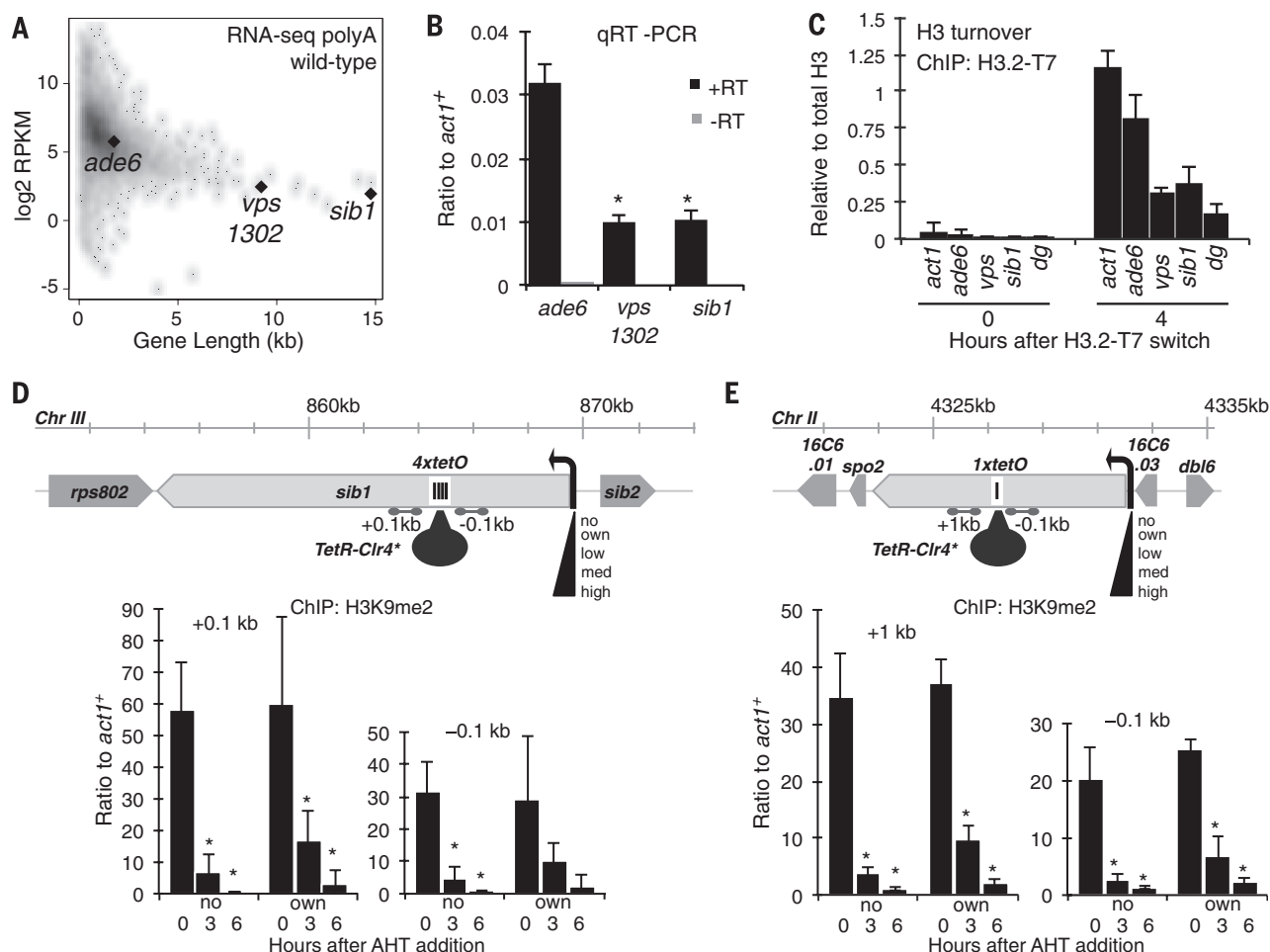
Fig. 2. Tethering TetR-Clr4* at loci with low expression and histone turnover does not stabilize H3K9 methylation. (A) Read distribution (log₂RPKM, where RPKM is reads per kilobase per million) from *S. pombe* polyA RNA sequencing (RNA-seq) relative to gene length. *ade6*$^+$, *sib1*$^+$, and *vps1302*$^+$ are indicated. (B) Quantitative reverse transcription polymerase chain reaction (qRT-PCR) of *ade6*$^+$, *sib1*$^+$, and *vps1302*$^+$ RNA levels. Data are mean ± SD (error bars) (n = 3). *P < 0.005 (t test). (C) Recombination-induced tag exchange monitoring incorporation of new H3-T7 on *act1*$^+$, *ade6*$^+$, *sib1*$^+$, *vps1302*$^+$, and *cen-dg* repeats. Data are mean ± SD (error bars) (n = 3). H3 turnover on *sib1*$^+$ and *vps1302*$^+$ was significantly lower

than on *act1*$^+$ and *ade6*$^+$. P < 0.05 (t test). (**D** and **E**) *sib1*$^+$ and *vps1302*$^+$ lose H3K9me2 after TetR-Clr4* release. The position of *tetO* sites within *sib1* and *vps1302* is shown. *own* promoters were replaced with *ura4*$^+$ (*no*) or swapped to low-, medium (*med*)–, or high-adh1 promoter versions (20). Dumbbells indicate primer pairs. qChIP of H3K9me2 levels, at time points relative to AHT addition, on *sib1:4xtetO* (D) and *vps1302:1xtetO* (E) with *no* or indicted promoters is shown. Data are mean ± SD (error bars) (n = 3); P < 0.05 (t test). The H3K9me2 level within *sib1* carrying its own promoter is decreased with a probability of, respectively, P = 0.068 and 0.051, 3 and 6 hours after TetR-Clr4* release.

also placed under the control of low, medium (*med*), and high versions of the constitutive *adh1* promoter (*20*). We also generated *sib1:4xtetO* and *vps1302:1xtetO* without promoters (*no*). All strains expressed WT Clr4 and TetR-Clr4*. Both *sib1+* and *vps1302+* were expressed at low levels when their promoters were removed and at much higher levels from *med-adh1* or *high-adh1* compared with their *own* or *low-adh1* promoters (fig. S4). TetR-Clr4* was unable to establish much H3K9me2 when tethered to *sib1:4xtetO* or *vps1302:1xtetO* expressed from *hi-adh1* and relatively low levels when expressed from *med-adh1*, but substantial H3K9me2 occurred when either gene had *no*, its *own*, or the *low-adh1* promoter (fig. S4). However, as with *4xtetO-ade6+*, rapid loss of H3K9me2 followed TetR-Clr4* release from even *no* and *own* promoter constructs; again, >90% was lost within 6 hours (Fig. 2, D and E). Although high levels of transcription across tethering sites prevents the establishment of H3K9me by TetR-Clr4*, neither low promoter strength nor low H3 turnover renders H3K9me more persistent upon methyltransferase release. Thus, the inability to maintain H3K9 methylation upon removal of the initiating tethered Clr4 methyltransferase is probably a general feature of euchromatic loci.

To determine whether the loss of H3K9 methylation from the tethering site is coupled to replication or passage through the cell cycle, we released TetR-Clr4* from *4xtetO-ade6+* in *cdc25-22* synchronized cultures (Fig. 3A). H3K9me2

levels on *4xtetO-ade6+* dropped by 70% within one cell cycle after the addition of AHT to these synchronized cultures, and no accelerated H3K9me2 loss was evident during S phase, which is coincident with septation (*21*). We also released TetR-Clr4* from *4xtetO-ade6+* in noncycling G_2 blocked *cdc25-22* cells (Fig. 3B). TetR-Clr4* was lost from *4xtetO-ade6* within 1 hour, and H3K9me declined to less than 25% of initial levels within 4 hours. Thus, after release of the initiating methyltransferase, rather than being passively diluted through chromatin replication, H3K9 methylation must be removed by an active process.

Known and putative histone demethylases might act to remove H3K9me and thus disassemble heterochromatin from TetR-Clr4* tethering sites. We therefore tested whether mutation of genes for six JmjC domain (Epe1, Jmj1, Jmj2, Jmj4, Lid2, and Msc1) (*22*) or two SWIRM/amino-oxidase domain proteins (Lsd1 and Lsd2) (*23*) allowed long-term *4xtetO-ade6+* silencing after tethered TetR-Clr4* release. WT *4xtetO-ade6+ TetR-Clr4** cells form red/*ade6*-repressed colonies on indicator plates lacking AHT, whereas white/*ade6*-expressing colonies appear on +AHT plates due to loss of H3K9me-dependent heterochromatin over *4xtetO-ade6+*. Of the eight tested mutants, only *epe1Δ* consistently formed red-pink colonies on +AHT plates, indicating that *4xtetO-ade6+* can remain repressed without bound TetR-Clr4* (Fig. 4A and figs. S5 and S6). Catalytically inactivating mutations in the Fe(II) or 2-oxyglutarate binding sites of the Epe1 putative demethylase (*epe1-H297A*

and *epe1-K314A*) had a similar phenotype (Fig. 4A, fig. S6, and table S3). The variable silencing and colony color most likely reflects stochastic events at the *4xtetO-ade6+* locus in *epe1Δ* cells in which H3K9me domains are known to expand and additional heterochromatin islands also appear, potentially titrating and redistributing heterochromatin proteins between various loci in individual cells (*24–27*). Maintenance of the silenced state in *epe1Δ* cells is not dependent on the RNAi component Ago1, as *ago1Δepe1Δ* cells form red/*ade6*-silent colonies on +AHT plates (fig. S7A), but it does require untethered WT Clr4 with an intact Clr4 chromodomain and Swi6 (fig. S8). This reliance on untethered, intact Clr4 and Swi6 is consistent with a simple read-write propagation mechanism (fig. S10).

Silencing of *4xtetO-ade6+* can be propagated through multiple cell divisions in *epe1* mutants (lost in 4% of cells per division), and a high proportion of descendant cells retain silencing of, and 30 to 70% of H3K9me2 on, *4xtetO-ade6+* after TetR-Clr4* release by AHT. In contrast, *4xtetO-ade6+* silencing and H3K9me2 are completely lost in WT cells (Fig. 4A and fig. S7, B to E). The relative levels of H3K9me2 and H3K9me3 detected on *4xtetO-ade6+* are similar in WT and *epe1Δ* cells, and surrounding genes are silenced by H3K9me2 in both WT and *epe1Δ*. (fig. S9). To determine whether H3K9me on *4xtetO-ade6+* in *epe1Δ* cells is maintained through meiosis in the absence of TetR-Clr4*, *epe1Δ 4xtetO-ade6+ tetr-clr4** cells (F_0) were crossed to *epe1Δ* cells devoid of both *4xtetO-ade6+* and TetR-Clr4*, and then F_1 *epe1Δ 4xtetO-ade6+* progeny lacking TetR-Clr4* were again crossed to *epe1Δ* cells. A high proportion of resulting F_2 *epe1Δ 4xtetO-ade6+* progeny formed red-pink/*ade6*-repressed colonies, and H3K9me2 was retained (Fig. 4B and fig. S6B). Thus, *epe1Δ* allows silencing and H3K9me to persist through multiple mitotic divisions and meiosis, in the complete absence of the tethered TetR-Clr4* that initiated H3K9me-dependent heterochromatin on *4xtetO-ade6+*. Crossing of red F2 *epe1Δ 4xtetO-ade6+* cells to WT *epe1+* cells resulted in loss of silencing (white colonies only) and H3K9me2 from the *4xtetO-ade6+* locus. Thus, provision of *epe1+* results in removal of persistent H3K9me and loss of silencing (Fig. 4B). Genetically identical naïve *epe1Δ 4xtetO-ade6+* cells that were never exposed to the TetR-Clr4* initiator formed only white/*ade6*-expressing colonies, and H3K9me2 was absent (Fig. 4B). We conclude that the transient tethering of TetR-Clr4* adjacent to *4xtetO-ade6+* allows establishment of H3K9me-dependent heterochromatin, which can be propagated epigenetically through mitotic cell divisions and meiosis using endogenous read-write copying mechanisms, provided that Epe1 is rendered nonfunctional (for a model, see fig. S10).

Propagation of heterochromatin on *4xtetO-ade6+* in *epe1* mutants requires recognition of TetR-Clr4*–mediated H3K9me by the chromodomain of Clr4 and also Swi6 (fig. S8). Epe1 associates with Swi6[HP1] and clearly opposes heterochromatin formation (*24–28*). Indeed, Epe1 associates with TetR-Clr4*–mediated heterochromatin (fig. S7C). Although
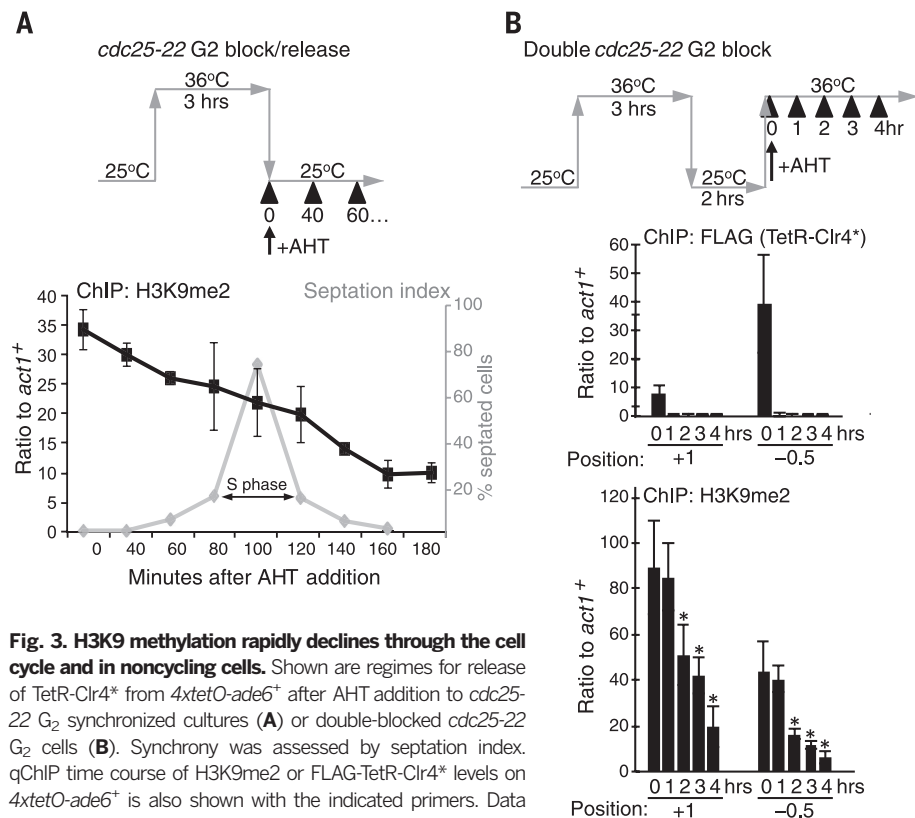
Fig. 3. H3K9 methylation rapidly declines through the cell cycle and in noncycling cells. Shown are regimes for release of TetR-Clr4* from *4xtetO-ade6+* after AHT addition to *cdc25-22* G_2 synchronized cultures (**A**) or double-blocked *cdc25-22* G_2 cells (**B**). Synchrony was assessed by septation index. qChIP time course of H3K9me2 or FLAG-TetR-Clr4* levels on *4xtetO-ade6+* is also shown with the indicated primers. Data are mean ± SD (error bars) (n = 3). T2, T3, and T4 H3K9me2 levels are significantly less than T0; *P < 0.05 (t test).
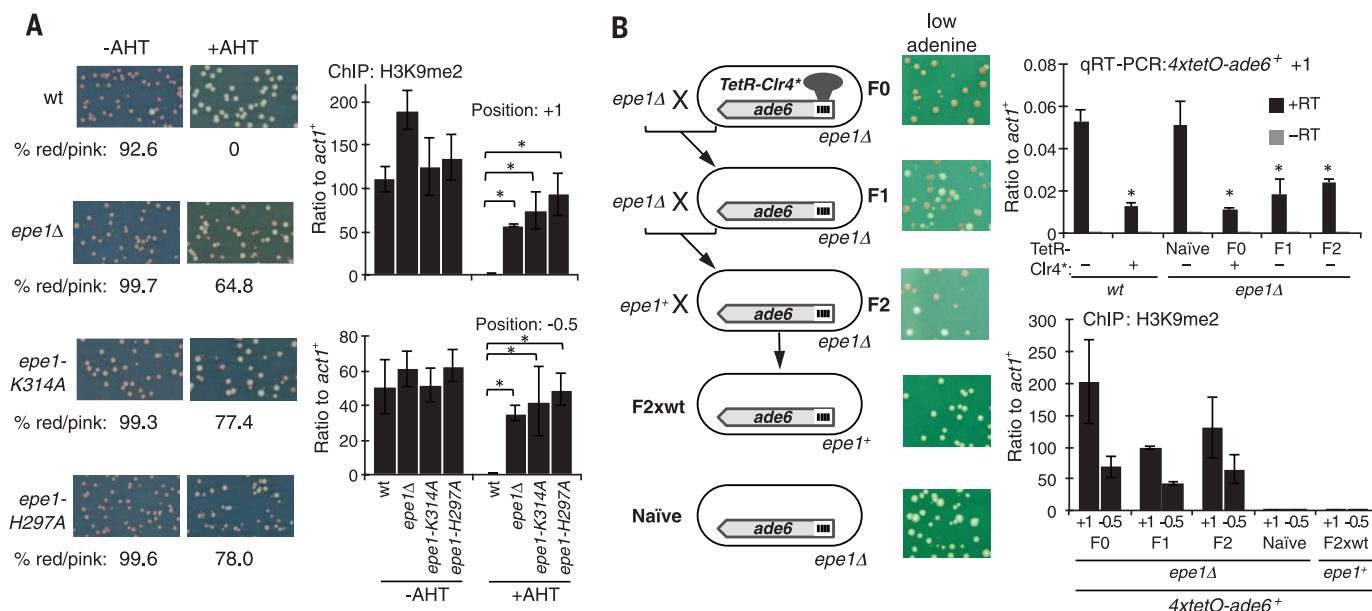
Fig. 4. *epe1* mutants retain heterochromatin without tethered Clr4 methyltransferase through multiple cell divisions and meiosis. (**A**) WT, *epe1Δ*, *epe1-K314A*, and *epe1-H297A* cells carrying *4xtetO-ade6⁺* and expressing TetR-Clr4* were grown with or without AHT. Colony color assay to assess *4xtetO-ade6⁺* silencing (red-pink colonies; percent of total indicated) and H3K9me2 qChIP on *4xtetO-ade6⁺* with (-AHT) or without (+AHT) tethered TetR-Clr4* are shown. Data are mean ± SD (error bars) (*n* = 3). *P* < 0.05 (*t* test). (**B**) TetR-Clr4* was completely removed from F₀ *epe1Δ 4xtetO-ade6⁺ tetR-Clr4*** cells by crossing to *epe1Δ* lacking TetR-Clr4* and *4xtetO-ade6⁺*. F₁ progeny were crossed to *epe1Δ* cells, generating *epe1Δ* F₂ progeny. *epe1⁺* F₂×WT progeny were produced by crossing *epe1⁺* into *epe1Δ 4xtetO-ade6⁺* F₂ cells. Naïve *epe1Δ 4xtetO-ade6⁺* cells never expressed TetR-Clr4*. Colony color, qRT-PCR, and qChIP assays were performed to assess silencing and transcription of *4xtetO-ade6⁺*, and H3K9me2 levels on *4xtetO-ade6⁺* in indicated cell types are shown. Data are mean ± SD (error bars) (*n* = 3). *4xtetO-ade6⁺* RNA levels are significantly reduced in F₀, F₁, and F₂ compared with WT cells without TetR-Clr4*. *P* < 0.05 (*t* test).

Epe1 contains a JmjC domain, its Fe(II) binding site is unusual, and histone demethylase activity has not been detected (*22*). However, the human PHF2 JmjC domain bears a similar anomaly but phosphorylation activates its latent H3K9 demethylase activity (*29*). The analyses presented here are consistent with Epe1 normally acting as an H3K9 demethylase that removes H3K9 methylation from ectopic sites of heterochromatin formation. Moreover, additional heterochromatin islands and domain expansion in *epe1* mutants are best explained by the loss of an H3K9 demethylase that prevents excessive H3K9me-dependent heterochromatin formation. Epe1-dependent removal of H3K9me ensures regulation of centromeric heterochromatin and makes the RNAi pathway essential for the systematic replenishment of H3K9me every cell cycle (*30, 31*). Epe1 itself may be regulated in response to environmental cues to retain or eliminate H3K9 methylation at specific locations (*26*). Indeed, Epe1 levels are regulated, and this may aid the persistence of centromeric H3K9me-dependent heterochromatin (*28*). Thus, opposing H3K9 methyltransferase and demethylase activities must be finely tuned to allow controlled heterochromatin formation and prevent its inappropriate mitotic and trans-generational inheritance. It seems counterintuitive for heterochromatin to carry a means of self-destruction; however, such an inbuilt safety mechanism averts the inappropriate, and potentially deleterious, silencing of genes by removing repressive heterochromatin and preventing its propagation.

REFERENCES AND NOTES

1. G. Almouzni, A. V. Probst, *Nucleus* **2**, 332–338 (2011).
2. A. J. Bannister *et al.*, *Nature* **410**, 120–124 (2001).
3. M. Lachner, D. O'Carroll, S. Rea, K. Mechtler, T. Jenuwein, *Nature* **410**, 116–120 (2001).
4. K. Zhang, K. Mosch, W. Fischle, S. I. Grewal, *Nat. Struct. Mol. Biol.* **15**, 381–388 (2008).
5. T. Wang *et al.*, *PLOS ONE* **7**, e52977 (2012).
6. S. A. Jacobs, W. Fischle, S. Khorasanizadeh, *Methods Enzymol.* **376**, 131–148 (2003).
7. L. Aagaard *et al.*, *EMBO J.* **18**, 1923–1938 (1999).
8. C. Rivera, Z. A. Gurard-Levin, G. Almouzni, A. Loyola, *Biochim. Biophys. Acta* **1839**, 1433–1439 (2014).
9. B. Zhu, D. Reinberg, *Cell Res.* **21**, 435–441 (2011).
10. X. Cheng, *Cold Spring Harbor Perspect. Biol.* **6**, a018747 (2014).
11. N. A. Hathaway *et al.*, *Cell* **149**, 1447–1460 (2012).
12. J. Nakayama, J. C. Rice, B. D. Strahl, C. D. Allis, S. I. Grewal, *Science* **292**, 110–113 (2001).
13. F. E. Reyes-Turcu, S. I. Grewal, *Curr. Opin. Genet. Dev.* **22**, 156–163 (2012).
14. S. E. Castel, R. A. Martienssen, *Nat. Rev. Genet.* **14**, 100–112 (2013).
15. A. Buscaino *et al.*, *EMBO J.* **32**, 1250–1264 (2013).
16. B. S. Wheeler, B. T. Ruderman, H. F. Willard, K. C. Scott, *Genetics* **190**, 549–557 (2012).
17. S. Jia, K. Noma, S. I. S. Grewal, *Science* **304**, 1971–1976 (2004).
18. A. Kagansky *et al.*, *Science* **324**, 1716–1719 (2009).
19. Materials and methods are available as supplementary materials on *Science* Online.
20. T. Sakuno, K. Tada, Y. Watanabe, *Nature* **458**, 852–858 (2009).
21. S. M. Kim, J. A. Huberman, *EMBO J.* **20**, 6115–6126 (2001).
22. Y. Tsukada *et al.*, *Nature* **439**, 811–816 (2006).
23. Y. Shi *et al.*, *Cell* **119**, 941–953 (2004).
24. M. Zofall, S. I. S. Grewal, *Mol. Cell* **22**, 681–692 (2006).
25. N. Ayoub *et al.*, *Mol. Cell. Biol.* **23**, 4356–4370 (2003).
26. M. Zofall *et al.*, *Science* **335**, 96–100 (2012).
27. S. C. Trewick, E. Minc, R. Antonelli, T. Urano, R. C. Allshire, *EMBO J.* **26**, 4670–4682 (2007).
28. S. Braun *et al.*, *Cell* **144**, 41–54 (2011).
29. A. Baba *et al.*, *Nat. Cell Biol.* **13**, 668–675 (2011).
30. E. S. Chen *et al.*, *Nature* **451**, 734–737 (2008).
31. A. Kloc, M. Zaratiegui, E. Nora, R. Martienssen, *Curr. Biol.* **18**, 490–495 (2008).

SUPPLEMENTARY MATERIALS

www.sciencemag.org/content/348/6230/132/suppl/DC1
Materials and Methods
Figs. S1 to S10
Tables S1 to S3
Reference (*32*)

ANTITUMOR IMMUNITY

A shed NKG2D ligand that promotes natural killer cell activation and tumor rejection

Weiwen Deng,[1] Benjamin G. Gowen,[1] Li Zhang,[1] Lin Wang,[1] Stephanie Lau,[1] Alexandre Iannello,[1] Jianfeng Xu,[1] Tihana L. Rovis,[2] Na Xiong,[3] David H. Raulet[1]*

Immune cells, including natural killer (NK) cells, recognize transformed cells and eliminate them in a process termed immunosurveillance. It is thought that tumor cells evade immunosurveillance by shedding membrane ligands that bind to the NKG2D-activating receptor on NK cells and/or T cells, and desensitize these cells. In contrast, we show that in mice, a shed form of MULT1, a high-affinity NKG2D ligand, causes NK cell activation and tumor rejection. Recombinant soluble MULT1 stimulated tumor rejection in mice. Soluble MULT1 functions, at least in part, by competitively reversing a global desensitization of NK cells imposed by engagement of membrane NKG2D ligands on tumor-associated cells, such as myeloid cells. The results overturn conventional wisdom that soluble ligands are always inhibitory and suggest a new approach for cancer immunotherapy.

Natural killer (NK) cells and some T cells use activating receptors such as NKG2D to recognize and eliminate infected and transformed cells that up-regulate ligands for these receptors (1). There are six to eight different NKG2D ligands, which are poorly expressed by normal cells but up-regulated in cancer cells (2). Many tumor cells release soluble NKG2D ligands through proteolytic shedding, alternative splicing, or exosome secretion (2, 3). Numerous reports conclude that excreted NKG2D ligands modulate NKG2D from the cell surface and desensitize antitumor effector cells (4, 5), although a functional impact of soluble NKG2D ligands is not always observed (6–9). To study shed NKG2D ligands in a controlled setting, we focused on the mouse ligand MULT1, which is commonly up-regulated in primary tumors (10) and is a transmembrane protein, as are the human ligands major histocompatibility complex (MHC) class I chain–related protein A (MICA), MICB, ULBP4, and ULBP5 (11). Analysis of fibroblasts transduced with either N- or C-terminally tagged MULT1 revealed an N-terminal species (23 kD after deglycosylation) shed into the culture supernatant (fig. S1A) and a 24 kD membrane "stub" in the cell lysates, in addition to full-length (around 42 kD) MULT1 (fig. S1B). Inhibiting matrix metalloproteinases blocked MULT1 shedding (fig. S1C).

Hemagglutinin (HA)–MULT1–transduced fibroblasts produced nearly eightfold more shed MULT1 than did untransduced fibroblasts (fig.

S2). WEHI-7.1 and C1498 but not human 293T cell lines excreted MULT1 produced endogenously. We detected serum MULT1 (mean concentration ~250 ng/ml) in most tumor-bearing Eμ-myc transgenic mice, which frequently develop MULT1+ tumors (10), but not in most nontransgenic littermates (Fig. 1A). Very high concentrations of soluble MULT1 were also detected in sera of Apoe−/− mice fed a high-fat diet (Fig. 1A). Given that atherosclerosis and liver inflammation in such mice are largely dependent on NKG2D function (12), it seemed unlikely that soluble MULT1 inhibits NKG2D function. Thus, MULT1 is released from cell lines that naturally or ectopically express MULT1 and accumulates in sera of animals with spontaneous tumors and NKG2D-dependent inflammatory disease.

Purified shed HA-MULT1 bound to NKG2D with high affinity [average dissociation constant (K_d) of 13 ± 3.8 nM] (fig. S3), similar to the affinity reported for recombinant MULT1 (13). In parallel, we engineered fibroblasts to secrete an ectodomain fragment of HA-MULT1 (which we call "secMULT"). SecMULT1 also bound to NKG2D with high affinity (19 ± 4.3 nM) (fig. S3).

To test the function of soluble MULT1, we engineered two NKG2D ligand-negative B6 strain tumor cell lines (the B16-BL6 melanoma and RMA lymphoma) to secrete secMULT1. Surprisingly, both cell lines were rejected by syngeneic B6 mice compared with cells transduced with empty vector (Fig. 1B and fig. S4A), despite the absence of cell surface MULT1 (fig. S4B). Tumor cells transduced with full-length MULT1 [mutated in the cytoplasmic tail to optimize cell surface expression (fig. S4B) (14)] were also rejected (Fig. 1B). B16-secMULT1 cells were still rejected in B6 hosts that had been depleted of CD8+ cells but grew progressively in B6 and Rag1−/− hosts that had been depleted of NK1.1+ cells (Fig. 1C and fig. S5). Hence, NK cells but

not CD8+ cells participate in the rejection of B16-secMULT1. B16 cells with inducible secMULT1 (fig. S6) were also partially rejected (Fig. 1D). In this case, the secMULT1 lacked an epitope tag, showing that rejection occurs without a tag. A mixture of B16 (90%) and B16-secMULT1 (10%) cells was also rejected, demonstrating that sec-MULT1 acts extrinsically (Fig. 1E). These data ruled out the possibility that rejection was solely due to intrinsic stress responses in sec-MULT1–expressing tumor cells. Instead, the data suggested that secMULT1 mobilizes or activates antitumor effector cells.

To address whether tumor cells secreting secMULT1 activate NK cells, we adapted a short-term in vivo NK induction protocol (15, 16) by injecting irradiated B6 cells intraperitoneally in normal mice. Injection of B16-secMULT1 or B16 cells induced similar modest increases in the percentages of NK cells in the peritoneal washes 3 days later (fig. S7), but B16-secMULT1 cells induced more potent ex vivo killing activity against NK-sensitive YAC-1 tumor cells (Fig. 2A). Similar results were obtained with RMA-secMULT1 cells (fig. S8A). Furthermore, higher percentages of peritoneal NK cells from mice injected with B16-secMULT1 cells produced interferon-γ (IFN-γ) after stimulation ex vivo with YAC-1 tumor cells (Fig. 2B) or immobilized antibodies against NK-activating receptors (Fig. 2C and fig. S8B). To allow the recovery of intratumoral NK cells at early times after subcutaneous transfer, we implanted 3×10^5 to 5×10^5 tumor cells mixed with matrigel. Seven days later, NK cells extracted from B16-secMULT1 tumors exhibited stronger IFN-γ responses after stimulation ex vivo (Fig. 2D). Therefore, soluble MULT1 stimulated NK cell functional capacities in both subcutaneous and peritoneal tumors.

Recombinant MULT1 (rMULT1) is similar in size to shed MULT1. When injected with B16 tumor cells (fig. S9A), rMULT1 resulted in partial tumor rejection (Fig. 2E and fig. S9B), and NK cells extracted from the tumors exhibited increased functional activity after stimulation ex vivo (Fig. 2F). The rMULT1 sample was devoid of endotoxin or other PAMPs that activate macrophages (fig. S9C). These data established that soluble MULT1 causes tumor rejection, likely by activating NK cells.

secMULT1 and shed MULT1 are monomeric (fig. S10, A to C) and should not cross-link NKG2D, which is typically necessary for immune receptor activation. Indeed, monomeric rMULT1 failed to stimulate IFN-γ production when incubated with peritoneal NK cells for 4 hours (fig. S11A). Soluble MULT1 may form a multivalent array in vivo, but preliminary staining analyses failed to detect such arrays. These data argue that soluble MULT1 stimulates NK cells by other mechanisms.

Target cells bearing membrane NKG2D ligands, including MULT1, caused down-regulation of cell surface NKG2D, presumably by aggregating the receptor and triggering receptor endocytosis (Fig. 3A) (8, 17). Tumor cells secreting secMULT1, in contrast, caused NKG2D up-regulation on

[1]Department of Molecular and Cell Biology, and Cancer Research Laboratory, University of California at Berkeley, Berkeley, CA 94720, USA. [2]Center for Proteomics University of Rijeka Faculty of Medicine Brace Branchetta 20, 51000 Rijeka, Croatia. [3]Department of Veterinary and Biomedical Sciences, Pennsylvania State University, 115 Henning Building, University Park, PA 16802, USA.
*Corresponding author. E-mail: raulet@berkeley.edu

NK cells in vivo (Fig. 3, A and B), without affecting an irrelevant receptor, DNAM-1 (Fig. 3B). NKG2D up-regulation occurred without increases in NKG2D mRNA (fig. S12) or intracellular protein. These findings suggested the following hypothesis (Fig. 3C): that untransformed host cells express membrane NKG2D ligands that persistently engage NK cells, cause NKG2D downregulation, and globally desensitize the NK cells as the tumors progress; and that soluble MULT1

enhances responsiveness and cell-surface NKG2D expression by blocking these interactions.

Consistent with the hypothesis, host CD11b$^+$F4/80$^+$ myeloid cells associated with either peritoneal or subcutaneous B16 or B16-secMULT1 tumors displayed the NKG2D ligand RAE-1 (but not MULT1) on the cell surface (Fig. 3, D and E). Monocytes in patients with several types of cancer also expressed NKG2D ligands (18). Tumors may cause an increase in RAE-1 expression by myeloid cells in the peritoneum (Fig. 3D) and possibly other sites (19). Hence, myeloid cells, and possibly other nontumor cells, express NKG2D ligands in vivo. We further demonstrated that rMULT1 competitively blocks binding of RAE-1e-Fc fusion protein to NKG2D on NK cells (Fig. 3F), confirming a distinct prediction of the hypothesis.

To test whether RAE-1 expressed on endogenous cells caused NK cell inactivation, we used
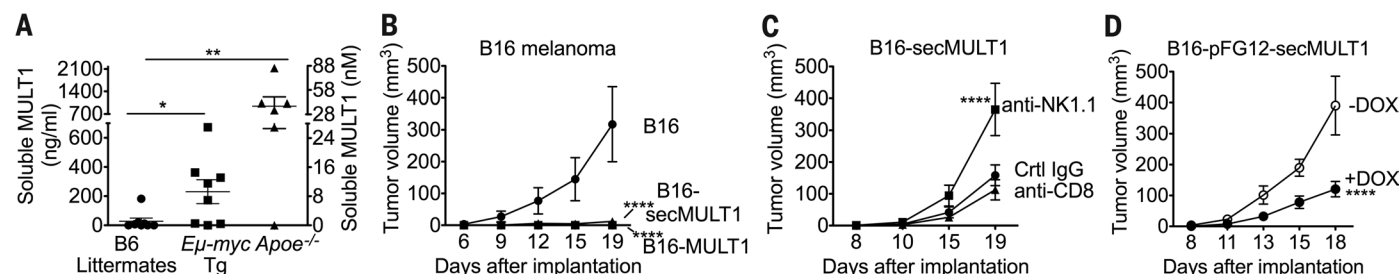
Fig. 1. NK cells promote the rejection of tumors that shed MULT1. (A) Enzyme-linked immunosorbent assay detection of soluble MULT1 in sera from tumor-bearing *Eµ-Myc* mice, nontransgenic littermates, and diseased *Apoe*$^{-/-}$ mice fed a Western diet (*n* = 6 to 8 mice). Each point represents a different mouse. **(B)** Comparison of growth of 2 × 10^4 subcutaneously transferred B16 melanoma tumor cells transduced with secMULT1, full-length MULT1, or empty vector, in wild-type (WT) B6 mice (*n* = 4 mice). Rejection was usually partial but was complete in some animals in some experiments. **(C)** Subcutaneous growth of B16-secMULT1 tumors in B6 mice (2 × 10^4 cells were inoculated) treated with control imuunoglobulin G (IgG), NK1.1 antibody, or CD8 antibody (*n* = 13 mice). **(D)** After inoculation of 2 × 10^4 B16 cells transduced with pFG12-secMULT1, mice were treated or not with doxycycline starting from the time of tumor implantation (*n* = 6 mice). **(E)** Mice (*n* = 6) received 2 × 10^4 B16 cells alone, or 2 × 10^4 B16 cells mixed with 2 × 10^3 B16-secMULT1 cells. Shown are representative examples of ≥3 [(B) and (E)] or 2 (D) experiments performed, whereas (C) includes combined data from 3 experiments. Tumor volumes ± SE are shown. (A) was analyzed with a Mann-Whitney test, and (B) to (E) were analyzed by two-way analysis of variance (ANOVA) with Bonferroni multiple comparison tests. *P < 0.05, **P < 0.01, ***P < 0.001 and ****P < 0.0001.
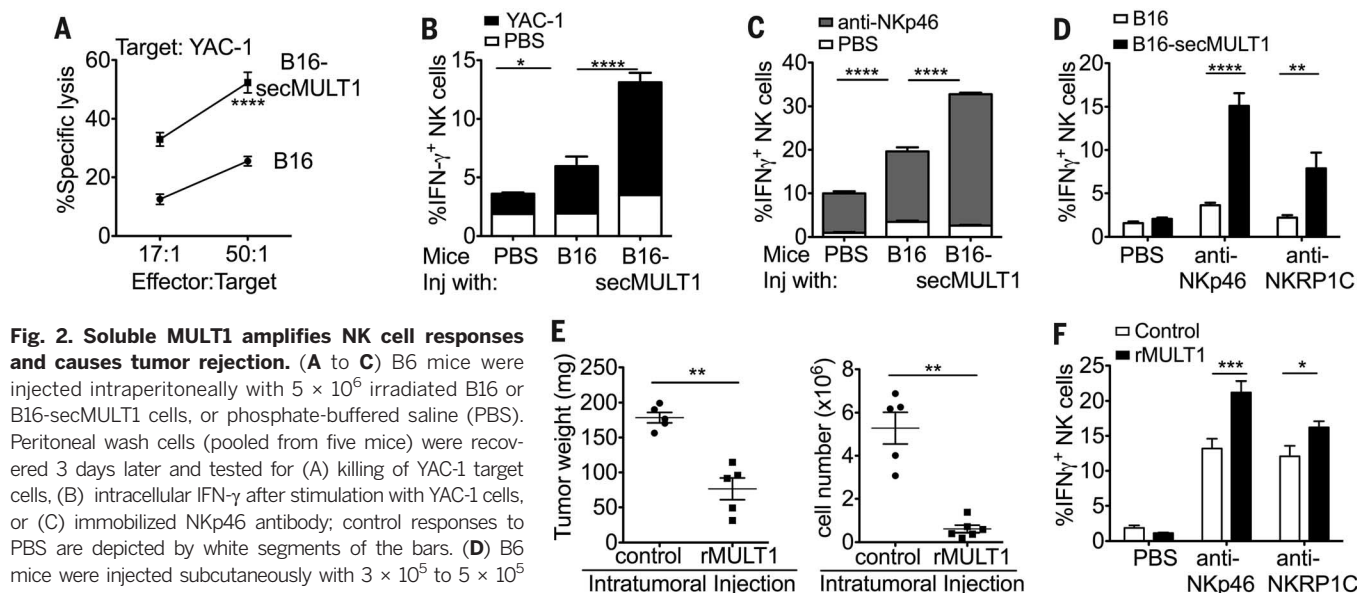
Fig. 2. Soluble MULT1 amplifies NK cell responses and causes tumor rejection. (A to C) B6 mice were injected intraperitoneally with 5 × 10^6 irradiated B16 or B16-secMULT1 cells, or phosphate-buffered saline (PBS). Peritoneal wash cells (pooled from five mice) were recovered 3 days later and tested for (A) killing of YAC-1 target cells, (B) intracellular IFN-γ after stimulation with YAC-1 cells, or (C) immobilized NKp46 antibody; control responses to PBS are depicted by white segments of the bars. **(D)** B6 mice were injected subcutaneously with 3 × 10^5 to 5 × 10^5 B16 or B16-secMULT1 cells in 100 µl matrigel. The tumors were dissociated 7 days later, and gated NK cells from individual mice (*n* = 5 mice) were tested for responses to immobilized NKp46 or NKRP1C Abs. **(E and F)** Subcutaneous tumors were established with 3 × 10^5 to 5 × 10^5 B16 cells in matrigel. The tumor cells in one group were mixed with 1 µg of recombinant MULT1 (rMULT1). After 4 days, an additional 1 µg of rMULT1 (or PBS for control mice) was injected into each matrigel/tumor for that group. On day 7, tumors were extracted, (E) weighed, dissociated, and (E) the tumor cells were counted. The immune cells within the tumors were stimulated with immobilized NKp46 and NKRP1C Abs, and (F) the IFN-γ responses of gated NK cells were determined. Shown are representative examples of 2 (A) or ≥3 [(B) to (F)] experiments performed. (A) to (D) and (F) were analyzed with two-way ANOVA with Bonferroni multiple comparison tests, (E) was analyzed with Mann-Whitney test. *P < 0.05, **P < 0.01, ***P < 0.001 and ****P < 0.0001.

Fig. 3. Mechanisms of immune activation by soluble MULT1. (**A** and **B**) Membrane NKG2D staining after exposure of NK cells to secMULT1 in intraperitoneal (A) or subcutaneous (B) tumors. (**C**) Model of secMULT1 action. Persistent NKG2D engagement by endogenous NKG2D ligand–expressing cells associated with the tumor desensitizes NK cells. Soluble MULT1 competitively blocks the NKG2D receptor, preventing NK cell desensitization and therefore augmenting tumor rejection mediated through distinct NK-activating receptors. (**D**) Expression of NKG2D ligand RAE-1 by gated CD11b$^+$F480$^+$ peritoneal myeloid cells in mice injected intraperitoneally 3 days before with PBS or 5×10^6 irradiated B16 or B16-secMULT1 tumor cells. Cells were stained with biotin-pan-RAE-1 Ab (blue). The staining was specific because it could be blocked by including an excess of unconjugated pan-RAE-1 antibody in the reaction (red). Gray shows isotype control staining. (**E**) Expression of RAE-1 by gated CD11b$^+$F480$^+$ intratumoral myeloid cells in mice injected subcutaneously with 2×10^4 B16 or B16-secMULT1 tumor cells 20 days before. (**F**) rMULT1 and NKG2D antibody [MI6 clone, in F(ab')$_2$ form] block RAE-1 binding to NKG2D on NK cells. The mean fluorescence intensity of RAE1ε-Fc staining of NK cells was used to calculate percent inhibition. (A) is combined data from 14 experiments. (B) and (D) to (F) show representative examples of ≥3 experiments performed. (A) was analyzed with one-way ANOVA Kruskal-Wallis test, (B) was analyzed with two-way ANOVA with Bonferroni multiple comparison tests; ns indicates $P > 0.05$, *$P < 0.05$, and ***$P < 0.001$.
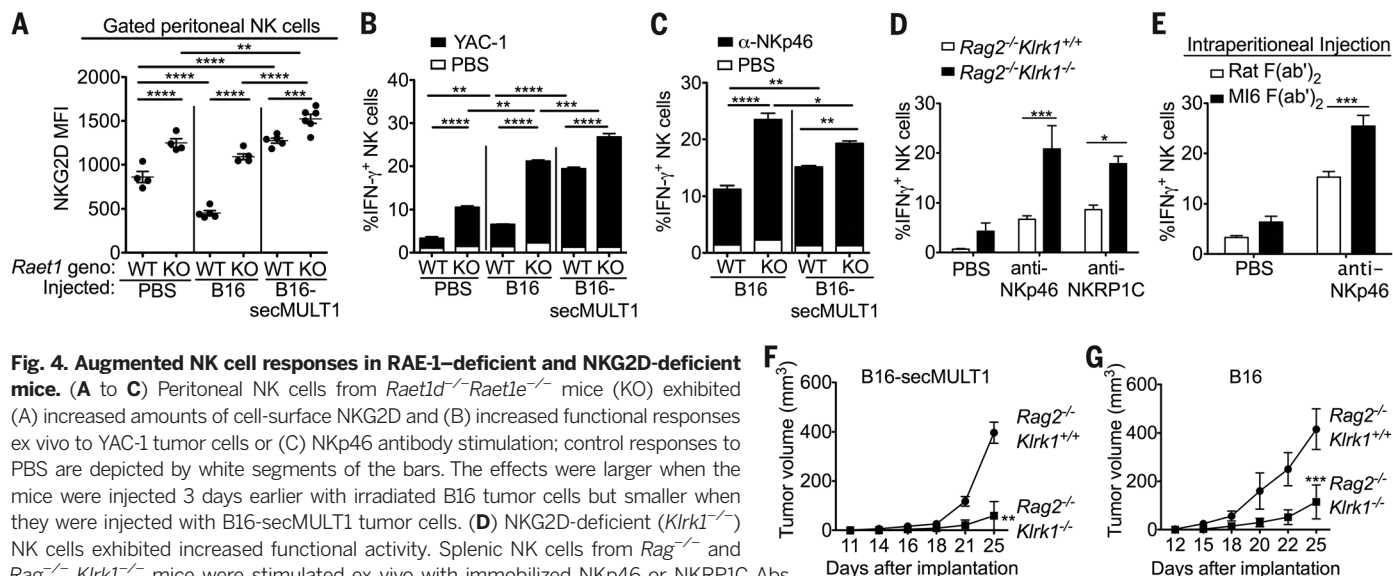
Fig. 4. Augmented NK cell responses in RAE-1–deficient and NKG2D-deficient mice. (**A** to **C**) Peritoneal NK cells from $Raet1d^{-/-}Raet1e^{-/-}$ mice (KO) exhibited (A) increased amounts of cell-surface NKG2D and (B) increased functional responses ex vivo to YAC-1 tumor cells or (C) NKp46 antibody stimulation; control responses to PBS are depicted by white segments of the bars. The effects were larger when the mice were injected 3 days earlier with irradiated B16 tumor cells but smaller when they were injected with B16-secMULT1 tumor cells. (**D**) NKG2D-deficient ($Klrk1^{-/-}$) NK cells exhibited increased functional activity. Splenic NK cells from $Rag^{-/-}$ and $Rag^{-/-}$ $Klrk1^{-/-}$ mice were stimulated ex vivo with immobilized NKp46 or NKRP1C Abs, and the IFN-γ responses of gated NK cells were determined. (**E**) B6 mice were injected intraperitoneally with 50 μg MI6 (anti-NKG2D) F(ab')$_2$ or F(ab')$_2$ of rat IgG on days 0, 3, and 6. On Day 8, peritoneal NK cells were stimulated ex vivo with immobilized NKp46 Abs, and the IFN-γ responses of gated NK cells were determined. (**F** and **G**) Increased tumor rejection responses in NKG2D-deficient mice. Growth of (F) B16-secMULT1 or (G) B16 tumor cells in $Rag2^{-/-}$ or $Rag2^{-/-}Klrk1^{-/-}$ mice ($n = 5$ mice). (F) and (G) are from separate experiments. Separate, direct comparisons showed retarded growth of B16-secMULT1 versus B16 tumors in $Rag2^{-/-}$ mice. All experiments show representative examples of ≥3 experiments performed. Tumor volumes ± SE are shown. (A) to (G) were analyzed with two-way ANOVA with Bonferroni multiple comparison tests. *$P < 0.05$, **$P < 0.01$, ***$P < 0.001$ and ****$P < 0.0001$.

the clustered regularly interspaced short palindromic repeat (CRISPR)/Cas9 method to disrupt both B6 strain RAE-1 genes, *Raet1d* and *Raet1e*. Peritoneal NK cells from $Raet1d^{-/-}Raet1e^{-/-}$ mice exhibited significant increases in membrane NKG2D expression as well as functional responses (Fig. 4, A to C). Greater differences occurred when the mice were injected with irradiated B16 tumor cells, suggesting that greater NK desensitization and NKG2D down-regulation occurs in the presence of tumors. The increase did not fully account for the effects of secMULT1 (Fig. 4, A and B), suggesting that secMULT1 may also operate by other mechanisms. NK cells in *Raet1*-deficient mice exhibited greater responses to both NKG2D-dependent stimuli (for example, to YAC-1 cells) (Fig. 4B) and NKG2D-independent stimuli (for example, to antibody to NKp46) (Fig. 4C), which is consistent with published reports that persistent stimulation by cells expressing NKG2D ligands results in a global desensitization of NK cells [17, 20]. In mice injected with B16-secMULT1 tumor cells, smaller differences were observed, as predicted if secMULT1 blocks NKG2D interactions with RAE-1-expressing cells. Indeed, addition of rMULT1 to cultures of peritoneal wash cells, which contain NK cells and RAE-1+ myeloid cells, resulted in increased responses of NK cells to stimulation, when tested 8 to 20 hours later (fig. S11, B and C). These data indicated that interactions of NK cells with RAE-1 molecules on nontumor cells cause NKG2D down-regulation and functional desensitization, and that this may be accentuated in tumor-bearing mice.

Our model further predicts that NKG2D receptor deficiency, or blocking with antibody, should have a similar effect as soluble MULT1. NK cells from NKG2D-deficient ($Klrk1^{-/-}$) mice exhibited a modest increase in functional activity (fig. S13A), confirming recent findings [21, 22]. A larger effect was evident in NKG2D-deficient NK cells on a $Rag2^{-/-}$ background (Fig. 4D). Similarly, intraperitoneal injections of B6 mice with F(ab')$_2$ fragments of blocking NKG2D antibody resulted in enhanced functional responses ex vivo (Fig. 4E). Most remarkably, NKG2D-deficient $Rag2^{-/-}$ mice exhibited a strongly enhanced rejection response against B16 and B16-secMULT1 tumors, compared with the responses of $Rag2^{-/-}$ mice (Fig. 4, F and G). Furthermore, incorporation of F(ab')$_2$ fragments of blocking NKG2D antibody into B16 tumors that were established in subcutaneous matrigel plugs resulted in partial tumor rejection and augmented responsiveness of NK cells within the residual tumors (fig. S13, B and C). Thus, NKG2D deficiency, or blockade, results in enhanced NK cell responsiveness and tumor rejection. These data strongly support the proposed model (Fig. 3C).

The finding that NK cells persistently stimulated through NKG2D or other receptors are broadly desensitized is consistent with published data [20, 23] and may reflect a defect in mitogen-activated protein kinase (MAPK)/extracellular signal–regulated kinase (ERK) signaling [23]. Blocking or disabling NKG2D restores killing of B16 cells because NK cells use receptors distinct from NKG2D to target B16 cells. A more complex outcome should pertain with tumor cells that express membrane NKG2D ligands because the NK cells, although more active, will be partly blocked in tumor cell recognition. Tumor cells often express multiple NKG2D ligands, suggesting that therapeutic efficacy may be maximized by blocking only the specific NKG2D ligands expressed by host cells, rather than by blocking NKG2D altogether.

Our results are surprising because they show that soluble NKG2D ligands in vivo stimulate tumor rejection and increase membrane NKG2D, whereas the literature suggests that they should suppress tumor rejection and decrease membrane NKG2D. However, NKG2D down-regulation is frequently not observed in patients with soluble MICA/MICB [6–9]. Moreover, MULT1 and MICA/MICB ligands differ in a key respect: affinity. Soluble MULT1 is a high-affinity ($K_d \sim 10$ nM) monomeric ligand. Soluble MICA and MICB are low-affinity ligands ($K_d \sim 1\ \mu$M), which are present in patient sera at concentrations below 1 nM [4, 24], meaning that NKG2D occupancy is predicted to be extremely low. This consideration suggests that systemic effects of soluble MICA and MICB may be indirect, or that the active form of soluble MICA or MICB is actually a multimeric exosome form [25, 26], which can bind and cross-link the receptors despite a low affinity and low concentration. Binding and cross-linking are conditions known to cause modulation of other immune receptors from the cell surface [27]. B16 cells secreting the low-affinity MICA ligand, when injected intraperitoneally, failed to induce significant NKG2D up-regulation or increased NK functional activity (fig. S14), which is in line with our expectations. The results identify an unexpected mechanism of immune activation and support efforts to evaluate the potential of soluble NKG2D ligands or antibodies that block NKG2D or its ligands for immunotherapy of cancer. Studies suggest that engagement of other NK-activating receptors, such as NKp46, may also lead to NK cell desensitization, suggesting that multiple targets exist for amplifying NK function [28].

REFERENCES AND NOTES

1. D. H. Raulet, *Nat. Rev. Immunol.* **3**, 781–790 (2003).
2. D. H. Raulet, S. Gasser, B. G. Gowen, W. Deng, H. Jung, *Annu. Rev. Immunol.* **31**, 413–441 (2013).
3. G. Chitadze, J. Bhat, M. Lettau, O. Janssen, D. Kabelitz, *Scand. J. Immunol.* **78**, 120–129 (2013).
4. V. Groh, J. Wu, C. Yee, T. Spies, *Nature* **419**, 734–738 (2002).
5. H. Song, J. Kim, D. Cosman, I. Choi, *Cell. Immunol.* **239**, 22–30 (2006).
6. H. R. Salih, D. Goehlsdorf, A. Steinle, *Hum. Immunol.* **67**, 188–195 (2006).
7. I. Waldhauer, A. Steinle, *Cancer Res.* **66**, 2520–2526 (2006).
8. K. Wiemann et al., *J. Immunol.* **175**, 720–729 (2005).
9. M. von Lilienfeld-Toal et al., *Cancer Immunol. Immunother.* **59**, 829–839 (2010).
10. N. Guerra et al., *Immunity* **28**, 571–580 (2008).
11. R. A. Eagle et al., *PLOS ONE* **4**, e4503 (2009).
12. M. Xia et al., *Circulation* **124**, 2933–2943 (2011).
13. L. N. Carayannopoulos, O. V. Naidenko, D. H. Fremont, W. M. Yokoyama, *J. Immunol.* **169**, 4079–4083 (2002).
14. T. J. Nice, L. Coscoy, D. H. Raulet, *J. Exp. Med.* **206**, 287–298 (2009).
15. R. Glas et al., *J. Exp. Med.* **191**, 129–138 (2000).
16. A. Diefenbach, E. R. Jensen, A. M. Jamieson, D. H. Raulet, *Nature* **413**, 165–171 (2001).
17. D. E. Oppenheim et al., *Nat. Immunol.* **6**, 928–937 (2005).
18. C. A. Crane et al., *Proc. Natl. Acad. Sci. U.S.A.* **111**, 12823–12828 (2014).
19. N. Nausch, I. E. Galani, E. Schlecker, A. Cerwenka, *Blood* **112**, 4080–4089 (2008).
20. J. D. Coudert, L. Scarpellino, F. Gros, E. Vivier, W. Held, *Blood* **111**, 3571–3578 (2008).
21. B. Zafirova et al., *Immunity* **31**, 270–282 (2009).
22. S. Sheppard et al., *Blood* **121**, 5025–5033 (2013).
23. M. Ardolino et al., *J. Clin. Invest.* **124**, 4781–4794 (2014).
24. A. Märten, M. von Lilienfeld-Toal, M. W. Büchler, J. Schmidt, *Int. J. Cancer* **119**, 2359–2365 (2006).
25. A. Clayton et al., *J. Immunol.* **180**, 7249–7258 (2008).
26. O. Ashiru et al., *Cancer Res.* **70**, 481–489 (2010).
27. R. B. Taylor, W. P. Duffus, M. C. Raff, S. de Petris, *Nat. New Biol.* **233**, 225–229 (1971).
28. E. Narni-Mancinelli et al., *Science* **335**, 344–348 (2012).

SUPPLEMENTARY MATERIALS

www.sciencemag.org/content/348/6230/136/suppl/DC1
Materials and Methods
Supplementary Text
Fig. S1 to S14
Table S1
References (29–32)

17 July 2014; accepted 30 January 2015
Published online 5 March 2015;
10.1126/science.1258867

ONE
FOR
ALL ALL
FOR
YOU

The Applied Biosystems™, Invitrogen™, Gibco™, and Ion Torrent™ brands are transitioning from Life Technologies to Thermo Fisher Scientific.

Alongside the Thermo Scientific brand, this combination creates our largest ever product offering, amplified by continuous innovation, enhanced support, and 50,000 employees focused on your success.

All from one company. All for you.

To learn more about your favorite brands, go to **lifetechnologies.com/allforyou**

Thermo
S C I E N T I F I C

appliedbiosystems

invitrogen

iontorrent

gibco

Thermo Físher
S C I E N T I F I C

TRANSLATE CANCER DISCOVERIES INTO
THERAPEUTICS
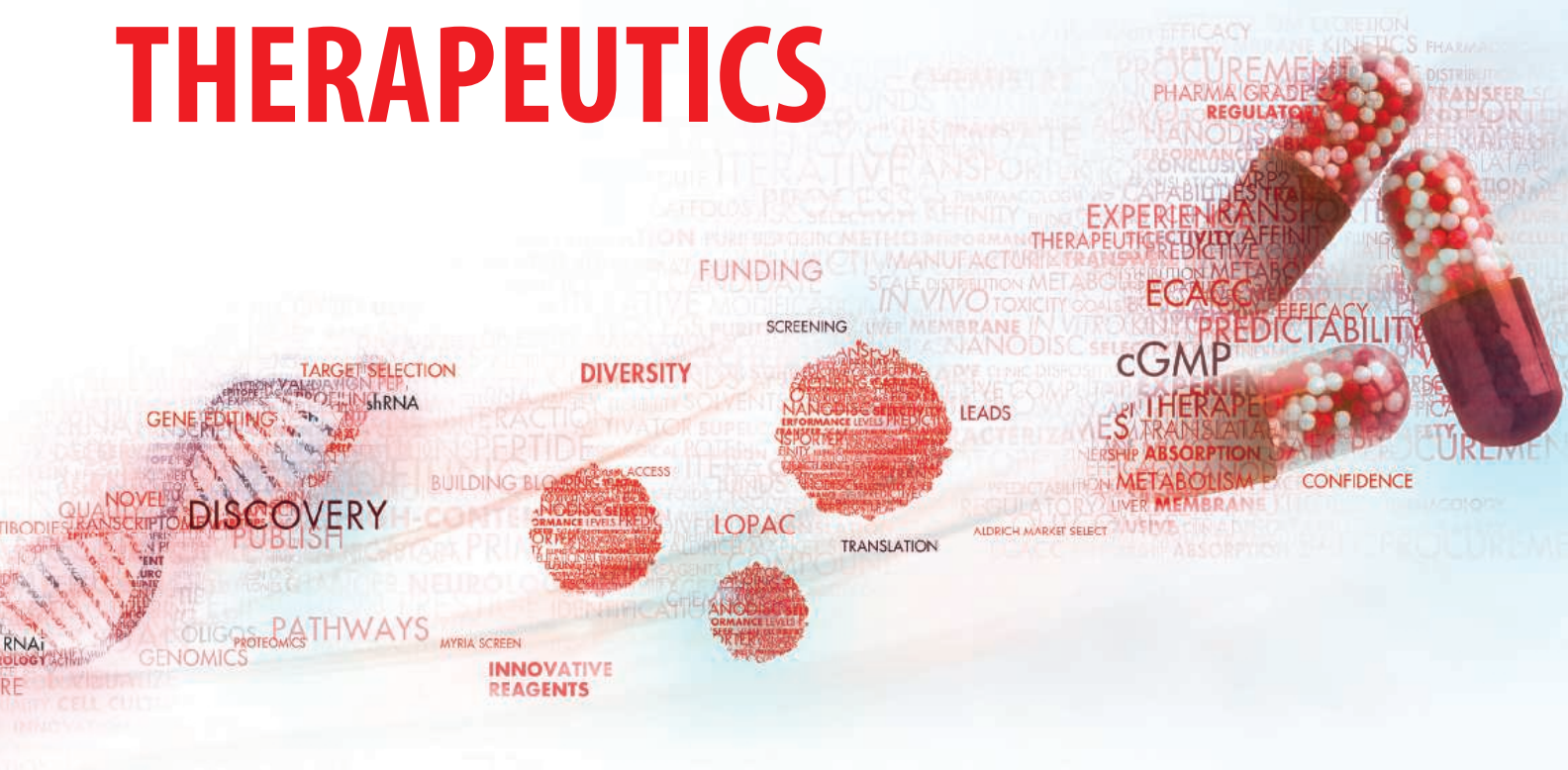
Advancing your Cancer research through better science

- Discover novel targets and pathways with quality reagents and cutting-edge gene editing technology

- Create diverse and unique compounds with the largest portfolio of building blocks, catalysts and reagents

- Accelerate novel compound discovery with chemically diverse compound arrays and screening libraries

Download our apps for more information
sigma-aldrich.com/cancer
#sigmaaldrich

TRANSLATIONAL RESEARCH SOLUTIONS

| TARGET ID & VALIDATION | LEAD DISCOVERY | LEAD OPTIMIZATION | PRE-CLINICAL DEVELOPMENT | CLINICAL DEVELOPMENT | MANUFACTURING |
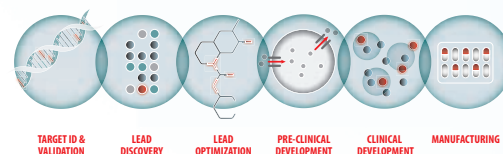
TEST YOUR KNOWLEDGE WITH OUR
CANCER RESEARCH TRIVIA BOWL
DURING THE AACR ANNUAL MEETING.
Monday - Wednesday at 10am and 2pm
Booth #519

SIGMA® | **ALDRICH**® | **SUPELCO**® | **SAFC**®

83344

SIGMA-ALDRICH®

BIO-RAD'S DROPLET DIGITAL™ PCR SYSTEMS

Over 200 Peer-Reviewed Droplet Digital PCR (ddPCR™) Publications*

From detection of rare mutations and cancer biomarkers to quantification of gene expression and miniscule viral loads, the QX100™ and QX200™ Droplet Digital PCR Systems have been used to redefine the limits of absolute nucleic acid quantification. With over 200 peer-reviewed publications, ddPCR platforms have outperformed other digital PCR systems by several orders of magnitude. The third-generation QX200™ AutoDG™ System now brings automation and scalability to digital PCR.

Visit **bio-rad.com/info/science200** for the publication list and to learn more.

BIO-RAD

* Based on PubMed data, February 2015.

eppendorf
& Science

PRIZE FOR
NEURO
BIOLOGY

2014年の優勝者
Eiman Azim博士
コロンビア大学
四肢の巧緻運動に関する
研究

Call for Entries

Eppendorf & Science Prize for Neurobiology
毎年開催される国際コンクール、エッペンドルフ&サイエンス神経生 物学賞は分子・細胞生物学の方法論に基づく神経生物学研究に優秀な貢献があった若手科学者を称えるものです。受賞者および最 終審査対象者はサイエンスの編集長ピーター・スターン博士が議長を務める独立科学者委員会により選定されます。応募資格は35歳以下です。

次の受賞者はあなたかも知れません
> 賞金25,000 USドル
> Science誌への論文掲載
> 米国神経科学学会年次総会に並行して開催される授賞式典への全額支援
> ドイツ ハンブルグのエッペンドルフ本社へご招待

応募は簡単です!

Learn more at: www.eppendorf.com/prize

eppendorf Science
AAAS

Help PNAS celebrate 100 years of service to science and society.

See the PNAS 100th Anniversary Portal
pnas100th.org

PNAS
Celebrating
100 Years
1915-2015
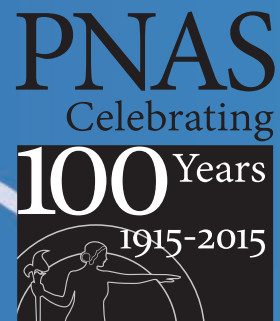
See the impact of PNAS over time through the Anniversary Timeline, Commentaries, Perspectives, Front Matter, Special Features, Landmark Papers, and more.

PNAS
www.pnas.org

Student Poster Competition Winners

The 2015 Student Poster Competition took place at the AAAS Annual Meeting in San Jose, 12–16 February. The student winners' work displayed originality and understanding that set them apart from their peers. The 2016 AAAS Annual Meeting poster entry site will open 13 May 2015.

BRAIN AND BEHAVIOR

Winner: Eden Barragan, University of California, Irvine
Effects of Anticonvulsants and Mono-amines on Seizures in Mutant Drosophila

Honorable Mention: Walter Guerrero, University of California, Irvine
PTEN/SOCS3 Co-Deletion Accelerates Functional Recovery Following Peripheral Nerve Damage

CELLULAR AND MOLECULAR BIOLOGY

Winner: Yasmynn Chowdhury and Setu Kaushal, Arizona State University
A Survey of Lectin Reactivity to Coccidioides in Infected Human Lung Tissue

Honorable Mention: Cole V. M. Helsell, Arizona State University
Comparitive Computational Models of TRPM8 Help Explain Modulation Mechanisms

DEVELOPMENTAL BIOLOGY, PHYSIOLOGY, AND IMMUNOLOGY

Winner: Michael Emami, University of California, Irvine
Investigating the Role of Meox2 in Myogenic and Tendon Differentiation

Sidney Lane, University of Miami
Transcriptomic Analysis of CD8 T cells from HIV+ Patients Using Fluidigm Technology

EDUCATION

Winner: Rachel Salter, North Dakota State University
Level Up: Capturing Upper-Division Student Understanding of Natural Selection

ENVIRONMENT AND ECOLOGY

Winner: Glenda L. Torres, Heritage University
Interactions Among Bactericera Cockerelli, Host Plants, and Liberibacter Solanacearum

Honorable Mention: Hector Felipe Sanchez, University of California, Irvine
Novel ampC Beta-Lactamase Genes from Morganella Morganii

MEDICINE AND PUBLIC HEALTH

Winner: Anthony R. Prosser, Emory University
Discovery and Synthesis of First-Generation Single-Drug "Cocktails" to Combat HIV

Honorable Mention: David Saldana, University of California, Irvine
Inhibition of Polo-like Kinase 4 as Therapy for Glioblastoma Primary Brain Tumors

PHYSICAL SCIENCES

Winner: Christopher Luna, Arizona State University
Neural Networks for Predicting Heat Transport in Tokamak Plasmas

SCIENCE AND SOCIETY

Winner: Rachel Gur-Arie, Arizona State University
University Student Knowledge and Perception of Influenza

Honorable Mention: Kristy Henson, Marshall University
Stories in Bone Still Told: Digitization and Replication of Human Remains

SOCIAL SCIENCES

Winner: Michael J. Bernstein, Arizona State University
Science Outside the Lab: Changing Perspective on the Role of Science and Engineering Society

Honorable Mention: Mariana Achirica Acosta, Autonomous University of Baja California
The Science-Policy Interface: Communication Between Academic Research and Governmental Decision-Makers

Honorable Mention: Wing H. Cheung, University of California, Irvine
A Democratic Process Framework for Enhancing Public Engagement in Citizen Science

TECHNOLOGY, ENGINEERING, AND MATH

Winner: Horacio M. Estabridis, University of California, Irvine
Elucidating the Stiffness of Extra-Cellular Matrix Fibers with High Speed Microscopy

Honorable Mention: Emily C. Hartman, Anum Azam and Kevin Metcalf, University of California, Berkeley
Antimicrobial Peptide Production using the Type 3 Secretion System in Salmonella

AAAS GENERAL POSTER SESSION ATTENDEES' CHOICE

Kirsten Olson, University of Alaska, Fairbanks
Modern Utilitarian Cermic Interpretation of Traditional Northern Native Designs

Chromatography Software

DataApex is pleased to announce the release of control drivers for Hitachi Chromaster and Primaide HPLC systems. Clarity Chromatography Software platform now enables both direct instrument control and digital data acquisition. The drivers have been released with Clarity version 5.0.5. Hitachi drivers will be available in selected territories through Hitachi official partners. Maximizing the portfolio of Clarity control drivers is very significant for us; the portfolio of controlled instruments is one of the greatest Clarity assets. Drivers for Hitachi HPLC systems were highly desired by Clarity users. Clarity Chromatography Software has a strong position in the chromatography data systems market. Clarity is highly regarded for its intuitive approach, excellent performance, cost-effectiveness, and proficient technical support. DataApex is solely focused on chromatography software development. A strong emphasis is placed on technological innovation, visionary adoption of new laboratory standards, best practices, and extensive customer support.

DataApex
For info: +420-251-013403
www.dataapex.com

Digital Microscope Camera

High-quality digital microscopy is now more accessible than ever with the new 5 megapixel SC50 microscope camera, bringing fast, full high-definition live imaging and more to a host of routine applications. Designed for the convenience of everyday use and ideal under low-light conditions, the new 5 megapixel SC50 microscope camera is built on the latest CMOS chip technology to deliver improved speed, sensitivity, and resolution. Achieving full high-definition images at 32 fps, high-speed imaging with the SC50 captures and records dynamic events. The camera delivers clear, high-quality images to nearly every kind of monitor or projector, ready to be further analyzed or shared with an audience and enhancing a range of applications throughout both life and materials science. The SC50 actively keeps noise under control with Olympus Smart Image Averaging technology. Designed for ease of use, the SC50 also boasts an automatic and continuous White Balance feature.

Olympus
For info: 484-896-5000
www.olympus.com
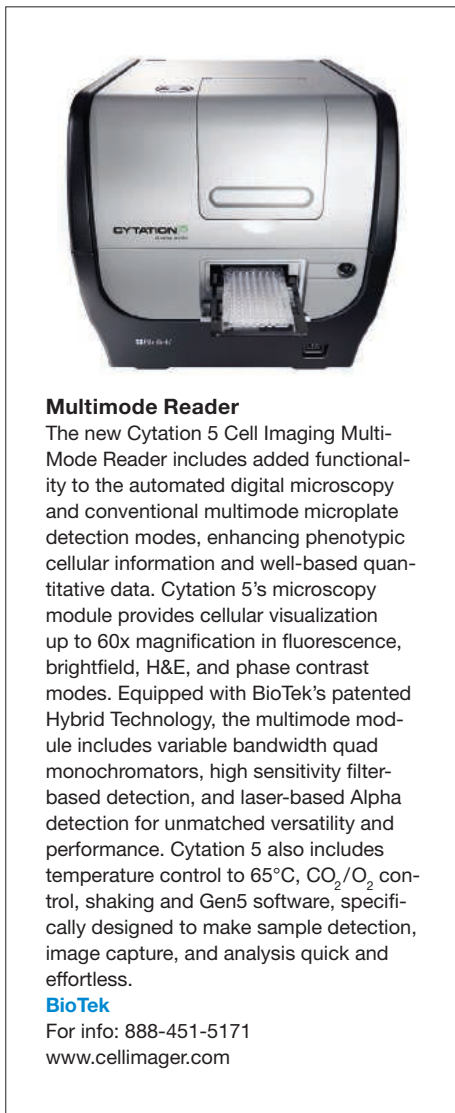
Multimode Reader

The new Cytation 5 Cell Imaging Multi-Mode Reader includes added functionality to the automated digital microscopy and conventional multimode microplate detection modes, enhancing phenotypic cellular information and well-based quantitative data. Cytation 5's microscopy module provides cellular visualization up to 60x magnification in fluorescence, brightfield, H&E, and phase contrast modes. Equipped with BioTek's patented Hybrid Technology, the multimode module includes variable bandwidth quad monochromators, high sensitivity filter-based detection, and laser-based Alpha detection for unmatched versatility and performance. Cytation 5 also includes temperature control to 65°C, CO_2/O_2 control, shaking and Gen5 software, specifically designed to make sample detection, image capture, and analysis quick and effortless.

BioTek
For info: 888-451-5171
www.cellimager.com

Low-Noise Data Acquisition System

Patch clamp recordings require significant preparation time not only for sample setup, but also for eliminating the 50 and 60 Hz line-frequency background noise that severely impairs analysis of biological signals. With traditional systems, this line-frequency noise may completely prevent data acquisition if its source cannot be identified. The Digidata 1550A Low-Noise Data Acquisition System is the first digitizer with built-in adaptive noise cancellation technology, called the HumSilencer, which provides single-click elimination of the 50 and 60 Hz line-frequency noise. The system rapidly identifies local line-frequency noise and suppresses extraneous noise amplitude up to 20V peak to peak at the analog input in less than one second, saving troubleshooting time and increasing the data quality of patch clamp recordings. When combined with the Axon family of products, the Digidata 1550A completes the setup required to perform electrophysiology recordings essential for basic ion channel research as well as cell pathway analysis and disease research.

Molecular Devices
For info: 800-635-5577
www.moleculardevices.com

Nucleic Acid Isolation

Small on space. Big on productivity. Introducing the revolutionary chemagic 360. Providing unparalleled sample volume flexibility and productivity for nucleic acid isolation, the chemagic 360 enables users to purify from 10 μL up to 10 mL of sample volume in batches varying from 1 to 96 samples at a time. Its modular set up allows for convenient integration with upstream and downstream platforms to provide a streamlined hands-free workflow. chemagen Technology by PerkinElmer also provides an extensive portfolio of kits to allow for nucleic acid isolation from various sample types. In addition, standard features such as an integrated dispenser for automated buffer filling, QA software, and barcode reading provide enhanced quality assurance to deliver results with certainty.

PerkinElmer
For info: +49-(0)-2401-805500
www.chemagen.com

Electronically submit your new product description or product literature information! Go to www.sciencemag.org/products/newproducts.dtl for more information.

Newly offered instrumentation, apparatus, and laboratory materials of interest to researchers in all disciplines in academic, industrial, and governmental organizations are featured in this space. Emphasis is given to purpose, chief characteristics, and availability of products and materials. Endorsement by *Science* or AAAS of any products or materials mentioned is not implied. Additional information may be obtained from the manufacturer or supplier.

DANA-FARBER
C A N C E R   I N S T I T U T E

Laboratory Investigator
Division of Hematologic Neoplasia

The Department of Medical Oncology at the Dana-Farber Cancer Institute and the Department of Medicine at Brigham and Women's Hospital announce a search for a laboratory investigator at the Assistant or Associate Professor level to join the Division of Hematologic Neoplasia. The investigator will be a central member of the newly formed Dana-Farber/ Brigham and Women's Leukemia Center. Appointment and compensation will be commensurate with experience and institutional policies.

The successful candidate will develop an independent, disease-based laboratory focused on hematologic malignancies. Areas of particular interest include the genetics of myeloid malignancies and the translation of genetic analyses to clinical trials and practice. The candidate must have an MD and/or PhD and a proven track record of outstanding laboratory research.

Interested candidates must submit a curriculum vitae, a research plan and three letters of reference to: Benjamin Ebert, MD, PhD; 1 Blackfan Circle, Karp 5.210, Boston, MA 02215. Please send submissions via email to Maria Kaplaukhova: mkaplaukhova@partners.org.

HARVARD MEDICAL SCHOOL

BRIGHAM AND WOMEN'S HOSPITAL

We are an equal opportunity employer and all qualified applicants will receive consideration for employment without regard to race, color, religion, sex, national origin, disability status, protected veteran status, or any other characteristic protected by law.

iCARE
International Cancer
Research Fellowships

iCARE is a fellowship program sponsored by the Italian Association for Cancer Research – **AIRC** in co-funding with the **European Union**.

iCARE offers three types of two-year fellowships, intended to promote the mobility of experienced researchers to and from Italy to work on a **cancer-focused** research project:

- **Outgoing Fellowships**, for researchers who have worked in Italy for more than 3 years, interested in a research experience in a scientific institution outside of Italy.
- **Incoming Fellowships**, for non-Italian scientists interested in a research experience in a scientific institution located in Italy.
- **Reintegration Fellowships**, for Italian researchers who have worked in a country outside Italy for at least 2 years, who wish to return and work in a research center in Italy.

Winners will be selected through a transparent and independent peer review process.

Detailed instructions to apply available at:
https://www.direzionescientifica.airc.it/ Calls/Default.aspx

The deadline for submission is May 19th, 2015

Faculty Position in Cancer Genomics

The Center for Genetic Medicine and the Robert H. Lurie Comprehensive Cancer Center of the Northwestern University Feinberg School of Medicine in downtown Chicago invite applications for a full time faculty position as Director of Cancer Genomics, at the rank of Professor or Associate Professor, in the area of cancer genomics. Start date is negotiable. Application deadline is **May 31, 2015**.

Applicants should have a Ph.D. or M.D. or M.D./Ph.D. and an outstanding record of research in cancer genomics or epigenomics, particularly the application of genomic profiling to human malignancy. The candidate should have experience in determining and interpreting genetic variation, preferably including whole genome/exome and/or RNA profiling approaches. We are seeking an individual with an established program in cancer genomics that is drawn to the broad opportunities at Northwestern with its collaborative clinical programs at Northwestern Memorial and Children's Memorial Hospitals. The Center for Genetic Medicine houses the NUgene biobank and the Robert H. Lurie Comprehensive Cancer Center offers a robust research infrastructure for translation.

Applicants should send (as a single PDF) a cover letter referencing search number **P-25102**, curriculum vitae, a two-page description of research accomplishments and plans, and the name and contact information for three references to: **CancerGenomicsSearch@northwestern.edu**

NORTHWESTERN UNIVERSITY
FEINBERG
SCHOOL OF MEDICINE

Northwestern University is an Affirmative Action, Equal Opportunity Employer. Women and minorities are encouraged to apply. Hiring is contingent upon eligibility to work in the United States.

Research Positions open at Soochow University
SOOCHOW UNIVERSITY

Soochow University, founded in 1900 in Suzhou, is a premier research university in clinical and basic hematology with wide international recognized program in immunology, leukemia and blood and marrow transplantation. With newly established Soochow Institute of Blood and Marrow Transplantation (SIBMT) and substantial funding from Jiangsu government and Soochow University, a major expansion of its research programs is under way.

We are seeking outstanding scientists in the areas of **immunology and malignant hematological disorders, biology of hematopoietic stem cells, blood and marrow transplantation** for Associate Professor and Professor positions. Candidates with strong background in immunology, molecular biology, and animal models are encouraged to apply. Candidates should have a Ph.D. or M.D., splendid track records of scientific achievements, the ability to develop independent research projects and strong interests in translational research. Our institute is dedicated to build a state-of-the-art research platform, offer large collections of clinical samples. Successful candidates will be provided with generous start-up funds and relocation packages and competitive salaries/benefits.

Please send your curriculum vitae, a statement of research interests and accomplishments, future research plans and a list of three references to:

Dr. Depei Wu (wudepei@medmail.com.cn) at the first affiliated hospital of Soochow University, 188# Shizi Street, Suzhou, 215006, China.

华北电力大学
NORTH CHINA ELECTRIC POWER UNIVERSITY

Faculty Positions Available in North China Electric Power University, China

Established in 1958, located in Beijing and Baoding (main campus in Beijing), North China Electric Power University (NCEPU) is one of the top research-oriented universities in China, focusing on fundamental cutting edge research and high-level education, covering diverse areas of science, engineering, technology, humanities, economics, management and law. NCEPU, as a key university jointly constructed by the Ministry of Education and the University Council, an organization composed of seven super-large Chinese power enterprises, China Electricity Council and NCEPU, is affiliated with the Ministry of Education, officially listed as one of the "211 Project" and "985 Project" universities as well as a "Predominant Discipline Innovation Platform". It owns 1 national key laboratory, 2 state science and technology innovation platforms and 11 provincial and ministerial key laboratories. At present, the campus covers one million square meters in total, with about 3000 faculty and staff.

North China Electric Power University is on a clear path to grow as a world-class university in engineering and science fields. As part of university's further pursuit for excellence in research and education, we have expanded a global search for the best research talents to join us.

North China Electric Power University invites applications for full-time Professors, Associate Professors and excellent scientists. Preference will be given to candidates whose research emphasis demonstrates the potential to complement and advance our existing research strengths on electric power, clean energy, energy power, mechanical engineering, automation, computer science, chemistry, economics, management, mathematics and physics. Successful candidates will be offered competitive salaries, appropriate positions and start-up funds.

Position Openings
- Position offered by the Recruitment Program of Global Experts (1000 Plan Professorship)
- Position offered by Chang Jiang Scholars Program
- Position offered by the Recruitment Program of Global Young Experts (1000 Plan Professorship for Young Talents)
- North China Electric Power University's Professors
- North China Electric Power University's Associate Professors
- North China Electric Power University's Teachers

Interested individuals should email his/her CV to ncepuscience@163.com, with "Faculty Application from Science" in the title. For more details, please visit our Talent Management Office's website at http://rcb.ncepu.edu.cn, or contact us by email ncepuscience@163.com, or telephone 86-010-61772414.

西南交通大学
Southwest Jiaotong University
Southwest Jiaotong University, P.R.China Anticipates Your Working Application

Southwest Jiaotong University (SWJTU), founded in 1896, situates itself in Chengdu, the provincial capital of Sichuan. It is a national key multidisciplinary "211" and "985 Feature" Projects university directly under the jurisdiction of the Ministry of Education, featuring engineering and a comprehensive range of study programs and research disciplines spreading across more than 20 faculties and institutes/centers. Boasting a complete Bachelor-Master-Doctor education system with more than 2,500 members of academic staff, our school also owns 2 first-level national key disciplines, 2 supplementary first-level national key disciplines (in their establishment), 15 first-level doctoral programs, 43 first-level master programs, 75 key undergraduate programs, 10 post-doctoral stations and more than 40 key laboratories at national and provincial levels.

Our university is currently implementing the strategy of "developing and strengthening the university by introducing and cultivating talents". Therefore, we sincerely look forward to your working application.

More information available at http://www.swjtu.edu.cn/

I. Positions and Requirements

A.High-level Leading Talents

It is required that candidates be listed in national top talents programs such as *Program of Global Experts, Top Talents of National Special Support Program, "Chang Jiang Scholars", China National Funds for Distinguished Young Scientists and National Award for Distinguished Teacher.*

Candidates are supposed to be no more than 50 years old. The limitation could be extended in the most-needed areas of disciplinary development.

Candidates who work in high-level universities/institutes and reach the above requirements are supposed to be no more than 45 years old.

B. Young Leading Scholars

Candidates are supposed to be listed in or qualified to apply for the following programs:
- *National Thousand Young Talents Program*
- *The Top Young Talents of National Special Support Program(Program for Supporting Top Young Talents)*
- *Science Foundation for the Excellent Youth Scholars*

Candidates should have good team spirit and leadership, outstanding academic achievements, broad academic vision and international cooperation experience and have the potential of being a leading academic researcher.

C. Excellent Young Academic Backbones

Candidates under 40 years old are expected to graduate from high-level universities/institutes either in China or other countries. Those who are professors, associate professors and other equal talents from high-level universities/institutes overseas could be employed as professors and associate professors as well.

D. Excellent Doctors and Post Doctoral Fellows

Candidates under 35 years old are supposed to be excellent academic researchers from high-level universities either in China or other countries.

II. Treatments

The candidates will be provided with competitive salaries and welfares that include settling-in allowance, subsidy of rental residence, start-up funds of scientific research, assistance in establishing scientific platform and research group as well as international-level training and promotion . As for outstanding returnees, we can offer further or specific treatments that can be discussed personally.

III . Contact us:

Contacts: Ye ZENG & Yinchuan LI   Telephone number: 86-28-66366202   Email: *talent@swjtu.edu.cn*
Address: Human Resources Department of SWJTU, the western park of high-tech zone, Chengdu, Sichuan, P.R.China, 611756

http://www.swjtu.edu.cn/

Faculty Position Available at China University of Petroleum in Qingdao

China University of Petroleum (UPC) is a national key university directly affiliated with the Ministry of Education and a member of the "211 Project" and "985 innovation platform for preponderant discipline" universities。 Honored as "the cradle of scientific and technological talents for petroleum industry", UPC is an important base of training high-level talents for the petroleum and petrochemical industry and has already developed into a multi-disciplinary, well-rounded university focusing on petroleum and engineering.

UPC now has two campuses in Shandong Province, one in Qingdao and one in Dongying. Qingdao Campus, the main and new campus, is located in Qingdao which enjoys a high reputation for its charming scenery and favorable climate.

We warmly welcome scientific and technological elites all over the world to join us and build our university into a national renowned, high-level, research-oriented institute with its petroleum-related disciplines reaching the world's first-class level.

UPC provides eligible talents with a good academic environment and excellent working and living conditions.

◎1.Tenured professor of well-known overseas universities or experts and scholars who have published a thesis as the original author in "Science" or "Nature" can be recruited as a high level professor at UPC，and will be offered 2 million RMB settling-in allowance or housing subsidy and 3-8 million RMB scientific research and academic funds after the evaluation.

◎2.Experts or scholars who have a high academic reputation and are qualified leader in certain disciplines can be recruited as a high level or regular professor，and will be offered 1 million RMB settling-in allowance or housing subsidy and 1-3 million RMB Scientific research and academic funds after the evaluation.

◎3.Youth talents who qualify for China's "Youth 1000 Talents projects" can be offered 0.5 million RMB annual salary, 1.5 million RMB settling-in allowance or housing subsidy and 1-3 million RMB scientific research and academic funds.

◎4.Youth talents who receive the position as postdoctoral, assistant professor, associate professor or have a PhD from a famous overseas university or research institution can be offered higher treatment than similar talents in China.

Further information is available at http:// rsc.upc.edu.cn
Contact us:
Tel: 0086-532-86981808; 86981806   E-mail: teacher@upc.edu.cn

NINGBO UNIVERSITY

Ningbo University invites you to apply for faculty positions

About Ningbo University

Founded in 1986 by Sir Yue-Kong Pao and autographed the name by Deng Xiaoping, Ningbo University (NBU) is a young and dynamic university located in the beautiful city of Ningbo by East China Sea, with five campuses covering 160 hectares of land. As a leading comprehensive university in Zhejiang Province, NBU offers programs in economics, law, education, liberal arts, history, science, engineering, agriculture, medicine, and management. The university now receives public funding, as well as continuous support and generous donations from many overseas Chinese and their families including Sir Yue-Kong Pao, Sir Run-Run Shaw, Chao An Chung, Hans Tang, Yue-shu Pao, Cao Guangbiao, Li Dashan, Zhu Xiushan, etc.

Academic Excellence

NBU consists of 22 faculties and offers 75 undergraduate programs, 116 master programs, and 12 Ph.D. programs. It enrolls 31,645 students including 26,527 full-time undergraduates and 5,118 graduate students. Currently NBU has around 1,400 full-time faculty members and 1,000 administrative staff members. Among them there are 5 academicians, 284 full professors, and 721 associate professors.

Research Achievements

With 77 research institutes and 14 key laboratories, NBU is the center of varieties of research and teaching activities. The research and development initiatives of the university, especially in marine science, information science and technology, engineering mechanics, and material science have contributed greatly to the economic development of the region and have been recognized by numerous national awards. The university library has a CNKI Network Administrative Service Center, and a collection of approximately 1,700,000 books and 11500GB digital resources.

International Programs

NBU maintains close links to 47 well-known institutions of higher education in Canada, Germany, France, Great Britain, USA, Sweden, Japan, South Korea and Australia. For example, the Sino-Canada joint-educational program is welcomed by international students with 100% satisfaction.

QUALIFICATIONS

Candidates should at least have (a) a Ph.D. degree in a related discipline, (b) adequate teaching ability and a strong passion for teaching, (c) an outstanding research background and influential publication record in recent three years, and (d) an ability to conducthigh-quality research and attract external funding.

REMUNERATION & CONDITIONS OF SERVICE

Salary offered will be commensurate with qualifications and experience. Remuneration package will be highly competitive. Forapplicants with titles of professor or associate professor, salary and housing compensation can be negotiated on the individual basis.For newly graduate PhD and Postdoctoral, initial appointment will be made on a fixed-term contract, with a housing compensation of 600,000 RMB upon fulfillment of the contract requirements. Re-engagement thereafter is subject to mutual agreement.

APPLICATION

Please submit completed application form, CV and cover letter via email to rsc@nbu.edu.cn. Application forms can be downloaded from http://www.nbu.edu.cn/shizi Recruitment stays open until positions are filled unless otherwise specified. Please visit http://rsc.nbu.edu.cn for more details.

INFORMATION ON POSITIONS

SCHOOL OF MARINE SCIENCE
Professor/Associate Professor
Marine Biotechnology/ Marine Sciences/Medicinal Chemistry/ Ocean Engineering/Marine planning and remote sensing /Sea port and environmental ecology/Marine Geographic Information Science

Faculty of Electrical Engineering and Computer Science
Professor/ Associate Professor Wireless Communications / New Generation Communication Networks / Underwater Acoustic Communication / Multimedia Information Processing / Embedded Systems / Integrated Circuit Design / Electronic Design Automation / Database System / Big Data Processing / Software and Theory / Information Security / Mobile Computing / Graphics and Image processing / Power system and Its Automation / Power Electronics / Pattern recognition and Intelligent system / Sensor and Intelligent detection

FACULTY OF SCIENCE
Professor/Associate Professor/Assistant Professor
Condensed Matter
Physics/Microelectronics/Optoelectronics/Solar Cell
Department of Mathematics/Computational
Mathematics/Probability and Statistics / Financial Mathematics

FACULTY OF MECHANICAL ENGINEERING AND MECHANICS
Professor/Associate Professor/Assistant Professor
Mechanics/Vehicle
Engineering/ Mechanical
Engineering/Industrial Design

INTERNATIONAL COLLEGE
Professor/Assistant Professor
Accounting

SCHOOL OF MATERIALS SCIENCE AND CHEMICAL ENGINEERING
Assistant/Associate/Full Professors
Polymer Science/Chemical Engineering/Materials Science

SCHOOL OF LAW
Professor/Associate Professor/Assistant Professor
Criminal Law/Criminal Procedure Law/Civil Procedure Law/Civil Law/Electronic Commerce Law

COLLEGE OF TEACHER EDUCATION
Professor/Associate Professor/Assistant Professor
Curriculum and Teaching Methodology/Higher Education/Preschool Education/Educational Economy and Management/Cognitive Psychology/Educational Psychology/Clinical Psychology/School Psychology/Experimental Psychology/Personality Psychology/Social Psychology/Management Psychology/Computer Graphics and Digital Image Processing/Electronic Music, Game Development/3D Animation and Game Development

FACULTY OF MARITIME AND TRANSPORTATION
Professor/Associate Professor/Assistant Professor
Department of Logistics and Transportation/Department ofMaritime Technology/Department of Marine Engineering/Department of Naval Architecture and Ocean Engineering

FACULTY OF PHYSICAL EDUCATION
Assistant Professor
Sport Management/Sport Sociology/Human Movement/Sport Training/Sport Physiology

MEDICAL SCHOOL
Professor / Associate Professor
Mechanism And Prevention Of Alzheimer's Disease; Oncology; Genetics; Human Anatomy; Histology And Embryology; Cell Biology; Immunology; Microbiology; Parasitology; Analytical Chemistry; Occupational And Environmental Health; Toxicology

COLLEGE OF ARTS
Professor / Associate Professor / Assistant Professor
Performance Of All Areas, Musicology (Ethnomusicology), Music Composition
Art Design Of All Areas, Digital Arts, Fine Art, Art History,Art/Music Industry, Art/Music Therapy

SCHOOL OF ARCHITECTURE, CIVIL ENGINEERING AND ENVIRONMENT
Professor /Associate Professor /Assistant Professor
Architecture Design/Urban Design/ Urban Planning/Architecture Technology/Human Geography/ Physical Geography/Cartography and Geographic Information System/Environmental Technology/Applied Environmental Microbiology/ Civil Engineering/Engineering Management

THE NEOTIA UNIVERSITY

ज्ञानम् आत्म प्रदीपाय

West Bengal State self-financed University

The Neotia University, one of India's most progressive and forward-looking universities, calls for the recruitment of **Assistant Professor**, **Associate Professor** and **Professor** in Marine Biotechnology and Bioinformatics, Marine Engineering, Robot Manufacturing, Automotive Manufacturing, Animation, Video Game Design, Energy Studies, Psychology, Applied Economics, English, Spanish and Mandarin. Check **www.tnu.in** for more details and send your applications within 15 days to **hr@tnu.in**

VACANCY ANNOUNCEMENT

DIRECTOR, OFFICE OF RESEARCH INTEGRITY

Department of Health and Human Services, Office of the Secretary

The Department of Health and Human Services is seeking candidates experienced and specially trained in the conduct of research and experienced in the conduct of investigations of research misconduct to apply for the position of Director of the Office of Research Integrity (ORI). As a regulatory agency, ORI promotes integrity in biomedical and behavioral research supported by the U.S. Public Health Service at more than 5,000 institutions worldwide by monitoring institutional investigations of research misconduct and facilitating educational programs in the responsible conduct of research.

The ORI Director provides executive leadership for ORI and serves as a liaison between the office and national and international partners committed to the promotion of research integrity across the U.S. and around the world.

This position is being announced as Director, Office of Research Integrity, Job Announcement Number: **HHS-OASH-RF-15-1356210**. Interested candidates are encouraged to visit **https://www.usajobs.gov/GetJob/ViewDetails/398039800** to access the full announcement and instructions on how to apply. This is an Excepted Service Position under Title 42 (salary range: $151,496.00 to $240,000.00 per year) based on a HHS-certified performance plan. Applications must be received by midnight of **May 15, 2015**.

IUSSTF
Indo-US Science and Technology Forum

INDO-U.S. SCIENCE AND TECHNOLOGY FORUM
NEW DELHI, INDIA

Vacancy Advertisement:
EXECUTIVE DIRECTOR

The governments of the United States of America and India, through an inter-governmental agreement, jointly established the Indo-U.S. Science and Technology Forum (IUSSTF) **http://iusstf.org** in 2000 as an autonomous organization in India. Its mission is to promote science and technology (S&T) innovation and entrepreneurship collaborations between the United States and India through efforts such as bilateral research centres, joint projects, academic, and industry exchanges, joint workshops, and training programs in basic and applied sciences.

IUSSTF invites applications for the position of Executive Director as per the details given below:

Tenure of appointment: 3 years with possibilities of extension(s).

Essential Qualification: Ph.D. in the sciences, engineering, or medicine. The applicant should be an Indian or U.S. citizen only.

Remuneration and other benefits: Annual compensation package will range between Indian Rupees 3.5 million to 4.0 million depending upon experience. Perks will include leased accommodation in Delhi or HRA, Medical insurance, Official Transport, Gratuity, Leave Travel Allowance etc.

Application procedure: Interested persons should send their applications to **recruitments@indousstf.org** in the prescribed IUSSTF application format with a 500 words vision statement on the future of the Forum and at least 3 references.

Application deadline is 11:59 p.m. IST, May 18, 2015.

For details on the opening and prescribed application format please visit the "**Announcements**" section at **http://iusstf.org**

THE UNIVERSITY OF HONG KONG
香 港 大 學

Lecturer in Common Core Curriculum
(Ref.: 201500260)

Applications are invited for appointment as Lecturer in Common Core Curriculum in the Faculty of Science, from as soon as possible, on a two-year term basis, with the possibility of renewal.

The University has established a Common Core Curriculum for all undergraduates since September 2012. The Faculty of Science offers courses in the area of Scientific and Technology Literacy to students from all ten faculties. A senior Professor in the Faculty of Science will lead the teaching of these courses and work with the Lecturer in the relevant area who will serve primarily as a tutor for small groups of students from multiple disciplines. The medium of instruction is English. Information about the Common Core Curriculum can be viewed at http://tl.hku.hk/common-core-curriculum.

Applicants should have a Ph.D. degree in Biological Sciences or Physical Sciences, and substantial teaching experience (at least 3 years) in subjects related to general education at the university level. The appointee's duties include conducting small-group tutorials for two courses per semester, marking assignments/examination scripts, preparing teaching materials, supervising student work, developing new courses, and undertaking other tasks related to science education. He/She will meet regularly with the Centre for the Enhancement of Teaching and Learning to reflect on and refine the teaching activities in Common Core courses.

A globally competitive remuneration package commensurate with qualifications and experience will be offered. At current rates, salaries tax does not exceed 15% of gross income. The appointment will attract a contract-end gratuity and University contribution to a retirement benefits scheme, totalling up to 15% of basic salary, as well as annual leave, and medical benefits. Please note that the University is not able to offer a relocation assistance package (including housing accommodation and a passage and baggage allowance) to the successful candidate recruited from overseas.

For enquiries about the specific job requirements, please write to Professor P. Chiu, Associate Dean (Teaching & Learning) (e-mail: sciappt@hku.hk). Applicants should send a completed application form, together with an up-to-date C.V. and a statement on teaching philosophy, which includes a portfolio of syllabi and descriptions of courses they have taught or co-taught by e-mail to sciappt@hku.hk. They should also arrange for submission of three references from senior academics who are familiar with their teaching approaches, skills and experience to sciappt@hku.hk. Please indicate clearly "Ref.: 201500260 (Lecturer in Common Core Curriculum)" in the subject of the e-mail. Application forms (341/1111) can be downloaded at http://www.hku.hk/apptunit/form-ext.doc. Further particulars can be obtained at http://jobs.hku.hk/. **Closes May 15, 2015**.

The University thanks applicants for their interest, but advises that only candidates shortlisted for interviews will be notified of the application result.

The University is an equal opportunities employer and is committed to a No-Smoking Policy

A career is like a love affair

intended to become a researcher. Instead I became a science journalist, then an editor, and finally CEO of the American Chemical Society (ACS) before I retired in February. At a recent event at Columbia University, hosted by the organization Women in Science at Columbia, I told my career story and passed along lessons I've learned about how women can make the most of their lives and careers. Here is some of the advice I offered at that event.

Believe in yourself, and never take "no" for an answer. In graduate school, I loved reading *Chemical & Engineering News* (*C&EN*). So I thought to myself, "Why not get a job there?" I called Richard Kenyon, who was the publisher at the time, to ask for an appointment. "Dr. Kenyon is busy all afternoon," his secretary said. "I suggest you send a résumé." Instead, I took a bus to Kenyon's office. "Do you mind if I wait?" I asked the secretary. "You can wait, but he won't be able to see you," she replied.

When Kenyon got off the elevator, I raced over. You can imagine the look of horror on the secretary's face when he said, "Come right in."

Never burn bridges, but know when it's time to move on. I was the youngest staff member at *C&EN* and the only woman. I loved working there. But when I discovered that my salary was 30% below a benchmark, I left. There were no hard feelings; I just took a better job, at the National Institutes of Health, and then another, at the National Bureau of Standards. I loved them both—and then I encountered the Boss From Hell.

Take control. Instead of mentoring and supporting me, he stood over my shoulder micromanaging and yelling. I left as soon as I could but not before learning a key lesson: Take control of your career. I encourage young women to construct 5-year plans focused on their aspirations and how to achieve them. Don't let others set the agenda, and never, ever let yourself be bullied.

Get a life. I landed at the Smithsonian Institution as chief science writer in the Office of Public Affairs. I stayed there 14 years. It was a wonderful place to work, but it was all consuming: It was not unusual to get calls at 3 a.m. asking about a new panda cub or a tornado at a storage facility. I sought a position where I could have a life outside of work. I returned to *C&EN* and soon became editor-in-chief.

"Don't let others set the agenda."

It was a demanding job, but I was more in control of my time. When my beloved father became ill with lymphoma, I left work every day at 5 p.m. to visit him, for 5 months. I cherish the time I spent with him. Barely a year after he died, I was diagnosed with breast cancer. I didn't miss a day of work (except for the surgery), but I was grateful for the flexibility to fit it all in. My cancer has been in remission for almost 18 years.

A career is like a love affair. There are many parallels: Both have ups and downs, it can be hard to find the right one, and sometimes we don't choose wisely. There might not be a single choice that gives satisfaction for a lifetime. To be worthwhile, relationships and careers must be rich and rewarding and provide an environment in which we can grow and learn. I can't imagine staying in a relationship that didn't have these qualities—and what else is a job except a relationship where you spend anywhere from 8 to 16 hours a day?

So, relationship or job, how do you find the right one? There's a Cole Porter musical called *Nymph Errant*, about Evangeline, an adventurous young woman who aims to lose her virginity—pretty advanced stuff for 1933. In a song called "Experiment," Ms. Pratt, Evangeline's chemistry teacher, exhorts her:

> To do what all good scientists do / Experiment /… / Be curious /… / Get furious / At each attempt to hold you down. / If this advice you always employ / The future can offer you infinite joy. /… / Experiment / And you'll see. ∎

ILLUSTRATION: ROBERT NEUBECKER